frontiers | Research Topics

Single-cell analysis on the pathophysiology of autoimmune diseases

Edited by
Shiang-Jong Tzeng, InKyeom Kim and Kuang-Hui Sun

Published in
Frontiers in Immunology

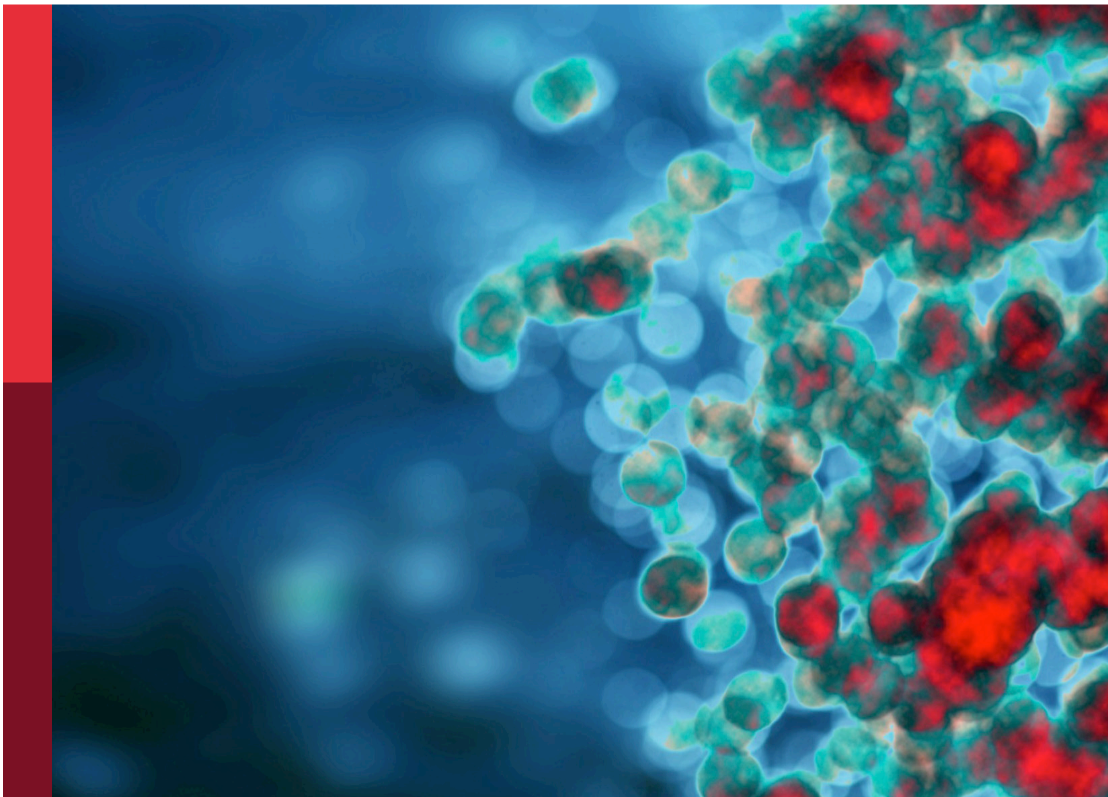

ISSN 1664-8714
ISBN 978-2-8325-5163-9
DOI 10.3389/978-2-8325-5163-9

About Frontiers

Frontiers is more than just an open access publisher of scholarly articles: it is a pioneering approach to the world of academia, radically improving the way scholarly research is managed. The grand vision of Frontiers is a world where all people have an equal opportunity to seek, share and generate knowledge. Frontiers provides immediate and permanent online open access to all its publications, but this alone is not enough to realize our grand goals.

Frontiers journal series

The Frontiers journal series is a multi-tier and interdisciplinary set of open-access, online journals, promising a paradigm shift from the current review, selection and dissemination processes in academic publishing. All Frontiers journals are driven by researchers for researchers; therefore, they constitute a service to the scholarly community. At the same time, the *Frontiers journal series* operates on a revolutionary invention, the tiered publishing system, initially addressing specific communities of scholars, and gradually climbing up to broader public understanding, thus serving the interests of the lay society, too.

Dedication to quality

Each Frontiers article is a landmark of the highest quality, thanks to genuinely collaborative interactions between authors and review editors, who include some of the world's best academicians. Research must be certified by peers before entering a stream of knowledge that may eventually reach the public - and shape society; therefore, Frontiers only applies the most rigorous and unbiased reviews. Frontiers revolutionizes research publishing by freely delivering the most outstanding research, evaluated with no bias from both the academic and social point of view. By applying the most advanced information technologies, Frontiers is catapulting scholarly publishing into a new generation.

What are Frontiers Research Topics?

Frontiers Research Topics are very popular trademarks of the *Frontiers journals series*: they are collections of at least ten articles, all centered on a particular subject. With their unique mix of varied contributions from Original Research to Review Articles, Frontiers Research Topics unify the most influential researchers, the latest key findings and historical advances in a hot research area.

Find out more on how to host your own Frontiers Research Topic or contribute to one as an author by contacting the Frontiers editorial office: frontiersin.org/about/contact

Single-cell analysis on the pathophysiology of autoimmune diseases

Topic editors
Shiang-Jong Tzeng — National Taiwan University, Taiwan
InKyeom Kim — Kyungpook National University, Republic of Korea
Kuang-Hui Sun — National Yang Ming Chiao Tung University, Taiwan

Citation
Tzeng, S.-J., Kim, I., Sun, K.-H., eds. (2024). *Single-cell analysis on the pathophysiology of autoimmune diseases*. Lausanne: Frontiers Media SA.
doi: 10.3389/978-2-8325-5163-9

Table of contents

frontiers | Frontiers in Immunology

TYPE Editorial
PUBLISHED 02 July 2024
DOI 10.3389/fimmu.2024.1451354

EDITED AND REVIEWED BY
Betty Diamond,
Feinstein Institute for Medical Research,
United States

*CORRESPONDENCE
Shiang-Jong Tzeng
✉ sjtzeng@ntu.edu.tw
InKyeom Kim
✉ inkim@knu.ac.kr
Kuang-Hui Sun
✉ khsun@nycu.edu.tw

RECEIVED 19 June 2024
ACCEPTED 24 June 2024
PUBLISHED 02 July 2024

CITATION
Tzeng S-J, Kim I and Sun K-H (2024)
Editorial: Single-cell analysis on the pathophysiology of autoimmune diseases.
Front. Immunol. 15:1451354.
doi: 10.3389/fimmu.2024.1451354

Editorial: Single-cell analysis on the pathophysiology of autoimmune diseases

Shiang-Jong Tzeng[1]*, InKyeom Kim[2,3,4]* and Kuang-Hui Sun[5]*

[1]Graduate Institute of Pharmacology, College of Medicine, National Taiwan University, Taipei, Taiwan, [2]Department of Pharmacology, School of Medicine, Kyungpook National University, Daegu, Republic of Korea, [3]BK21 Plus Kyungpook National University (KNU) Biomedical Convergence Program, School of Medicine, Kyungpook National University, Daegu, Republic of Korea, [4]Cardiovascular Research Institute, School of Medicine, Kyungpook National University, Daegu, Republic of Korea, [5]Department of Biotechnology and Laboratory Science in Medicine, National Yang Ming Chiao Tung University, Taipei, Taiwan

KEYWORDS

autoimmune disease, single-cell RNA sequencing (scRNA-seq), transcriptomics, epigenomics, mass cytometry, CITE-seq, pathophysiology, therapy

Editorial on the Research Topic
Single-cell analysis on the pathophysiology of autoimmune diseases

Autoimmune diseases are characterized by a complex interplay of diverse immune cell types, each fulfilling unique roles and functions. Traditional bulk analysis methods tend to average signals across mixed cell populations, thereby obscuring the contributions of individual cell types. In contrast, single-cell analysis enables the precise identification of specific cell subsets that play pivotal roles in driving disease pathogenesis and progression, thus providing novel insights into autoimmune disorders. Moreover, this approach facilitates the detection and characterization of rare cells with significant pathogenic potential, enhancing our understanding of their functional roles and contributions to disease mechanisms. By scrutinizing the transcriptome, proteome, or epigenome of individual cells, researchers can uncover distinct gene expression patterns, protein profiles, and regulatory mechanisms specific to particular cell types or disease states. This comprehensive molecular profiling not only aids in identifying biomarkers crucial for diagnosis, prognosis, and the development of therapeutic targets, but also reveals intricate details that might be overlooked by bulk analysis methods.

In this Research Topic on single-cell analysis, we present a collection of 15 papers exploring various aspects of autoimmune diseases, including sequencing methods, genetic and epigenetic contributions, molecular mechanisms and pathogenesis, biomarkers, and therapeutic implications. By examining these factors at the single-cell level, we aim to enhance our understanding of autoimmune diseases and highlight new potential diagnostics and therapeutics.

Three studies are related to single-cell methods. The cellular indexing of transcriptomes and epitopes by sequencing (CITE-seq) enables the identification cell types through the expression of surface markers not captured by single-cell RNA sequencing (scRNA-seq), while simultaneously quantifying gene and protein surface expressions (1). Colpitts et al. used paired CITE-seq and flow cytometry to characterize resident immune cells in human islets that would have been difficult to detect based on mRNA expression alone. Their analysis revealed valuable insights into the cellular dynamics within human islets. In analytic methods, Fritz et al. reviewed advancements in single-cell computational machine learning to characterize the heterogeneity of fibroblasts and uncover novel fibroblast-macrophage interactions driving immune-mediated inflammatory diseases such as rheumatoid arthritis (RA) and psoriasis. Their review unraveled promising therapeutic targets, including CSF1R, PDGFR, and EGFR, which could lead to new treatment strategies for these diseases. Balog et al. employed single-cell mass cytometry (or CyTOF, cytometry by time-of-flight) (2) to comprehensively characterize and compare 17 immune cell populations in peripheral blood samples from healthy controls, treatment-naive patients with RA, systemic sclerosis, and systemic lupus erythematosus (SLE). They utilized 34 markers and analyzed 59 scatter plots to elucidate disease-specific population frequencies and expression patterns of immune cells. Their study represents a valuable single-cell data resource that enhances our understanding of the immune cell landscape in these autoimmune diseases.

Four studies have employed single-cell analysis to investigate SLE. Patients with lupus nephritis (LN) are susceptible to irreversible kidney damage or failure. Daamen et al. conducted scRNA-seq on the kidneys of female lupus-prone NZM2328 mice at acute, transitional, and chronic stages of the disease. They compared gene expression profiles between these mice and human LN patients to elucidate molecular mechanisms driving LN progression. Utilizing unsupervised gene co-expression network analysis, such as MEGENA (3), they characterized molecular profiles correlating with disease severity. Their gene expression analysis offers a method to stage LN in lupus-prone mice and translate these findings to human LN patients. Additionally, Daamen et al. explored the heterogeneity of splenic IL-10 producing regulatory B cells (Breg) across disease stages in lupus-prone mice, revealing several insights from scRNA-seq analysis: active disease is marked by a loss of marginal zone-lineage Bregs, an increase in plasmablast/plasma cell-lineage Bregs, and overall elevation in inflammatory gene signatures. These findings underscore the dynamic changes in Breg populations and their roles in lupus pathogenesis. Filia et al. performed a comprehensive analysis of hematopoietic stem and progenitor cells (HSPCs) in SLE patients. Their study revealed a decrease in non-proliferating early progenitors with an interferon (IFN) signature, implicated in the functional loss and depletion of HSPCs. The data suggest that HSPCs act as sensors of IFN-related inflammatory signals, initiating the inflammatory processes characteristic of SLE. Of interest, Cui et al. explored the shared mechanisms between SLE and primary Sjögren's syndrome (pSS) by analyzing shared hub genes, related pathways, and transcription factors (TFs) in scRNA-seq datasets from the peripheral blood of patients with SLE and pSS. They identified IFI44L, ISG15 and ITGB2 as shared hub genes involved in the IFN response and ITGB2 signaling pathways. Additionally, they found that STAT1 and IRF7 are common TFs associated with monocytes and dendritic cells (DCs) in both SLE and pSS patients.

Three single-cell studies have investigated autoimmune disorders affecting the skin. Kim et al. analyzed human psoriasis lesions before and after 12 weeks of systemic IL-17A blockade using a multi-omics approach that integrated immune cell-enriched scRNA-seq, microarray, and immunohistochemistry data. They discovered that systemic IL-17A inhibition not only blocked the entire IL-23/T17 cell axis in T cells, DCs, and keratinocytes, but also promoted regulatory gene expression in regulatory DCs present in human psoriasis skin, such as BDCA-3 (THBD) and DCIR (CLEC4A). Gao et al. explored the epigenetic pathogenesis of psoriasis by analyzing the involvement of long non-coding RNAs (lncRNAs) known to participate in immune regulation. They conducted an analysis for differentially expressed lncRNAs, co-regulated gene patterns, and GO-bioprocess enrichment to identify lncRNAs that modulate cellular inflammation in psoriasis at the single-cell level. Their study highlights the therapeutic potential of lncRNAs in managing this disease. Epidermolysis bullosa acquisita (EBA) is a chronic autoimmune disorder characterized by subepidermal blistering of the skin and mucous membranes. The condition arises from antibodies (Abs) targeting type VII collagen, the primary constituent of anchoring fibrils responsible for connecting the basement membrane to dermal structures (4). Guerrero-Juarez et al. performed scRNA-seq of whole blood and skin dissociates to characterize the transcriptome of perturbed neutrophils in patients with EBA. Their findings revealed that the upregulation of C-type lectin receptors (Clec4n, Clec4d, and Clec4e) is a hallmark of activated dermal neutrophil populations. However, despite this upregulation, the individual contribution of these genes to the pathogenesis of EBA was found to be dispensable. This highlights the complexity of EBA pathogenesis and underscores the need for further research to uncover critical molecular targets for therapy.

Two studies are related to RA. Methylation of adenosine at N6 position (m6A) is mediated by distinct enzymes and occurs on both coding and non-coding RNAs (5). Geng et al. investigated the m6A methylation regulators in RA. They identified two m6A methylation regulators, IGF2BP3 and YTHDC2, as significant biomarkers for RA. Using consensus feature selection from four methods, these biomarkers were found to predict RA diagnosis with high accuracy. Pathway and network analysis revealed a novel role for IGF2BP3 in M1 macrophage polarization during the progression of RA, offering new strategies for early diagnosis and targeted therapy. In a brief report on a case of COVID-19 vaccination, Ishikawa et al.'s scRNA-seq analysis identified a distinct monocyte population with RA signatures, such as cathepsin L (CTSL) and CXCL8, in peripheral blood during the acute phase of encephalitis (day 3). It remains unclear whether this specific classical monocyte population is commonly observed in COVID-19 vaccination-related CNS diseases or if it reflects the enhanced dysregulated immunity unique to each specific disease. Further studies are needed to determine the generalizability of these findings across different cases of vaccination-related CNS diseases.

Anti-N-methyl-D-aspartate receptor encephalitis (anti-NMDARE) is a rare autoimmune disease characterized by Abs against the glutamate receptor N1 (GluN1) subunit of NMDAR (6). Using scRNA-seq, Jiang et al. observed that patients in the acute phase expressed high levels of DC_CCR7 in peripheral myeloid cells. DC_CCR7 is known to play crucial roles in T-cell activation, differentiation, and the expansion of IgG-producing B cells. This finding implies that DC_CCR7 may contribute to lymphocyte activation during the acute stage of anti-NMDARE, highlighting its potential significance in the disease's pathogenesis.

Lastly, the topic editor Kim et al.'s group addressed the critical role of immune cells in the development of hypertension (7). They performed scRNA-seq on peripheral blood and lamina propria cells from salt-sensitive male rats receiving a high-fructose solution. Their study pointed out a pivotal role for the upregulation of IFN pathway in B cells in the development of hypertension. This suggests a potential autoimmune factor contributing to the pathogenesis of fructose-induced hypertension in the intestine. Furthermore, their findings indicate that targeting B cells could be a potential intervention strategy to reduce blood pressure in individuals with fructose-induced hypertension, highlighting a novel therapeutic approach in managing this condition.

In conclusion, the findings presented here contribute significantly to identifying pathogenic cell populations, elucidating their interactions, and deciphering the regulatory mechanisms at play. The precision achieved in understanding disease mechanisms holds promise for designing more effective treatments tailored to meet the individual needs of patients. This marks a significant advancement towards personalized medicine in the field of autoimmune disease research, paving the way for innovative therapeutic strategies that could greatly improve patient outcomes.

Author contributions

S-JT: Writing – original draft, Writing – review & editing. IK: Writing – review & editing. K-HS: Writing – review & editing.

Acknowledgments

We greatly appreciate the contributions to this Research Topic by all authors and reviewers. We also thank all the guest associated editors of the Research Topic, and the editorial board of the journal of Frontiers, for their support.

Conflict of interest

The authors declare that the research was conducted in the absence of any commercial or financial relationships that could be construed as a potential conflict of interest.

Publisher's note

References

1. Stoeckius M, Hafemeister C, Stephenson W, Houck-Loomis B, Chattopadhyay PK, Swerdlow H, et al. Simultaneous epitope and transcriptome measurement in single cells. *Nat Methods*. (2017) 14:865–8. doi: 10.1038/nmeth.4380

2. Spitzer MH, Nolan GP. Mass cytometry: single Cells, many Features. *Cell*. (2016) 165:780–91. doi: 10.1016/j.cell.2016.04.019

3. Song WM, Zhang B. Multiscale embedded gene co-expression network analysis. *PloS Comput Biol*. (2015) 11:e1004574. doi: 10.1371/journal.pcbi.1004574

4. Kridin K, Kneiber D, Kowalski EH, Valdebran M, Amber KT. Epidermolysis bullosa acquisita: A comprehensive review. *Autoimmun Rev*. (2019) 18:786–95. doi: 10.1016/j.autrev.2019.06.007

5. Sommer S, Lavi U, Darnell JE Jr. The absolute frequency of labeled N-6-methyladenosine in HeLa cell messenger RNA decreases with label time. *J Mol Biol*. (1978) 124:487–99. doi: 10.1016/0022-2836(78)90183-3

6. Zhao X, Teng Y, Ni J, Li T, Shi J, Wei M. Systematic review: clinical characteristics of anti-N-methyl-D-aspartate receptor encephalitis. *Front Hum Neurosci*. (2023) 17:1261638. doi: 10.3389/fnhum.2023.1261638

7. Drummond GR, Vinh A, Guzik TJ, Sobey CG. Immune mechanisms of hypertension. *Nat Rev Immunol*. (2019) 19:517–32. doi: 10.1038/s41577-019-0160-5

frontiers | Frontiers in Immunology

TYPE Original Research
PUBLISHED 02 December 2022
DOI 10.3389/fimmu.2022.1075675

EDITED BY
Rui Li,
University of Pennsylvania,
United States

REVIEWED BY
Le Yang,
Air Force Military Medical University,
China
Feng Yi,
Guangdong-Hong Kong-Macao
Greater Bay Area Center for Brian
Science and Brain-Inspired
Intelligence, China
Uma Sriram,
Temple University, United States

*CORRESPONDENCE
Wei Li
liwei71@126.com
Yushu Jiang
jiangecho1988@zzu.edu.cn

SPECIALTY SECTION
This article was submitted to Autoimmune and Autoinflammatory Disorders: Autoimmune Disorders, a section of the journal Frontiers in Immunology

RECEIVED 20 October 2022
ACCEPTED 22 November 2022
PUBLISHED 02 December 2022

CITATION
Jiang Y, Dai S, Jia L, Qin L, Zhang M, Liu H, Wang X, Pang R, Zhang J, Peng G and Li W (2022) Single-cell transcriptomics reveals cell type–specific immune regulation associated with anti-NMDA receptor encephalitis in humans. *Front. Immunol.* 13:1075675. doi: 10.3389/fimmu.2022.1075675

Single-cell transcriptomics reveals cell type–specific immune regulation associated with anti-NMDA receptor encephalitis in humans

Yushu Jiang[1]*, Shuhua Dai[2], Linlin Jia[1], Lingzhi Qin[1], Milan Zhang[1], Huiqin Liu[1], Xiaojuan Wang[1], Rui Pang[1], Jiewen Zhang[1], Gongxin Peng[3] and Wei Li[1]*

[1]Department of Neurology, Henan Joint International Research Laboratory of Accurate Diagnosis, Treatment, Research and Development, Henan Provincial People's Hospital, People's Hospital of Zhengzhou University, Zhengzhou, Henan, China, [2]Department of Neurology, Henan Provincial People's Hospital, Xinxiang Medical University, Zhengzhou, Henan, China, [3]China Center for Bioinformatics, Institute of Basic Medical Sciences, Peking Union Medical College, Chinese Academy of Medical Sciences and School of Basic Medicine, Beijing, China

Introduction: Anti-N-methyl-D-aspartate receptor encephalitis (anti-NMDARE) is a rare autoimmune disease, and the peripheral immune characteristics associated with anti-NMDARE antibodies remain unclear.

Methods: Herein, we characterized peripheral blood mononuclear cells from patients with anti-NMDARE and healthy individuals by single-cell RNA sequencing (scRNA-seq).

Results: The transcriptional profiles of 129,217 cells were assessed, and 21 major cell clusters were identified. B-cell activation and differentiation, plasma cell expansion, and excessive inflammatory responses in innate immunity were all identified. Patients with anti-NMDARE showed higher expression levels of CXCL8, IL1B, IL6, TNF, TNFSF13, TNFSF13B, and NLRP3. We observed that anti-NMDARE patients in the acute phase expressed high levels of DC_CCR7 in human myeloid cells. Moreover, we observed that anti-NMDARE effects include oligoclonal expansions in response to immunizing agents. Strong humoral immunity and positive regulation of lymphocyte activation were observed in acute stage anti-NMDARE patients.

Discussion: This high-dimensional single-cell profiling of the peripheral immune microenvironment suggests that potential mechanisms are involved in the pathogenesis and recovery of anti-NMDAREs.

KEYWORDS

anti-N-methyl-D-aspartate receptor encephalitis, peripheral blood mononuclear cell, single-cell RNA sequencing, B cells, plasma cells

1 Introduction

Anti-N-methyl-D-aspartate receptor encephalitis (anti-NMDARE) is a rare autoimmune disorder characterized by a complex neuropsychiatric condition (1) associated with antibodies against the glutamate receptor N1 (GluN1) subunit of NMDAR (2). Steroids and intravenous immunoglobulins (IVIG) are all used as first-line therapies for anti-NMDAREs (1, 3). However, approximately 40% of patients with anti-NMDARE showed no improvement after four weeks of first-line therapy (3). Due to the lack of disease awareness and late diagnosis, approximately 70% of anti-NMDARE patients are admitted to intensive care units with symptoms of persistent dysautonomia, consciousness fluctuation, or breathing dysfunction (4). Therefore, a thorough investigation of this disease is required to identify new markers and underlying mechanisms to cope with the severity of symptoms.

Susceptibility genes for anti-NMDARE include interferon regulatory factor 7 (IRF7), B cell scaffold with ankyrin repeats 1 (BANK1), T-Box Transcription Factor Protein 21 (TBX21), and human leukocyte antigen (HLA), as identified in genome-wide association studies (GWAS) (5–7). However, the association between these genes and disease susceptibility is weak; therefore, a thorough investigation is required to elucidate the exact mechanism. Tumors and herpes simplex encephalitis are recognized as the major causes of anti-NMDARE (8, 9), while molecular mimicry and chronic polyclonal expansions have been proposed as underlying pathogenic mechanisms (10, 11). Autoantibodies bind to and cross-link endogenous NMDARs, disturbing the interaction with the receptor tyrosine kinase EphB2, which leads to internalization and ultimately affects the function of NMDARs (12, 13). The reduced function of NMDARs results in learning and memory deficiencies and prominent psychiatric or behavioral symptoms in approximately 90% of patients (14). Some researchers believe that antibody titers can be used to make better clinical decisions; however, there is no reliable data to support this notion (15). Although its auto-antigen and effector mechanisms are well defined, the cellular and molecular mechanisms involved in anti-NMDARE are still poorly understood (1). Therefore, greater understanding of the activation and immune system patterns could provide important information regarding the pathogenesis of anti-NMDARE.

During the acute phase of anti-NMDARE, the levels of pro-inflammatory cytokines, such as interleukin (IL)-1β, IL-6, IL-17, and chemokines, such as CXCL-10, and CXCL-13 in the cerebrospinal fluid, and the pro-inflammatory cytokine IL-2 in plasma are elevated (16). Among these pro-inflammatory cytokines and chemokines, CXCL13 is involved in B cell-mediated neuroinflammation (17). B- cells differentiate into plasma cells and are involved in the production of anti-NMDAR-IgG and neuronal damage (18). The levels of the type 1 T helper (Th1) axis (IFN-γ, TNF-α, CCL3, and CXCL10), Th2 axis (CCL1, CCL8, CCL17, CCL22), Treg axis (IL-10), Th17 axis (IL-7), B cell axis (CXCL13), cytokines, and T cells also contribute to the clinical stages of the disease (16, 19, 20). The immune system comprises a vast variety of cells in different states; however, previous studies conducting immunophenotypic analysis were based on low-flux assays confined to selected cell types and markers (21, 22). Therefore, a better understanding of immune system modulation in response to anti-NMDARE using high-flux assays is required.

In the current study, we performed scRNA-seq of peripheral blood mononuclear cells (PBMC) using supervised and unsupervised machine-learning tools to dissect immune dysregulation in anti-NMDARE. This analysis identified 21 major cell groups, allowing us to assess the primary alterations in these major cell types. We found that patients with anti-NMDARE disease expressed high levels of IL-1B, IL-6, IL-8, TNF, CXCL8, TNFSF13B, TNFSF13, and NLRP3, whereas in the acute phase, high levels of DC_CCR7 were expressed in human myeloid cells. Moreover, in the acute phase of disease in patients with anti-NMDARE antibodies, strong humoral immunity and positive regulation of lymphocyte activation had developed. This high-dimensional single-cell profile of the peripheral immune microenvironment suggests that several potential mechanisms are involved in the pathogenesis and recovery of anti-NMDAREs. Moreover, we observed that, compared to HCs, anti-NMDARE patients produced elevated levels of pro-inflammatory cytokines and chemokines. The present study was designed to obtain a better understanding of the heterogeneity within the immune system related to anti-NMDARE through high-flux assays, predominantly single-cell RNA sequencing (scRNA-seq).

Abbreviations: anti-NMDARE, anti-N-methyl-D-aspartate receptor encephalitis; ASCs, antibody-secreting cells; BANK1, B cell scaffold with ankyrin repeats 1; BCR, B cell receptor; BCLs, base call files; CSF, cerebrospinal fluid; CDR3, complementary determining region 3; CHI3L1, chitinase-3-like 1; DEGs, differentially expressed genes; DCs, dendritic cells; GluN1, glutamate receptor N1; GWAS, genome-wide association studies; GEM, gel bead in emulsion; GO, Gene Ontology; HLA, human leukocyte antigen; HCs, healthy controls; HVGs, highly variable genes; IVIG, intravenous immunoglobulins; IRF7, interferon regulatory factor 7; IL, interleukin; KEGG, Kyoto Encyclopedia of Genes and Genomes; MΦ, macrophages; MCs, mast cells; Mgk, megakaryocytes; MBCs, memory B cells; NK, natural killer; PBMC, peripheral blood mononuclear cell; PBS, phosphate-buffered saline; PCA, principal component analysis; PBs, patients prior to first-line therapies; PAs, patients after first-line therapies; PTX3, pentraxin 3; scRNA-seq, single-cell RNA sequencing; scBCR-seq, single-cell BCR sequencing; scTCR-seq, single-cell TCR sequencing; SA-PE, streptavidin-phycoerythrin; TBX21, T-Box Transcription Factor Protein 21; Th1, type 1 T helper; TCR, T-cell receptor; TLRs, toll-like receptors; TNF, tumor necrosis factor; UMI, unique molecular identifier; UMAP, uniform manifold approximation and projection.

2 Materials and methods

2.1 Processing of patient samples

This study was approved by the Ethics Committee of Henan Provincial People's Hospital. 34 suspected anti-NMDARE patients were enrolled in the Neurology Department of Henan Provincial Peoples Hospital between December 2020 and January 2022.

The inclusion criteria for patients with anti-NMDARE were as follows: (1) diagnosis of anti-NMDARE according to the Graus and Dalmau criteria (23); (2) in the cerebrospinal fluid (CSF), antibody titers of more than 1:100–1:320 were considered for anti-NMDARE. The exclusion criteria were as follows: (1) definite or suspected central nervous system infection; (2) definite or suspected peripheral infection; (3) definite or suspected neuromyelitis optica spectrum disorders or multiple sclerosis (MS); (4) definite or suspected systemic immune disease; (5) history of malignant tumor; (6) pregnancy; and (7) history of high-dose methylprednisolone pulse, intravenous immunoglobulin, or plasma exchange treatment. Finally, 10 patients were included in the study cohort (Supplementary Figure 1). In addition, five age- and sex- matched HCs were enrolled. The first cohort, including anti-NMDARE (n = 5) and HCs (n = 5), was used for 10X genomics scRNA-sEq. The second cohort, including anti-NMDARE (n = 10) and HCs (n = 5), was used for multiple microsphere flow immunofluorescence analysis (Supplementary Table 1). Ten patients with anti-NMDARE received high-dose methylprednisolone pulse therapy and intravenous immunoglobulin. Peripheral blood was collected the day before and ten days after the onset of first-line therapy. Informed consent was obtained from all patients and HCs.

2.2 Generation and sequencing of single-cell libraries

Fresh blood samples were diluted in phosphate- buffered saline (PBS), and the PBMC fraction was isolated using SepMate 50 tubes (Stemcell Technologies) and human Lymphocyte Separation Medium (Cedarlane). The cell pellets were resuspended at 2-4 × 10^6 cells/mL in serum-free, animal protein-free cell freezing medium, immediately cryopreserved at −80° Celsius for no more than one week. Then they were transferred to liquid nitrogen storage before further processing. After resuscitation of frozen aliquots, cell viability was assessed using 0.4% trypan blue (Thermo Fisher, Cat. no. 14190144) on a Countess® II Automated Cell Counter (Thermo Fisher Scientific). ScRNA-seq libraries were constructed with the 5' Library and Gel Bead Kit and V(D)J Enrichment Kit and prepared per the Chromium Single Cell 5' library preparation kit user guide (10X Genomics). 10X library preparation and sequencing Beads with a unique molecular identifier (UMI) and cell barcodes were loaded close to saturation so that each cell was paired with a bead in a gel bead in emulsion (GEM). After exposure to the cell lysis buffer, polyadenylated RNA molecules were hybridized to the beads. Beads were retrieved in a single tube for reverse transcription. For cDNA synthesis, each cDNA molecule was tagged on the 5'end (corresponding to the 3' end of a messenger RNA transcript) with UMI and a cell label indicating its cell of origin. Subsequently, 10X beads were subjected to second-strand cDNA synthesis, adaptor ligation, and universal amplification. Sequencing libraries were prepared using randomly interrupted whole-transcriptome amplification products to enrich the 3' end of transcripts linked to the cell barcode and UMI. All remaining procedures, including library construction, were performed in accordance with the manufacturer's protocol (CG000206 RevD). ScRNA-Seq libraries were sequenced on NovaSeq6000 (Illumina) with paired-end 150bp sequencing.

2.3 The V (d) J library preparation and sequencing

Individual cells were encapsulated together with gel beads with a bar code and primer inside an oil droplet using a microfluidics system. Subsequently, the gel beads within each oil droplet were dissolved, and the cells were split to release mRNA. The mRNA was reverse transcribed into cDNA using the 10X barcode and UMI. After breaking the emulsions, the cDNA was split into two parts for gene expression and library construction. The V (d) J sequences of T-cell receptor (TCR) and B cell receptor (BCR) were amplified by PCR using nested primers designed for region C. Due to the mRNA information retaining the 5'-ends of reads, unlike the 10X Genomics 3'mRNA library, the sequencing then allowed accessing to the large amounts of single-cell gene expression and immune-group library data.

2.4 ScRNA-seq bioinformatics analysis

2.4.1 Construction, quality control, and filtering of feature-barcode matrix

During initial procession 10X data "mkfastq" module of the Cell Ranger (5.0.0) pipeline was operated to demultiplex the Illumina raw base call files (BCLs) obtained from Illumina sequencing into FASTQ files. FASTQs generated from the above workflow subsequently underwent several processing steps, as shown below. Specifically, according to default and recommended parameters based on the Cellranger "count" module (https://support.10Xgenomics.com/single-cell-gene-expression/software/pipelines/latest/using/count), the FASTQ sequences were aligned and quantified to the GRCh38 1.2.0

human reference genome obtained from 10X Genomics. The outputs generated by multiple runs of the Cellranger "count" were aggregated into a new feature-barcode matrix (barcodes, features, and count matrix) using the "aggr" pipeline. The matrix from the above operations was then imputed into the Seurat R package (4.1.3) for quality control and downstream analyses. To exclude low-quality cells from all samples, we adopted three criteria to remove genes detected in less than three cells, cells with less than 200 or over 6000 expressed genes, and cells expressing >0.1 of mitochondrial genes. After filtering, 116,916 cells with a median gene count of 18827 genes were maintained for the subsequent analysis, as shown in Supplementary Table 2. Finally, we corrected the batch effects between samples using the R package Seurat prior to clustering.

2.4.2 Feature selection, dimension reduction, and visualization for high-dimensional data

The "LongNormalize" method was used for normalization based on the filtered gene-barcode matrices obtained in the previous step. The "MVP" method was used to identify 494 highly variable genes (HVGs). We retained only the genes that contributed to group variability after controlling for the strong relationship between variability and average expression. Next, data from different samples were identified as 'anchors' and integrated. FindIntegrationAnchors and IntegrateData in the Seurat package were used to obtain pairs of cell anchor points when the cells of the query data set and the cells of the reference data set had common molecular characteristics. We subsequently performed principal component analysis (PCA) for linear dimension reduction and reduced the data to the top 20 PCs based on the elbow plot after scaling. Clustering was further performed using the Seurat FindClusters function with a resolution of 0.5, and the clusters were visualized on a 2D map produced with uniform manifold approximation and projection (UMAP). The final 12 cell clusters were determined using the above method. For sub-clustering, we applied the same procedure of scaling, dimensionality reduction, and clustering to a specific set of data (usually restricted to one type of cell).

2.4.3 Identification of differentially expressed genes (DEGs) and marker genes

Specific marker genes for each cluster were calculated using the Seurat "FindAllMarkers" function, with the parameters: logfc.threshold > 0.25, min.diff.pct > 0.25, min.pct > 0.1. DEGs were then identified by comparing cells from the target cluster to all other cells from the remaining clusters using Wilcoxon rank-sum tests. Finally, according to the statistical test results, the genes with the highest ranking from DEGs were set as specific marker genes of that cluster based on LFC > 0.5 and P-value < 0.05. Furthermore, marker genes were simultaneously defined as those with the highest mean expression in that cluster.

2.4.4 Functional enrichment analysis of DEGs

The ClusterRprofile R package (v4.2.2) was used to perform Gene Ontology (GO) analysis and Kyoto Encyclopedia of Genes and Genomes (KEGG) pathway analysis.

2.4.5 Pseudo time-trajectory analysis of different cell types

We used DDRTree's reduction method in Monocle3 (R package) with default parameters to reconstruct pseudo- time trajectories of 'target cells' to predict cellular differentiation pathways. First, we filtered all the differences of the cell clusters after converting normalized data to a Monocle object in R, and reduced the dimension for building minimum generating trees. Second, we searched for the optimal sorting of single -cell data in high-dimensional and low-dimensional spaces. Finally, we fitted the pseudo- time trajectory curve for the best cell development or differentiation. The criteria applied for gene selection included the following analysis: Genes expressed in less than 10 cells, or with a minimum normalized expression greater than 0.1 were filtered out, 2) q-value<0.01 in DEGs expression analysis.

2.4.6 BCR and TCR data analysis

The reads of a single barcode from the scRNA-seq were put into the vdj pipeline from the Cell Ranger V(D)J pipeline (v3.1.0, 10X Genomics), and these reads were glued to assemble a set of contigs to produce the best estimation of the current transcriptional sequence. The purpose of V(D)J contig annotation was to compare V, D, and J fragments to a contig; thus, we identified complementary determining region 3 (CDR3) sequences and rearranged full-length BCR/TCR V(D)J segments, as well as clonotype frequency. Next, the following sequences were obtained for downstream analysis: 1) high-confidence, detectable V genes, J genes, CDR3 nucleotides, and 2) more than two unique molecular identifier (UMI) counts. In cases with more than one assembled heavy-light chain pair, the one with higher UMI counts was chosen as the dominant in the corresponding cells. T or B cells that shared the same CDR3 nucleotide sequence of the VJ and VDJ chains were considered to be one clonotype that has the same adaptive immune receptor and epitopes. The Sc-BCR/Sc-TCR data were analyzed using the R package scRepertoire v1.5.2., following to the official vignette.

2.4.7 Statistical analysis

Shapiro-Wilk normality test and Levene's test were used to determining the normality and variance homogeneity. The wilcox-test was used for statistical analysis to determine the genes expression regulation change among multiple cell clusters. All statistical analyses were performed using the open-source statistical package R version 4.0.3 (R Project for Statistical Computing, Vienna, Austria).

2.5 Cytokine and chemokine measurement

Several cytokines and chemokines, including IL-1β, IL-2, IL-4, IL-5, IL-6, IL-8, IL-10, IL-17, IFN-α, IFN-γ, and TNF-α, were detected by multiple microsphere flow immunofluorescence. Cytokine detection reagent was provided by Qingdao Raisecare Biotechnology Co., Ltd. (Shandong, China). Briefly, EDTA-K2 anti-coagulated whole blood was centrifuged at 1,000 g for 30 min, and plasma was collected. Subsequently, 25 µL each of experimental buffer, centrifuged plasma, capture microsphere antibody, and detection antibodies were mixed in flow tubes and placed on a shaker at 500 RPM for 2 h at room temperature. Then, 25 µL of streptavidin-phycoerythrin (SA-PE) was added to the flow tubes, which were then placed on a shaker at 500 RPM for an additional 30 min. Data were then obtained using an automatic flow cytometer (Raisecare).

3 Results

3.1 Study design and single-cell survey of major changes in transcriptional profiles between anti-NMDARE patients and HCs

Ten fresh peripheral blood samples were obtained from five patients with anti-NMDARE (P1-P5), in whom the diagnosis of anti-NMDARE was based on the Graus and Dalmau criteria (23). Blood samples were obtained twice from each patient, once the day before the onset of first-line therapy (steroids and intravenous immunoglobulins) and once ten days later. Peripheral blood samples were collected from five age- and sex- matched healthy donors as controls (HC1-HC5). The clinical characteristics of the patients are presented in Supplementary Table 3.

A total of 129,217 cells were analyzed by scRNA-seq using the 10X genomics sequencing technology. Among these, 37,696 were derived from patients prior to first-line therapies (PBs), 38,396 after therapy (PAs), and 53,125 from HCs (Figure 1A). The sequencing information of each sample is presented in Supplementary Table 2. The single-cell profiles were divided into 21 clusters (Supplementary Figure 2), of which the major cell types included CD4+T cells, CD8+ T cells, B cells, monocytes, natural killer (NK) cells, macrophages (MΦ), mast cells (MCs), dendritic cells (DCs), and residual megakaryocytes (Mgk) mixed in PBMCs (Figure 1B). Most marker genes of each cluster were calculated based on highly DEGs (Supplementary Table 4). The cell types were identified using known unique signature and marker genes. Subsequently, 13 cell types were generated: naïve CD4+ T cells, memory CD4+ T cells, naïve CD8+ T cells, memory CD8+ T cells, proliferative CD8+ T cells, B cells, plasma B cells, NK cells, monocytes, MΦ, MCs, DCs, and Mgk (Figure 1C). Cluster annotation was confirmed by gene set enrichment analysis. GO analysis (Supplementary Figure 3) demonstrated that clusters 8, 9, and 17 were associated with B- cell receptor signaling; c lusters 0, 2, 4, 6, 7,11 and 16 were associated with T- cell activation and differentiation; clusters 1, 5, and 13 were found to regulate cytokine production and myeloid cell activation and differentiation, and c luster 15 was associated with antigen processing and presentation. These results were consistent with the KEGG pathway analysis (Supplementary Figure 4).

Compared to HCs, anti-NMDAR patients demonstrated a notable difference in the amount of cell subtypes (Figure 1D and Supplementary Figure 5). Compared with HCs, pre-treatment anti-NMDARE patients showed a higher proportion of monocytes and DCs, and a lower proportion of B cells and T cells. (Figure 1E and Supplementary Figure 6). Moreover, we assessed differences in subtype representations between PBs and PAs, finding that the population of B cells and myeloid cells demonstrated a decrease in PAs and DCs, while MΦ, in terms of myeloid cells, demonstrated a prominently lower population than HCs (Figures 1D, E, Supplementary Figure 6).

BCR and TCR information was retained by single-cell BCR sequencing (scBCR-seq) and single-cell TCR sequencing (scTCR-seq), based on scRNA-seq libraries. After quality control, 9,992 and 46,420 cells were detected with BCR (IGH) and TCR (TCR α–β pair) signatures, respectively (Supplementary Tables 5, 6). Among them, 8,817 B cells with a single productive IGH allele (1,941 from PBs, 1,899 from PAs, and 4,977 from HCs) and 41,475 T cells with a single productive TCRα-β pair (11,691 from PBs, 8,860 from PAs, and 20,924 from HCs) were detected. In the remainder of the study, we focused predominantly on B cells because of their importance in anti-NMDARE (Figures 1D, E). The proportion of unique clonal BCRs of HCs, PBs and PAs is 84.49%, 68.61% and 65.67%, respectively (Figure 1F). A significant decrease in proportion of unique clonal BCRs was observed in all anti-NMDARE patients compared to HCs. And this decrease continued after the first-line therapy. The large and hyperexpanded categories is uncommon in HCs, according to Supplementary Figure 7. The large and hyperexpanded categories is significantly taken into consideration in the PBs and PAs, particularly in P1a_PA and P4b_PB. The relative abundance of large and hyperexpanded categories demonstrated an increase in anti-NMDAR patients group compared to HC group. Our observations suggested that anti-NMDARE comprises oligoclonal expansions in response to immunizing antigens. Overall, the major immune cells and characterized cell proportions in anti-NMDARE patients were identified and compared to HCs, revealing prominent changes in B cells and myeloid cells.

3.2 Anti-NMDARE induces strong humoral immune responses

B cells were further divided into more homogeneous subsets, and 11 distinct sub-clusters were obtained (Figure 2A). Given the reported marker genes (24, 25), NRGN+ naive B cells

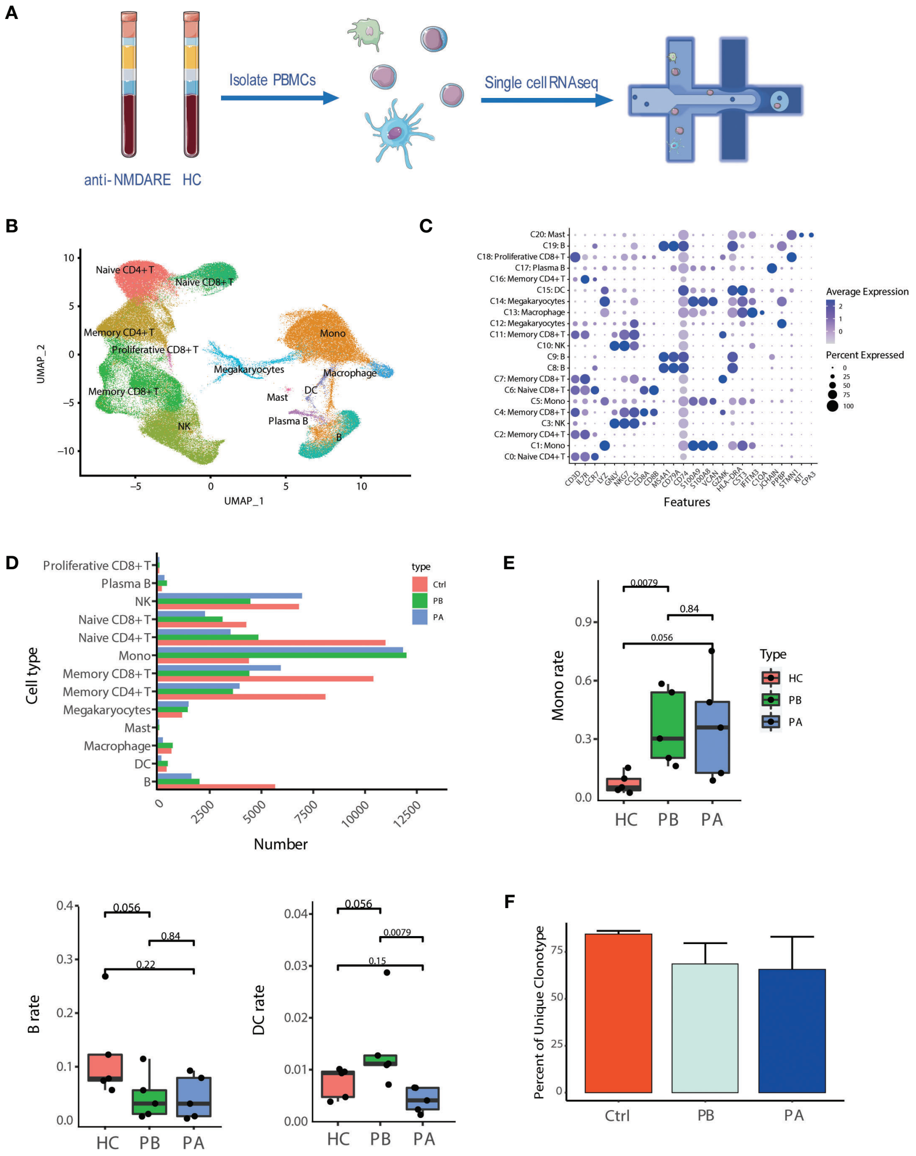

FIGURE 1
Assessment of major changes in transcriptional profiles in anti-NMDARE patients and HCs: **(A)** Schematic representation of scRNA-seq analysis; **(B)** Uniform manifold approximation and projection (UMAP) representation of scRNA-seq data; **(C)** Cluster annotation of expression values of selected genes (x axis) across each cluster (y axis) was shown by dot plot represents; **(D)** The alignment of the number of each cell type was shown by histogram across HCs (n = 5), PB (n = 5) and PA (n = 5); **(E)** The proportions of the major immune cell types among HCs, PBs and Pas; **(F)** Percent of unique clonotype across PBs, PAs and HCs.

(cluster 4), NRGN- naive B cells (cluster 5), germinal center B cells (cluster 2), CD27- memory B cells (cluster 0), CD27+ memory B cells (cluster 1), class-switched memory B cells (cluster 8), Plasmablast B cells (cluster 7), Plasma B cells (cluster 3), myeloid-like plasma B cells (cluster 9), CD14+ atypical B cells (cluster 6), and Age-associated B cells (cluster 10) were identified (Figure 2B).

Differential analysis revealed that naive B cells expressed the marker genes IGHD, IGHM, and CD37, but very low levels of CD27. Memory B cells (MBCs) expressed very low levels of IGHD. Unbiased analysis revealed two sub-clusters of naive B cells: NRGN^{high} and NRGN^{low} B cells. Neurogranin, encoded by NRGN, bidirectionally modulates synaptic plasticity *via* the calmodulin-dependent regulation of the neuronal phosphoproteome (26). Additionally, three sub-clusters of MBCs were identified. Cluster 8 was identified as class-switched memory B cells with upregulated CD99 and low IGHM levels (27). CD27 memory B cells are increased in the elderly and in patients with specific autoimmune diseases (28).

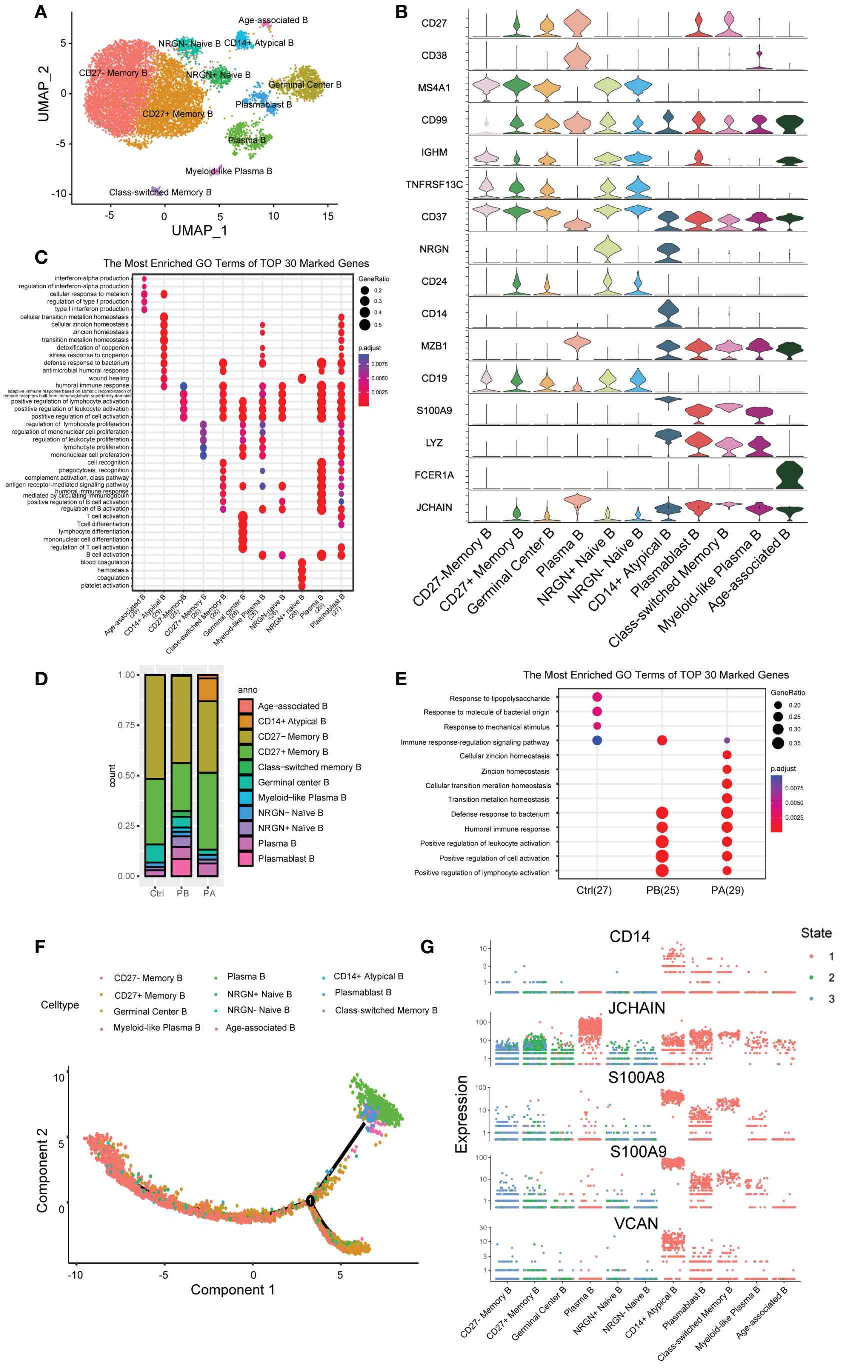

FIGURE 2
Assessment of changes in B cells in transcriptional profiles in anti-NMDARE patients and HCs: **(A)** The heterogeneous clusters of B cells were shown by UMAP; **(B)** The key gene markers across B cell subsets were shown by Violin plots; **(C)** The DEGs in B cell subsets; **(D)** Percentage of B cell types under each condition; **(E)** Enrichment analysis of DEGs from B cells in PBs, PAs and HCs; **(F)** B cells sorted using the DDRTree algorithm and projected onto the different cell states; **(G)** Key genes related to differentiation in B cell subsets across each state.

Germinal center B Cells had a higher expression of TNFRSF13C, and persistent germinal center activity may be responsible for the ongoing production of NR1-IgG, which strongly contributes to the initial peripheral generation of NR1 antibodies (29, 30). Antibody-secreting cells (ASCs) comprising plasmablasts, plasma cells, and myeloid-like plasma B cells expressed higher CD27 and CD38, concurrent with the low expression of CD19 and MS4A1. One cluster of ITGAX^{high} TBX21^{high}IGHD^{low}CD27^{low}CD24^{low} B cells was identified as age-associated B cells (ABCs), which have attracted significant attention in recent years (31). The high expression of FCER1A in age-associated B cells suggests increased antigen-presenting activity. ABCs may be potential triggers for autoimmune diseases (32). CD14+ atypical B- cells, characterized by the absence of CD21 and CD27, mainly exist in PAs. MT2A, MT1G, MTIX, and MTIE are predominantly expressed by CD14+ atypical B cells, which affect apoptotic and autophagy pathways in various diseases (33).

Furthermore, we characterized the transcriptomic changes in B cells of all clusters (Figure 2C, Supplementary Tables 7 and 8). GO analysis revealed that cluster 0 was associated with positive regulation of lymphocyte activation, cytokines, toll-like receptors (TLRs), and B- cell receptor signaling pathways. Conversely, cluster 1 was associated with regulation of lymphocyte proliferation, positive regulation of cell adhesion, antigen processing, and presentation of peptide antigens. Cluster 3 was associated with intrinsic signaling, including protein maturation, ERAD pathway, and complement activation. Cluster 6 was associated with phagocytosis, cell chemotaxis, and cell migration. Cluster 10 was associated with ATP metabolic processes and material transport. KEGG analysis further showed that clusters 3 and 7 shared similar pathways, such as the cell cycle set, indicating that they were highly activated.

3.3 Extensive B cell heterogeneity

The B cell compartments differed greatly in composition across the different cell groups (Figure 2D, Supplementary Figure 8). Compared with HCs, PBs showed an increased proportion of class-switched memory B Cells and ASCs, along with a decreased proportion of MBCs and germinal center B cells. These proportional changes indicate a strong humoral immune response induced by anti-NMDARE. After first-line therapy, the proportion of ASCs and class-switched memory B cells in total B cells decreased with an increase in ABCs and CD14+ Atypical B cells. In summary, strong humoral immunity develops in patients with anti-NMDARE in the acute stage. Considering that ASCs were significantly expanded in PAs and demonstrated essential roles at producing high-affinity antibodies, we were able to transcriptional changes between anti-NMDARE patients and HCs.

GO analysis suggested that the DEGs were mainly involved in the positive regulation of lymphocyte activation and humoral immune response (Figure 2E). Genes involved in lymphocyte activation, that is, IGHA1, IGHG1, IGHV3-30, IL7R, CCL5, TYROBP, LGALS1, and IGKC, were upregulated in anti-NMDARE patients compared to HCs. Genes upregulated in the humoral immune response in PBs compared to HCs included S100A4, S100A9, S100A8, S100A12, LYZ, GNLY, IGHV3-23, and JCHAIN. After therapy, genes involved in the response to steroids and those involved in the apoptotic process of leukocytes were induced, including TSC22D3, DDIT4, GPX1, and TXNIP. In general, immune response signaling and lymphocyte activation pathways were activated in PBs, whereas apoptotic signaling pathways were upregulated in PAs.

Further, we analyzed the trajectory of B cells in each sample (Figure 2F, Supplementary Figure 9). In HCs, trajectory analysis revealed a gradual transition from naïve B cells and germinal center B cells to ASCs or MBCs, with most cells undergoing differentiation into MBCs. MBCs had low progression along pseudonyms, indicating a close relationship to naïve B cells, which marked the beginning of the pseudotime. In anti-NMDARE patients, although the differentiation pathways were similar, more cells differentiated into ASCs. After therapy, the end of the branch generated ABCs and CD14+ Atypical B cells, which were closely associated with the immune senescence, including reduced B cell genesis and a dampened immune responses (34). The branch consisting of ASCs, ABCs, CD14+ Atypical B, and Class-switched memory B cells progressed further along pseudotime, showing that these cell populations were differentiated further away from naive B cells compared to MBCs. ASCs highly expressed JCHAIN, which is required for immunoglobulin polymerization (Figure 2G), J chain is a small glycopeptide linked to IgA and IgM by disulfide bonds which has also been detected in IgG- and IgD-containing cells (35, 36). Clusters 6 and 8 contained elevated levels of S100A8 and S100A9, which are considered alarming and damage-associated molecules, respectively (37). The above analysis revealed an enhanced propensity for differentiation towards the ASC phenotype in anti-NMDARE patients, and a highly activated state of ABCs and CD14+ Atypical B cells.

3.4 Characterization of BCRs

The dynamics of BCR repertoires during acute anti-NMDARE were dissected (Figure 3A). The PBs of clonally expanded B cells showed transcriptional homogeneity; however, a diffusive distribution indicated transcriptional heterogeneity in the HCs (Figure 3B). Moreover, the number of clonal BCRs increased significantly in plasma B cells and myeloid-like plasma B cells (Figure 3C). Prior to undergoing first-line therapies, the majority of clone types from plasmablast B cells and myeloid-like plasma B cells were large (5<X<=100), but exhibited various expression patterns in PAs. However, after first-line therapy, the proportion of IGHA and IGHG increased significantly (Figure 3D), indicating that B cell activation led to the conversion of immunoglobulin from IgM/IgD to IgG/IgA. Significant oligoclonal expansion in ASCs was observed, among which the lgG subtype was predominantly found in myeloid-like plasma B cells and IgA in plasma and plasmablast B cells (Figure 3E, Supplementary Figure 10). In general, our data suggested that a larger proportion of ASCs with highly expanded features and transcriptional homogeneity were

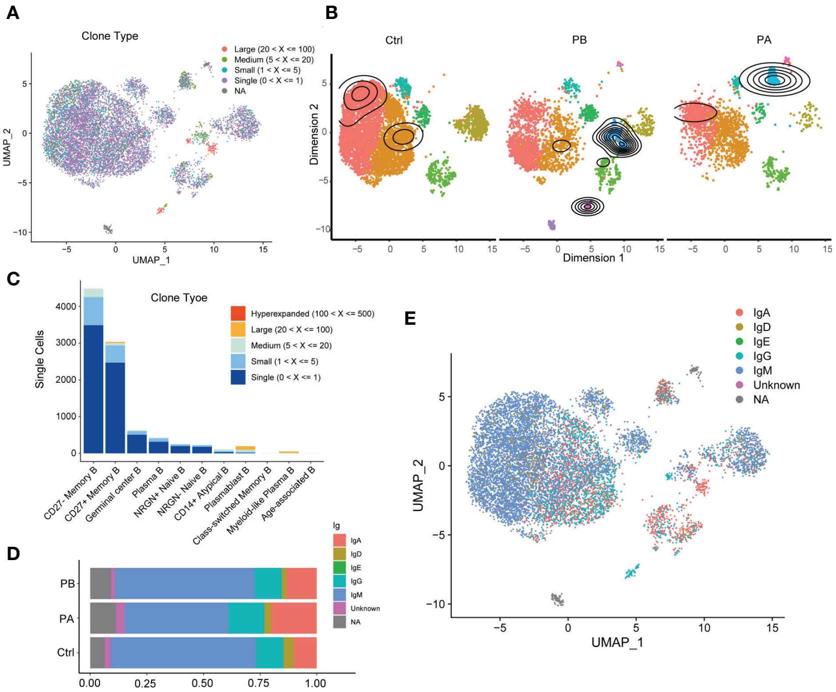

FIGURE 3
Characterization of BCR repertoires during acute anti-NMDARE state: **(A)** The clonal expansion status in B cells shown by UMAP; **(B)** The clonal expansion status of B cell subsets in PBs, PAs and HCs; **(C)** BCR clonotype tracking in B cell subsets; **(D)** The percentage of IGHA and IGHG in BCRs across PBs, PAs and HCs; **(E)** The IGH isotypes in each B cluster shown by UMAP.

present in patients with anti-NMDARE antibodies, and that significant oligoclonal expansions were dominated by IgA and IgG isotypes.

3.5 Expression of inflammatory cytokines and chemokines in myeloid subsets

Furthermore, we quantitatively evaluated the anti-NMDARE-driven changes in myeloid cells. Human peripheral blood myeloid cells, including monocytes, DCs, and MΦ, promote antigen presentation and inflammatory activity (38). Myeloid cells were sub-grouped into 13 clusters, numbered from 0 to 12 (Figures 4A, B). The three myeloid subsets were defined as monocytes (clusters 0, 1, and 2), of which Mono1 (Cluster 0) was the most abundant. The expression levels of S100A8, S100A9, and LYZ were higher in mono1 (cluster 0). In mono2 cells (cluster 1), the expression levels of IL-32, PRF1, and GNLY were higher. M ono _THBS1 (cluster 2) was a minor subset expressing THBS1. The myeloid subset MΦ (cluster 4) highly expressed FCGR3A (cluster 4). Myeloid_IGHV2-5 (cluster 11) highly expressed IGHV2-5 (cluster 11). Mgk (cluster 5) and MCs (cluster 10) highly expressed surface markers STMN1 and PPBP. A few cells, defined as B cells, NK cells, and red blood cells were combined with myeloid cells (clusters 6, 9, and 12). The myeloid subsets DC_FCER1A (cluster 8) and DC_CCR7 (cluster 3) highly expressed FCER1A and CCR7, respectively (Figures 4A, B).

We subsequently compared the expression levels of different myeloid clusters (Figure 4C). In both mono1 and mono2, monocyte expansion was prominent (Figure 4D). After first-line therapy, mono_THBS1 was highly expressed in patients. The proportion of mono_THBS1 remained significantly higher in patients with anti-NMDARE post-treatment than in HCs. Mono1 showed high expression levels of S100A8 and S100A9, which exert pro-inflammatory effects in a range of diseases (39). Mono2 highly expresses IL32 and PRF1. IL-32 may further play a role in innate and adaptive immune responses, which induce other cytokines involved in inflammation, including tumor necrosis factor (TNF)-α, IL-6, and IL-1β, and activate typical cytokine signaling pathways of NF-κB and p38 MAPK (40). PRF1 is important for immunity (41). Thus, anti-NMDARE patients showing an inflammatory state were caused by the expansion of mono1 and mono2. Moreover, we observed that during the acute phase in anti-NMDARE patients, higher levels of DC_CCR7 were expressed in human myeloid cells (Figure 4C). The composition of mono1 and mono2 in the PB and PA groups were similar, suggesting that immunological changes were sustained during convalescence. However, the increased proportion of mono_THBS1, along with a decreased

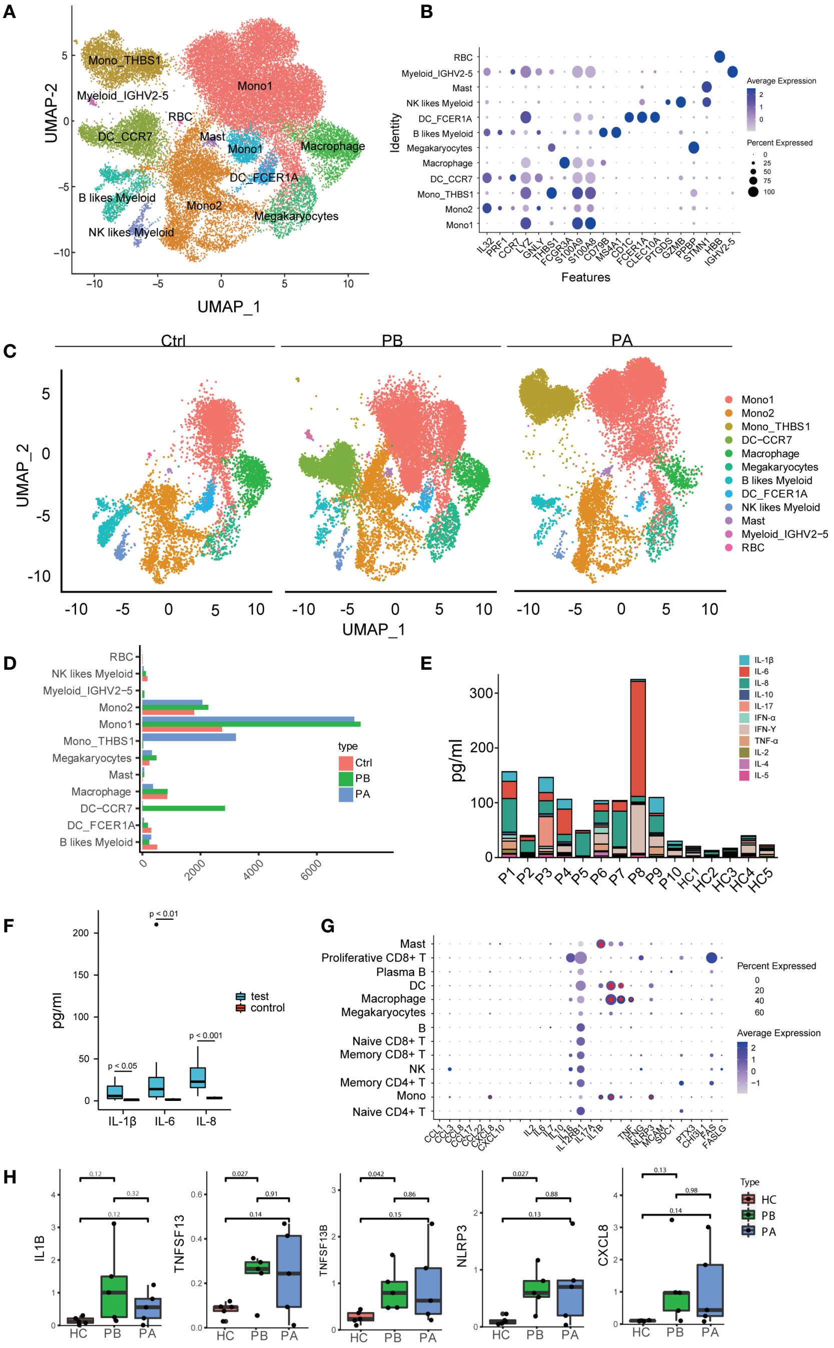

FIGURE 4
Assessment of changes in myeloid cells in transcriptional profiles between anti-NMDARE patients and HCs: **(A)** The heterogeneous clusters of myeloid cells were shown by UMAP; **(B)** The key gene markers across myeloid cell subsets were shown by violin plots. The dot plot represents the expression values of selected genes (x axis) across each cluster (y axis). The percentage of cells expressing the marker of interest were shown by dot size and the mean expression within expressing cells was shown by color intensity. **(C)** The major myeloid subsets from the HC, PB, and PA groups were shown by UMAP; **(D)** Cell abundance across PBs, PAs and HCs; **(E)** The alignment of the levels of selected cytokines and chemokines in peripheral blood in HCs (n = 5), PBs (n = 10); **(F)** The levels of IL-1β, IL-6 and IL-8 in peripheral blood in HCs (n = 5), PBs (n = 10). P-value was adjusted by false discovery rate; **(G)** Expression patterns of molecular biomarkers in anti-NMDARE. The dot plot represented average expression levels and percentage of cells expressing the molecular biomarkers genes across peripheral PBMC; **(H)** Expression levels of IL1B, TNFSF13B, TNFSF13 and NLRP3 in PBMCs of HCs (n = 5), PBs (n = 5) and PAs (n = 5).

proportion of DC_CCR7 in PAs suggests that excessive inflammatory responses were inhibited.

Furthermore, the levels of several cytokines and chemokines in the peripheral blood of the anti-NMDARE patients were measured (Figure 4E, Supplementary Table 1). Compared with HCs, anti-NMDARE patients had much higher levels of IL-1β, IL-6, and IL-8 inflammatory cytokines (Figure 4F, Supplementary Figure 11). The expression of molecular biomarkers in patients with anti-NMDARE was also measured (Figure 4G). IL-6 and IL-2 are crucial inflammatory mediators that stimulate both B and T cells in autoimmune processes, and have been used as therapeutic targets to treat anti-NMDAREs (42, 43). Overall, we found that IL6 was predominantly expressed in B cells, while CXCL8, IL1B, TNFSF13B, TNFSF13, TNF, and NLRP3 were mainly expressed in myeloid cells and upregulated in PBs (Figures 4G, H). In addition, CXCL8 and NLRP3 were mainly expressed in monocytes. TNFSF13 and TNF were mainly expressed in macrophages, whereas TNFSF13B was mainly expressed in monocytes, DCs, and macrophages (Supplementary Figure 12). These results suggest that as myeloid abundance increases, the production of total chemokines and other molecular biomarkers in anti-NMDARE patients is expected to increase.

4 Discussion

Anti-NMDARE is the most frequently recognized neuronal antibody-mediated encephalitis (44). ASCs enter the central nervous system through the blood-brain barrier and secrete antibodies, leading to their internalization and subsequently reduced functioning of NMDARE, delineating the pathogenesis of the disease (45, 46). The immune system is dysregulated in anti-NMDARE patients, and significant efforts have been made in the research and treatment of anti-NMDARE (47). However, further investigation of the regulation of the immune system in peripheral blood is still required to develop novel therapies and to achieve improved curative effects in less time.

In the current study, we aimed to understand the cellular transcriptional changes in anti-NMDARE patients. To the best of our knowledge, this is the first study to create a high-resolution map of transcriptional changes and systematically discuss cellular heterogeneity and impaired peripheral tolerance in anti-NMDARE patients.

We performed scRNA-seq to assess the transcriptional profiles of 129,217 cells and identified and annotated 21 major cell clusters, after which we performed by DEG and pathway analysis. First, we identified 21 cell clusters comprising CD4+T cells, CD8+ T cells, B cells, monocytes, NK cells, MΦ, MCs, Mgk, and DCs. B cell differentiation and activation, plasma cell expansion, and excessive inflammatory responses in innate immunity were all identified. Furthermore, we found some interesting results: anti-NMDARE promotes B-cell polarization from naive to ASC with higher CD27 and CD38 expression, and low expression of CD19 and MS4A1, and anti-NMDARE induces a dysregulation in the balance of myeloid subsets (e.g., a significant increase in mono1, mono2, and DC _CCR7). NMDAR are taken up by antigen- presenting cells (APCs), and present to the immune system, resulting in the differentiation of naive B cells into MBCs, and plasma cells in local lymph nodes (48, 49). Based on these two studies, we speculated that in patients with anti-NMDARE, naive B cells differentiate into more plasma cells with the help of APCs. Previous studies of pathology in anti-NMDARE have focused on adaptive immunity (50), finding that monocytes and DCs were significantly expanded in PBs compared to HCs; this suggests that, both innate and adaptive immunity are involved in the occurrence and development of diseases.

In the current study, we identified DEGs and observed remarkable oligoclonal expansions in anti-NMDARE patients, which may provide a reference for studying the pathological roles of immune cell subsets and discovering potential drug targets to treat these diseases.

B cells are the dominant cell type for maintaining humoral defenses (51). They are also associated with the development and control of autoimmunity that targets self-antigens (52, 53). Various B cell categories exhibit the ability for both self-protection and self-destruction (52). Patients with anti-NMDARE carry major B cell alterations, including expansion of the activated plasma B cell phenotype (54), with higher concentrations of NR1-IgG in the serum than the CSF (55, 56). These alterations suggest that the periphery is likely the site of primary immunization. We found that although the total B cell abundance decreased in anti-NMDARE patients, the proportion of class-switched memory B cells and ASCs among the B cells increased.

Moreover, we observed extensive oligoclonal expansion of BCRs and isotype switching from IgM/IgD to IgG/IgA. All the evidence supports the hypothesis that due to some specific antigens, the acquired immune responses thus generated leads to anti-NMDARE (13, 57). B rain biopsy or autopsy findings suggested that during anti-NMDARE, B cells and plasma cells infiltrate brain tissue along with IgG deposits, resulting in little neuron loss (58, 59), which confirmed that adaptive immunity is involved in the occurrence of diseases. The detection of synthetic antibodies based on oligoclonal IgAs and lgGs can be used as a specific diagnostic test for anti-NMDARE (47, 60, 61). The DEG analysis in our study indicated that genes involved in positive regulation of lymphocytes and humoral immune responses such as IL-7R, CCL5, LYZ, GNLY, JCHAIN, and S100 were upregulated. The expression levels of IGHA1, IGHG1, IGHV3-30, and IGHV3-23 encoding immunoglobulin heavy chains were high before first-line therapy and returned to normal levels after therapy, suggesting that the immunomodulatory effect of steroids and IVIG may be related to the blockage of activated immunoglobulin (62, 63). In autoimmune disorders, the expansion of ABCs and CD14+ Atypical B cells is significantly higher (64, 65); therefore, conditional targeting of the transcription factor T-bet encoded by TBX21, which is important and sufficient for ABCs formation (66), could be an efficient and novel therapeutic target.

Previous studies have focused on adaptive immunity in anti-NMDARE (1); however, we observed remarkable expansion and alterations in the differentiation of myeloid cells. In our study, mono1 and mono2 highly expressed S100A8, S100A9, IL32, and PRF1, indicating an inflammatory state in patients with anti-NMDARE. S100A8 and S100A9 can also amplify the inflammatory response by promoting the secretion of pro-inflammatory cytokines (TNF, IL6, etc.), and exert a chemo-attractive function that allows the recruitment and adhesion of leukocytes (67).

Our data showed a dysregulation in the balance of myeloid populations in anti-NMDARE patients, as manifested by a substantial increase in monocyte subsets and DC_CCR7. The central chemokine receptor CCR7 plays a role in T-cell activation, differentiation, and expansion of IgG-producing B cells (68). Blocking CCR7 signaling seems to reduce both humoral and immune cell-mediated pathogenic courses, making CCR7 a potential target for interference with anti-NMDARE. Thus, we suggest CCR7 as a possible target for potential future drugs with an antagonistic effect in inhibiting disease progression by reducing inflammation (69).

Furthermore, we found an increased percentage of mono_THBS1, a potent inhibitor of T cell and DC activation which dampens an excessive inflammatory response (70, 71), after first-line therapy, Therefore, we propose that mono_THBS1 could be used as an indicator to monitor the curative effect. However, the increased proportion of mono_THBS1 and the decreased proportion of DC_CCR7 in PAs suggests that excessive inflammatory responses were inhibited.

Patients with anti-NMDARE have higher levels of IL-1β, IL-6, IL-8 and higher expression of inflammatory factors, particularly CXCL8, IL1B, TNFSF13B, TNFSF13, TNF, and NLRP3, than in HCs. Our data suggest that myeloid cells in patients with anti-NMDARE may contribute to local inflammation, and cytokine storms are associated with disease severity. Moreover, several studies have confirmed that some cytokines/chemokines and other molecular biomarkers, such as the NLRP3 inflammasome, soluble Fas and FasL, chitinase-3-like 1 (CHI3L1), pentraxin 3 (PTX3), and CD40L, are associated with clinical activity, inflammation, and long-term outcomes (72).

However, our study has several limitations. The sample size for scRNA-seq analysis was small and heterogeneous. This study was carried out on PBMCs, and therefore could not reflect the inflammatory responses in the cerebrospinal fluid. F actors such as age, disease severity, and immunoregulatory therapies were not comprehensively assessed. Moreover, more patients with herpes simplex encephalitis or teratoma should be included in future studies to accurately determine the relationship between different infections and immune responses.

Data availability statement

The RNA-seq data reported in this article has been deposited in the Genome Sequence Archive (GSA) for human in BIG Data Center, Beijing Institute of Genomics, Chinese Academy of Sciences and is accessible through accession number HRA003508.

Ethics statement

This study was approved by the ethics committee of Henan Provincial Peoples Hospital. Written informed consent to participate in this study was provided by the participants' legal guardian/next of kin.

Author contributions

YJ played a major role in the design of the research, conduction of the experiments, acquisition and analysis of the data, drafting, and revision of the manuscript. SD was involved in the sample collection, conduction of the experiments and analysis of the data. LJ, XW, and RP collected the sample. GP analyzed the data. LQ, MZ, and HL edited and revised manuscript. WL and JZ co-directed the study. WL revised manuscript and provided financial support. All authors contributed to the article and approved the submitted version.

Funding

This work was supported by grant to WL from the Medical Science and Technology Project of Henan Province (NO. SBGJ2018077). The funder had no role in study design, data collection and analysis, decision to publish, or preparation of the manuscript.

Acknowledgments

Figure 1A was constructed in part using Servier Medical Art (https://smart.servier.com/), licensed under a Creative Common Attribution 3.0 Generic License. (https://creativecommons.org/licenses/by/3.0/).

Conflict of interest

The authors declare that the research was conducted in the absence of any commercial or financial relationships that could be construed as a potential conflict of interest.

Publisher's note

Supplementary material

The Supplementary Material for this article can be found online at: https://www.frontiersin.org/articles/10.3389/fimmu.2022.1075675/full#supplementary-material

References

1. Dalmau J, Armangué T, Planagumà J, Radosevic M, Mannara F, Leypoldt F, et al. An update on anti-NMDA receptor encephalitis for neurologists and psychiatrists: mechanisms and models. *Lancet Neurol* (2019) 18(11):1045–57. doi: 10.1016/S1474-4422(19)30244-3

2. Dalmau D, Gleichman AJ, Hughes EG, Rossi JE, Peng X, Lai M, et al. Anti-NMDA-receptor encephalitis: case series and analysis of the effects of antibodies. *Lancet Neurol* (2008) 7(12):1091–8. doi: 10.1016/S1474-4422(08)70224-2

3. Titulaer MJ, McCracken L, Gabilondo I, Armangué T, Glaser C, Iizuka T, et al. Treatment and prognostic factors for long-term outcome in patients with anti-NMDA receptor encephalitis: an observational cohort study. *Lancet Neurol* (2013) 12(2):157–65. doi: 10.1016/S1474-4422(12)70310-1

4. Montmollin E, Demeret S, Brulé N, Conrad M, Dailler F, Lerolle N, et al. Anti-N-Methyl-d-Aspartate receptor encephalitis in adult patients requiring intensive care. *Am J Respir Crit Care Med* (2017) 195(4):491–9. doi: 10.1164/rccm.201603-0507OC

5. Ciano-Petersen NL, Cabezudo-García P, Muñiz-Castrillo S, Honnorat J, Serrano-Castro PJ, Oliver-Martos B. Current status of biomarkers in anti-N-Methyl-D-Aspartate receptor encephalitis. *Int J Mol Sci* (2021) 22(23):13127. doi: 10.3390/ijms222313127

6. Shu Y, Guo J, Ma X, Yan Y, Wang Y, Chen C, et al. Anti-N-methyl-D-aspartate receptor (NMDAR) encephalitis is associated with IRF7, BANK1 and TBX21 polymorphisms in two populations. *Eur J Neurol* (2021) 28(2):595–601. doi: 10.1111/ene.14596

7. Shu Y, Qiu W, Zheng J, Sun X, Yin J, Yang X, et al. HLA class II allele DRB1*16:02 is associated with anti-NMDAR encephalitis. *J Neurol Neurosurg Psychiatry* (2019) 90(6):652–8. doi: 10.1136/jnnp-2018-319714

8. Wu C-Y, Wu J-D, Chen C-C. The association of ovarian teratoma and anti-N-Methyl-D-Aspartate receptor encephalitis: An updated integrative review. *Int J Mol Sci* (2021) 22(20):10911. doi: 10.3390/ijms222010911

9. Nosadini M, Mohammad SS, Corazza F, Ruga EM, Kothur K, Perilongo G, et al. Herpes simplex virus-induced anti-n-methyl-d-aspartate receptor encephalitis: a systematic literature review with analysis of 43 cases. *Dev Med Child Neurol* (2017) 59(8):796–805. doi: 10.1111/dmcn.13448

10. Chefdeville A, Treilleux I, Mayeur M-E, Couillault C, Picard G, Bost C, et al. Immunopathological characterization of ovarian teratomas associated with anti-N-methyl-D-aspartate receptor encephalitis. *Acta Neuropathol Commun* (2019) 7(1):38. doi: 10.1186/s40478-019-0693-7

11. Schwenkenbecher P, Skripuletz T, Lange P, Dürr M, Konen FF, Möhn N, et al. Intrathecal antibody production against Epstein-Barr, herpes simplex, and other neurotropic viruses in autoimmune encephalitis. *Neurol Neuroimmunol Neuroinflamm* (2021) 8(6):e1062. doi: 10.1212/NXI.0000000000001062

12. Huang Y-Q, Xiong H. Anti-NMDA receptor encephalitis: a review of mechanistic studies. *Int J Physiol Pathophysiol Pharmacol* (2021) 13(1):1–11.

13. Mikasova L, de RP, Bouchet D, Georges F, Rogemond V, Didelot A, et al. Disrupted surface cross-talk between NMDA and ephrin-B2 receptors in anti-NMDA encephalitis. *Brain* (2012) 135(Pt5):1606–21. doi: 10.1093/brain/aws092

14. Kayser MS, Titulaer MJ, Gresa-Arribas N, Dalmau J. Frequency and characteristics of isolated psychiatric episodes in anti–n-methyl-d-aspartate receptor encephalitis. *JAMA Neurol* (2013) 70(9):1133–9. doi: 10.1001/jamaneurol.2013.3216

15. Gresa-Arribas N, Titulaer MJ, Torrents A, Aguilar E, McCracken L, Leypoldt F, et al. Antibody titres at diagnosis and during follow-up of anti-NMDA receptor encephalitis: a retrospective study. *Lancet Neurol* (2014) 13(2):167–77. doi: 10.1016/S1474-4422(13)70282-5

16. Liu J, Liu L, Kang W, Peng G, Yu D, Ma Q, et al. Cytokines/Chemokines: Potential biomarkers for non-paraneoplastic anti-N-Methyl-D-Aspartate receptor encephalitis. *Front Neurol* (2020) 11:582296. doi: 10.3389/fneur.2020.582296

17. Körtvelyessy P, Goihl A, Guttek K, Schraven B, Prüss H, Reinhold D. Serum and CSF cytokine levels mirror different neuroimmunological mechanisms in patients with LGI1 and Caspr2 encephalitis. *Cytokine* (2020) 135:155226. doi: 10.1016/j.cyto.2020.155226

18. Wagnon I, Hélie P, Bardou I, Regnauld C, Lesec L, Leprince J, et al. Autoimmune encephalitis mediated by b-cell response against n-methyl-d-aspartate receptor. *Brain* (2020) 143(10):2957–72. doi: 10.1093/brain/awaa250

19. Pilli D, Zou A, Tea F, Dale RC, Brilot F. Expanding role of T cells in human autoimmune diseases of the central nervous system. *Front Immunol* (2017) 8:652. doi: 10.3389/fimmu.2017.00652

20. Liba Z, Kayserova J, Elisak M, Marusic P, Nohejlova H, Hanzalova J, et al. Anti-N-methyl-D-aspartate receptor encephalitis: the clinical course in light of the chemokine and cytokine levels in cerebrospinal fluid. *J Neuroinflamm* (2016) 13(1):55. doi: 10.1186/s12974-016-0507-9

21. Feng J, Fan S, Sun Y, Ren H, Guan H, Wang J. Comprehensive b-cell immune repertoire analysis of anti-NMDAR encephalitis and anti-LGI1 encephalitis. *Front Immunol* (2021) 12:717598. doi: 10.3389/fimmu.2021.717598

22. Malviya M, Barman S, Golombeck KS, Planagumà J, Mannara F, Strutz-Seebohm N, et al. NMDAR encephalitis: passive transfer from man to mouse by a recombinant antibody. *Ann Clin Transl Neurol* (2017) 4(11):768–83. doi: 10.1002/acn3.444

23. Graus F, Titulaer MJ, Balu R, Benseler S, Bien CG, Cellucci T, et al. A clinical approach to diagnosis of autoimmune encephalitis. *Lancet Neurol* (2016) 15(4):391–404. doi: 10.1016/S1474-4422(15)00401-9

24. Zhang C, Zhang T-X, Liu Y, Jia D, Zeng P, Du C, et al. B-cell compartmental features and molecular basis for therapy in autoimmune disease. *Neurol Neuroimmunol Neuroinflamm* (2021) 8(6):e1070. doi: 10.1212/NXI.0000000000001070

25. King HW, Orban N, Riches JC, Clear AJ, Warnes G, Teichmann SA, et al. Single-cell analysis of human b cell maturation predicts how antibody class

switching shapes selection dynamics. *Sci Immunol* (2021) 6(56):eabe6291. doi: 10.1126/sciimmunol.abe6291

26. Hwang H, Szucs MJ, Ding LJ, Allen A, Ren X, Haensgen H, et al. Neurogranin, encoded by the schizophrenia risk gene NRGN, bidirectionally modulates synaptic plasticity *via* calmodulin-dependent regulation of the neuronal phosphoproteome. *Biol Psychiatry* (2021) 89(3):256–69. doi: 10.1016/j.biopsych.2020.07.014

27. Descatoire M, Weller S, Irtan S, Sarnacki S, Feuillard J, Storck S, et al. Identification of a human splenic marginal zone b cell precursor with NOTCH2-dependent differentiation properties. *J Exp Med* (2014) 211(5):987–1000. doi: 10.1084/jem.20132203

28. Wu Y-CB, Kipling D, Dunn-Walters DK. The relationship between CD27 negative and positive b cell populations in human peripheral blood. *Front Immunol* (2011) 2:81. doi: 10.3389/fimmu.2011.00081

29. Makuch M, Wilson R, Al-Diwani A, Varley J, Kienzler A-K, Taylor J, et al. N-methyl-D-aspartate receptor antibody production from germinal center reactions: Therapeutic implications. *Ann Neurol* (2018) 83(3):553–61. doi: 10.1002/ana.25173

30. Rüegg S, Irani SR. The trouble with plasma cells: Getting to the root cause. *Neurology* (2017) 88(4):340–1. doi: 10.1212/WNL.0000000000003545

31. Abplanalp WT, John D, Cremer S, Assmus B, Dorsheimer L, Hoffmann J, et al. Single-cell RNA-sequencing reveals profound changes in circulating immune cells in patients with heart failure. *Cardiovasc Res* (2021) 117(2):484–94. doi: 10.1093/cvr/cvaa101

32. Jin W, Yang Q, Peng Y, Yan C, Li Y, Luo Z, et al. Single-cell RNA-seq reveals transcriptional heterogeneity and immune subtypes associated with disease activity in human myasthenia gravis. *Cell Discovery* (2021) 7(1):85. doi: 10.1038/s41421-021-00314-w

33. Sutton HJ, Aye R, Idris AH, Vistein R, Nduati E, Kai O, et al. Atypical b cells are part of an alternative lineage of b cells that participates in responses to vaccination and infection in humans. *Cell Rep* (2021) 34(6):108684. doi: 10.1016/j.celrep.2020.108684

34. Cancro MP. Age-associated b cells. *Annu Rev Immunol* (2020) 38:315–40. doi: 10.1146/annurev-immunol-092419-031130

35. Li Y, Wang G, Li N, Wang Y, Zhu Q, Chu H, et al. Structural insights into immunoglobulin m. *Science* (2020) 367(6481):1014–7. doi: 10.1126/science.aaz5425

36. Zheng Y, Lu P, Deng Y, Wen L, Wang Y, Ma X, et al. Single-cell transcriptomics reveal immune mechanisms of the onset and progression of IgA nephropathy. *Cell Rep* (2020) 33(12):108525. doi: 10.1016/j.celrep.2020.108525

37. Mondet J, Chevalier S, Mossuz P. Pathogenic roles of S100A8 and S100A9 proteins in acute myeloid and lymphoid leukemia: Clinical and therapeutic impacts. *Molecules* (2021) 26(5):1323. doi: 10.3390/molecules26051323

38. Ströher U, West E, Bugany H, Klenk HD, Schnittler HJ, Feldmann H. Infection and activation of monocytes by marburg and Ebola viruses. *J Virol* (2001) 75(22):11025–33. doi: 10.1128/JVI.75.22.11025-11033.2001

39. Perera C, McNeil HP, Geczy CL. S100 calgranulins in inflammatory arthritis. *Immunol Cell Biol* (2010) 88(1):41–9. doi: 10.1038/icb.2009.88

40. Albuquerque R, Komsi E, Starskaia I, Ullah U, Lahesmaa R. The role of interleukin-32 in autoimmunity. *Scand J Immunol* (2021) 93(2):e13012. doi: 10.1111/sji.13012

41. Sidore C, Orrù V, Cocco E, Steri M, Inshaw JR, Pitzalis M, et al. PRF1 mutation alters immune system activation, inflammation, and risk of autoimmunity. *Mult Scler* (2021) 27(9):1332–40. doi: 10.1177/1352458520963937

42. Lee W-J, Lee S-T, Moon J, Sunwoo J-S, Byun J-I, Lim J-A, et al. Tocilizumab in autoimmune encephalitis refractory to rituximab: An institutional cohort study. *Neurotherapeutics* (2016) 13(4):824–32. doi: 10.1007/s13311-016-0442-6

43. Lim J-A, Lee S-T, Moon J, Jun J-S, Park B-S, Byun J-I, et al. New feasible treatment for refractory autoimmune encephalitis: Low-dose interleukin-2. *J Neuroimmunol* (2016) 299:107–11. doi: 10.1016/j.jneuroim.2016.09.001

44. Dalmau J, Graus F. Antibody-mediated encephalitis. *N Engl J Med* (2018) 378(9):840–51. doi: 10.1056/NEJMra1708712

45. Ladépêche L, Planagumà J, Thakur S, Suárez I, Hara M, Borbely JS, et al. NMDA receptor autoantibodies in autoimmune encephalitis cause a subunit-specific nanoscale redistribution of NMDA receptors. *Cell Rep* (2018) 23(13):3759–68. doi: 10.1016/j.celrep.2018.05.096

46. Moscato EH, Peng X, Jain A, Parsons TD, Dalmau J, Balice-Gordon RJ. Acute mechanisms underlying antibody effects in anti-N-methyl-D-aspartate receptor encephalitis. *Ann Neurol* (2014) 76(1):108–19. doi: 10.1002/ana.24195

47. Abboud H, Probasco JC, Irani S, Ances B, Benavides DR, Bradshaw M, et al. Autoimmune encephalitis: proposed best practice recommendations for diagnosis and acute management. *J Neurol Neurosurg Psychiatry* (2021) 92(7):757–68. doi: 10.1136/jnnp-2020-325300

48. Dalmau J. NMDA receptor encephalitis and other antibody-mediated disorders of the synapse: The 2016 cotzias lecture. *Neurology* (2016) 87(23):2471–82. doi: 10.1212/WNL.0000000000003414

49. Feng J, Fan S, Sun Y, Zhang Z, Ren H, Li W, et al. Study of b cell repertoire in patients with anti-N-Methyl-D-Aspartate receptor encephalitis. *Front Immunol* (2020) 11:1539. doi: 10.3389/fimmu.2020.01539

50. Huang Q, Xie Y, Hu Z, Tang X. Anti-N-methyl-D-aspartate receptor encephalitis: A review of pathogenic mechanisms, treatment, prognosis. *Brain Res* (2020) 1727:146549. doi: 10.1016/j.brainres.2019.146549

51. Cancro MP, Tomayko MM. Memory b cells and plasma cells: The differentiative continuum of humoral immunity. *Immunol Rev* (2021) 303(1):72–82. doi: 10.1111/imr.13016

52. Rawlings DJ, Metzler G, Wray-Dutra M, Jackson SW. Altered b cell signalling in autoimmunity. *Nat Rev Immunol* (2017) 17(7):421–36. doi: 10.1038/nri.2017.24

53. Raza IGA, Clarke AJ. B cell metabolism and autophagy in autoimmunity. *Front Immunol* (2021) 12:681105. doi: 10.3389/fimmu.2021.681105

54. Irani SR, Bera K, Waters P, Zuliani L, Maxwell S, Zandi MS, et al. N-methyl-D-aspartate antibody encephalitis: temporal progression of clinical and paraclinical observations in a predominantly non-paraneoplastic disorder of both sexes. *Brain* (2010) 133(Pt 6):1655–67. doi: 10.1093/brain/awq113

55. Kreye J, Wenke NK, Chayka M, Leubner J, Murugan R, Maier N, et al. Human cerebrospinal fluid monoclonal n-methyl-D-aspartate receptor autoantibodies are sufficient for encephalitis pathogenesis. *Brain* (2016) 139(Pt 10):2641–52. doi: 10.1093/brain/aww208

56. Suh-Lailam BB, Haven TR, Copple SS, Knapp D, Jaskowski TD, Tebo AE. Anti-NMDA-receptor antibody encephalitis: performance evaluation and laboratory experience with the anti-NMDA-receptor IgG assay. *Clin Chim Acta* (2013) 421:1–6. doi: 10.1016/j.cca.2013.02.010

57. Geis C, Planagumà J, Carreño M, Graus F, Dalmau J. Autoimmune seizures and epilepsy. *J Clin Invest* (2019) 129(3):926–40. doi: 10.1172/JCI125178

58. Dalmau J, Tüzün E, Wu H, Masjuan J, Rossi JE, Voloschin A, et al. Paraneoplastic anti-N-methyl-D-aspartate receptor encephalitis associated with ovarian teratoma. *Ann Neurol* (2007) 61(1):25–36. doi: 10.1002/ana.21050

59. Bien CG, Vincent A, Barnett MH, Becker AJ, Blümcke I, Graus F, et al. Immunopathology of autoantibody-associated encephalitides: clues for pathogenesis. *Brain* (2012) 135(Pt 5):1622–38. doi: 10.1093/brain/aws082

60. Zuliani L, Graus F, Giometto B, Bien C, Vincent A. Central nervous system neuronal surface antibody associated syndromes: review and guidelines for recognition. *J Neurol Neurosurg Psychiatry* (2012) 83(6):638–45. doi: 10.1136/jnnp-2011-301237

61. Huang X, Fan C, Wu J, Ye J, Zhan S, Song H, et al. Clinical analysis on anti-N-methyl-D-aspartate receptor encephalitis cases: Chinese experience. *Int J Clin Exp Med* (2015) 8(10):18927–35.

62. Nosadini M, Mohammad SS, Ramanathan S, Brilot F, Dale RC. Immune therapy in autoimmune encephalitis: a systematic review. *Expert Rev Neurother* (2015) 15(12):1391–419. doi: 10.1586/14737175.2015.1115720

63. Tha-In T, Bayry J, Metselaar HJ, Kaveri SV, Kwekkeboom J. Modulation of the cellular immune system by intravenous immunoglobulin. *Trends Immunol* (2008) 29(12):608–15. doi: 10.1016/j.it.2008.08.004

64. Rubtsov AV, Rubtsova K, Fischer A, Meehan RT, Gillis JZ, Kappler JW, et al. Toll-like receptor 7 (TLR7)-driven accumulation of a novel $CD11c^+$ b-cell population is important for the development of autoimmunity. *Blood* (2011) 118(5):1305–15. doi: 10.1182/blood-2011-01-331462

65. Isnardi I, Ng Y-S, Menard L, Meyers G, Saadoun D, Srdanovic I, et al. Complement receptor 2/CD21- human naive b cells contain mostly autoreactive unresponsive clones. *Blood* (2010) 115(24):5026–36. doi: 10.1182/blood-2009-09-243071

66. Sachinidis A, Xanthopoulos K, Garyfallos A. Age-associated b cells (ABCs) in the prognosis, diagnosis and therapy of systemic lupus erythematosus (SLE). *Mediterr J Rheumatol* (2020) 31(3):311–8. doi: 10.31138/mjr.31.3.311

67. Simard J-C, Cesaro A, Chapeton-Montes J, Tardif M, Antoine F, Girard D, et al. S100A8 and S100A9 induce cytokine expression and regulate the NLRP3 inflammasome *via* ROS-dependent activation of NF-κB(1*.). PloS One* (2013) 8(8):e72138. doi: 10.1371/journal.pone.0072138

68. Brandum EP, Jørgensen AS, Rosenkilde MM, Hjortø GM. Dendritic cells and CCR7 expression: An important factor for autoimmune diseases, chronic inflammation, and cancer. *Int J Mol Sci* (2021) 22(15):8340. doi: 10.3390/ijms22158340

69. Moschovakis GL, Bubke A, Friedrichsen M, Ristenpart J, Back JW, Falk CS, et al. The chemokine receptor CCR7 is a promising target for rheumatoid arthritis therapy. *Cell Mol Immunol* (2019) 16(10):791–9. doi: 10.1038/s41423-018-0056-5

70. Miller TW, Soto-Pantoja DR, Schwartz AL, Sipes JM, DeGraff WG, Ridnour LA, et al. CD47 receptor globally regulates metabolic pathways that control resistance to ionizing radiation. *J Biol Chem* (2015) 290(41):24858–74. doi: 10.1074/jbc.M115.665752

71. Peñaloza HF, Olonisakin TF, Bain WG, Qu Y, van der Geest R, Zupetic J, et al. Thrombospondin-1 restricts interleukin-36γ-Mediated neutrophilic inflammation during pseudomonas aeruginosa pulmonary infection. *mBio* (2021) 12(2):e03336-20. doi: 10.1128/mBio.03336-20

72. Kothur K, Wienholt L, Mohammad SS, Tantsis EM, Pillai S, Britton PN, et al. Utility of CSF Cytokine/Chemokines as markers of active intrathecal inflammation: Comparison of demyelinating, anti-NMDAR and enteroviral encephalitis. *PloS One* (2016) 11(8):e0161656. doi: 10.1371/journal.pone.0161656

frontiers | Frontiers in Immunology

TYPE Original Research
PUBLISHED 13 December 2022
DOI 10.3389/fimmu.2022.1041284

EDITED BY
Jing Ni,
Anhui Medical University, China

REVIEWED BY
Xulong Zhang,
Capital Medical University, China
Huw Lewis,
GlaxoSmithKline, United Kingdom

*CORRESPONDENCE
Cheng Xiao
xc2002812@126.com
Tingting Deng
ttdeng1983@163.com

SPECIALTY SECTION
This article was submitted to Autoimmune and Autoinflammatory Disorders : Autoimmune Disorders, a section of the journal Frontiers in Immunology

RECEIVED 10 September 2022
ACCEPTED 28 November 2022
PUBLISHED 13 December 2022

CITATION
Geng Q, Cao X, Fan D, Gu X, Zhang Q, Zhang M, Wang Z, Deng T and Xiao C (2022) Diagnostic gene signatures and aberrant pathway activation based on m6A methylation regulators in rheumatoid arthritis.
Front. Immunol. 13:1041284.
doi: 10.3389/fimmu.2022.1041284

Diagnostic gene signatures and aberrant pathway activation based on m6A methylation regulators in rheumatoid arthritis

Qishun Geng[1,2], Xiaoxue Cao[1,2], Danping Fan[3], Xiaofeng Gu[4], Qian Zhang[4], Mengxiao Zhang[2], Zheng Wang[5], Tingting Deng[2*] and Cheng Xiao[1,2,6*]

[1]China-Japan Friendship Hospital (Institute of Clinical Medical Sciences), Chinese Academy of Medical Sciences and Peking Union Medical College, Beijing, China, [2]Institute of Clinical Medical Sciences, China-Japan Friendship Hospital, Beijing, China, [3]Beijing Key Laboratory of Research of Chinese Medicine on Prevention and Treatment for Major Diseases, Experimental Research Center, China Academy of Chinese Medical Sciences, Beijing, China, [4]Biotechnology Research Institute, Chinese Academy of Agricultural Sciences, Beijing, China, [5]Laboratory for Bone and Joint Diseases, RIKEN Center for Integrative Medical Sciences, Tokyo, Japan, [6]Department of Emergency, China-Japan Friendship Hospital, Beijing, China

Purpose: Rheumatoid arthritis (RA) is a chronic autoimmune disease (AD) characterized by persistent synovial inflammation, bone erosion and progressive joint destruction. This research aimed to elucidate the potential roles and molecular mechanisms of N6-methyladenosine (m6A) methylation regulators in RA.

Methods: An array of tissues from 233 RA and 126 control samples was profiled and integrated for mRNA expression analysis. Following quality control and normalization, the cohort was split into training and validation sets. Five distinct machine learning feature selection methods were applied to the training set and validated in validation sets.

Results: Among the six models, the LASSO_λ-1se model not only performed better in the validation sets but also exhibited more stringent performance. Two m6A methylation regulators were identified as significant biomarkers by consensus feature selection from all four methods. IGF2BP3 and YTHDC2, which are differentially expressed in patients with RA and controls, were used to predict RA diagnosis with high accuracy. In addition, IGF2BP3 showed higher importance, which can regulate the G2/M transition to promote RA-FLS proliferation and affect M1 macrophage polarization.

Conclusion: This consensus of multiple machine learning approaches identified two m6A methylation regulators that could distinguish patients with RA from controls. These m6A methylation regulators and their target genes may provide insight into RA pathogenesis and reveal novel disease regulators and putative drug targets.

KEYWORDS

rheumatoid arthritis, N6-methyladenosine, IGF2BP3, cell cycle, M1 macrophages

Introduction

Rheumatoid arthritis (RA) is a chronic autoimmune disease (AD) characterized by tumour-like hyperplasia of synovial tissue, persistent synovial inflammation, bone erosion and progressive joint destruction (1). RA usually occurs in middle-aged women. Currently, we attribute the development of RA to genetic and environmental factors, such as smoking, obesity, stress, neurodepression, and female hormones. Patients with RA have a higher risk of developing malignancies than the general population (2). Recently, the management of clinical symptoms and complications in RA patients has received increasing attention from medical workers (3, 4). An in-depth understanding of the mechanisms underlying RA occurrence and development can help to detect RA and its complications earlier so that measures can be taken to control the development and reduce the activity of the disease.

Previous studies have shown that T/B lymphocytes, macrophages, fibroblast-like synoviocytes (FLSs) and other cells are involved in the pathogenesis of RA (5). Activated FLSs in synovial tissue exacerbate the inflammatory response by secreting proinflammatory factors, chemokines and cell adhesion molecules, which can recruit additional immune cells to synovial tissue (6). Although the pathogenesis of RA remains incompletely elucidated, immune cells and FLSs undoubtedly play a crucial role in the progressive joint destruction and inflammatory response (7). Therefore, studying strategies to inhibit the proliferation and migration of FLSs and the inflammatory response in RA is highly important for elucidating the disease mechanism and developing treatments.

The study of epigenetics, especially RNA modifications, is a hotspot in life science research. Recently, with the development of the first RNA N6-methyladenosine (m6A) map by Cornell University and the discovery of its ubiquity in mRNA, transcriptional modification has gradually become the focus of the biomedical community (8). Among RNA modifications, m6A accounts for the largest proportion of base modifications in mRNAs and functions to regulate RNA stability, protein synthesis and translation; stem cell stress responses, cytotoxic stress responses; and mRNA export (9, 10). Currently, the known m6A methylation regulators consist of eight writers (METTL3, METTL14, WTAP, KIAA1429, RBM15, RBM15B, CBLL1 and ZC3H13), two readers (FTO and ALKBH5) and thirteen erasers (YTHDF1, YTHDF2, YTHDF3, YTHDC1, YTHDC2, HNRNPC, HNRNPA2B1, IGF2BP1, IGF2BP2, IGF2BP3, FMR1, ELAVL1 and LRPPRC) (11). Previous studies have shown that these regulators are involved in biological processes (BPs) such as cell differentiation and apoptosis and immune regulation, which are closely related to cancers and immune diseases (12–14). However, few studies have addressed the regulatory mechanism of m6A in RA, and more attention is needed.

In this study, we selected 19 m6A methylation regulators with expression data in the GSE12021, GSE55235, GSE55457, GSE55584, GSE77298 and GSE153105 datasets. Based on five distinct supervised machine learning approaches, we assessed the potential of these m6A methylation regulators as diagnostic tools by creating binary predictive classification models and assessing their accuracy. Then, by analysing the target genes and pathways of the m6A methylation regulators, we gained a further understanding of the roles of m6A methylation regulators in the pathogenesis of RA (Figure 1). This study is of great significance for elucidating the potential roles and molecular mechanisms of m6A methylation regulators in RA and for exploring new RA biomarkers.

Materials and methods

Dataset collection and processing

Data for 384 samples were accessed *via* the Gene Expression Omnibus (GEO) repository (Supplementary Table 1). The data from GSE12021, GSE55235, GSE55457 and GSE55584 were retrieved from the Affymetrix$^{®}$ GPL96 platform (Human Genome U133A Array), and the data from GSE77298 and GSE153105 were retrieved from the Affymetrix$^{®}$ GPL570 platform (Human Genome U133 Plus 2.0 Array). The raw

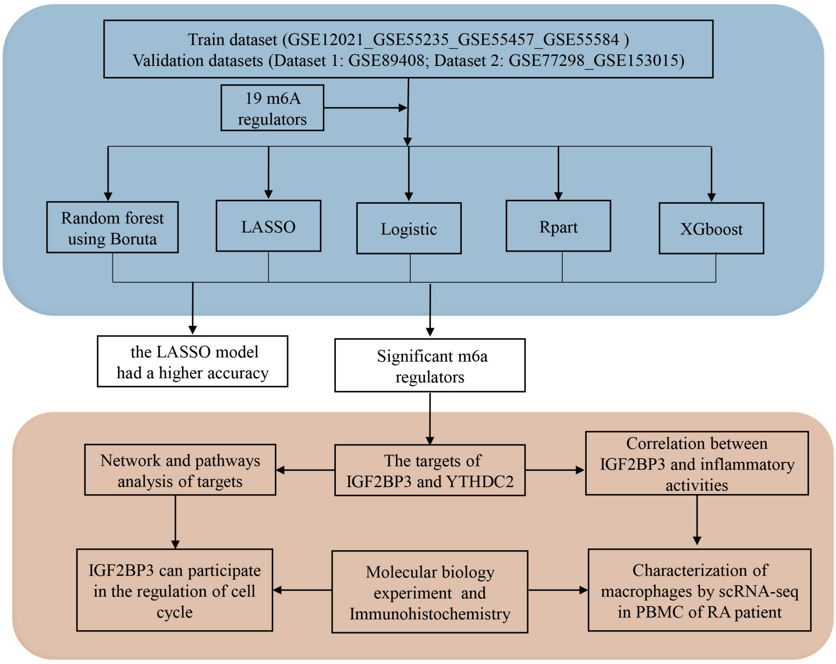

FIGURE 1
Diagram of the study.

data from the Affymetrix® platforms were processed *via* the robust multiarray averaging (RMA) algorithm implemented in the Affy package. After removal of batch effects with the ComBat algorithm, the training dataset was generated by combining the GEO datasets from the Affymetrix® GPL96 platform. Validation dataset 1 was generated by combining the GEO datasets from the Affymetrix® GPL570 platform. GSE89408 (platform: GPL1154) was considered validation dataset 2. In this research, for comparison with the RA group, we defined healthy individuals and patients with osteoarthritis (OA) as the control group.

The samples in GSE12021, GSE55235, GSE55457, GSE55584, GSE77298 and GSE153105 were extracted from synovial tissues. The samples in GSE90081 were taken from peripheral blood mononuclear cells (PBMCs). To investigate the relationship between IGF2BP3 expression and M1 macrophages, single-cell RNA sequencing (scRNA-seq) data from the GSE159117 dataset were analysed.

Cell lines and cell transfection

RA-FLSs were isolated from RA synovium. The cells were maintained in Dulbecco's modified Eagle's medium (DMEM) (Gibco, Grand Island, NY, USA) supplemented with 15% foetal bovine serum (FBS) (Thermo, USA) and cultured at 37°C in 5% CO_2 and saturated humidity. The ethics committee of China-Japan Friendship Hospital approved the research (approval number 2021-153-K111).

To silence the expression of IGF2BP3, an IGF2BP3 siRNA (siIGF2BP3) and a control siRNA (siNC) were chemically synthesized by Tsingke Biotechnology Co., Ltd (Beijing, China) and transfected into RA-FLSs and RAW 264.7 cells. The siIGF2BP3 target sequences are shown below: human si-IGF2BP3, 5'- GCAAAGGATT CGGAAACTT -3'; mouse si-Igf2bp3, 5'- GGAGGUGCUGGAUAGUUUACU -3'. JetPRIME® Transfection Reagent was used for cell transfection (Polyplus Transfection, USA).

Random forest optimization using boruta

Boruta has high feature variable selection accuracy in biological data. We used the default settings in the Boruta package (v7.0.0) to evaluate variable importance with 300 iterations (15). After 300 iterations, the confirmed variables were identified. Then, these confirmed variables selected by Boruta were used to construct a random forest model by using the caret package (v.6.0-92). After tuning and modelling, the final selected model was obtained and used to determine whether the subjects were RA patients or non-RA patients.

Regression partition tree

Rpart is a commonly used decision tree modelling method with a good visualization effect and straightforward results. We used the Rpart (v4.1-15) package to build a classification tree model. To avoid overfitting, some rules with weak classification and descriptive abilities were removed to improve the prediction accuracy. The classification tree model was optimized based on the minimum Xerror value, and the optimal classification tree model was used to determine whether the subjects were RA patients or non-RA patients.

Least absolute shrinkage and selection operator

LASSO has the advantage of preserving subset shrinkage and is a biased estimator for dealing with data with complex collinearity. Lasso allows a more refined model to be obtained by constructing a penalty function such that some coefficients are compressed and some coefficients are set to zero (16). LASSO-penalized logistic regression was performed with the glmnet package (version 4.1-4), which then calculated two automatic λ values—one that minimizes the binomial deviance and one representing the largest λ that is still within 1 standard error of the minimum binomial deviance. Both λ values (λ-min=0.02395, λ-1se=0.09203) were selected and used to refit the model, which resulted in a stricter penalty that allowed us to reduce the number of covariates even further than with the former λ. A probability threshold of > 0.5 was used to determine whether the subjects were RA patients or non-RA patients.

Extreme gradient boosting

XGBoost is an extreme gradient boosting algorithm that ranks features from most important to least important and has been used very effectively in diverse classification problems. Based on the default parameters, we used the XGBoost package (version 1.6.0.1) to build the final model for disease diagnosis and rank the features by importance. Features contributing to more than a 5% improvement in accuracy to their branches were selected as ‘important’ (17). The trained model was used to determine whether the subjects were RA patients or non-RA patients.

Logistic regression

Logistic regression is a machine learning method used to solve binary classification problems to estimate the likelihood of an event. The glmnet package (version 4.1-4) was used to build the final model for disease diagnosis, which was used to determine whether the subjects were RA patients or non-RA patients.

Pathway analysis

M6A2Target (http://m6a2target.canceromics.org/) is a comprehensive database for determining the target genes of writers, erasers and readers (WERs) of m6A modification. It integrates highly confidential targets validated by low-throughput experiments and potential targets with binding evidence indicated by high-throughput sequencing or inferred from m6A WER perturbation followed by high-throughput sequencing. The gene targets of the more important m6A regulators in disease diagnosis were inferred using m6A2Target (18). Then, ClueGO (version 3.0.3) was used for BP functional annotation analysis of the gene targets (19). The clusterProfiler package (version 4.2.2), a universal enrichment tool for interpreting omics data, was used for functional enrichment analysis.

scRNA-seq analysis

First, we imported the H5 file and converted the data to a Seurat object. Then, with the Seurat (version 4.1.1) package, data quality control and clustering were performed on the PBMC population. Each cell subset was annotated based on the celldex package (version 1.4.0).

Real-time qPCR analysis and western blot analysis

RNA isolation and RT–qPCR analysis were carried out according to previous studies (20). β-actin served as an internal control. The sequences of the primers used in the experiment are as follows. Human IGF2BP3: 5′- TCGAGG CGCTTTCAGGTAAA-3′ (forward), 5′- AAACTATCCAGCA CCTCCCAC-3′ (reverse). Mouse Igf2bp3: 5′- CCTGGTGA AGACGGGCTAC-3′ (forward), 5′- TCAACTTCCATCGGTT TCCCA-3′ (reverse).

Protein extraction and Western blot analysis were carried out according to previous studies (20). The primary antibodies included rabbit anti-IGF2BP3 (1:1000, Proteintech, Chicago, USA), anti-CCNB1 (1:1000, Shanghai, China) and anti-C-Myc (1:2,000, Cell Signaling Technology, Beverly, MA, USA). Band densities on autoradiograms were densitometrically quantified (Quantity One software; Bio-Rad), with GAPDH serving as the internal control.

Cell viability assay and cell cycle analysis

The cell viability assay was performed 24 h after transfection of siNC and siIGF2BP3 with a CCK-8 kit from Beyotime (Beijing, China). After transfection, cells were plated in 96-well dishes at a concentration of 5×10^3 cells/well and cultured in DMEM containing 15% FBS for cell attachment. Cell viability was measured with CCK-8 reagent following the manufacturer's protocol at the indicated time points (24, 48 and 72 h).

Cell cycle analysis was performed 48 h after transfection of siNC and siIGF2BP3. Cells were washed twice with ice-cold PBS, harvested, and fixed with 70% ethanol at 4°C overnight. Then, the cells were stained with a Cell Cycle and Apoptosis Analysis Kit (Beyotime, Beijing, China) at 37°C for 30 minutes and detected by flow cytometry (Becton-Dickinson, San Jose, CA, USA). Cell cycle distributions were analysed with ModFit LT 3.1 software (verity Software House, Inc., Topsham, ME, USA).

Flow cytometric analysis and enzyme linked immunosorbent assay

Analysis was performed 48 h after transfection of siNC and iIGF2BP3. After 6h of LPS (100ng/ml) stimulation, cells were collected and washed with PBS. Subsequently, the cells were directly surface stained using anti-CD86 antibodies (Biolegend, California, USA) for 20 min at 4°C. Signals were detected by flow cytometry (Becton-Dickinson, San Jose, CA, USA). Data analysis was conducted with FlowJo software version 10.0 (Tree Star, Inc., Ashland, OR, USA).

After transfection and stimulation, the cell supernatant was collected. According to the protocol of Mouse TNF-alpha ELISA Kit (ABclonal, Wuhan, China), the content of TNF-α in cell supernatant was detected.

Immunohistochemistry

The synovium tissues of six RA patients and six OA patients are obtained from China-Japan Friendship Hospital. Sample processing and data analysis were performed as previously described (20). The ethics committee of China-Japan Friendship Hospital approved the research (approval number 2021-153-K111).

Statistical analyses

Statistical analyses were performed using GraphPad Prism Software (GraphPad Software, San Diego, CA) and R version 4.0.4 software (Institute for Statistics and Mathematics, Vienna, Austria; https://www.r-project.org). We used a leave-one-out (LOO) cross-validation approach to evaluate the performance of the classifiers in the training set. Student's t test was used for comparisons between groups. Measurement data are expressed as the means ± standard deviations, and $P< 0.05$ indicates statistical significance.

Results

Performance of RA classification approaches using the m6A regulators

Considering the important role of m6A methylation regulators in tumour and immune disease progression, we used a public dataset to comprehensively explore the importance of 19 m6A methylation regulators for RA diagnosis. Based on the expression levels of these 19 m6A methylation regulators, a disease diagnosis model (RA *vs*. non-RA) was constructed using five different machine learning methods: random forest optimization using Boruta, Rpart, LASSO, XGBoost and logistic regression. The cross-validation performance in the training set is presented in Supplementary Table 2. The accuracy and AUC of all models except for the Rpart model were greater than 0.8. To compare the performance of each machine learning method, we observed the performance of each model as a classifier in the validation sets. The performance of each machine learning method in the validation sets was also variable (Tables 1, 2; Figures 2A-F). In validation dataset 1, the logistic regression model and LASSO_λ-min model had the highest AUC (0.90), but the LASSO_λ-min model had a higher accuracy (0.901). The Rpart model had the lowest AUC (0.8). In validation dataset 2, the LASSO_λ-min model and LASSO_λ-1se model had the highest accuracy (0.89) and AUC (0.88). Among the models, the Rpart model had the poorest performance. In addition, the number of m6A methylation regulators selected by each machine learning method differed, with Boruta selecting the most (14 regulators) and the Rpart model selecting just one regulator. Considering the performance of each machine learning method in the validation sets and the number of regulators that it selects in the models, the LASSO_λ-1se model not only performed better in the validation sets but also exhibited more stringent in variable screening. These results indicate that the LASSO_λ-1se model has good clinical application value and practicality. Therefore, we further compared the performance of the LASSO_λ-1se model in whole blood samples and calculated an AUC value of 0.83 (Figure 2G), further suggesting that the LASSO_λ-1se model has clinical application prospects in blood-based diagnosis of RA.

TABLE 1 Model performance of the six classifiers in validation set 1: A random forest wrapper (Boruta), LASSO_λ-min, LASSO_λ-1se, logistic regression, regression partition trees (Rpart) and extreme gradient boosting (XGBoost).

	Random forest	LASSO_min	LASSO_1se	Logistic	Rpart	XGBoost
Regulators selected by model, n	14	11	4	13	1	5
Best threshold	0.481 (0.22,0.829)	0.520 (0.28,0.961)	1.280 (0.26,0.895)	-293.891 (0.3,0.934)	0.5014 (0.24,0.829)	0.903 (0.22,0.809)
Sensitivity	0.78	0.72	0.74	0.7	0.76	0.78
Specificity	0.8289	0.961	0.8947	0.9342	0.8289	0.8092
Positive predictive value	0.6	0.8571	0.6981	0.7778	0.5938	0.5735
Negative predictive value	0.9197	0.9125	0.9128	0.9045	0.913	0.9179
Acuracy (95%)	0.8168 (0.7565~0.8676)	0.901 (0.8512-0.9385)	0.8564 (0.8004-0.9017)	0.8762 (0.8227-0.9183)	0.812 (0.7511-0.8633)	0.802 (0.7403-0.8546)
AUC (95%)	0.811 (0.735-0.888)	0.895 (0.841-0.948)	0.89 (0.830-0.944)	0.899 (0.847-0.95)	0.794 (0.728-0.861)	0.853 (0.792-0.914)

The more important m6A methylation regulators in the RA classification

Different candidate biomarkers were selected by these multivariable machine learning methods. However, biomarkers often have equal accuracy and importance (17). Considering the poorest performance of the Rpart model, we focused on the overlapping m6A methylation regulators selected by the different machine learning methods, including of random forest optimization using Boruta, LASSO, XGBoost and logistic regression (Figure 3A; Supplementary Table 3). Two of the overlapping m6A methylation regulators were selected by every model: IGF2BP3 and YTHDC2. The expression levels of the 19 m6A methylation regulators were further compared in the training dataset. The expression levels of IGF2BP3 and YTHDC2 were significantly different in RA and non-RA patients (Figure 3B). More importantly, based on transcript levels, IGF2BP3 and YTHDC2 also performed well in the diagnosis of RA in the training set (Figure 3C), with AUC values of 0.85 and 0.75, respectively. In addition, when the Boruta (Figure 3D), Rpart (Figure 3E) and XGBoost (Figure 3F) algorithms were used to calculate the importance of the 19 m6A methylation regulators, IGF2BP3 and YTHDC2 were ranked high; and IGF2BP3 has the highest importance.

Pathway and network analysis of the IGF2BP3 and YTHDC2 targets

To investigate the novel roles that these m6A methylation regulators play in RA and examine the related pathways, we predicted their target genes using m6A2Target. IGF2BP3 and YTHDC2 had 287 predicted gene targets in total (Supplementary Table 4); IGF2BP3 had 16 verified targets and 190 predicted targets, and YTHDC2 had 9 verified targets and 77 predicted targets. Based on the predicted gene targets, KEGG pathway enrichment analysis was performed using the ClusterProfiler package (version 4.2.2) to analyse the signalling pathways in which IGF2BP3 and YTHDC2 participate. These predicted gene targets were highly enriched in the following functions and pathways: MYC_TARGETS_V1, E2F_TARGETS, G2M_CHECKPOINT, MITOTIC_SPINDLE, ESTROGEN_RESPONSE_LATE, ALLOGRAFT_REJECTION, OXIDATIVE_PHOSPHORYLATION, DNA_REPAIR, UNFOLDED_PROTEIN_RESPONSE, MYC_TARGETS_V2, and

TABLE 2 Model performance of the six classifiers in validation set 2: A random forest wrapper (Boruta), LASSO_λ-min, LASSO_λ-1se, logistic regression, regression partition trees (Rpart) and extreme gradient boosting (XGBoost).

	Random forest	LASSO_min	LASSO_1se	Logistic	Rpart	XGBoost
Regulators selected by model, n	14	11	4	13	1	5
Best threshold	0.693 (0.273,0.778)	-2.229 (0.273,0.944)	-1.588 (0.273,0.944)	-7331.730 (0.091,0.472)	NA	0.007 (0.273,0.556)
Sensitivity	0.7273	0.7273	0.7273	0.9091	1	0.7273
Specificity	0.7778	0.9444	0.9444	0.4722	0	0.5556
Positive predictive value	0.5	0.8	0.8	0.3448	0.234	0.3333
Negative predictive value	0.9032	0.9189	0.9189	0.9444	NA	0.8696
Acuracy (95%)	0.766 (0.6197, 0.877)	0.8936 (0.769,0.9645)	0.8936 (0.769,0.9645)	0.5745 (0.4218-0.7174)	0.234 (0.123-0.3803)	0.5957 (0.4427-0.7363)
AUC (95%)	0.782 (0.641-0.923)	0.884 (0.780-0.988)	0.881 (0.778-0.984)	0.707 (0.525-0.889)	0.5	0.667 (0.518-0.816)

NA, Not Applicable.

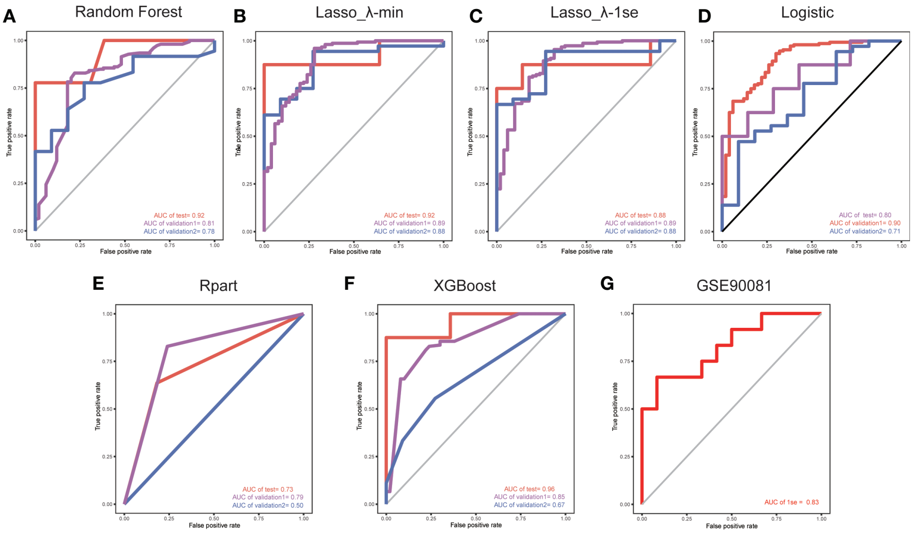

FIGURE 2
ROC curves for validation set 1 and validation set 2, with the model trained on a separate set. The red lines indicate the models trained using a LOO cross-validation approach across the training set. We used five methods to develop models based on the training set: **(A)** a random forest wrapper (Boruta), **(B)** LASSO_λ-min, **(C)** LASSO_λ-1se, **(D)** logistic regression, **(E)** regression partition trees (Rpart) and **(F)** extreme gradient boosting (XGBoost). **(G)** ROC curve of the LASSO_λ-1se model in whole blood samples.

so on (Figure 3G). Interestingly, BP functional enrichment analysis carried out by ClueGO showed that the predicted gene targets participated mainly in processes related to the mitotic cell cycle, translation, cytoplasmic translation and regulation of DNA metabolic processes, which play key roles in the occurrence and development of RA (Figure 3H). To better demonstrate the relationship between IGF2BP3 and YTHDC2, their predicted gene targets and the related pathways, Cytoscape (version 3.9.0) was used to construct a network, which indicated that IGF2BP3 and YTHDC2 can regulate the G2M_CHECKPOINT, MYC_TARGETS_V1 and E2F_TARGETS pathways by acting on CDK1, CDK2, MYC and other targets (Figure 4A).

The importance of IGF2BP3 in the viability and cell cycle of RA-FLSs

Based on the pathway enrichment analysis results, IGF2BP3 and YTHDC2 are closely related to the cell cycle. But, when the Boruta (Figure 3D), Rpart (Figure 3E) and XGBoost (Figure 3F) algorithms were used to calculate the importance of the 19 m6A methylation regulators, IGF2BP3 ranked first, while YTHDC2 ranked lower. In addition, compared with YTHDC2, IGF2BP3 performed better in the diagnosis of RA (Figure 3C). Therefore, we further explored the regulatory effects of IGF2BP3 on the viability and cell cycle of RA-FLSs through molecular biology experiments. To explore the effects of IGF2BP3 on RA-FLSs, siRNAs were transfected into RA-FLSs. The transfection results were confirmed by RT–qPCR and Western blotting and indicated that the siRNA had a good knockdown efficiency (Figures 4B-D). Then, we studied the effect of IGF2BP3 on RA-FLS viability *in vitro*. The CCK-8 cytotoxicity assay revealed that downregulation of IGF2BP3 in RA-FLSs significantly reduced cell viability compared to that of the control cells ($P < 0.05$, Figure 4E). The cell proliferation assay also revealed that downregulation of IGF2BP3 in RA-FLSs significantly inhibited cell proliferation compared to that of the control cells ($P < 0.05$, Figure 4F). In addition, the flow cytometry results showed that low expression of IGF2BP3 had an obvious effect on the G2/M transition. Compared with that in the control group, the proportion of G2/M-phase cells in the siIGF2BP3 group was significantly increased ($P < 0.05$, Figures 4G, H). We also measured the expression of cell cycle-related proteins, showing that siIGF2BP3 reduced CCNB1 and C-MYC expression (Figures 4C, D). In addition, the expression of IGF2BP3 in synovial tissues of patients with OA and RA was detected. We found that IGF2BP3 expression was significantly higher in synovial tissues of RA patients, further affirming the importance of IGF2BP3 in the progression of RA (Figure 4I).

Correlation between IGF2BP3 expression and inflammatory activity

Increasing evidence suggests that m6A modification is an important regulator of immune response regulatory mechanisms and inflammatory regulatory networks (21). To identify the IGF2BP3-associated immune signature in RA, we determined the immune scores and the proportions of immune cells with

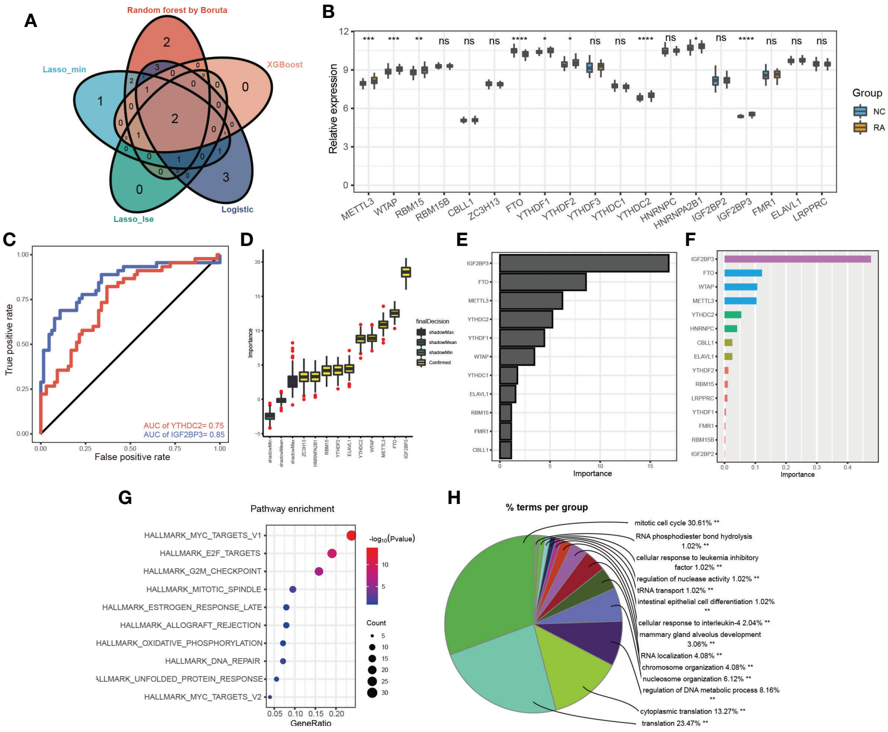

FIGURE 3
The more important m6A methylation regulators in RA classification. **(A)** Venn diagram of the m6A methylation regulators selected by the different machine learning methods; **(B)** the expression levels of 19 m6A methylation regulators in the training dataset; **(C)** the ROC curves for IGF2BP3 and YTHDC2 in the training set; the importance of the 19 m6a methylation regulators calculated by the Boruta **(D)**, Rpart **(E)** and XGBoost **(F)** algorithms; KEGG pathway **(G)** and BP **(H)** enrichment analyses of the gene targets of IGF2BP3 and YTHDC2 *p < 0.05, **p < 0.01, ***p < 0.001, ****p < 0.0001, ns (p > 0.05).

xCell (22). First, we found significant differences in the immune score between the two groups, with higher immune scores in the RA patient group than in the NC patient group ($P < 0.001$; Figure 5A). Then, the proportions of immune cells were compared between the two groups. There were significant differences in the proportions of many immune cells, including interdigitating cells (IDCs), natural killer T (NKT) cells, classical dendritic cells (cDCs), macrophages, mast cells, M2 macrophages, Th2 cells, M1 macrophages, and myocytes (Figures 5B, C). Among these cell types, we focused on M1 macrophages because of the closely relationship between M1 macrophages and RA (23). The proportion of M1 macrophages in RA patients was significantly higher than that in control patients. In addition, we investigated the relationship between the proportion of M1 macrophages and the expression level of IGF2BP3 in RA patients and found that they were strongly correlated (Figure 5D). IGF2BP3 expression was also significantly correlated with the expression of M1 macrophage markers, including IL1A, CD86 and TLR2 (Figures 5E-G). Therefore, we thought that IGF2BP3 can participate in the regulation of M1 macrophage polarization.

To further explore the effect of IGF2BP3 on M1 macrophage polarization, we transfected RAW264.7 cells with Igf2bp3-siRNA or NC-siRNA (negative control). RT–qPCR and Western blot analysis were performed to confirm the efficiency of gene silencing and indicated that the siRNA had a good knockdown efficiency (Figures 5H, I). Forty-eight hours after transfection, RAW264.7 cells were treated with 100 ng/ml LPS for 24 h. Then, by measuring the expression of the surface marker (CD86) of M1 macrophages by flow cytometry, we found that the expression level of CD86 in siIgf2bp3 cells was significantly lower than that in siNC cells (Figure 5J). In addition, we further detected the content of TNF-a in the cell supernatant, which indicated that the content of TNF-a in siIgf2bp3 cells was lower than that in siNC cells (Figure 5K). These results further validated the involvement of IGF2BP3 in the regulation of M1 macrophage polarization.

scRNA-seq revealed the relationship between IGF2BP3 expression and M1 macrophage polarization

To further characterize the relationship between IGF2BP3 expression and M1 macrophage polarization, we conducted scRNA-seq in the GSE159117 dataset. Fourteen cell clusters were

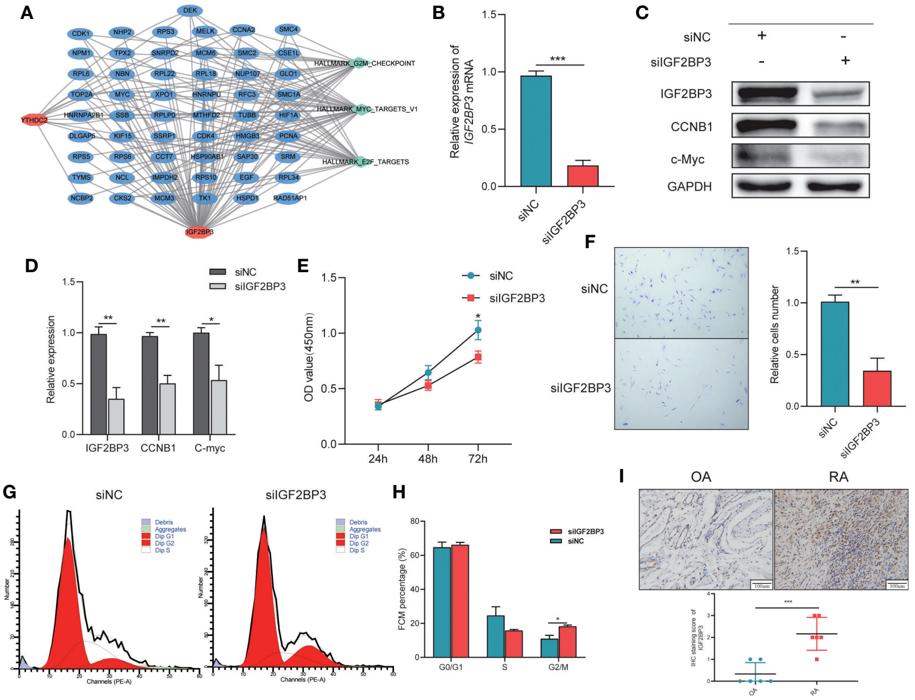

FIGURE 4
The importance of IGF2BP3 in the Viability and Cell Cycle of RA-FLSs. **(A)** The network connecting IGF2BP3 and YTHDC2 pathways and other targets; **(B)** RT–qPCR results showing the efficient depletion of IGF2BP3 expression in RA-FLSs compared with siNC-transfected RA-FLSs; **(C, D)** Expression of IGF2BP3, c-MYC and CCNB1 in RA-FLSs after transfection; **(E)** The proliferative ability of RA-FLSs after transfection was evaluated by a CCK-8 assay; **(F)** Representative images (left) and histograms (right) showing the effect of siFN1 on the cell proliferation of RA-FLSs; **(G, H)** Flow cytometric analysis was used to evaluate the cell cycle distribution of RA-FLSs after transfection; **(I)** Representative IHC staining and IHC staining score of Synovial tissues. **p* < 0.05, ***p* < 0.01, ****p* < 0.001.

obtained by a combined uniform manifold approximation and projection (UMAP) analysis (Figure 6A). SingleR (version 1.8.1) was used to identify 7 cell types: B cells, CD4$^+$ T cells, CD8$^+$ T cells, dendritic cells, monocytes, NK cells and T cells (Figure 6B). IGF2BP3 was found to be expressed mainly on monocytes and B cells among the seven cell types (Figure 6C; clusters 4 and 8). Macrophages are the main type of cell derived from monocytes. Therefore, the relationship between CD86 and IGF2BP3 expression was explored in monocytes, and CD86 and IGF2BP3 were found to have a coexpression trend (Figure 6D). Then, we preliminarily investigated the expression of several macrophage markers in monocytes. M1 macrophage markers (including CD86, IL1B, TLR2 and TLR4) were significantly upregulated but M2 macrophage markers (including MSR1, IL10, MMP14 and VEGFA) were downregulated in monocytes (Figure 6E).

Discussion

RA is a systemic autoimmune disorder affecting the synovium of peripheral joints. The average life expectancy of patients with RA is shorter than that of the overall population, and patients with active disease are also prone to develop various diseases, such as cardiovascular disease, pulmonary interstitial disease, and osteoporosis (24, 25). m6A methylation has been shown to be associated with tumours, neurological disorders, metabolic diseases, ADs, viral infections and so on (26). Mutations in the genes encoding m6A methylation regulators are closely associated with inflammation-related diseases, and changes in their expression levels have been observed in RA (21, 27). Therefore, exploring the diagnostic value and mechanism of m6A methylation regulators in RA is highly important for the effective treatment of RA and the improvement of its prognosis.

In this study, based on m6A methylation regulator expression profiles and consensus machine learning approaches, we constructed binary predictive classification models and assessed their accuracy. Among the models, the LASSO_λ-1se model not only performed better in the validation sets but also exhibited more stringent performance. In addition, the LASSO_λ-1se model exhibited better performance in whole blood samples, further suggesting that the LASSO_λ-1se model has application prospects in blood-based diagnosis of RA. Our primary aim in this study was to investigate the relationships between m6A methylation regulators and clinical classification rather than to develop a

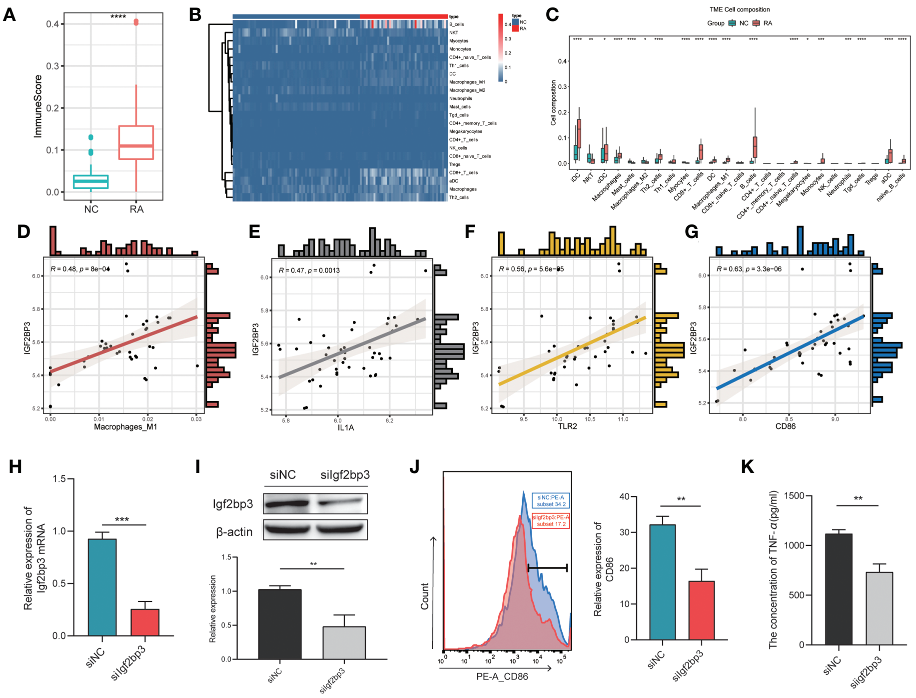

FIGURE 5

Correlation between IGF2BP3 expression and inflammatory activity. Immune scores **(A)** and proportions of immune cells **(B, C)** in the RA and NC groups; **(D)** correlation between the proportion of M1 macrophages and the expression level of IGF2BP3 in RA patients; **(E–G)** correlations between the expression levels of M1 macrophage markers (IL1A, CD86 and TLR2) and IGF2BP3; **(H, I)** RT–qPCR and Western blot analysis confirmed the efficiency of gene silencing; **(J)** expression level of CD86 in RAW264.7 cells after transfection; **(K)** the content of TNF-α in RAW264.7 cells after transfection. *$p < 0.05$, **$p < 0.01$, ***$p < 0.001$, ****$p < 0.0001$.

diagnostic tool. Combined with the comprehensive imaging, haematological and gene expression analyses, a diagnostic model of RA has more clinical diagnostic significance and higher accuracy. This study lays the foundation for the establishment of diagnostic tools by evaluating the accuracy of m6A methylation regulators for clinical classification and affirms the potential diagnostic value of m6A methylation regulators. A limitation of this study is the relatively small sample size used to generate and validate the m6A methylation regulators as classifiers. This may have led to overfitting of some models and thus to overestimation of effect sizes. To alleviate this issue, we validated each model's diagnostic value in different published datasets and validated potentially interesting genes using molecular biology experiments. To develop accurate diagnostic tools, further studies based on larger retrospective and prospective clinical cohorts are warranted.

Machine learning provides an unbiased approach to predict patient status while also offering the potential to identify previously unknown interactions and identify novel biological signatures (17, 28). Our approach of investigating the biomarkers identified through multiple feature selection techniques increases confidence in the generation of reproducible biomarker panels and reduces the number of m6A methylation regulators for potential clinical investigation. The selected m6A methylation regulators (IGF2BP3 and YTHDC2) ranked highly in variable importance. Previous studies have shown that IGF2BP3 and YTHDC2 are closely related to cell proliferation and migration, cell cycle regulation, and immune and inflammatory regulation (29–31). In addition, the study by Fan et al. confirmed that IGF2BP3 not only was significantly overexpressed in RA synovial tissue but also might be a therapeutic target of thymopentin (TP) during RA treatment (32). The above literature reports provide supporting evidence that IGF2BP3 and YTHDC2, identified here as candidate biomarkers, may be associated with disease progression in RA, validating our machine learning approach to identify relevant m6A methylation regulator biomarkers. Pathway enrichment analysis showed that IGF2BP3 and YTHDC2 were involved in the regulation of MYC_TARGETS_V1, E2F_TARGETS, G2M_CHECKPOINT and other pathways, which are closely related to the cell cycle. In particular, IGF2BP3 not only was ranked highest by the Boruta, Rpart and XGBoost methods but also showed better diagnostic value in the training set. We focused on verifying the relationship between IGF2BP3 expression and the cell cycle and further confirmed that IGF2BP3 may affect the proliferation of

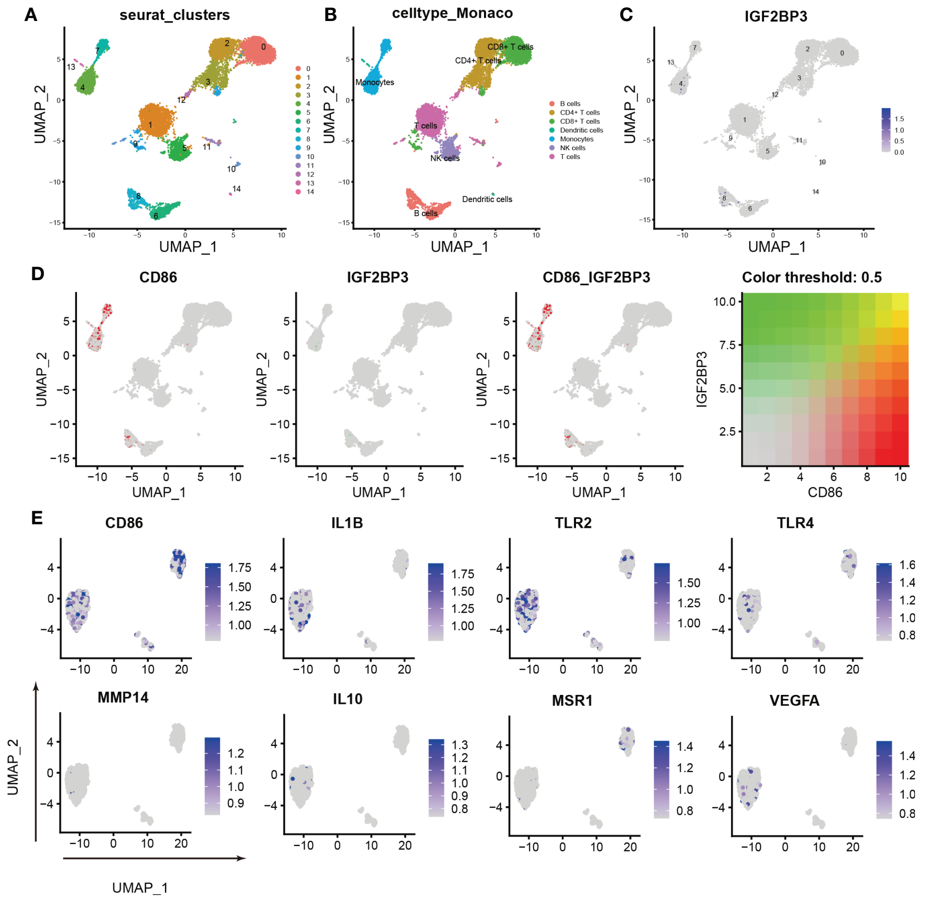

FIGURE 6
Characterization of macrophages by scRNA-seq in PBMCs. **(A)** UMAP plot showing the sources of the collected scRNA-seq cell samples; **(B)** UMAP plot showing 14 cell clusters of 7 cell types in the collected samples; **(C)** UMAP plot showing the IGF2BP3 expression level in the 14 cell clusters; **(D)** scRNA-seq analysis revealed the correlation between IGF2BP3 and CD86 expression; **(E)** UMAP plot showing the expression levels of M1 and M2 macrophage markers.

RA-FLSs by regulating the G2/M transition. Inflammatory cells can secrete a large amount and variety of inflammatory factors and chemokines, leading to the activation of more FLSs and promoting their proliferation and migration, thereby further aggravating the inflammatory response in the disease (33). Among these immune cell types, M1 macrophages attracted our attention for the following three reasons: 1. M1 macrophages, also called classical macrophages, can produce proinflammatory cytokines and thus have potent microbicidal ability but are also prone to cause tissue destruction and exacerbate inflammatory processes that are detrimental to health (34); 2. The synovial lining of RA patients exhibits cell proliferation and a large amount of inflammatory cell infiltration in the interstitium. The degree of inflammatory infiltration determines the severity of the disease (35). 3. Among the inflammatory cells involved in RA, macrophages play a key role. These cells can polarize into different phenotypes and mediate the immune/inflammatory response as well as the repair phase when possible (23). By analysing the relationship between IGF2BP3 expression and M1 macrophage polarization in RA RNA-seq datasets and scRNA-seq datasets, we found that IGF2BP3 plays a crucial role in M1 macrophage polarization. CD86, also known as B7.2, is a T lymphocyte activation antigen with a molecular weight of 80 kD and can be expressed in dendritic cells, monocytes, T lymphocytes and B lymphocytes. Previous studies have shown that CD86 can serve as a marker to elevate the proportion of M1 macrophages (36, 37). By measuring the expression of CD86 by flow cytometry, we found that the expression level of CD86 in siIgf2bp3 RAW264.7 cells was significantly lower than that in siNC RAW264.7 cells. Yang et al. also showed that siIGF2BP3 can reduce MALAT1 expression, thereby impeding p38/mitogen-activated protein kinase phosphorylation and macrophage-mediated inflammation (38). These studies all further verified that IGF2BP3 can regulate macrophage polarization and inflammatory exacerbation during RA progression.

The RA diagnostic model established based on public databases had good performance in multiple validation sets. However, further validation of the diagnostic value of established models in larger independent cohorts is warranted before considering their clinical application. Furthermore, we used five machine learning feature selection algorithms on data from patient synovial tissue to identify two signature m6A methylation regulators in RA, and our findings may provide a new RA marker and reveal novel disease mechanisms. Moreover, this study is the first to confirm the effect of the m6A reader protein IGF2BP3 on the progression of RA and verify its biological function through bioinformatics analysis and molecular biology experiments. This study provides new ideas and strategies for the early diagnosis and targeted therapy of RA and has theoretical innovation prospects. Moreover, it provides theoretical support for the discovery of new markers and drug targets for RA.

Data availability statement

The original contributions presented in the study are included in the article/Supplementary Material. Further inquiries can be directed to the corresponding authors.

Ethics statement

The ethics committee of China-Japan Friendship Hospital approved the research (approval number 2021-153-K111). Written informed consent for participation was not required for this study in accordance with the national legislation and the institutional requirements.

Author contributions

QG and CX designed and wrote the manuscript. The other authors participated in discussions associated with the manuscript and revised the manuscript. All authors contributed to the article and approved the submitted version.

Funding

This study was financially supported by the National Natural Science Foundation of China (U22A20374) and the National Natural Science Foundation of China (Grant number 82073677).

Conflict of interest

The authors declare that the research was conducted in the absence of any commercial or financial relationships that could be construed as a potential conflict of interest.

Publisher's note

Supplementary material

The Supplementary Material for this article can be found online at: https://www.frontiersin.org/articles/10.3389/fimmu.2022.1041284/full#supplementary-material

SUPPLEMENTARY TABLE 1
Sample information from the different public datasets.

SUPPLEMENTARY TABLE 2
The leave-one-out (LOO) cross-validation performance in the training set a random forest wrapper (Boruta), LASSO_λ-min, LASSO_λ-1se, logistic regression, regression partition trees (Rpart) and extreme gradient boosting (XGBoost).

SUPPLEMENTARY TABLE 3
The selected genes in different machine learning methods.

SUPPLEMENTARY TABLE 4
The gene targets of IGF2BP3 and YTHDC2.

References

1. Scott DL, Wolfe F, Huizinga TW. Rheumatoid arthritis. *Lancet* (2010) 376 (9746):1094–108. doi: 10.1016/s0140-6736(10)60826-4

2. Smolen JS. Rheumatoid arthritis primer - behind the scenes. *Nat Rev Dis Primers* (2020) 6(1):32. doi: 10.1038/s41572-020-0168-y

3. Serhal L, Lwin MN, Holroyd C, Edwards CJ. Rheumatoid arthritis in the elderly: Characteristics and treatment considerations. *Autoimmun Rev* (2020) 19 (6):102528. doi: 10.1016/j.autrev.2020.102528

4. Xi X, Ye Q, Fan D, Cao X, Wang Q, Wang X, et al. Polycyclic aromatic hydrocarbons affect rheumatoid arthritis pathogenesis *via* aryl hydrocarbon receptor. *Front Immunol* (2022) 13:797815. doi: 10.3389/fimmu.2022.797815

5. Scherer HU, Häupl T, Burmester GR. The etiology of rheumatoid arthritis. *J Autoimmun* (2020) 110:102400. doi: 10.1016/j.jaut.2019.102400

6. Aihaiti Y, Song Cai Y, Tuerhong X, Ni Yang Y, Ma Y, Shi Zheng H, et al. Therapeutic effects of naringin in rheumatoid arthritis: Network pharmacology and experimental validation. *Front Pharmacol* (2021) 12:672054. doi: 10.3389/fphar.2021.672054

7. Kim EK, Kwon JE, Lee SY, Lee EJ, Kim DS, Moon SJ, et al. IL-17-mediated mitochondrial dysfunction impairs apoptosis in rheumatoid arthritis synovial fibroblasts through activation of autophagy. *Cell Death Dis* (2017) 8(1):e2565. doi: 10.1038/cddis.2016.490

8. Zhao BS, Roundtree IA, He C. Post-transcriptional gene regulation by mRNA modifications. *Nat Rev Mol Cell Biol* (2017) 18(1):31–42. doi: 10.1038/nrm.2016.132

9. Sun T, Wu R, Ming L. The role of m6A RNA methylation in cancer. *BioMed Pharmacother* (2019) 112:108613. doi: 10.1016/j.biopha.2019.108613

10. Zhang H, Shi X, Huang T, Zhao X, Chen W, Gu N, et al. Dynamic landscape and evolution of m6A methylation in human. *Nucleic Acids Res* (2020) 48 (11):6251–64. doi: 10.1093/nar/gkaa347

11. Zhang X, Zhang S, Yan X, Shan Y, Liu L, Zhou J, et al. m6A regulator-mediated RNA methylation modification patterns are involved in immune microenvironment regulation of periodontitis. *J Cell Mol Med* (2021) 25 (7):3634–45. doi: 10.1111/jcmm.16469

12. Yin H, Zhang X, Yang P, Zhang X, Peng Y, Li D, et al. RNA m6A methylation orchestrates cancer growth and metastasis *via* macrophage reprogramming. *Nat Commun* (2021) 12(1):1394. doi: 10.1038/s41467-021-21514-8

13. Chong W, Shang L, Liu J, Fang Z, Du F, Wu H, et al. m(6)A regulator-based methylation modification patterns characterized by distinct tumor microenvironment immune profiles in colon cancer. *Theranostics* (2021) 11 (5):2201–17. doi: 10.7150/thno.52717

14. Fan D, Xia Y, Lu C, Ye Q, Xi X, Wang Q, et al. Regulatory role of the RNA N (6)-methyladenosine modification in immunoregulatory cells and immune-related bone homeostasis associated with rheumatoid arthritis. *Front Cell Dev Biol* (2020) 8:627893. doi: 10.3389/fcell.2020.627893

15. Kursa MB, Rudnicki WR. Feature selection with the boruta package. *J Stat Softw* (2010) 36(11):1–13. doi: 10.18637/jss.v036.i11

16. McEligot AJ, Poynor V, Sharma R, Panangadan A. Logistic LASSO regression for dietary intakes and breast cancer. *Nutrients* (2020) 12(9):2652. doi: 10.3390/nu12092652

17. Errington N, Iremonger J, Pickworth JA, Kariotis S, Rhodes CJ, Rothman AM, et al. A diagnostic miRNA signature for pulmonary arterial hypertension using a consensus machine learning approach. *EBioMedicine* (2021) 69:103444. doi: 10.1016/j.ebiom.2021.103444

18. Deng S, Zhang H, Zhu K, Li X, Ye Y, Li R, et al. M6A2Target: a comprehensive database for targets of m6A writers, erasers and readers. *Brief Bioinform* (2021) 22(3):bbaa055. doi: 10.1093/bib/bbaa055

19. Bindea G, Mlecnik B, Hackl H, Charoentong P, Tosolini M, Kirilovsky A, et al. ClueGO: a cytoscape plug-in to decipher functionally grouped gene ontology and pathway annotation networks. *Bioinformatics* (2009) 25(8):1091–3. doi: 10.1093/bioinformatics/btp101

20. Geng QS, Yang MJ, Li LF, Shen ZB, Wang LH, Zheng YY, et al. Over-expression and prognostic significance of FATP5, as a new biomarker, in colorectal carcinoma. *Front Mol Biosci* (2021) 8:770624. doi: 10.3389/fmolb.2021.770624

21. Wu S, Li XF, Wu YY, Yin SQ, Huang C, Li J. N(6) -methyladenosine and rheumatoid arthritis: A comprehensive review. *Front Immunol* (2021) 12:731842. doi: 10.3389/fimmu.2021.731842

22. Aran D, Hu Z, Butte AJ. xCell: digitally portraying the tissue cellular heterogeneity landscape. *Genome Biol* (2017) 18(1):220. doi: 10.1186/s13059-017-1349-1

23. Tardito S, Martinelli G, Soldano S, Paolino S, Pacini G, Patane M, et al. Macrophage M1/M2 polarization and rheumatoid arthritis: A systematic review. *Autoimmun Rev* (2019) 18(11):102397. doi: 10.1016/j.autrev.2019.102397

24. Lin YJ, Anzaghe M, Schülke S. Update on the pathomechanism, diagnosis, and treatment options for rheumatoid arthritis. *Cells* (2020) 9(4):880. doi: 10.3390/cells9040880

25. Aletaha D, Smolen JS. Diagnosis and management of rheumatoid arthritis: A review. *JAMA* (2018) 320(13):1360–72. doi: 10.1001/jama.2018.13103

26. Nombela P, Miguel-López B, Blanco S. The role of m(6)A, m(5)C and Ψ RNA modifications in cancer: Novel therapeutic opportunities. *Mol Cancer* (2021) 20(1):18. doi: 10.1186/s12943-020-01263-w

27. Zhang M, Song J, Yuan W, Zhang W, Sun Z. Roles of RNA methylation on tumor immunity and clinical implications. *Front Immunol* (2021) 12:641507. doi: 10.3389/fimmu.2021.641507

28. Neumann U, Riemenschneider M, Sowa JP, Baars T, Kälsch J, Canbay A, et al. Compensation of feature selection biases accompanied with improved predictive performance for binary classification by using a novel ensemble feature selection approach. *BioData Min* (2016) 9:36. doi: 10.1186/s13040-016-0114-4

29. Wang J, Tan L, Jia B, Yu X, Yao R, OUYang N, et al. Downregulation of m (6)A reader YTHDC2 promotes the proliferation and migration of malignant lung cells *via* CYLD/NF-κB pathway. *Int J Biol Sci* (2021) 17(10):2633–51. doi: 10.7150/ijbs.58514

30. Yang Z, Wang T, Wu D, Min Z, Tan J, Yu B. RNA N6-methyladenosine reader IGF2BP3 regulates cell cycle and angiogenesis in colon cancer. *J Exp Clin Cancer Res* (2020) 39(1):203. doi: 10.1186/s13046-020-01714-8

31. Wan W, Ao X, Chen Q, Yu Y, Ao L, Xing W, et al. METTL3/IGF2BP3 axis inhibits tumor immune surveillance by upregulating N(6)-methyladenosine modification of PD-L1 mRNA in breast cancer. *Mol Cancer* (2022) 21(1):60. doi: 10.1186/s12943-021-01447-y

32. Fan D, Liu B, Gu X, Zhang Q, Ye Q, Xi X, et al. Potential target analysis of triptolide based on transcriptome-wide m(6)A methylome in rheumatoid arthritis. *Front Pharmacol* (2022) 13:843358. doi: 10.3389/fphar.2022.843358

33. Du H, Zhang X, Zeng Y, Huang X, Chen H, Wang S, et al. A novel phytochemical, DIM, inhibits proliferation, migration, invasion and TNF-α induced inflammatory cytokine production of synovial fibroblasts from rheumatoid arthritis patients by targeting MAPK and AKT/mTOR signal pathway. *Front Immunol* (2019) 10:1620. doi: 10.3389/fimmu.2019.01620

34. Kalkman HO, Feuerbach D. Antidepressant therapies inhibit inflammation and microglial M1-polarization. *Pharmacol Ther* (2016) 163:82–93. doi: 10.1016/j.pharmthera.2016.04.001

35. Buckley CD, Ospelt C, Gay S, Midwood KS. Location, location, location: how the tissue microenvironment affects inflammation in RA. *Nat Rev Rheumatol* (2021) 17(4):195–212. doi: 10.1038/s41584-020-00570-2

36. Dong P, Ma L, Liu L, Zhao G, Zhang S, Dong L, et al. CD86$^+$/CD206$^+$, diametrically polarized tumor-associated macrophages, predict hepatocellular carcinoma patient prognosis. *Int J Mol Sci* (2016) 17(3):320. doi: 10.3390/ijms17030320

37. Väyrynen JP, Haruki K, Lau MC, Väyrynen SA, Zhong R, Dias Costa A, et al. The prognostic role of macrophage polarization in the colorectal cancer microenvironment. *Cancer Immunol Res* (2021) 9(1):8–19. doi: 10.1158/2326-6066.Cir-20-0527

38. Yang L, Fu J, Han X, Zhang C, Xia L, Zhu R, et al. Hsa_circ_0004287 inhibits macrophage-mediated inflammation in an N(6)-methyladenosine-dependent manner in atopic dermatitis and psoriasis. *J Allergy Clin Immunol* (2022) 149 (6):2021–33. doi: 10.1016/j.jaci.2021.11.024

frontiers | Frontiers in Immunology

TYPE Review
PUBLISHED 04 January 2023
DOI 10.3389/fimmu.2022.1076700

OPEN ACCESS

EDITED BY
Mojca Frank Bertoncelj,
BioMed X Institute, Germany

REVIEWED BY
Muriel Elhai,
University Hospital Zürich, Switzerland
Margaret Chang,
Division of Immunology, Boston Children's Hospital and Harvard Medical School, United States

*CORRESPONDENCE
Fan Zhang
✉ fan.3.zhang@cuanschutz.edu

SPECIALTY SECTION
This article was submitted to Autoimmune and Autoinflammatory Disorders: Autoimmune Disorders, a section of the journal Frontiers in Immunology

RECEIVED 21 October 2022
ACCEPTED 01 December 2022
PUBLISHED 04 January 2023

CITATION
Fritz D, Inamo J and Zhang F (2023) Single-cell computational machine learning approaches to immune-mediated inflammatory disease: New tools uncover novel fibroblast and macrophage interactions driving pathogenesis.
Front. Immunol. 13:1076700.
doi: 10.3389/fimmu.2022.1076700

Single-cell computational machine learning approaches to immune-mediated inflammatory disease: New tools uncover novel fibroblast and macrophage interactions driving pathogenesis

Douglas Fritz[1,2,3], Jun Inamo[2,3] and Fan Zhang[2,3]*

[1]Medical Scientist Training Program, University of Colorado School of Medicine, Aurora, CO, United States, [2]Division of Rheumatology, Department of Medicine, University of Colorado School of Medicine, Aurora, CO, United States, [3]Center for Health Artificial Intelligence, Department of Biomedical Informatics, University of Colorado School of Medicine, Aurora, CO, United States

Recent advances in single-cell sequencing technologies call for greater computational scalability and sensitivity to analytically decompose diseased tissues and expose meaningful biological relevance in individual cells with high resolution. And while fibroblasts, one of the most abundant cell types in tissues, were long thought to display relative homogeneity, recent analytical and technical advances in single-cell sequencing have exposed wide variation and sub-phenotypes of fibroblasts of potential and apparent clinical significance to inflammatory diseases. Alongside anticipated improvements in single cell spatial sequencing resolution, new computational biology techniques have formed the technical backbone when exploring fibroblast heterogeneity. More robust models are required, however. This review will summarize the key advancements in computational techniques that are being deployed to categorize fibroblast heterogeneity and their interaction with the myeloid compartments in specific biological and clinical contexts. First, typical machine-learning-aided methods such as dimensionality reduction, clustering, and trajectory inference, have exposed the role of fibroblast subpopulations in inflammatory disease pathologies. Second, these techniques, coupled with single-cell predicted computational methods have raised novel interactomes between fibroblasts and macrophages of potential clinical significance to many immune-mediated inflammatory diseases such as rheumatoid arthritis, ulcerative colitis, lupus, systemic sclerosis, and others. Third, recently developed scalable integrative methods have the potential to map cross-cell-type spatial interactions at the single-cell level while cross-tissue analysis with these models reveals shared biological mechanisms between disease contexts. Finally, these advanced computational omics approaches have the potential to be leveraged toward therapeutic strategies that target fibroblast-macrophage interactions in a wide variety of inflammatory diseases.

KEYWORDS

computational biology, machine learning, single-cell omics, spatial transcriptomics, immune-mediated inflammatory disease, rheumatoid arthritis, fibroblast-macrophage interaction

Introduction

Immune-mediated inflammatory diseases (IMIDs) are roughly categorized by abnormal or maladaptive inflammation of specific tissues within the human body and are thought to affect nearly 3% of the population (1). The increasing prevalence of IMID diseases such as inflammatory joint disease and inflammatory bowel disease and their respective subphenotypes has driven additional research into the genetic and immunogenomic mechanisms involved in their development, progression, and treatment (2, 3). Because of fibroblasts' ubiquity in the lining of interior surfaces of the human body and their role in mediating the extracellular matrix, fibroblasts have recently become an area of intense research and a key component of the study of IMIDs (4, 5).

Fibroblasts play a critical role in inflammatory disease by directing or suppressing the inflammatory cascade and repair at sites of injury or invasion through the release of cytokines and other effector molecules (6). In addition, bone and extracellular metabolic pathways are also involved in pathogenesis: activated fibroblasts produce receptor activator of NF-κB ligand (RANKL), which promotes differentiation of osteoclast precursors into bone-resorbing osteoclasts, leading to bone erosion in Rheumatoid Arthritis (RA) (7). They also produce metalloproteinases such as MMP-1 and MMP-3, which cause cartilage degradation. As a result, understanding these and other intercellular communications between fibroblasts and surrounding cell types is an area of rapid research and critical to understanding the microbiological contexts of IMID toward developing new drug targets (4, 8, 9). While the communications between fibroblasts and immune cells such as macrophages is a common focus of cancer research (10), applying this framework to the study of IMIDs has also proved consequential in determining an approach to treatment (11). However, these interactions are often highly tissue-specific and microenvironment-specific and require precise study using high-resolution single-cell multiomic technologies.

The challenge of mapping these cellular interactions in inflammatory microenvironments, then, becomes one that is highly dependent on advances in single-cell transcriptomics, single-cell multimodal techniques, and recent single-cell spatial transcriptomics (12, 13). While collecting omics data at the single-cell level has been commonly applied to discrete cellular suspensions *via* microfluidics (12, 14–17), collecting single-cell spatiotemporal data and prevailing tissue microenvironment intact has proved elusive and high-throughput techniques with these capabilities are hotly anticipated by the field (18). At present, technical resolution remains a challenge to mapping the complex tissue intercellular interactions thought to be pivotal toward IMID treatments, but this challenge is exacerbated by the enormous volumes of data that near-single cell omics technologies create. This review outlines how computational methods including machine learning and deep learning approaches are used to analyze high-dimensional data from existing single-cell technologies, which expand the capabilities and resolution of these experimental approaches to uncover novel pathways in fibroblasts. Then, this paper summarizes the computational approaches to cell-cell interactions that can be used to uncover these interactomes underlying IMIDs using single-cell transcriptomics and spatial transcriptomics, respectively. Further, opportunities and challenges of integrating single-cell profiles from multiple tissue sources to reveal shared and unique pathogenic pathways are described. Lastly, we explore the potential for developing therapeutic approaches that target pathogenic fibroblast and macrophage interactions.

Fibroblasts play important roles in different inflammatory disease tissue pathology

Long thought to be relatively homogeneous in nature, recent discoveries (18–22) have uncovered a likely vast number of fibroblast subpopulations with discrete markers that have been implicated in mediating inflammation and damage in different IMIDs (23–25). In RA synovial tissue, Zhang et al. analyzed the synovial tissues from patients with RA and osteoarthritis (OA) using a multi-technology-approach by integrating single-cell RNA-seq (scRNA-seq), mass cytometry, and bulk RNA-seq data to identify robust and biologically meaningful cell-state clusters (26). An integrative computational strategy was developed based on canonical correlation analysis (CCA) to align datasets from different technologies into a joint low-dimensional space by maximizing the correlation between them, which elucidated significant sublining fibroblast phenotypes, CD34+ (SC-F1), HLA-DRhi (SC-F2), and DKK3+ (SC-F3), and a type of CD55+ lining fibroblasts (SC-F4). In parallel, Croft et al. used single-cell transcriptomic analysis in a mouse model to untangle two pathologically distinct RA fibroblast subsets FAPα+THY1+ and FAPα+THY1-. Deletion of fibroblast-activation-protein-alpha-positive (FAPα^{+}) fibroblasts suppressed both inflammation and bone erosions in mouse models (27). Separate studies have revealed pathological functions of stromal cells in other IMID tissues, including the gut of Ulcerative Colitis (UC) (8), the ileum of Crohn's Disease (CD) (28), and the lungs of systemic sclerosis (29) patients, respectively. Interestingly, similar THY1+ fibroblasts are revealed in inflamed CD ileum, and an activated fibroblast phenotype with a strong cytokine-chemokine expression profile in this tissue may contribute to the resistance to anti-TNF therapy. In parallel, inflammatory fibroblasts that highly expressed IL11 and IL24, were identified at 189-fold levels in inflamed gut compared to non-inflamed/healthy gut; this phenotype also expressed cancer-associated fibroblast markers, including FAP and WNT2, indicating the important pathology underlying multiple disease contexts (8).

In these studies, several computational methods are used to facilitate the single-cell transcriptomic analysis to reveal fibroblast heterogeneity (Figure 1). In particular, dimensionality reduction techniques including principal component analysis (PCA) and non-linear tSNE are standard approaches to identify meaningful biological variation. Additionally, graph-based clustering techniques group fibroblasts with similar transcriptomic profiles together. To better account for non-linear geometry and time components in the single-cell data, trajectory inferences have been widely used to allocate and order cells into lineages as pseudotime gradients. Pseudotime reflects continuous changes in expression to quantitatively capture a biological progression, such as cell differentiation. Based on global topology theory, several computational methods have been developed, including Monocle, which is built based on DDRTree (Discriminative dimensionality reduction *via* learning a tree) (30, 31). To predict the future state of individual cells, RNA velocity algorithms (32) estimate the time derivative of the gene expression state by distinguishing unspliced and spliced mRNAs from single-cell transcriptomic data. These trajectory analyses have been deployed to analyze fibroblast lineages to reveal a NOTCH3 signaling gradient in RA synovial fibroblasts (33).

As the recent development of single-cell multimodal technologies, single-cell joint modelings are used to provide further insights into mesenchymal cell heterogeneity using single-cell multimodal data, including CITE-seq that quantifies gene and protein surface expressions simultaneously (34), single-cell multiome that profiles gene expression and open chromatin from the same cells, and spatial transcriptomics

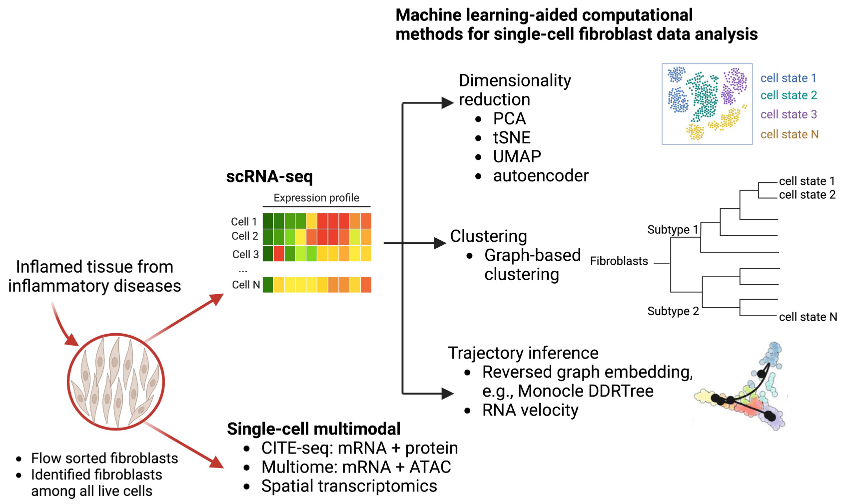

FIGURE 1
Computational machine learning algorithms that drive single-cell transcriptomics and other multimodal data analysis to study fibroblast heterogeneity. Disaggregated cells are sequenced by either multimodal technologies or scRNA-seq technologies to generate a large dataset of thousands of variables that can be modeled and analyzed *via* machine learning approaches. Graphical exploration of gene expression variation across cells can be done through clustering for dimensionality reduction. Continuous gene expression changes for specific cell differentiation processes can be modeled with trajectory inference.

(ST) that provides spatial information to the gene expression. Multimodal data integrations provide additional biological perspectives, through the combination of proteomics (CITE-seq), epigenetics (multiome), or spatial locations (ST), in addition to transcriptomics, which can reveal novel immunological or disease-driven insights. A very recent study with a collaborative effort from AMP (Accelerating Medicines Partnership) RA/SLE network used CITE-seq to reveal 10 distinct stromal populations and emphasized which of these populations are expanded in a particular patient group (35). Using three-dimensional spatial transcriptomics, Vickovic et al. uncovers colocalization of THY1+ fibroblast and synovial macrophages in seropositive RA synovium samples (36).

Single-cell transcriptomics-driven computational methods reveal predicted interactomes between fibroblasts and myeloid cells

Deciphering cell–cell communications from gene expression is an area of intensive research (37). Many computational methods have been developed based on ligand-receptor expression patterns between cell types, such as fibroblasts and myeloid cells (macrophages, monocytes, neutrophils, and dendritic cells). Examples of these techniques are: CellphoneDB (38), NicheNet (39), CellChat (40), and ICELLNET (41), each of which took a slightly different methodology to predict potential cell-cell interactions in scRNA-seq data (Figure 2A). CellphoneDB was first demonstrated (38), and has since been updated through multiple iterations of a ligand-receptor mapping tool (42). NicheNet incorporates prior knowledge on gene regulatory pathways to generate a biologically meaningful pathway that propagates the signal from a ligand, through receptors, signaling proteins, and transcriptional regulators to the targeted genes from cell types of interest. CellChat, on the other hand, uses network analysis, and identifies complex patterns in the data from skin or other tissues; while ICELLNET calculates a communication score to predict interactions and reveals hypothesized interactions that can be verified experimentally. In short, these cell-cell interaction prediction methods are widely used to prioritize putative interactions between fibroblasts and other immune cells, such as macrophages, from different disease contexts, including tumor (10), fibrosis (43), and cardiovascular disease (44). As fibroblasts and macrophages play indispensable roles in the tissue destruction of IMIDs, disentangling the fibroblast-myeloid interactions in each IMID disease context is still forthcoming (45). A recent single-cell driven research approach identified a MerTK+ macrophage phenotype in synovial tissues and revealed that a low frequency of this phenotype in RA remission was associated with increased risk of disease flare (46). Further examination of which pathogenic fibroblast phenotypes could interact with the MerTK+ or other inflammatory and anti-inflammatory macrophage phenotypes is needed. In another IMID, a single-cell transcriptomics and histopathology approach to inflammatory bowel disease (IBD)

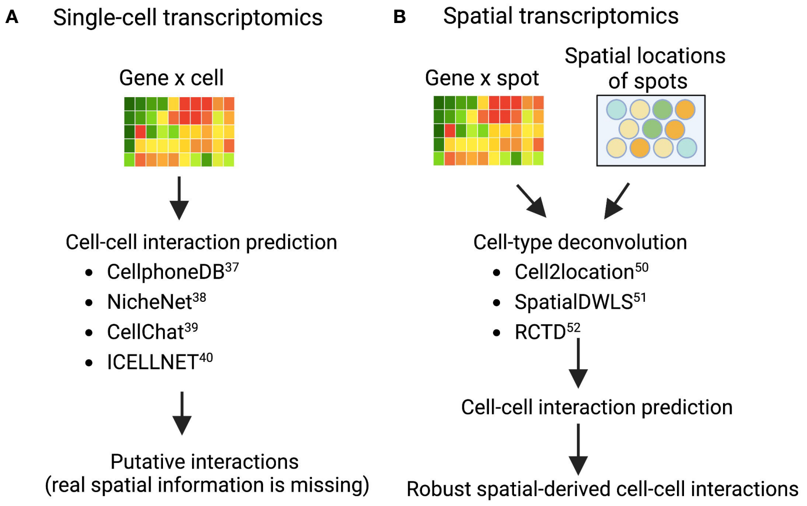

FIGURE 2
Validated computational packages to predict cell-cell interactions using **(A)** single-cell transcriptomics and **(B)** spatial transcriptomics, respectively Cell-cell interaction prediction algorithms **(A)** are quite adept at mapping interactions from single-cell transcriptomics where tissue architecture information was lost in sample preparation. As a result, interactions revealed in analysis are theoretical and merely suggest that cells co-located in the sample tissue. However, combining these interaction-prediction-algorithms with spatial cell-type deconvolution modeling **(B)**. The sample tissue's spatial architecture is conserved by modeling cells that are both co-locating in the tissue and interacting.

revealed an IL-1+ driven fibroblast-neutrophil interaction in a subset of patients with IBD that did not respond to therapies (47), which highlights another fibroblast-neutrophil IL-1 signaling pathway for ulcerating disease.

Novel computational approaches to spatial transcriptomics reveal spatial interactions across cell types

While CellPhoneDB and similar packages are useful for revealing interactomes in scRNA-seq data, decomposing the data spatially within tissues remains a challenge. Spatial Transcriptomics (ST) technology development and the improvement of its resolution enabled the identification of cross-cell type interactions from both gene expression co-varying patterns and spatial information. The widely used commercialized ST technologies include 10X Visium, Nanostring GeoMX, and single-molecule fluorescent *in situ* hybridization (smFISH)-based technology such as MERFISH commercialized by Vizgen (48, 49). These ST datasources require new computational algorithms to infer biologically meaningful findings and to spur further widespread adoption of these techniques across IMIDs.

Given the constraint of greater-than-single-cell resolution of many commercialized ST technologies, more than 16 computational methods have been developed to perform cell-type deconvolution for ST data to infer single-cell interactions (50). As a result (Figure 2B), Cell2location (51), SpatialDWLS (52), and RCTD (53) are particularly powerful approaches that perform cell-type deconvolution. Cell2location is developed to integrate scRNA-seq data from an adjacent tissue slice with the spatial information from the microarray, which can effectively identify the spatial co-occurrence of diverse cell types in complex tissues such as lymph nodes (51). SpatialDWLS adapts the idea of dampened weighted least squared to infer cell-type composition while minimizing the overall relative error rate. RCTD fits the raw counts using Poisson-based statistical model to leverage cell-type mixtures while accounting for artifact from sequencing platforms. Many groups have demonstrated that these techniques work well in tumors from the well-characterized organs such as brain (54, 55), but in some heterogeneous or not well-characterized tissue structures such as synovium and kidney tissues it remains to be evaluated whether these techniques can be deployed. Ongoing efforts from the AMP-AIM (Accelerating Medicines Partnership-Autoimmune and Immune-Mediated Diseases) network are actively testing multiple ST technologies on IMIDs disease tissues. We look forward to both the deployment of newer and higher-resolution techniques that might be better suited to these IMID tissue-structures and to further benchmarking of existing and forthcoming computational models. With these efforts, more in-depth spatial-aware interactions between fibroblasts and myeloid cells will be revealed using ST data with the assistance of more robust computational methods.

Cross-tissue single-cell integrative analysis reveals shared mechanisms

Recent developments of computational integration algorithms enable the cross-tissue, cross-disease comparisons for IMIDs to reveal shared mechanisms and pathways using single-cell datasets (Figure 3A). To facilitate unbiased integrative analysis, two major types of methods have been developed including joint clustering and reference mapping (Figures 3B, C). In joint clustering, batch correction methods, such as soft clustering-based mixed effect models (56), canonical correlation analysis (57), mutual nearest-neighbors and manifold learning (58), have been developed to enforce projecting the cells from different tissues, donors, and clinical cohorts into a joint low-dimensional embeddings (i.e. multiple variables captured on a 2D graph) (Figure 3B). Additionally, recent single-cell reference mapping methods, including PCA-based approaches, transfer learning, and autoencoder, enable an automatic way to map query cells to an existing reference with cell-type annotations (59–62) (Figure 3C). These offer a more efficient framework to compare query cell phenotypes with an existing cell reference. A recent study performed joint clustering analysis to reveal two shared pathogenic phenotypes of fibroblasts, a CXCL10+ CCL19+ inflammatory fibroblast phenotype localizing to a T cell enriched niche and a SPARC+ COL3A1+ fibroblast phenotype localizing to a perivascular niche, from four chronic inflammatory diseased tissues including lung, intestine, salivary gland, and synovium (63). Another study built fibroblast atlases using around 230,000 fibroblasts across 17 mouse tissues and revealed that many fibroblast transcriptional states were conserved between humans and mice (64). In parallel, we identified shared inflammatory macrophage phenotypes from five inflamed tissues, including synovium, ileum, colon, lung, and kidney (65). These recent cross-tissue single-cell computation-driven transformative research open new possibilities beyond well-known cell types and pathways.

However, key aspects of these techniques need to be validated to interpret single-cell integrative results more precisely regarding disease-specific implications. First, sufficient power is required to reveal statistical significance of associating single-cell results with clinical metrics and demographic features. A large-scale cohort with balanced disease and healthy controls and well characterized medications is ideal. Second, reproducible analysis of computational pipelines is sometimes neglected. For example, it remains largely under-explored whether the same common fibroblast phenotypes can be recapitulated in another clinical cohort. It is possible that the tissue-specific fibroblast phenotypes

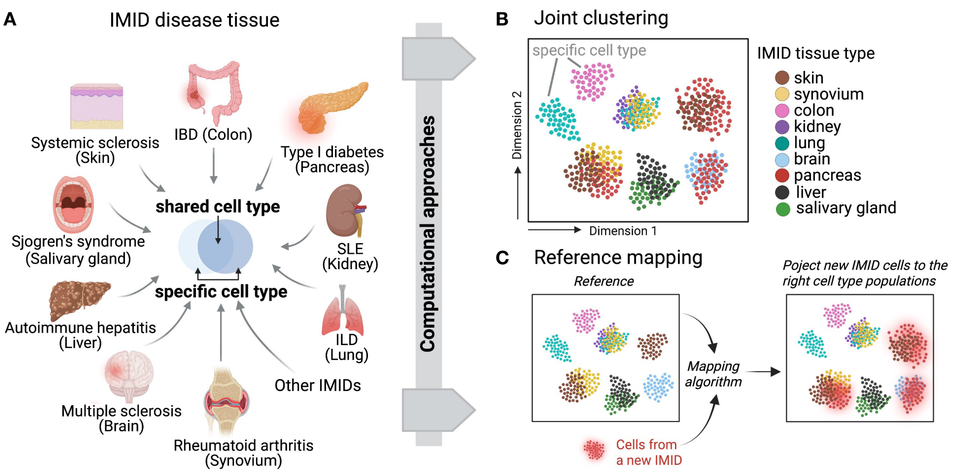

FIGURE 3

Across IMID single-cell integrative analysis. **(A)** Multiple IMIDs (organ systems) where inflammatory and pathogenic cells display both heterogeneity and similarity between tissue types and within disease contexts. Computational approaches can be deployed to disentangle the shared and specific pathways between IMIDs while also controlling for tissue heterogeneity. Two main computational frameworks include **(B)** integrative and joint clustering analysis and **(C)** reference mapping approach. **(B, C)** indicate the low-dimensional projections of cells across IMIDs.

found in a certain diseased context are actually due to unbalanced cell numbers in the cross-sample analysis. Yet, as an active computational and systems immunology area, we expect these computational machine learning algorithms and future developments will boost the transformative research to elucidate shared pathogenic pathways and treatment areas.

Opportunities for developing therapeutical strategies targeting fibroblast and macrophage interactions for inflammatory diseases

Remarkable recent advances in understanding the molecular pathogenesis of IMIDs have elucidated relevant pathophysiological pathways and therapeutic targets. Inhibition of TNF and IL6 signaling, for example, has shown some efficacy in treating various IMID contexts, including RA and ulcerative colitis (66–68). Similarly, in systemic sclerosis, in which fibroblasts and macrophages are deeply involved in the pathogenesis of lung damage, IL6 blockade delayed decline in key lung function measures compared with the placebo groups in a double-blind phase II randomized clinical trial (69, 70). Additionally, although strong evidence from experimental models and human data *in vivo* and *in situ* suggested potential of anti-IL17 blockade as a therapeutic target in RA (71, 72), psoriasis (73), and spondyloarthritis (74), strong efficacy for RA and other similar diseases has not shown in comparison to placebo (75). Thus, ineligible patients with IMIDs still suffer from progressive functional disability from a substantial burden of lifelong treatment—highlighting the existence of the remaining pathological molecular signatures and the urgent need to link them to targeted core-pathogenic phenotypes, such as mesenchymal and immune cell interactions at the site of inflammation.

A precise understanding of fibroblasts and macrophages, major tissue components in IMIDs, may promote the development of novel therapeutic targets. Key interactions based on the well-known pathways and new mechanisms revealed by single-cell computational omics are summarized in Figure 4. Fibroblasts and macrophages produce CSF1 (Colony Stimulating Factor 1) and PDGFs (platelet-derived growth factors), respectively, and bind to each other's receptors to promote survival, maintenance, and proliferation, forming a synergistic loop in a steady-state (76, 77) and upon activation (78, 79). In a radiation-induced pulmonary fibrosis model, depletion of tissue-infiltrating macrophages, but not alveolar macrophages, using a clinically available CSF1R neutralizing antibody ameliorated fibrosis (79). Similarly, Aran et al. demonstrated that inhibition of Pdgf-aa produced by the inflammatory macrophage identified by single-cell sequence suppressed fibroblast growth in bleomycin-induced lung fibrosis in mice (78). Accumulating evidence of clinical efficacy of inhibition of tyrosine-kinase, which is a downstream molecule of CSF1R and PDGFR, for IMIDs suggests that targeting the interactions between fibroblasts and macrophages are highly promising strategies towards individualized and targeted treatments of IMIDs (80–82). Using single-cell transcriptomics, Kuo et al. reported that a particular HBEGF (Heparin Binding EGF Like Growth Factor)+ inflammatory macrophage phenotype was induced by fibroblasts and TNF in RA synovium, subsequently promoted fibroblast

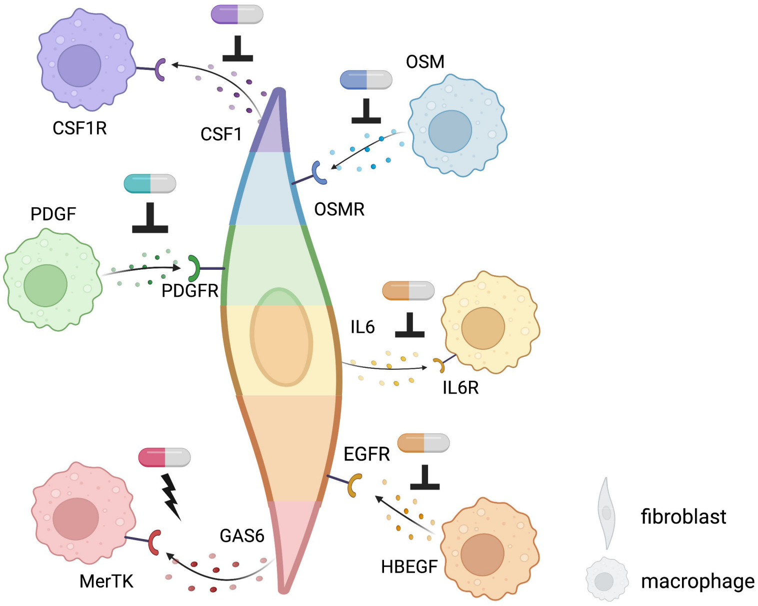

FIGURE 4
Potential targets of fibroblast-macrophage interacting revealed by single-cell computational methods using existing receptor-ligand pairs in IMIDs. Targets of novel therapeutics: potential sites of inhibition are indicated by an upside-down T while sites of activation are indicated by a lightning bolt. Different colors of each fibroblast and macrophage indicate different phenotypes of each cell type. Pill icons indicate potential, experimental, or existing therapeutics.

invasiveness (83). They also found that this interaction was inhibited by anti-EGFR (Epidermal Growth Factor Receptor) antibody, which decreased pathogenic fibroblast invasiveness in the destruction of cartilage and bone. Further experimental evidence and case reports support the potential of EGFR as a promising therapeutic target for RA (84–86).

In IBD, anti-TNF agents bring about clinical response in about two-thirds of patients, but around 30% of patients are resistant to treatment (87, 88). Using single-cell omics, inflammatory fibroblasts and inflammatory monocytes were identified to be expanded in inflamed colon lesion and expressed Oncostatin M (OSM) and OSM receptor (8), respectively, which is associated with anti-TNF response, suggesting that the inflammatory fibroblasts and monocytes might be implicated in OSM-mediated anti-TNF resistance (89). Methods that not only inhibit interactions but also exploit interactions with anti-inflammatory effects may be promising therapeutic targets. The addition of GAS6 from THY1+CXCL14+ sublining synovial fibroblasts, reduced proinflammatory cytokines produced by MerTK+ macrophages in synovial tissues of RA (46). On the flip side, GAS6 and MerTK are reported to be overexpressed in tumor which could promote tumorigenesis (90–92). It is necessary to clarify the difference between malignancy and inflammation in this pathway and to examine what route of administration, such as intra-articular injection, is appropriate for therapeutic targeting.

So far, no drugs targeting specifically fibroblasts have been approved by the U.S. Food and Drug Administration (FDA). Thus, identification of promising across cell-type interactome targets, such as fibroblasts and macrophages in inflammatory lesions, using single-cell technologies combined with powerful computational tools could lead to the development of effective therapeutics for IMIDs, as in the area of oncology (43). If markers characteristic of disease-specific cell types that play a central role in the pathogenesis utilizing single-cell high granular results can be identified, more accurate therapeutic agents can be developed to minimize the adverse event and improve precision medicine.

Future directions

Most of these computational methods described above can be generalized to many inflammatory disease studies. For example, t-SNE and UMAP are used widely for dimensionality reduction analysis for many IMID research projects. Additionally, techniques like graph-based clustering and trajectory analysis are umbrella classifications that are highly modified and adapted depending on data type and context. Yet, each computational method may have specific limitations derived from disease tissue (e.g., tissue disaggregation approaches) or technology (e.g., high dropout rates, non-single-cell resolution in the recent spatial transcriptomics) when applied across multiple IMID contexts. This review summarizes the most recent computational advancements and major novel disease-specific findings combined with cutting-edge single-cell techniques to IMIDs, so we expect more generalized applications of these interdisciplinary approaches along with computational machine learning algorithms can be adapted to more understudied IMIDs. Taking advantage of the power of these computational algorithms helps generate novel cell phenotype and highlight theoretical cell-cell interactions in humans. More in-depth functionally validations (e.g., knockout specific target, *in vivo* or *in vitro* stimulation) are needed, however, to determine the function mechanisms of these interactions and disease etiology in human and non-human models.

To develop personalized treatment for IMIDs, it is necessary to identify the cell-type that forms the core of the pathogenesis in stratified patient groups. For example, analysis of bulk RNA-seq from skin lesions from systemic sclerosis patients using cell-type deconvolution methods demonstrated that certain types of serum autoantibodies were associated with dysregulated molecular pathways as well a predictable abundance of fibroblasts and macrophages at the skin lesion (93). In RA, bulk RNA-seq studies defined three histological subgroups or "pathotypes": lympho-myeloid, diffuse-myeloid, and pauci-immune (94, 95). The myeloid signature is associated with response to TNF inhibition, while the pauci-immune group, predominated with fibroblasts, is associated with refractory to multi-drugs (94). This indicates that mesenchymal cell compartment is a key population for further study using higher-resolution technologies, such as single-cell omics, as it is unclear whether the specific high-granularity pathogenic subphenotypes underlying these pathotypes are targetable therapeutically.

More recently, Zhang et al. demonstrated that in-depth stratification of RA synovial biopsies based on single-cell multimodal integrative analysis combined with covarying neighborhood analysis can associate cellular heterogeneity to stratified RA synovial phenotypes. Specifically, RA synovial heterogeneity was classified into six distinct subgroups or "cell type abundance phenotypes" (CTAPs) based on major cell-type abundance (35): 1) endothelial, fibroblast, and myeloid cells, 2) fibroblasts, 3) T cells and fibroblasts, 4) T and B cells, 5) T and myeloid cells, and 6) myeloid cells. Three of the CTAPs have associations with fibroblast and their immune interaction abundances suggesting that different patients, even with the same disease, have different tissue phenotypes at the core of their pathology, and accordingly, different molecules to be targeted for therapy. Notably, CTAPs are associated with disease-relevant cytokines, histology, and serology metrics, which indicates that the CTAP classification schema could guide appropriate targeted therapeutic treatment.

Yet, knowledge in this area is limited by the availability of biopsies from inflamed lesions derived from IMID patients. To address this, better single-cell power analysis of study design, demographic information, and technical confounders need to be considered to strengthen biologically relevant findings. Moreover, identifying the right computational and machine learning approaches is critical for downstream analysis. For example, more reproducible single-cell analytical methods with open-source code and well-benchmarked machine learning methods regarding stability and accuracy need to be provided and further improved. Given the complexity of the immunological questions, new computational and disease-driven tools using AI approaches may provide further insights into disease etiology. In all, comprehensive characterization of cellular and molecular heterogeneity in inflamed lesions using single-cell computational machine learning approaches will enhance our understanding of disease heterogeneity, which will provide a promising way to stratify patient cohorts to optimize personalized therapies for IMIDs.

Author contributions

DF and FZ conceived of the idea for this review, compiled literature, and reviewed relevant manuscripts. DF led the writing of the manuscript as was supported by JI and FZ on particular subsections. JI and FZ lead figure design. All authors provided critical feedback and helped shape the research and manuscript. All authors contributed to the article and approved the submitted version.

Funding

DF is supported by National Research Service Award (NRSA) Institutional Research Training Grant (T32) GM008497; FZ is supported by PhRMA Foundation Faculty Starter Grant for Translational Medicine.

Acknowledgments

Figures were created with BioRender.com.

Conflict of interest

The authors declare that the research was conducted in the absence of any commercial or financial relationships that could be construed as a potential conflict of interest.

Publisher's note

References

1. Schett G, McInnes IB, Neurath MF. Reframing immune-mediated inflammatory diseases through signature cytokine hubs. *N Engl J Med* (2021) 385:628–39. doi: 10.1056/NEJMra1909094

2. Bach J-F. The effect of infections on susceptibility to autoimmune and allergic diseases. *N Engl J Med* (2002) 347:911–20. doi: 10.1056/NEJMra020100

3. F. Farrokhyar ET. Swarbrick e. a critical review of epidemiological studies in inflammatory bowel disease. *Scand J Gastroenterol* (2001) 36:2–15. doi: 10.1080/00365520150218002

4. Smith TJ. Insights into the role of fibroblasts in human autoimmune diseases. *Clin Exp Immunol* (2005) 141:388. doi: 10.1111/j.1365-2249.2005.02824.x

5. Glaros T, Larsen M, Li L. Macrophages and fibroblasts during inflammation, tissue damage and organ injury. *Front Biosci* (2009) 14. doi: 10.2741/3506

6. Buechler MB, Turley SJ. A short field guide to fibroblast function in immunity. *Semin Immunol* (2018) 35:48–58. doi: 10.1016/j.smim.2017.11.001

7. Smolen JS, Aletaha D, McInnes IB. Rheumatoid arthritis. *Lancet* (2016) 388:2023–38. doi: 10.1016/S0140-6736(16)30173-8

8. Smillie CS, Biton M, Ordovas-Montanes J, Sullivan KM, Burgin G, Graham DB, et al. Intra- and inter-cellular rewiring of the human colon during ulcerative colitis. *Cell* (2019) 178:714–730.e22. doi: 10.1016/j.cell.2019.06.029

9. Shipman WD, Sandoval MJ, Veiga K, Donlin LT, Lu TT. Fibroblast subtypes in tissues affected by autoimmunity: with lessons from lymph node fibroblasts. *Curr Opin Immunol* (2020) 64:63. doi: 10.1016/j.coi.2020.03.002

10. Qi J, Sun H, Zhang Y, Wang Z, Xun Z, Li Z, et al. Single-cell and spatial analysis reveal interaction of FAP+ fibroblasts and SPP1+ macrophages in colorectal cancer. *Nat Commun* (2022) 13:1742. doi: 10.1038/s41467-022-29366-6

11. Komatsu N, Takayanagi H. Mechanisms of joint destruction in rheumatoid arthritis - immune cell-fibroblast-bone interactions. *Nat Rev Rheumatol* (2022) 18:415–29. doi: 10.1038/s41584-022-00793-5

12. Rao A, Barkley D, França GS, Yanai I. Exploring tissue architecture using spatial transcriptomics. *Nature* (2021) 596:211. doi: 10.1038/s41586-021-03634-9

13. Fan J, Slowikowski K, Zhang F. Single-cell transcriptomics in cancer: computational challenges and opportunities. *Exp Mol Med* (2020) 52:1452–65. doi: 10.1038/s12276-020-0422-0

14. Gawad C, Koh W, Quake SR. Single-cell genome sequencing: current state of the science. *Nat Rev Genet* (2016) 17:175–88. doi: 10.1038/nrg.2015.16

15. Zenobi R. Single-cell metabolomics: analytical and biological perspectives. *Science* (2013) 342:1243259. doi: 10.1126/science.1243259

16. Schwartzman O, Tanay A. Single-cell epigenomics: techniques and emerging applications. *Nat Rev Genet* (2015) 16:716–26. doi: 10.1038/nrg3980

17. Kolodziejczyk AA, Kim JK, Svensson V, Marioni JC, Teichmann SA. The technology and biology of single-cell RNA sequencing. *Mol Cell* (2015) 58:610–20. doi: 10.1016/j.molcel.2015.04.005

18. Chen KH, Boettiger AN, Moffitt JR, Wang S, Zhuang X. RNA Imaging. spatially resolved, highly multiplexed RNA profiling in single cells. *Science* (2015) 348:aaa6090. doi: 10.1126/science.aaa6090

19. Fries KM, Blieden T, Looney RJ, Sempowski GD, Silvera MR, Willis RA, et al. Evidence of fibroblast heterogeneity and the role of fibroblast subpopulations in fibrosis. *Clin Immunol Immunopathol* (1994) 72:283–92. doi: 10.1006/clin.1994.1144

20. Borrello MA, Phipps RP. Differential thy-1 expression by splenic fibroblasts defines functionally distinct subsets. *Cell Immunol* (1996) 173:198–206. doi: 10.1006/cimm.1996.0268

21. Bordin S, Kolb WP, Page RC. C1Q receptors on cultured human gingival fibroblasts: analysis of binding properties. *J Immunol* (1983) 130:1871–5.

22. Gabbiani G, Ryan GB, Majne G. Presence of modified fibroblasts in granulation tissue and their possible role in wound contraction. *Experientia* (1971) 27:549–50. doi: 10.1007/BF02147594

23. Plikus MV, Wang X, Sinha S, Forte E, Thompson SM, Herzog EL, et al. Fibroblasts: Origins, definitions, and functions in health and disease. *Cell* (2021) 184:3852–72. doi: 10.1016/j.cell.2021.06.024

24. Davidson S, Coles M, Thomas T, Kollias G, Ludewig B, Turley S, et al. Fibroblasts as immune regulators in infection, inflammation and cancer. *Nat Rev Immunol* (2021) 21:704–17. doi: 10.1038/s41577-021-00540-z

25. Koliaraki V, Prados A, Armaka M, Kollias G. The mesenchymal context in inflammation, immunity and cancer. *Nat Immunol* (2020) 21:974–82. doi: 10.1038/s41590-020-0741-2

26. Zhang F, Wei K, Slowikowski K, Fonseka CY, Rao DA, Kelly S, et al. Defining inflammatory cell states in rheumatoid arthritis joint synovial tissues by integrating single-cell transcriptomics and mass cytometry. *Nat Immunol* (2019) 20:928–42. doi: 10.1038/s41590-019-0378-1

27. Croft AP, Campos J, Jansen K, Turner JD, Marshall J, Attar M, et al. Distinct fibroblast subsets drive inflammation and damage in arthritis. *Nature* (2019) 570:246–51. doi: 10.1038/s41586-019-1263-7

28. Martin JC, Chang C, Boschetti G, Ungaro R, Giri M, Grout JA, et al. Single-cell analysis of crohn's disease lesions identifies a pathogenic cellular module associated with resistance to anti-TNF therapy. *Cell* (2019) 178:1493–1508.e20. doi: 10.1016/j.cell.2019.08.008

29. Valenzi E, Bulik M, Tabib T, Morse C, Sembrat J, Trejo Bittar H, et al. Single-cell analysis reveals fibroblast heterogeneity and myofibroblasts in systemic sclerosis-associated interstitial lung disease. *Ann Rheumatol Dis* (2019) 78:1379–87. doi: 10.1136/annrheumdis-2018-214865

30. Cao J, Spielmann M, Qiu X, Huang X, Ibrahim DM, Hill AJ, et al. The single-cell transcriptional landscape of mammalian organogenesis. *Nature* (2019) 566:496–502. doi: 10.1038/s41586-019-0969-x

31. Qiu X, Mao Q, Tang Y, Wang L, Chawla R, Pliner HA, et al. Reversed graph embedding resolves complex single-cell trajectories. *Nat Methods* (2017) 14:979–82. doi: 10.1038/nmeth.4402

32. La Manno G, Soldatov R, Zeisel A, Braun E, Hochgerner H, Petukhov V, et al. RNA Velocity of single cells. *Nature* (2018) 560:494–8. doi: 10.1038/s41586-018-0414-6

33. Wei K, Korsunsky I, Marshall JL, Gao A, Watts GFM, Major T, et al. Notch signalling drives synovial fibroblast identity and arthritis pathology. *Nature* (2020) 582:259–64. doi: 10.1038/s41586-020-2222-z

34. Stoeckius M, Hafemeister C, Stephenson W, Houck-Loomis B, Chattopadhyay PK, Swerdlow H, et al. Simultaneous epitope and transcriptome measurement in single cells. *Nat Methods* (2017) 14:865–8. doi: 10.1038/nmeth.4380

35. Zhang F, Jonsson AH, Nathan A, Wei K, Millard N, Xiao Q, et al. Cellular deconstruction of inflamed synovium defines diverse inflammatory phenotypes in rheumatoid arthritis. *bioRxiv* (2022). doi: 10.1101/2022.02.25.481990

36. Vickovic S, Schapiro D, Carlberg K, Lötstedt B, Larsson L, Hildebrandt F, et al. Three-dimensional spatial transcriptomics uncovers cell type localizations in the human rheumatoid arthritis synovium. *Commun Biol* (2022) 5:1–11. doi: 10.1038/s42003-022-03050-3

37. Armingol E, Officer A, Harismendy O, Lewis NE. Deciphering cell–cell interactions and communication from gene expression. *Nat Rev Genet* (2020) 22:71–88. doi: 10.1038/s41576-020-00292-x

38. Vento-Tormo R, Efremova M, Botting RA, Turco MY, Vento-Tormo M, Meyer KB, et al. Single-cell reconstruction of the early maternal-fetal interface in humans. *Nature* (2018) 563:347–53. doi: 10.1038/s41586-018-0698-6

39. Browaeys R, Saelens W, Saeys Y. NicheNet: modeling intercellular communication by linking ligands to target genes. *Nat Methods* (2019) 17:159–62. doi: 10.1038/s41592-019-0667-5

40. Jin S, Guerrero-Juarez CF, Zhang L, Chang I, Ramos R, Kuan C-H, et al. Inference and analysis of cell-cell communication using CellChat. *Nat Commun* (2021) 12:1–20. doi: 10.1038/s41467-021-21246-9

41. Noël F, Massenet-Regad L, Carmi-Levy I, Cappuccio A, Grandclaudon M, Trichot C, et al. Dissection of intercellular communication using the transcriptome-based framework ICELLNET. *Nat Commun* (2021) 12:1–16. doi: 10.1038/s41467-021-21244-x

42. Efremova M, Vento-Tormo M, Teichmann SA, Vento-Tormo R. CellPhoneDB: inferring cell–cell communication from combined expression of multi-subunit ligand–receptor complexes. *Nat Protoc* (2020) 15:1484–506. doi: 10.1038/s41596-020-0292-x

43. Buechler MB, Fu W, Turley SJ. Fibroblast-macrophage reciprocal interactions in health, fibrosis, and cancer. *Immunity* (2021) 54:903–15. doi: 10.1016/j.immuni.2021.04.021

44. Van Linthout S, Miteva K, Tschöpe C. Crosstalk between fibroblasts and inflammatory cells. *Cardiovasc Res* (2014) 102:258–69. doi: 10.1093/cvr/cvu062

45. Cheng L, Wang Y, Wu R, Ding T, Xue H, Gao C, et al. New insights from single-cell sequencing data: Synovial fibroblasts and synovial macrophages in rheumatoid arthritis. *Front Immunol* (2021) 12:709178. doi: 10.3389/fimmu.2021.709178

46. Alivernini S, MacDonald L, Elmesmari A, Finlay S, Tolusso B, Gigante MR, et al. Distinct synovial tissue macrophage subsets regulate inflammation and remission in rheumatoid arthritis. *Nat Med* (2020) 26:1295–306. doi: 10.1038/s41591-020-0939-8

47. Friedrich M, Pohin M, Jackson MA, Korsunsky I, Bullers SJ, Rue-Albrecht K, et al. IL-1-driven stromal–neutrophil interactions define a subset of patients

with inflammatory bowel disease that does not respond to therapies. *Nat Med* (2021) 27:1970–81. doi: 10.1038/s41591-021-01520-5

48. Larsson L, Frisén J, Lundeberg J. Spatially resolved transcriptomics adds a new dimension to genomics. *Nat Methods* (2021) 18:15–8. doi: 10.1038/s41592-020-01038-7

49. Moses L, Pachter L. Museum of spatial transcriptomics. *Nat Methods* (2022) 19:534–46. doi: 10.1038/s41592-022-01409-2

50. Li B, Zhang W, Guo C, Xu H, Li L, Fang M, et al. Benchmarking spatial and single-cell transcriptomics integration methods for transcript distribution prediction and cell type deconvolution. *Nat Methods* (2022) 19:662–70. doi: 10.1038/s41592-022-01480-9

51. Kleshchevnikov V, Shmatko A, Dann E, Aivazidis A, King HW, Li T, et al. Cell2location maps fine-grained cell types in spatial transcriptomics. *Nat Biotechnol* (2022) 40:661–71. doi: 10.1038/s41587-021-01139-4

52. Dong R, Yuan G-C. SpatialDWLS: accurate deconvolution of spatial transcriptomic data. *bioRxiv* (2021) 2021:2.02.429429. doi: 10.1101/2021.02.02.429429

53. Cable DM, Murray E, Zou LS, Goeva A, Macosko EZ, Chen F, et al. Robust decomposition of cell type mixtures in spatial transcriptomics. *Nat Biotechnol* (2021) 40:517–26. doi: 10.1038/s41587-021-00830-w

54. Hunter MV, Moncada R, Weiss JM, Yanai I, White RM. Spatially resolved transcriptomics reveals the architecture of the tumor-microenvironment interface. *Nat Commun* (2021) 12:1–16. doi: 10.1038/s41467-021-26614-z

55. Ravi VM, Will P, Kueckelhaus J, Sun N, Joseph K, Salié H, et al. Spatially resolved multi-omics deciphers bidirectional tumor-host interdependence in glioblastoma. *Cancer Cell* (2022) 40:639–655.e13. doi: 10.1016/j.ccell.2022.05.009

56. Korsunsky I, Millard N, Fan J, Slowikowski K, Zhang F, Wei K, et al. Fast, sensitive and accurate integration of single-cell data with harmony. *Nat Methods* (2019) 16:1289–96. doi: 10.1038/s41592-019-0619-0

57. Butler A, Hoffman P, Smibert P, Papalexi E, Satija R. Integrating single-cell transcriptomic data across different conditions, technologies, and species. *Nat Biotechnol* (2018) 36:411–20. doi: 10.1038/nbt.4096

58. Hie B, Bryson B, Berger B. Efficient integration of heterogeneous single-cell transcriptomes using scanorama. *Nat Biotechnol* (2019) 37:685–91. doi: 10.1038/s41587-019-0113-3

59. Stuart T, Butler A, Hoffman P, Hafemeister C, Papalexi E, Mauck WM 3rd, et al. Comprehensive integration of single-cell data. *Cell* (2019) 177:1888–1902.e21. doi: 10.1016/j.cell.2019.05.031

60. Kang JB, Nathan A, Weinand K, Zhang F, Millard N, Rumker L, et al. Efficient and precise single-cell reference atlas mapping with symphony. *Nat Commun* (2021) 12:5890. doi: 10.1038/s41467-021-25957-x

61. Lotfollahi M, Naghipourfar M, Luecken MD, Khajavi M, Büttner M, Wagenstetter M, et al. Mapping single-cell data to reference atlases by transfer learning. *Nat Biotechnol* (2021) 40:121–30. doi: 10.1038/s41587-021-01001-7

62. Lotfollahi M, Naghipourfar M, Theis FJ, Wolf FA. Conditional out-of-distribution generation for unpaired data using transfer VAE. *Bioinf 36* (2020) 36: i610–17. doi: 10.1093/bioinformatics/btaa800

63. Korsunsky I, Wei K, Pohin M, Kim EY, Barone F, Major T, et al. Cross-tissue, single-cell stromal atlas identifies shared pathological fibroblast phenotypes in four chronic inflammatory diseases. *Med (N Y)* (2022) 3:481–518.e14. doi: 10.1016/j.medj.2022.05.002

64. Buechler MB, Pradhan RN, Krishnamurty AT, Cox C, Calviello AK, Wang AW, et al. Cross-tissue organization of the fibroblast lineage. *Nature* (2021) 593:575–9. doi: 10.1038/s41586-021-03549-5

65. Zhang F, Mears JR, Shakib L, Beynor JI, Shanaj S, Korsunsky I, et al. IFN-γ and TNF-α drive a CXCL10+ CCL2+ macrophage phenotype expanded in severe COVID-19 lungs and inflammatory diseases with tissue inflammation. *Genome Med* (2021) 13:64. doi: 10.1186/s13073-021-00881-3

66. Smolen JS, Aletaha D. Rheumatoid arthritis therapy reappraisal: strategies, opportunities and challenges. *Nat Rev Rheumatol* (2015) 11:276–89. doi: 10.1038/nrrheum.2015.8

67. Choy EH, De Benedetti F, Takeuchi T, Hashizume M, John MR, Kishimoto T. Translating IL-6 biology into effective treatments. *Nat Rev Rheumatol* (2020) 16:335–45. doi: 10.1038/s41584-020-0419-z

68. Kobayashi T, Siegmund B, Le Berre C, Wei SC, Ferrante M, Shen B, et al. Ulcerative colitis. *Nat Rev Dis Primers* (2020) 6:74. doi: 10.1038/s41572-020-0205-x

69. Khanna D, Denton CP, Jahreis A, van Laar JM, Frech TM, Anderson ME, et al. Safety and efficacy of subcutaneous tocilizumab in adults with systemic sclerosis (faSScinate): a phase 2, randomised, controlled trial. *Lancet* (2016) 387:2630–40. doi: 10.1016/S0140-6736(16)00232-4

70. Denton CP, Ong VH, Xu S, Chen-Harris H, Modrusan Z, Lafyatis R, et al. Therapeutic interleukin-6 blockade reverses transforming growth factor-beta pathway activation in dermal fibroblasts: insights from the faSScinate clinical trial in systemic sclerosis. *Ann Rheumatol Dis* (2018) 77:1362–71. doi: 10.1136/annrheumdis-2018-213031

71. Bush KA, Farmer KM, Walker JS, Kirkham BW. Reduction of joint inflammation and bone erosion in rat adjuvant arthritis by treatment with interleukin-17 receptor IgG1 fc fusion protein. *Arthritis Rheumatol* (2002) 46:802–5. doi: 10.1002/art.10173

72. Shen H, Goodall JC, Hill Gaston JS. Frequency and phenotype of peripheral blood Th17 cells in ankylosing spondylitis and rheumatoid arthritis. *Arthritis Rheumatol* (2009) 60:1647–56. doi: 10.1002/art.24568

73. Langley RG, Elewski BE, Lebwohl M, Reich K, Griffiths CEM, Papp K, et al. Secukinumab in plaque psoriasis–results of two phase 3 trials. *N Engl J Med* (2014) 371:326–38. doi: 10.1056/NEJMoa1314258

74. Deodhar A, Blanco R, Dokoupilová E, Hall S, Kameda H, Kivitz AJ, et al. Improvement of signs and symptoms of nonradiographic axial spondyloarthritis in patients treated with secukinumab: Primary results of a randomized, placebo-controlled phase III study. *Arthritis Rheumatol* (2021) 73:110–20. doi: 10.1002/art.41477

75. Blanco FJ, Möricke R, Dokoupilova E, Codding C, Neal J, Andersson M, et al. Secukinumab in active rheumatoid arthritis: A phase III randomized, double-blind, active comparator- and placebo-controlled study. *Arthritis Rheumatol* (2017) 69:1144–53. doi: 10.1002/art.40070

76. Bellomo A, Mondor I, Spinelli L, Lagueyrie M, Stewart BJ, Brouilly N, et al. Reticular fibroblasts expressing the transcription factor WT1 define a stromal niche that maintains and replenishes splenic red pulp macrophages. *Immunity* (2020) 53:127–142.e7. doi: 10.1016/j.immuni.2020.06.008

77. Zhou X, Franklin RA, Adler M, Jacox JB, Bailis W, Shyer JA, et al. Circuit design features of a stable two-cell system. *Cell* (2018) 172:744–757.e17. doi: 10.1016/j.cell.2018.01.015

78. Aran D, Looney AP, Liu L, Wu E, Fong V, Hsu A, et al. Reference-based analysis of lung single-cell sequencing reveals a transitional profibrotic macrophage. *Nat Immunol* (2019) 20:163–72. doi: 10.1038/s41590-018-0276-y

79. Meziani L, Mondini M, Petit B, Boissonnas A, Thomas de Montpreville V, Mercier O, et al. CSF1R inhibition prevents radiation pulmonary fibrosis by depletion of interstitial macrophages. *Eur Respir J* (2018) 51. doi: 10.1183/13993003.02120-2017

80. Eklund KK, Joensuu H. Treatment of rheumatoid arthritis with imatinib mesylate: clinical improvement in three refractory cases. *Ann Med* (2003) 35:362–7. doi: 10.1080/07853890310001339

81. Zarrin AA, Bao K, Lupardus P, Vucic D. Kinase inhibition in autoimmunity and inflammation. *Nat Rev Drug Discovery* (2021) 20:39–63. doi: 10.1038/s41573-020-0082-8

82. Flaherty KR, Wells AU, Cottin V, Devaraj A, Walsh SLF, Inoue Y, et al. Nintedanib in progressive fibrosing interstitial lung diseases. *N Engl J Med* (2019) 381:1718–27. doi: 10.1056/NEJMoa1908681

83. Kuo D, Ding J, Cohn IS, Zhang F, Wei K, Rao DA, et al. HBEGF+ macrophages in rheumatoid arthritis induce fibroblast invasiveness. *Sci Transl Med* (2019) 11. doi: 10.1126/scitranslmed.aau8587

84. Yuan F-L, Li X, Lu W-G, Sun J-M, Jiang D-L, Xu R-S. Epidermal growth factor receptor (EGFR) as a therapeutic target in rheumatoid arthritis. *Clin Rheumatol* (2013) 32:289–92. doi: 10.1007/s10067-012-2119-9

85. Niu J, Li C, Jin Y, Xing R, Sun L, Yu R, et al. Identification and suppression of epidermal growth factor receptor variant III signaling in fibroblast-like synoviocytes from aggressive rheumatoid arthritis by the mimotope. *Immunol Lett* (2018) 198:74–80. doi: 10.1016/j.imlet.2018.04.009

86. Sullivan T, Benjamin CG, Kempf PW, Deeken JF. Cetuximab in the treatment of rheumatoid arthritis. *J Clin Rheumatol* (2010) 16:32–3. doi: 10.1097/RHU.0b013e3181c8e176

87. Rutgeerts P, Sandborn WJ, Feagan BG, Reinisch W, Olson A, Johanns J, et al. Infliximab for induction and maintenance therapy for ulcerative colitis. *N Engl J Med* (2005) 353:2462–76. doi: 10.1056/NEJMoa050516

88. Sandborn WJ, Hanauer SB, Rutgeerts P, Fedorak RN, Lukas M, MacIntosh DG, et al. Adalimumab for maintenance treatment of crohn's disease: results of the CLASSIC II trial. *Gut* (2007) 56:1232–9. doi: 10.1136/gut.2006.106781

89. West NR, Oxford IBD Cohort Investigators, Hegazy AN, Owens BMJ, Bullers SJ, Linggi B, et al. Oncostatin m drives intestinal inflammation and predicts response to tumor necrosis factor–neutralizing therapy in patients with inflammatory bowel disease. *Nat Med* (2017) 23:579–89. doi: 10.1038/nm.4307

90. Huelse JM, Fridlyand DM, Earp S, DeRyckere D, Graham DK. MERTK in cancer therapy: Targeting the receptor tyrosine kinase in tumor cells and the immune system. *Pharmacol Ther* (2020) 213:107577. doi: 10.1016/j.pharmthera.2020.107577

91. Graham DK, DeRyckere D, Davies KD, Earp HS. The TAM family: phosphatidylserine sensing receptor tyrosine kinases gone awry in cancer. *Nat Rev Cancer* (2014) 14:769–85. doi: 10.1038/nrc3847

92. Nguyen K-QN, Tsou W-I, Calarese DA, Kimani SG, Singh S, Hsieh S, et al. Overexpression of MERTK receptor tyrosine kinase in epithelial cancer cells drives

efferocytosis in a gain-of-function capacity. *J Biol Chem* (2014) 289:25737–49. doi: 10.1074/jbc.M114.570838

93. Inamo J. Association of differentially expressed genes and autoantibody type in patients with systemic sclerosis. *Rheumatology* (2021) 60:929–39. doi: 10.1093/rheumatology/keaa447

94. Rivellese F, Surace AEA, Goldmann K, Sciacca E, Çubuk C, Giorli G, et al. Rituximab versus tocilizumab in rheumatoid arthritis: synovial biopsy-based biomarker analysis of the phase 4 R4RA randomized trial. *Nat Med* (2022) 28:1256–68. doi: 10.1038/s41591-022-01789-0

95. Humby F, Lewis M, Ramamoorthi N, Hackney JA, Barnes MR, Bombardieri M, et al. Synovial cellular and molecular signatures stratify clinical response to csDMARD therapy and predict radiographic progression in early rheumatoid arthritis patients. *Ann Rheumatol Dis* (2019) 78:761–72. doi: 10.1136/annrheumdis-2018-214539

frontiers | Frontiers in Immunology

TYPE Brief Research Report
PUBLISHED 23 February 2023
DOI 10.3389/fimmu.2023.998233

OPEN ACCESS

EDITED BY
Rui Li,
University of Pennsylvania,
United States

REVIEWED BY
Hanane Touil,
Columbia University Irving Medical Center,
United States
Dorin Dragoş,
Carol Davila University of Medicine and
Pharmacy, Romania

*CORRESPONDENCE
Makoto Kinoshita
✉ mkinoshita@neurol.med.osaka-u.ac.jp
Daisuke Okuzaki
✉ dokuzaki@biken.osaka-u.ac.jp

†These authors have contributed equally to this work

SPECIALTY SECTION
This article was submitted to Autoimmune and Autoinflammatory Disorders : Autoimmune Disorders, a section of the journal Frontiers in Immunology

RECEIVED 19 July 2022
ACCEPTED 06 February 2023
PUBLISHED 23 February 2023

CITATION
Ishikawa M, Shimada Y, Ozono T, Matsumoto H, Ogura H, Kihara K, Mochizuki H, Okuno T, Sakakibara S, Kinoshita M and Okuzaki D (2023) Single-cell RNA-seq analysis identifies distinct myeloid cells in a case with encephalitis temporally associated with COVID-19 vaccination. *Front. Immunol.* 14:998233. doi: 10.3389/fimmu.2023.998233

Single-cell RNA-seq analysis identifies distinct myeloid cells in a case with encephalitis temporally associated with COVID-19 vaccination

Masakazu Ishikawa[1,2†], Yuki Shimada[3†], Tatsuhiko Ozono[3], Hisatake Matsumoto[2,4], Hiroshi Ogura[4], Keigo Kihara[3], Hideki Mochizuki[3], Tatsusada Okuno[3], Shuhei Sakakibara[4], Makoto Kinoshita[3*] and Daisuke Okuzaki[1,2,6,7*]

[1]Laboratory of Human Immunology (Single Cell Genomics), WPI Immunology Frontier Research Center, Osaka University, Osaka, Japan, [2]Center for Infectious Disease Education and Research, Osaka University, Osaka, Japan, [3]Department of Neurology, Graduate School of Medicine, Osaka University, Osaka, Japan, [4]Department of Traumatology and Acute Critical Medicine, Graduate School of Medicine, Osaka University, Osaka, Japan, [5]Laboratory of Immune Regulation, WPI Immunology Frontier Research Center, Osaka University, Osaka, Japan, [6]Genome Information Research Center, Research Institute for Microbial Diseases, Osaka University, Osaka, Japan, [7]Institute for Open and Transdisciplinary Research Initiatives, Osaka University, Osaka, Japan

Recently accumulating evidence has highlighted the rare occurrence of COVID-19 vaccination-induced inflammation in the central nervous system. However, the precise information on immune dysregulation related to the COVID-19 vaccination-associated autoimmunity remains elusive. Here we report a case of encephalitis temporally associated with COVID-19 vaccination, where single-cell RNA sequencing (scRNA-seq) analysis was applied to elucidate the distinct immune signature in the peripheral immune system. Peripheral blood mononuclear cells (PBMCs) were analyzed using scRNA-seq to clarify the cellular components of the patients in the acute and remission phases of the disease. The data obtained were compared to those acquired from a healthy cohort. The scRNA-seq analysis identified a distinct myeloid cell population in PBMCs during the acute phase of encephalitis. This specific myeloid population was detected neither in the remission phase of the disease nor in the healthy cohort. Our findings illustrate induction of a unique myeloid subset in encephalitis temporally associated with COVID-19 vaccination. Further research into the dysregulated immune signature of COVID-19 vaccination-associated autoimmunity including the cerebrospinal fluid (CSF) cells of central nervous system (CNS) is warranted to clarify the pathogenic role of the myeloid subset observed in our study.

KEYWORDS

single-cell RNA-seq, myeloid cells, COVID-19, vaccination, encephalitis

Introduction

The outbreak of severe acute respiratory syndrome called coronavirus disease-2019 (COVID-19) was caused by a novel coronavirus (SARS-CoV-2) infection (1). The SARS-CoV-2 infection has spread rapidly worldwide by high human-to-human transmission, resulting in a public health emergency of international concern. The ongoing COVID-19 pandemic has been described as 'an explosive pandemic of historic proportions', with over 200 million confirmed cases and over 5 million confirmed deaths worldwide (2). Several mRNA vaccination applications have prevented severe SARS-CoV-2 disease outcomes (3). Accumulating evidence demonstrates that mRNA vaccination is highly effective in eliciting the production of antibodies against SARS-CoV-2 (3–5). Despite the well-acknowledged efficacy of mRNA vaccination of SARS-CoV-2, the precise alteration of immune responses elicited by mRNA vaccination remains to be clarified. Although several studies suggest the safety of mRNA vaccination for patients suffering from autoimmune neurological diseases (6, 7), reports showing the rare occurrence of autoimmune diseases affecting peripheral or central nervous system is accumulating (8–10). The frequency of encephalitis after COVID-19 mRNA vaccination is estimated to be 2 in 10 million (11). Thus, it is crucial to clarify the immune dysregulation triggered and identify the cellular population contributing to the development of COVID-19 vaccination associated-autoimmunity. Improvements in DNA library preparation technology for sequencing have enabled RNA sequencing to comprehensively analyze gene expression levels at the single-cell level (12). Single cell RNA-sequencing (scRNA-seq) provides information on both the proportion of each specific cellular subset, and the gene signature of the cells (13). Here, we describe a case where augmentation of autoimmune encephalitis was observed after COVID-19 vaccination using scRNA-seq of peripheral blood mononuclear cells (PBMCs), and further demonstrate distinct myeloid cell population identified in PBMCs at the acute phase of the disease.

Materials and methods

Subjects and PBMC preparation

PBMCs were chronologically collected from the patient at the onset of encephalitis (day 0), two days after the onset of the disease (day 3), and at the remission of the disease (day 17). Written informed consent was obtained from the participant prior to the participation in the study. The protocol was reviewed and approved by the Ethics Committee of Osaka University and in accordance with the tenets set forth in the Declaration of Helsinki.

Isolation of PBMCs

PBMCs were isolated using Histopaque 1077 (Sigma) by centrifugation at 800g for 15 min at room temperature. PBMCs at the interface were collected, rinsed twice with phosphate buffered saline (PBS) and 2% bovine serum albumin (BSA), and cryopreserved in fetal bovine serum with 10% dimethyl sulfoxide. All samples were processed within 4 hours of collection. The preserved PBMCs were thawed immediately at 37°C, transferred to a 50-ml tube, and ten volumes of prewarmed PBS was added slowly and dropwisely, followed by centrifugation at 500g for 5 min. The pellet was resuspended in 1 ml of PBS with 2% BSA, and the viability of each sample was assessed by counting using trypan blue and a Countess II FL Automated Cell Counter (Thermo Fisher Scientific).

TotalSeq-C hashtag antibody staining, single cell library preparation and sequencing

The PBMCs from each donor were stained with Human TruStain FcX Fc Blocking Reagent (BioLegend, 422302) for 10 min at 4°C. Subsequently, the cells were then stained with a TotalSeq-C hashtag (BioLegend) for 30 min at 4°C. The cells were then washed twice using centrifugation at 500g for 5 min at 4°C with PBS supplemented with 2% (vol/vol) BSA. Each sample's cell number and viability were determined using trypan blue and a Countess II FL Automated Cell Counter, then pooled together in equal numbers. The cells were counted again and processed immediately for a 10x 5' single-cell system followed by Chromium Next GEM Single Cell V(D)J Reagent Kit v2 with Feature Barcoding technology for Cell-Surface Protein-Rev D protocol. Gene expression and feature barcode libraries were prepared according to the manufacturer's protocol (10x Genomics). All libraries were sequenced using the DNBSEQ-G400 (MGI) to achieve a minimum of 20,000 paired-end reads per cell for gene expression and 5,000 paired-end reads per cell for cell-surface protein.

Bioinformatics analysis

Sequencing data obtained from MGISEQ-G400 were aligned to the GRCh38 genome using Cell Ranger (v.6.1.0). We have also obtained the public data from Wang et al. (2022) (reference number: OMIX001295) as healthy subjects, which samples were analyzed immediately after the second dose of mRNA-1273 vaccination (14). Filtered matrices were loaded into the R package Seurat (v.4.0) (15) and conducted data filtering, normalization, scaling, dimensional reduction, clustering, and visualization were conducted using Seurat. After clustering, cell types were automatically determined by using ScType (16). The gene expression information of surface proteins is shown in Supplementary Table 1. Differential gene expression (DE) analysis was conducted by FindMarker script implemented in Seurat. The results of DE analysis were used in volcano plot and Gene Ontology (GO) enrichment analysis. The figure of the volcano plot was plotted by hand-made scripts, and GO enrichment analysis was conducted by using the compareCluster function in the R package clusterProfiler (17). Genes differentially expressed were identified as p_val_adj < 0.1 and |Log2 FC| > 1.

Data availability

Data that support the findings of this study are available from the corresponding author upon reasonable request. Data for all scRNA-seq will be available through GEO at accession number GSE205606 and GSE205607.

Results

Case presentation

A 25-year-old Asian woman had been experiencing swelling and pain in her right toe interphalangeal joint and finger proximal interphalangeal joint. She was diagnosed with rheumatoid arthritis and commenced treatment with methotrexate after a positive blood test for rheumatoid factor and joint echo results. Subsequently, she developed a generalized convulsive seizure and was transferred to her previous physician. MRI T2-weighted head images showed high-signal areas just below the cerebral cortex in the right frontal and parietal lobes, and both symptoms and imaging findings improved with antiepileptic drugs and oral steroids. Accordingly, the patient was discharged with a diagnosis of autoimmune encephalitis associated with the extra-articular manifestation of rheumatoid arthritis. Four months later, the seizures recurred again, and the patient was transferred to our hospital for specialist care with increased doses of oral steroids and antiepileptic drugs. At the time of transfer, there were no obvious neurological abnormalities, and CSF examination was normal. The patient was scheduled for discharge from the hospital after a gradual reduction of steroids. However, when the second dose of COVID-19 vaccination (mRNA-1273) was administered in the same month, the patient developed fever during the night on the same day and generalized tonic-clonic seizures in the early morning of the next day (day 0). MRI images of the head revealed a high-signal area in the subcortical white matter in the fluid-attenuated inversion recovery scan (Figure 1A), and CSF examination showed an elevated cell count of 32 cells/μL (Figure 1B). The patient was ventilated for seizures and treated with diazepam, fosphenytoin, midazolam, and propofol. Three days later (day 3), the patient was extubated and treated with steroid pulse therapy, and tacrolimus was introduced in addition to oral steroids to prevent further relapses of encephalitis. No residual neurological symptoms were observed, and the patient was discharged from the hospital. On day 17 spinal fluid findings were normalized, and the lesion had markedly resolved on head MRI imaging (Figures 1A, B).

Distinct myeloid cell population can be observed in the acute phase of encephalitis

We generated single-cell transcriptome data of PBMCs obtained from the patient at day 0, day 3 and day 17 (Figure 2A). We obtained 16,295 cells in total from the 3 conditions after doublet removal. Figure 2B shows the landscape of each immune subset after analyzing the combined scRNA-seq results of the 3 samples. When scRNA-seq results of each sample were analyzed respectively, PBMCs obtained at day 0 and day 3 of the patient revealed the appearance of a distinct cellular population compared to those of day 17 in the cluster island annotated as classical monocytes (Figure 2C). There were no other distinct cellular subsets or clonal predominance observed in the acute phase of the disease (Supplementary Tables 2, 3).

Immunological pathways specific to the distinct myeloid cell population at the acute phase of encephalitis

To clarify whether the distinctive classical monocytes observed at the acute phase of the disease in our patient was not the immune alteration shared with healthy subjects receiving vaccination, PBMCs obtained at day 0 were compared with the healthy controls receiving COVID-19 vaccination from public database. Both samples were obtained one day after the mRNA-1273 vaccine. Figure 3 shows the distinct monocyte clusters between day 0 of the patient and the healthy controls. Differential expression gene (DEG) analysis was further performed among the classical monocytes between day 0 of the patient and the healthy controls. DEGs were defined by the threshold as p_val_adj < 0.1 and |Log2Fold| > 1. The most highly up-regulated genes of the classical monocytes of day 0 were *G0S2* (G0/G1 Switch 2), *TIMP1* (TIMP Metallopeptidase Inhibitor 1), *ASPH* (Aspartate Beta-Hydroxylase), and *HMOX1* (Heme Oxygenase 1), whereas the most prominently down-regulated genes were *FOS* (Fos Proto-Oncogene), *DUSP1* (Dual Specificity Phosphatase 1), *RHOB* (Ras Homolog Family Member B), and *MNDA* (Myeloid Cell Nuclear Differentiation Antigen) (Supplementary Table 4).

To further elucidate the molecular pathway representing the overall gene signature characteristic to the distinct monocyte cluster observed at the acute phase of day 0, Kyoto Encyclopedia of Genes and Genomes Enrichment analysis (KEGG) Enrichment analysis was performed. As shown in Figure 4A, the pathway term “Rheumatoid arthritis” represented the up-regulated gene signature of the monocyte cluster observed at day 0. No pathway terms were enriched for genes down-regulated in the monocyte cluster.

The DEGs which contributed to the pathway term “Rheumatoid arthritis” were *CXCL8* (C-X-C Motif Chemokine Ligand 8), *CTSL* (Cathepsin L), *CXCL2* (C-X-C Motif Chemokine Ligand 2), and *CCL2* (C-C Motif Chemokine Ligand 2) (Figure 4B).

Discussion

In the COVID-19 pandemic era, clinical trials have revealed that mRNA vaccines, a novel vaccine modality, prevent COVID-19 infection at a high rate and reduce the risk of severe disease (3). Adverse reactions are not severe in the majority of vaccine recipients; however, rare adverse reactions of autoimmune neurological diseases have been reported (8–10).

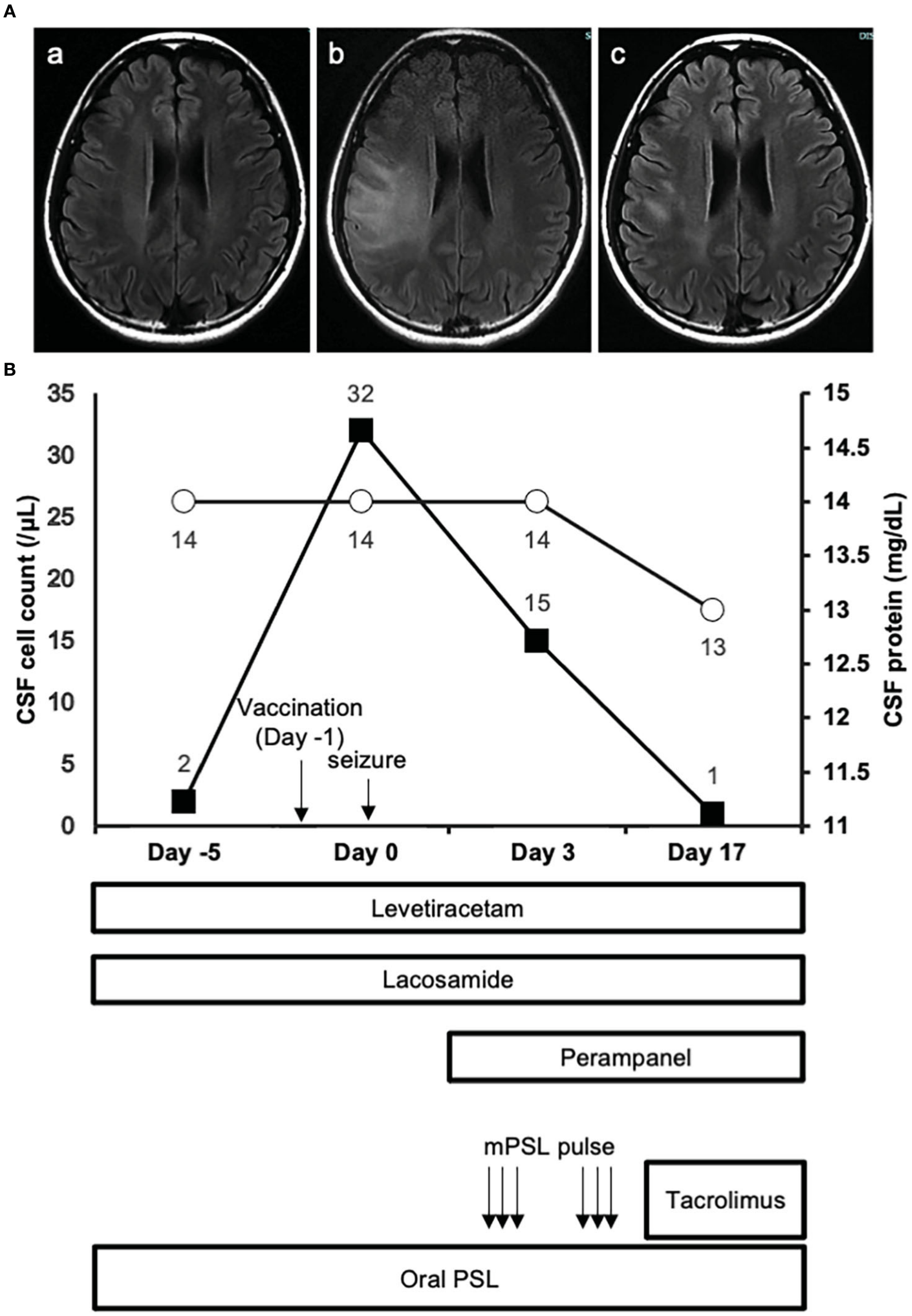

FIGURE 1
MRI images and clinical course. **(A.a)** FLAIR image of the brain obtained 2 days before the vaccination. **(A.b)** FLAIR image of the brain on day 0 show extensive development of high intensity lesions predominantly at the white matter. **(A.c)** FLAIR image of the brain on day 24 reveals the amelioration of high intensity lesions observed at the acute phase of the disease. **(B)** The closed squares and open circles represent CSF cell count and protein concentration of each timepoint respectively.

Typical COVID-19 vaccination-related autoimmune neurological diseases reported include cranial nerve palsies (18), Guillain-Barré syndrome (9, 19), myelitis (20), and encephalitis (10), but the details of the altered immune responses that contribute to their pathogenesis remain unresolved.

Our patient is a rare case of rheumatoid encephalitis with acute exacerbation, which was observed after the vaccine booster immunization. It remains elusive whether the specific classical monocyte population identified in our case is observed in COVID-19 vaccination-related CNS diseases in general, or is rather reflecting enhanced dysregulated immunity of each specific disease. Accumulating evidence is warranted to clarify the potential role of the specific classical monocyte population to utilize as the surrogate marker of immune flare in COVID-19 vaccination-related CNS diseases.

Recent reports of detailed single-cell analysis after mRNA vaccine administration have revealed that vaccination induces

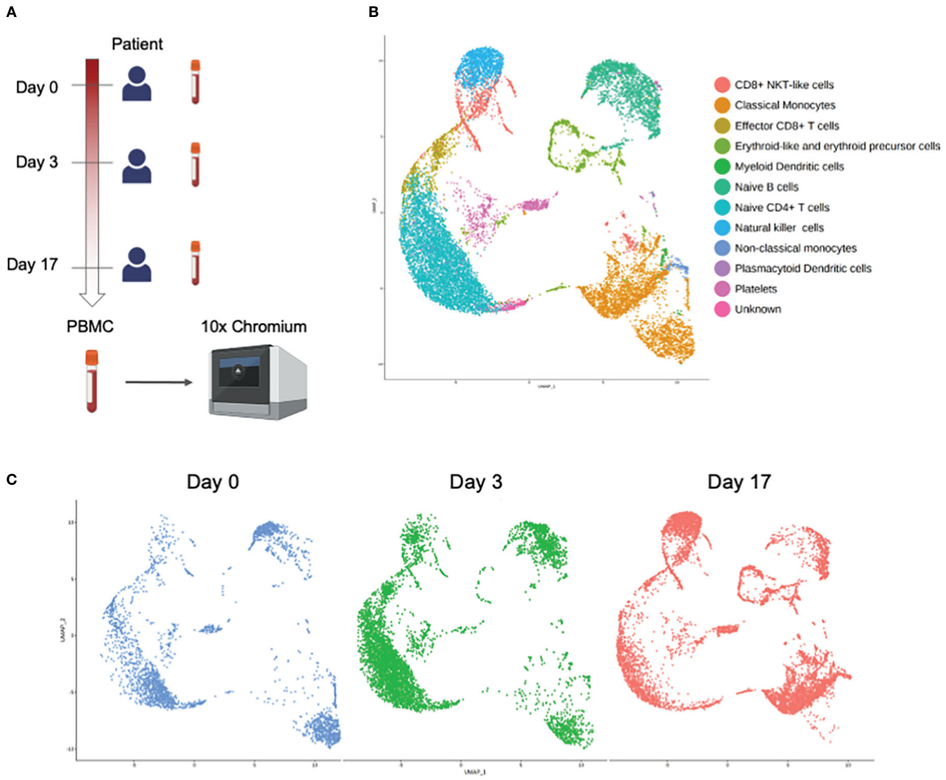

FIGURE 2
Single-cell RNA-seq analysis of PBMCs obtained at day 0, day 3, and day 17 from the patient. **(A)** Experimental design of the study. Figure was created using BioRender.com. **(B)** UMAP projection of all PBMCs with major subsets annotated. **(C)** UMAP projection of all PBMCs split by samples.

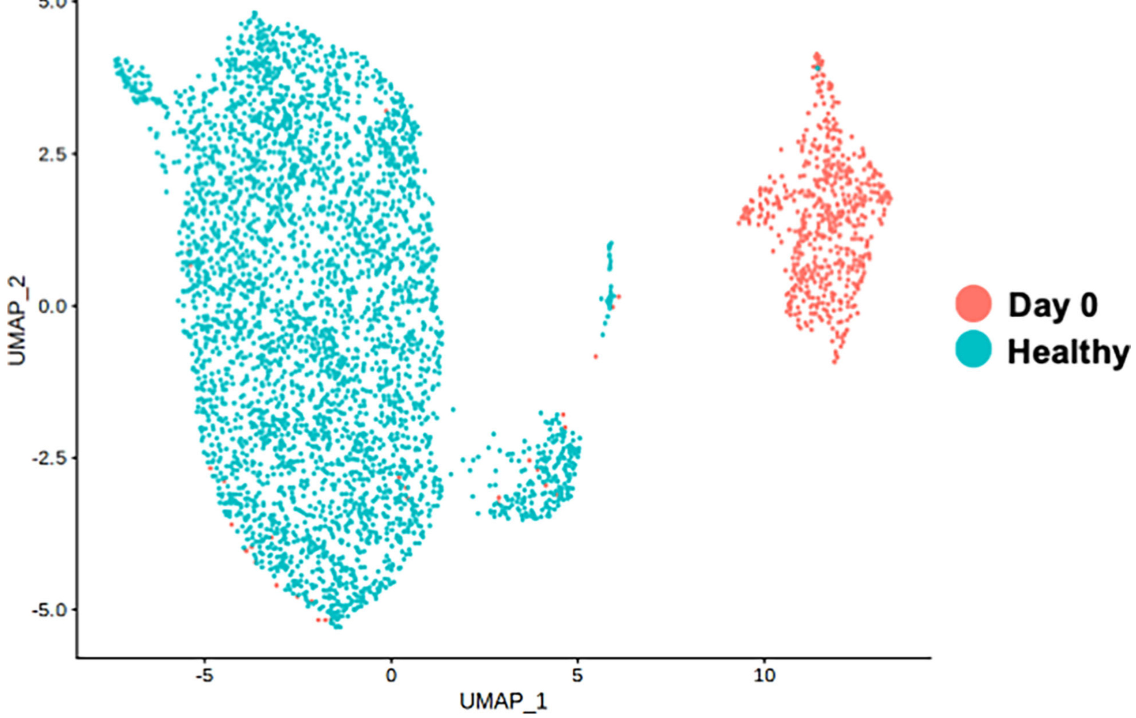

FIGURE 3
Single-cell RNA-seq analysis of classical monocyte cell population. UMAP visualization of classical monocytes colored by sample conditions. “Day 0” depicts the samples obtained from the patient on day 0. “Healthy” depicts the samples obtained from the public healthy control data OMIX001295.

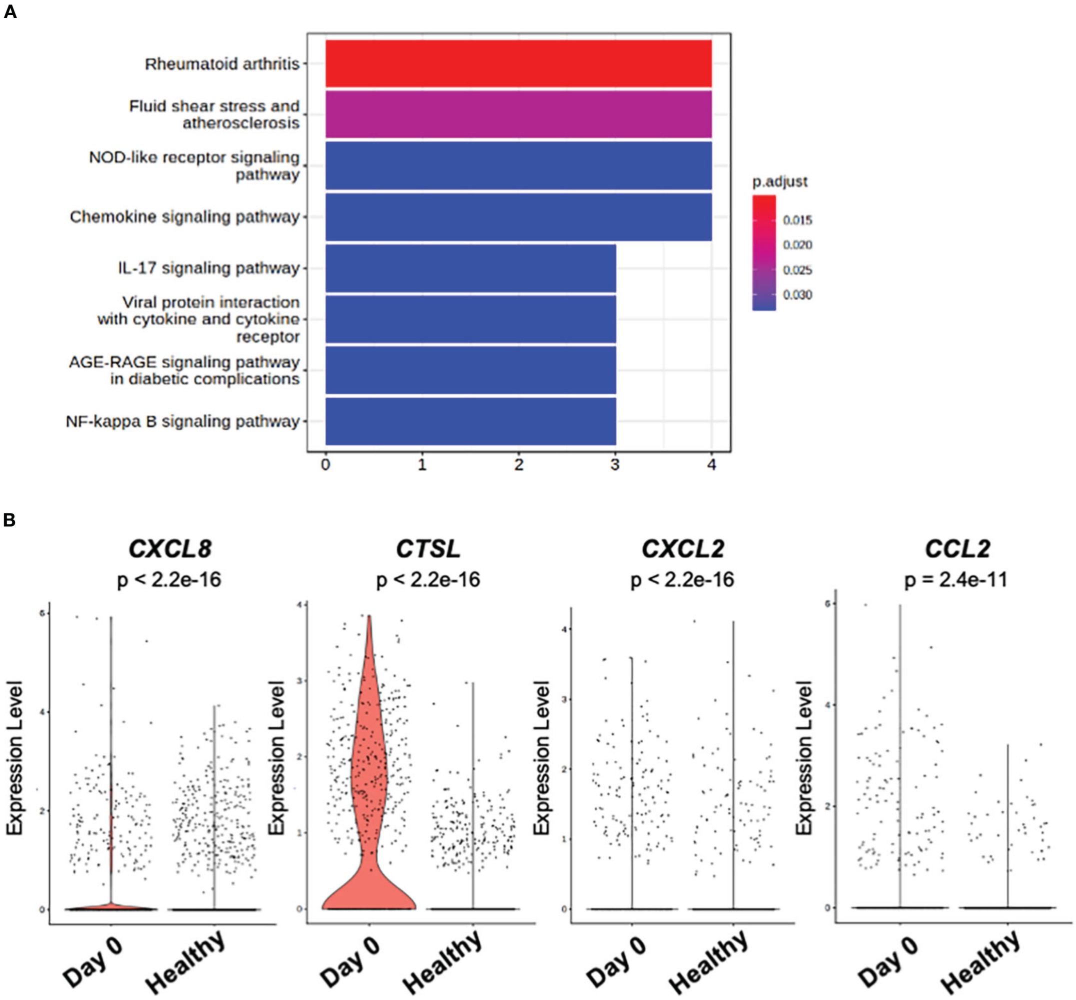

FIGURE 4

KEGG pathway and DEG analysis of classical monocytes. **(A)** Bar plot of KEGG pathway enriched in significantly (p_val_adj < 0.1 and |avg_log2FC| > 1) up-regulated genes among classical monocytes at day 0 and day 3 of the patient. **(B)** Violin plot of the genes related to KEGG pathway term "Rheumatoid arthritis" in **(A)**. "Day 0" depicts the samples obtained from the patient on day 0. "Healthy" depicts the samples obtained from the public healthy control data OMIX001295.

specific acquired immune activation, including antigen-specific CD4-positive T cells and CD8-positive T cells, while booster vaccination induces notably enhanced innate immune responses (21). The enhanced responses of CD4- and CD8-positive T cells after the booster vaccination is also demonstrated in another study (22), while memory B cells are also demonstrated to be primed by mRNA vaccine (23). Furthermore, immunosuppressant medication is shown to inhibit the efficacious germinal center responses elicited by mRNA vaccine (24).

The specific classical monocyte population we identified in this study is characterized by high expression of CXCL8, CTSL, CXCL2, and CCL2, all of which are molecules associated with rheumatic disease activity, and we hypothesized that the COVID-19 vaccination may have been the trigger for the rheumatic activity in our patients. CXCL8 is known to be elevated in PBMCs of patients with active rheumatoid arthritis (25). The cathepsins including CTSL is known to be expressed at high levels in the joints of rheumatoid arthritis (26). It is also reported that CXCL2 is significantly elevated in the serum of rheumatoid arthritis compared to healthy controls (27). In addition, CCL2 has been reported to be elevated in the serum of rheumatoid patients compared to healthy controls (28).

Large clinical studies of rheumatoid arthritis have reported that COVID-19 vaccine does not clearly increase the risk of recurrence (29), but there are rare reports of increased disease activity and recurrence (30). Rheumatoid arthritis is mainly characterized by joint symptoms, but can be complicated by various central nervous system symptoms, including meningitis and encephalitis (31).

It remains to be clarified whether the specific classical monocyte population we identified in this study directly contributes to the development of encephalitis by infiltrating the brain or by enhancing systemic production of inflammatory cytokines, leading to brain lesions. In this regard, further analysis of CSF cells, which was not feasible in our study due to insufficient number of cells collected, will provide more convincing evidence to show the pathogenic immune subsets responsible for encephalitis development after COVID-19 vaccination.

Another limitation of this study is that the patients were under treatment with various types of medication at the time of sample collection. In this regard, we cannot exclude the possibility that these multi-factorial effects altered the gene expression pattern of our scRNA-seq results of the patient.

Considering the autoimmune background of rheumatoid arthritis in our patient, it is also interesting to elucidate whether COVID-19 vaccination can activate the immune signature underlying the pathogenesis characteristic of each disease related to autoimmunity in the future studies.

Data availability statement

Data that supports the findings of this study are available from the corresponding author upon reasonable request. Data for all scRNA-seq are available through GEO at accession number GSE205606 and GSE205607.

Ethics statement

The studies involving human participants were reviewed and approved by the Ethics Committee of Osaka University. The patients/participants provided their written informed consent to participate in this study. Written informed consent was obtained from the individual(s) for the publication of any potentially identifiable images or data included in this article.

Author contributions

MI, SS, MK, and DO designed research; MI, YS, TOz, HMa, HO, KK, HMo, TOk, SS, MK, and DO performed research; MI, SS, MK, and DO analyzed data; MI, SY, and MK wrote the paper. All authors contributed to the article and approved the submitted version.

Funding

This work was supported by the Japan Society for the Promotion of Science (JSPS) through Grant-in-Aid for Scientific Research (C) (grant number 20K08356), the Japan Agency for Medical Research and Development (grant number 20fk0108404h0001), the Mitsubishi Foundation, and the NIPPON Foundation for social innovation.

Acknowledgments

We thank the members of our laboratory and the NGS core facility of the Genome Information Research Center at the Research Institute for Microbial Diseases of Osaka University for helpful discussions in analyzing the data.

Conflict of interest

The authors declare that the research was conducted in the absence of any commercial or financial relationships that could be construed as a potential conflict of interest.

Publisher's note

Supplementary material

The Supplementary Material for this article can be found online at: https://www.frontiersin.org/articles/10.3389/fimmu.2023.998233/full#supplementary-material

References

1. Gorbalenya AE, Baker SC, Baric RS, de Groot RJ, Drosten C, Anastasia A, et al. The species severe acute respiratory syndrome-related coronavirus: classifying 2019-nCoV and naming it SARS-CoV-2. *Nat Microbiol* (2020) 5:536–44. doi: 10.1038/s41564-020-0695-z

2. Escobedo RA, Kaushal D, Singh DK. Insights into the changing landscape of coronavirus disease 2019. *Front Cell Infect Microbiol* (2022) 11:761521. doi: 10.3389/fcimb.2021.761521

3. Sharif N, Alzahrani KJ, Ahmed SN, Dey SK. Efficacy, immunogenicity and safety of COVID-19 vaccines: A systematic review and meta-analysis. *Front Immunol* (2021) 12:714170. doi: 10.3389/fimmu.2021.714170

4. Polack FP, Thomas SJ, Kitchin N, Absalon J, Gurtman A, Lockhart S, et al. Safety and efficacy of the BNT162b2 mRNA covid-19 vaccine. *N Engl J Med* (2020) 383:2603–15. doi: 10.1056/NEJMc2036242

5. Frenck RW, Klein NP, Kitchin N, Gurtman A, Absalon J, Lockhart S, et al. Safety, immunogenicity, and efficacy of the BNT162b2 covid-19 vaccine in adolescents. *N Engl J Med* (2021) 385:239–50. doi: 10.1056/NEJMoa2107456

6. Giannoccaro MP, Vacchiano V, Leone M, Camilli F, Zenesini C, Panzera I, et al. Difference in safety and humoral response to mRNA SARS-CoV-2 vaccines in patients with autoimmune neurological disorders: The ANCOVAX study. *J Neurol* (2022) 269:4000–4012. doi: 10.1007/s00415-022-11142-7

7. Dinoto A, Gastaldi M, Iorio R, Marini S, Damato V, Farina A, et al. Safety profile of SARS-CoV-2 vaccination in patients with antibody-mediated CNS disorders. *Mult Scler Relat Disord* (2022) 63:103827. doi: 10.1016/j.msard.2022.103827

8. Oonk NGM, Ettema AR, van Berghem H, de Klerk JJ, van der Vegt JPM, van der Meulen M. SARS-CoV-2 vaccine-related neurological complications. *Neurol Sci* (2022) 43:2295–7. doi: 10.1007/s10072-022-05898-z

9. Finsterer J. Neurological side effects of SARS-CoV-2 vaccinations. *Acta Neurol Scand* (2022) 145:5–9. doi: 10.1111/ane.13550

10. Kania K, Ambrosius W, Tokarz Kupczyk E, Kozubski W. Acute disseminated encephalomyelitis in a patient vaccinated against SARS-CoV-2. *Ann Clin Transl Neurol* (2021) 8:2000–3. doi: 10.1002/acn3.51447

11. Zuhorn F, Graf T, Klingebiel R, Schäbitz WR, Rogalewski A. Postvaccinal encephalitis after ChAdOx1 nCov-19. *Ann Neurol* (2021) 90:506–11. doi: 10.1002/ana.26182

12. Shapiro E, Biezuner T, Linnarsson S. Single-cell sequencing-based technologies will revolutionize whole-organism science. *Nat Rev Genet* (2013) 14:618–30. doi: 10.1038/nrg3542

13. Papalexi E, Satija R. Single-cell RNA sequencing to explore immune cell heterogeneity. *Nat Rev Immunol* (2018) 18:35–45. doi: 10.1038/nri.2017.76

14. Wang Y, Wang X, Luu LDW, Li J, Cui X, Yao H, et al. Single-cell transcriptomic atlas reveals distinct immunological responses between COVID-19 vaccine and natural SARS-CoV-2 infection. *J Med Virol* (2022) 94:5304–24. doi: 10.1002/jmv.28012

15. Stuart T, Butler A, Hoffman P, Hafemeister C, Papalexi E, Mauck WM III, et al. Comprehensive integration of single-cell data resource comprehensive integration of single-cell data. *Cell.* (2019) 177:1888–1902.e21. doi: 10.1016/j.cell.2019.05.031

16. Ianevski A, Giri AK, Aittokallio T. Fully-automated and ultra-fast cell-type identification using specific marker combinations from single-cell transcriptomic data. *Nat Commun* (2022) 13:1–10. doi: 10.1038/s41467-022-28803-w

17. Yu G, Wang LG, Han Y, He QY. ClusterProfiler: An r package for comparing biological themes among gene clusters. *Omi A J Integr Biol* (2012) 16:284–7. doi: 10.1089/omi.2011.0118

18. Manea MM, Dragoş D, Enache I, Sirbu AG, Tuta S. Multiple cranial nerve palsies following COVID-19 vaccination-case report. *Acta Neurol Scand* (2022) 145:257–9. doi: 10.1111/ane.13548

19. Koike H, Chiba A, Katsuno M. Emerging infection , vaccination , and Guillain – barre Syndrome : A review. *Neurol Ther* (2021) 10:523–37. doi: 10.1007/s40120-021-00261-4

20. Khan E, Shrestha AK, Colantonio MA, Liberio RN, Sriwastava S. Acute transverse myelitis following SARS – CoV – 2 vaccination : a case report and review of literature. *J Neurol* (2022) 269:1121–32. doi: 10.1007/s00415-021-10785-2

21. Arunachalam PS, Scott MKD, Hagan T, Li C, Feng Y, Wimmers F, et al. Systems vaccinology of the BNT162b2 mRNA vaccine in humans. *Nature.* (2021) 596:410–6. doi: 10.1038/s41586-021-03791-x

22. Painter MM, Mathew D, Goel RR, Apostolidis SA, Pattekar A, Kuthuru O, et al. Rapid induction of antigen-specific CD4+ T cells is associated with coordinated humoral and cellular immunity to SARS-CoV-2 mRNA vaccination. *Immunity.* (2021) 54:2133–2142.e3. doi: 10.1016/j.immuni.2021.08.001

23. Goel RR, Apostolidis SA, Painter MM, Mathew D, Pattekar A, Kuthuru O, et al. Distinct antibody and memory b cell responses in SARSCoV-2 naïve and recovered individuals following mRNA vaccination. *Sci Immunol* (2021) 6:1–19. doi: 10.1126/sciimmunol.abi6950

24. Lederer K, Bettini E, Parvathaneni K, Painter MM, Agarwal D, Lundgreen KA, et al. Germinal center responses to SARS-CoV-2 mRNA vaccines in healthy and immunocompromised individuals. *Cell.* (2022) 185:1008–1024.e15. doi: 10.1016/j.cell.2022.01.027

25. Petrackova A, Horak P, Radvansky M, Fillerova R, Smotkova Kraiczova V, Kudelka M. Revealed heterogeneity in rheumatoid arthritis based on multivariate innate signature analysis. *Clin Exp Rheumatol* (2020) 38:289–98. doi: 10.55563/clinexprheumatol/qb2ha3

26. Clanchy FIL, Borghese F, Bystrom J, Balog A, Penn H, Taylor PC, et al. Disease status in human and experimental arthritis, and response to TNF blockade, is associated with MHC class II invariant chain (CD74) isoform expression. *J Autoimmun* (2022) 128:102810. doi: 10.1016/j.jaut.2022.102810

27. Wang X, Sun L, He N, An Z, Yu R, Li C, et al. Increased expression of CXCL2 in ACPA-positive rheumatoid arthritis and its role in osteoclastogenesis. *Clin Exp Immunol* (2021) 203:194–208. doi: 10.1111/cei.13527

28. Zhang L, Yu M, Deng J, Lv X, Liu J, Xiao Y, et al. Chemokine signaling pathway involved in CCL2 expression in patients with rheumatoid arthritis. *Yonsei Med J* (2015) 56:1134–42. doi: 10.3349/ymj.2015.56.4.1134

29. Li X, Tong X, Yeung WWY, Kuan P, Hin Hei Yum S, Ling Chui CS, et al. Two-dose COVID-19 vaccination and possible arthritis flare among patients with rheumatoid arthritis in Hong Kong. *Ann Rheum Dis* (2022) 81:564–8. doi: 10.1136/annrheumdis-2021-221571

30. Spinelli FR, Favalli EG, Garufi C, Cornalba M, Colafrancesco S, Conti F, et al. Low frequency of disease flare in patients with rheumatic musculoskeletal diseases who received SARS-CoV-2 mRNA vaccine. *Arthritis Res Ther* (2022) 24:1–8. doi: 10.1186/s13075-021-02674-w

31. Higashida-Konishi M, Izumi K, Tsukamoto M, Ohya H, Takasugi N, Hama S, et al. Correction to: Anti-cyclic citrullinated peptide antibody in the cerebrospinal fluid in patients with rheumatoid arthritis who have central nervous system involvement. *Clin Rheumatology;* (2020) 39:2441–8. doi: 10.1007/s10067-020-05044-0

frontiers | Frontiers in Immunology

TYPE Original Research
PUBLISHED 01 March 2023
DOI 10.3389/fimmu.2023.1147526

OPEN ACCESS

EDITED BY
Giuseppe Murdaca,
University of Genoa, Italy

REVIEWED BY
Sun Jung Kim,
Northwell Health, United States
Kevin M. Nickerson,
University of Pittsburgh, United States

*CORRESPONDENCE
Peter E. Lipsky
peterlipsky@comcast.net

SPECIALTY SECTION
This article was submitted to Autoimmune and Autoinflammatory Disorders : Autoimmune Disorders, a section of the journal Frontiers in Immunology

RECEIVED 18 January 2023
ACCEPTED 15 February 2023
PUBLISHED 01 March 2023

CITATION
Daamen AR, Wang H, Bachali P, Shen N, Kingsmore KM, Robl RD, Grammer AC, Fu SM and Lipsky PE (2023) Molecular mechanisms governing the progression of nephritis in lupus prone mice and human lupus patients. *Front. Immunol.* 14:1147526. doi: 10.3389/fimmu.2023.1147526

Molecular mechanisms governing the progression of nephritis in lupus prone mice and human lupus patients

Andrea R. Daamen[1], Hongyang Wang[2,3], Prathyusha Bachali[1], Nan Shen[4], Kathryn M. Kingsmore[1], Robert D. Robl[1], Amrie C. Grammer[1], Shu Man Fu[2,3] and Peter E. Lipsky[1]*

[1]AMPEL BioSolutions LLC, Charlottesville, VA, United States, [2]Center for Immunity, Inflammation, and Regenerative Medicine, Department of Medicine, University of Virginia School of Medicine, Charlottesville, VA, United States, [3]Division of Rheumatology, Department of Medicine, University of Virginia School of Medicine, Charlottesville, VA, United States, [4]Shanghai Institute of Rheumatology, Renji Hospital, Shanghai Jiao Tong University School of Medicine, Shanghai, China

Introduction: Pathologic inflammation is a major driver of kidney damage in lupus nephritis (LN), but the immune mechanisms of disease progression and risk factors for end organ damage are poorly understood.

Methods: To characterize molecular profiles through the development of LN, we carried out gene expression analysis of microdissected kidneys from lupus-prone NZM2328 mice. We examined male mice and the congenic NZM2328.R27 strain as a means to define mechanisms associated with resistance to chronic nephritis. Gene expression profiles in lupus mice were compared with those in human LN.

Results: NZM2328 mice exhibited progress from acute to transitional and then to chronic glomerulonephritis (GN). Each stage manifested a unique molecular profile. Neither male mice nor R27 mice progressed past the acute GN stage, with the former exhibiting minimal immune infiltration and the latter enrichment of immunoregulatory gene signatures in conjunction with robust kidney tubule cell profiles indicative of resistance to cellular damage. The gene expression profiles of human LN were similar to those noted in the NZM2328 mouse suggesting comparable stages of LN progression.

Conclusions: Overall, this work provides a comprehensive examination of the immune processes involved in progression of murine LN and thus contributes to our understanding of the risk factors for end-stage renal disease. In addition, this work presents a foundation for improved classification of LN and illustrates the applicability of murine models to identify the stages of human disease.

KEYWORDS

lupus, nephritis, transcriptomics, bioinformatics, translational, mouse models

Introduction

Systemic lupus erythematosus (SLE) is an autoimmune disorder that can affect a variety of tissues, including the kidney (1). Lupus nephritis (LN) affects approximately 40% of adult lupus patients with 10-20% of patients developing end-stage renal disease (ESRD) (2). Disease is thought to initiate in the kidney glomerulus with immune complex (IC) deposition and complement activation leading to the release of damage associated molecular patterns (DAMPS), cytokine production, and the infiltration of inflammatory cells that amplify and sustain inflammation (3, 4). Damage to the kidney glomerulus promotes ischemic damage and chronic hypoxia, compromising the downstream blood supply to the tubulointerstitium (TI) and reducing tubule cell viability, which serve as prognostic markers for the development of ESRD (5–7). Despite advances in understanding of LN, there remains no clear indication of factors controlling the conversion of acute to chronic nephritis and no proven treatments to prevent ESRD (8–10).

Previous studies established the NZM2328 lupus-prone mouse strain as a model of human LN, with severe IC-mediated nephritis and early mortality predominantly affecting female mice (11–13). These studies determined that disease in female NZM2328 mice presents in two stages termed acute glomerulonephritis (AGN) with pathology largely confined to the glomerulus, and chronic GN (CGN) in which inflammation and tissue damage are also found amongst and between the tubules (12, 13). AGN and CGN were associated with a genetic loci on chromosome 1, the *Agnz1* and *Cgnz1* regions respectively. In addition, the NZM2328.Lc1R27 (R27) recombinant strain was generated by replacing the *Cgnz1* region of NZM2328 with that from the C57BL/J strain, such that female R27 mice develop AGN but do not progress to CGN. Similarly, male NZM2328 mice develop a milder, acute form of nephritis but do not exhibit severe proteinuria or progress to chronic disease (14, 15).

The heterogeneity in disease presentation among LN patients and difficulty in predicting therapeutic responses have highlighted the utility of molecular profiling to improve classification of lupus kidney pathology (10, 16). Here, to understand the pathogenesis of LN and especially the relationship between acute and chronic disease in greater detail, we utilized transcriptome analysis to define the stages of GN in NZM2328 mice and identify pathologic immune populations and processes associated with disease progression. In addition, we identified distinct mechanisms of resistance to chronic disease based on differences in gender and genetics and demonstrated similarities in gene expression profiles between human and murine LN, suggesting comparable progression with implications for elucidating risk factors for development of ESRD in human lupus patients.

Materials and methods

Mice

NZM2328 and NZM2328.R27 congenic mice were obtained/generated as previously described (11, 13). All mice were housed at the University of Virginia (UVA) Center of Comparative Medicine under pathogen-free conditions.

Histological characterization

Kidneys of NZM2328 and R27 mice were harvested and the stage of GN was confirmed by histological classification (Supplementary Table 1) as previously described (11, 13). Briefly, mice were sacrificed at 8-9 weeks for the control group and 26-38 weeks for diseased mice. Before sacrifice, the presence of nephritis in diseased mice was assayed using proteinuria test strips. Mice were classified into AGN, TGN, or CGN stages by assessment of glomerular size and cellularity, mesangial expansion, glomerular sclerosis, kidney fibrosis, tubular cell dilation, tubular atrophy, and immune cell infiltration. IgG, C3, and ANA staining were performed as previously described.

Laser microdissection and microarray hybridization

LMD of snap frozen kidney sections was performed as previously described (17). Frozen sections were cut by Cryostat to 5-micron thickness and placed on dry ice. The sections were fixed in 70% ethanol followed by hematoxylin and eosin (H&E) staining. LMD was performed along and including the Bowman's capsule to isolate kidney glomeruli while tubulointerstitial tissue was collected from approximately 3-4 layers of cells outside of the microdissected glomeruli. For each mouse, 40 glomeruli/tissue picks were collected and pooled to prepare each RNA sample.

Total RNA was isolated from LMD-derived cells using PicoPure RNA isolation kit (Applied Biosystems). RNA quality was detected by Agilent Pico Gel. Array hybridization was carried out by the UT Southwestern Microarray Core facility for the Affymetrix Clariom D Array of NZM2328 female and R27 mice and by the UVA Genome Analysis and Technology Core for the GeneChip Mouse 430 v2.0 array of NZM2328 female and male mice according to standard Affymetrix protocols.

Microarray data processing

Raw CEL files from the publicly available murine IFNα-NZB (GSE86423) and human microdissected kidney (GSE32591) microarray datasets were derived from GEO using the R/Bioconductor package GEOquery. Processing of raw microarray data from all murine and human microarray datasets was carried out with the R/Bioconductor packages oligo, affy, affycoretools, and simpleaffy. Affymetrix CEL files were background corrected and normalized using the Robust Multiarray Average (RMA) or GeneChip Robust Multiarray Average (GCRMA) methods depending on the microarray platform. Normalized data was transformed into $\log_2$ intensity values and formatted as R expression set objects (E-sets). Principal component analysis

(PCA) was used to inspect the datasets for outliers. E-sets were annotated using chip definition files (CDFs) corresponding to Affymetrix Clariom D (NZM2328 female and R27 mice), Mouse 430 v2.0 (NZM2328 male mice), HT_MG-430_PM (IFNα-NZB mice), HGU133A_CDF_ENTREZG_10 (human microdissected kidney), or HG-U133_Plus_2 (human whole kidney) arrays. Low intensity probes were filtered by visual selection of thresholds at the dip in histograms of binned $\log_2$-transformed probe intensities. Variance correction was carried out using the ebayes function in the R/Bioconductor LIMMA package. Resulting p-values were adjusted for multiple comparisons using the Benjamini-Hochberg correction that produced a false discovery rate (FDR) for each comparison. Probes were distilled down to differentially expressed (DE) probes with FDR < 0.2 which were considered statistically significant.

Gene set variation analysis (GSVA)

The R/Bioconductor package GSVA (18) (v1.36.3) was used as a non-parametric, unsupervised method to estimate the variation in enrichment of pre-defined gene sets in microarray data from NZM2328 mice. The input for GSVA was a matrix of $\log_2$ expression values for all samples and a collection of gene signatures for immune cell types and functional pathways. Genes with multiple Affymetrix identifiers were selected based on the highest interquartile range (IQR) and probes with IQR=0 were filtered out. GSVA enrichment scores were calculated on a per sample basis, without specifying the sample labels, using a Kolgomorov-Smirnoff (KS)-like random walk statistic comparing the distribution of genes in the specific gene modules to those not in the module and were scaled across all samples to values between -1 and +1 indicative of negative enrichment and positive enrichment, respectively.

GSVA gene set generation

Gene sets used as input for GSVA are listed in Supplementary Table 2. Cell type and pathway gene signatures were generated based on literature mining, Mouse Genome Informatics (MGI) (19) gene ontology (GO) terms, and immune cell-specific expression derived from the Immunological Genome Project Consortium (ImmGen) (20). The glycolysis, oxidative phosphorylation, amino acid metabolism, and fatty acid oxidation gene signatures have been previously described (21). The cell type gene signatures were derived from Mouse CellScan, a tool for identification of cellular origin from mouse gene expression datasets. The pathway gene signatures were derived from the Mouse Biologically Informed Gene Clustering (BIG-C) tool for categorization of biological functions in mouse gene expression datasets.

Linear regression analysis

Linear regression analysis between GSVA enrichment scores and $\log_2$ gene expression values was carried out using GraphPad Prism software (v9.3.1). The goodness of fit is displayed as the R^2 value. The *p*-value indicates the significance of the slope of the regression line.

Ingenuity pathway analysis (IPA)

Molecules upstream of selected *Cgnz1* locus genes were identified using IPA upstream regulator (UPR) analysis (Qiagen) (22). UPRs with an overlap p-value < 0.01 were considered significant.

Multiscale embedded gene co-expression network analysis (MEGENA)

The MEGENA R package (23) was used to generate gene co-expression networks for NZM2328 mouse glomerulus and TI by inputting the top 5,000 row variance genes from the respective gene expression matrices. A planar filtered network (PFN) was formed using a false discovery rate (FDR) of 0.2. MEGENA multi-scale clustering analysis (MCA) used the PFN to form lineages of gene modules which were assigned "lineage" names based on their descendance from the root MEGENA module. Modules were functionally annotated by overlapping their gene symbols with curated mouse-specific functional signatures, immune cell, and kidney tissue cell signatures as well as the top GO terms (24) exhibiting the greatest coverage for each module. Annotations of MEGENA modules were considered significant if there were at least 3 overlapping gene symbols between the module gene symbols and annotation signature gene symbols, and the Fisher's p-value statistic of the overlap was p<0.2. A module eigengene (ME) was calculated for each module equivalent to the first principal component of a module's gene expression. Intracorrelations of sample traits were calculated for brief inspection. MEs were correlated to all sample traits and correlations were zeroed out where the p-value of the correlation was >=0.2. All second generation (gen2) MEGENA modules were retained for ensuing analysis. A gene expression set from human whole kidney biopsies was subjected to MEGENA analysis in a similar manner. Gen2 MEGENA modules from NZM2328 glomerulus and TI were examined for preservation in the MEGENA human kidney modules by utilizing an algorithm that generates z.summ composite scores of 20 preservation metrics (25).

K-means clustering

GSVA enrichment scores of gen2 MEGENA modules (Supplementary Table 4) or 22 curated immune cell, kidney cell, and metabolic pathway gene signatures (Supplementary Table 2) were used as input for k-means clustering performed with 1000 iterations to identify the most stable clusters for each dataset. Clustering results were visualized using the R package ComplexHeatmap (v 2.12) (26).

Statistical analysis

P-values and odds ratios (ORs) for the overlap of DEGs with inflammatory cell types and pathways were calculated with a two-sided fisher's exact test in R with a confidence level of 0.95. All other statistical tests were carried out with GraphPad Prism (v9.3.1). Comparisons for two groups (CTL, AGN) were calculated using an unpaired, two-sided Welch's t-test. Comparisons for more than two groups (CTL, AGN, TGN, CGN) were calculated using Brown Forsythe and Welch's ANOVA followed by Dunnett's T3 multiple comparisons test.

Study approval

Mice were kept at the University of Virginia Center of Comparative Medicine. All experimental protocols were approved by the Institutional Animal Care and Use committee.

Data availability

The murine microarray dataset generated for the current study is available from NCBI's GEO database under accession GSE206806. The human microarray dataset generated for the current study has been submitted to ArrayExpress with accession E-MTAB-12257. The publicly available murine and human microarray datasets analyzed in the current study can be found under GEO accessions GSE86423 and GSE32591, respectively.

Results

Renal disease of NZM2328 mice is characterized by escalating stages of inflammation

To identify different stages of GN in the kidneys of female NZM2328 mice, we carried out histological studies at regular intervals throughout disease progression (Figures 1A–D; Supplementary Table 1). Tissues from young mice, before disease development and without evidence of kidney pathology were used as a control (Figure 1A). At the AGN stage, glomeruli were increased in size with evidence of immune cell infiltration and immune complex deposition including IgG, C3, and anti-nuclear antibody (ANA) deposits (Figure 1B). There were no changes to tubule cells of AGN mice and they exhibited mild immune cell infiltration in the interstitium. We identified an additional intermediate stage of disease progression not previously reported termed transitional GN (TGN) at which, like the AGN stage, glomeruli exhibited immune cell infiltration, but levels of IgG and C3 deposition as well as serum levels of anti-DNA antibodies were elevated over AGN mice (Figure 1C). The interstitium of TGN mice had more inflammatory cells than at the AGN stage and tubular cells showed some dilation and atrophy. However, tubule damage was not evident histologically. At the CGN stage, mice exhibited glomerular sclerosis, fibrosis with interstitial inflammation, and the highest level of immune complex deposition as compared to earlier disease stages (Figure 1D). In CGN stage mice, >80% of tubular cells had tubular dilation with increased evidence of atrophy and tubular casts as compared to the TGN stage.

Transcriptional profiling uncovers immune populations present at the onset of GN in NZM2328 mice

To establish the inflammatory environment in the kidney at disease onset, we analyzed the transcriptomes of microdissected glomeruli and TI from the kidneys of female NZM2328 mice. Tissues from 8-9 week-old (CTL) mice were used as a control (11–13). Using Gene Set Variation Analysis (GSVA) (18) with a battery of curated gene sets (Supplementary Table 2), glomeruli of histologically-defined AGN mice were found to be enriched for gene signatures of a number of immune/inflammatory cell types, including myeloid cells, M1 macrophages (Mϕs), antigen presenting cells (APCs), CD8 T cells, and T follicular helper (Tfh) cells (Figure 1E). In addition, genes encoding immune cell receptors, including pattern recognition receptors (PRRs) as well as major histocompatibility complex (MHC) class I and II were significantly elevated in AGN glomeruli. The TI of AGN mice was enriched for many of the same immune signatures, including myeloid cells, M1 Mϕs, APCs, and MHC class II as well as the IG chain signature indicative of the presence of a plasma cell (PC) infiltrate (Figure 1F). However, despite the presence of signatures indicative of immune cells, gene signatures of podocytes in the glomeruli (Figure 1G) and of tubule cells in the TI (Figure 1H) were not significantly different than CTL. Thus, the kidneys of mice with AGN are enriched for predominantly innate immune cell gene signatures with no evidence of damage to the kidney cells.

Transcriptomic analysis reveals distinct immune profiles of acute, transitional, and chronic GN in NZM2328 mice

Next, we compared the transcriptomes of glomeruli and TI from pre-disease CTL mice to mice with progressively more severe stages of disease. Overall, we found that the more robust gene signature enrichment in later stages of disease decreased the significant differences between AGN and CTL mice (Figures 2A, C). The immune profile of glomeruli of TGN mice reflected an intermediate stage of renal disease and the peak of inflammatory signature enrichment. We found enrichment of gene signatures of germinal center (GC) B cells, myeloid cells, and Mϕs, including both M1 and M2 subsets, as well as signatures of interferon (IFN) stimulated genes, MHC class I, the cell cycle, and the Hif1a signaling pathway (Figure 2A). In addition, the inflammatory signatures enriched in AGN mice were increased further at the transitional stage. Glomeruli of CGN mice were enriched for platelets and WNT signaling and de-enriched for gene signatures of mitochondrial function and amino acid metabolism (Figure 2A).

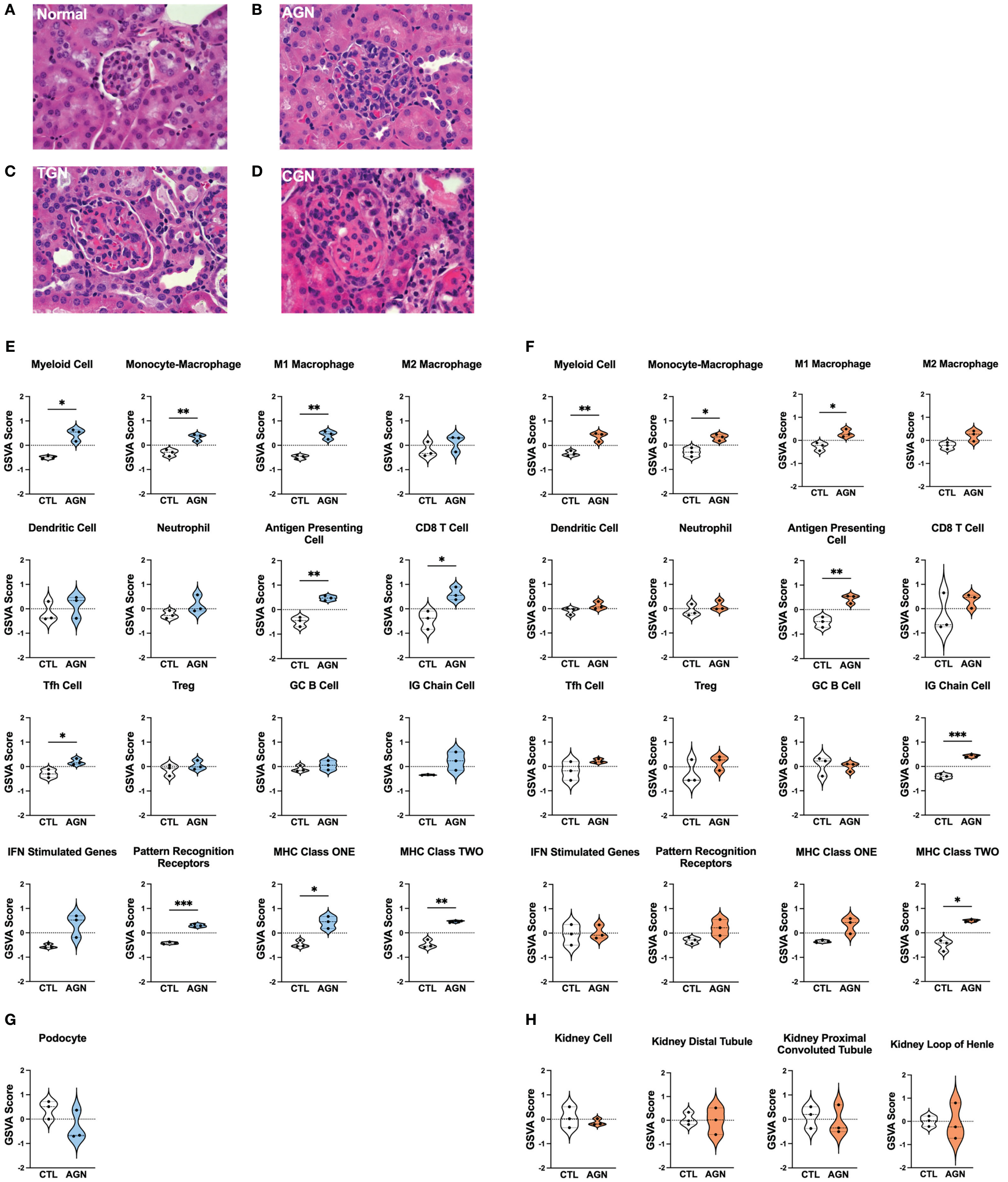

FIGURE 1
Histologic and transcriptional analysis of immune populations in NZM2328 mice with GN. **(A-D)** H&E staining of kidneys from normal/CTL **(A)** NZM2328 females and mice with acute **(B)**, transitional **(C)**, and chronic **(D)** stage GN. Individual sample gene expression from glomeruli **(E, G)** and TI **(F, H)** of CTL and AGN mice was analyzed by GSVA for enrichment of immune cells/inflammatory pathways **(E, F)** and kidney tissue cells **(G, H)**. Enrichment scores are shown as violin plots. *p<0.05, **p<0.01, ***p<0.001.

Along with the enrichment of gene signatures of inflammatory cells and pathways, we also found evidence of kidney damage in TGN and CGN mice with de-enrichment of the gene signature for podocytes (Figure 2B).

Relative gene expression results from the TI of NZM2328 kidneys showed a progressive pattern of inflammation and kidney cell loss. The TI regions of TGN kidneys were enriched for numerous immune and inflammatory signatures, including Th17

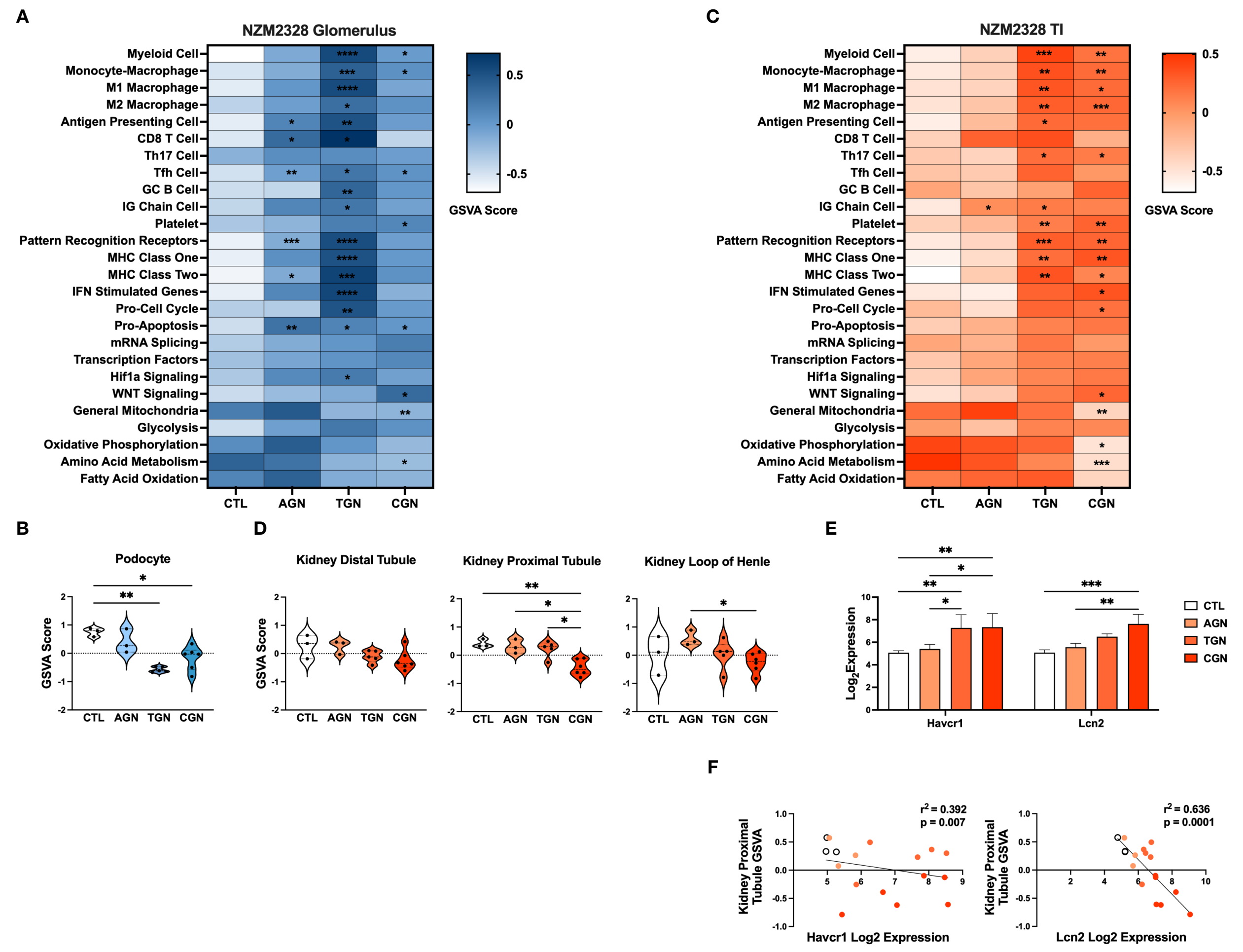

FIGURE 2
Transcriptomic analysis of GN disease stages in glomeruli and TI of NZM2328 mice. **(A)** Heatmap of GSVA scores for enrichment of immune cell and pathway gene signatures in glomeruli of CTL, AGN, TGN, and CGN mice. Asterisks indicate significant comparisons with CTL mice. **(B)** GSVA enrichment of podocytes in cohorts shown in **(A)**. **(C)** Heatmap of GSVA scores in the TI of cohorts shown in **(A)**. **(D)** GSVA enrichment of kidney tubule cell gene signatures in cohorts from **(C)**. **(E)** Log_2 expression values of kidney tubule damage-associated genes for cohorts from **(C)**. **(F)** Linear regression between log_2 expression of kidney tubule damage genes and GSVA scores of kidney tubule cells. *$p<0.05$, **$p<0.01$, ***$p<0.001$, ****$p<0.000$.

cells, PRRs, MHC class I and II, myeloid cells, and M1 and M2 Mϕs (Figure 2C). The TI of CGN mice exhibited enrichment of IFN stimulated genes, the cell cycle, and WNT signaling as well as decreases in gene signatures for mitochondria, amino acid metabolism, and oxidative phosphorylation (Figure 2C). We found further indicators of damage to the kidney tubules in CGN mice with decreases in kidney tubule cell gene signatures (Figure 2D) that correlated with significant increases in the expression of the kidney tubule damage-associated genes, *Havcr1* and *Lcn2* (Figures 2E, F). Overall, these results suggest that renal disease in female NZM2328 mice progresses from the glomerulus to the tubules and that inflammation established in the acute and transitional stages promotes a decrease in kidney cell signatures, indicative of cell damage.

Lack of a robust inflammatory signature in glomeruli of NZM2328 male mice is associated with absence of progression to chronic renal disease

To gain insight into the basis of the difference in gender-based resistance to chronic disease, we evaluated the transcriptomes of glomeruli from male NZM2328 mice with AGN at 10 months of age as compared to pre-disease, 8-9-week-old mice (Figure 3). Even though male mice were selected because they had evident immune complex deposition, male AGN mice, in contrast to the females, were not enriched for gene signatures indicative of a robust adaptive immune response or increased inflammation in the kidneys (Figure 3A). Instead, males exhibited enrichment for signatures of mRNA splicing

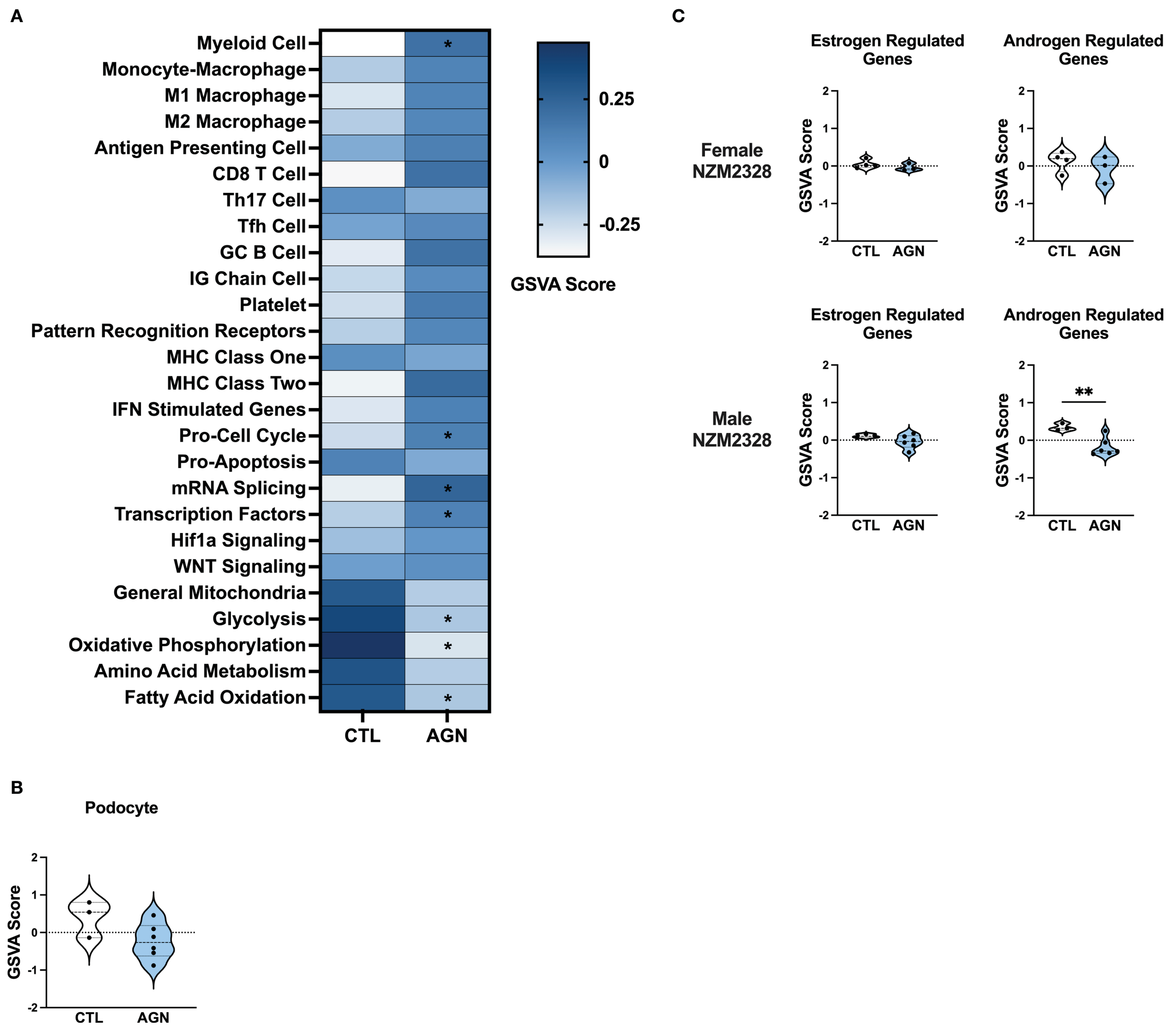

FIGURE 3

Male NZM2328 mice lack inflammatory signature enrichment associated with progression to chronic GN. **(A)** Heatmap of GSVA scores for enrichment of immune cell and pathway gene signatures in glomeruli of male CTL and AGN mice. Asterisks indicate significant comparisons with CTL mice. **(B)** GSVA enrichment of podocytes in cohorts shown in **(A)**. **(C)** GSVA enrichment of signatures for estrogen-regulated and androgen-regulated genes in glomeruli of female and male AGN mice. *p<0.05, **p<0.01.

and transcription factors and de-enrichment of metabolic pathways, including glycolysis, oxidative phosphorylation, and fatty acid oxidation. In addition, there was no difference in expression of kidney tissue signatures in male AGN mice as compared to normal controls (Figure 3B).

To assess the role of sex hormones in renal disease in NZM2328 mice, we developed signatures of estrogen- and androgen-regulated genes and compared their enrichment in female and male mice with AGN as compared to normal controls (Figure 3C). Female AGN mice exhibited no differences in enrichment of hormone-regulated gene signatures. However, in males, androgen-regulated genes were decreased in AGN mice. Furthermore, most androgen-regulated genes de-enriched in male mice were related to mitochondrial function and metabolic pathways, including *Akap1, Cox6b1, Iapp, Mrps6, Mybbp1a, Ndufa1, Phkg2, Prelid1, Sord*, and *Tmem86a*. This result suggested that decreased expression of male hormone response genes in AGN mice may contribute to resistance to disease progression by regulating metabolism and dampening inflammation.

Inflammatory gene signatures in glomeruli of R27 mice differ from those in NZM2328 mice

We next examined the R27 congenic mouse strain as female R27 mice develop AGN with similar kidney pathology to NZM2328 mice, but do not progress further to severe proteinuria and ESRD. We compared gene expression profiles from glomeruli and TI of normal, CTL R27 mice (8-9 weeks) and R27 mice with AGN (12 months). R27 mice were selected for the presence of proteinuria and glomerular deposits of immunoglobulin detected by immunofluorescence. Examination of differentially expressed genes (DEGs) from glomeruli of NZM2328 and R27 mice relative to their respective CTLs (Supplementary Table 3, Supplementary Figure 1A) revealed significant overlaps with increased expression of APC, myeloid cell, Mϕ, and MHC signatures. In contrast, DEGs from NZM2328 but not R27 AGN mice showed overexpression of PRRs and IFN stimulated genes, suggesting a more severe inflammatory environment.

GSVA analysis of R27 AGN glomeruli (Figures 4A, C) demonstrated enrichment of gene signatures indicative of inflammation, including APCs, IG Chains, Mϕs, and MHC class I and II (Figure 4A). Notably, analysis of Mϕ subsets revealed enrichment of anti-inflammatory M2, but not pro-inflammatory M1 Mϕs in R27 mice. No enrichment of IFN stimulated genes, PRRs, or Hif1a signaling between R27 control and AGN mice was detected. Moreover, no evidence of change in kidney cell-specific gene signatures was found in R27 AGN (Figure 4B).

NZM2328.R27 mice exhibit resistance to kidney tubule damage

Next we compared DEGs expressed in the TI of R27 AGN mice relative to NZM2328 mice with AGN (Supplementary Table 3, Supplementary Figure 1B). DEGs from the TI of NZM2328 AGN mice were indicative of APCs, myeloid cells, Mϕs, and MHC class II, indicating the presence of some immune infiltrates but not to the

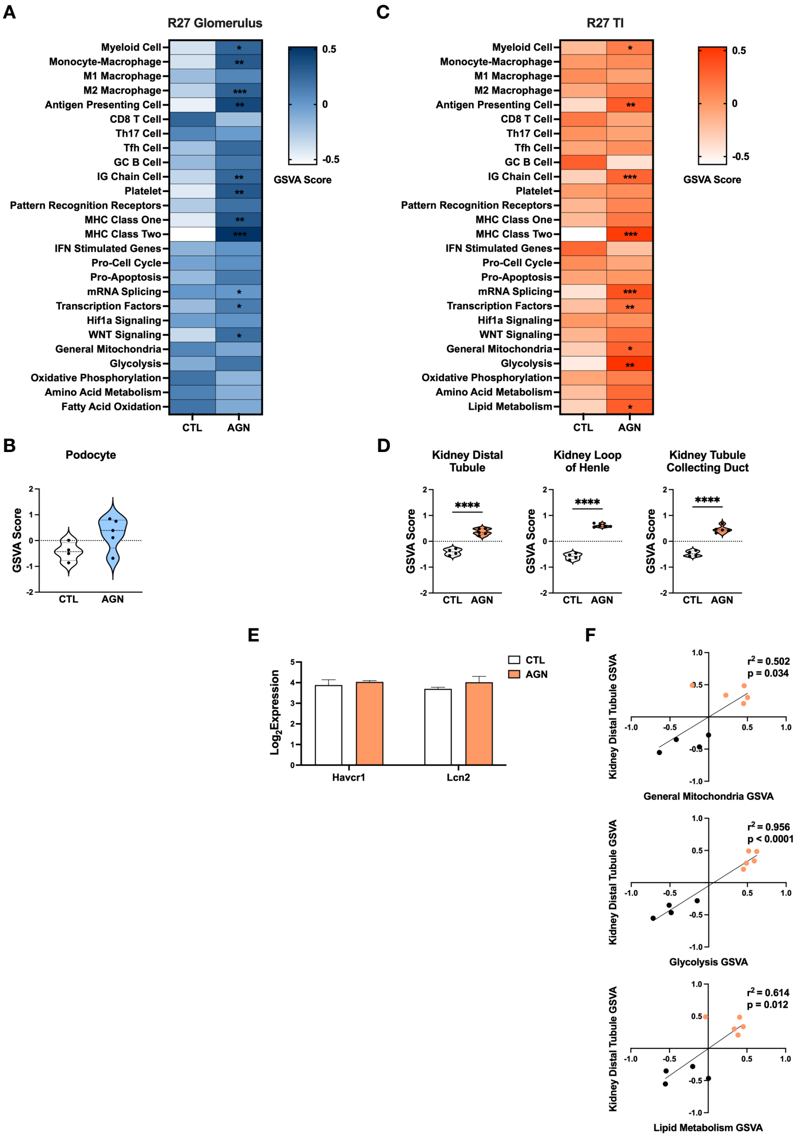

FIGURE 4
Molecular profiles of R27 mice differ from NZM2328 mice and indicate resistance to kidney tubule damage. **(A)** Heatmap of GSVA scores for enrichment of immune cell and pathway gene signatures in the glomeruli of R27 CTL and AGN mice. Asterisks indicate significant comparisons with CTL mice. **(B)** GSVA enrichment of podocytes in cohorts shown in A. **(C)** Heatmap of GSVA scores in the TI of cohorts shown in A. **(D)** GSVA enrichment of kidney tissue cell signatures in cohorts shown in C. **(E)** Log2 expression values of kidney tubule damage-associated genes for cohorts from C. **(F)** Linear regression between GSVA scores of kidney tubule cell and metabolic pathway gene signatures. *p < 0.05, **p < 0.01, ***p < 0.001, ****p < 0.0001.

same extent as the inflammation in the glomeruli at this early point in disease. In contrast, DEGs from R27 AGN mice were only indicative of APC and MHC class II and were not associated with other inflammatory signatures.

Similarly, GSVA of the TI of R27 AGN mice confirmed the enrichment of APCs, IG chains, and myeloid cell signatures, but not Mϕs, denoting a less extensive infiltration of immune/inflammatory cells in the R27 mice. (Figure 4C). Previous studies using the R27 strain found evidence that resistance to end organ damage might contribute to their decreased development of CGN (13). In support of this, we found that kidney tubule cell signatures were significantly increased in R27 AGN mice (Figure 4D), whereas the kidney damage-associated genes, *Havcr1* and *Lcn2*, were unchanged (Figure 4E). We also found that gene signatures related to mitochondria, glycolysis, and lipid metabolism were increased (Figure 4C) and were significantly correlated with the kidney tubule cell gene signature (Figure 4F), suggesting that robust mitochondrial function may contribute to the kidney tubule cell enrichment observed in R27 AGN mice.

Kidney cell signatures enriched in NZM2328.R27 mice correlate with expression of chronic GN risk locus genes

The risk for progression to CGN in NZM2328 mice was associated with a 1.34 Mb region of chromosome 1 (*Cgnz1*) containing 45 genes (13). We analyzed differential expression of these CGN susceptibility genes in glomeruli and TI of female NZM2328 AGN/TGN/CGN, and R27 AGN mice as compared to normal controls to determine their contribution to renal disease progression (Figure 5). In the glomerulus, we found that genes encoding receptors expressed on immune cells and associated with inflammation, including *Cd244, Fcer1g, Fcgr3, Fcgr4*, and *Slamf7*, were significantly increased in NZM2328 AGN, whereas none was overexpressed in R27 kidneys (Figure 5A; Supplementary Figure 2). Expression of these genes as well as additional immune-associated *Cgnz1* locus genes was further increased at the height of inflammatory cell and pathway gene signature enrichment at the TGN stage and either maintained or decreased at the CGN stage in glomeruli of NZM2328 mice.

In the TI, there were no significant differences in expression of *Cgnz1* locus genes in NZM2328 or R27 female AGN mice as compared to normal controls (Supplementary Figure 3). Furthermore, this result was consistent with the minimal inflammatory signature observed in AGN mice. However, at the TGN stage of NZM2328 mice, expression of immune-associated *Cgnz1* locus genes increased significantly over normal control mice, providing further evidence for the critical role of the CGN risk locus in progression to chronic disease (Figure 5B)

To investigate the relationship between CGN risk locus gene expression and kidney tubule cell enrichment in R27 female AGN mice, we carried out linear regression analysis (Figure 5C), and found that $\log_2$ expression values for 7 of the 45 genes composing the *Cgnz1* locus (*Apoa2, Fcer1g, Ncstn, Ndufs2, Nit1, Pex19, Sdhc*) were significantly correlated with GSVA scores for kidney distal tubule cells and thus could play a role in promoting resistance to kidney damage. Notably, we found that the proteins encoded by these genes were involved in mitochondrial respiration (*Ndufs2, Sdhc*), metabolite processing (*Apoa2, Ncstn, Nit1, Pex19*) and immune signaling (*Fcer1g*). Furthermore, $\log_2$ expression values for 4 of these genes (*Apoa2, Ndufs2, Nit1*, and *Sdhc*) were significantly correlated with kidney tubule cell GSVA scores and significantly decreased in the TI of NZM2328 CGN mice as compared to normal controls (Figures 5D, E).

To delve further into the functional pathways involving these kidney cell-associated genes, we identified upstream regulators (UPRs) using Ingenuity Pathway Analysis (IPA) (22) (Supplementary Table 4). Notable UPRs predicted to drive expression of the 7 *Cgnz1* genes correlated to kidney tubule cell enrichment included Rb1, Rictor, Wnt3a, Ctnnb1, and Hif1a and thus reflected the involvement of cell growth regulation, WNT signaling, and hypoxic stress response pathways in the kidneys of R27 AGN mice. These results suggest that the cellular functions associated with expression of some of the *Cgnz1* risk locus genes in R27 mice could contribute to robust mitochondrial function and promote resistance to kidney tissue damage in the context of acute nephritis.

Gene co-expression network analysis identifies molecular profiles correlating with disease progression in NZM2328 mice

As an orthogonal approach to identify molecular patterns reflective of disease stage in NZM2328 mice in an unsupervised manner, we generated a network of co-expressed gene modules using multiscale embedded gene co-expression network analysis (MEGENA) (23) and correlated individual gene modules with mouse GN stages (Figure 6). MEGENA of gene expression results from NZM2328 mice generated 60 co-expressed gene modules for the glomerulus and 48 modules for the TI that were divided into three megaclusters and annotated based on gene overlap with curated gene signatures as well as gene ontology (GO) terms (Supplementary Table 5). Overall, the MEGENA-derived gene modules were representative of the major cell types and processes we had previously associated with GN using curated gene signatures, including inflammatory myeloid cells, kidney tissue cells, and metabolic processes. Furthermore, k-means clustering based on the MEGENA modules successfully separated mice into cohorts based on disease severity. In the glomerulus (Figure 6A), the coral cluster of CTL and AGN mice was positively correlated with gene modules associated with kidney cells and metabolic processes, and negatively correlated with gene modules related to the immune/inflammatory response. Two clusters (maroon and green) contained a combination of TGN and CGN mice and were positively correlated with immune response modules and negatively correlated with kidney cell and metabolism modules. The final cluster of CGN mice (blue) had a negative correlation with immune response and kidney/metabolic modules but retained a high positive correlation with secreted immune factors. MEGENA results and correlations with disease stage in the TI (Figure 6B) were

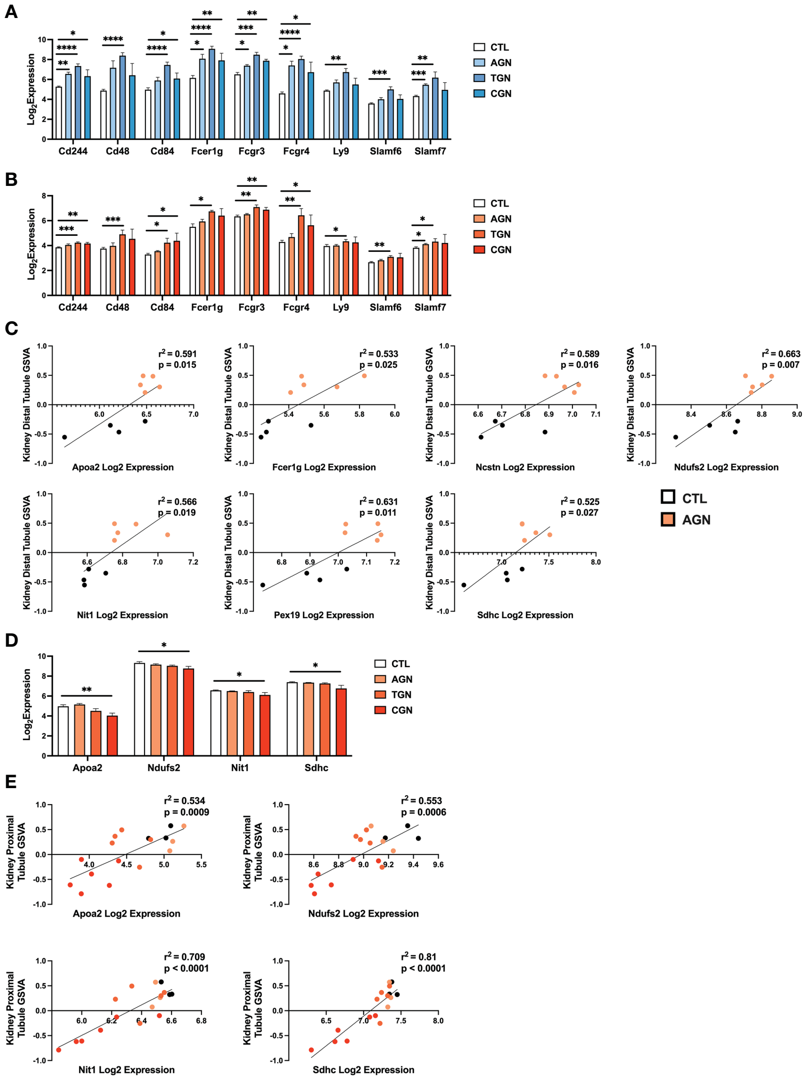

FIGURE 5

Expression of chronic risk locus genes is associated with disease severity and kidney tubule resistance in NZM2328 and R27 AGN mice. **(A, B)** Log$_2$ expression values of immune receptor genes in the *Cgnz1* risk locus from glomeruli **(A)** and TI **(B)** of NZM2328 CTL, AGN, TGN, and CGN mice. **(C)** Linear regression between log$_2$ expression of *Cgnz1* locus genes and GSVA scores of kidney tubule cells from the TI of R27 mice. All statistically significant correlations are shown. **(D)** Linear regression between log$_2$ expression of *Cgnz1* locus genes from C and GSVA scores of kidney tubule cells from the TI of NZM2328 mice. All statistically significant correlations are shown. **(E)** Log$_2$ expression values *Cgnz1* locus genes from C in the TI of NZM2328 CTL, AGN, TGN, and CGN mice. $^*p<0.05$, $^{**}p<0.01$, $^{***}p<0.001$, $^{****}p<0.0001$.

similar to the glomerulus, but the resulting gene modules were more heavily skewed toward mitochondrial metabolism and the blue cluster of CGN mice was still positively correlated with the immune response-associated modules. In summary, this unsupervised approach employing co-expressed gene modules yielded results that closely resemble our previously identified molecular profiles of disease progression in NZM2328 mice.

Identification of gene signatures characterizing GN stages in NZM2328 mice

We next sought to assemble a panel of curated gene signatures that would characterize the inflammatory environment in different stages of murine GN and determine whether similar immune profiles could be identified in human LN kidneys. To accomplish this, a core set of 22 GSVA gene signatures was selected based on significant enrichment in AGN, TGN, or CGN NZM2328 mice (Supplementary Table 2; Figures 2A, C). GSVA scores were then used as input for k-means clustering to form 4 clusters of mice from the glomerulus and TI gene expression datasets (Figures 7A, B). In the glomerulus, AGN mice in the maroon cluster were characterized by slightly increased enrichment of inflammatory immune cells compared to CTL mice but retained enrichment of kidney tissue cell and metabolism gene signatures (Figure 7A). TGN mice in the green cluster exhibited the highest enrichment of all inflammatory gene signatures accompanied by a decrease in metabolic and kidney cell signatures. CGN mice were divided among multiple clusters and thus reflected heterogeneity in

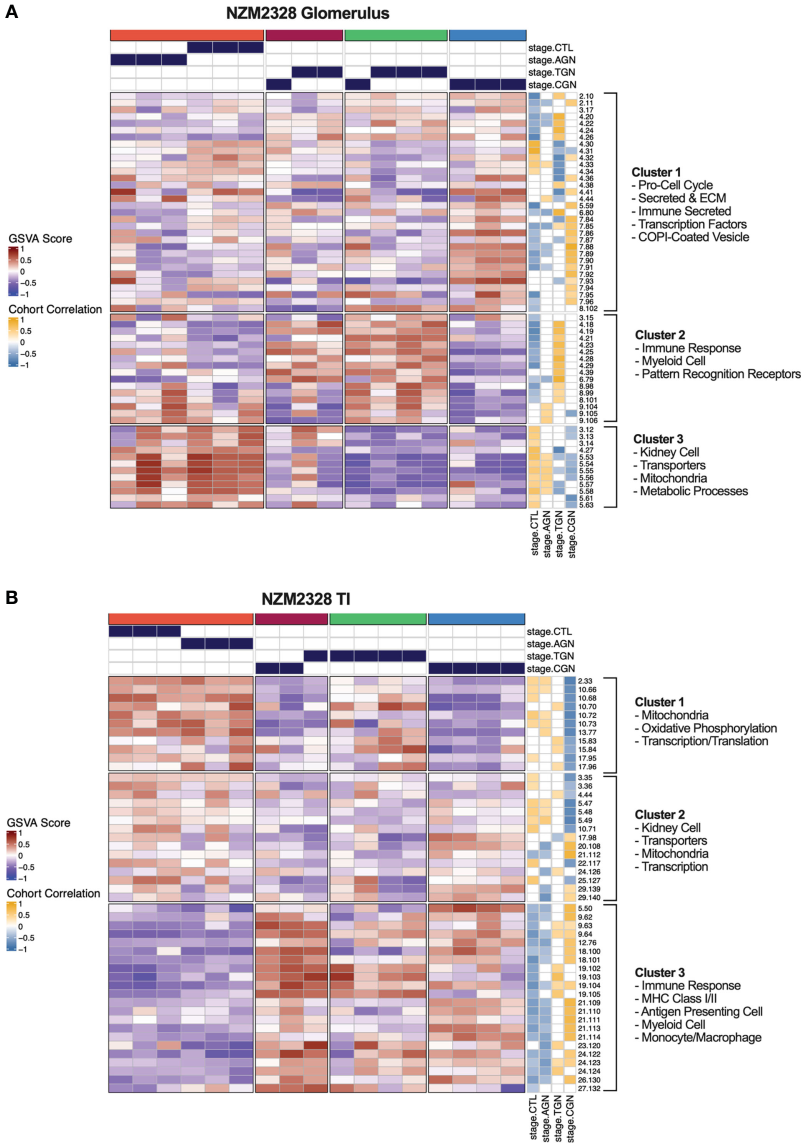

FIGURE 6
Unsupervised gene co-expression network analysis defines molecular profiles of NZM2328 mice correlated with disease severity. **(A, B)** K-means clustering (k=4) of NZM2328 CTL, AGN, TGN, and CGN mouse glomeruli **(A)** and TI **(B)** based on GSVA enrichment scores of MEGENA modules. The optimal number of module clusters was defined by the silhouette method and annotated by gene overlap with curated immunologic signatures and GO terms. Heatmap visualizations depict positive to negative GSVA scores on a red to blue gradient and positive to negative correlations between GSVA scores and disease classification on a gold to blue gradient.

immune profiles among mice at this stage of disease. Two CGN mice were placed in the coral cluster with CTL mice reflecting waning inflammation and retention of metabolic and kidney cell signatures. Another group of CGN mice with continued evidence of inflammatory gene signatures were found in the green cluster with TGN mice. Finally, the blue cluster of CGN mice exhibited a relative de-enrichment of immune cells, kidney cells, and metabolic pathways indicative of a post-inflammatory state with evidence of end organ damage.

Gene expression-based clustering of the TI yielded similar results as the glomerulus with increasing inflammation and decreasing metabolism and kidney tubule cell gene signatures marking progression in disease severity (Figure 7B). However, in the TI, the AGN mice clustered with CTLs and more of the CGN mice appeared to retain immune cell enrichment, reflecting persistent immune cell infiltration.

Validation of NZM2328 gene expression patterns in an unrelated dataset

To validate the findings in NZM2328 mice in another lupus-prone strain, we applied the same approach to analysis of publicly available gene expression data from whole kidney tissue of the IFNα-

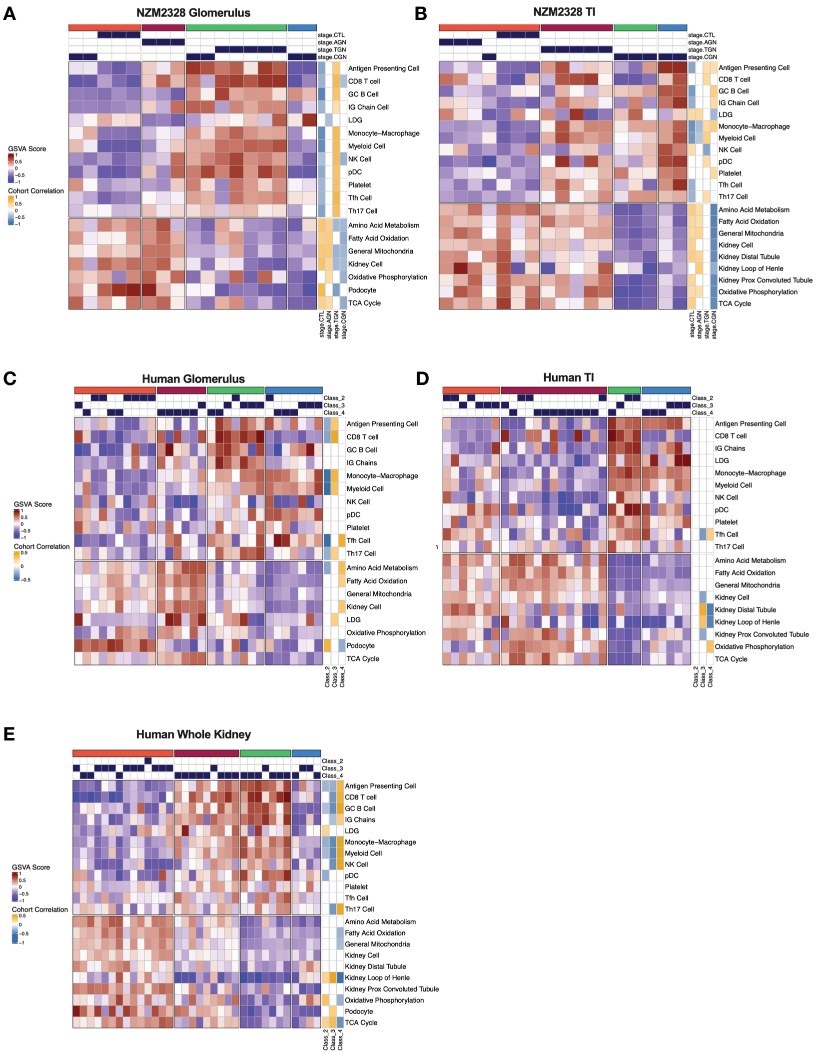

FIGURE 7

Gene signature-based clustering of GN stages in NZM2328 mice translates to human LN patients. **(A, B)** K-means clustering (k=4) of NZM2328 CTL, AGN, TGN, and CGN mouse glomeruli **(A)** and TI **(B)** based on GSVA enrichment scores of selected immune cell, kidney cell, and metabolic pathway gene sets. **(C-E)** K-means clustering (k=4) of microdissected glomeruli **(C)**, TI **(D)**, and whole kidney **(E)** from human LN patients based on GSVA score from human orthologs of the mouse gene sets used in **(A, B)**. Heatmap visualizations depict positive to negative GSVA scores on a red to blue gradient and positive to negative correlations between GSVA scores and disease classification on a gold to blue gradient.

accelerated NZB/W model (IFNα-NZB, GSE86423). Notably, the 22 curated gene expression signatures used to separate disease stages in NZM2328 mice, followed a similar enrichment pattern over a 9-week time course in IFNα-NZB mice indicating that this result was not unique to the gene expression dataset we generated from the NZM2328 strain (Supplementary Figure 4).

Gene signatures characterizing GN stages in NZM2328 mice identify analogous subsets of human LN patients

To determine whether immune profiles of NZM2328 mice with different stages of GN would translate to human lupus patients, we analyzed a publicly available gene expression dataset of microdissected glomeruli and TI from kidneys of patients with International Society of Nephrology (ISN) class II-IV LN as determined by histological classification (GSE32591) (27). We carried out GSVA using human orthologs of the 22 curated mouse gene signatures and identified 4 molecular endotypes by k-means clustering based on the pattern of enriched gene signatures in each individual patient (Supplementary Table 1; Figures 7C–E). GSVA results of glomeruli and TI from kidneys of LN patients formed 4 patient clusters that exhibited similar gene set enrichment profiles to the nephritic kidneys of NZM2328 mice (Figures 7C, D). In both the glomerulus and TI, we observed a clear progression with increased enrichment of inflammatory cells corresponding with de-enrichment of kidney tissue cells as well as metabolic pathway signatures. In addition, the cohort correlations between LN classification and gene signature enrichment revealed increased correlations with pro-inflammatory cells in proliferative nephritis, particularly in the glomerulus, and corresponding negative correlations with kidney tissue cell signatures. However, whereas in the mouse kidneys we observed a post-inflammatory cluster of CGN stage mice, human LN samples with the greatest de-enrichment in metabolic and kidney cell signatures also retained a relatively high enrichment of immune/inflammatory cell signatures.

To confirm these results, we generated and analyzed a second gene expression dataset from whole kidneys of human LN patients in a similar manner (Figure 7E). Notably, gene signature enrichment profiles of each human whole kidney subset more closely resembled clusters from mouse GN, including a cluster of samples that exhibited both de-enrichment of inflammatory signatures and metabolic signatures. GSVA of human whole kidney gene expression using the unsupervised MEGENA modules generated for NZM2328 mouse kidneys (Figure 6) also yielded similar patterns of gene expression enrichment across LN patient clusters (Supplementary Figure 5). As an additional approach to establish similarities between mouse and human kidney gene expression profiles, we carried out MEGENA using the human LN whole kidney dataset. Then, MEGENA modules generated for the NZM2328 mouse (Figure 6) were used as a reference to determine the preservation of gene module assignment between the mouse and human kidney gene co-expression networks (Supplementary Table 5). The results indicated that 22 MEGENA modules from the mouse glomerulus and 31 MEGENA modules from the mouse TI had a significant module preservation score (z-score > 2) with human kidney modules indicating a high degree of overlap in their gene expression profiles. Overall, these results demonstrate that gene expression analysis can be used to classify stages of GN in lupus-prone mice and that mouse kidney endotypes can be translated to human LN patients.

Discussion

The challenge of classifying disease pathology in heterogeneous presentations of LN has highlighted the need for a better understanding of disease progression in the kidneys of lupus patients and the risk factors for ESRD. To begin to address this, we utilized gene expression analysis to characterize stages of autoimmune inflammation leading up to the development of chronic disease in an established murine model of human GN. Mice were classified in disease stages by histological comparison, matching mice by level of disease pathology and amount of IC deposition. This analysis revealed distinct immune profiles for acute disease, after initial IC deposition in the kidney glomerulus, transitional disease in which inflammatory cell and pathway enrichment is at its peak, and chronic disease in which the accumulated insults result in irreversible damage to the kidney tissue.

We found evidence of selective immune cell infiltration in glomeruli of AGN mice, including enrichment for Monocyte/Mϕ, APC, MHC Class II, and Tfh cell gene signatures. This result reflects a limited set of immune/inflammatory cells present in the tissues at the initiation of AGN and likely reflects the cellular response to IC deposition (1, 12, 28). Enrichment of apoptosis and PRR gene signatures at the AGN stage may reflect the widening innate immune response triggered by early DAMP release from the kidney tissue. At the AGN stage, glomeruli of NZM2328 mice were also enriched for CD8 T cells, which studies have found to be elevated in both human and mouse GN and have been linked with disease severity (29–31). However, it is possible that in the context of AGN, these CD8 T cells act in a more regulatory rather than effector cell capacity, as previously suggested (32).

Our classification of the progression of GN in NZM2328 mice uncovered a newly recognized transitional stage during which we observed the greatest level of immune activity. As NZM2328 mice progressed to TGN, we observed a striking increase in innate immune response pathways and evidence of significant myeloid cell infiltration in the kidney tissue. Previous molecular studies of LN report a robust IFN response as the key feature distinguishing kidneys of lupus patients from healthy individuals and the TGN stage is when we first observed significant enrichment of an IFN signature in glomeruli of diseased mice (33–35). In line with this result, we also found significant enrichment of Mϕ populations in TGN mice and, in particular, those with a pro-inflammatory, M1 rather than an alternatively activated, M2 gene signature. Mϕs with both an M1 and an M2 phenotype have been described in mouse models of LN and associated with disease pathogenesis (36–39). However, despite the production of anti-inflammatory molecules by M2 Mϕs, the amplification of inflammatory cytokine production by immune and kidney tissue cells was found to overwhelm any regulatory response and promote disease progression. Kidney-infiltrating Mϕs are also important mediators of damage to the kidney tissue and we found that increases in Mϕ signatures in TGN mice were accompanied by decreases in kidney cell signatures and, in particular, podocytes. Podocytes are frequent targets of immune infiltration in the glomerulus and podocyte injury has been associated with proteinuria in lupus patients and is regarded as a precursor to end organ renal damage (40–42).

It has been reported that the low oxygen tension environment in the kidney becomes more hypoxic in LN, correlates with disease severity, and is associated with mitochondrial dysfunction in lupus mouse models (43, 44). In addition, several studies supporting the "chronic hypoxia hypothesis" have identified hypoxia-induced damage in the TI as the final critical pathway leading to ESRD in human patients (3, 5, 45). Our results align with these studies as we observed enrichment of the hypoxia response pathway through Hif1a in the glomeruli of TGN mice. Furthermore, heightened severity of disease pathology in CGN mice was accompanied by evidence of further damage to the kidney tissue, as well as a loss of mitochondrial and metabolic gene signatures suggestive of mitochondrial dysfunction. Therefore, our results support previous assertions that targeting the hypoxia response and mitochondrial dysfunction may be beneficial in the treatment of lupus patients (44, 46).

Glomeruli serve as the first connection points of kidney nephrons with the vasculature before disease progresses downstream to the kidney tubules such that kidney tubule damage is regarded as a diagnostic marker for progression to

ESRD (7, 47). In line with this, enrichment of inflammatory cell and pathway gene signatures was delayed in the TI as compared to glomeruli of nephritic mice and resulted in de-enrichment of kidney tubule cell gene signatures in the TI of CGN mice. We also found that the expression of kidney-damage associated genes *Havcr1* and *Lcn2* (48–51) was significantly elevated in the TI of CGN mice. In addition, de-enrichment of metabolic gene signatures indicative of mitochondrial dysfunction was more prevalent in the TI of CGN mice suggesting that mitochondrial stress contributed to kidney tubule damage in late-stage disease.

Here, we also examined the mechanism(s) of resistance to chronic disease based on differences in gender and genetic background of lupus-prone NZM2328 mice. The increased prevalence of SLE in females over males in both human lupus patients and certain lupus mouse models implicates sex hormones in the pathogenesis of LN (52–55). Our analysis by both histology and gene expression-based approaches confirmed that male NZM2328 lupus-prone mice develop a milder form of AGN than female mice that does not progress to CGN (14). In addition, critical metabolic signatures, including glycolysis and oxidative phosphorylation, were decreased in male AGN mice suggestive of a dampened inflammatory response. Analysis of sex hormone-regulated gene signatures in the kidney did not indicate a difference in the estrogen response of female or male mice, which has been associated with lupus pathogenesis in both humans and mouse models (56–59). However, in many cases, the effects of estrogen regulation have been on immune cell populations and, therefore, we cannot discount an influence of estrogen regulation on circulating immune cells outside of the kidney tissue. In contrast to estrogens, androgens have been implicated in immunosuppression with decreased levels found in autoimmunity (60, 61). In line with this, androgen-regulated genes were de-enriched in male NZM2328 AGN mice and the genes contributing to this decrease were involved in cellular metabolism, suggesting a mechanism of androgen regulated immunosuppression through targeting metabolic pathways that is decreased in NZM nephritic mice.

We investigated the genetic-based resistance to chronic disease using female mice of the congenic strain, NZM2328.R27 (13). Interestingly, glomeruli of R27 mice exhibited evidence of anti-inflammatory, M2 Mϕ infiltration with no enrichment of the pro-inflammatory, M1, gene signature observed in the base strain. This result suggests that the altered nature of the inflammatory response in R27 AGN mice contributes to end organ resistance to disease. Furthermore, the TI of R27 AGN mice exhibited enrichment of gene signatures indicating a resistance to damaging pathologic processes stemming from inflamed glomeruli including increased kidney tubule cell signatures in conjunction with increased mitochondrial and metabolic gene signatures.

Since the R27 strain was derived by replacing the chronic disease risk locus, *Cgnz1*, of NZM2328, we examined the potential contribution of the 45 genes within this locus to resistance to CGN. We uncovered several pro-inflammatory genes with elevated expression in NZM2328 female mice, that would promote the activation of pathogenic immune populations such as M1 Mϕs and have been implicated in GN (62, 63). Furthermore, 7 risk locus genes that significantly correlated with kidney tubule cell signature enrichment in R27 AGN mice were involved in cell growth, metabolism, and WNT signaling. Involvement in boosting mitochondrial function could counteract the risk of mitochondrial stress and loss of function that were present in late-stage NZM2328 female mice. In addition, WNT signaling has been shown to have a positive role in resolving acute kidney injury, whereas it may promote maladaptive responses during chronic disease (64).

We have identified multiple mechanisms by which lupus-prone mice acquire resistance to chronic nephritis with implications for identifying risk factors for ESRD in human lupus patients. Interestingly, these mechanisms appear to be independent of the amount of IC deposition as all AGN mice (NZM2328 female, NZM2328 male, and R27 female) were matched by the level of pathology before monitoring disease progression. Resistance to chronic disease in male NZM2328 mice may have occurred at the initial point of IC deposition in the glomerulus, which failed to elicit a potent inflammatory response, possibly related to androgen-dependent suppression of energy-producing metabolic pathways. Resistance to chronic disease in R27 mice was associated with an altered composition of immune cells in the glomerulus that resulted in a lack of immune pathology downstream in the tubules. Moreover, the tubules in the R27 mice appear to be resistant to damage, as manifested by enhanced metabolic signatures. The resistance of tubules to damage related to immune activity in the glomerulus and/or hypoxia could play a pivotal role in preventing the typical inflammatory infiltrate in the TI of CGN, Thus, the absence of tubular dysfunction may have limited the inflammatory infiltrate in the TI and ultimately prevented additional damage to the kidney tissue.

Using a gene expression-based clustering approach, we have identified a core set of curated gene signatures able to classify disease stages of murine GN into molecular endotypes that effectively translate to human LN patients. Notably, human orthologs of the murine GN gene signatures identified a similar pattern in two independent cohorts of human LN patients consisting of increased enrichment of inflammatory cells and corresponding de-enrichment of metabolic pathways and kidney tissue cells associated with more advanced stages of kidney pathology. In current practice, the severity of LN pathogenesis is determined by histological classification, which is used to drive therapeutic decisions and assess the potential for terminal kidney damage (27, 65, 66). We found only modest correlation between ISN histological classification of renal pathology in human LN patients and molecular classification by gene expression profiling and the gene signature correlations that were identified were inconsistent across patients with the same ISN class and between datasets. This result emphasizes the subjectivity of histological assessment of renal pathology, and suggests that molecular classification may be a more robust and reproducible approach to classification of human LN.

An orthogonal, unsupervised approach to generate co-expressed gene modules (MEGENA) also identified similar molecular patterns that effectively classified mouse GN stages, human LN patients, and were highly conserved between species. This unsupervised approach supplies further validation for gene expressed-based profiles derived from curated gene signatures as well as the utility of lupus mice to recapitulate human LN at the molecular level. In summary, this work provides a comprehensive examination of the immune processes involved in progression of murine GN to chronic disease resulting in renal failure. In addition, this work presents a foundation for improved classification of LN based on molecular endotypes and illustrates the applicability of murine models to better understand the stages of human disease.

Data availability statement

The murine microarray dataset generated for the current study is available from NCBI's GEO database under accession GSE206806. The human microarray dataset generated for the current study is available from ArrayExpress under accession E-MTAB-12257. The publicly available murine and human microarray datasets analyzed in the current study can be found under GEO accessions GSE86423 and GSE32591, respectively.

Ethics statement

The studies involving human participants were reviewed and approved by Shanghai Institute of Rheumatology. The patients/participants provided their written informed consent to participate in this study. The animal study was reviewed and approved by the University of Virginia Animal Care and Use Committee.

Author contributions

Conceptualization: AD, HW, SF, and PL. Methodology: AD, HW, SF, and PL. Software: PB. Formal analysis: AD, HW, PB, KK, and RR. Data Curation: HW, SF, NS, PB, KK, and RR. Writing – original draft: AD. Writing – review & editing: AD, HW, KK, NS, RR, and PL. Visualization: AD and HW. Supervision: NS, SF, AG, and PL. Project administration: NS, SF, AG, and PL. Funding acquisition: SF, AG, and PL. All authors contributed to the article and approved the submitted version.

Funding

NIH Grants R01 AR-047988 and R01 AI-148231 (SF). RILITE Research Foundation (AG, PL).

Acknowledgments

We thank the UT Southwestern Microarray Core facility, UVA Genome Analysis and Technology Core, and Shanghai Institute of Rheumatology for assistance in preparation of mouse and human microarrays. We thank the authors of previous studies who made their data publicly available and facilitated our validation analyses.

Conflict of interest

Authors AD, PB, KK, RR, AG, and PL were employed by AMPEL BioSolutions LLC.

The remaining authors declare that the research was conducted in the absence of any commercial or financial relationships that could be construed as a potential conflict of interest.

Publisher's note

Supplementary material

The Supplementary Material for this article can be found online at: https://www.frontiersin.org/articles/10.3389/fimmu.2023.1147526/full#supplementary-material

References

1. Davidson A. What is damaging the kidney in lupus nephritis? *Nat Rev Rheumatol* (2016) 12:143–53. doi: 10.1038/nrrheum.2015.159

2. Maria NI, Davidson A. Protecting the kidney in systemic lupus erythematosus: from diagnosis to therapy. *Nat Rev Rheumatol* (2020) 16:255–67. doi: 10.1038/s41584-020-0401-9

3. Mimura I, Nangaku M. The suffocating kidney: Tubulointerstitial hypoxia in end-stage renal disease. *Nat Rev Nephrol* (2010) 6:667–78. doi: 10.1038/nrneph.2010.124

4. Suárez-Fueyo A, Bradley SJ, Klatzmann D, Tsokos GC. T Cells and autoimmune kidney disease. *Nat Rev Nephrol* (2017) 13:329–43. doi: 10.1038/nrneph.2017.34

5. Nangaku M. Chronic hypoxia and tubulointerstitial injury: a final common pathway to end-stage renal failure. *J Am Soc Nephrol* (2006) 17:17–25. doi: 10.1681/ASN.2005070757

6. Leatherwood C, Speyer CB, Feldman CH, D'Silva K, Gómez-Puerta JA, Hoover PJ, et al. Clinical characteristics and renal prognosis associated with interstitial fibrosis and tubular atrophy (IFTA) and vascular injury in lupus nephritis biopsies. *Semin Arthritis Rheum* (2019) 49:396–404. doi: 10.1016/j.semarthrit.2019.06.002

7. Liu B-C, Tang T-T, Lv L-L, Lan H-Y. Renal tubule injury: a driving force toward chronic kidney disease. *Kidney Int* (2018) 93:568–79. doi: 10.1016/j.kint.2017.09.033

8. Schwartz MM, Lan SP, Bernstein J, Hill GS, Holley K, Lewis EJ. Irreproducibility of the activity and chronicity indices limits their utility in the management of lupus nephritis. lupus nephritis collaborative study group. *Am J Kidney Dis Off J Natl Kidney Found* (1993) 21:374–7. doi: 10.1016/s0272-6386(12)80263-0

9. Mubarak M, Nasri H. ISN/RPS 2003 classification of lupus nephritis: time to take a look on the achievements and limitations of the schema. *J Nephropathol* (2014) 3:87–90. doi: 10.12860/jnp.2014.17

10. Almaani S, Prokopec SD, Zhang J, Yu L, Avila-Casado C, Wither J, et al. Rethinking lupus nephritis classification on a molecular level. *J Clin Med* (2019) 8. doi: 10.3390/jcm8101524

11. Waters ST, Fu SM, Gaskin F, Deshmukh US, Sung SS, Kannapell CC, et al. NZM2328: a new mouse model of systemic lupus erythematosus with unique genetic susceptibility loci. *Clin Immunol* (2001) 100:372–83. doi: 10.1006/clim.2001.5079

12. Waters ST, McDuffie M, Bagavant H, Deshmukh US, Gaskin F, Jiang C, et al. Breaking tolerance to double stranded DNA, nucleosome, and other nuclear antigens is not required for the pathogenesis of lupus glomerulonephritis. *J Exp Med* (2004) 199:255–64. doi: 10.1084/jem.20031519

13. Ge Y, Jiang C, Sung SSJ, Bagavant H, Dai C, Wang H, et al. Cgnz1 allele confers kidney resistance to damage preventing progression of immune complex-mediated acute lupus glomerulonephritis. *J Exp Med* (2013) 210:2387–401. doi: 10.1084/jem.20130731

14. Bagavant H, Deshmukh US, Wang H, Ly T, Fu SM. Role for nephritogenic T cells in lupus glomerulonephritis: Progression to renal failure is accompanied by T cell activation and expansion in regional lymph nodes. *J Immunol* (2006) 177:8258–65. doi: 10.4049/jimmunol.177.11.8258

15. Fu SM, Wang H, Dai C, Sung S-SJ, Gaskin F. Pathogenesis of proliferative lupus nephritis from a historical and personal perspective. *Clin Immunol* (2017) 185:51–8. doi: 10.1016/j.clim.2016.07.024

16. Peterson KS, Huang J-F, Zhu J, D'Agati V, Liu X, Miller N, et al. Characterization of heterogeneity in the molecular pathogenesis of lupus nephritis from transcriptional profiles of laser-captured glomeruli. *J Clin Invest* (2004) 113:1722–33. doi: 10.1172/JCI19139

17. Espina V, Wulfkuhle JD, Calvert VS, VanMeter A, Zhou W, Coukos G, et al. Laser-capture microdissection. *Nat Protoc* (2006) 1:586–603. doi: 10.1038/nprot.2006.85

18. Hänzelmann S, Castelo R, Guinney J. GSVA: gene set variation analysis for microarray and RNA-seq data. *BMC Bioinf* (2013) 14:7. doi: 10.1186/1471-2105-14-7

19. Bult CJ, Blake JA, Smith CL, Kadin JA, Richardson JE. Mouse genome database (MGD) 2019. *Nucleic Acids Res* (2019) 47:D801–6. doi: 10.1093/nar/gky1056

20. Heng TSP, Painter MW, Elpek K, Lukacs-Kornek V, Mauermann N, Turley SJ, et al. The immunological genome project: networks of gene expression in immune cells. *Nat Immunol* (2008) 9:1091–4. doi: 10.1038/ni1008-1091

21. Kingsmore KM, Bachali P, Catalina MD, Daamen AR, Heuer SE, Robl RD, et al. Altered expression of genes controlling metabolism characterizes the tissue response to immune injury in lupus. *Sci Rep* (2021) 11:14789. doi: 10.1038/s41598-021-93034-w

22. Krämer A, Green J, Pollard JJ, Tugendreich S. Causal analysis approaches in ingenuity pathway analysis. *Bioinformatics* (2014) 30:523–30. doi: 10.1093/bioinformatics/btt703

23. Song WM, Zhang B. Multiscale embedded gene Co-expression network analysis. *PloS Comput Biol* (2015) 11. doi: 10.1371/journal.pcbi.1004574

24. The gene ontology resource: enriching a GOld mine. *Nucleic Acids Res* (2021) 49:D325–34. doi: 10.1093/nar/gkaa1113

25. Langfelder P, Horvath S. WGCNA: An r package for weighted correlation network analysis. *BMC Bioinf* (2008) 9. doi: 10.1186/1471-2105-9-559

26. Gu Z, Eils R, Schlesner M. Complex heatmaps reveal patterns and correlations in multidimensional genomic data. *Bioinformatics* (2016) 32:2847–9. doi: 10.1093/bioinformatics/btw313

27. Markowitz GS, D'Agati VD. The ISN/RPS 2003 classification of lupus nephritis: An assessment at 3 years. *Kidney Int* (2007) 71:491–5. doi: 10.1038/sj.ki.5002118

28. Mannik M, Merrill CE, Stamps LD, Wener MH. Multiple autoantibodies form the glomerular immune deposits in patients with systemic lupus erythematosus. *J Rheumatol* (2003) 30:1495–504.

29. Reynolds J, Norgan VA, Bhambra U, Smith J, Cook HT, Pusey CD. Anti-CD8 monoclonal antibody therapy is effective in the prevention and treatment of experimental autoimmune glomerulonephritis. *J Am Soc Nephrol* (2002) 13:359–69. doi: 10.1681/ASN.V132359

30. Chen A, Lee K, Guan T, He JC, Schlondorff D. Role of CD8+ T cells in crescentic glomerulonephritis. *Nephrol Dial Transplant Off Publ Eur Dial Transpl Assoc Eur Ren Assoc* (2020) 35:564–72. doi: 10.1093/ndt/gfz043

31. Couzi L, Merville P, Deminière C, Moreau J-F, Combe C, Pellegrin J-L, et al. Predominance of CD8+ T lymphocytes among periglomerular infiltrating cells and link to the prognosis of class III and class IV lupus nephritis. *Arthritis Rheum* (2007) 56:2362–70. doi: 10.1002/art.22654

32. Kim HJ, Wang X, Radfar S, Sproule TJ, Roopenian DC, Cantor H. CD8+ T regulatory cells express the Ly49 class I MHC receptor and are defective in autoimmune prone B6-yaa mice. *Proc Natl Acad Sci U.S.A.* (2011) 108:2010–5. doi: 10.1073/pnas.1018974108

33. Arazi A, Rao DA, Berthier CC, Davidson A, Liu Y, Hoover PJ, et al. The immune cell landscape in kidneys of patients with lupus nephritis. *Nat Immunol* (2019) 20:902–14. doi: 10.1038/s41590-019-0398-x

34. Toro-Domínguez D, Martorell-Marugán J, Goldman D, Petri M, Carmona-Sáez P, Alarcón-Riquelme ME. Stratification of systemic lupus erythematosus patients into three groups of disease activity progression according to longitudinal gene expression. *Arthritis Rheumatol* (2018) 70:2025–35. doi: 10.1002/art.40653

35. Der E, Suryawanshi H, Morozov P, Kustagi M, Goilav B, Ranabathou S, et al. Tubular cell and keratinocyte single-cell transcriptomics applied to lupus nephritis reveal type I IFN and fibrosis relevant pathways. *Nat Immunol* (2019) 20:915–27. doi: 10.1038/s41590-019-0386-1

36. Sung SJ, Ge Y, Dai C, Wang H, Fu SM, Sharma R, et al. Dependence of glomerulonephritis induction on novel intraglomerular alternatively activated bone marrow–derived macrophages and mac-1 and PD-L1 in lupus-prone NZM2328 mice. *J Immunol* (2017) 198:2589–601. doi: 10.4049/jimmunol.1601565

37. Sung S-SJ, Fu SM. Interactions among glomerulus infiltrating macrophages and intrinsic cells *via* cytokines in chronic lupus glomerulonephritis. *J Autoimmun* (2020) 106:102331. doi: 10.1016/j.jaut.2019.102331

38. Kuriakose J, Redecke V, Guy C, Zhou J, Wu R, Ippagunta SK, et al. Patrolling monocytes promote the pathogenesis of early lupus-like glomerulonephritis. *J Clin Invest* (2019) 129:2251–65. doi: 10.1172/JCI125116

39. Schiffer L, Bethunaickan R, Ramanujam M, Huang W, Schiffer M, Tao H, et al. Activated renal macrophages are markers of disease onset and disease remission in lupus nephritis. *J Immunol* (2008) 180:1938–47. doi: 10.4049/jimmunol.180.3.1938

40. Ma R, Jiang W, Li Z, Sun Y, Wei Z. Intrarenal macrophage infiltration induced by T cells is associated with podocyte injury in lupus nephritis patients. *Lupus* (2016) 25:1577–86. doi: 10.1177/0961203316646861

41. Sakhi H, Moktefi A, Bouachi K, Audard V, Hénique C, Remy P, et al. Podocyte injury in lupus nephritis. *J Clin Med* (2019) 8. doi: 10.3390/jcm8091340

42. Tian Y, Guo H, Miao X, Xu J, Yang R, Zhao L, et al. Nestin protects podocyte from injury in lupus nephritis by mitophagy and oxidative stress. *Cell Death Dis* (2020) 11:319. doi: 10.1038/s41419-020-2547-4

43. Deng W, Ren Y, Feng X, Yao G, Chen W, Sun Y, et al. Hypoxia inducible factor-1 alpha promotes mesangial cell proliferation in lupus nephritis. *Am J Nephrol* (2014) 40:507–15. doi: 10.1159/000369564

44. Chen PM, Wilson PC, Shyer JA, Veselits M, Steach HR, Cui C, et al. Kidney tissue hypoxia dictates T cell–mediated injury in murine lupus nephritis. *Sci Transl Med* (2020) 12. doi: 10.1126/scitranslmed.aay1620

45. Fine LG, Bandyopadhay D, Norman JT. Is there a common mechanism for the progression of different types of renal diseases other than proteinuria? towards the unifying theme of chronic hypoxia. *Kidney Int Suppl* (2000) 75:S22–6. doi: 10.1046/j.1523-1755.57.s75.12.x

46. Fortner KA, Blanco LP, Buskiewicz I, Huang N, Gibson PC, Cook DL, et al. Targeting mitochondrial oxidative stress with MitoQ reduces NET formation and kidney disease in lupus-prone MRL- lpr mice. *Lupus Sci Med* (2020) 7. doi: 10.1136/lupus-2020-000387

47. Hong S, Healy H, Kassianos AJ. The emerging role of renal tubular epithelial cells in the immunological pathophysiology of lupus nephritis. *Front Immunol* (2020) 11:578952. doi: 10.3389/fimmu.2020.578952

48. Bonventre JV. Kidney injury molecule-1 (KIM-1): A urinary biomarker and much more. *Nephrol Dial Transplant* (2009) 24:3265–8. doi: 10.1093/ndt/gfp010

49. Zhou Y, Vaidya VS, Brown RP, Zhang J, Rosenzweig BA, Thompson KL, et al. Comparison of kidney injury molecule-1 and other nephrotoxicity biomarkers in urine and kidney following acute exposure to gentamicin, mercury, and chromium. *Toxicol Sci* (2008) 101:159–70. doi: 10.1093/toxsci/kfm260

50. Castillo-Rodriguez E, Fernandez-Prado R, Martin-Cleary C, Pizarro-Sánchez MS, Sanchez-Ninõ MD, Sanz AB, et al. Kidney injury marker 1 and neutrophil gelatinase-associated lipocalin in chronic kidney disease. *Nephron* (2017) 136:263–7. doi: 10.1159/000447649

51. Moschen AR, Adolph TE, Gerner RR, Wieser V, Tilg H. Lipocalin-2: A master mediator of intestinal and metabolic inflammation. *Trends Endocrinol Metab* (2017) 28:388–97. doi: 10.1016/j.tem.2017.01.003

52. Moulton VR. Sex hormones in acquired immunity and autoimmune disease. *Front Immunol* (2018) 9:2279. doi: 10.3389/fimmu.2018.02279

53. Schwartzman-Morris J, Putterman C. Gender differences in the pathogenesis and outcome of lupus and of lupus nephritis. *Clin Dev Immunol* (2012) 2012:604892. doi: 10.1155/2012/604892

54. Ansar Ahmed S, Penhale WJ, Talal N. Sex hormones, immune responses, and autoimmune diseases. mechanisms of sex hormone action. *Am J Pathol* (1985) 121:531–51.

55. Cutolo M, Wilder RL. Different roles for androgens and estrogens in the susceptibility to autoimmune rheumatic diseases. *Rheum Dis Clin North Am* (2000) 26:825–39. doi: 10.1016/s0889-857x(05)70171-x

56. Shim G-J, Kis LL, Warner M, Gustafsson J-Å. Autoimmune glomerulonephritis with spontaneous formation of splenic germinal centers in mice lacking the *estrogen receptor alpha* gene. *Proc Natl Acad Sci* (2004) 101:1720–4. doi: 10.1073/pnas.0307915100

57. Rider V, Jones SR, Evans M, Abdou NI. Molecular mechanisms involved in the estrogen-dependent regulation of calcineurin in systemic lupus erythematosus T cells. *Clin Immunol* (2000) 95:124–34. doi: 10.1006/clim.2000.4844

58. Lang TJ, Nguyen P, Papadimitriou JC, Via CS. Increased severity of murine lupus in female mice is due to enhanced expansion of pathogenic T cells. *J Immunol* (2003) 171:5795–801. doi: 10.4049/jimmunol.171.11.5795

59. Graham JH, Yoachim SD, Gould KA. Estrogen receptor alpha signaling is responsible for the female sex bias in the loss of tolerance and immune cell activation induced by the lupus susceptibility locus Sle1b. *Front Immunol* (2020) 11:582214. doi: 10.3389/fimmu.2020.582214

60. Cutolo M, Seriolo B, Villaggio B, Pizzorni C, Craviotto C, Sulli A. Androgens and estrogens modulate the immune and inflammatory responses in rheumatoid arthritis. *Ann N Y Acad Sci* (2002) 966:131–42. doi: 10.1111/j.1749-6632.2002.tb04210.x

61. Gubbels Bupp MR, Jorgensen TN. Androgen-induced immunosuppression. *Front Immunol* (2018) 9:794. doi: 10.3389/fimmu.2018.00794

62. Aitman TJ, Dong R, Vyse TJ, Norsworthy PJ, Johnson MD, Smith J, et al. Copy number polymorphism in Fcgr3 predisposes to glomerulonephritis in rats and humans. *Nature* (2006) 439:851–5. doi: 10.1038/nature04489

63. Stratigou V, Doyle AF, Carlucci F, Stephens L, Foschi V, Castelli M, et al. Altered expression of signalling lymphocyte activation molecule receptors in T-cells from lupus nephritis patients-a potential biomarker of disease activity. *Rheumatol (United Kingdom)* (2017) 56:1206–16. doi: 10.1093/rheumatology/kex078

64. Zhou D, Tan RJ, Fu H, Liu Y. Wnt/β-catenin signaling in kidney injury and repair: A double-edged sword. *Lab Investig* (2016) 96:156–67. doi: 10.1038/labinvest.2015.153

65. Weening JJ, D'Agati VD, Schwartz MM, Seshan SV, Alpers CE, Appel GB, et al. The classification of glomerulonephritis in systemic lupus erythematosus revisited. *J Am Soc Nephrol* (2004) 15:241–50. doi: 10.1097/01.ASN.0000108969.21691.5D

66. Ortega LM, Schultz DR, Lenz O, Pardo V, Contreras GN. Lupus nephritis: Pathologic features, epidemiology and a guide to therapeutic decisions. *Lupus* (2010) 19:557–74. doi: 10.1177/0961203309358187

Frontiers in Immunology

TYPE Methods
PUBLISHED 01 March 2023
DOI 10.3389/fimmu.2023.1107582

OPEN ACCESS

EDITED BY
Kuang-Hui Sun,
National Yang Ming Chiao Tung University, Taiwan

REVIEWED BY
Howard Davidson,
University of Colorado, United States
Yanshan Dai,
Bristol Myers Squibb, United States

*CORRESPONDENCE
Megan K. Levings
✉ mlevings@bcchr.ca
Sarah Q. Crome
✉ sarah.crome@utoronto.ca
C. Bruce Verchere
✉ bverchere@bcchr.ca

†These authors have contributed equally to this work and share first authorship

‡These authors have contributed equally to this work and share senior authorship

SPECIALTY SECTION
This article was submitted to Autoimmune and Autoinflammatory Disorders : Autoimmune Disorders, a section of the journal Frontiers in Immunology

RECEIVED 25 November 2022
ACCEPTED 30 January 2023
PUBLISHED 01 March 2023

CITATION
Colpitts SJ, Budd MA, Monajemi M, Reid KT, Murphy JM, Ivison S, Verchere CB, Levings MK and Crome SQ (2023) Strategies for optimizing CITE-seq for human islets and other tissues. *Front. Immunol.* 14:1107582.
doi: 10.3389/fimmu.2023.1107582

Strategies for optimizing CITE-seq for human islets and other tissues

Sarah J. Colpitts[1,2†], Matthew A. Budd[3,4†], Mahdis Monajemi[3,4†], Kyle T. Reid[1,2], Julia M. Murphy[1,2], Sabine Ivison[3,4], C. Bruce Verchere[3,4,5*‡], Megan K. Levings[3,4,6*‡] and Sarah Q. Crome[1,2*‡]

[1]Department of Immunology, Temerty Faculty of Medicine, University of Toronto, Toronto, ON, Canada, [2]Toronto General Hospital Research Institute, Ajmera Transplant Centre, University Health Network, Toronto, ON, Canada, [3]Department of Surgery, University of British Columbia, Vancouver, BC, Canada, [4]BC Children's Hospital Research Institute, Vancouver, BC, Canada, [5]Department of Pathology and Laboratory Medicine, Canada and Centre for Molecular Medicine and Therapeutics, University of British Columbia, Vancouver, BC, Canada, [6]School of Biomedical Engineering, University of British Columbia, Vancouver, BC, Canada

Defining the immunological landscape of human tissue is an important area of research, but challenges include the impact of tissue disaggregation on cell phenotypes and the low abundance of immune cells in many tissues. Here, we describe methods to troubleshoot and standardize Cellular Indexing of Transcriptomes and Epitopes by sequencing (CITE-seq) for studies involving enzymatic digestion of human tissue. We tested epitope susceptibility of 92 antibodies commonly used to differentiate immune lineages and cell states on human peripheral blood mononuclear cells following treatment with an enzymatic digestion cocktail used to isolate islets. We observed CD4, CD8a, CD25, CD27, CD120b, CCR4, CCR6, and PD1 display significant sensitivity to enzymatic treatment, effects that often could not be overcome with alternate antibodies. Comparison of flow cytometry-based CITE-seq antibody titrations and sequencing data supports that for the majority of antibodies, flow cytometry accurately predicts optimal antibody concentrations for CITE-seq. Comparison by CITE-seq of immune cells in enzymatically digested islet tissue and donor-matched spleen not treated with enzymes revealed little digestion-induced epitope cleavage, suggesting increased sensitivity of CITE-seq and/or that the islet structure may protect resident immune cells from enzymes. Within islets, CITE-seq identified immune cells difficult to identify by transcriptional signatures alone, such as distinct tissue-resident T cell subsets, mast cells, and innate lymphoid cells (ILCs). Collectively this study identifies strategies for the rational design and testing of CITE-seq antibodies for single-cell studies of immune cells within islets and other tissues.

KEYWORDS

CITE-seq, tissue immunity, flow cytometry, pancreas, single cell RNA seq

1 Introduction

Type 1 diabetes (T1D) is an autoimmune disease characterized by T-cell mediated destruction of insulin-producing beta cells in pancreatic islets (1). The balance between beta cell function and regeneration versus dysfunction and death is influenced by a variety of islet-proximal immune cells such as macrophages and other innate cells, as well as effector and regulatory T cells and other lymphoid populations (2–7). However, much of our current understanding comes from studies in mice (8–12) and there is a need to better understand cellular-cross talk mechanisms that control the function of human islets in both health and T1D. Characterization of human islet-resident immune cells and their interactions has proven challenging, however, due to low frequency of immune cells within islets and effects of dissociating tissue that can impact surface antigens (13–17).

Phenotyping of human tissue-resident immune cells has been significantly advanced by the advent of Cellular Indexing of Transcriptomes and Epitopes by sequencing (CITE-seq). This method allows simultaneous capture of cell surface protein and messenger RNA (mRNA) expression of single cells (18), and is particularly useful for detecting immune cell lineage markers with low mRNA expression (19) as well as unbiased capture of the transcriptome of novel cell types (20). For example, T cell populations such as γ/δ and mucosal-associated invariant T cells, and cell types such as innate lymphoid cells (ILCs) and neutrophils are not well identified by single-cell RNA sequencing due to low RNA content of lineage defining transcripts, high levels of RNase (20–22), and mRNA expression patterns that do not correlate with protein expression (19). Thus, annotating immune populations solely on the basis of mRNA expression can lead to misidentification or an inability to distinguish distinct populations with overlapping transcriptional characteristics.

Despite the advantages of assessing surface protein expression using CITE-seq, there are several methodological challenges. One obstacle is the identification of optimal antibody titrations, as hyper-concentration can lead to high background signal and increased sequencing costs without adding sequencing depth, whereas insufficient antibody can lead to insufficient signal to distinguish positive expression patterns (23). Flow cytometry is often used as a surrogate to define CITE-seq antibody titrations, on the basis of the assumption that the signals of oligo-tagged antibodies correlate to those from the same clone in a fluorochrome-tagged format (18). However, due to differences in antibody lots, tissue source, fluorescence spillover, tissue autofluorescence, and non-specific background binding, optimal concentrations of flow cytometry versus CITE-seq antibodies may differ.

Another challenge in studying human tissue samples is the use of enzymatic digestion to create single cell suspensions. The type of enzymes used and length of digestion time can significantly affect the presence of cell surface proteins (24). For islets, a variety of purified digestive enzymes can be used during the isolation process for clinical or research applications, including collagenase NB1 (Nordmark; Uetersen, Germany), Liberase^{TM} (Roche; Basel, Switzerland) and/or Collagenase Gold (Vitacyte; Indianapolis IN, USA) (25, 26). The comparison between these collagenase enzymes used in islet isolation shows that they produce similar islet purity and viability (27). During the tissue digestion process, cell surface molecules on both immune and parenchymal populations may be damaged (17, 24), necessitating assessment of the digestion-induced destruction of epitopes of interest to accurately assess the phenotype of resident immune cells (17).

Herein, we assessed the impact of pancreas digestion and islet isolation on extracellular immune cell lineage and phenotype markers, and identified antibody clones that are sensitive or resistant to the digestion process. We also optimized titration of antibodies for CITE-seq using flow cytometry, and characterized expression of immune cell markers in healthy human islets by paired flow cytometry and CITE-seq.

2 Materials and methods

2.1 Experimental design

To evaluate the effect of digestive enzymes used during islet isolation on CITE-seq oligo-antibodies, peripheral blood mononuclear cells (PBMCs) were treated with enzymes to mimic the process used by the University of Alberta IsletCore (26). Splenocytes were used in during CITE-seq antibody titrations. All donor information can be found in Supplemental Table S1. Cells were incubated for 30 minutes, with or without digestion enzymes, and then stained with a variety of antibody panels to comprehensively classify and characterize T cell-, myeloid-, and ILC-derived subpopulations. We then compared the proportion of cells positive for each antibody stain in a common parent cell type: either lymphoid or myeloid, depending on the marker of interest (Figure 1A and Supplemental Figure S1).

2.2 PBMC and spleen preparation

Human tissue specimens were collected in accordance with biosafety and ethical protocols approved by the University of British Columbia Clinical Research Ethics Board (B22-0075 and H18-02553, respectively) and Canadian Blood Services, and the University Health Networks Research Ethics Board and biosafety protocols (17-6229 and 20-5206, respectively). PBMCs were derived from venous blood and cryopreserved in aliquots as previously described (28).

For digestion experiments, PBMCs were thawed in a 37°C water bath and transferred to pre-warmed (37°C) X-VIVO cell culture media containing 5% human serum at a concentration of 1 million cells/mL. For panels consisting of markers requiring immune activation, cells were

---

Abbreviations: CITE-seq, Cellular indexing of transcriptomes and epitopes by sequencing; EDTA, Ethylenediaminetetraacetic acid; FACS, Fluorescence-activated cell sorting; FBS, Fetal bovine serum; ILC, Innate lymphoid cell; mRNA, Messenger RNA; PBMC, Peripheral blood mononuclear cell; PCA, Principal component analysis; RC, Relative change; T1D, Type 1 diabetes; UMAP, Uniform manifold approximation and projection; UMI, Unique molecular identifier; ADT, Antibody-derived tags; DEGs, Differentially expressed genes; DEPs, Differentially expressed proteins.

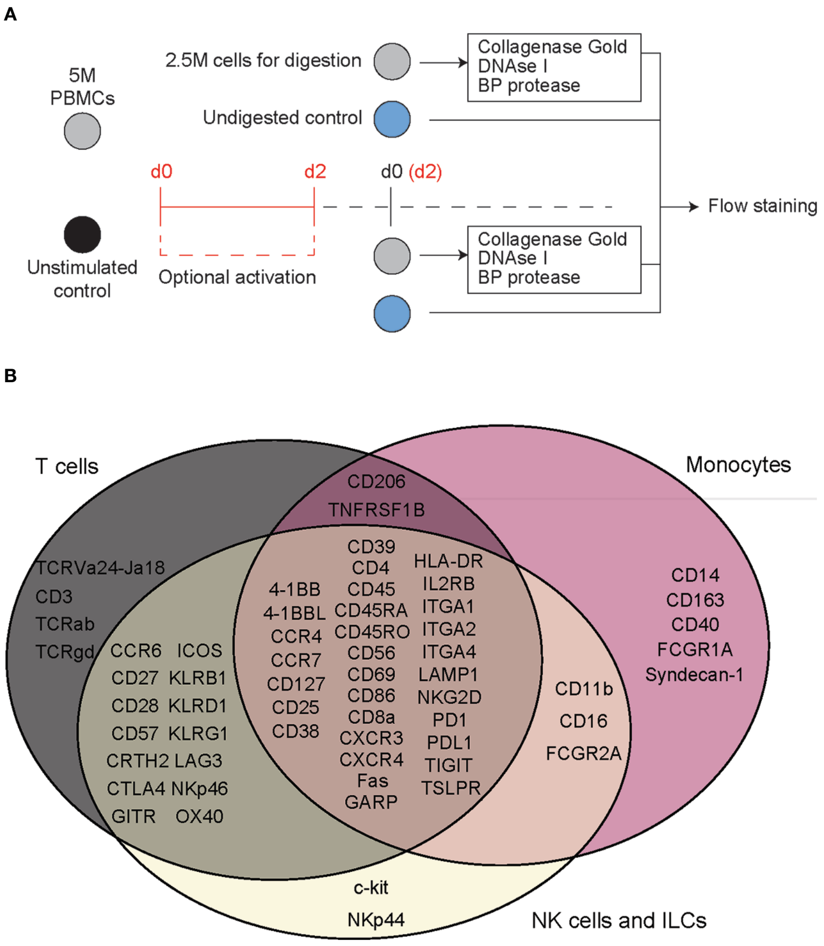

FIGURE 1
Flow cytometry reveals T cell specific, deleterious effects of islet digestive enzymes on staining of antibody clones used for generation of TotalSeq-C oligo-antibodies. **(A)** Activated or non-activated PBMCs were treated with a digestive enzyme solution and stained with flow cytometry antibodies corresponding to clones used in the TotalSeq-C commercial antibody catalogue of oligo-antibodies used for CITE-seq. **(B)** Markers were selected to identify key cellular subsets of T lymphocytes, monocytes, and innate lymphoid cells, in addition to other antibodies used for e.g., leukocyte selection, stress indicators, and immune activation.

divided into two equal-volume aliquots, one of which was activated with CytoStim^{TM} polyclonal T cell stimulant to a concentration of 1:200 (stimulant to media) and cultured for 48 hours at 37°C.

Islet perfusion solution was prepared following a standardized protocol from the University of Alberta (26) from HBSS with 3.6 mM calcium chloride, 0.81 mM magnesium sulfate, 4.2 mM sodium bicarbonate, 10 mM HEPES, and 100 U penicillin-streptomycin adjusted to a pH value of 7.35. Perfusion buffer was combined with a digestion solution of 2.8 mg/mL Collagenase Gold, 12,500 U/g BP Protease, and 5.6 mg/mL DNAse I, Grade II. Up to 2x10^{6} PBMCs were then incubated for 30 min at 37°C in the combination perfusion buffer/digestive solution. The vials were gently agitated at 10-minute intervals. After digestion cells were washed in PBS containing 0.5 mM EDTA and resuspended in 4.5 mL PBS/EDTA. Trypsin (390 µL of 0.25%) was added to the cell suspension and incubated at 37°C for 10 min. The reaction was stopped by adding 10 mL PBS containing 1% fetal bovine serum (**FBS**), 1 mM EDTA, and 11 mM GlutaMAX^{TM}. Finally, cells were transferred to a 96-well V-bottom polystyrene plate for flow cytometry staining.

Spleens were received from the University of Alberta IsletCore or the Ajmera Transplant Centre Islet Transplant Program. Samples were cut into small pieces using a sterile scalpel then placed into gentleMACS C-tubes with 10 mL PBS plus 2% FBS and placed in a gentleMACS dissociator using the m_spleen_01_01 setting. After dissociation, the slurry was mashed through a 70 µm cell strainer and ACK lysed to remove red blood cells (29). Cell pellets were resuspended in 50 mL RPMI media and 1x10^{6} cells were removed per well, centrifuged and resuspended in 50 µL master mixes containing cell staining buffer and either flow cytometry or CITE-seq antibodies.

2.3 Flow cytometry of PBMCs to assess clonal sensitivity to enzymatic digestion

PBMCs, either exposed to islet perfusion solution or unexposed controls, were stained with a combination of the 61 anti-human antibodies listed in Supplemental Table S2. Each staining panel was selected to distinguish key subpopulations of myeloid cells and lymphocytes. For each cell surface marker, at least one of the antibody clones tested matched that of the corresponding marker in BioLegend's TotalSeq^{TM}-C Human Universal Cocktail selection kit. Panels were designed to allow standard lineage gating of immune cell phenotypes whenever possible. Samples for flow cytometry were acquired on the FACS Symphony A5 platform and analyzed using FlowJo software (BD Biosciences; version 10.8.1). All events were gated on live, single lymphoid or myeloid populations as applicable (gating strategy shown in Supplemental Figure S1). Gates were set on undigested cells and then applied to the digested cells. Markers were assigned to either a myeloid lineage or activated/non-activated lymphocyte lineage, and percent positive of parent populations reported. Figures were generated with Prism 9 (GraphPad Software; version 9.3.1) and the R statistical computing environment (version 4.2.0). Figure 2 was generated using the ComplexUpset package (30).

All data pertaining to fluorophore-conjugated antibody staining of cells treated with digestion enzymes were considered for quality-related inclusion or exclusion from the study at the time of data collection and analysis. Our *a priori* criteria for inclusion of data in the final assessment were as follows: 1) Data for n=2 or more PBMC donors; 2) a population of positive cells clearly identifiable in the undigested cell sample; 3) for markers on activated cells, a sufficient

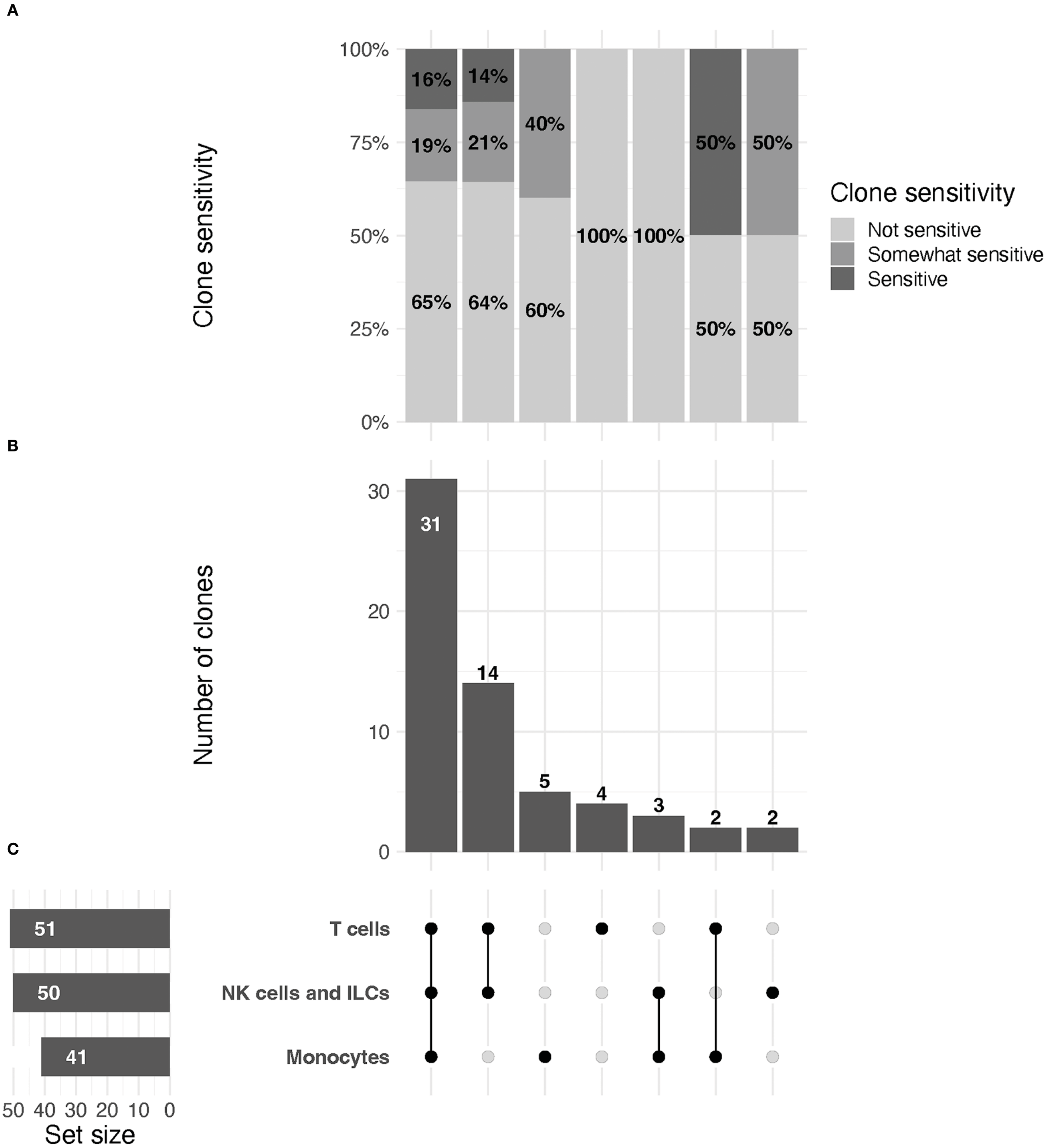

FIGURE 2
UpSet plot of clones included in the study, organized by immune cell lineage (T cell, NK/ILC, or monocyte).**(A)** Relative proportions of sensitive, partially sensitive, and insensitive clones per grouping. **(B)** Histogram representing number of clones tested per grouping. (**C**, left) From top to bottom, total number of clones tested for markers that are expressed by T cells, NK/ILCs, and monocytes, respectively. Line plot (right) signifies groupings of markers for data in **(A, B)** that are expressed by one, two, or all three cell types, as indicated by connected dots (e.g., the first column describes data for markers that are expressed by all three cell types, the second column for markers expressed only by T cells and NK/ILCs, etc.). Groupings are exclusive.

activation signal, determined *via* CD69 staining, must be visible in the flow cytometry output.

Readings of identical clone-fluorophore combinations during a single flow cytometry experiment (e.g., repeat measurements from different staining panels on the same day) were used to determine mean values and recorded in the final dataset. Digestion sensitivity of technical replicates (or the mean value for repeated measurements) for each antibody was assessed by calculating the relative change (**RC**) of the positive population in digested cells (to undigested cells) and converting to a percentage (see **Equation 1**).

$$RC = 100 * \frac{\%\ positive\ \ (undigested) - \%\ positive\ \ (digested)}{\%\ positive\ \ (undigested)}$$

Equation 1. Expression for quantifying relative change in positive staining for flow cytometry antibodies in digested and undigested cells.

A sample was considered sensitive if the RC was ≥ 50, and partially sensitive if 25 ≤ RC ≤ 50. As the equation is biased to output large values for small inputs (e.g., markers for rare cell populations), replicates with ≤ 5% positivity of the undigested cells were assessed for sensitivity *via* standard flow gating. If a positive population for the antibody was visible, it was considered insensitive to digestion.

Subsequently, overall clone sensitivity to digestion was assessed by computing the proportion of replicates for each clone with full or partial sensitivity. Antibody clones were considered sensitive if the majority of replicates had an RC ≥ 50; partially sensitive if the majority of clones had an RC ≥ 25 but ≤ 50; and insensitive if the majority of replicates had an RC ≤ 25. Clones with a 50% split between full/partial or partial/insensitive replicates were categorized as partially sensitive.

2.4 Human islet preparation

Human islets were received in accordance with research ethics protocols 20-5206 (UHN) and H20-01930 (UBC). Human islets (~10,000 islet equivalents) were obtained from the IsletCore (University of Alberta) and shipped overnight in CMRL 1066 media. Prior to CITE-seq staining, islets were dissociated into a single cell suspension by centrifugation (800 rpm, 5 min), resuspended in 5 mL trypLE, and incubated in a 37°C water bath. After 2 minutes, the islets were removed, pipetted vigorously, and returned to the water bath for an additional 3 minutes. Islets were counted and immune cells enriched using an Easysep human CD45 Depletion kit II. Cells were resuspended at $1.0x10^8$ cells/mL in EasySep^{TM} buffer and 12.5 µL/mL EasySep Human CD45 Depletion Cocktail II was added and incubated for 5 minutes at room temperature. EasySep Dextran RapidSpheres (20 µL/mL) were then added and incubated for 3 minutes at room temperature. The mixture was then topped up to 2.5 mL with EasySep buffer and placed in an EasySep purple magnet for 5 minutes. The CD45-negative fraction was decanted, and the positive fraction added to the magnet for an additional 5 minutes in 2.5 mL EasySep buffer. The resulting CD45-positive fraction was then counted, $1x10^6$ cells were removed, centrifuged, and resuspended in 50 µL master mix containing cell staining buffer and flow cytometry antibodies or TotalSeq-C antibodies for CITE-seq, or a mix of both for ILC enrichment.

As ILCs are present in very low abundance and display significant overlap in protein and RNA level expression of molecules expressed by T cells, we also performed an ILC enrichment on the same sample. CD45-enriched islet cells ($1x10^6$) were stained with flow cytometry antibodies as well as the TotalSeq^{TM}-C antibody cocktail (at a 1:1 ratio) and flow sorted before sequencing. FITC-conjugated antibodies against B cells, T cells, and myeloid cells were used to differentiate these immune cells from ILCs. Antibodies used for lineage exclusion are listed in Table 1. We also used a live/dead dye (FVS700) and antibodies directed against CD45 (APC Cy7, clone HI30), CD56 (BV605, clone HCD56), and CD127 (PE, clone hIL-7R-M21) to differentiate helper ILCs from NK cells. Cells were sorted as Live, CD45$^+$, Lineage$^-$ (Supplemental Figure S2) washed as above and sent for sequencing.

2.5 Assessing optimal antibody titrations using splenic samples

To capture tissue-resident myeloid populations, such as those seen in islets, we used human splenocytes for flow cytometry-based CITE-seq antibody titrations. Splenocytes were thawed in pre-warmed, serum-free RPMI, washed and resuspended at $5x10^6$ cells/mL in RPMI containing 5% human serum and 1% penicillin/streptomycin. Since some markers of interest were only expressed upon activation, cells were either activated (with LPS + IFNγ or PMA/ionomycin) or rested for 6 hours in complete RPMI at 37°C. If the marker of interest was expressed more abundantly on myeloid lineage cells, cells were activated with 10 ng/mL LPS + 100 ng/mL IFNγ. If the marker of interest was expressed more abundantly on ILCs or T cells, cells were activated in PMA/Ionomycin cell stimulation cocktail. After stimulation, $3x10^6$ cells were washed with PBS plus 2% FBS (FACS buffer), resuspended in 75 µL Human TruStain FcX^{TM} Fc Blocking reagent (at a 1:10 dilution in FACS buffer) and $1x10^6$ cells (25 µl of Fc blocked cells) were plated in a V-bottom plate for 15 minutes at 4°C. Each antibody was tested in 3 dilutions: 2x, 1x and 0.5x the recommended dilution and added to 25µl of FACS buffer. Samples were stained for 30 minutes at 4°C and washed in FACS buffer. Acquisition was performed on a BD LSRFortessa flow cytometer and analyzed using FlowJo software (BD Biosciences; version 10.8.1).

2.6 CITE-seq staining of spleen and islets

Surface staining was performed as described in the BioLegend protocol (31). Briefly, $1x10^6$ cells were resuspended in 45 µL Cell Staining Buffer in 1.5 mL microcentrifuge tubes. Human TruStain FcX^{TM} Fc Blocking reagent (5 µL) was added, and cells were incubated for 10 minutes at 4°C. TotalSeq^{TM}-C antibody cocktails were made during the incubation using concentrations determined by previous flow-cytometry-based CITE-seq titrations. All TotalSeq^{TM}-C antibodies added can be found in Supplemental Table S3. The resulting cocktail was then added to cells and incubated for 30 minutes at 4°C. After incubation, cell pellets were resuspended with 1 mL PBS plus 0.05% BSA and centrifuged for 5 minutes at 400*g*. The wash was repeated twice more for a total of 3 washes, and the final

TABLE 1 Flow cytometry antibodies used to identify cells positive for classical immune cell lineage markers.

Antibody	Clone
CD3	OKT3
CD3	UCHT1
CD4	RPA-T4
CD8a	RPA-T8
CD14	M5E2
CD15	W6D3
CD19	HIB19
CD20	2H7
TCR a/b	IP26
TCR g/d	B1
CD33	HIM3-4
CD34	583
CD203c	NP4D6
FceR1a	AER37
CD79a	HM47
CD138	MI15

concentration was adjusted to 1200 cells/μL and sent for sequencing to a local biomedical research core.

2.7 CITE-seq data analysis pipeline

Samples were prepared for sequencing using the 10X Genomics Single Cell 5' v2 platform in accordance with manufacturer's instructions for capture of 12,000 cells per sample. Reverse transcription, cDNA amplification and sequencing libraries were generated using 10X Genomics Single Cell 5' v2 reagents. Across samples, cells were sequenced to a target depth of 40,000 reads per cell. Read alignment to the reference human genome (GRCh38/hg38) and gene expression matrices were generated by the 10X Genomics CellRanger pipeline (version 6.1.2) 7. In line 640 please remove "to generate UMAPS.

Data were loaded into R and Seurat objects were created individually for both islets and spleen. High mitochondrial content cells were removed from the islet clusters by removing cells with >10% of Unique Molecular Identifiers (**UMIs**) mapped to mitochondrial genes and <200 unique genes. For splenocytes, cells which had >20% of UMIs mapped to mitochondrial genes and <200 unique genes were removed. Data were normalized with SCTransform (32), principal component analysis was used for dimensionality reduction (RunPCA) and cells were clustered using the Louvain algorithm with 30 principal components (FindNeighbors and FindClusters) in Seurat (33). Clusters were visualized using the Uniform Manifold Approximation and Projection (**UMAP**) algorithm (34).

In each object, immune cells (identified as clusters expressing *PTPRC*), were used to create an immune cell-only object. The individual datasets were then merged and integrated using harmony (RunHarmony) (35). Cell type-specific thresholds were set to remove low quality cells and all cells with >10% of UMIs mapped to mitochondrial genes, as above. Cells with low transcript abundance (<200 features) and high antibody expression indicative of antibody aggregates were removed. Integrated data was then normalized following the same process above. Cell types and lineages were annotated by analysing the top differentially expressed genes and/or proteins (FindMarkers) and manually labelled. T cell UMAPs were generated by selecting cells which expressed either *CD3E* or CD3 and re-clustered.

3 Results

3.1 Epitopes for several antibody clones in the TotalSeq™-C kit are affected by digestive enzymes

We performed flow cytometry on PBMCs which were or were not exposed to a mock islet digestion protocol using a total of 92 antibody clones specific for 64 immune cell markers (Figure 1). Surface marker expression by cell type is displayed in Figure 1B. Up to five antibody clones were tested per marker, with 2-18 replicates per clone on cells from 2-4 PBMC donors. In the final analysis, data from 75/92 (82%) of tested clones, specific for 61 immune cell markers were included.

To assess epitope sensitivity to digestive enzymes, we first analyzed data *via* traditional flow cytometry to identify potentially problematic clones/markers for which no positive population was observed in the digestion condition. We then assessed the quantity of cells positive for each marker as a proportion of the parent cell population.

Across all replicates included in the final analysis (n=216), we observed a median relative change of 8.2 (IQR: -1.1 to 52.7), with values ranging from −188% to 100% (Note: RC values correspond to relative change of mean fluorescence intensity for the marker of interest in digested versus undigested cells). We found that 37/216 (17%) replicates displayed low, but quantifiable, relative expression in the parent population of cells in both the digested and undigested samples, and we treated these replicates for reporting purposes as non-sensitive. A total of 116/216 (54%) replicates were non-sensitive with >5% positivity in the undigested parent cells (i.e. true non-sensitives), 20/216 (9%) partially sensitive, and 43/216 (20%) significantly sensitive. A summary of these observations stratified by immune cell type is provided in Figure 2.

We found that most (47/75, 63%) antibody clones tested using flow cytometry that align with TotalSeq-C oligo-antibodies were not sensitive to the enzymatic digestion process, with some notable exceptions (Figure 3; Table 2). We observed partial sensitivity in n=16 (21%) of clones tested, and high sensitivity in n=12 (16%) of clones. A library of figures for each marker is included as a supplementary download, indicating the proportion of parent cells positive for each antibody stain and subsetted by clone tested. Of the n=12 clones found to be highly sensitive, n=8 (75%) belonged to the TotalSeq-C library, summarized in Table 2. Additionally, Figure 4 summarizes the sensitivity of each clone included in our final results in a hierarchical heatmap format.

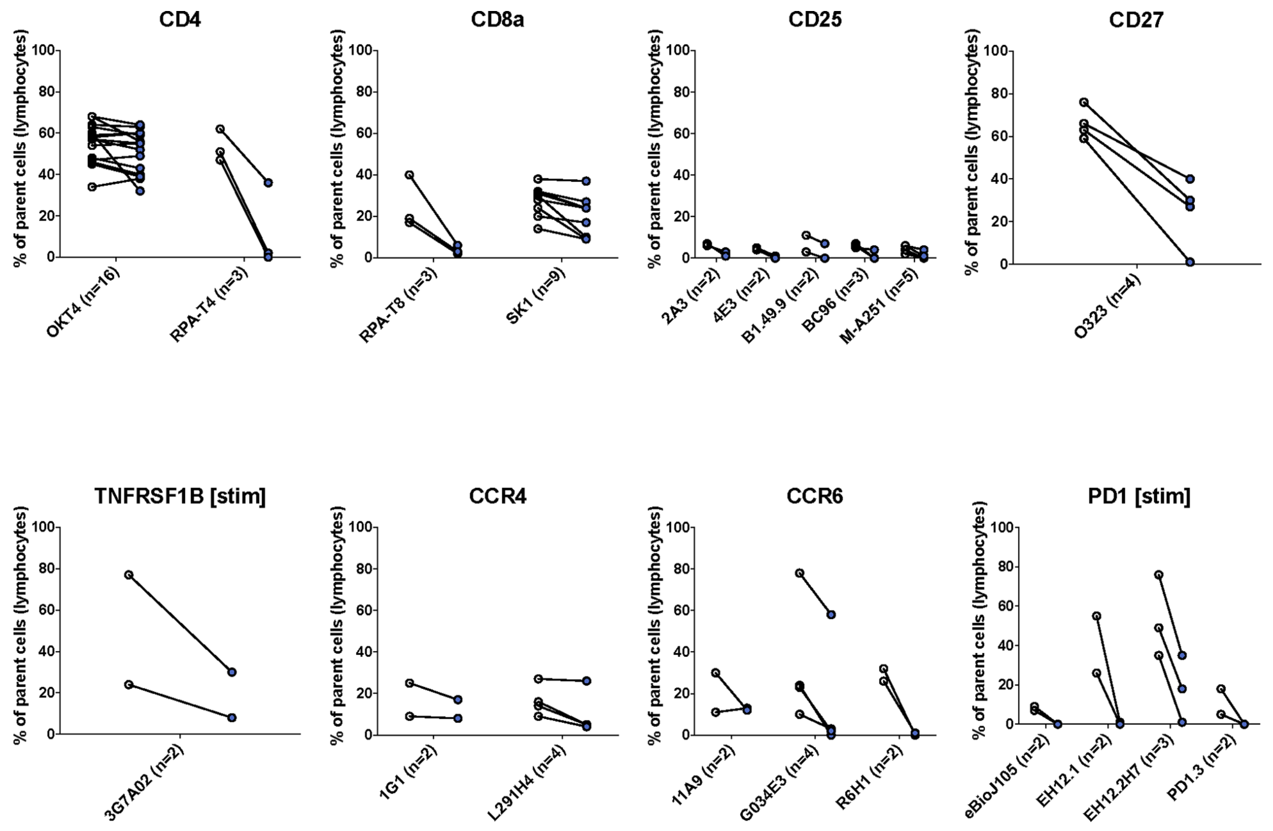

FIGURE 3
The effects of enzymatic digestion on key phenotypic markers of concern in the TotalSeq-C antibody library. White and blue circles indicate pre- and post-digestion values, respectively. Each pairing signifies an independent experimental replicate of pre- and post-treatment measurements, and the proportion of cells positive for the marker of interest was determined using standard flow gating. Parent cells were total live lymphocytes after applying quality control gating as outlined in Supplemental Figure S1.

3.2 Flow cytometry antibody titrations allow estimates of antibody concentrations for CITE-seq studies

Flow-based antibody titrations were used to determine the optimal concentration for CITE-seq staining, as prior studies suggested flow-based signal would be analogous to CITE-seq signals (18). PE-conjugated antibodies corresponding to the same markers and epitopes (clones) as the TotalSeq-C antibodies were utilized. Three titrations were performed on each antibody of interest with the middle concentration being that recommended by the vendor (BioLegend). Flow cytometric analysis was used to determine the lowest amount of PE-conjugated antibody needed to generate a positive signal (Table 3; Figure 5). As some populations of interest are rare or absent in PBMCs, we used human splenocytes to perform the antibody titrations. For markers which were more highly expressed upon activation, cells were activated for 6 hours before staining. For activation markers on myeloid cells (e.g., CD80, CD86 and CD163), cells were stimulated with a combination of LPS and IFNγ, and for those on T cells and/or ILCs (e.g. CD69, ICOS, and CD107a), cells were activated with PMA/Ionomycin. Concentrations were assessed by the ratio of percent positive signal plus noise (gated based on unstained) to the percent positive signal (gated based on peak separation). The optimal antibody concentration was determined to be that which gave a positive peak with the lowest positive signal plus noise (Figure 5A). Titration results for each marker are listed in Table 3 and Figure 5B gives examples of titration plots for markers affected by enzymatic digestion and Figure 5C is the legend for these plots, with the titration concentration selected to move forward with shown in blue. For 15 antibodies, the recommended dilution (titration concentration #2) was appropriate. However, for only 1 marker (CD11b), the highest concentration (titration concentration #3) gave a positive signal without substantial background staining (signal – (signal + noise) ratio). For the remainder and majority of antibodies (47), we noted the lowest concentration, titration #1, to be optimal. We therefore moved forward with the appropriate concentration based on these results for CITE-seq studies.

3.3 CITE-seq antibody concentrations determined by flow cytometry allow identification of islet-resident immune populations

To test the effects of enzymatic digestion on CITE-seq samples, enzymatically dissociated islets and donor-matched spleen (mechanically dissociated only) from one individual were stained with a panel of 67 oligo-tagged antibodies associated with myeloid, T cell and ILC populations (Supplemental Table S3) and sequenced. As

TABLE 2 List of clones tested for key markers of concern.

Clone tested	Clone with best observed staining	Number of donors> clone was tested with	Number of replicates included	Proportion of replicates sensitive (%)	Proportion of replicates partially sensitive (%)	Proportion of replicates not sensitive (%)
CD4	OKT4					
OKT4		4	16	0	0	100
RPA-T4		2	3	67	33	0
CD8a	SK1					
RPA-T8		2	3	100	0	0
SK1		3	9	22	22	56
CD25 (IL2R)	4E3					
2A3		2	2	100	0	0
4E3		2	2	0	0	100
B1.49.9		2	2	0	50	50
BC96		3	3	67	0	33
M-A251		3	5	20	20	60
CD27	O323					
O323		2	4	75	25	0
CD120b (TNFRSF1B)	3G7A02					
3G7A02		2	2	100	0	0
CD194 (CCR4)	1G1					
1G1		2	2	0	50	50
L291H4		3	4	75	0	25
CD196 (CCR6)	11A9					
11A9		2	2	50	0	50
G034E3		3	4	75	25	0
R6H1		2	2	100	0	0
CD279 (PD1)	PD1.3					
eBioJ105		2	2	100	0	0
EH12.1		2	2	100	0	0
EH12.2H7		3	3	100	0	0
PD1.3		2	2	50	0	50

TotalSeq-C clones highlighted in bold text.

we were primarily focused on how enzymatic digestion impacted epitopes on immune cells and how CITE-seq could aid in better delineation of immune cell subsets, the panel of antibodies selected included markers commonly used to distinguish immune cell subsets and activation states.

To ensure sufficient immune cells were captured by sequencing, CD45-enrichment using magnetic separation was performed on islets, as immune cells account for only 1-2% of cells within human islets (15). To further enrich for rare ILC populations, which can have overlapping transcriptomic signatures with $CD4^+$ T cell subsets, ILCs were isolated *via* flow cytometry sorting by negatively gating on expression of lineage markers (Table 1) on islet-resident $CD45^+$ cells (Supplemental Figure S2). This ILC-enriched sample was sequenced along with the donor-matched CD45-enriched sample (Figure 6A). Donor-matched spleen was also sequenced to serve as a control for assessing epitopes negatively impacted by enzymatic digestion and to aid in annotation of immune populations.

After sequencing, islet CD45-enriched and islet ILC-enriched samples were integrated (Figure 6B) and populations defined by RNA expression and antibody-derived tags (ADT) were compared

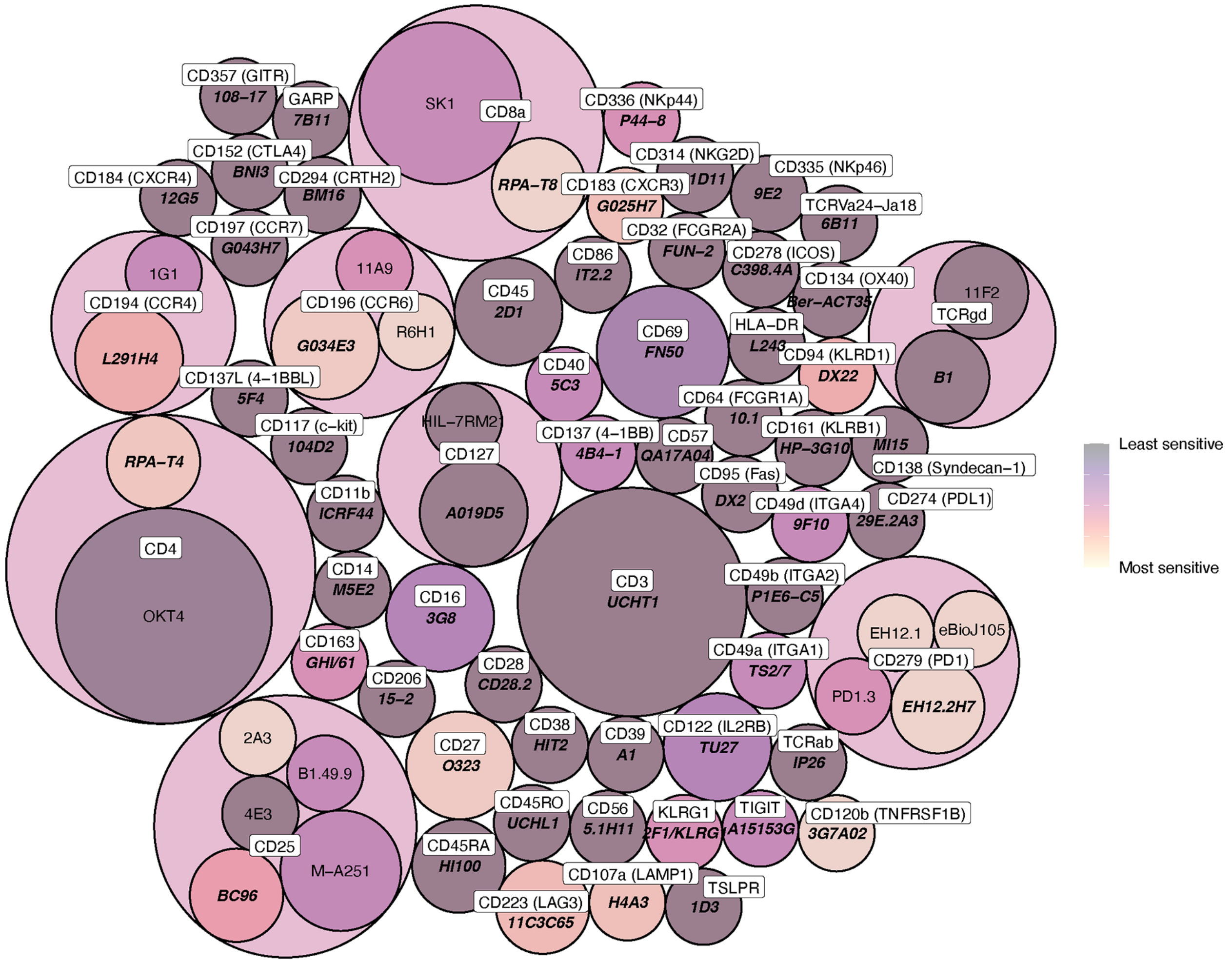

FIGURE 4
Circle packing heat map of clone sensitivity to digestive enzymes. The colour scale indicates relative proportion of replicates sensitive or partially sensitive to digestion, and the size of each circle indicates the number of replicates included in analysis. Circle containers indicate successive levels of hierarchy, where clones are grouped according to immune marker (the colour of these encapsulating hierarchy circles, which contain multiple daughter clones, is not indicative of daughter clone sensitivity).

to those observed in donor-matched spleen (Figure 6B). Individual islet and spleen UMAPs with clustering based on combined RNA expression and ADT were annotated based on cell types and origin (CD45-enriched or sorted) (Figure 6B). Next, islet-resident immune cells were merged with the splenocytes and normalization, PCA and cell-clustering analysis performed. Clusters in the merged islet and spleen dataset were then manually annotated based on cell lineage and cell type and compared across tissue of origin (islet or spleen) (Figure 6C). We noted the contribution and proportion of each cell type from islets or spleen differed (Figure 6D). Mast cells originated primarily from islets whereas B cells and plasma cells were predominantly from the spleen (Figure 6D). To annotate subsets of immune cell lineages, the expression of genes and proteins associated with T cells and ILCs (Figure 6E), myeloid cells (Figure 6F) and plasma cells, B cells and mast cells (Figure 6G) were assessed. Unique to islets, we also identified a CD8 T cell population with surface protein expression of NKG2D and CD94 (Figure 6E).

We noted, however, that although flow cytometric titrations were performed to optimize antibody dilutions for CITE-seq, the concentrations used based on this optimization were not always ideal, with some markers displaying a large degree of non-specific background signal. In particular, 4-1BBL, CD138, TCR γ/δ, CD64, NKp44 and OX40 contained notable background contamination. To correct this, minimum cut-offs were used to eliminate background signal from non-specific binding of oligo-tagged antibodies (Supplemental Figure S3).

To validate the CITE-seq protein data based on ADT, flow cytometry analysis was performed on islets from n=4 donors. Proportions of immune cells in healthy human islets (Figure 7A) were used to compare expression patterns in myeloid, T cell and ILC populations (Figures 7B–D). CD14 and CD68 were used to identify myeloid populations (Figure 7B) and the expression of HLA-DR and CD206 was validated in healthy human islets in comparison to PBMC control myeloid cells. CD3, CD4, and CD8 were used to identify T cell populations. CITE-seq revealed that islet-resident CD4$^+$ T cells expressed CCR4 and CD45RO, which was also observed *via* flow cytometry (Figure 7C). In CD8$^+$ T cells, high expression of CD103 and CD45RO was observed *via* both CITE-seq and flow cytometry (Figure 7C). Thus, there was concordance in positive expression between protein detected by flow cytometry and protein detected by CITE-seq in islet resident immune cells.

TABLE 3 List of antibodies titrated, stimulation condition, recommended titration from the vendor and 3 point titration values.

Antibody	Stimulation condition	Recommended Titration	Titration 1	Titration 2	Titration 3
CD56	–	0.05 - 0.8	**0.05**	0.425	0.8
CD161	–	0.125 - 2	**0.125**	1.0625	2
CD117 (c-kit)	–	0.25-1	**0.25**	0.625	1
CD16	–	0.025 - 0.4	**0.025**	0.2125	0.4
TIGIT (VSTM3)	–	0.125 - 2	**0.125**	1.0625	2
CD335 (NKp46)	–	0.05 - 0.8	**0.05**	0.425	0.8
CD294 (CRTH2)	–	>0.5	0.5	**1.25**	2
CD127 (IL-7Rα)	–	0.05 - 0.8	**0.05**	0.425	0.8
CD196 (CCR6)	–	0.0125 - 0.2	**0.0125**	0.106	0.2
CD314 (NKG2D)	PMA	0.0625 - 1	0.0625	**0.53125**	1
CD336 (NKp44)	–	>0.5	0.5	**1.25**	2
CD94	–	0.025 - 0.4	**0.025**	0.2125	0.4
KLRG1 (MAFA)	–	0.1-0.5	**0.1**	0.3	0.5
CD183 (CXCR3)	–	0.05 - 0.8	**0.05**	0.425	0.8
TCR γ/δ	–	N/A	0.05	**0.425**	0.8
CD45	–	0.01-0.1	**0.01**	0.055	0.1
TCR Vα24-Jα18 (iNKT cell)	–	N/A	**0.5**	1.25	2
TCR α/β	–	0.015 - 0.24	**0.015**	0.1275	0.24
CD8a	–	N/A	**0.025**	0.2125	0.4
CD3	–	0.0125 - 0.2	**0.0125**	0.106	0.2
CD4	–	0.025 - 0.4	**0.025**	0.2125	0.4
CD138 (Syndecan-1)	–	N/A	0.05	**0.425**	0.8
CD14	–	0.025 - 0.4	**0.025**	0.2125	0.4
CD206 (MMR)	–	0.25-1	**0.25**	0.625	1
HLA-DR	–	0.0125 - 0.2	0.0125	**0.106**	0.2
CD45RA	–	0.03125 - 0.5	**0.03125**	0.2656	0.5
CD45RO	–	0.125 - 2	**0.125**	1.0625	2
CD25	PMA	0.025 - 0.4	**0.025**	0.2125	0.4
CD223 (LAG-3)	PMA	0.125 - 2	**0.125**	1.0625	2
CX3CR1	–	0.0625-1	**0.0625**	0.53125	1
TSLPR (TSLP-R)	–	>0.5	**0.5**	1.25	2
CD49b	–	0.025 - 0.4	**0.025**	0.2125	0.4
CD38	PMA	0.05 - 0.8	**0.05**	0.425	0.8
CD57 Recombinant	–	0.025 - 0.4	**0.0.25**	0.2125	0.4
CD49a	–	0.025 - 0.4	**0.025**	0.2125	0.4
CD278 (ICOS)	PMA	0.0625 - 1	**0.0625**	0.53125	1
CD357 (GITR)	PMA	N/A	**0.5**	1.25	2
CD39	PMA	0.0125 - 0.2	**0.0125**	0.10625	0.2
CD69	PMA	0.025 - 0.4	**0.025**	0.2125	0.4
CD279 (PD-1)	PMA	0.125 - 2	**0.125**	1.0625	2

(Continued)

TABLE 3 Continued

Antibody	Stimulation condition	Recommended Titration	Titration 1	Titration 2	Titration 3
CD152 (CTLA-4)	PMA	0.25-1	**0.25**	0.625	1
CD107a (LAMP-1)	PMA	0.0625 - 1	**0.0625**	0.53125	1
CD95 (Fas)	PMA	0.125 - 2	**0.125**	1.0625	2
CD134 (OX40)	PMA	0.125 - 2	**0.125**	1.0625	2
CD137L (4-1BB Ligand)	PMA	>0.5	**0.5**	1.25	2
CD40	LPS/IFN	0.025 - 0.4	**0.025**	0.2125	0.4
CD137 (4-1BB)	PMA	0.125 - 2	0.125	**1.0625**	2
CD194 (CCR4)	–	0.0125-0.2	0.0125	**0.10625**	0.2
CD27	–	0.005 - 0.08	0.005	**0.0425**	0.08
CD28	–	0.03125 - 0.5	**0.03125**	0.2656	0.5
GARP (LRRC32)	–	0.125-0.5	**0.125**	0.375	0.5
CD122 (IL-2Rβ)	–	0.0625 - 1	**0.0625**	0.53125	1
CD184 (CXCR4)	–	>0.5	**0.5**	1.25	2
CD49d	PMA	0.0125 - 0.2	**0.0125**	0.10625	0.2
CD274 (B7-H1, PD-L1)	PMA	0.0625-1	**0.0625**	0.53125	1
CD120b	LPS/IFN	N/A	0.01	**0.255**	0.5
CD80	LPS/IFN	0.25-1	0.25	**0.625**	1
CD32/Fcg RII	LPS/IFN	0.0125 - 0.2	0.0125	**0.10625**	0.2
CD11b	LPS/IFN	0.0125 - 0.2	0.0125	0.10625	**0.2**
CD64 (FCGR1A)	LPS/IFN	0.0125 - 0.2	0.0125	**0.10625**	0.2
CD86	LPS/IFN	0.005 - 0.08	0.005	**0.0425**	0.08
CD163	LPS/IFN	0.0625 - 1	0.0625	**0.53125**	1
CD197 (CCR7)	–	>0.5	**0.5**	1.25	2

All titration values are µg per 100µl with 1 million splenocytes. Chosen titration values are bolded. N/A stands for Not Available.

To examine whether combined RNA and protein data allowed for better delineation of cell types than either individually, we performed normalization and UMAP projections based on either RNA or ADT data alone from the merged islet and spleen dataset (Supplemental Figure S4). Manual annotation of the UMAPs was informed by heatmaps of select differentially expressed genes (DEGs) or differentially expressed proteins (DEPs) present in clusters defined by RNA, ADT, and/or combined RNA and ADT (Supplemental Figure S5). We found that analysis using RNA, ADT or RNA with ADT all generated UMAPs with 14 clusters (Supplemental Figure S4A). Populations labelled as 'Unclear' in Supplemental Figure S4B were those which lacked lineage defining markers by either RNA or ADT. Notably, manual annotation with information from either RNA or ADT alone did not match annotations derived from RNA and ADT (Supplemental Figure S4B). Specifically, clusters 0, 1, 2, 3, 4, 5, 8, 9, 11, and 14 were not accurately annotated using RNA or ADT data alone. Further, UMAPs derived from combined RNA and protein data were necessary to identify CD4$^+$ T cells, NK/CD8$^+$ T cells, NK cell/ILCs and CD8$^+$ T cells as key lineage markers were not highly expressed at the RNA level. These findings emphasize the importance of including protein data to accurately distinguish T cell, ILC and NK cell types.

We also assessed how protein and mRNA expression levels were correlated in human islet-resident immune cells by comparing lineage markers associated with T cells, ILCs, myeloid and plasma cells, as well as molecules associated with activation or inhibition (Figure 8A). Of the markers included in our CITE-seq panel, 15/67 had positive mRNA expression levels that overlapped with positive protein levels, 37/67 had some overlap between protein and corresponding mRNA expression and 10/61 did not overlap in either islet and spleen populations (visualized by FeaturePlot and DotPlot). Markers not assessed did not have RNA level equivalents, such as CD45RA. For example, consistent expression patterns of CD3, CD127 and CD14 were observed at both the protein and mRNA levels. In contrast CD8, CD4, CD56 and CD138 were not highly expressed at the mRNA level but could be readily detected at the protein level. (Figure 8A). Importantly, protein level data within the CITE-seq dataset increased the resolution and accuracy of our annotations. For example, T cell populations can be more clearly delineated by distinct surface level CD4 and CD8 expression and likewise,

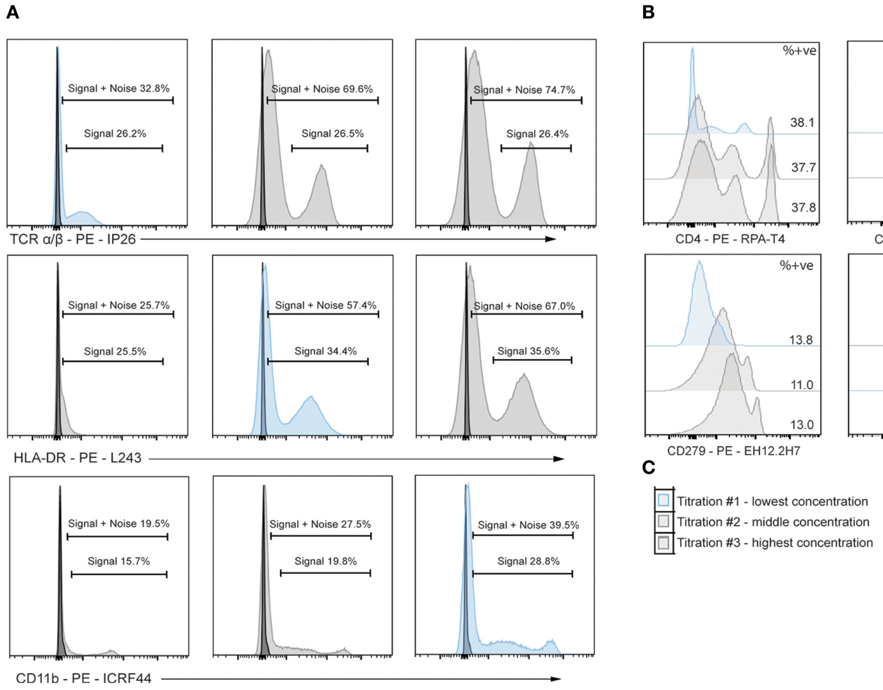

FIGURE 5
Titrations of flow cytometry antibodies corresponding to oligo-antibody clones in the TotalSeq-C catalogue reveals optimal staining conditions. PBMCs were stained using PE antibodies against the marker of interest and performed in 3-fold serial dilutions. Dilution chosen is shown in blue. **(A)** Example titrations showing percent positive noise + signal and percent positive signals. The titration chosen is the dilution that does not lose positive signal yet has the least signal + noise percent positive. **(B)** 3-point titrations performed on markers affected by enzymatic digestion. **(C)** Example legend for histograms shown in B, where the top plot is titration #1 and the lowest dilution, middle plot is titration #2 and the middle concentration, and the bottom plot is titration #3 and highest concentration of antibody.

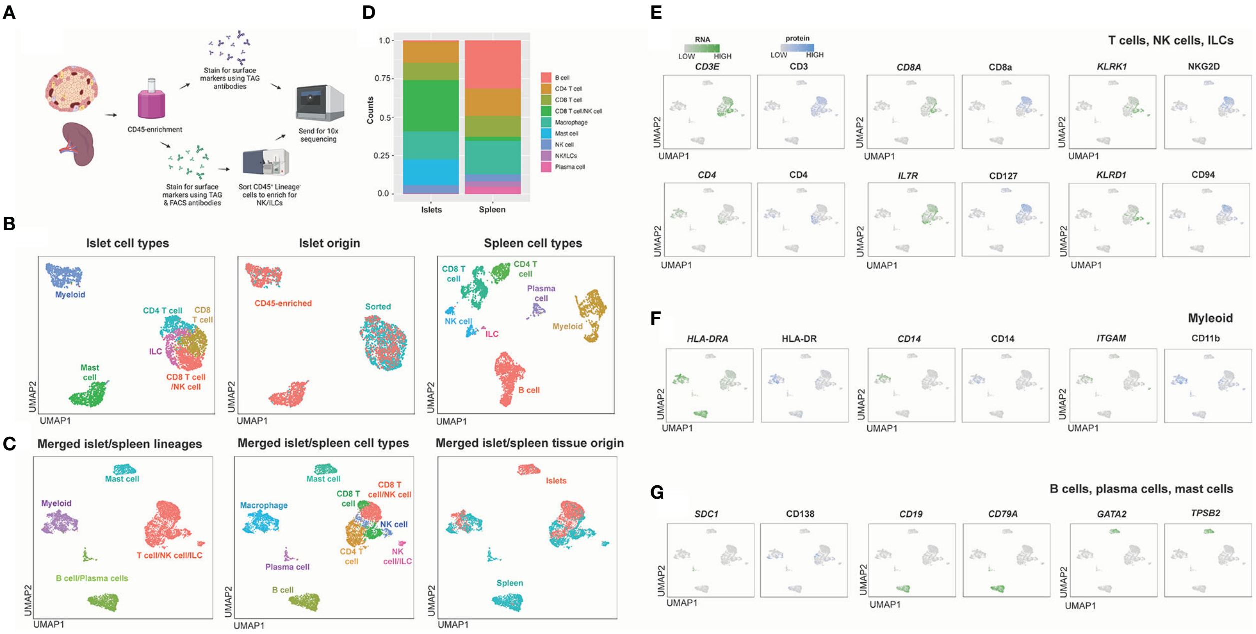

FIGURE 6
Workflow and combined islet and spleen lineage maps. **(A)** Example workflow of CITE-seq. Spleen and islet samples were enriched for CD45$^+$ immune cells. Immune cells from spleen were stained with oligo-antibody conjugated TotalSeqC antibodies and sent for 10x sequencing. Islet immune cells were either were stained with oligo-antibody conjugated TotalSeqC antibodies or stained for both oligo-antibody conjugated TotalSeqC and flow cytometry antibodies at the same time and FACS sorted to enrich for NK cells and ILCs and then sent for 10x sequencing. **(B)** UMAPs of islet cell types, islet cell origin (FACS sorted or CD45-enriched), and spleen cell types. **(C)** Merged islet and spleen lineage, cell types and tissue of origin UMAPs. **(D)** Composition of cell types from each organ. **(E)** T, NK and ILC lineage markers. **(F)** Myeloid lineage markers. **(G)** B cell, plasma cell and mast cell lineage markers.

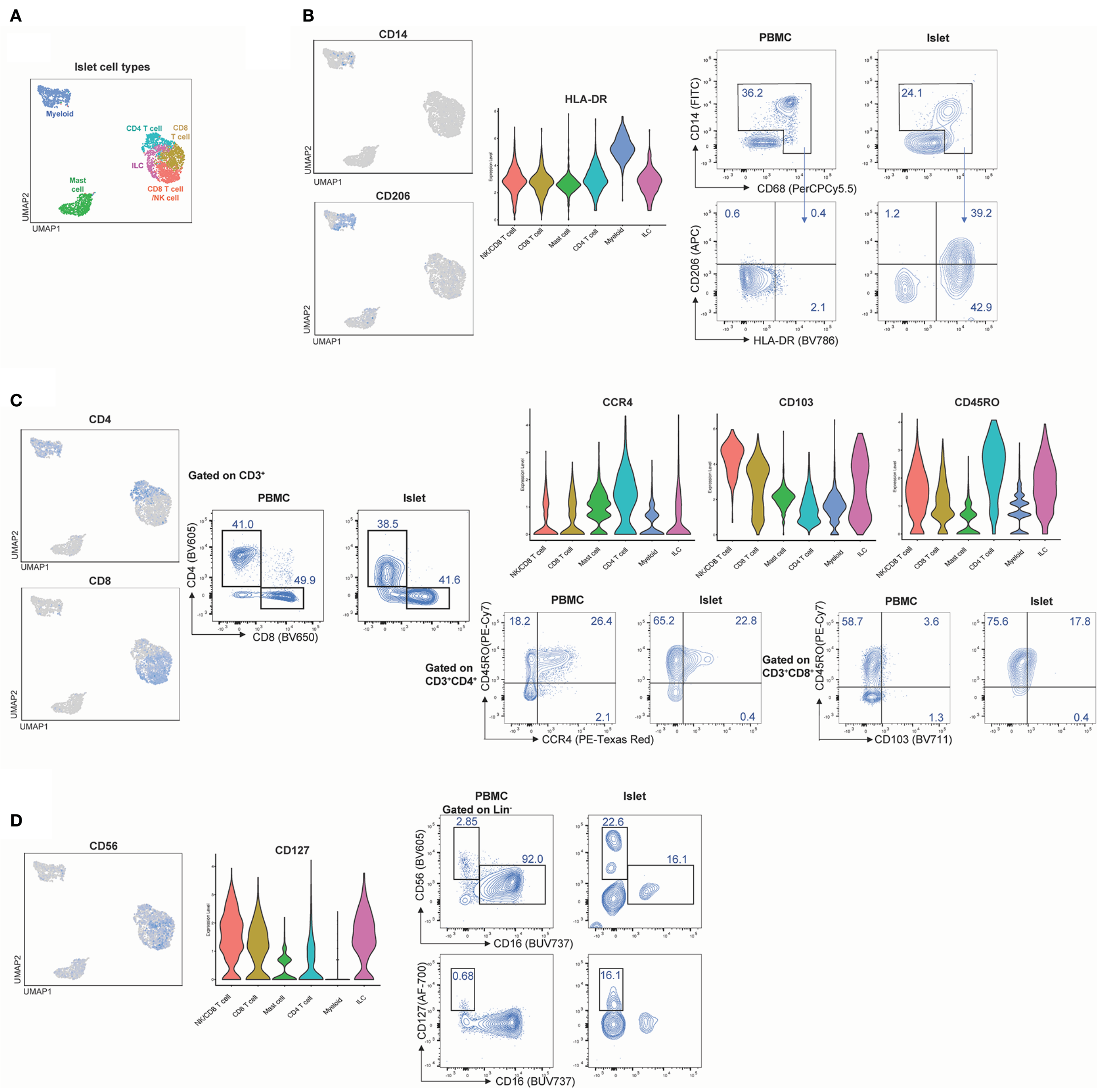

FIGURE 7
CITE-Seq protein expression is validated by flow cytometry on healthy human islets. Healthy human islets were analyzed by CITE-seq and flow cytometry. Surface marker proteins found to be expressed by islet-resident immune cells by CITE-seq were analyzed by flow cytometry in order to validate CITE-seq findings. PBMCs were used a staining control for flow cytometry analysis. **(A)** human islet UMAP, **(B)** Myeloid population analysis of CD14, CD206 and HLA-DR expression. **(C)** T cell population analysis of CD4, CD8, CD45Ro, CCR4 and CD103. **(D)** ILC analysis of CD56 and CD127.

cytotoxic T cell and NK cell populations can be delineated with clear expression of surface CD56.

We also compared mRNA to protein expression on islet- and spleen-derived T cells to determine whether protein level quantification may have been affected by digestion (Figures 8B, C). T cells from the merged spleen and islet Seurat object were re-clustered (Figure 8B), and T-cell-associated gene and protein expression were compared between digested (islet), and undigested (spleen) tissue. While all 67 CITE-seq proteins were assessed, we focused on analysis of CD4, CD8A, CD25, PD1, CD27 and CCR6 (Figure 8C), since flow cytometry studies identified these markers as being highly susceptible to digestion (Figure 3). Minimal differences in protein expression between the two measurement methods were observed.

4 Discussion

In this study we examined strategies to optimize CITE-seq of resident immune cells by testing epitope susceptibility to an enzymatic digestion cocktail commonly used to isolate islets, titrating antibodies for CITE-seq by flow cytometry, and comparing CITE-seq data generated with 67 oligo-conjugated antibodies in parallel samples of spleen and islet immune cells. This work revealed epitopes that are highly susceptible to enzymatic digestion, but that were still detectable on cells within the islet capsule. Parallel analysis of flow cytometry and CITE-seq-detected protein expression revealed good data concordance and enabled identification of islet resident immune cells that would have been difficult to detect on the basis of mRNA expression alone.

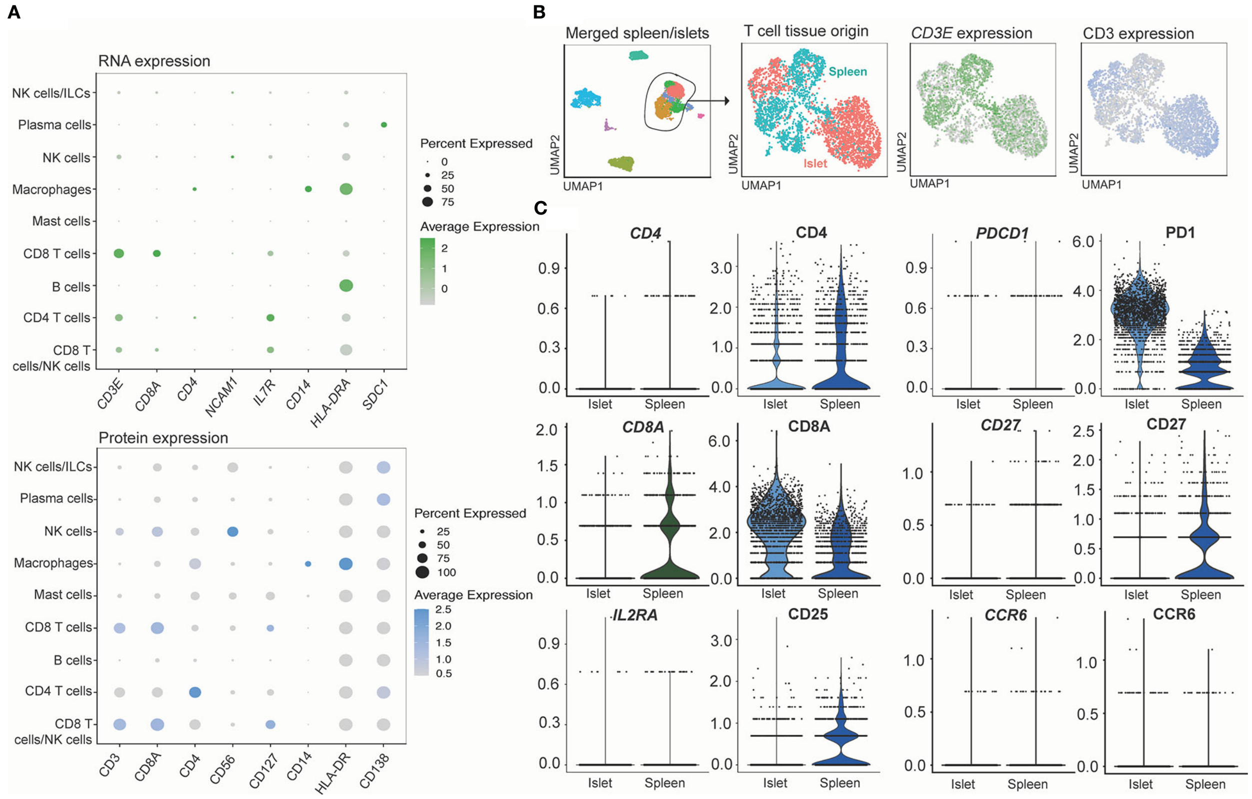

FIGURE 8
CITE-seq allows identification cell types through the expression of surface markers not captured by single cell RNA sequencing. **(A)** RNA (genes shown in green) and protein (surface markers shown in blue) expression of matched molecules. **(B)** Markers shown to be sensitive to digestion by flow cytometry on T cells. T cells subsets were extracted from the combined islet/spleen objects and **(C)** titration markers were compared between the digested (islets) and non-digested (spleen) samples.

Digestion of the exocrine pancreas in collagenase is a well-established method for human islet isolation in preparation for transplantation or for laboratory studies of islets, beta cells and/or islet-resident immune cells (27, 36). To determine whether this process could affect cell surface proteins on immune cells, we performed flow cytometry with PBMCs experimentally exposed to enzymes commonly used in the preparation of islets. These data showed that depending on the antibody clone, the ability to detect CD4, CD8a, CD25, CD27, CCR6, and PD-1 can be affected by enzymatic digestion. In accordance with our findings, CD4, CD8a, CD25, and CD27 have also been observed by other groups to be sensitive to digestion (24).

To further assess the impact of collagenase on cell surface marker expression by CITE-seq, we compared protein and mRNA expression in digested islets and mechanically dissociated spleen, focusing on the proteins found to be most cleavage-susceptible by flow cytometry. Contrary to flow cytometry data, protein expression of CD8a and PD-1 was higher in islets (digested) than in spleen (undigested). These findings suggest that while these epitopes are sensitive to enzymatic digestion, CITE-seq has sufficient sensitivity to detect expression. Similar expression of CD4 in islets and spleen at the protein and mRNA was observed, suggesting that digestion did not negatively affect the ability to detect this marker by CITE-seq. We did not detect CD25 or CD27 protein expression on immune cells from human islets but could observe immune cells expressing these markers in spleen. This may be a result of collagenase-induced cleavage, but as reported by other groups (15) it is more likely that CD25^{+} cells are not present in islet-resident immune cells from people without T1D, as it was also not detected by flow cytometry or at the mRNA level. Further, *FOXP3* mRNA (expressed by CD25^{hi} Tregs) was not detected. We noted low *CD27* gene expression in both tissues, making it unclear if the difference in CD27 expression between islets and spleen are a result of collagenase-induced cleavage or reflective of biological differences in immune cells from these distinct tissues. Finally, we observed no CCR6 protein or mRNA expression in either islets or spleen, so while this marker is sensitive to digestion, it was likely not expressed by immune cells within tissues studied within this donor.

Surface protein cleavage by collagenase can be impacted by the length of digestion time and concentration of the enzyme. In human islet isolation protocols, collagenase is typically delivered *via* the common bile duct for dispersal throughout the pancreas (26, 36). Exposure of islet-resident immune cells to collagenase during this process varies among donors, collagenase lots (36), and islet preparations. We theorize that the epitopes of immune cells within islets may have been shielded by cells that comprise the islet mantle, minimizing the exposure of immune cells to digestion enzymes and mitigating any potential proteolytic effect. Thus, our assessment of the impact of collagenase on PBMCs may not enable direct comparison to islet-resident immune cell cleavage after digestion. Nonetheless, identifying the epitopes most susceptible to cleavage is still important to determine whether differences in cell surface expression might be biological or related to the islet digestion protocol. Our study highlights the utility of parallel sequencing of control tissues (e.g., splenocytes) that do not require enzymatic digestion to create single cell suspensions, whenever possible.

Titrating oligo-conjugated antibodies for multimodal single-cell analysis is important for improving sensitivity, lowering background signal, and reducing sequencing costs (23). In our study, we did 3-point serial dilutions with the middle concentration being suggested by the manufacturer (BioLegend) using PE-conjugated versions of the same clones used for CITE-seq. We noted that the manufacturer's recommended antibody staining concentration, which had been optimized on circulating immune cells in blood, was only optimal for 15 of 67 antibodies, suggesting antibody optimization may have to be tailored for tissue studies. By using splenocytes rather than PBMCs for optimizations, we were better able to select a concentration which had the optimal balance between positive signal and low background. This observation is of note, as unlike antibody titrations for flow cytometry, with CITE-seq it is important to not use saturating amounts of antibody, as this may result in sequencing of unbound, aggregated antibodies and reduced overall sequencing depth (23).

Due to the high cost of sequencing and the rarity of human islet donors, we performed our antibody titrations using flow cytometry analysis of human splenocytes, rather than with human islets and sequencing. While this enhanced our ability to select optimal antibody dilution for most markers, it may also have led to sub-optimal selection of CITE-seq antibody concentrations for islet studies. We noted that while helpful for many epitopes, the use of PE-conjugated antibodies as a proxy for CITE-seq oligo-tagged antibodies was imperfect. This could in part be due to the variance in conjugation stoichiometry that is often not consistent between varying formats and batches of fluorescent antibodies (37). It may also be due to differences in sensitivity of ADT sequencing as compared to fluorescent antibody detection (38). While flow based titration methods are used widely as an economical and relatively quick method of antibody optimizations for CITEseq studies, this may lead to using sub-optimal CITE-seq antibody concentrations. Despite this, in cases where there was a background signal, we were able to perform manual modifications of signal expression to visualize the differential expression, leading us to conclude that oligo-conjugated antibody titration by flow cytometry is for the most part a helpful technique to obtain concentrations needed for CITE-seq but the source of immune cells can influence selection of appropriate concentration.

CITE-seq allows for optimal annotation of cell populations and identification of rare cells that cannot be identified by RNA sequencing alone. We found that protein expression data from 67 surface markers increased our ability to annotate myeloid cells, T cells, NK cells and other ILCs, as well as mast cells in human islets. As ILCs are present in low abundance in islets, and can have very similar profiles at the RNA level to T cell populations, including expression of CD3 at the transcriptional level (39, 40), we enriched NK cells and helper ILCs by flow cytometry-sorting prior to sequencing. CITE-seq enabled clear differentiation of helper ILCs from T cells by positive expression of CD127 without high surface CD4 and CD8 protein expression. There were discrepancies between mRNA and protein expression for ILC markers including *IL7R* and CD127, *KLRD1* and CD94, and CD56 and *NCAM1*. The latter is particularly relevant, as CD56 is expressed by several ILCs – NK cells, key among – but also natural killer T cells and activated T cells. The poor capture of *NCAM1* in mRNA data illustrates the benefit of CITE-seq versus single cell RNA sequencing to identify CD56-expressing cells (41).

In summary, we found that although digestion of immune cells with islet isolation enzymes has the potential to significantly affect cell surface expression of several epitopes, the structure of islets might mitigate any proteolytic effects on resident immune cells. With the use of accurately titrated antibodies, CITE-seq adds a valuable layer of information to single-cell RNA sequencing in the characterization of islet-resident immune cell subsets. This work sets the stage for a more comprehensive investigation of how these cells change in health and disease.

Data availability statement

The original contributions presented in the study are publicly available. This data can be found here: Gene Expression Omnibus, GSE224767.

Ethics statement

The studies involving human participants were reviewed and approved by University of British Columbia Clinical Research Ethics Board (B22-0075 and H18-02553), Canadian Blood Services, and the University Health Network Research Ethics Board (17-6229 and 20-5206). The patients/participants provided their written informed consent to participate in this study.

Author contributions

SJC, MB, and MM contributed equally to this work and share first authorship. CV, ML, and SQC contributed equally to this work and share senior authorship. KR, JM, and SI contributed to experimental design and analysis. SJC, MB, MM, CV, ML, and SQC wrote the manuscript, which all authors reviewed and edited. All authors contributed to the article and approved the submitted version.

Funding

This study was funded by the Canadian Institutes of Health Research Human Immunology Initiative (HUI-159423 and HH3-168005), and JDRF Canada (4-SRA-2020-953-A-N). SJC was supported by a Banting and Best Novo Nordisk Scholarship and a Queen Elizabeth II/Dr. Dina Gordon Malkin Graduate Scholarship in Science and Technology. The funder was not involved in the study design, collection, analysis, interpretation of data, the writing of this article, or the decision to submit it for publication. MB is supported by a CIHR doctoral award. MKL and CBV receive salary awards from the BC Children's Hospital Research Institute. ML holds a Canada Research Chair in Engineered Immune Tolerance. SQC holds a Canada Research Chair in Tissue-Specific Immune Tolerance and was also supported by the Medicine by Design program (Canada First Research Excellence Fund), the Ajmera Transplant Centre and the Canada Foundation for Innovation (38308).

Acknowledgments

Thank you to Robert McCarthy, Vitacyte president and co-founder, for aiding in the experimental protocol design, donating the requisite enzymes for experimentation, and providing helpful discussions. We thank Patrick MacDonald and team at the University of Alberta IsletCore, as well as Trevor Reichman and Justin Manuel at the Ajmera Transplant Centre for facilitation islet and splenic tissue collection.

Conflict of interest

The authors declare that the research was conducted in the absence of any commercial or financial relationships that could be construed as a potential conflict of interest.

Publisher's note

Supplementary material

The Supplementary Material for this article can be found online at: https://www.frontiersin.org/articles/10.3389/fimmu.2023.1107582/full#supplementary-material

References

1. Burrack AL, Martinov T, Fife BT. T Cell-mediated beta cell destruction: Autoimmunity and alloimmunity in the context of type 1 diabetes. *Front Endocrinol* (2017) 8:343. doi: 10.3389/fendo.2017.00343

2. Dalmas E, Lehmann FM, Dror E, Wueest S, Thienel C, Borsigova M, et al. Interleukin-33-Activated islet-resident innate lymphoid cells promote insulin secretion through myeloid cell retinoic acid production. *Immunity* (2017) 47(5):928–942.e7. doi: 10.1016/j.immuni.2017.10.015

3. Molofsky AB, Nussbaum JC, Liang HE, Van Dyken SJ, Cheng LE, Mohapatra A, et al. Innate lymphoid type 2 cells sustain visceral adipose tissue eosinophils and alternatively activated macrophages. *J Exp Med* (2013) 210(3):535–49. doi: 10.1084/jem.20121964

4. Xiao X, Gittes GK. Concise review: New insights into the role of macrophages in β-cell proliferation. *Stem Cells Transl Med* (2015) 4(6):655–8. doi: 10.5966/sctm.2014-0248

5. Zhou L, He X, Cai P, Li T, Peng R, Dang J, et al. Induced regulatory T cells suppress Tc1 cells through TGF-β signaling to ameliorate STZ-induced type 1 diabetes mellitus. *Cell Mol Immunol* (2021) 698–710. doi: 10.1038/s41423-020-00623-2

6. Budd MA, Monajemi M, Colpitts SJ, Crome SQ, Verchere CB, Levings MK. Interactions between islets and regulatory immune cells in health and type 1 diabetes. *Diabetologia* (2021) 64(11):2378–88. doi: 10.1007/s00125-021-05565-6

7. Nackiewicz D, Dan M, Speck M, Chow SZ, Chen YC, Pospisilik JA, et al. Islet macrophages shift to a reparative state following pancreatic beta-cell death and are a major source of islet insulin-like growth factor-1. *iScience* (2020) 23(1):100775. doi: 10.1016/j.isci.2019.100775

8. Denroche HC, Miard S, Sallé-Lefort S, Picard F, Verchere CB. T Cells accumulate in non-diabetic islets during ageing. *Immun Ageing.* (2021) 18(1):8. doi: 10.1186/s12979-021-00221-4

9. Zinselmeyer BH, Vomund AN, Saunders BT, Johnson MW, Carrero JA, Unanue ER. The resident macrophages in murine pancreatic islets are constantly probing their local environment, capturing beta cell granules and blood particles. *Diabetologia* (2018) 61(6):1374–83. doi: 10.1007/s00125-018-4592-4

10. Brissova M, Aamodt K, Brahmachary P, Prasad N, Hong JY, Dai C, et al. Islet microenvironment, modulated by vascular endothelial growth factor-a signaling, promotes β cell regeneration. *Cell Metab* (2014) 19(3):498–511. doi: 10.1016/j.cmet.2014.02.001

11. Han JM, Wu D, Denroche HC, Yao Y, Verchere CB, Levings MK. IL-33 reverses an obesity-induced deficit in visceral adipose tissue ST2+ T regulatory cells and ameliorates adipose tissue inflammation and insulin resistance. *J Immunol Baltim Md 1950* (2015) 194 (10):4777–83. doi: 10.4049/jimmunol.1500020

12. Winer DA, Winer S, Shen L, Wadia PP, Yantha J, Paltser G, et al. B cells promote insulin resistance through modulation of T cells and production of pathogenic IgG antibodies. *Nat Med* (2011) 17(5):610–7. doi: 10.1038/nm.2353

13. Grange C, Létourneau J, Forget MA, Godin-Ethier J, Martin J, Liberman M, et al. Phenotypic characterization and functional analysis of human tumor immune infiltration after mechanical and enzymatic disaggregation. *J Immunol Methods* (2011) 372(1):119–26. doi: 10.1016/j.jim.2011.07.002

14. Quatromoni JG, Singhal S, Bhojnagarwala P, Hancock WW, Albelda SM, Eruslanov E. An optimized disaggregation method for human lung tumors that preserves the phenotype and function of the immune cells. *J Leukoc Biol* (2015) 97 (1):201–9. doi: 10.1189/jlb.5TA0814-373

15. Radenkovic M, Uvebrant K, Skog O, Sarmiento L, Avartsson J, Storm P, et al. Characterization of resident lymphocytes in human pancreatic islets. *Clin Exp Immunol* (2017) 187(3):418–27. doi: 10.1111/cei.12892

16. Waise S, Parker R, Rose-Zerilli MJJ, Layfield DM, Wood O, West J, et al. An optimised tissue disaggregation and data processing pipeline for characterising fibroblast phenotypes using single-cell RNA sequencing. *Sci Rep* (2019) 9(1):9580. doi: 10.1038/s41598-019-45842-4

17. de Vos P, Smink AM, Paredes G, Lakey JRT, Kuipers J, Giepmans BNG, et al. Enzymes for pancreatic islet isolation impact chemokine-production and polarization of insulin-producing β-cells with reduced functional survival of immunoisolated rat islet-allografts as a consequence. *PloS One* (2016) 11(1):e0147992. doi: 10.1371/journal.pone.0147992

18. Stoeckius M, Zheng S, Houck-Loomis B, Hao S, Yeung BZ, Mauck WM, et al. Cell hashing with barcoded antibodies enables multiplexing and doublet detection for single cell genomics. *Genome Biol* (2018) 19(1):224. doi: 10.1186/s13059-018-1603-1

19. Stoeckius M, Hafemeister C, Stephenson W, Houck-Loomis B, Chattopadhyay PK, Swerdlow H, et al. Simultaneous epitope and transcriptome measurement in single cells. *Nat Methods* (2017) 14(9):865–8. doi: 10.1038/nmeth.4380

20. Scheyltjens I, Van Hove H, De Vlaminck K, Kancheva D, Bastos J, Vara-Pérez M, et al. Single-cell RNA and protein profiling of immune cells from the mouse brain and its border tissues. *Nat Protoc* (2022) 17:1–35. doi: 10.1038/s41596-022-00716-4

21. Hao Y, Hao S, Andersen-Nissen E, Mauck WM, Zheng S, Butler A, et al. Integrated analysis of multimodal single-cell data. *Cell* (2021) 184(13):3573–3587.e29. doi: 10.1016/j.cell.2021.04.048

22. Mazzurana L, Czarnewski P, Jonsson V, Wigge L, Ringnér M, Williams TC, et al. Tissue-specific transcriptional imprinting and heterogeneity in human innate lymphoid cells revealed by full-length single-cell RNA-sequencing. *Cell Res* (2021) 31(5):554–68. doi: 10.1038/s41422-020-00445-x

23. Buus TB, Herrera A, Ivanova E, Mimitou E, Cheng A, Herati RS, et al. Improving oligo-conjugated antibody signal in multimodal single-cell analysis. *eLife* (2021) 10: e61973. doi: 10.7554/eLife.61973

24. Autengruber A, Gereke M, Hansen G, Hennig C, Bruder D. Impact of enzymatic tissue disintegration on the level of surface molecule expression and immune cell function. *Eur J Microbiol Immunol* (2012) 2(2):112–20. doi: 10.1556/EuJMI.2.2012.2.3

25. Corbin KL, West HL, Brodsky S, Whitticar NB, Koch WJ, Nunemaker CS. A practical guide to rodent islet isolation and assessment revisited. *Biol Proced Online.* (2021) 23(1):7. doi: 10.1186/s12575-021-00143-x

26. Lyon J, Manning Fox JE, Spigelman AF, Kim R, Smith N, O'Gorman D, et al. Research-focused isolation of human islets from donors with and without diabetes at the Alberta diabetes institute IsletCore. *Endocrinology* (2016) 157(2):560–9. doi: 10.1210/en.2015-1562

27. Rheinheimer J, Ziegelmann PK, Carlessi R, Reck LR, Bauer AC, Leitão CB, et al. Different digestion enzymes used for human pancreatic islet isolation: A mixed treatment comparison (MTC) meta-analysis. *Islets* (2014) 6(4):e977118. doi: 10.4161/19382014.2014.977118

28. Ivison S, Malek M, Garcia RV, Broady R, Halpin A, Richaud M, et al. A standardized immune phenotyping and automated data analysis platform for multicenter biomarker studies. *JCI Insight* (2018) 3(23):121867. doi: 10.1172/jci.insight.121867

29. Bossuyt X, Marti GE, Fleisher TA. Comparative analysis of whole blood lysis methods for flow cytometry. *Cytometry* (1997) 30(3):124–33. doi: 10.1002/(SICI)1097-0320(19970615)30:3<124::AID-CYTO3>3.0.CO;2-L

30. Lex A, Gehlenborg N, Strobelt H, Vuillemot R, Pfister H. UpSet: Visualization of intersecting sets. *IEEE Trans Vis Comput Graph.* (2014) 20(12):1983–92. doi: 10.1109/TVCG.2014.2346248

31. *Protocol - TotalSeq™-b or -c with 10x feature barcoding technology.* Available at: https://www.biolegend.com/en-us/protocols/totalseq-b-or-c-with-10xfeature-barcoding-technology.

32. Hafemeister C, Satija R. Normalization and variance stabilization of single-cell RNA-seq data using regularized negative binomial regression. *Genome Biol* (2019) 20:296. doi: 10.1186/s13059-019-1874-1

33. Stuart T, Butler A, Hoffman P, Hafemeister C, Papalexi E, Mauck WM, et al. Comprehensive integration of single-cell data. *Cell* (2019) 177(7):1888–1902.e21. doi: 10.1016/j.cell.2019.05.031

34. Becht E, McInnes L, Healy J, Dutertre CA, Kwok IWH, Ng LG, et al. Dimensionality reduction for visualizing single-cell data using UMAP. *Nat Biotechnol* (2018) 38–44. doi: 10.1038/nbt.4314

35. Korsunsky I, Millard N, Fan J, Slowikowski K, Zhang F, Wei K, et al. Fast, sensitive and accurate integration of single-cell data with harmony. *Nat Methods* (2019) 16 (12):1289–96. doi: 10.1038/s41592-019-0619-0

36. Kin T, Zhai X, Murdoch TB, Salam A, Shapiro AMJ, Lakey JRT. Enhancing the success of human islet isolation through optimization and characterization of pancreas dissociation enzyme. *Am J Transplant Off J Am Soc Transplant Am Soc Transpl Surg* (2007) 7(5):1233–41. doi: 10.1111/j.1600-6143.2007.01760.x

37. Ivell R, Teerds K, Hoffman GE. Proper application of antibodies for immunohistochemical detection: Antibody crimes and how to prevent them. *Endocrinology* (2014) 155(3):676–87. doi: 10.1210/en.2013-1971

38. Stoeckius M, Hafemeister C, Stephenson W, Houck-Loomis B, Chattopadhyay PK, Swerdlow H, et al. Large-Scale simultaneous measurement of epitopes and transcriptomes in single cells. *Nat Methods* (2017) 14(9):865–8. doi: 10.1038/nmeth.4380

39. Björklund ÅK, Forkel M, Picelli S, Konya V, Theorell J, Friberg D, et al. The heterogeneity of human CD127 + innate lymphoid cells revealed by single-cell RNA sequencing. *Nat Immunol* (2016) 17(4):451–60. doi: 10.1038/ni.3368

40. Suffiotti M, Carmona SJ, Jandus C, Gfeller D. Identification of innate lymphoid cells in single-cell RNA-seq data. *Immunogenetics* (2017) 69(7):439–50. doi: 10.1007/s00251-017-1002-x

41. Lawlor N, Nehar-Belaid D, Grassmann JDS, Stoeckius M, Smibert P, Stitzel ML, et al. Single cell analysis of blood mononuclear cells stimulated through either LPS or anti-CD3 and anti-CD28. *Front Immunol* (2021) 12:636720. doi: 10.3389/fimmu.2021.636720

frontiers | Frontiers in Immunology

TYPE Original Research
PUBLISHED 08 August 2023
DOI 10.3389/fimmu.2023.1212330

Exploring the shared molecular mechanisms between systemic lupus erythematosus and primary Sjögren's syndrome based on integrated bioinformatics and single-cell RNA-seq analysis

Yanling Cui[1,2†], Huina Zhang[1,2†], Zhen Wang[1,2†], Bangdong Gong[3], Hisham Al-Ward[1,2], Yaxuan Deng[1,2], Orion Fan[1,2], Junbang Wang[1], Wenmin Zhu[1] and Yi Eve Sun[1,2*]

[1]Stem Cell Translational Research Center, Tongji Hospital, School of Medicine, Tongji University, Shanghai, China, [2]Shanghai Institute of Stem Cell Research and Clinical Translation, Shanghai East Hospital, School of Medicine, Tongji University, Shanghai, China, [3]Division of Rheumatology, Tongji Hospital of Tongji University School of Medicine, Shanghai, China

OPEN ACCESS

EDITED BY
Kuang-Hui Sun,
National Yang Ming Chiao Tung University,
Taiwan

REVIEWED BY
Anela Tosevska,
Medizinische Universitaet Wien, Austria
Juliana Imgenberg-Kreuz,
Uppsala University, Sweden

*CORRESPONDENCE
Yi Eve Sun
✉ yi.eve.sun@gmail.com

†These authors have contributed equally to this work

RECEIVED 26 April 2023
ACCEPTED 19 July 2023
PUBLISHED 08 August 2023

CITATION
Cui Y, Zhang H, Wang Z, Gong B, Al-Ward H, Deng Y, Fan O, Wang J, Zhu W and Sun YE (2023) Exploring the shared molecular mechanisms between systemic lupus erythematosus and primary Sjögren's syndrome based on integrated bioinformatics and single-cell RNA-seq analysis. *Front. Immunol.* 14:1212330. doi: 10.3389/fimmu.2023.1212330

Background: Systemic lupus erythematosus (SLE) and primary Sjögren's syndrome (pSS) are common systemic autoimmune diseases that share a wide range of clinical manifestations and serological features. This study investigates genes, signaling pathways, and transcription factors (TFs) shared between SLE and pSS.

Methods: Gene expression profiles of SLE and pSS were obtained from the Gene Expression Omnibus (GEO). Weighted gene co-expression network analysis (WGCNA) and differentially expressed gene (DEG) analysis were conducted to identify shared genes related to SLE and pSS. Overlapping genes were then subject to Gene Ontology (GO) and protein-protein interaction (PPI) network analyses. Cytoscape plugins cytoHubba and iRegulon were subsequently used to screen shared hub genes and predict TFs. In addition, gene set variation analysis (GSVA) and CIBERSORTx were used to calculate the correlations between hub genes and immune cells as well as related pathways. To confirm these results, hub genes and TFs were verified in microarray and single-cell RNA sequencing (scRNA-seq) datasets.

Results: Following WGCNA and limma analysis, 152 shared genes were identified. These genes were involved in interferon (IFN) response and cytokine-mediated signaling pathway. Moreover, we screened six shared genes, namely *IFI44L, ISG15, IFIT1, USP18, RSAD2* and *ITGB2*, out of which three genes, namely *IFI44L, ISG15* and *ITGB2* were found to be highly expressed in both microarray and scRNA-seq datasets. IFN response and ITGB2 signaling pathway were identified as potentially relevant pathways. In addition, STAT1 and IRF7 were identified as common TFs in both diseases.

Conclusion: This study revealed *IFI44L, ISG15* and *ITGB2* as the shared genes and identified STAT1 and IRF7 as the common TFs of SLE and pSS. Notably, the IFN response and ITGB2 signaling pathway played vital roles in both diseases. Our study revealed common pathogenetic characteristics of SLE and pSS. The particular roles of these pivotal genes and mutually overlapping pathways may provide a basis for further mechanistic research.

KEYWORDS

systemic lupus erythematosus, primary Sjögren's syndrome, bioinformatics, hub genes, TFs, scRNA-seq

Introduction

Systemic lupus erythematosus (SLE) and primary Sjögren's syndrome (pSS) are among the most common systemic autoimmune diseases and exhibit numerous shared clinical symptoms, serological profiles and immunological characteristics (1–3). Both SLE and pSS exhibit a predominance in females, and cases frequently present overlapping clinical symptoms, such as arthralgia, myalgia, and leukopenia (4). SLE and pSS preferentially target specific organs. SLE is characterized by a variety of disease-specific clinical manifestations, including skin rash, arthritis, lupus nephritis and hematological symptoms (5, 6). The pSS is a chronic inflammation condition that primarily affects the exocrine glands (salivary and lacrimal glands), resulting in oral and ocular dryness (7). Beyond affecting organs, peripheral blood plays an indispensable role in manifesting the immune pathophysiology for SLE and pSS. Peripheral blood mononuclear cells (PBMCs) are the immune cells most responsible for initiating the autoimmune inflammatory process against the target organs (8). Thus, the transcriptomic profiles of PBMC could provide pertinent insights into the molecular characteristics of the immune cells in SLE and pSS.

The etiologies and pathogeneses of SLE and pSS remain elusive and may be related to various factors, such as genetic predisposition, environmental triggers and epigenetic mechanisms (9). Genetic risk loci, including HLA class II, *IL12A* and *BLK* (associated with adaptive immunity), *IRF5* and *STAT4* (associated with innate immunity) are shared in these two diseases (10–12). Environmental factors such as Epstein-Barr virus (EBV) infection and alterations in gut microbial composition have been frequently observed in individuals with SLE and pSS (13–16). Various studies have reported that viral infections promote the development and progression of pSS through type I interferon (IFN). It has been demonstrated that the gene regulation by type I IFN is linked to an escalation disease activity in both SLE and pSS (9, 17–19). In recent studies, widespread changes in DNA methylation have been identified in SLE and pSS by epigenome-wide association studies (EWAS) (1, 20–22). Although these findings suggest the presence of common pathogenetic mechanisms between SLE and pSS, systematic cross-comparative analyses at the genetic level have yet to be conducted.

The rapid development of bioinformatics approaches has facilitated a more robust comprehension of disease pathobiology at the genetic level (23). The identification of common transcriptional features between SLE and pSS may provide valuable insights into shared pathogenetic characteristics of these two diseases. To this end, we performed comprehensive bioinformatics analyses in microarray and single-cell RNA sequencing (scRNA-seq) datasets to identify shared hub genes, related pathways and transcription factors (TFs) in SLE and pSS. We further investigated the correlation between hub gene and immune cell as well as related pathway, and validated their expression and location using scRNA-seq data. Finally, we predicted and verified TFs both in microarray and scRNA-seq datasets. Collectively, the shared hub genes, relevant pathways and TFs identified in this study have the potential to provide new insights to the genetic etiologies of SLE and pSS.

Materials and methods

Data source

Gene Expression Omnibus (GEO) (http://www.ncbi.nlm.nih.gov/geo/) is an extensive and publicly available database that contains numerous high-throughput sequencing and microarray datasets related to many diseases. The keywords "systemic lupus erythematosus" and "primary Sjögren's syndrome" were used to search SLE and pSS gene expression datasets. The selected datasets for analysis strictly consisted of gene expression profiles for both cases and controls, generated from the same sequencing platform and exclusively from human specimens. Datasets GSE50772 (24), GSE81622 (25) and GSE135779 (26) were selected for SLE; GSE84844 (27), GSE48378 (28) and GSE157278 (29) were selected for pSS. The datasets were downloaded from GEO for subsequent analyses. For SLE, dataset GSE50772 includes 61 SLE samples and 20 healthy control samples (Platform: GPL570 Affymetrix Human Genome U133 Plus 2.0 Array); GSE81622 contains 30 SLE samples and 25 healthy control samples (Platform: GPL10558 Illumina HumanHT-12 V4.0 expression bead chip); and GSE135779 consists of 42 SLE samples and 17 control samples (Platform : GPL20301 Illumina HiSeq 4000). For pSS, dataset GSE84844 includes 30 pSS samples and 30 healthy control samples (Platform : GPL570); GSE48378 contains 11 pSS samples and 16 healthy control samples (Platform: GPL5175 Affymetrix Human Exon 1.0 ST Array); and GSE157278 consists of 5 pSS samples and 5 control samples (Platform: GPL24676 Illumina NovaSeq 6000). For microarray datasets, the series matrix files provided by the contributors include data processed by MAS5 or RMA algorithms. We read the data with the GEOquery package and matched the probes to their gene symbols according to the annotation documents of corresponding platforms. Finally, the gene matrix with row names as gene symbols and column names as sample names was obtained for subsequent analyses.

Weighted gene co-expression network analysis

To identify gene co-expression modules associated with SLE and pSS, we conducted weighted gene co-expression network analysis (WGCNA) on the GSE50772 and GSE84844 datasets. The WGCNA R package was used to conduct the analysis (30). We selected the top 5000 genes of the median absolute deviation in the expression matrix of the dataset for WGCNA. Prior to the analysis, the 'Hclust' function was used to eliminate outlier samples. The parameters were networkType = "signed" and TOMType = "signed". We then selected an optimal soft threshold ranging from 1 to 20 using the 'pickSoftThreshold' function to build an adjacency matrix, which was then transformed into a topological overlap matrix (TOM). Co-expression modules were identified through hierarchical clustering, followed by Pearson correlation analysis to compute the correlation between the module eigengene and clinical feature to obtain the expression profile of each module. We then chose the modules with high correlation coefficients with SLE and pSS and obtained genes from these modules for further analysis.

Identification of DEGs

The differentially expressed genes (DEGs) in SLE and pSS were determined by using the limma R package (31). First, the GSE50772 and GSE84844 datasets were converted into an expression matrix and grouped. Next, the limma package was used to normalize and analyze the datasets to obtain DEGs. Genes with adjusted p-value [false discovery rate (FDR)] < 0.05 and $|\log2FC$ (fold change) $| \geq 0.5$ were considered as DEGs (32). Furthermore, genes were classified as upregulated or downregulated based on their log2FC value being greater than 0.5 or less than -0.5, respectively. The overlapping DEGs of SLE and pSS were identified by using an online Venn diagram tool.

Functional enrichment analysis

Gene ontology (GO) is a comprehensive resource regarding the functions of genes and gene products, providing annotations for gene products related to molecular functions, biological processes, and cellular components (33). Hallmark gene sets represent biological states or processes derived from the Molecular Signatures Database (MSigDB) (34). The "clusterProfiler" R package was used to conduct GO and Hallmark functional annotation analyses. Significantly enriched outcomes were recognized by p-values less than 0.05.

PPI network construction and module analysis

STRING is an online search tool for the retrieval of interacting genes (STRING; http://string-db.org) (35). WGCNA results and DEGs were combined and imported into the STRING database to construct the protein- protein interaction (PPI) network; the interaction score used for the PPI network was set at > 0.4. Analysis of the PPI network and visualization were carried out using Cytoscape (http://www.cytoscape.org) (36). The molecular complex detection technology (MCODE), a Cytoscape plug-in, was used to conduct key functional module analysis. The employed parameters were as follows: degree cutoff = 2, max depth = 100, node score cutoff = 0.2 and K-core = 2.

Selection and validation of hub genes

The 96 common module genes and 91 common DEGs were combined and subsequently imported into the STRING database to construct a PPI network. To identify hub genes, the cytoHubba plug-in Cytoscape was applied (37). Five algorithms (MCC [maximal clique centrality], MNC [maximum neighborhood component], Closeness, Radiality and EPC [edge percolated component]) were used from cytoHubba to identify and validate the hub genes.

In order to verify the hub genes expression, the GSE81622 and GSE48378 datasets were downloaded. The GSE81622 dataset includes PBMC expression data from 25 patients diagnosed with SLE and 30 healthy controls. The GSE48378 dataset contains expression data of 11 patients diagnosed with pSS and 16 healthy controls. The Shapiro-Wilks test was performed in R to test for the normality of the variables. The w-value was close to 1, and p-value > 0.05. The comparison was then performed using the t-test in these two datasets, separately (38); p-values < 0.05 were considered significant.

Pathways analysis and the correlation with hub genes

Gene Set Variation Analysis (GSVA) is a non-parametric and unsupervised methodology that is employed to evaluate gene set enrichment (GSE) in gene expression microarray and RNA-seq data (39). The GSVA R package was used to find the related pathways in SLE and pSS, by quantifying the activities of the 50 hallmark pathways. Correlations between hub gene and pathway were evaluated by Pearson correlation coefficient. R packages "ggplot2" and "pheatmap" were used for visualization.

Single-cell RNA-Seq data analysis

The scRNA-seq datasets GSE135779 for SLE and GSE157278 for pSS were downloaded from GEO. Down-stream analyses were performed using the Seurat R package (version 4.1.0) (40). Following quality control (QC), cells with fewer than 200 expressed genes and >10% mitochondria-related genes were excluded. After normalization, the top 3000 highly variable genes (HVGs) in each Seurat object were selected for subsequent analysis, including ScaleData, RunPCA, RunTSNE and RunUMAP. The cells were then clustered using the FindNeighbors and FindClusters functions. The generated clusters were visualized using uniform manifold approximation and projection (UMAP) plot. Cell types were identified using classical marker genes and the SingleR algorithm (41). The gene list used to generate IFN-response score comprises the following *IFI27, IFI6, RSAD2, IFI44, IFI44L, IFITM1, IFNGR1, IFIT2, MX2, OASL, GBP1, USP18, LY6E, OAS1, SIGLEC1, ISG15, IFIT1, OAS3, HERC5, MX1, LAMP3, EPSTI1, IFIT3, OAS2, RTP4, PLSCR1, DNAPTP6, TYK1* and *CXCL10* (42–45). The AddModuleScore function in Seurat R was used to calculate the IFN-response score. Differential expression analysis was performed on scRNA-seq datasets using the “FindMarkers” function in the Seurat package with default parameters. This analysis aimed to compare the expression profiles of different cell types between different groups (SLE/HC and pSS/HC). Adjusted p-value < 0.05 and $|\log2FC| > 0.25$ was used to define significant DEGs.

Estimation of immune cell fractions and the correlation with hub genes

CIBERSORTx is a suite of machine learning tools designed for detecting the abundance of cell types in bulk RNA-seq and microarray data (46, 47). We used the GSE135779 and GSE157278 scRNA-seq datasets to build scRNA-seq signature matrices with CIBERSORTx, respectively. After following the instruction to format and upload the single-cell reference matrix file, we ran the “Create Signature Matrix” module to build the scRNA-seq signature matrix (47). We used the generated signature matrices to perform CIBERSORTx deconvolution on the GSE50772 and GSE84844 datasets, separately. p-value < 0.05 was considered statistically significant. To visualize the proportion of each immune cell type, boxplots were constructed, with red and blue color-coding to indicate disease and healthy control (HC) status, respectively. The correlation between each hub gene and immune cell type was evaluated by Pearson correlation coefficient. R packages “ggplot2” and “pheatmap” were used for visualization.

Cell-cell communication analysis

The CellChat package is a powerful tool that facilitates the quantitative inference and analysis of intercellular communication networks from scRNA-seq data. CellChat is capable of predicting the major signaling inputs and outputs for cells, as well as how these signals coordinate for various cellular functions. Once cell types have been identified, CellChat can be further used to analyze cell-cell communication (48). In this study, we generated new CellChat objects from the Seurat objects. The CellChatDB was set as the reference database. The two scRNA-seq data were further divided into two groups each based on their respective conditions (HC vs SLE, HC vs pSS). Thereafter, the variations in ligand-receptor interactions and signaling pathways among these states were thoroughly examined.

Prediction and verification of transcription factors

iRegulon is a computational method to reverse-engineer the transcriptional regulatory network underlying a co-expressed gene set using cis-regulatory sequence analysis. This method utilizes a genome-wide ranking-and-recovery approach to detect enriched transcription factor (TF) motifs and their optimal sets of direct targets (49). In this study, we employed iRegulon to predict the TFs of hub genes, and their expression levels were subsequently validated in microarray datasets. Furthermore, we confirmed the expression and localization of these TFs in scRNA-seq data. The major parameters in iRegulon were the following: Species and gene nomenclature = “Homo sapiens, HGNC symbols”, Motif collection = “10K (9713 PWMs)”, Track collection = “1120 ChIP-seq tracks (ENCODE raw signals)”, Putative regulatory region = “20kb centered around TSS”, Enrichment score threshold = 3.0, ROC threshold for AUC calculation = 0.03 and the rank threshold = 5000.

Gene regulatory network

Single-cell regulatory network inference and clustering (SCENIC) is a computational method to infer cell type-specific gene regulatory networks (GRNs) from scRNA-seq data (50). The input matrices were the raw unique molecular identifier (UMI) counts for each sample obtained from Seurat. Genes present in RcisTarget’s databases (hg19-500 bp-upstream-7species. mc9nr. feather and hg19-tss-centered-10 kb-7species. mc9nr.feather) were utilized. Following the SCENIC pipeline, the GENIE3 method and GRNBoost were used to identify potential TF targets, and the regulon-specific score (RSS) was generated. Only significantly upregulated regulons were involved in further analysis.

Results

GEO information

The workflow of this study is illustrated in Figure 1. Four microarray datasets, including GSE50772, GSE81622, GSE84844 and GSE48378, along with two scRNA-seq datasets, namely GSE157278 and GSE135779, were downloaded from GEO. Information from these datasets, including GSE number, detection platforms, samples and source types, is provided in

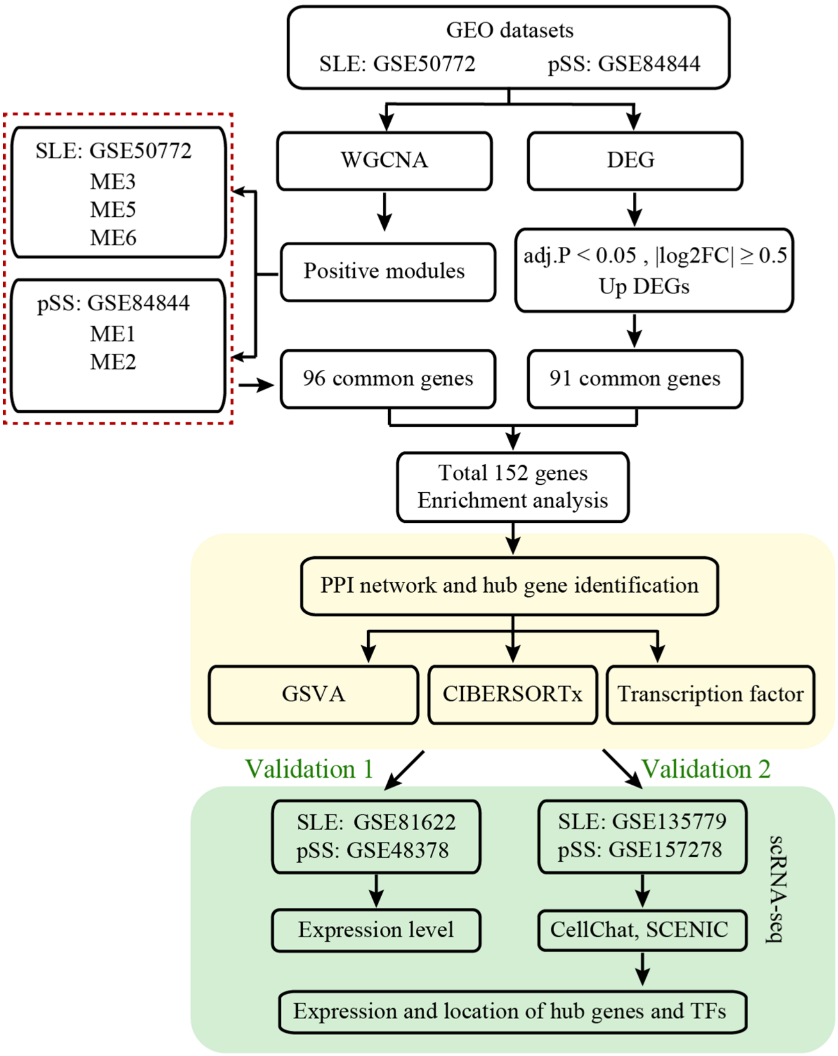

FIGURE 1
Workflow diagram of this work.

Supplementary Table 1. WGCNA, DEGs, GSVA and immune cell analyses were performed on GSE50772 and GSE84844 datasets. Expression levels for hub genes and TFs were validated using GSE81622 and GSE48378. Additionally, the hub genes and TFs expression patterns were further validated in scRNA-seq datasets, namely GSE135779 and GSE157278.

Weighted gene co-expression network analysis of SLE and pSS

In WGCNA, the module-trait relationship heatmap according to the Pearson correlation coefficient showed the correlation between each module and the clinical trait. After processing with 'Hclust', one SLE sample was eliminated in GSE50772 dataset, and two pSS samples were eliminated in GSE84844 (Supplementary Figure 1). A total of 12 modules were identified in GSE50772, and 11 modules were identified in GSE84844. Afterwards, the correlation between each module and clinical trait was calculated. In GSE50772 database, the ME3, ME5 and ME6 modules had high positive correlations with SLE (r = 0.62, 0.65 and 0.57), comprising 1120 genes. The ME10 and ME11 modules were negatively correlated with SLE (r = -0.72 and -0.55), and comprised a total of 453 genes (Figure 2A). In GSE84844 database, the ME1 and ME2 modules showed high positive correlation with pSS (r = 0.73 and 0.65), containing 2796 genes. The ME6 and ME7 modules had negative correlations with pSS (r = -0.71 and -0.39), comprising a total of 637 genes (Figure 2C).

Further, we performed GO enrichment analysis on the positively related modules. For SLE, our results showed that the ME3 module was mainly associated with type I IFN response and innate immune response. The ME5 module was mainly related to cell chemotaxis and cytokine-mediated signaling pathway. Additionally, the ME6 module was involved in immune response (Figure 2B). For pSS, functional enrichment analysis indicated that the ME1 module was mainly associated with T cell activation and differentiation, and ME2 module was related to type I IFN response and cytokine production (Figure 2D). Therefore, type I IFN

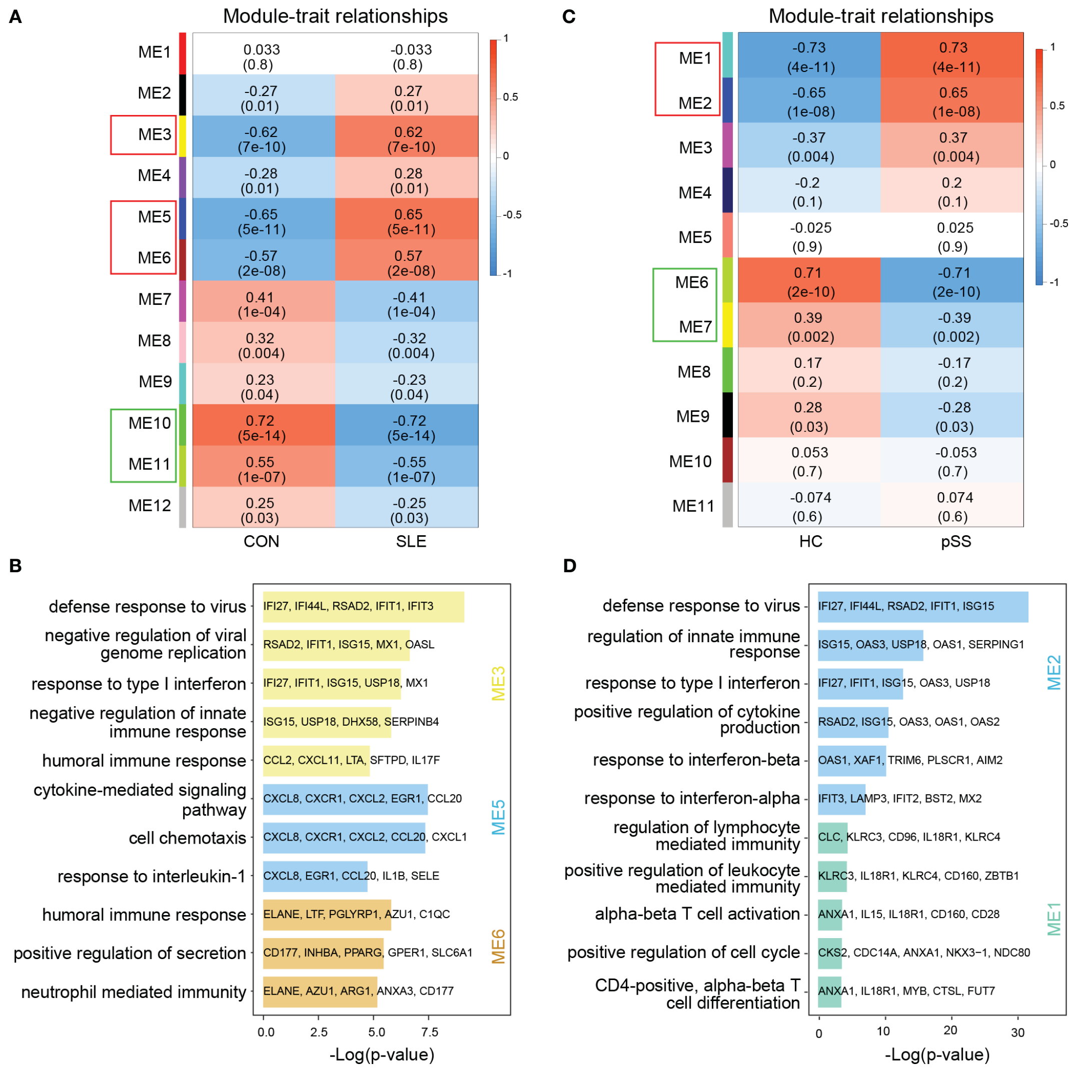

FIGURE 2
Weighted gene co-expression network analysis (WGCNA) and GO (Gene ontology) analysis of GSE50772 and GSE84844 datasets. **(A)** Heatmap of module-trait relationships in SLE. Each cell contains the corresponding correlation and *p*-value. **(B)** GO biological process analyses of three positively related modules with SLE. **(C)** Heatmap of module-trait relationships in pSS. Each cell contains the corresponding correlation and *p*-value. **(D)** GO biological process analyses of two positively related modules with pSS. SLE, systemic lupus erythematosus; pSS, primary Sjögren's syndrome.

response and cytokine-mediated signaling pathway collectively participated in the pathogenesis of SLE and pSS.

Enrichment analysis of common gene from WGCNA

The common genes were screened between SLE positively related modules (ME3, ME5 and ME6 modules) and pSS positively related modules (ME1 and ME2 module). 96 genes overlapped in positively related modules from SLE and pSS (Figure 3A). Enrichment analysis results showed that the 96 genes were mainly associated with type I IFN response and cytokine-mediated signaling pathway (Figure 3B). There were 4 genes that overlapped in negatively related modules from SLE and pSS (Supplementary Figures 2A, B).

Identification and function analyses of common DEGs

The limma R package was utilized to perform an analysis of DEGs on the GSE50772 and GSE84844 datasets. Volcano plots showed the identified DEGs. For SLE dataset GSE50772, 2918 DEGs were identified, among which 1366 genes were upregulated and 1552 genes were downregulated (Figure 4A; Supplementary File 1). 1597 DEGs were obtained from the pSS dataset GSE84844, out of which 1315 DEGs were upregulated and 282 DEGs were downregulated (Figure 4B; Supplementary File 2). After examining the intersection for the DEGs, 91 shared upregulated DEGs and 11 shared downregulated DEGs were identified. The overlapping DEGs were visualized by Venn diagrams (Figure 4C; Supplementary Figure 2C, Supplementary File 3). To further analyze the underlying biological information associated with the common DEGs, GO analysis was performed. The results

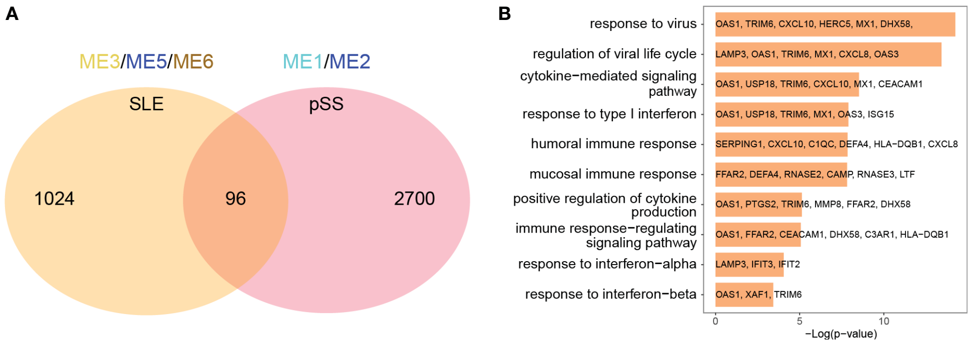

FIGURE 3

Venn diagrams and enrichment analysis of common genes from WGCNA. **(A)** Venn diagrams showing the overlap genes in positive related modules in SLE and pSS. **(B)** GO enrichment analysis of the 96 common genes. GO, gene ontology; SLE, systemic lupus erythematosus; pSS, primary Sjögren's syndrome.

showed that the commonly upregulated DEGs were mainly enriched in type I IFN and cytokine stimulus response, which were consistent with the results of WGCNA (Figure 4D). These findings strongly indicated that type I IFN response and cytokine stimulus jointly participated in the development and progression of these two autoimmune diseases. We also performed the GO analysis on the upregulated DEGs in SLE and pSS, respectively. In addition to type I IFN response, inflammatory, immune response and T cell activation were also significantly enriched in SLE (Supplementary Figure 3A). For the upregulated DEGs in pSS, response to tumor necrosis factor (TNF), I-kappa B kinase/NF–kappa B signaling were also enriched (Supplementary Figure 3B).

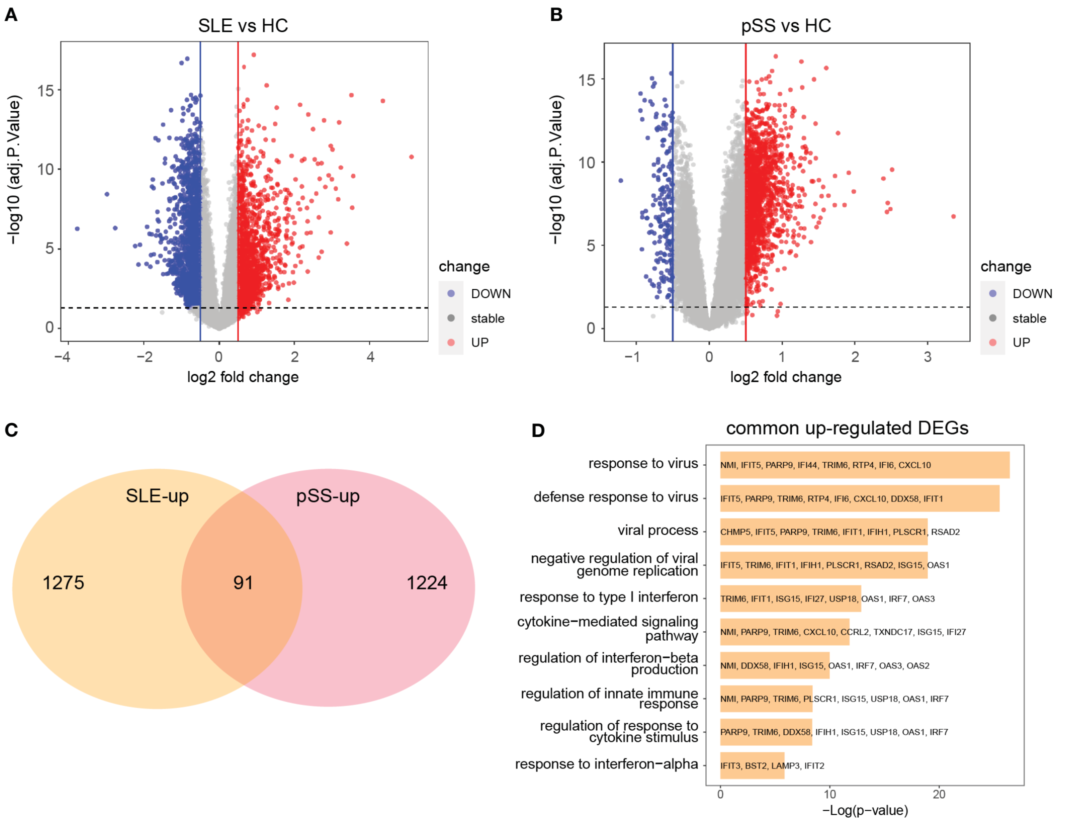

FIGURE 4

Identification common DEGs and functional enrichment analysis. **(A)** Volcano plot of GSE50772. **(B)** Volcano plot of GSE84844. Red dots indicate upregulated genes and blue dots indicate downregulated genes. **(C)** 91 upregulated DEGs overlapped in the two datasets. **(D)** GO enrichment analysis of common upregulated DEGs. DEGs, differentially expressed genes; GO, gene ontology; SLE, systemic lupus erythematosus; pSS, primary Sjögren's syndrome.

Selection and analysis of hub genes

The 91 commonly upregulated DEGs and 96 shared genes determined by the positively correlated modules in both autoimmune diseases were combined to yield 152 candidate genes for the subsequent analyses. Subsequently, a PPI network of the candidate genes was constructed, and the three clustering modules from closely connected genes were further extracted through MCODE analysis (Figure 5A). Cluster 1 contained 42 nodes and 789 edges. Enrichment analysis results showed that the genes in cluster 1 were mainly associated with type I IFN and cytokine stimulus response. Cluster 2 comprised 38 nodes and 282 edges, and linked to cellular organismal processes. Cluster 3 contained 13 nodes and 33 edges, and involved in leukocyte activation (Figure 5B). Thus, clusters 1 and 3 were considered as key modules that may play crucial roles in disease development. To identify the top 15 genes in cluster 1, we utilized five algorithms of the plug-in cytoHubba (MCC, MNC, EPC, Closeness and Radiality) (Supplementary Table 2). By intersecting the Venn diagrams, we identified 5 common genes (*IFI44L, ISG15, IFIT1, USP18* and *RSAD2*) in cluster 1 (Figure 5C). For cluster 3, we selected the top three genes (*PTPRC, CXCR8* and *ITGB2*) for subsequent analyses (Figure 5D).

Validation of hub genes expression

The expression levels of eight genes were verified in SLE dataset GSE81622 and pSS dataset GSE48378. The results demonstrated that *IFI44L, ISG15, IFIT1, USP18, RSAD2* and *ITGB2* were

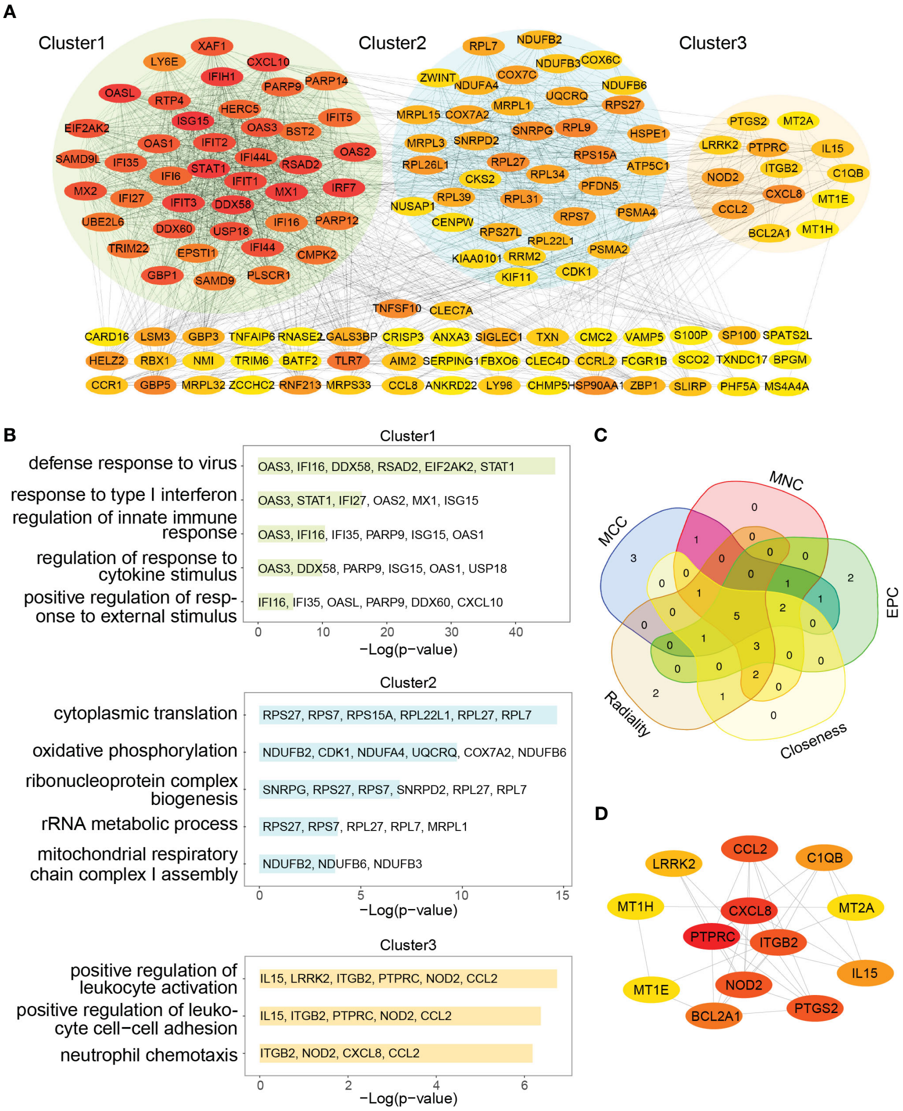

FIGURE 5

PPI network and Venn diagram of shared genes among SLE and pSS. **(A)** PPI network of combined common module genes and DEGs. The network has 140 nodes and 1610 edges. **(B)** GO analysis of three clusters. **(C)** The Venn diagram showed 5 overlapping genes screened by 5 algorithms. **(D)** PPI network of cluster 3. DEGs, differentially expressed genes; GO, gene ontology; SLE, systemic lupus erythematosus; pSS, primary Sjögren's syndrome.

significantly upregulated in SLE (Figure 6A). Additionally, the expression levels of these genes in pSS were also higher than those in healthy control samples (Figure 6B). The expression of *PTPRC* and *CXCR8* showed no significant difference in both diseases. Consequently, *IFI44L, ISG15, IFIT1, USP18, RSAD2* and *ITGB2* were identified as hub genes for subsequent analyses (Supplementary Table 3). A t-test was conducted to compare the two subsets in these each dataset, separately. A significance level of $p < 0.05$ was applied.

Pathways involvement and correlation with hub genes

GSVA was performed to identify the relevant pathways, and Pearson correlation analysis was employed to evaluate the correlation between hub gene and relevant pathway in SLE and pSS (Figure 7). A total of 50 hallmark pathways were subjected to GSVA analysis. Overall, the results suggested a strong and consistent correlation between the hub genes (*IFI44L, ISG15, IFIT1, USP18,* and *RSAD2*) and the INTERFERON_ALPHA_RESPONSE, INTERFERON_GAMMA_RESPONSE pathways in both SLE and pSS.

The expression of hub genes in single-cell RNA-Seq datasets

The PBMC scRNA-seq datasets GSE135779 and GSE157278 were downloaded for subsequent analyses. We selected 5 healthy controls and 7 adults with SLE from the GSE135779 dataset, while the GSE157278 dataset contained 5 pSS patients and 5 normal controls. The two datasets were analyzed separately. Following the Seurat pipeline, and combining the SingleR algorithm with canonical gene markers including *CD3E, CD3D, CD4, CD8A, CCR7, SELL, S100A4, CD79A, MS4A1, GNLY, NCAM1, NKG7, GZMK, GZMB, CD14, LYZ, FCGR3A, MS4A7, FCER1A, CD1C, CLEC4C, LILRA4, PPBP, PF4, SLC4A10, TRDC, TRDV2, FOXP3* as well as *IL2RA*, we identified cell populations. Among the identified populations were CD4 naïve T cells, CD4 memory T cells, CD8 naïve T cells, CD8 memory T cells, CD8 effector T cells, monocytes, NK cells, B cells, DCs and some other cells in the two datasets (Figures 8A, B). The dot plot depicted the cell-type-specific markers (Supplementary Figure 4). Cell composition analysis revealed that monocytes (HC, 16.3%; SLE, 28.1%) and CD8 effector T cells (HC, 13.3%; SLE, 17.3%) were expanded, while CD4 naïve T cells (HC, 33.5%; SLE, 22.2%.) were decreased in SLE patients compared to HCs (Figure 8C). For the pSS dataset, NK cells (HC, 12.9%; pSS, 20.6%), B cells (HC, 5.4%; pSS, 7.5%) and CD8 effector T cells (HC, 8.0%; pSS, 11.3%) were expanded, while CD4 naïve T cells (HC, 17.7%; pSS, 10.9%) and CD8 naïve T cells (HC, 12.0%; pSS, 5.5%) were decreased in pSS patients compared to HCs (Figure 8D). The violin plot showed that the expression levels of three hub genes (*IFI44L, ISG15* and *ITGB2*) were elevated in both SLE and pSS in most cell types, especially in monocytes, NK cells and CD8 effector T cells. (Figures 8E, F). In summary, the results showed that the proportion of CD8 effector T cells increased, however the proportion of CD4 naïve T cells decreased in SLE and pSS patients. We performed DEG analysis in scRNA-seq datasets. For SLE dataset GSE135779, 230 DEGs were upregulated, meanwhile 537 DEGs were upregulated in pSS dataset GSE157278. After performing an intersection of the upregulated DEGs, 97 shared upregulated DEGs were identified (Supplementary Figure 5A). The GO results showed that the shared upregulated DEGs were mainly associated with IFN response (Supplementary Figure 5B), which was consistent with the results of WGCNA and DEGs analysis in GSE50772 and GSE84844 datasets. The results of GO analysis on the upregulated DEGs in SLE and pSS were highly consistent with the previous results (Supplementary Figures 5C, D). We conducted Hallmark annotation analysis on the upregulated DEGs in all cell types (Supplementary Figures 5E, F). The results consistently showed enrichment in the IFN response across all cell types in both SLE and pSS.

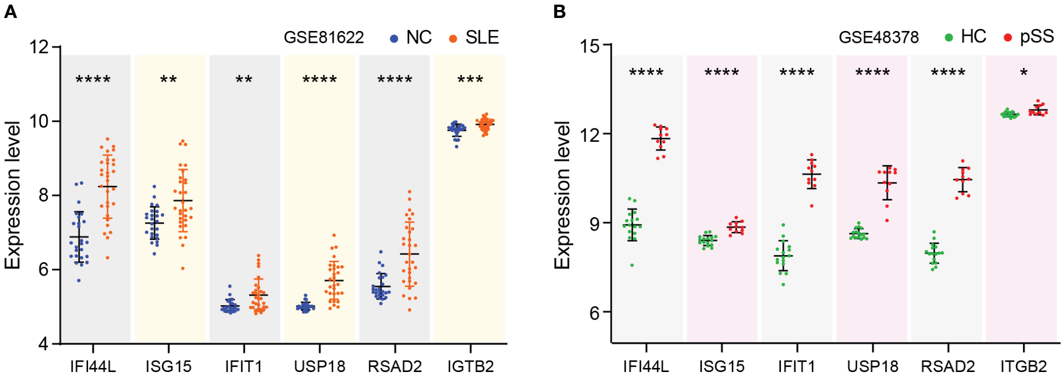

FIGURE 6
Verification of hub genes expression. **(A)** Expression of hub genes verified in GSE81622. **(B)** Expression of hub genes verified in GSE48378. The comparison in the two sets of data used the mean t-test, separately; p -value < 0.05 was considered statistically significant. *p < 0.05, **p < 0.01, ***p < 0.001, ****p < 0.0001.

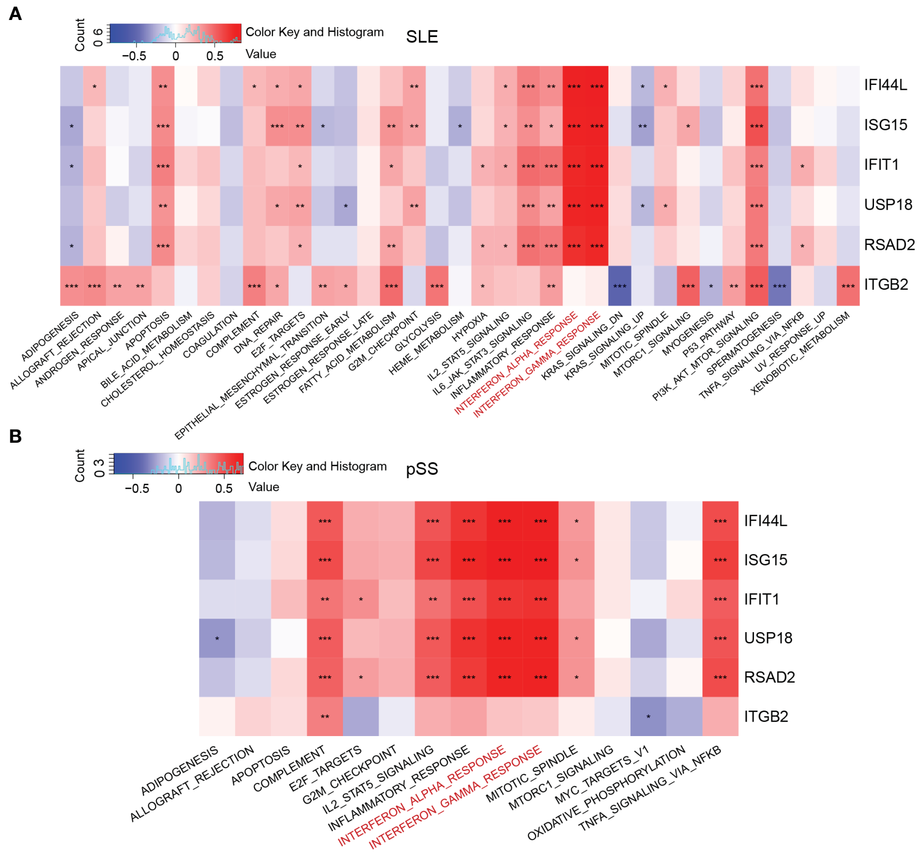

FIGURE 7
Correlation matrix between hallmark pathways and hub genes. **(A)** Correlation matrix of hallmark pathways and hub genes in SLE. **(B)** Correlation matrix of hallmark pathways and hub genes in pSS. Red: positive correlation; Blue: negative correlation. SLE, systemic lupus erythematosus; pSS, primary Sjögren's syndrome. *$p < 0.05$, **$p < 0.01$, ***$p < 0.001$.

Immune cell fractions and the correlation with hub genes

The CIBERSORTx method was used to evaluate the immune cell (IC) composition in peripheral blood using GSE135779 and GSE157278 scRNA-seq datasets as reference matrices for deconvolution on the SLE (GSE50772) and pSS (GSE84844) datasets separately. The boxplot showed that the proportion of CD4 naïve T cells in SLE samples was lower than that in HC samples, despite lack of statistical significance. Interestingly, CD8 effector T cells and monocytes were significantly increased in SLE patients compared to HCs ($p < 0.05$) (Figure 9A). Furthermore, Pearson correlation analysis was performed to investigate the correlations between hub genes and ICs in SLE. The heatmap revealed that three hub genes (*IFI44L, ISG15* and *ITGB2*) had positive correlations with monocytes and CD8 effector T cells, while having negative correlations with CD4 naïve T cells ($p < 0.05$) (Figure 9B).

In comparison to HCs, the proportion of monocytes exhibited significant increase in pSS samples ($p < 0.05$). Additionally, B cells and CD8 effector T cells displayed increasing trend in pSS, though statistically insignificant. More importantly, CD4 naïve T cells exhibited significant decrease in pSS (Figure 9C). The correlations between hub genes and ICs in pSS demonstrated that three hub genes (*IFI44L, ISG15* and *ITGB2*) had positive correlations with monocytes, B cells and CD8 effector T cells, while had significant negative correlations with CD4 naïve T cells ($p < 0.05$) (Figure 9D). In summary, the results showed a consistent pattern of increase in CD8 effector T cells, and decrease in CD4 naïve T cells in both SLE and pSS patients, which was consistent with our results of scRNA-seq analysis. Meanwhile, hub genes (*IFI44L, ISG15* and *ITGB2*) exhibited positive correlations with monocytes in SLE and pSS, especially *ITGB2*. The correlations between genes (*IFIT1, USP18* and *RSAD2*) and ICs are provided in Supplementary Figure 6.

Single-cell analysis for the expression of related pathways

According to the previous GSVA results (Figures 7A, B), hub genes (*IFI44L* and *ISG15*) exhibited significant positive correlations with INTERFRON_ALPHA_RESPONSE and INTERFRON_GAMMA_RESPONSE pathways. Therefore, an evaluation of the expression level of INTERFRON RESPONSE in SLE and pSS was performed. We discovered that the INTERFRON RESPONSE was increased in both SLE and pSS patients,

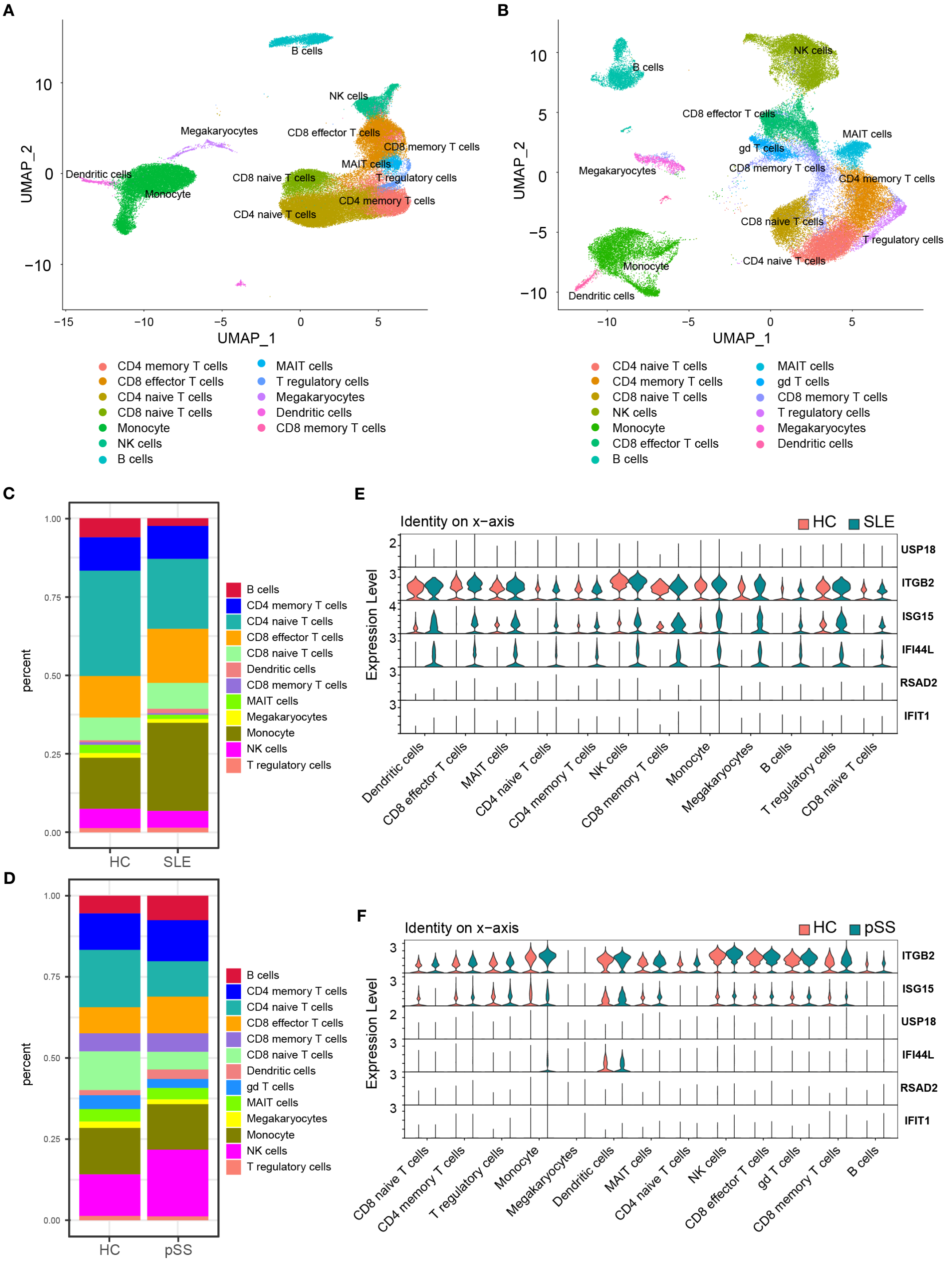

FIGURE 8

Validation of hub genes in scRNA-seq datasets. (A) UMAP visualization GSE157278 scRNA-seq datasets. (B) UMAP visualization GSE135779 scRNA-seq datasets; Different colors indicate distinct cell types. (C) Cellular composition in SLE and HCs group (D) Cellular composition in pSS and HCs group. The colors represent different cell types. (E) Violin plot of hub genes expression in different cell types in SLE. (F) Violin plot of hub genes expression in different cell types in pSS. SLE, systemic lupus erythematosus; pSS, primary Sjögren's syndrome.

particularly in monocytes (Figures 10A, B). Besides INTERFRON RESPONSE, we also explored and identified *ITGB2* as a hub gene. Furthermore, we used CellChat to investigate the putative interactions among the major cell types in disease versus control. The results showed that the activity of ITGB2 signaling pathway was increased in SLE and pSS patients, and the ITGB2 signaling pathway was most enriched from monocytes to CD4 T cells and CD8 effector T cells (Figures 10C, D). The *ITGB2, ICAM1, ICAM2, CD226* and *ITGAL* expression levels related to ITGB2 signaling pathway were verified both in scRNA-seq and microarray datasets

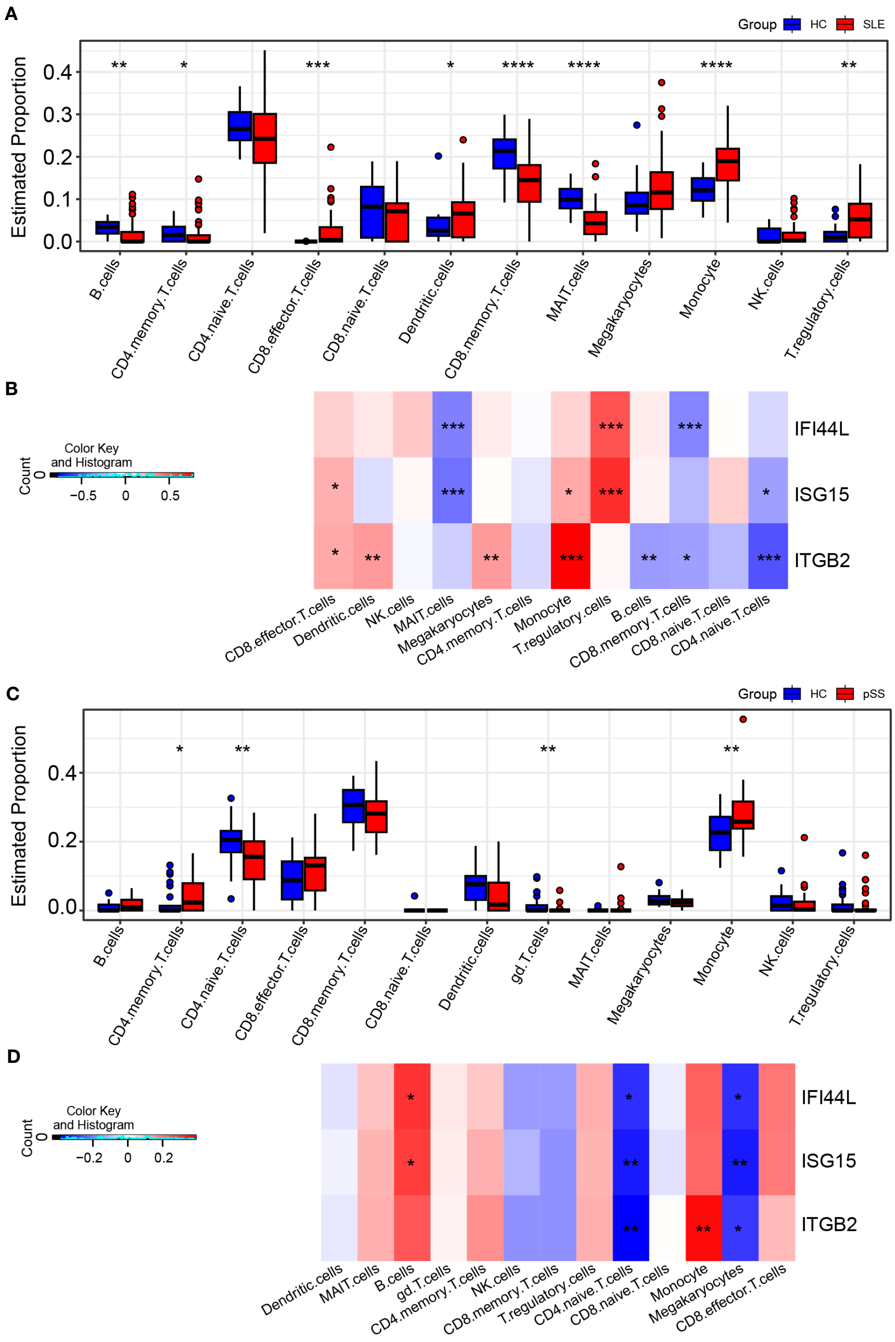

FIGURE 9
Landscape map of IC in SLE and pSS datasets. **(A)** Boxplot showing the differences of IC between SLE and HC. **(B)** Correlation matrix between IC and hub gene in SLE. **(C)** Boxplot showing the differences of IC between pSS and HC. **(D)** Correlation matrix between IC and hub gene in pSS. Red: positive correlation; blue: negative correlation. SLE, systemic lupus erythematosus; pSS, primary Sjögren's syndrome. *p < 0.05, **p < 0.01, ***p < 0.001, ****p < 0.0001.

between disease conditions and healthy controls (51, 52) (Supplementary Figure 7). The results demonstrated that ITGB2 signaling pathway related genes were upregulated both in SLE and pSS patients, though some were not statistically significantly so. Further analysis showed monocytes are the prominent sender and influencer of the ITGB2 signaling pathway (Figures 10E, F). The results indicated that monocytes may play vital roles in IFN response and ITGB2 signaling pathway in the pathogenesis of SLE and pSS, which were consistent with our results of immune cell analysis.

Prediction and verification of TFs

Based on the iRegulon algorithm, we have identified the top 6 TFs that may regulate the expression of hub genes (*IFI44L, ISG15* and

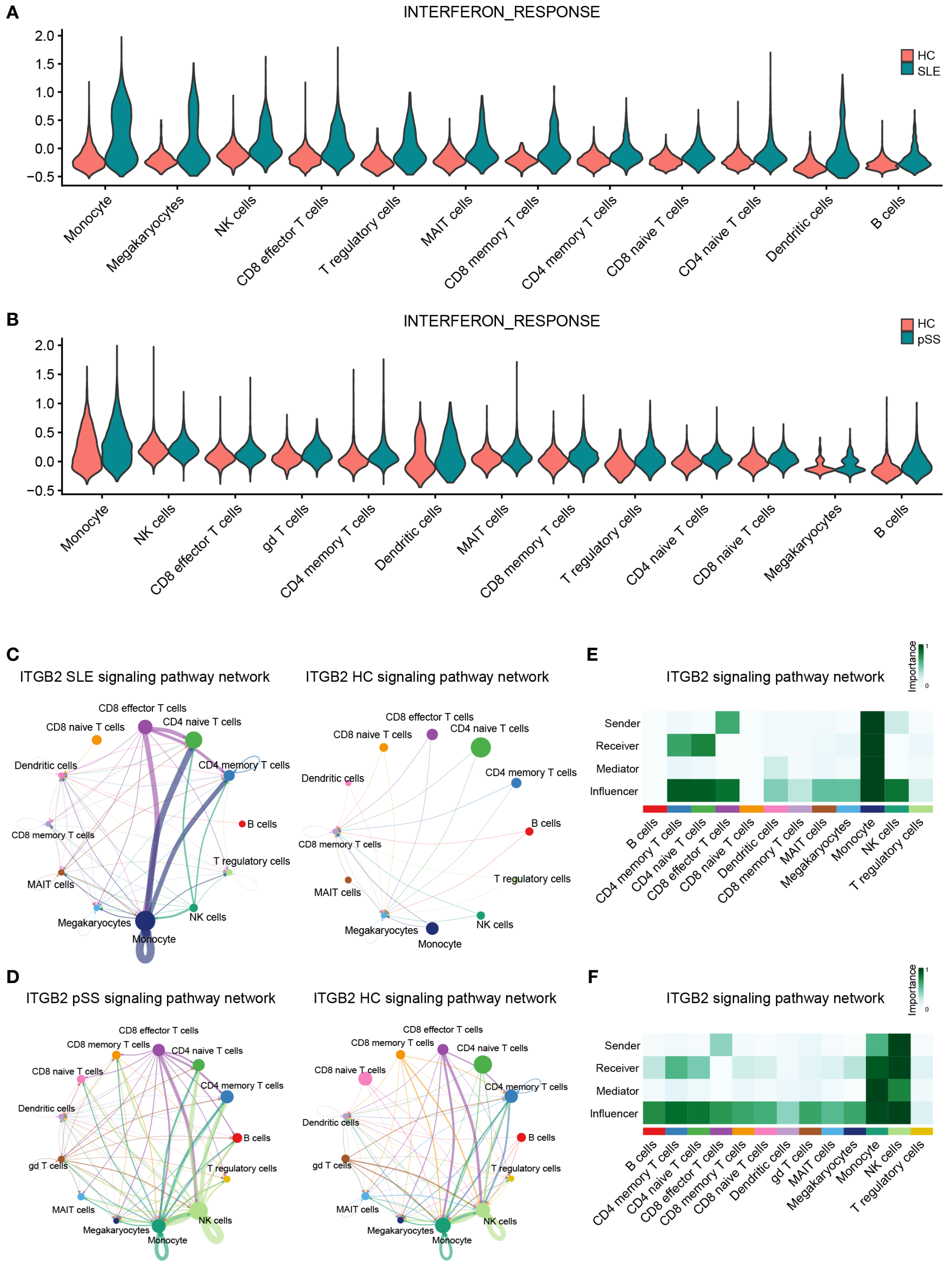

FIGURE 10
Verification of related pathways in scRNA-seq datasets. **(A)** Violin plot of INTERFERON_RESPONSE expression in SLE. **(B)** Violin plot of INTERFERON_RESPONSE expression in pSS. **(C)** Circos plot showing the ITGB2 signaling pathway network across major cell types in SLE and HCs. **(D)** Circos plot showing the ITGB2 signaling pathway network across major cell types in pSS and HCs. **(E)** Heatmap showing the relative importance of each cell type based on the computed four network centrality measures of the ITGB2 signaling pathway in SLE. **(F)** Heatmap showing the relative importance of each cell type based on the computed four network centrality measures of the ITGB2 signaling pathway in pSS. SLE, systemic lupus erythematosus; pSS, primary Sjögren's syndrome.

ITGB2) (Figure 11A). We found that three TFs (STAT1, STAT2 and IRF7) were highly expressed in SLE and pSS validation datasets (Figure 11B). To further validate our findings, we employed SCENIC to infer the TF regulatory information underlying each cell type. Remarkably, the SCENIC analysis revealed that STAT1 was upregulated in both diseases and mainly concentrated in monocytes and DCs. Additionally, IRF7 was upregulated and concentrated in DCs in SLE (Figures 12A, B). The violin plot showed that expression levels of 3 TFs (STAT1, STAT2 and IRF7) were significantly elevated in SLE and pSS, especially IRF7 in DCs (Figures 12C, D).

Discussion

SLE and pSS are chronic autoimmune diseases predominantly affecting women and exhibit overlapping clinical and serologic

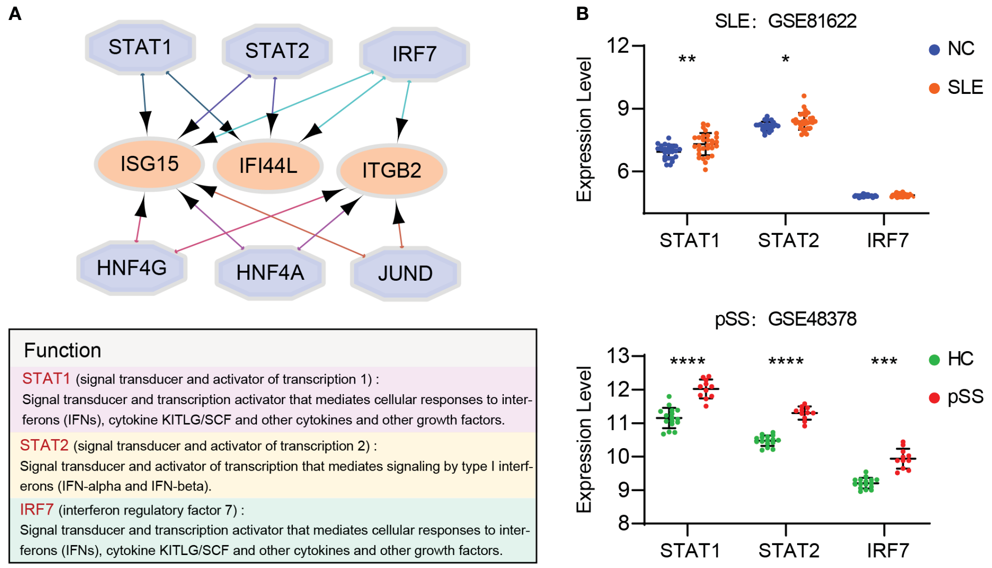

Function

STAT1 (signal transducer and activator of transcription 1) :
Signal transducer and transcription activator that mediates cellular responses to interferons (IFNs), cytokine KITLG/SCF and other cytokines and other growth factors.

STAT2 (signal transducer and activator of transcription 2) :
Signal transducer and activator of transcription that mediates signaling by type I interferons (IFN-alpha and IFN-beta).

IRF7 (interferon regulatory factor 7) :
Signal transducer and transcription activator that mediates cellular responses to interferons (IFNs), cytokine KITLG/SCF and other cytokines and other growth factors.

FIGURE 11
Prediction and verification of TFs. **(A)** iRegulon plug-in predicted TFs of hub genes. **(B)** Expression of TFs verified in GSE81662 and GSE48378. SLE, systemic lupus erythematosus; pSS, primary Sjögren's syndrome. $*p < 0.05$, $**p < 0.01$, $***p < 0.001$, $****p < 0.0001$.

characteristics. In a subset of pSS patients, the disease may progress to clinical manifestations, serological profiles and immunological characteristics shared with SLE, leading to fulfillment of classification criteria for both diseases. This condition is commonly referred to as pSS/SLE overlap (53). Despite the increasing knowledge regarding environmental triggers and epigenetic mechanisms, the genetic factors underlying SLE and pSS remain elusive. In this study, we aimed to investigate common target genes, relevant pathways and TFs in SLE and pSS through integrative bioinformatic analyses of transcriptomes. Firstly, we conducted analyses of common genes in the WGCNA module genes and shared DEGs of SLE and pSS. Enrichment analysis showed that these genes were involved in both type I IFN response and cytokine-mediated signaling pathway. Subsequently, we combined the common genes in WGCNA and DEGs, and obtained 152 shared candidate genes. Next, we identified 6 hub genes (*IFI44L, ISG15, IFIT1, USP18, RSAD2* and *ITGB2*) by the PPI network and cytoHuba algorithms, and verified their expression levels. The expression of hub genes was further verified in scRNA-seq datasets. The results showed that 3 hub genes- *IFI44L, ISG15* and *ITGB2*- were upregulated in disease groups. Additionally, we evaluated the correlations between hub genes and ICs as well as related pathways. The results showed that hub genes (*IFI44L* and *ISG15*) had positive correlations with monocytes, as well as the IFN response pathway. *ITGB2* had a significant positive correlation with monocytes and mainly involved in ITGB2 signaling pathway. The IFN response and ITGB2 signaling pathway were increased and enriched in monocytes in SLE and pSS. Finally, TFs (STAT1, STAT2 and IRF7) were predicted and verified, and only STAT1 and IRF7 were upregulated in scRNA-seq data. Notably, IRF7 was specially enriched in DCs.

The biological processes involved in the IFN response, inflammatory, immune response and T cells activation were enriched among the upregulated DEGs in SLE. Activated IFN response has been well recognized as an important feature in SLE (54). The abnormal activation of T cells appears to be involved in the pathogenesis of SLE. An analysis of lymphocyte composition revealed a reduction in naïve CD4 T cells and an increase in CD8 T cells in SLE patients (55). The autoantibodies and immune complex mediated cytokines, such as IL-1, would cause persistent inflammatory response in SLE (56). Besides, the neutrophil extracellular traps and neutrophil to lymphocyte ratio played essential roles in the pathogenesis of SLE (57, 58). Besides IFN response, the upregulated DEGs associated with TNF response, I-kappa B kinase/NF-kappa B signaling were also identified by GO analysis in pSS patients. Serum level of TNF-α has been identified as the most discriminating factor associated with the presence of interstitial lung disease (ILD) in pSS patients (59). B cell-activating factor of the TNF family (BAFF) may contribute to focal lymphocytic infiltration and is an essential cytokine in pSS physiopathology (60). In PBMC from pSS patients, phosphorylated inhibitor of κB (IκB) kinase (IKK) ϵ (IKKϵ), total IKKϵ, pIKKα/β and pNF-κB p65 were significantly increased compared to healthy controls (61). Knockdown of RSAD2 attenuated pSS B cell hyperactivity via suppressing NF-κB signaling (62). Owing to the multitude of influencing factors observed in previous studies as well as our own analyses, comprehensive understanding of the pathogeneses of SLE and pSS remains an ongoing project. The high IFN response plays a critical role both in SLE and pSS.

IFNs are a class of cytokines that exhibit antiviral effects and are induced by viral infections, ultimately leading to the expression of IFN-stimulated genes (ISGs) and further exerting antiviral effects (63, 64). Type I IFNs, including IFN-α, IFN-β, IFN-ϵ and IFN-κ, are the primary interferons capable of exerting antiviral effects. Studies have reported that IFNs can not only act on viruses to interfere with their replication but enhance cellular immunity by

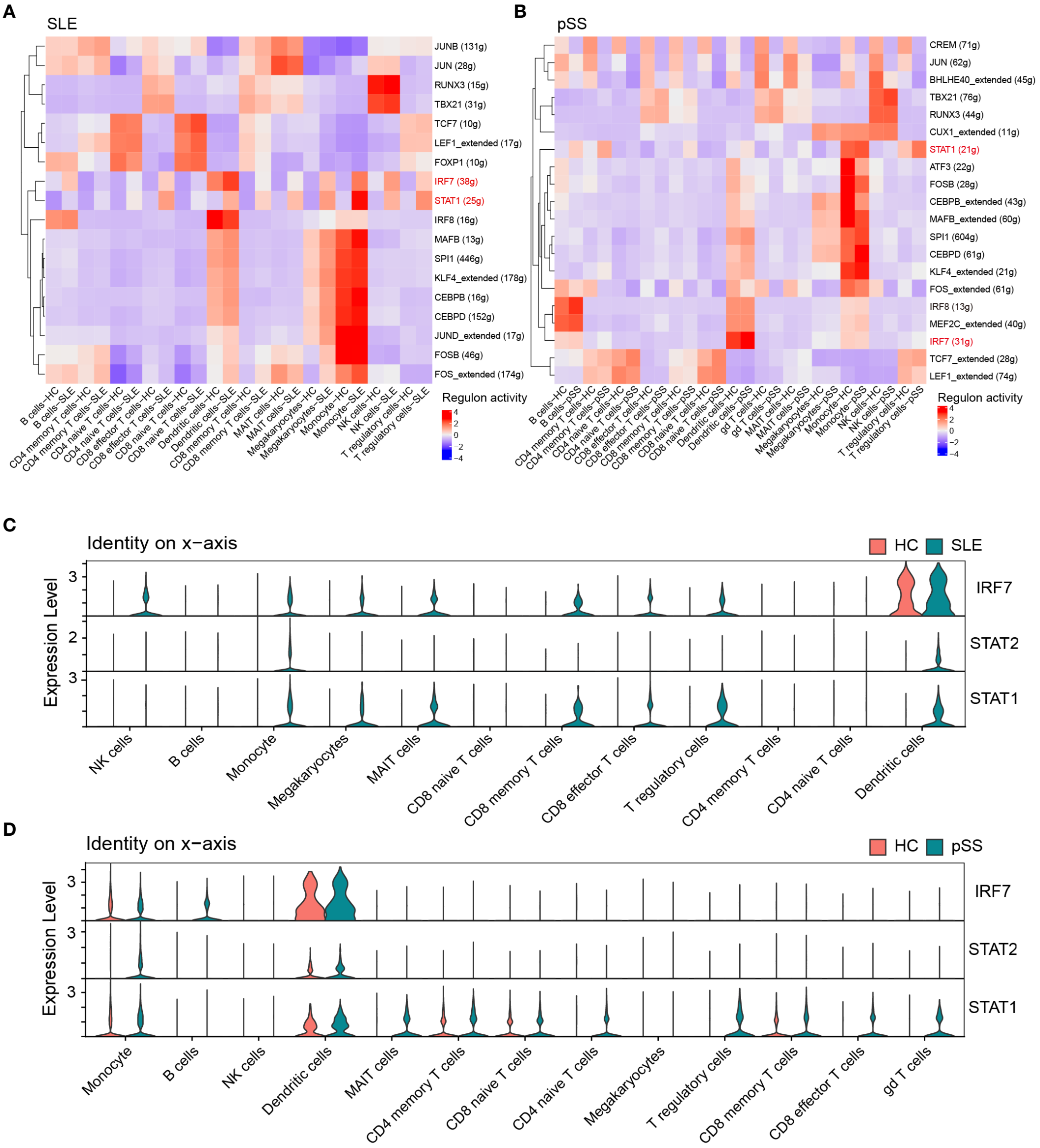

FIGURE 12
Verification of TFs in scRNA-seq datasets. **(A)** SCENIC analysis revealed TF regulatory information of each cell type in SLE. **(B)** SCENIC analysis revealed TF regulatory information of each cell type in pSS. Red: up-regulated TFs; blue: down-regulated TF. **(C)** Violin plot of TF expression in different cell types in SLE. **(D)** Violin plot of TF expression in different cell types in pSS. SLE, systemic lupus erythematosus; pSS, primary Sjögren's syndrome.

acting on T/B cell proliferation and differentiation (65, 66). Type I IFNs stimulate monocytes differentiation and induce immature DCs to express chemokines and costimulatory molecules, which contributes to the pathogenesis of SLE (67). BAFF is stimulated by type I IFNs and promotes B-cell activation, involved in the pathogenesis of pSS (68). Our enrichment analysis of common upregulated DEGs and overlapping genes from positively correlated modules further demonstrates the importance of the type I IFN response in diseases. We also employed GSVA and found hub genes exhibited significant positive correlations with IFNα and IFNγ response pathways. Moreover, a meta-analysis of transcriptomes has identified shared type I IFN- stimulated genes among rheumatoid arthritis (RA), SLE and pSS, such as *IFI44L, IFI44, IFI27* and *IFIT1* (9). Unlike previous studies, our research employed comprehensive and improved bioinformatic methods, and paid more attention to the exploration of hub genes, related pathways and TFs in peripheral blood that are common in SLE and pSS (69, 70). We identified 3 hub genes (*IFI44L, ISG15* and *ITGB2*). *IFI44L* is a type I IFN-stimulated gene, which has benn found to be upregulated in patients with pSS and was markedly increased following with either IFN-α or IFN-β stimulation (71). STAT3 promoted the overexpression of *IFI44L* in monocytes, which contributes to the pathogenesis of SLE. *IFI44L* is expected to become a new therapeutic target for SLE treatment (67, 72). Interferon-stimulated gene 15 (*ISG15*) is a ubiquitin-like protein that is conjugated to intracellular target proteins upon activation by

IFN-α and IFN-β (73). The expression level of *ISG15* was higher in saliva and serum from pSS patients than from controls. The expression of ISG15 is relatively high in patients with SLE and correlates with disease activity prior to treatment (74). We identified *IFI44L* and *ISG15* as common hub genes in the two diseases.

However, the pathogeneses of SLE and pSS are exceptionally complicated. Besides IFN response, we also explored and identified *ITGB2* as a hub gene. Integrin subunit β2 (*ITGB2*) encodes integrin β2 protein (CD18) (75). Integrins are heterodimeric transmembrane proteins consisting of alpha and beta subunits. Integrins regulate immune cell trafficking by modulating leukocyte adhesion to blood vessels and facilitating their extravasation into tissues. These proteins play important roles in inflammatory and autoimmune responses (76, 77). Behera and colleagues reported that osteopontin can bind αvβ3 integrin and induce JAK2/STAT3 activation in human breast cancer cells (78). Mastrangeli and colleagues reported the binding properties of deamidated IFN-β to αvβ3 integrin in triple-negative breast cancer (79). The link between interferons and integrins remains for further investigation. Beta2-integrins are leukocyte-specific adhesion molecules that are essential for leukocyte trafficking and immune cell activation. As a result, beta2-integrins may be involved in many autoimmune diseases. *ITGB2* was upregulated in PBMCs from systemic sclerosis (SSc) patients, which may participate in immune cell migration to involved tissues. Splenic B cells from NZB/NZW F1 lupus mice showed ITGB2 activation compared to normal C57Bl/6 mice (75, 80, 81). However, there are no studies reporting its role in pSS, which provides a springboard for future research. Our results are the first to demonstrate increased ITGB2 signaling pathway activity, and upregulated *ITGB2* expression in both SLE and pSS patients. Vedolizumab (targets integrin α4β7), and etrolizumab (anti β7) have been approved by the FDA for the treatment of inflammatory bowel disease (IBD), namely ulcerative colitis (UC) and Crohn's disease (CD). These drugs have demonstrated efficacy with minimal systemic adverse effects (82, 83). The research about integrins antagonists underscores the central role of these proteins in autoimmune diseases. Additionally, organ-specific delivery of drugs to targeted tissue may further increase the therapeutic potential for anti-integrin agents (84). Lifitegrast, a small-molecule inhibitor that targets integrin αLβ2 has been approved for the topical treatment of dry eye disease (DED). Topical application of lifitegrast provides improvement in inferior corneal staining score and eye dryness (85). Our study revealed that *ITGB2* may be a novel therapeutic target in SLE and pSS. Development of drug delivery strategies will provide greater therapeutic opportunities for targeting integrins.

In addition, we also analyzed TFs and verified their expression levels in microarray and scRNA-seq datasets. We found that 6 TFs may regulate the expression of hub genes. Upon further verification, two TFs (STAT1 and IRF7) are highly expressed in SLE and pSS. Signal transducer and activator of transcription (STAT) families and IFN regulatory factor (IRF) have been demonstrated to play essential roles in regulating type I IFN response (86). All STAT family members primarily function within the Janus kinase-signal transducer and activator of transcription (JAK-STAT) pathway (87). IFNs cause STAT activation and subsequently trigger ISG expression (88, 89). STAT1, STAT2 and IRF9 are capable of amplifying JAK-STAT signaling to reinforce IFN response (90). The JAK-STAT pathway transduces intracellular signals of multiple cytokines, and is critical to the pathogenesis of autoimmune diseases. SLE patients showed substantially higher STAT1 in B cells and plasmablasts (91). STAT1 expression is also increased in labial salivary glands from pSS patients (92). Our study confirmed the essential role of STAT1 in both SLE and pSS. STATs, as JAK substrates, have been investigated as attractive therapeutic targets in autoimmune diseases. However, challenges in the development of STAT inhibitors include issues with bioavailability, *in vivo* efficacy and selectivity (93). Thus, Janus kinase inhibitors (Jakinibs), targeting JAK-STAT pathways, hold promise to block STAT expression. Currently, Jakinibs are most commonly used for RA treatment. In SLE, tofacitinib has been used in phases of clinical trials. Lee and colleagues (94) performed a series of experiments to determine the safety and efficacy of filgotinib for pSS treatment, and suggested that filgotinib has potential for pSS treatment. The mammalian IRF family proteins (IRF1-9) are TFs that play crucial roles in connecting microbial signaling to the responses of IFNs, pro-inflammatory cytokines and innate immune responses (95, 96). IRF3 and IRF7 play pivotal roles in the induction of type I IFN gene transcription (97). IRF7 is a lymphoid TF that is constitutively expressed only in B cells, monocytes and plasmacytoid dendritic cells (pDCs), and is particularly highly expressed in pDCs (98), which was consistent with our study. IRF7 was specifically concentrated in DCs from both SLE and pSS. IRFs can induce the expression of ISGs through a pathway that may depend on or be independent of JAK-STAT signaling (99). IRF7 as transcriptional regulators of type I IFNs and certain single nucleotide polymorphisms (SNPs) in IRF7 to the onset of SLE have been substantiated in previous literature (100). However, the limited studies about IRF7 function regulation in SLE are mainly on murine models. With respect to pSS, IRF7 was upregulated in B cells from patients compared from healthy controls (101). In our study, IRF7 was identified as a pivotal TF in both SLE and pSS. Firstly, the functions of TFs need to be further verified with *in vitro* models. Secondly, STAT1 and IRF7 might act as reporter genes for preliminary screening of drug candidates in SLE and pSS diseases in the future.

There are some limitations in our study. Although we employed comprehensive and improved bioinformatic methods and verified our results in other gene expression profiles, the analysis remains speculative. Further experimental research is needed to confirm the findings in this study, which provides a theoretical basis for future research in the field.

Conclusions

In summary, we explored and identified the shared hub genes, related pathways and TFs in peripheral blood from SLE and pSS patients for the first time. The hub genes (I*FI44L, ISG15* and *ITGB2*) were identified, and relevant pathways (IFN response and ITGB2 signaling pathway) were found in SLE and pSS. In addition, STAT1 and IRF7 were identified as common TFs, associated with monocytes and DCs. Moreover, IRF7 was predominantly expressed in DCs. This study provides novel insights for further pathogenesis studies of SLE and pSS. In conclusion, a better understanding of the pathogenesis of each disease is of fundamental importance for identifying new therapeutic targets and immunomodulatory agents in future management of SLE and pSS.

Data availability statement

The datasets presented in this study can be found in online repositories. The names of the repository/repositories and accession number(s) can be found in the article.

Author contributions

These authors contributed equally: YC, HZ and ZW. YC performed data analyses. HZ was responsible for visualization the figures. YC, HZ, ZW, BG, HA-W, YD, OF, JW and WZ wrote and revised the manuscript draft. YS revised and finalized the manuscript. All authors contributed to the article and approved the submitted version.

Funding

This work was supported by the National Key R&D Program of China (2020YFC2002804), the State Key Program of the Nation al Natural Science Foundation of China (82030035), the Foundation of Shanghai Municipal Education Commission (2019-01- 07-00-07-E00055) and the Key R&D Program of Jiangsu (BE2020026).

Acknowledgments

We are grateful to the Gene Expression Omnibus database, and researchers for freely sharing their invaluable data.

Conflict of interest

The authors declare that the research was conducted in the absence of any commercial or financial relationships that could be construed as a potential conflict of interest.

Publisher's note

Supplementary material

The Supplementary Material for this article can be found online at: https://www.frontiersin.org/articles/10.3389/fimmu.2023.1212330/full#supplementary-material

References

1. Imgenberg-Kreuz J, Almlof JC, Leonard D, Sjowall C, Syvanen AC, Ronnblom L, et al. Shared and unique patterns of DNA methylation in systemic lupus erythematosus and primary Sjogren's syndrome. *Front Immunol* (2019) 10:1686. doi: 10.3389/fimmu.2019.01686

2. Martin-Gutierrez L, Peng J, Thompson NL, Robinson GA, Naja M, Peckham H, et al. Stratification of patients with Sjogren's syndrome and patients with systemic lupus erythematosus according to two shared immune cell signatures, with potential therapeutic implications. *Arthritis Rheumatol* (2021) 73(9):1626–37. doi: 10.1002/art.41708

3. Goldblatt F, O'Neill SG. Clinical aspects of autoimmune rheumatic diseases. *Lancet* (2013) 382(9894):797–808. doi: 10.1016/S0140-6736(13)61499-3

4. Pasoto SG, Adriano de Oliveira Martins V, Bonfa E. Sjogren's syndrome and systemic lupus erythematosus: links and risks. *Open Access Rheumatol* (2019) 11:33–45. doi: 10.2147/OARRR.S167783

5. Teruel M, Alarcon-Riquelme ME. Genetics of systemic lupus erythematosus and Sjogren's syndrome: an update. *Curr Opin Rheumatol* (2016) 28(5):506–14. doi: 10.1097/BOR.0000000000000310

6. Pisetsky DS. Evolving story of autoantibodies in systemic lupus erythematosus. *J Autoimmun* (2020) 110:102356. doi: 10.1016/j.jaut.2019.102356

7. Nocturne G, Mariette X. Advances in understanding the pathogenesis of primary Sjogren's syndrome. *Nat Rev Rheumatol* (2013) 9(9):544–56. doi: 10.1038/nrrheum.2013.110

8. Wang Y, Xie X, Zhang C, Su M, Gao S, Wang J, et al. Rheumatoid arthritis, systemic lupus erythematosus and primary Sjogren's syndrome shared megakaryocyte expansion in peripheral blood. *Ann Rheum Dis* (2022) 81(3):379–85. doi: 10.1136/annrheumdis-2021-220066

9. Toro-Dominguez D, Carmona-Saez P, Alarcon-Riquelme ME. Shared signatures between rheumatoid arthritis, systemic lupus erythematosus and Sjogren's syndrome uncovered through gene expression meta-analysis. *Arthritis Res Ther* (2014) 16(6):489. doi: 10.1186/s13075-014-0489-x

10. Imgenberg-Kreuz J, Sandling JK, Nordmark G. Epigenetic alterations in primary Sjogren's syndrome - an overview. *Clin Immunol* (2018) 196:12–20. doi: 10.1016/j.clim.2018.04.004

11. Li Y, Zhang K, Chen H, Sun F, Xu J, Wu Z, et al. A genome-wide association study in Han Chinese identifies a susceptibility locus for primary Sjogren's syndrome at 7q11.23. *Nat Genet* (2013) 45(11):1361–5. doi: 10.1038/ng.2779

12. Nordmark G, Kristjansdottir G, Theander E, Eriksson P, Brun JG, Wang C, et al. Additive effects of the major risk alleles of IRF5 and STAT4 in primary Sjogren's syndrome. *Genes Immun* (2009) 10(1):68–76. doi: 10.1038/gene.2008.94

13. Chen B, Sun L, Zhang X. Integration of microbiome and epigenome to decipher the pathogenesis of autoimmune diseases. *J Autoimmun* (2017) 83:31–42. doi: 10.1016/j.jaut.2017.03.009

14. Correa JD, Calderaro DC, Ferreira GA, Mendonca SM, Fernandes GR, Xiao E, et al. Subgingival microbiota dysbiosis in systemic lupus erythematosus: association with periodontal status. *Microbiome* (2017) 5(1):34. doi: 10.1186/s40168-017-0252-z

15. de Paiva CS, Jones DB, Stern ME, Bian F, Moore QL, Corbiere S, et al. Altered mucosal microbiome diversity and disease severity in Sjogren syndrome. *Sci Rep* (2016) 6:23561. doi: 10.1038/srep23561

16. van der Meulen TA, Harmsen HJM, Vila AV, Kurilshikov A, Liefers SC, Zhernakova A, et al. Shared gut, but distinct oral microbiota composition in primary Sjogren's syndrome and systemic lupus erythematosus. *J Autoimmun* (2019) 97:77–87. doi: 10.1016/j.jaut.2018.10.009

17. Crow MK. Type I interferon in the pathogenesis of lupus. *J Immunol* (2014) 192 (12):5459–68. doi: 10.4049/jimmunol.1002795

18. Nezos A, Gravani F, Tassidou A, Kapsogeorgou EK, Voulgarelis M, Koutsilieris M, et al. Type I and II interferon signatures in Sjogren's syndrome pathogenesis: Contributions in distinct clinical phenotypes and Sjogren's related lymphomagenesis. *J Autoimmun* (2015) 63:47–58. doi: 10.1016/j.jaut.2015.07.002

19. Thorlacius GE, Wahren-Herlenius M, Ronnblom L. An update on the role of type I interferons in systemic lupus erythematosus and Sjogren's syndrome. *Curr Opin Rheumatol* (2018) 30(5):471–81. doi: 10.1097/BOR.0000000000000524

20. Imgenberg-Kreuz J, Rasmussen A, Sivils K, Nordmark G. Genetics and epigenetics in primary Sjogren's syndrome. *Rheumatol (Oxford)* (2021) 60(5):2085–98. doi: 10.1093/rheumatology/key330

21. Lanata CM, Chung SA, Criswell LA. DNA methylation 101: what is important to know about DNA methylation and its role in SLE risk and disease heterogeneity. *Lupus Sci Med* (2018) 5(1):e000285. doi: 10.1136/lupus-2018-000285

22. Mazzone R, Zwergel C, Artico M, Taurone S, Ralli M, Greco A, et al. The emerging role of epigenetics in human autoimmune disorders. *Clin Epigenet* (2019) 11 (1):34. doi: 10.1186/s13148-019-0632-2

23. Yao M, Zhang C, Gao C, Wang Q, Dai M, Yue R, et al. Exploration of the shared gene signatures and molecular mechanisms between systemic lupus erythematosus and pulmonary arterial hypertension: evidence from transcriptome data. *Front Immunol* (2021) 12:658341. doi: 10.3389/fimmu.2021.658341

24. Kennedy WP, Maciuca R, Wolslegel K, Tew W, Abbas AR, Chaivorapol C, et al. Association of the interferon signature metric with serological disease manifestations but not global activity scores in multiple cohorts of patients with SLE. *Lupus Sci Med* (2015) 2(1):e000080. doi: 10.1136/lupus-2014-000080

25. Zhu H, Mi W, Luo H, Chen T, Liu S, Raman I, et al. Whole-genome transcription and DNA methylation analysis of peripheral blood mononuclear cells identified aberrant gene regulation pathways in systemic lupus erythematosus. *Arthritis Res Ther* (2016) 18(1):162. doi: 10.1186/s13075-016-1050-x

26. Nehar-Belaid D, Hong S, Marches R, Chen G, Bolisetty M, Baisch J, et al. Mapping systemic lupus erythematosus heterogeneity at the single-cell level. *Nat Immunol* (2020) 21(9):1094–106. doi: 10.1038/s41590-020-0743-0

27. Tasaki S, Suzuki K, Nishikawa A, Kassai Y, Takiguchi M, Kurisu R, et al. Multiomic disease signatures converge to cytotoxic CD8 T cells in primary Sjögren's syndrome. *Ann Rheumatic Dis* (2017) 76(8):1458–66. doi: 10.1136/annrheumdis-2016-210788

28. Sjöstrand M, Ambrosi A, Brauner S, Sullivan J, Malin S, Kuchroo VK, et al. Expression of the immune regulator Tripartite-motif 21 is controlled by IFN regulatory factors. *J Immunol* (2013) 191(7):3753–63. doi: 10.4049/jimmunol.1202341

29. Hong X, Meng S, Tang D, Wang T, Ding L, Yu H, et al. Single-cell RNA sequencing reveals the expansion of cytotoxic CD4+ T lymphocytes and a landscape of immune cells in Primary Sjögren's syndrome. *Front Immunol* (2021) 11:594658. doi: 10.3389/fimmu.2020.594658

30. Langfelder P, Horvath S. WGCNA: an R package for weighted correlation network analysis. *BMC Bioinf* (2008) 9:559. doi: 10.1186/1471-2105-9-559

31. Ritchie ME, Phipson B, Wu D, Hu Y, Law CW, Shi W, et al. limma powers differential expression analyses for RNA-sequencing and microarray studies. *Nucleic Acids Res* (2015) 43(7):e47. doi: 10.1093/nar/gkv007

32. Lv Y, Zhang T, Cai J, Huang C, Zhan S, Liu J. Bioinformatics and systems biology approach to identify the pathogenetic link of Long COVID and Myalgic Encephalomyelitis/Chronic Fatigue Syndrome. *Front Immunol* (2022) 13:952987. doi: 10.3389/fimmu.2022.952987

33. The Gene Ontology C. Expansion of the Gene Ontology knowledgebase and resources. *Nucleic Acids Res* (2017) 45(D1):D331–D8. doi: 10.1093/nar/gkw1108

34. Liberzon A, Birger C, Thorvaldsdottir H, Ghandi M, Mesirov JP, Tamayo P. The Molecular Signatures Database (MSigDB) hallmark gene set collection. *Cell Syst* (2015) 1(6):417–25. doi: 10.1016/j.cels.2015.12.004

35. Franceschini A, Szklarczyk D, Frankild S, Kuhn M, Simonovic M, Roth A, et al. STRING v9.1: protein-protein interaction networks, with increased coverage and integration. *Nucleic Acids Res* (2013) 41(Database issue):D808–15. doi: 10.1093/nar/gks1094

36. Smoot ME, Ono K, Ruscheinski J, Wang PL, Ideker T. Cytoscape 2.8: new features for data integration and network visualization. *Bioinformatics* (2011) 27 (3):431–2. doi: 10.1093/bioinformatics/btq675

37. Chin CH, Chen SH, Wu HH, Ho CW, Ko MT, Lin CY. cytoHubba: identifying hub objects and sub-networks from complex interactome. *BMC Syst Biol* (2014) 8 Suppl 4(Suppl 4):S11. doi: 10.1186/1752-0509-8-S4-S11

38. Mo L, Ma C, Wang Z, Li J, He W, Niu W, et al. Integrated bioinformatic analysis of the shared molecular mechanisms between osteoporosis and atherosclerosis. *Front Endocrinol (Lausanne)* (2022) 13:950030. doi: 10.3389/fendo.2022.950030

39. Ferreira MR, Santos GA, Biagi CA, Silva Junior WA, Zambuzzi WF. GSVA score reveals molecular signatures from transcriptomes for biomaterials comparison. *J BioMed Mater Res A* (2021) 109(6):1004–14. doi: 10.1002/jbm.a.37090

40. Stuart T, Butler A, Hoffman P, Hafemeister C, Papalexi E, Mauck WM. 3rd, et al. *Compr Integration Single-Cell Data Cell* (2019) 177(7):1888–902 e21. doi: 10.1016/j.cell.2019.05.031

41. Aran D, Looney AP, Liu L, Wu E, Fong V, Hsu A, et al. Reference-based analysis of lung single-cell sequencing reveals a transitional profibrotic macrophage. *Nat Immunol* (2019) 20(2):163–72. doi: 10.1038/s41590-018-0276-y

42. Northcott M, Jones S, Koelmeyer R, Bonin J, Vincent F, Kandane-Rathnayake R, et al. Type 1 interferon status in systemic lupus erythematosus: a longitudinal analysis. *Lupus Sci Med* (2022) 9(1):e000625. doi: 10.1136/lupus-2021-000625

43. Rice GI, Forte GM, Szynkiewicz M, Chase DS, Aeby A, Abdel-Hamid MS, et al. Assessment of interferon-related biomarkers in Aicardi-Goutieres syndrome associated with mutations in TREX1, RNASEH2A, RNASEH2B, RNASEH2C, SAMHD1, and ADAR: a case-control study. *Lancet Neurol* (2013) 12(12):1159–69. doi: 10.1016/S1474-4422(13)70258-8

44. Wright HL, Thomas HB, Moots RJ, Edwards SW. Interferon gene expression signature in rheumatoid arthritis neutrophils correlates with a good response to TNFi therapy. *Rheumatol (Oxford)* (2015) 54(1):188–93. doi: 10.1093/rheumatology/keu299

45. Singhania A, Graham CM, Gabrysova L, Moreira-Teixeira L, Stavropoulos E, Pitt JM, et al. Transcriptional profiling unveils type I and II interferon networks in blood and tissues across diseases. *Nat Commun* (2019) 10(1):2887. doi: 10.1038/s41467-019-10601-6

46. Newman AM, Steen CB, Liu CL, Gentles AJ, Chaudhuri AA, Scherer F, et al. Determining cell type abundance and expression from bulk tissues with digital cytometry. *Nat Biotechnol* (2019) 37(7):773–82. doi: 10.1038/s41587-019-0114-2

47. Steen CB, Liu CL, Alizadeh AA, Newman AM. Profiling cell type abundance and expression in bulk tissues with CIBERSORTx. *Methods Mol Biol* (2020) 2117:135–57. doi: 10.1007/978-1-0716-0301-7_7

48. Jin S, Guerrero-Juarez CF, Zhang L, Chang I, Ramos R, Kuan CH, et al. Inference and analysis of cell-cell communication using CellChat. *Nat Commun* (2021) 12(1):1088. doi: 10.1038/s41467-021-21246-9

49. Janky R, Verfaillie A, Imrichova H, Van de Sande B, Standaert L, Christiaens V, et al. iRegulon: from a gene list to a gene regulatory network using large motif and track collections. *PloS Comput Biol* (2014) 10(7):e1003731. doi: 10.1371/journal.pcbi.1003731

50. Aibar S, Gonzalez-Blas CB, Moerman T, Huynh-Thu VA, Imrichova H, Hulselmans G, et al. SCENIC: single-cell regulatory network inference and clustering. *Nat Methods* (2017) 14(11):1083–6. doi: 10.1038/nmeth.4463

51. Miao R, Dong X, Gong J, Li Y, Guo X, Wang J, et al. Single-cell RNA-sequencing and microarray analyses to explore the pathological mechanisms of chronic thromboembolic pulmonary hypertension. *Front Cardiovasc Med* (2022) 9:900353. doi: 10.3389/fcvm.2022.900353

52. Wei J, Huang XJ, Huang Y, Xiong MY, Yao XY, Huang ZN, et al. Key immune-related gene ITGB2 as a prognostic signature for acute myeloid leukemia. *Ann Transl Med* (2021) 9(17):1386. doi: 10.21037/atm-21-3641

53. Manoussakis MN, Georgopoulou C, Zintzaras E, Spyropoulou M, Stavropoulou A, Skopouli FN, et al. Sjogren's syndrome associated with systemic lupus erythematosus: clinical and laboratory profiles and comparison with primary Sjogren's syndrome. *Arthritis Rheum* (2004) 50(3):882–91. doi: 10.1002/art.20093

54. Psarras A, Wittmann M, Vital EM. Emerging concepts of type I interferons in SLE pathogenesis and therapy. *Nat Rev Rheumatol* (2022) 18(10):575–90. doi: 10.1038/s41584-022-00826-z

55. Perez RK, Gordon MG, Subramaniam M, Kim MC, Hartoularos GC, Targ S, et al. Single-cell RNA-seq reveals cell type-specific molecular and genetic associations to lupus. *Science* (2022) 376(6589):eabf1970. doi: 10.1126/science.abf1970

56. Tsokos GC, Lo MS, Costa Reis P, Sullivan KE. New insights into the immunopathogenesis of systemic lupus erythematosus. *Nat Rev Rheumatol* (2016) 12 (12):716–30. doi: 10.1038/nrrheum.2016.186

57. Qin B, Ma N, Tang Q, Wei T, Yang M, Fu H, et al. Neutrophil to lymphocyte ratio (NLR) and platelet to lymphocyte ratio (PLR) were useful markers in assessment of inflammatory response and disease activity in SLE patients. *Mod Rheumatol* (2016) 26(3):372–6. doi: 10.3109/14397595.2015.1091136

58. Chapman EA, Lyon M, Simpson D, Mason D, Beynon RJ, Moots RJ, et al. Caught in a trap? Proteomic analysis of neutrophil extracellular traps in rheumatoid arthritis and systemic lupus erythematosus. *Front Immunol* (2019) 10:423. doi: 10.3389/fimmu.2019.00423

59. Weng L, Chen Y, Liang T, Lin Y, Liu D, Yu C, et al. Biomarkers of interstitial lung disease associated with primary Sjogren's syndrome. *Eur J Med Res* (2022) 27 (1):199. doi: 10.1186/s40001-022-00828-3

60. Ittah M, Miceli-Richard C, Eric Gottenberg J, Lavie F, Lazure T, Ba N, et al. B cell-activating factor of the tumor necrosis factor family (BAFF) is expressed under stimulation by interferon in salivary gland epithelial cells in primary Sjogren's syndrome. *Arthritis Res Ther* (2006) 8(2):R51. doi: 10.1186/ar1912

61. Chen W, Lin J, Cao H, Xu D, Xu B, Xu L, et al. Local and systemic IKKepsilon and NF-kappaB signaling associated with Sjogren's syndrome immunopathogenesis. *J Immunol Res* (2015) 2015:534648. doi: 10.1155/2015/534648

62. Zhu H, Zheng J, Zhou Y, Wu T, Zhu T. Knockdown of RSAD2 attenuates B cell hyperactivity in patients with primary Sjogren's syndrome (pSS) via suppressing NF-kappab signaling pathway. *Mol Cell Biochem* (2021) 476(5):2029–37. doi: 10.1007/s11010-021-04070-z

63. Wang W, Xu L, Su J, Peppelenbosch MP, Pan Q. Transcriptional regulation of antiviral interferon-stimulated genes. *Trends Microbiol* (2017) 25(7):573–84. doi: 10.1016/j.tim.2017.01.001

64. Park A, Iwasaki A. Type I and type III interferons - induction, signaling, evasion, and application to combat COVID-19. *Cell Host Microbe* (2020) 27(6):870–8. doi: 10.1016/j.chom.2020.05.008

65. Chenna Narendra S, Chalise JP, Biggs S, Kalinke U, Magnusson M. Regulatory T-cells mediate IFN-α-induced resistance against antigen-induced arthritis. *Front Immunol* (2018) 9:285. doi: 10.3389/fimmu.2018.00285

66. Graalmann T, Borst K, Manchanda H, Vaas L, Bruhn M, Graalmann L, et al. B cell depletion impairs vaccination-induced CD8+T cell responses in a type I interferon-dependent manner. *Ann Rheumatic Dis* (2021) 80(12):1537–44. doi: 10.1136/annrheumdis-2021-220435

67. Luo S, Wu R, Li Q, Zhang G. Epigenetic regulation of IFI44L expression in monocytes affects the functions of monocyte-derived dendritic cells in systemic lupus erythematosus. *J Immunol Res* (2022) 2022:4053038. doi: 10.1155/2022/4053038

68. Nocturne G, Mariette X. B cells in the pathogenesis of primary Sjogren syndrome. *Nat Rev Rheumatol* (2018) 14(3):133–45. doi: 10.1038/nrrheum.2018.1

69. Fang X, Duan SF, Gong YZ, Wang F, Chen XL. Identification of key genes associated with changes in the host response to severe burn shock: A bioinformatics analysis with data from the gene expression omnibus (GEO) database. *J Inflammation Res* (2020) 13:1029–41. doi: 10.2147/JIR.S282722

70. Yang S, Cao C, Xie Z, Zhou Z. Analysis of potential hub genes involved in the pathogenesis of Chinese type 1 diabetic patients. *Ann Transl Med* (2020) 8(6):295. doi: 10.21037/atm.2020.02.171

71. Jara D, Carvajal P, Castro I, Barrera MJ, Aguilera S, Gonzalez S, et al. Type I interferon dependent hsa-miR-145-5p downregulation modulates MUC1 and TLR4 overexpression in salivary glands from Sjogren's syndrome patients. *Front Immunol* (2021) 12:685837. doi: 10.3389/fimmu.2021.685837

72. Zhao M, Zhou Y, Zhu B, Wan M, Jiang T, Tan Q, et al. IFI44L promoter methylation as a blood biomarker for systemic lupus erythematosus. *Ann Rheum Dis* (2016) 75(11):1998–2006. doi: 10.1136/annrheumdis-2015-208410

73. Zhang X, Bogunovic D, Payelle-Brogard B, Francois-Newton V, Speer SD, Yuan C, et al. Human intracellular ISG15 prevents interferon-alpha/beta over-amplification and auto-inflammation. *Nature* (2015) 517(7532):89–93. doi: 10.1038/nature13801

74. Yuan Y, Ma H, Ye Z, Jing W, Jiang Z. Interferon-stimulated gene 15 expression in systemic lupus erythematosus: Diagnostic value and association with lymphocytopenia. *Z Rheumatol* (2018) 77(3):256–62. doi: 10.1007/s00393-017-0274-8

75. Dashti N, Mahmoudi M, Gharibdoost F, Kavosi H, Rezaei R, Imeni V, et al. Evaluation of ITGB2 (CD18) and SELL (CD62L) genes expression and methylation of ITGB2 promoter region in patients with systemic sclerosis. *Rheumatol Int* (2018) 38 (3):489–98. doi: 10.1007/s00296-017-3915-y

76. Slack RJ, Macdonald SJF, Roper JA, Jenkins RG, Hatley RJD. Emerging therapeutic opportunities for integrin inhibitors. *Nat Rev Drug Discovery* (2022) 21 (1):60–78. doi: 10.1038/s41573-021-00284-4

77. Ghilardi N, Pappu R, Arron JR, Chan AC. 30 years of biotherapeutics development-what have we learned? *Annu Rev Immunol* (2020) 38:249–87. doi: 10.1146/annurev-immunol-101619-031510

78. Behera R, Kumar V, Lohite K, Karnik S, Kundu GC. Activation of JAK2/STAT3 signaling by osteopontin promotes tumor growth in human breast cancer cells. *Carcinogenesis* (2010) 31(2):192–200. doi: 10.1093/carcin/bgp289

79. Mastrangeli R, D'Amici F, D'Acunto CW, Fiumi S, Rossi M, Terlizzese M, et al. A deamidated interferon-beta variant binds to integrin alphavbeta3. *Cytokine* (2018) 104:38–41. doi: 10.1016/j.cyto.2018.01.024

80. Baker KF, Isaacs JD. Novel therapies for immune-mediated inflammatory diseases: What can we learn from their use in rheumatoid arthritis, spondyloarthritis, systemic lupus erythematosus, psoriasis, Crohn's disease and ulcerative colitis? *Ann Rheum Dis* (2018) 77(2):175–87. doi: 10.1136/annrheumdis-2017-211555

81. Nakou M, Bertsias G, Stagakis I, Centola M, Tassiulas I, Hatziapostolou M, et al. Gene network analysis of bone marrow mononuclear cells reveals activation of multiple kinase pathways in human systemic lupus erythematosus. *PloS One* (2010) 5(10): e13351. doi: 10.1371/journal.pone.0013351

82. Feagan BG, Rutgeerts P, Sands BE, Hanauer S, Colombel JF, Sandborn WJ, et al. Vedolizumab as induction and maintenance therapy for ulcerative colitis. *N Engl J Med* (2013) 369(8):699–710. doi: 10.1056/NEJMoa1215734

83. Sandborn WJ, Feagan BG, Rutgeerts P, Hanauer S, Colombel JF, Sands BE, et al. Vedolizumab as induction and maintenance therapy for Crohn's disease. *N Engl J Med* (2013) 369(8):711–21. doi: 10.1056/NEJMoa1215739

84. Haber SL, Benson V, Buckway CJ, Gonzales JM, Romanet D, Scholes B. Lifitegrast: a novel drug for patients with dry eye disease. *Ther Adv Ophthalmol* (2019) 11:2515841419870366. doi: 10.1177/2515841419870366

85. Mitroulis I, Alexaki VI, Kourtzelis I, Ziogas A, Hajishengallis G, Chavakis T. Leukocyte integrins: role in leukocyte recruitment and as therapeutic targets in inflammatory disease. *Pharmacol Ther* (2015) 147:123–35. doi: 10.1016/j.pharmthera.2014.11.008

86. Mogensen TH. IRF and STAT transcription factors - from basic biology to roles in infection, protective immunity, and primary immunodeficiencies. *Front Immunol* (2018) 9:3047. doi: 10.3389/fimmu.2018.03047

87. Platanitis E, Decker T. Regulatory networks involving STATs, IRFs, and NFkappaB in inflammation. *Front Immunol* (2018) 9:2542. doi: 10.3389/fimmu.2018.02542

88. Wack A, Terczynska-Dyla E, Hartmann R. Guarding the frontiers: the biology of type III interferons. *Nat Immunol* (2015) 16(8):802–9. doi: 10.1038/ni.3212

89. Platanias LC. Mechanisms of type-I- and type-II-interferon-mediated signalling. *Nat Rev Immunol* (2005) 5(5):375–86. doi: 10.1038/nri1604

90. Ivashkiv LB, Donlin LT. Regulation of type I interferon responses. *Nat Rev Immunol* (2014) 14(1):36–49. doi: 10.1038/nri3581

91. Aue A, Szelinski F, Weissenberg SY, Wiedemann A, Rose T, Lino AC, et al. Elevated STAT1 expression but not phosphorylation in lupus B cells correlates with disease activity and increased plasmablast susceptibility. *Rheumatol (Oxford)* (2020) 59 (11):3435–42. doi: 10.1093/rheumatology/keaa187

92. Li M, Li M, Qiao L, Wu C, Xu D, Zhao Y, et al. Role of JAK-STAT signaling pathway in pathogenesis and treatment of primary Sjogren's syndrome. *Chin Med J (Engl)* (2023). doi: 10.1097/CM9.0000000000002539

93. Banerjee S, Biehl A, Gadina M, Hasni S, Schwartz DM. JAK-STAT signaling as a target for inflammatory and autoimmune diseases: current and future prospects. *Drugs* (2017) 77(5):521–46. doi: 10.1007/s40265-017-0701-9

94. Lee J, Lee J, Kwok SK, Baek S, Jang SG, Hong SM, et al. JAK-1 inhibition suppresses interferon-induced BAFF production in human salivary gland: potential therapeutic strategy for primary Sjogren's syndrome. *Arthritis Rheumatol* (2018) 70 (12):2057–66. doi: 10.1002/art.40589

95. Chiang HS, Liu HM. The molecular basis of viral inhibition of IRF- and STAT-dependent immune responses. *Front Immunol* (2018) 9:3086. doi: 10.3389/fimmu.2018.03086

96. Ikushima H, Negishi H, Taniguchi T. The IRF family transcription factors at the interface of innate and adaptive immune responses. *Cold Spring Harb Symp Quant Biol* (2013) 78:105–16. doi: 10.1101/sqb.2013.78.020321

97. Honda K, Takaoka A, Taniguchi T. Type I interferon [corrected] gene induction by the interferon regulatory factor family of transcription factors. *Immunity* (2006) 25 (3):349–60. doi: 10.1016/j.immuni.2006.08.009

98. Au WC, Moore PA, LaFleur DW, Tombal B, Pitha PM. Characterization of the interferon regulatory factor-7 and its potential role in the transcription activation of interferon A genes. *J Biol Chem* (1998) 273(44):29210–7. doi: 10.1074/jbc.273.44.29210

99. Wu J, Chen ZJ. Innate immune sensing and signaling of cytosolic nucleic acids. *Annu Rev Immunol* (2014) 32:461–88. doi: 10.1146/annurev-immunol-032713-120156

100. Jefferies CA. Regulating IRFs in IFN driven disease. *Front Immunol* (2019) 10:325. doi: 10.3389/fimmu.2019.00325

101. Riviere E, Pascaud J, Tchitchek N, Boudaoud S, Paoletti A, Ly B, et al. Salivary gland epithelial cells from patients with Sjogren's syndrome induce B-lymphocyte survival and activation. *Ann Rheum Dis* (2020) 79(11):1468–77. doi: 10.1136/annrheumdis-2019-216588

frontiers | Frontiers in Immunology

TYPE Correction
PUBLISHED 08 December 2023
DOI 10.3389/fimmu.2023.1339929

Check for updates

OPEN ACCESS

EDITED AND REVIEWED BY
Kuang-Hui Sun,
National Yang Ming Chiao
Tung University, Taiwan

*CORRESPONDENCE
Yi Eve Sun
yi.eve.sun@gmail.com

†These authors have contributed equally to this work

RECEIVED 17 November 2023
ACCEPTED 27 November 2023
PUBLISHED 08 December 2023

CITATION
Cui Y, Zhang H, Wang Z, Gong B, Al-Ward H, Deng Y, Fan O, Wang J, Zhu W and Sun YE (2023) Corrigendum: Exploring the shared molecular mechanisms between systemic lupus erythematosus and primary Sjögren's syndrome based on integrated bioinformatics and single-cell RNA-seq analysis. *Front. Immunol.* 14:1339929. doi: 10.3389/fimmu.2023.1339929

Corrigendum: Exploring the shared molecular mechanisms between systemic lupus erythematosus and primary Sjögren's syndrome based on integrated bioinformatics and single-cell RNA-seq analysis

Yanling Cui[1,2†], Huina Zhang[1,2†], Zhen Wang[1,2†], Bangdong Gong[3], Hisham Al-Ward[1,2], Yaxuan Deng[1,2], Orion Fan[1,2], Junbang Wang[1], Wenmin Zhu[1] and Yi Eve Sun[1,2*]

[1]Stem Cell Translational Research Center, Tongji Hospital, School of Medicine, Tongji University, Shanghai, China, [2]Shanghai Institute of Stem Cell Research and Clinical Translation, Shanghai East Hospital, School of Medicine, Tongji University, Shanghai, China, [3]Division of Rheumatology, Tongji Hospital of Tongji University School of Medicine, Shanghai, China

KEYWORDS

systemic lupus erythematosus, primary Sjögren's syndrome, bioinformatics, hub genes, TFs, scRNA-seq

A corrigendum on
Exploring the shared molecular mechanisms between systemic lupus erythematosus and primary Sjögren's syndrome based on integrated bioinformatics and single-cell RNA-seq analysis

by Cui Y, Zhang H, Wang Z, Gong B, Al-Ward H, Deng Y, Fan O, Wang J, Zhu W and Sun YE (2023). *Front. Immunol.* 14:1212330. doi: 10.3389/fimmu.2023.1212330

In the published article, there was an error in Figures 8C, 9A, 9B, 10C, 10E and Supplementary Figures S5E, S6A, S7E as published. We noticed that a cell type was incorrectly described. The "gd T cells" should be "CD8 memory T cells" in our article since the R codes were not revised in time. The corrected Figures 8, 9, 10 and Supplementary Figures 5, 6 and 7 and their captions "FIGURE 8 Validation of hub genes in scRNA-seq datasets", "FIGURE 9 Landscape map of IC in SLE and pSS datasets", "FIGURE 10 Verification of related pathways in scRNA-seq datasets", "Supplementary Figure 5 Functional analysis of upregulated DEGs in scRNA-seq", "Supplementary Figure 6 Heatmap of correlation matrix", "Supplementary Figure 7 The expression levels of ITGB2 signaling pathway related genes (ITGB2, ICAM1, ICAM2, CD226 and ITGAL)" appear below or can be found in the Supplementary Material of the original article.

The authors apologize for this error and state that this does not change the scientific conclusions of the article in any way. The original article has been updated.

Publisher's note

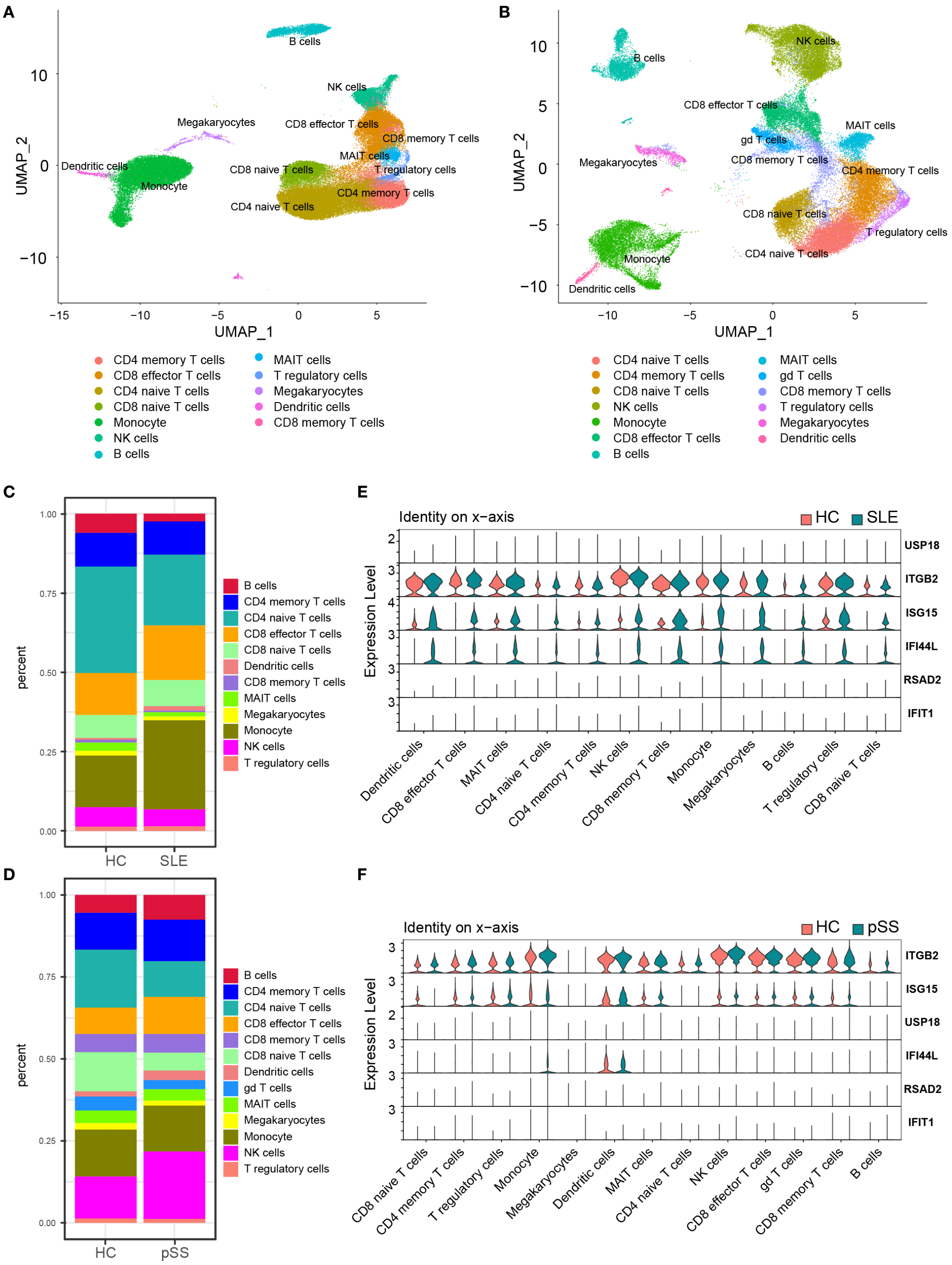

FIGURE 8
Validation of hub genes in scRNA-seq datasets. **(A)** UMAP visualization GSE157278 scRNA-seq datasets. **(B)** UMAP visualization GSE135779 scRNAseq datasets; Different colors indicate distinct cell types. **(C)** Cellular composition in SLE and HCs group **(D)** Cellular composition in pSS and HCs group. The colors represent different cell types. **(E)** Violin plot of hub genes expression in different cell types in SLE. **(F)** Violin plot of hub genes expression in different cell types in pSS. SLE, systemic lupus erythematosus; pSS, primary Sjögren's syndrome.

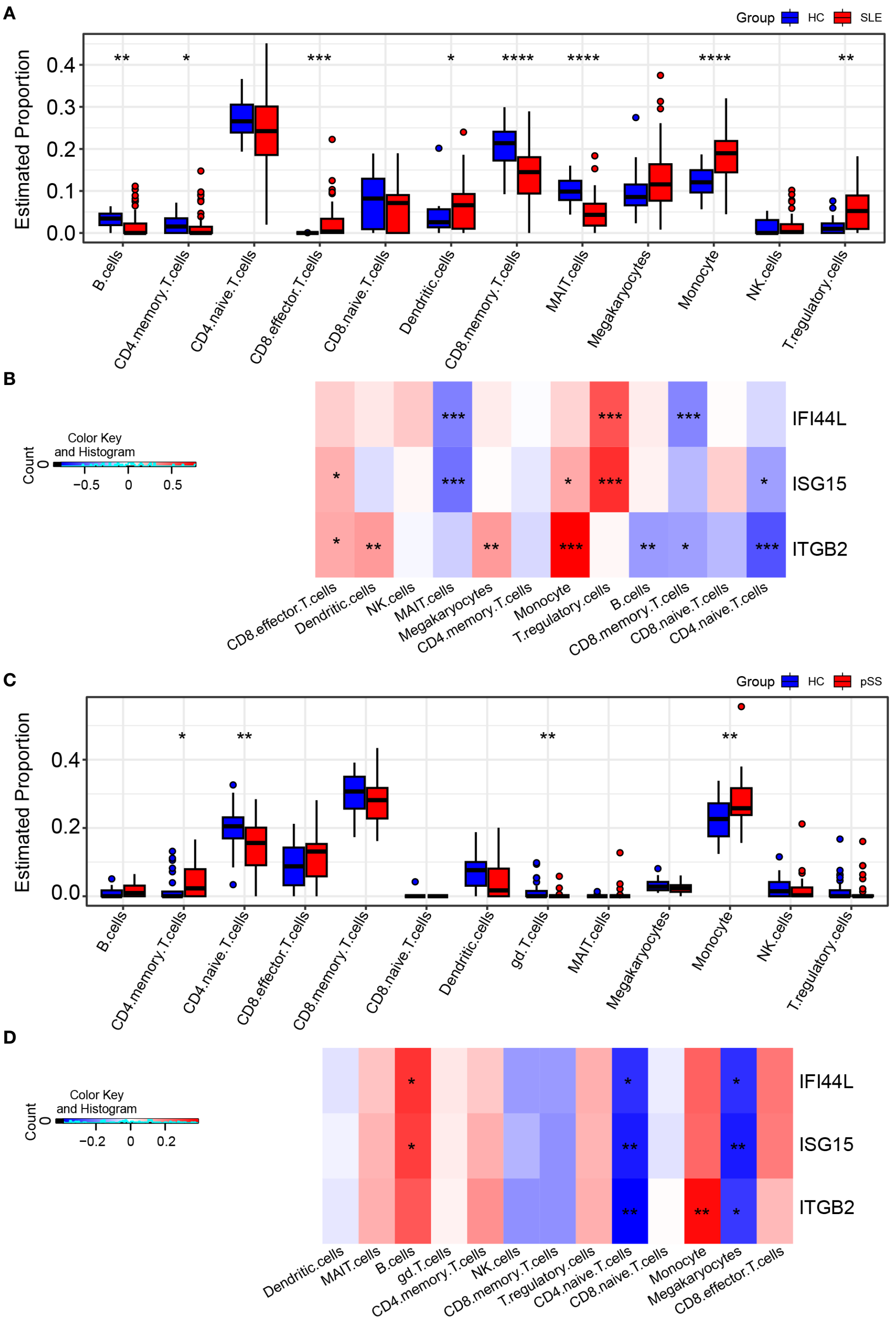

FIGURE 9
Landscape map of IC in SLE and pSS datasets. **(A)** Boxplot showing the differences of IC between SLE and HC. **(B)** Correlation matrix between IC and hub gene in SLE. **(C)** Boxplot showing the differences of IC between pSS and HC. **(D)** Correlation matrix between IC and hub gene in pSS. Red: positive correlation; blue: negative correlation. SLE, systemic lupus erythematosus; pSS, primary Sjögren's syndrome. **p* < 0.05, ***p* < 0.01, ****p* < 0.001, *****p* < 0.0001.

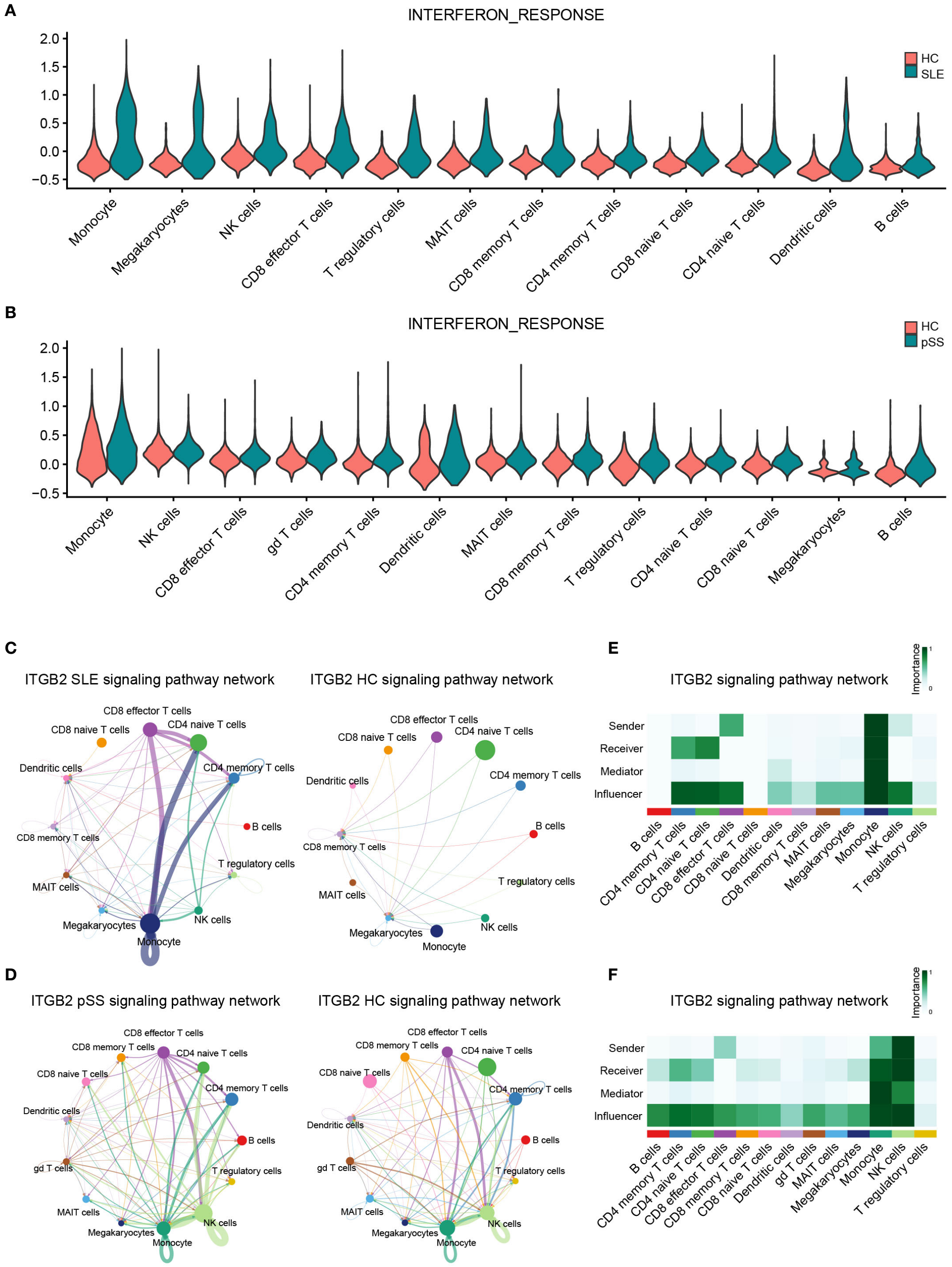

FIGURE 10

Verification of related pathways in scRNA-seq datasets. **(A)** Violin plot of INTERFERON_RESPONSE expression in SLE. **(B)** Violin plot of INTERFERON_RESPONSE expression in pSS. **(C)** Circos plot showing the ITGB2 signaling pathway network across major cell types in SLE and HCs. **(D)** Circos plot showing the ITGB2 signaling pathway network across major cell types in pSS and HCs. **(E)** Heatmap showing the relative importance of each cell type based on the computed four network centrality measures of the ITGB2 signaling pathway in SLE. **(F)** Heatmap showing the relative importance of each cell type based on the computed four network centrality measures of the ITGB2 signaling pathway in pSS. SLE, systemic lupus erythematosus; pSS, primary Sjögren's syndrome.

frontiers | Frontiers in Immunology

TYPE Original Research
PUBLISHED 12 September 2023
DOI 10.3389/fimmu.2023.1250504

OPEN ACCESS

EDITED BY
Shiang-Jong Tzeng,
National Taiwan University, Taiwan

REVIEWED BY
Stephanie Schell,
The Pennsylvania State University,
United States
Yale Liu,
The Second Affiliated Hospital of Xi'an
Jiaotong University, China

*CORRESPONDENCE
Jaehwan Kim
✉ derkim@ucdavis.edu
James G. Krueger
✉ jgk@rockefeller.edu

RECEIVED 30 June 2023
ACCEPTED 28 August 2023
PUBLISHED 12 September 2023

CITATION
Kim J, Lee J, Li X, Kunjravia N, Rambhia D, Cueto I, Kim K, Chaparala V, Ko Y, Garcet S, Zhou W, Cao J and Krueger JG (2023) Multi-omics segregate different transcriptomic impacts of anti-IL-17A blockade on type 17 T-cells and regulatory immune cells in psoriasis skin. *Front. Immunol.* 14:1250504. doi: 10.3389/fimmu.2023.1250504

Multi-omics segregate different transcriptomic impacts of anti-IL-17A blockade on type 17 T-cells and regulatory immune cells in psoriasis skin

Jaehwan Kim[1,2,3*], Jongmi Lee[2], Xuan Li[1], Norma Kunjravia[1], Darshna Rambhia[1], Inna Cueto[1], Katherine Kim[2,3], Vasuma Chaparala[2], Younhee Ko[3,4], Sandra Garcet[1,5], Wei Zhou[6], Junyue Cao[6] and James G. Krueger[1*]

[1]Laboratory for Investigative Dermatology, The Rockefeller University, New York, NY, United States, [2]Dermatology Section, Veterans Affairs Northern California Health Care System, Mather, CA, United States, [3]Department of Dermatology, University of California, Davis, Sacramento, CA, United States, [4]Division of Biomedical Engineering, Hankuk University of Foreign Studies, Seoul, Republic of Korea, [5]Research Bioinformatics, Center for Clinical and Translational Science, The Rockefeller University, New York, NY, United States, [6]Laboratory of Single-cell Genomics and Population Dynamics, The Rockefeller University, New York, NY, United States

Durable psoriasis improvement has been reported in a subset of psoriasis patients after treatment withdrawal of biologics blocking IL-23/Type 17 T-cell (T17) autoimmune axis. However, it is not well understood if systemic blockade of the IL-23/T17 axis promotes immune tolerance in psoriasis skin. The purpose of the study was to find translational evidence that systemic IL-17A blockade promotes regulatory transcriptome modification in human psoriasis skin immune cell subsets. We analyzed human psoriasis lesional skin 6 mm punch biopsy tissues before and after systemic IL-17A blockade using the muti-genomics approach integrating immune cell-enriched scRNA-seq ($n = 18$), microarray ($n = 61$), and immunohistochemistry ($n = 61$) with repository normal control skin immune cell-enriched scRNA-seq ($n = 10$) and microarray ($n = 8$) data. For the T17 axis transcriptome, systemic IL-17A blockade depleted 100% of *IL17A*$^+$ T-cells and 95% of *IL17F*$^+$ T-cells in psoriasis skin. The expression of *IL23A* in DC subsets was also downregulated by IL-17A blockade. The expression of IL-17-driven inflammatory mediators (*IL36G*, *S100A8*, *DEFB4A*, and *DEFB4B*) in suprabasal keratinocytes was correlated with psoriasis severity and was downregulated by IL-17A blockade. For the regulatory DC transcriptome, the proportion of regulatory semimature DCs expressing regulatory DC markers of *BDCA-3* (*THBD*) and *DCIR* (*CLEC4A*) was increased in posttreatment psoriasis lesional skin compared to pretreatment psoriasis lesional skin. In addition, IL-17A blockade induced higher expression of *CD1C* and *CD14*, which are markers of CD1c$^+$ CD14$^+$ dendritic cell (DC) subset that suppresses antigen-specific T-cell responses, in posttreatment regulatory semimature DCs compared to pretreatment regulatory semimature DCs. In conclusion, systemic IL-17A inhibition not only blocks the entire IL-23/T17 cell axis but also promotes regulatory gene expression in regulatory DCs in human psoriasis skin.

KEYWORDS

psoriasis, multi-omics, single-cell RNA sequencing, IL-17, biologics impacts of IL-17A blockade on skin immune cell subsets

Introduction

Psoriasis is one of the most common organ-specific autoimmune diseases in the human population affecting 3.2% of the adult population (1–3). Psoriasis originates from the skin, but it progressively induces systemic inflammation that may accompany psoriatic arthritis, metabolic syndrome, diabetes, overt vascular inflammation, and cardiovascular disease (4–7). Increasing evidence indicates that the systemic impact of psoriasis shortens the lifespan of affected individuals by at least 3–5 years (8).

Psoriasis persists as a lifelong disease that rarely improves without treatment, but systemic administration of recent monoclonal antibodies targeting the IL-23/Type 17 T-cell (T17) autoimmune axis is highly effective for psoriasis treatment (3). In the current model of psoriasis immunopathogenesis, IL-23 from dendritic cells (DCs) triggers T-cells (T17 cells) to produce IL-17, and IL-17 induces inflammatory mediators in keratinocytes (KCs) such as IL-36γ. The inflammatory mediators from KCs amplify DC and T-cell recruitment and activation completing the feed-forward inflammatory loop.

Genomic medicine mapping of psoriasis-associated immune pathways in the human skin enabled the therapeutic success of IL-23/IL-17 antagonists. The high efficacy of most IL-23/IL-17 antagonists was identified through early phase IIb studies that incorporated total skin gene expression profiles on relatively small numbers of patients, often with <10 in a treatment cohort (9–11). Large phase II and III studies were needed mainly to develop safety profiles on a sufficient number of patients for new drug registration.

However, total skin gene expression profiling is confronting limitations to dissect the IL-23/T17 autoimmune axis for explaining recent clinical trial findings (1): systemic administration of an anti-IL-17A monoclonal antibody increased the expression of genes involved in skin homeostasis promotion and KC stem cell activation in psoriasis skin (10). (2) systemic administration of an anti-IL-17A or anti-IL-23p19 monoclonal antibody produced durable psoriasis improvement maintenance even after treatment withdrawal in a subset of psoriasis patients (9, 12–15). To understand immune tolerance promotion induced by IL-23/T17 autoimmune axis blockade, we need to segregate and compare the transcriptome of regulatory immune cell subsets in human psoriasis skin before and after blocking the IL-23/T17 autoimmune axis.

We recently used RT-PCR analyses of total skin from a randomized placebo-controlled clinical trial (ClinicalTrial.gov identifier: NCT03131570) to study psoriasis skin transcriptome modifications induced by systemic IL-17A blockade (10). Here, we used archived samples from this trial for further analysis, applying a multi-omics approach. We performed single cell RNA-sequencing (scRNA-seq) analyses of T-cell, DC, and KC subsets isolated from psoriasis skin. We also used whole psoriasis skin for microarray, RT-PCR, and IHC analyses (Figure 1). Our multi-omics approach provides novel translational evidence in human psoriasis skin that systemic anti-IL-17A monoclonal antibody

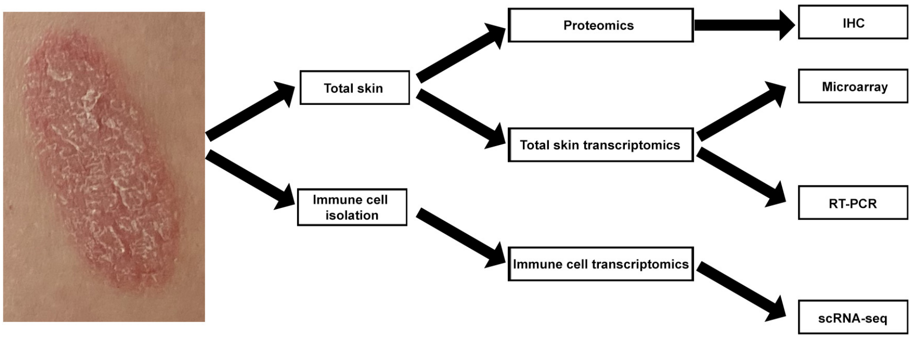

FIGURE 1
Schematic view of multi-omics strategy for mapping human psoriasis skin transcriptome.

administration not only blocks the entire feed-forward inflammatory amplification loop between T-cells, DCs, and KCs, but also promotes regulatory transcriptome modification in regulatory DCs.

Materials and methods

Human psoriasis skin before and after systemic IL-17A blockade

23 adult psoriasis patients received anti-IL-17A monoclonal antibody (secukinumab) injections for more than 12 weeks in the phase II clinical trial (ClinicalTrial.gov identifier: NCT03131570). Patients received the anti-IL-17A monoclonal antibody at a dose of 300 mg with injections administered once weekly at baseline and at weeks 1, 2, 3, and 4 and then every 4 weeks. The clinical responses of patients and RT-PCR analyses of psoriasis skin were previously published (10).

For this study, psoriasis skin biopsy samples obtained from the clinical trial (10) were further analyzed by immune cell-enriched scRNA-seq (n = 18; GSE183047), microarray (n = 61; GSE226244), and immunohistochemistry (n = 61) together with our repository normal control skin immune cell-enriched scRNA-seq data (n = 10) (16) and microarray data (n = 8) (Supplementary Table 1). To minimize the batch effects, all the molecular experiments from the initial sample processing to cDNA library construction were performed by the same investigators under the same protocol.

Lesional biopsy specimens were harvested with a 6 mm punch biopsy from areas with representative psoriasis lesions. The individual skin sample information, including age, gender, psoriasis versus (*vs.*) control, and timepoint of biopsy is summarized in Supplementary Table 1. Psoriasis lesional skin biopsy samples before anti-IL-17A monoclonal antibody injections (pretreatment) and psoriasis lesional skin biopsy samples after 12 weeks of anti-IL-17 monoclonal antibody injections (posttreatment) were compared for this study.

Harvested skin samples were bisected immediately after the skin biopsy. Half of the two bisected skin tissue was incubated in a culture medium for single-cell RNA sequencing (scRNA-seq) experiments. Another half of the bisected skin tissue was snap-frozen and embedded in the Optimal Cutting Temperature (OCT) compound (Ted Pella, Redding, CA) for microarray and immunohistochemistry experiments.

Immune cell-enriched single-cell RNA sequencing analyses of human psoriasis skin

Harvesting emigrating cells from skin biopsy tissues for immune cell-enriched scRNA-seq

Skin biopsy samples were incubated in culture medium for harvesting emigrating cells (16). To split the epidermis and dermis where most of the inflammatory cells were located, harvested skin tissue was immediately placed in 0.2% Dispase II (Sigma-Aldrich, St. Louis, MO) and incubated in a humidified incubator at 37°C and 5% CO_2 for 3 hours. Then, the epidermis and dermis were separated with forceps and sliced into small pieces with #10 blade scalpels. The epidermis and dermis were separately incubated in RPMI-1640 medium with L-glutamine (Cytiva, Marlborough, MA) supplemented with 10% human albumin serum (Sigma-Aldrich, St. Louis, MO) in a humidified incubator at 37°C and 5% CO_2. Nonplastic adherent cells that had emigrated out of the epidermis and dermis were harvested after 48 hours. The harvested cells from the epidermis and dermis were filtered through a 40-μm cell strainer (Corning, Glendale, AZ) and stored on ice. The cell numbers and viability were determined using a Countess automated cell counter (Invitrogen, Carlsbad, CA) and trypan blue staining (BioRad, Hercules, CA).

Single-cell capture and cDNA library preparation

The 10x Genomics Chromium Single Cell 3′ Reagents Kit user guide (https://support.10xgenomics.com) was used to prepare the single-cell suspension. The appropriate volume of each sample was diluted to recover 10,000 cells. Subsequently, the single-cell suspension, gel beads, and oils were added to the 10X Genomics single-cell chip. After droplet generation, samples were transferred into PCR tubes and we performed reverse transcription using a ProFlex PCR Thermocycler System (Applied Biosystems, Foster City, CA). After reverse transcription, cDNA was recovered using a recovery agent, provided by 10X Genomics, followed by silane DynaBead clean-up as outlined in the user guide.

Single-cell RNA sequencing data generation

The raw sequencing data for individual samples were processed using the 10X Genomics standard sequencing protocol without modifications. The FASTQ files were aligned to the human genome reference sequence GRCh38. Cell Ranger was applied to FASTQ files to generate files containing a barcode table, a gene table, and a gene expression matrix. The number of reads, mean reads per cell, valid barcodes, sequencing saturation, and other scRNA-seq parameters are detailed in Supplementary Table 1. The scRNA-seq data have been deposited in NCBI's Gene Expression Omnibus and are publicly accessible through GEO Series accession number GSE183047. There is no restriction on the use of the data.

Single-cell data quality control

We used the *Seurat* R package (version 4.0) installed in R (version 4.0.2) for the downstream single-cell analyses (17–19). Before data integration, single-cell data quality control was performed separately for each sample as previously described for human skin single-cell RNA sequencing analyses (16, 20–22). Genes expressed in <3 cells, and cells with <100 or >5,000 genes and a mitochondrial gene percentage of >25% were filtered out to eliminate partial cells and doublets. Ubiquitously expressed ribosomal protein-coding (RPS and RPL) and MALAT noncoding RNA, miRNA, and snoRNA genes were excluded from the analysis as we described in our prior single-cell analysis publication with the publicly available R scripts (16). Seurat objects were created followed by normalizing data, scaling data, and finding variable 2,000 genes.

Single-cell data integration and harmonization

We first merged single-cell data of samples with the identical reagent kit version and the identical sequencer. To harmonize merged groups into a single dataset reducing batch effects, correspondences between cells in merged datasets were identified by the FindIntegrationAnchors function, and the correspondences were used for data integration with the IntegratedData function as detailed by Stuart et al. (18).

Non-linear dimension reduction and clustering analysis

Principal component analysis and graph-based clustering analysis were performed, and sixty principal components (PCs) were selected for Uniform Manifold Approximation and Projection for Dimension Reduction. With a resolution of 0.8, cells were clustered by the FindClusters function. The average gene expression of psoriasis *vs*. control cells within a cluster was calculated by the AverageExpression function.

When 10,000 cells are submitted to a microfluidic platform for droplet-based single-cell library construction, 2.3% to 4.6% of single-cell data could be technical artifacts caused by cell doublets formed during cell capture (Chromium Next GEM Single Cell 3′ Reagent Kits User Guide, 10X Genomics, USA). To remove clusters with possible doublets for downstream single-cell analysis, we excluded clusters expressing gene signatures of more than two different immune cell types (Supplementary Figure 1). We also excluded clusters of a minimal number of cells that were spatially separated from the analogous type of cells. To compare psoriasis and control cells within clusters representing each type of skin immune cells, we merged adjacent clusters of common immune cell subsets.

Microarray analyses of human skin

Skin biopsy samples were frozen and then mechanically disaggregated before RNA extraction. RNA was extracted with RNA isolation kits (Qiagen) according to the manufacturer's protocol. A total of 100 ng of biotinylated cDNA was hybridized to the GeneChip Human Genome U133 Plus 2.0 Array (Affymetrix). The expression values were obtained using the GCRMA algorithm (23), while normalization across samples was carried out using quantile normalization. The raw microarray data have been deposited in NCBI's Gene Expression Omnibus (GEO) and are accessible through accession number GSE226244.

RT-PCR analyses of human skin

Total RNA was extracted from frozen skin biopsies by the Qiagen miNeasy Mini Kit (Valencia, CA, USA). DNA was removed with on-column DNase digestion by the Qiagen RNase-free DNase Set (Valencia, CA, USA). The quality of extracted RNA was examined using Agilent Bioanalyzer 2100 (Agilent Technologies, Palo Alto, CA). Real-time PCR was performed on QuantStudio 7 Flex Real-Time PCR System (Thermo Fisher Scientific, Waltham, MA) with TaqMan Array Cards (384-well plates preloaded with TaqMan assays, Thermo Fisher Scientific, Waltham, MA). All primers are listed in Supplementary Table 2.

Immunohistochemistry analyses of human skin

For immunostaining, vertical sections were cut to a thickness of 6 µm (+/- 1 µm) from the frozen skin biopsy tissues embedded in the OCT compound. Frozen sections were dried at room temperature and then fixed for 2 minutes in acetone. Next, the samples were blocked with 10% normal serum of the species in which the secondary antibody was made, and then the samples were incubated overnight at 4°C with the appropriate primary antibody. Primary antibodies used in this study were all mouse antibodies: KRT16 (LSBio, Seattle, WA; clone 7A4, dilution 1:500), CD3 (BD Biosciences, San Jose, CA; clone SK7, dilution 1:100), and CD11c (BD Biosciences, San Jose, CA; clone Bly6, dilution 1:100). Biotin-labeled horse anti-mouse antibodies (Vector Laboratories, Burlingame, CA) were used to detect the primary antibodies. The staining signal was amplified with avidin-biotin complex (Vector Laboratories, Burlingame, CA) and developed using chromogen 3-amino-9-ethyl carbazole (Sigma-Aldrich, St. Louis, MO). Section images were acquired at ×10 magnification. The number of immunostaining-positive cell counts per section was manually counted using computer-assisted image analysis software (ImageJ V1.48, National Institute of Health, Bethesda, MD). 61 sections were quantified for CD3 immunostaining (n = 40 for pretreatment sections and n = 21 for posttreatment sections) and 60 sections were quantified for CD11c immunostaining (n = 40 for pretreatment sections and n = 20 for posttreatment sections).

Statistics

Statistical analyses of scRNA-seq data at the level of total T-cells, DCs, or KCs were performed under the general framework of the Seurat R package (17–19). We used a Wilcoxon rank sum test to define differentially expressed genes. A value of $p < 0.05$ was considered statistically significant.

Statistical analyses of scRNA-seq data at the level of T-cell and KC subsets were performed under the trajectory inference framework of Monocle3 R package (24, 25). We used a spatial autocorrelation analysis called Moran's I (25) with the graph-test function, which Cao et al. (24) showed to be effective in finding genes that are differentially expressed in single-cell RNA sequencing data. A *p*-value that has been adjusted for the False Discovery rate < 0.05 was considered statistically significant (Supplementary Tables 3, 4). Spearman's rank correlation coefficient was calculated to test inter-correlations between the single-cell data.

For statistical analyses of microarray data, log2-transformed expression values were modeled using linear mixed-effects models. *P*-values from moderated t-tests were adjusted for multiple hypotheses across genes using the Benjamini-Hochberg procedure. A value of $p < 0.05$ and a fold change ratio > 2 was considered statistically significant.

For statistical analyses of RT-PCR data, RT-PCR results were modeled with the delta Ct (ΔΔCt) method for relative quantification to a housekeeping gene *RPLP0* (Ribosomal Protein Lateral Stalk Subunit P0) and calibration with a reference sample Control01 under the general framework of *pcr_analyze* R package (26) as we described in our prior publication (10). Two-sided Wilcoxon rank-sum test was used to compare RT-PCR experiment results between group 1 and group 2. A value of $p < 0.05$ was considered statistically significant.

For statistical analyses of immunohistochemistry data, we used a Wilcoxon rank sum test to compare measures between groups. A value of $p < 0.05$ was considered statistically significant.

Study approval

The study protocol and informed consent were approved by the Institutional Review Board of the Rockefeller University, New York, NY, USA. The study was conducted in accordance with Good Clinical Practice and the Declaration of Helsinki, and all subjects provided written informed consent before entering the study.

Results

IL-17A blockade reduces T-cell signatures, dendritic cell signatures, and keratinocyte hyperproliferation signatures and increases regulatory molecular expression in psoriasis lesional skin at total skin transcriptome levels

We first studied how the immune cell numbers are changed in psoriasis skin after systemic IL-17A blockade, and how the immune cell number changes are reflected in total skin transcriptome. KC hyperproliferation [KRT16 staining (27)], T-cell numbers (CD3 staining), and DC numbers (ITGAX (CD11c) staining) were decreased in psoriasis lesional skin after 12 weeks of anti-IL-17A monoclonal antibody injections (posttreatment) compared to pretreatment psoriasis lesional skin of the same patients (Figure 2A, $p < 0.05$).

Reflecting the decreased T-cell numbers by systemic IL-17A blockade, total skin transcriptome of T17 responses (*IL17A*, *IL26*, *IL12B*, and *IL20*) (3, 28), T-cell regulation (*IL24* and *CTLA4*) (29, 30), resident memory T-cells (Trms) [*ITGAE* (*CD103*)] (31) and regulatory T-cells (Tregs) (*FOXP3*) (32) was decreased in posttreatment psoriasis lesional skin compared to pretreatment psoriasis lesional skin in both microarray and RT-PCR experiments (Figures 2B, C, $p < 0.05$).

Reflecting the decreased DC numbers by systemic IL-17A blockade, total skin transcriptome of T17 cell-stimulating DCs (*IL23A*) (3) and mature DCs (*LAMP3* (*DC-LAMP*), *CD274* (*PD-L1*) and *IDO1*) (16, 33, 34) were decreased in posttreatment psoriasis lesional skin compared to pretreatment psoriasis lesional skin in both microarray and RT-PCR experiments (Figures 2B, C, $p < 0.05$).

Reflecting the decreased KC hyperproliferation by systemic IL-17A blockade, total skin transcriptome of KC cytokines that stimulate DCs and T-cells in feed-forward mechanisms (*S100A8* and *IL36G*) (3) was decreased in posttreatment psoriasis lesional skin compared to pretreatment psoriasis lesional skin in both microarray and RT-PCR experiments (Figures 2B, C, $p < 0.05$).

In contrast, total skin transcriptome of Treg-specific cytokine that mediates immune tolerance [*IL34* (35–37)], an anti-inflammatory cytokine that inhibits innate immune signaling [*IL37* (38, 39)], and KC stem cell marker of quiescence [*KRT15* (40)] were increased in posttreatment psoriasis lesional skin compared to pretreatment psoriasis lesional skin in both microarray and RT-PCR experiments, albeit the decreased T-cell, DC, and KC numbers (Figures 2B, C, $p < 0.05$).

IL-17A blockade reduces type 17 T-cell signatures in psoriasis lesional skin at single-cell cluster levels.

We next studied how systemic IL-17A blockade modified transcriptome of T17 cells and transcriptome of Tregs differently with single-cell analyses. Clustering analysis of 40,026 single cells from 28 samples of 20 subjects identified clusters of NK cells, CD161$^+$ T-cells, CD8$^+$ T-cells, CD4$^+$ T-cells, Tregs, mature DCs, semimature DCs, melanocytes, KCs in different layers of Stratum (S.) corneum, S. granulosum, S. spinosum, S. basale, endothelial cells, and fibroblasts without subclustering (Figure 3A and Supplementary Figure 2). The identity of each cluster was determined by the expression of established cell type markers (Figure 3B). To characterize T17 cell transcriptome in psoriasis skin, we segregated T-cell (CD161$^+$ T-cell, CD8$^+$ T-cell, CD4$^+$ T-cell, and Treg) clusters in the scRNA-seq data and tested if psoriasis T-cells express more T17 cell genes than control T-cells. The expression of T17 cell genes [*KLRB1* (*CD161*) (41), *IL17A*, *IL17F*, and *IL26* (42, 43)], a cytokine that represents a particularly T17-specific abnormality and positively associates with psoriasis severity (*CXCL13*) (44–47), and Treg genes (*FOXP3*, *IL2RA* (*CD25*), and *TIGIT*) was increased in pretreatment psoriasis lesional skin T-cells compared to control skin T-cells (Figure 4A, $p < 0.05$).

When we defined T17 cells as T-cell cluster cells expressing *IL17A* and/or *IL17F*, the majority of T17 cells were within the CD161$^+$ T-cell cluster. 5.5% of total T-cells were CD161$^+$ T-cell cluster cells and 15.0% of CD161$^+$ T-cell cluster cells were T17 cells (Figure 4C). 76.5% of *IL17A*$^+$ T-cells, 61.4% of *IL17F*$^+$ T-cells, and 100% of *IL17A*$^+$ *IL17F*$^+$ T-cells were within the CD161$^+$ T-cell cluster in pretreatment psoriasis lesional skin. In addition, 84.7% of CD161$^+$ T-cell cluster cells expressed *CXCL13*, while only 1.6% of

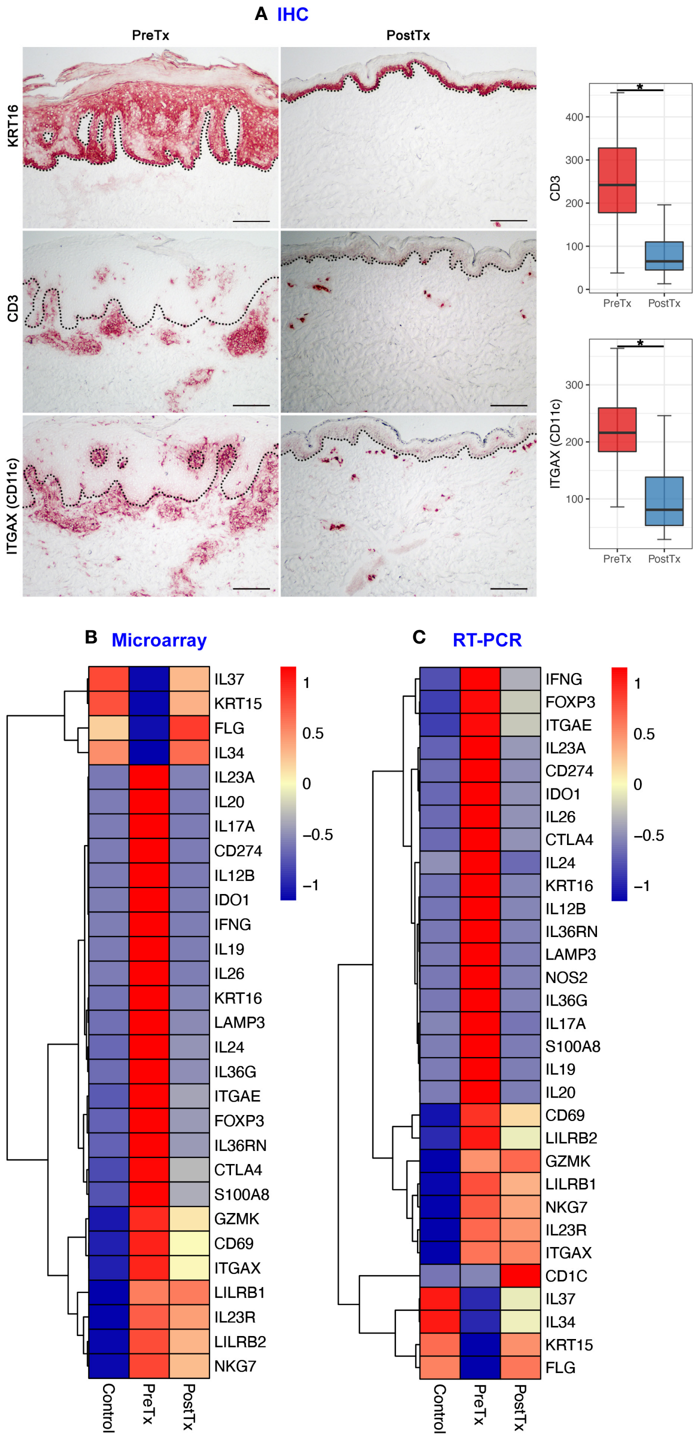

FIGURE 2

IL-17A blockade reduces T-cell signatures, dendritic cell signatures, and keratinocyte hyperproliferation signatures and increases regulatory molecular expression in psoriasis lesional skin at total skin transcriptome levels. **(A)** Immunohistochemistry of keratinocyte hyperproliferation (KRT16), CD3$^+$ T-cells, and ITGAX (CD11c)$^+$ dendritic cells (DCs) before (PreTx) and after (PostTx) 12 weeks of systemic anti-IL-17A monoclonal antibody (secukinumab) administration. Bar graphs display CD3$^+$ T-cell (n = 40 for PreTx and n = 21 for PostTx) and ITGAX (CD11c)$^+$ DC (n = 40 for PreTx and n = 20 for PostTx) number changes induced by systemic anti-IL-17A blockade. *$p < 0.05$. Black dotted lines delineate the junction between the epidermis and dermis (Scale bar = 200 μm). **(B, C)**, Differentially expressed genes (DEGs) between PreTx and PostTx at total skin transcriptome levels. DEGs that are relevant to psoriasis pathogenesis and statistically significant in both microarray (B, fold change ratio > 2 and $p < 0.05$) and RT-PCR (C, $p < 0.05$) experiments are displayed.

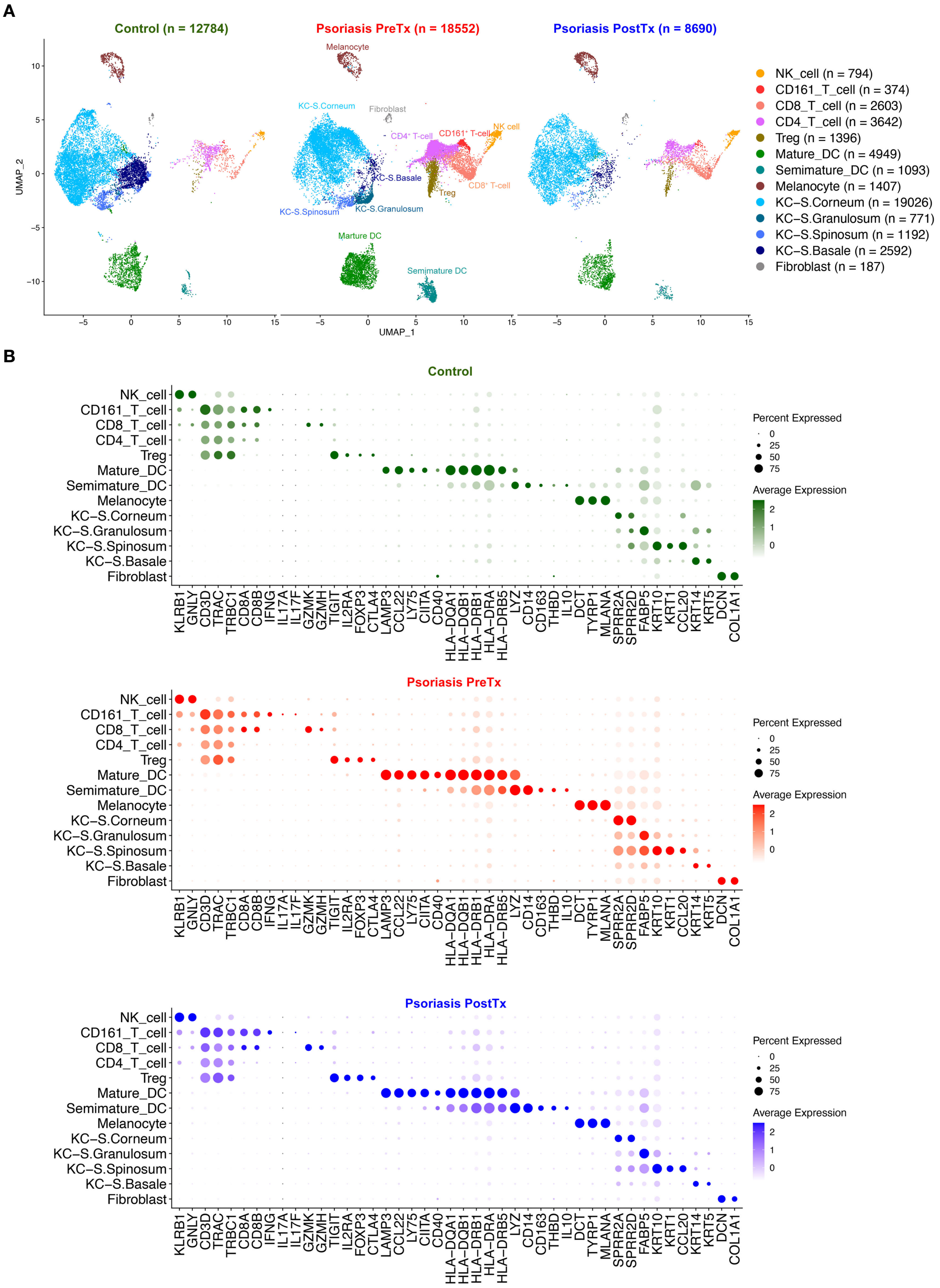

FIGURE 3
Human skin immune cell subset single-cell transcriptome comparison between psoriasis pretreatment (PreTx), psoriasis posttreatment (PostTx), and control (healthy volunteers). Psoriasis posttreatment is after anti-IL-17A monoclonal antibody (secukinumab) subcutaneous injections at a dose of 300 mg at baseline and weeks 1, 2, 3, 4, 8, and 12 (12 weeks of injections). **(A)** The Uniform Manifold Approximation and Projection plot (UMAP). **(B)** Dot plots displaying expression levels of cluster-defining genes.

$CD8^+$ T-cell cluster cells, 2.5% of $CD4^+$ T-cell cluster cells, and 0.6% of Treg cluster cells expressed *CXCL13* in pretreatment psoriasis lesional skin (Figure 4B).

After systemic IL-17A blockade (12 weeks of anti-IL-17A monoclonal antibody injections), the expression of *IL17A* in the $CD161^+$ T-cell cluster was decreased to zero in psoriasis lesional skin (Figures 4B, C, and Supplementary Table 3; $p < 0.05$). Although anti-IL-17A monoclonal antibody does not directly target IL-17F, the expression of *IL17F* was also decreased in the $CD161^+$ T-cell cluster in psoriasis lesional skin after IL-17A blockade (Figure 4B and Supplementary Table 3, $p < 0.05$). When all T-cell cluster cells were considered, IL-17A blockade decreased 95% of *IL17F*$^+$ T-cells (Figure 4C).

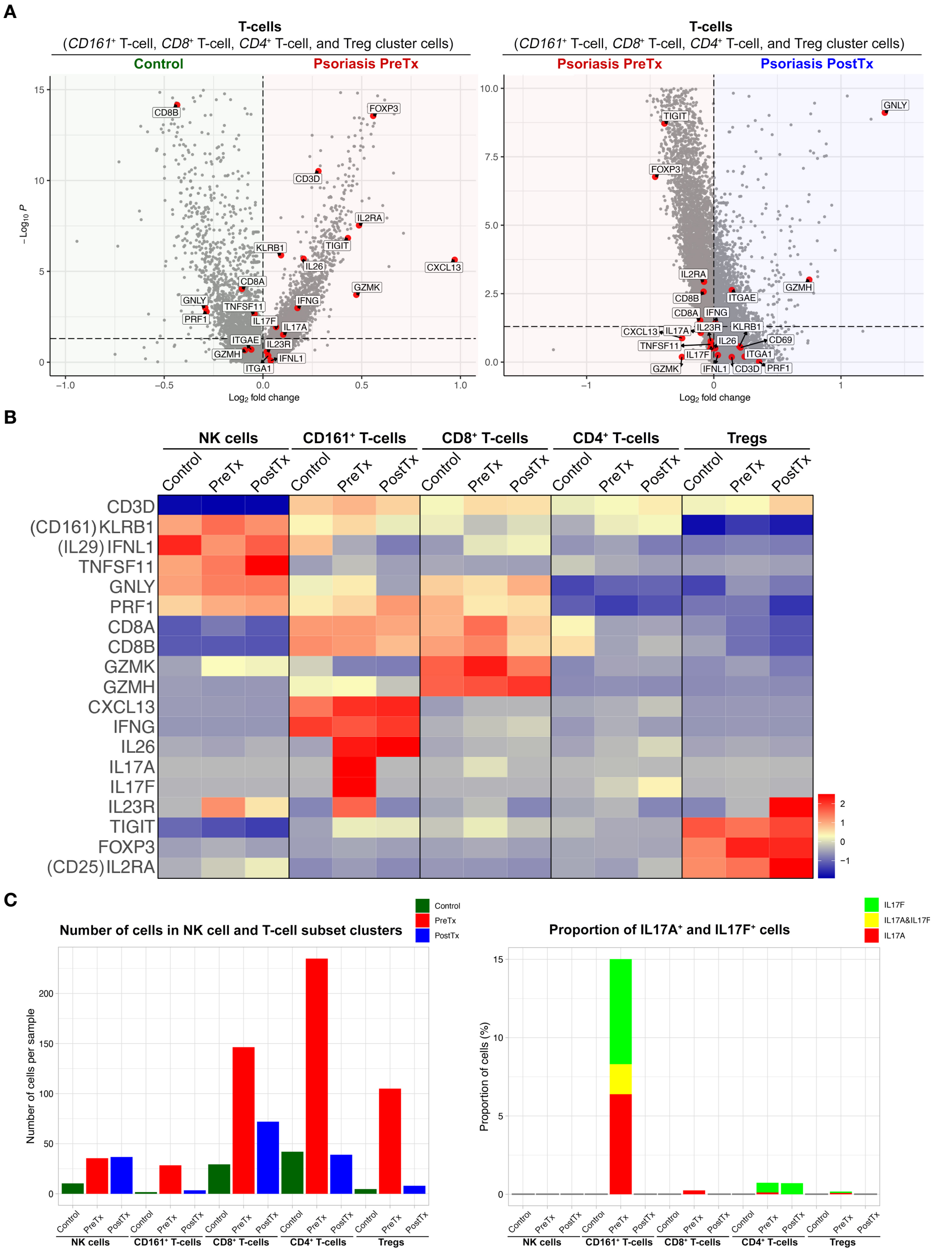

FIGURE 4
IL-17A blockade reduces Type 17 T-cell signatures and modifies regulatory T-cell signatures in psoriasis lesional skin at single-cell cluster levels. **(A)** Volcano plots displaying differentially expressed genes between control skin T-cells, psoriasis lesional skin T-cells before treatment (PreTx), and psoriasis lesional skin T-cells after 12 weeks of systemic anti-IL-17A monoclonal antibody (secukinumab) administration (PostTx). **(B)** Heatmap illustrating the average gene expression in clusters of NK cell and T-cell subsets, split by psoriasis PreTx, psoriasis PostTx, and control skin. **(C)** (Left) Number of cells per sample and (Right) proportion of *IL17A*$^+$ and *IL17F*$^+$ cells in NK cell and T-cell subset clusters, split by control, psoriasis PreTx, and psoriasis PostTx.

IL-17A blockade increases regulatory dendritic cell signatures in psoriasis lesional skin at single-cell cluster levels

We next studied how systemic IL-17A blockade modified transcriptome of different DC subsets that we previously described in our prior single-cell studies of human psoriasis skin (16). When we segregated DC subset (mature DC and semimature DC) clusters in the scRNA-seq data and compared their transcriptome, mature DCs in psoriasis skin were characterized by relatively high expression of MHC class II molecules (*HLA-DRA* and *HLA-DPB1*) and upregulated maturation markers [*CD86* (48) and *DC-LAMP* (*LAMP3*) (49)] (16) (Figure 5A). In contrast, semimature DCs in psoriasis skin were characterized by relatively low expression of MHC class II molecules (*HLA-DRA* and *HLA-DPB1*) and upregulated inflammatory monocyte receptor markers [*CD14* and *CD64* (*FCGR1A*) (50)] (Figure 5B, $p < 0.05$). Semimature DCs were characterized as regulatory DCs expressing high levels of *IL10*, *THBD* (*BDCA-3*), *LILRB2*, and

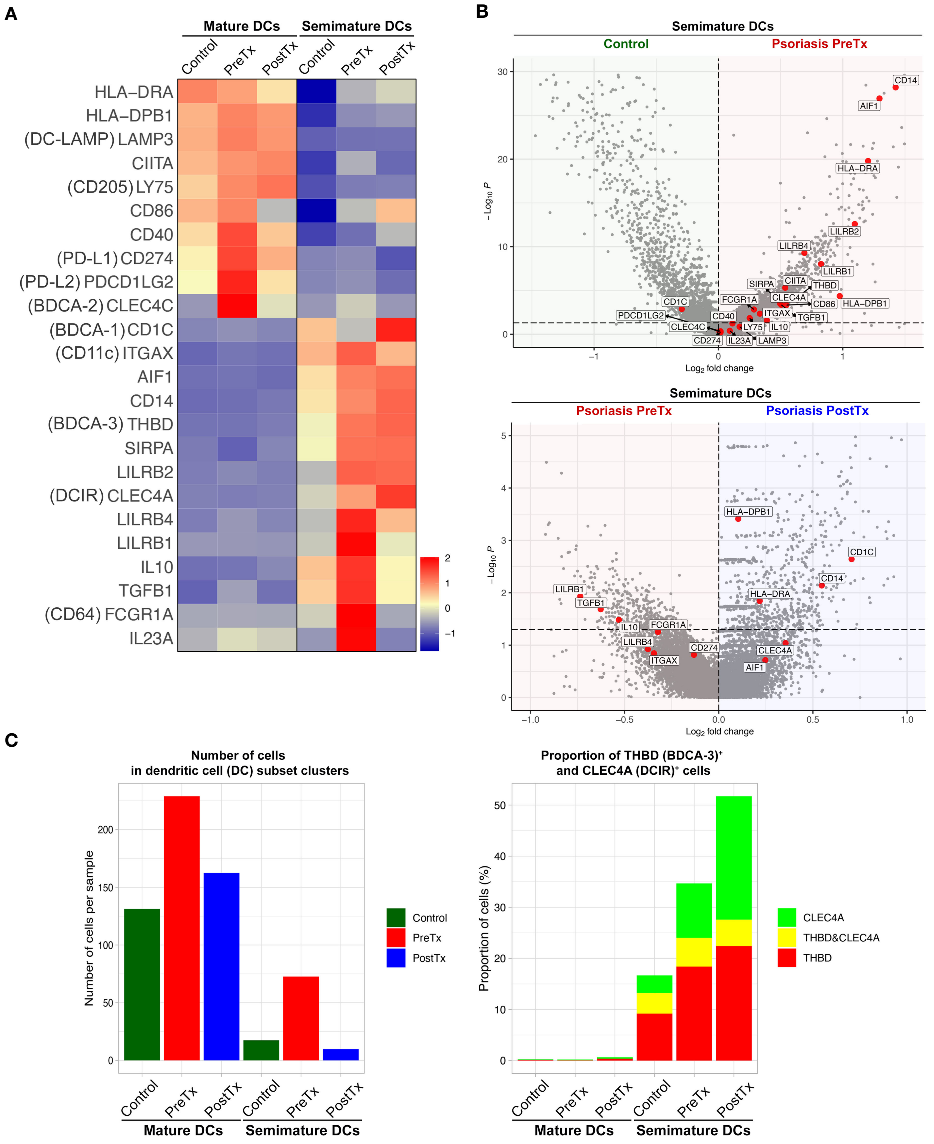

FIGURE 5

IL-17A blockade increases regulatory dendritic cell signatures in psoriasis lesional skin at single-cell cluster levels. **(A)** Heatmap illustrating the average gene expression in clusters of mature DCs and semimature DCs, split by control skin DCs, psoriasis lesional skin DCs before treatment (PreTx), and psoriasis lesional skin DCs after 12 weeks of systemic anti-IL-17A monoclonal antibody (secukinumab) administration (PostTx). **(B)** Volcano plots displaying differentially expressed genes between control skin DCs, psoriasis PreTx DCs, and psoriasis PostTx DCs. **(C)** (Left) Number of cells per sample and (Right) proportion of *THBD* (*BDCA-3*)$^+$ and *CLEC4A* (*DCIR*)$^+$ cells in DC subset clusters, split by control, psoriasis PreTx, and psoriasis PostTx.

CLEC4A (*DCIR*) (51, 52) (Figure 5B, $p < 0.05$). We previously reported that both mature and semimature DCs in psoriasis lesional skin expressed high levels of *IL23A* compared to control skin (16) (Figure 5A). Our current study showed that the expression of *IL23A* in both mature and semimature DCs was decreased after systemic IL-17A blockade in posttreatment psoriasis lesional skin compared to pretreatment psoriasis lesional skin (Figure 5A, $p < 0.05$).

Reflecting the decreased DC numbers after systemic IL-17A blockade in the immunohistochemistry experiment (Figure 2A), both mature and semimature DC numbers were decreased in posttreatment psoriasis lesional skin compared to pretreatment psoriasis lesional skin in scRNA-seq data (Figure 5C). Although semimature DC cell numbers were decreased after systemic IL-17A blockade, regulatory transcriptome expression of the semimature DCs was increased after systemic IL-17A blockade – 1) The proportion of semimature DCs expressing regulatory DC markers of *BDCA-3* (*THBD*) (51) and *DCIR* (*CLEC4A*) (52) was increased in posttreatment psoriasis lesional skin compared to pretreatment psoriasis lesional skin (Figure 5C). 2) The expression of *CD1C* and *CD14*, which are genes of a CD1c$^+$ CD14$^+$ DC subset that suppresses antigen-specific T-cell responses (53, 54), was increased in posttreatment psoriasis lesional skin semimature DCs compared to pretreatment psoriasis lesional skin semimature DCs (Figure 5B, $p < 0.05$).

IL-17A blockade reduces IL-17-driven inflammatory mediator expression in suprabasal keratinocytes and increases keratinocyte stem cell marker expression in basal keratinocytes in psoriasis lesional skin at single-cell cluster levels

We next studied how systemic IL-17A blockade modified transcriptome of KCs in different layers of epidermis. We segregated KC clusters representing different layers of the epidermis (S. corneum, S. granulosum, S. spinosum, and S. basale) and tested if psoriasis KCs express more IL-17-driven inflammatory mediators than control KCs. The expression of inflammatory mediators induced by IL-17 in keratinocytes (*IL36G*, *S100A8*, *DEFB4A*, and *DEFB4B* (3)) was increased in pretreatment psoriasis lesional skin KCs compared to control skin KCs (Figure 6A, $p < 0.05$). After systemic IL-17A blockade, the expression of those inflammatory mediators (*IL36G*, *S100A8*,

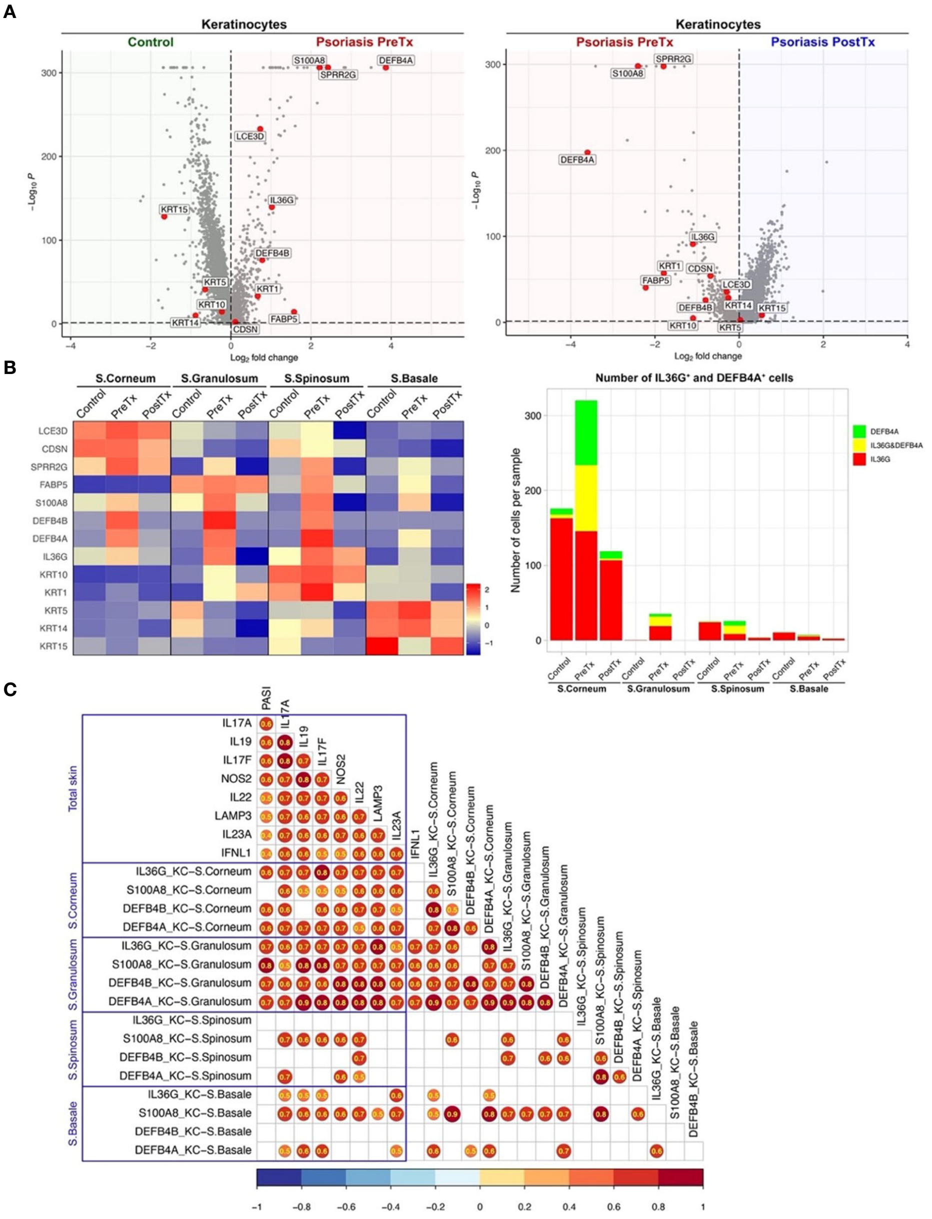

FIGURE 6

IL-17A blockade reduces IL-17-driven inflammatory mediator expression in suprabasal keratinocytes and increases keratinocyte stem cell marker expression in basal keratinocytes in psoriasis lesional skin at single-cell cluster levels. **(A)** Volcano plots displaying differentially expressed genes between control skin KCs, psoriasis lesional skin KCs before treatment (PreTx), and psoriasis lesional skin KCs after 12 weeks of systemic anti-IL-17A monoclonal antibody (secukinumab) administration (PostTx). **(B)** Heatmap illustrating the average gene expression in KC clusters representing different layers of epidermis (Stratum (S.) corneum, S. granulosum, S. spinosum, and S. basale), split by psoriasis PreTx, psoriasis PostTx, and control skin. Bar graphs displaying *IL36G*$^+$ and *DEFB4A*$^+$ cell numbers in KC clusters, split by control, psoriasis PreTx, and psoriasis PostTx. **(C)** Correlation plots displaying inter-correlations between Psoriasis Area-and-Severity Index (PASI), IL-23/T17 axis gene expression in total skin, and IL-17-driven KC inflammatory mediator expression in different epidermal layers. Circled numbers = correlation coefficients with $p < 0.05$.

DEFB4A, and *DEFB4B*) was decreased in posttreatment psoriasis lesional skin KCs compared to pretreatment psoriasis lesional skin KCs (Figure 6A, $p < 0.05$).

When we compared KC transcriptome in different epidermal layers, the expression of IL-17-driven inflammatory mediators (*IL36G*, *S100A8*, *DEFB4A*, and *DEFB4B*) was localized to suprabasal layers (S. corneum, S. granulosum, and S. spinosum) in pretreatment psoriasis lesional skin (Figure 6B). A high proportion of *IL36G* expressing KCs co-expressed *DEFB4A* in suprabasal layers (37.7% in S. corneum, 39.9% in S. granulosum and 56.7% in S. spinosum). Reflecting that inflammation in the upper layers of the epidermis determines psoriasis disease severity (erythema, thickness, and scaling components of Psoriasis Area-and-Severity Index (PASI)), KC expression of *IL36G*, *DEFB4A*, and *DEFB4B* in S. corneum and S. granulosum was correlated with PASI (Figure 6C, $p < 0.05$). After IL-17A blockade, KC expression of *IL36G*, *S100A8*, *DEFB4A*, and *DEFB4B* in S. corneum and S. granulosum decreased in posttreatment psoriasis lesional skin compared to pretreatment psoriasis lesional skin (Figure 6B and Supplementary Table 4, $p < 0.05$). The number of *IL36G* and/or *DEFB4A* expressing KCs in S. corneum and S. granulosum was decreased by 3 times from pretreatment psoriasis lesional skin to posttreatment psoriasis lesional skin (Figure 6B).

In contrast to the inflammatory mediators induced by IL-17, the expression of the KC stem cell marker (*KRT15*) was decreased in pretreatment psoriasis lesional skin KCs compared to control skin KCs (Figure 6A, $p < 0.05$). After systemic IL-17A blockade, the expression of *KRT15* was increased in posttreatment psoriasis lesional skin KCs compared to pretreatment psoriasis lesional skin KCs (Figure 6A, $p < 0.05$). The expression of *KRT15* in pretreatment psoriasis lesional skin was localized to the basal layer in pretreatment psoriasis lesional skin (Figure 6B). After IL-17A blockade, KC expression of *KRT15* in S. basale increased in posttreatment psoriasis lesional skin compared to pretreatment psoriasis lesional skin (Figure 6B and Supplementary Table 4, $p < 0.05$).

Discussion

In this study, we applied multi-omics to human psoriasis skin providing a unique opportunity to compare the transcriptome of total skin (microarray and RT-PCR) and the transcriptome of skin immune cell subsets (scRNA-seq) generated from the same tissues with different techniques. When skin transcriptome changes by systemic IL-17A blockade were compared between total skin and skin immune cell subsets, IL-23/T17 axis cytokine expression was downregulated at both total skin levels and skin immune cell subset levels. The quantity of overall immune cells, including both pathogenic and regulatory subsets, was decreased in posttreatment psoriasis lesional skin compared to pretreatment psoriasis lesional skin (Figure 2A). Since the IL-23/T17 axis cytokine sources (T-cells, DCs, and KCs) were decreased in the predetermined volume of skin biopsy tissue (6 mm punch), total skin transcriptome of IL-23/T17 axis cytokines (*IL17A* and *IL26* from T-cells, *IL23A*, *IL12B*, and *IL20* from DCs, and *S100A8* and *IL36* from KCs) was decreased in posttreatment psoriasis lesional skin compared to pretreatment psoriasis lesional skin (Figure 2B).

Paired skin immune cell subset transcriptome analyses with scRNA-seq further elucidated which immune cell subsets were expressing the IL-23/T17 axis cytokines and how their transcriptome was affected by systemic IL-17A blockade. For T-cell subsets, our study showed that 1) CD161$^+$ T-cell cluster was the major T17 cell cluster, but only 15.0% of CD161$^+$ T-cell cluster cells were T17 cells. Single-cell clustering of immune cell subsets presented in this study was consistent with our previous single-cell paper (16), but T-cell clustering evolved as we increased the total number of single-cells for dimension reduction analyses from 23,220 to 40,026 (Figure 3). Our new dimension reduction and clustering analyses revealed that the majority of T17 cells in psoriasis skin were contained in the CD161$^+$ T-cell cluster consistent with previous CD161$^+$ T-cell studies (55) (Figure 4C). CD161 is a marker of all human T-cell subsets with the ability to produce IL-17, and it has been reported that IL-17-producing cells exclusively originate from naïve CD161$^+$ T-cell precursors (56). In psoriasis, it has been reported that more CD161$^+$ T-cells are present in psoriasis lesional skin compared to psoriasis nonlesional skin or normal skin (57, 58), and the greater frequency of CD161$^+$ T-cells are present in prepsoriatic skin compared to normal skin, suggesting the role of CD161$^+$ T-cells in the initial development of psoriatic lesions (57, 59). 2) CD161$^+$ T-cell cluster was the major T-cell subset cluster expressing *CXCL13*, which is a cytokine that represents a particularly T17-specific abnormality and positively associates with psoriasis severity (44–47) (Figure 4B). In our single-cell dataset, 70.2% of *CXCL13*-expressing cells was T-cell cluster cells, and 73.2% of *CXCL13*-expressing T-cell cluster cells were CD161$^+$ T-cell cluster cells.

For single-cell transcriptome modification of the IL-23/T17 cell axis induced by systemic IL-17A blockade, our study showed that 1) The expression of *IL23A* in dendritic cell subsets in psoriasis skin lesions was downregulated by systemic IL-17A blockade, potentially by blocking the entire feed-forward inflammatory amplification loop between T-cells, DCs, and KCs (Figure 5A), 2) Systemic IL-17A blockade removed 100% of *IL17A*-expressing T-cells. Although anti-IL-17A monoclonal antibody does not directly target IL-17F, systemic IL-17A blockade also removed 95% of *IL17F*-expressing T-cells in psoriasis skin, potentially mediated by IL-23 reduction in dendritic cells (Figure 4C). 2) The expression of IL-17-driven inflammatory mediators (*IL36G*, *S100A8*, *DEFB4A*, and *DEFB4B*) in KCs was localized to suprabasal KCs (Figure 6B). The expression of those IL-17-driven inflammatory mediators in suprabasal KCs was correlated with psoriasis severity (Figure 6C) and was downregulated by systemic IL-17A blockade (Figure 6B).

Mapping regulatory DC transcriptome is challenging because a master regulator of regulatory DCs is not identified. All regulatory DC markers of *BDCA-3* (*THBD*) (51), *DCIR* (*CLEC4A*) (52), *LILRB1* (60), *LILRB2* (*ILT4*) (61), *LILRB4* (*ILT3*) (61) and combination of *CD1C* and *CD14* (53, 54) are surface markers that are not specific for DCs. Since the markers are expressed in other skin cells, total skin transcriptome changes of those markers did not represent transcriptome changes of regulatory DCs (Figure 2B). Instead, skin immune cell subset transcriptome analyses of the semimature DC cluster, which we previously reported as regulatory DCs in psoriasis skin (16), showed regulatory transcriptome promotion by systemic IL-17A blockade in regulatory DCs – 1) The proportion of semimature DCs expressing regulatory DC markers of *BDCA-3* (*THBD*) (51) and *DCIR* (*CLEC4A*) (52) was increased in posttreatment psoriasis lesional skin compared to pretreatment psoriasis lesional skin (Figure 5C). 2) The expression of *CD1C* and *CD14* [markers of CD1c$^+$ CD14$^+$ DC subset that suppresses antigen-specific T-cell responses (53, 54)] was increased in posttreatment psoriasis lesional skin semimature DCs compared to pretreatment psoriasis lesional skin semimature DCs (Figure 5B, $p < 0.05$).

Clinically, when moderate-to-severe psoriasis patients were treated with systemic anti-IL-17A monoclonal antibody (secukinumab) administration for 52 weeks and then stopped the treatment, 16.0% of them maintained response after treatment withdrawal over the next 52 weeks without need for retreatment (12, 13). Our study may explain how those patients restored immune tolerance to psoriasis autoantigens that may have prevented recurrence of psoriasis off the treatment. In addition to the co-modulation of IL-17A and IL-17F by direct and indirect effects on T-cells including IL-23 reduction in dendritic cells, systemic IL-17A blockade may have effectively modified regulatory transcriptome of regulatory DCs (Figures 5B, 6C) in those patients.

Our study has limitations: 1) Our single-cell analysis approach relied on immune cell emigration from the skin biopsies in culture. Whilst this is a recognized approach to isolate immune cells from the skin (16), some skin resident immune cells may not be migratory and may have been excluded in the immune cell subset analyses. 2) The unique challenges of scRNA-seq data analysis, including the sparsity of the scRNA-seq dataset and the dropout of lowly expressed genes, are widely acknowledged (62–67). In particular, differentially expressed gene analyses of scRNA-seq data are biased towards highly expressed genes (68), while the target genes investigated in the study (T17 axis cytokines) are lowly expressed genes in specific T-cell or DC subsets (16). To maximize the recovery of differentially expressed genes, we used a Wilcoxon rank sum test at total immune cell (T-cell, DC, or KC) levels and a spatial autocorrelation analysis (24, 25) at immune cell subset levels. However, we observed the discrepancies of IL23R status between the average expression visualized in the heatmap (Figure 4B) and the spatial autocorrelation test results (Supplementary Table 3) in Treg cluster analyses. The average expression of IL23R was higher in posttreatment Tregs compared to pretreatment Tregs (Figure 4B) but the difference was not statistically significant in the spatial autocorrelation test. 3) The transcriptome analyses were not validated by functional studies at protein levels. 4) Different body sites can harbor different microbes and may have different immune cell compositions, but the location of skin biopsies was not matched between comparison groups (Skin biopsy location of each sample is listed in Supplementary Table 1).

Conclusion

Our study provides an early demonstration that systemic anti-IL-17A monoclonal antibody administration blocks the entire IL-23/T17 cell axis depleting or modulating 100% of *IL17A*$^+$ T17 cells and 95% of *IL17F*$^+$ T17 cells at single-cell levels (Supplementary Figure 3). In addition, systemic anti-IL-17A monoclonal antibody administration promotes regulatory DCs, while strongly downregulating the expression of *IL23A* in dendritic cells in psoriasis skin lesions. Thus, we hypothesize that a monoclonal blockade of pathogenic T-cells, such as an IL-17A blockade or an IL-23p19 blockade, may induce expansion of regulatory immune cells subsets or expression of cytokines involved in skin homeostasis (9, 10, 69). To further test the hypothesis, we are currently conducting a clinical trial of short-term anti-IL-23p19 monoclonal antibody administration to induce long-term disease remission that incorporates scRNA-seq analyses of human skin before/after the monoclonal antibody administration (NCT04630652). We are hoping to better understand the regulatory immune cell promotion by blocking the IL-23/T17 cell axis and develop personalized medicine approaches to cure psoriasis without recurrence.

Data availability statement

The datasets presented in this study can be found in online repositories. The names of the repository/repositories and accession number(s) can be found below: GSE183047 and GSE226244 (GEO).

Ethics statement

The study protocol and informed consent were approved by the Institutional Review Board of the Rockefeller University, New York, NY, USA. The study was conducted in accordance with Good Clinical Practice and the Declaration of Helsinki, and all subjects provided written informed consent before entering the study. The studies were conducted in accordance with the local legislation and institutional requirements. The participants provided their written informed consent to participate in this study.

Author contributions

All the authors have made substantial contributions to the acquisition, analysis, or interpretation of the data. In addition, all the authors have contributed to the drafting or editing of the manuscript and gave their approval for the version submitted. JK and JGK designed the clinical trial, experiments, and laboratory protocols. JK, NK, IC, KK, and VC contributed to patient consent and care. JL and XL conducted single-cell and microarray studies. DR conducted immunohistochemistry studies. JK, YK, SG, WZ, JC, and JGK interpreted the data. JK and JGK verified all the underlying data. All authors contributed to the article and approved the submitted version.

Funding

This work was supported, in part, by grant no. UL1TR001866 from the National Center for Advancing Translational Sciences

(NCATS), National Institutes of Health (NIH) Clinical and Translational Science Award (CTSA) program. JK was supported by NIAMS K23 Career Development Award (K23AR080043). JK was also supported by the Group for Research and Assessment of Psoriasis and Psoriatic Arthritis (GRAPPA) pilot grant award.

Conflict of interest

JK has received research funds from AbbVie and Novartis. JGK. has received research support from Pfizer, Amgen, Janssen, Lilly, Merck, Novartis, Kadmon, Dermira, Boehringer, Innovaderm, Kyowa, BMS, Serono, BiogenIdec, Delenex, AbbVie, Sanofi, Baxter, Paraxel, Xenoport, and Kineta.

The remaining authors declare that the research was conducted in the absence of any commercial or financial relationships that could be construed as a potential conflict of interest.

Publisher's note

Supplementary material

The Supplementary Material for this article can be found online at: https://www.frontiersin.org/articles/10.3389/fimmu.2023.1250504/full#supplementary-material

SUPPLEMENTARY FIGURE 1

The Uniform Manifold Approximation and Projection plot (UMAP) of the initial non-linear dimension reduction and clustering analysis **(A)** and the final clusters for the downstream differential expression testing **(B)**.

SUPPLEMENTARY FIGURE 2

Alluvial diagram visualizing how individual immune cells in single-cell RNA sequencing data are allocated across categorical dimensions. Left column: Patients -10 psoriasis patients and 10 control healthy volunteers. Middle column: Treatment - psoriasis pretreatment (Psoriasis_preTx), psoriasis posttreatment (Psoriasis_postTx) after weeks 12, 24, and 48 of systemic anti-IL-17A administration, and control, Right column: immune cell clusters – NK cell, CD161 T-cell, CD8 T-cell, CD4 T-cell, regulatory T-cell (Treg), mature dendritic cell (DC), semimature DC, melanocyte, Keratinocyte in S (Stratum) corneum, S. granulosum, S. spinosum, S. basale, and fibroblast clusters.

SUPPLEMENTARY FIGURE 3

A summary of different transcriptomic impacts of anti-IL-17A blockade on human psoriasis skin at the levels of total skin and clusters of T-cell, dendritic cell, and keratinocyte subsets. DC = dendritic cell, KC = keratinocyte.

References

1. Rachakonda TD, Schupp CW, Armstrong AW. Psoriasis prevalence among adults in the United States. *J Am Acad Dermatol* (2014) 70:512–6. doi: 10.1016/j.jaad.2013.11.013

2. Armstrong AW, Mehta MD, Schupp CW, Gondo GC, Bell SJ, Griffiths CEM. Psoriasis prevalence in adults in the United States. *JAMA Dermatol* (2021) 157:940–6. doi: 10.1001/jamadermatol.2021.2007

3. Kim J, Krueger JG. Highly effective new treatments for psoriasis target the IL-23/type 17 T cell autoimmune axis. *Annu Rev Med* (2017) 68:255–69. doi: 10.1146/annurev-med-042915-103905

4. Sterry W, Strober BE, Menter AInternational Psoriasis Council. Obesity in psoriasis: the metabolic, clinical and therapeutic implications. Report of an interdisciplinary conference and review. *Br J Dermatol* (2007) 157:649–55. doi: 10.1111/j.1365-2133.2007.08068.x

5. Gisondi P, Tessari G, Conti A, Piaserico S, Schianchi S, Peserico A, et al. Prevalence of metabolic syndrome in patients with psoriasis: a hospital-based case-control study. *Br J Dermatol* (2007) 157:68–73. doi: 10.1111/j.1365-2133.2007.07986.x

6. Cohen AD, Dreiher J, Shapiro Y, Vidavsky L, Vardy DA, Davidovici B, et al. Psoriasis and diabetes: a population-based cross-sectional study. *J Eur Acad Dermatol Venereol* (2008) 22:585–9. doi: 10.1111/j.1468-3083.2008.02636.x

7. Armstrong EJ, Harskamp CT, Armstrong AW. Psoriasis and major adverse cardiovascular events: a systematic review and meta-analysis of observational studies. *J Am Heart Assoc* (2013) 2:e000062. doi: 10.1161/JAHA.113.000062

8. Gelfand JM, Troxel AB, Lewis JD, Kurd SK, Shin DB, Wang X, et al. The risk of mortality in patients with psoriasis: results from a population-based study. *Arch Dermatol* (2007) 143:1493–9. doi: 10.1001/archderm.143.12.1493

9. Krueger JG, Ferris LK, Menter A, Wagner F, White A, Visvanathan S, et al. Anti-IL-23A mAb BI 655066 for treatment of moderate-to-severe psoriasis: Safety, efficacy, pharmacokinetics, and biomarker results of a single-rising-dose, randomized, double-blind, placebo-controlled trial. *J Allergy Clin Immunol* (2015) 136:116–124.e7. doi: 10.1016/j.jaci.2015.01.018

10. Kim J, Lee J, Hawkes JE, Li X, Kunjravia N, Rambhia D, et al. Secukinumab improves mild-to-moderate psoriasis: A randomized, placebo-controlled exploratory clinical trial. *J Am Acad Dermatol* (2023) 88:428–30. doi: 10.1016/j.jaad.2022.04.060

11. Harden JL, Johnson-Huang LM, Chamian MF, Lee E, Pearce T, Leonardi CL, et al. Humanized anti-IFN-γ (HuZAF) in the treatment of psoriasis. *J Allergy Clin Immunol* (2015) 135:553–6. doi: 10.1016/j.jaci.2014.05.046

12. Langley RG, Sofen H, Dei-Cas I, Reich K, Sigurgeirsson B, Warren RB, et al. Secukinumab long-term efficacy and safety in psoriasis through to year 5 of treatment: results of a randomized extension of the phase III ERASURE and FIXTURE trials. *Br J Dermatol* (2023) 188:198–207. doi: 10.1093/bjd/ljac040

13. Blauvelt A, Reich K, Warren RB, Szepietowski JC, Sigurgeirsson B, Tyring SK, et al. Secukinumab re-initiation achieves regain of high response levels in patients who interrupt treatment for moderate to severe plaque psoriasis. *Br J Dermatol* (2017) 177:879–81. doi: 10.1111/bjd.15656

14. Papp KA, Blauvelt A, Bukhalo M, Gooderham M, Krueger JG, Lacour J-P, et al. Risankizumab versus ustekinumab for moderate-to-severe plaque psoriasis. *N Engl J Med* (2017) 376:1551–60. doi: 10.1056/NEJMoa1607017

15. Gordon KB, Armstrong AW, Foley P, Song M, Shen Y-K, Li S, et al. Guselkumab efficacy after withdrawal is associated with suppression of serum IL-23-regulated IL-17 and IL-22 in psoriasis: VOYAGE 2 study. *J Invest Dermatol* (2019) 139:2437–2446.e1. doi: 10.1016/j.jid.2019.05.016

16. Kim J, Lee J, Kim HJ, Kameyama N, Nazarian R, Der E, et al. Single-cell transcriptomics applied to emigrating cells from psoriasis elucidate pathogenic versus regulatory immune cell subsets. *J Allergy Clin Immunol* (2021) 148:1281–92. doi: 10.1016/j.jaci.2021.04.021

17. Hao Y, Hao S, Andersen-Nissen E, Mauck WM 3rd, Zheng S, Butler A, et al. Integrated analysis of multimodal single-cell data. *Cell* (2021) 184:3573–3587.e29. doi: 10.1016/j.cell.2021.04.048

18. Stuart T, Butler A, Hoffman P, Hafemeister C, Papalexi E, Mauck WM 3rd, et al. Comprehensive integration of single-cell data. *Cell* (2019) 177:1888–1902.e21. doi: 10.1016/j.cell.2019.05.031

19. Satija R, Farrell JA, Gennert D, Schier AF, Regev A. Spatial reconstruction of single-cell gene expression data. *Nat Biotechnol* (2015) 33:495–502. doi: 10.1038/nbt.3192

20. Der E, Ranabothu S, Suryawanshi H, Akat KM, Clancy R, Morozov P, et al. Single cell RNA sequencing to dissect the molecular heterogeneity in lupus nephritis. *JCI Insight* (2017) 2:e93009. doi: 10.1172/jci.insight.93009

21. Der E, Suryawanshi H, Morozov P, Kustagi M, Goilav B, Ranabothu S, et al. Tubular cell and keratinocyte single-cell transcriptomics applied to lupus nephritis reveal type I IFN and fibrosis relevant pathways. *Nat Immunol* (2019) 20:915–27. doi: 10.1038/s41590-019-0386-1

22. He H, Suryawanshi H, Morozov P, Gay-Mimbrera J, Del Duca E, Kim HJ, et al. Single-cell transcriptome analysis of human skin identifies novel fibroblast

subpopulation and enrichment of immune subsets in atopic dermatitis. *J Allergy Clin Immunol* (2020) 145:1615–28. doi: 10.1016/j.jaci.2020.01.042

23. Wu Z, Irizarry RA. Preprocessing of oligonucleotide array data. *Nat Biotechnol* (2004) 22:656–8. doi: 10.1038/nbt0604-656b

24. Cao J, Spielmann M, Qiu X, Huang X, Ibrahim DM, Hill AJ, et al. The single-cell transcriptional landscape of mamMalian organogenesis. *Nature* (2019) 566:496–502. doi: 10.1038/s41586-019-0969-x

25. Moran PAP. Notes on continuous stochastic phenomena. *Biometrika* (1950) 37:17–23. doi: 10.1093/biomet/37.1-2.17

26. Livak KJ, Schmittgen TD. Analysis of relative gene expression data using real-time quantitative PCR and the 2(-Delta Delta C(T)) Method. *Methods* (2001) 25:402–8. doi: 10.1006/meth.2001.1262

27. Leigh IM, Navsaria H, Purkis PE, McKay IA, Bowden PE, Riddle PN. Keratins (K16 and K17) as markers of keratinocyte hyperproliferation in psoriasis *in vivo* and *in vitro*.. *Br J Dermatol* (1995) 133:501–11. doi: 10.1111/j.1365-2133.1995.tb02696.x

28. Wolk K, Witte K, Witte E, Raftery M, Kokolakis G, Philipp S, et al. IL-29 is produced by TH17 cells and mediates the cutaneous antiviral competence in psoriasis. *Sci Transl Med* (2013) 5:204ra129–204ra129. doi: 10.1126/scitranslmed.3006245

29. Chikuma S. CTLA-4, an essential immune-checkpoint for T-cell activation. *Curr Top Microbiol Immunol* (2017) 410:99–126. doi: 10.1007/82_2017_61

30. Zhang Y, Liu Y, Xu Y. Interleukin-24 regulates T cell activity in patients with colorectal adenocarcinoma. *Front Oncol* (2019) 9:1401. doi: 10.3389/fonc.2019.01401

31. Watanabe R, Gehad A, Yang C, Scott LL, Teague JE, Schlapbach C, et al. Human skin is protected by four functionally and phenotypically discrete populations of resident and recirculating memory T cells. *Sci Transl Med* (2015) 7:279ra39s. doi: 10.1126/scitranslmed.3010302

32. Bovenschen HJ, van de Kerkhof PC, van Erp PE, Woestenenk R, Joosten I, Koenen HJPM. Foxp3+ regulatory T cells of psoriasis patients easily differentiate into IL-17A-producing cells and are found in lesional skin. *J Invest Dermatol* (2011) 131:1853–60. doi: 10.1038/jid.2011.139

33. Peng Q, Qiu X, Zhang Z, Zhang S, Zhang Y, Liang Y, et al. PD-L1 on dendritic cells attenuates T cell activation and regulates response to immune checkpoint blockade. *Nat Commun* (2020) 11:4835. doi: 10.1038/s41467-020-18570-x

34. Mellor AL, Munn DH. IDO expression by dendritic cells: tolerance and tryptophan catabolism. *Nat Rev Immunol* (2004) 4:762–74. doi: 10.1038/nri1457

35. Bézie S, Picarda E, Ossart J, Tesson L, Usal C, Renaudin K, et al. IL-34 is a Treg-specific cytokine and mediates transplant tolerance. *J Clin Invest* (2015) 125:3952–64. doi: 10.1172/JCI81227

36. Lelios I, Cansever D, Utz SG, Mildenberger W, Stifter SA, Greter M. Emerging roles of IL-34 in health and disease. *J Exp Med* (2020) 217:e20190290. doi: 10.1084/jem.20190290

37. Farrag DA, Asaad MK, Ghobrial CK. Evaluation of IL-34 in psoriasis and psoriatic arthritis patients: correlation with disease activity and severity. *Egypt Rheumatol* (2017) 39:25–31. doi: 10.1016/j.ejr.2016.05.008

38. Allaire JM, Poon A, Crowley SM, Han X, Sharafian Z, Moore N, et al. Interleukin-37 regulates innate immune signaling in human and mouse colonic organoids. *Sci Rep* (2021) 11:8206. doi: 10.1038/s41598-021-87592-2

39. Rønholt K, Nielsen AL-L, Johansen C, Vestergaard C, Fauerbye A, López-Vales R, et al. IL-37 expression is downregulated in lesional psoriasis skin. *Immunohorizons* (2020) 4:754–61. doi: 10.4049/immunohorizons.2000083

40. Garza LA, Yang C-C, Zhao T, Blatt HB, Lee M, He H, et al. Bald scalp in men with androgenetic alopecia retains hair follicle stem cells but lacks CD200-rich and CD34-positive hair follicle progenitor cells. *J Clin Invest* (2011) 121:613–22. doi: 10.1172/JCI44478

41. Cosmi L, De Palma R, Santarlasci V, Maggi L, Capone M, Frosali F, et al. Human interleukin 17-producing cells originate from a CD161+CD4+ T cell precursor. *J Exp Med* (2008) 205:1903–16. doi: 10.1084/jem.20080397

42. Dambacher J, Beigel F, Zitzmann K, De Toni EN, Göke B, Diepolder HM, et al. The role of the novel Th17 cytokine IL-26 in intestinal inflammation. *Gut* (2009) 58:1207–17. doi: 10.1136/gut.2007.130112

43. Donnelly RP, Sheikh F, Dickensheets H, Savan R, Young HA, Walter MR. Interleukin-26: an IL-10-related cytokine produced by Th17 cells. *Cytokine Growth Factor Rev* (2010) 21:393–401. doi: 10.1016/j.cytogfr.2010.09.001

44. Liu J, Chang H-W, Huang Z-M, Nakamura M, Sekhon S, Ahn R, et al. Single-cell RNA sequencing of psoriatic skin identifies pathogenic Tc17 cell subsets and reveals distinctions between CD8+ T cells in autoimmunity and cancer. *J Allergy Clin Immunol* (2021) 147:2370–80. doi: 10.1016/j.jaci.2020.11.028

45. Liu Y, Wang H, Cook C, Taylor MA, North JP, Hailer A, et al. Defining patient-level molecular heterogeneity in psoriasis vulgaris based on single-cell transcriptomics. *Front Immunol* (2022) 13:842651. doi: 10.3389/fimmu.2022.842651

46. Liu Y, Wang H, Taylor M, Cook C, Martínez-Berdeja A, North JP, et al. Classification of human chronic inflammatory skin disease based on single-cell immune profiling. *Sci Immunol* (2022) 7:eabl9165s. doi: 10.1126/sciimmunol.abl9165

47. Liu W, Zhou X, Wang A, Ma J, Bai Y. Increased peripheral helper T cells type 17 subset correlates with the severity of psoriasis vulgaris. *Immunol Lett* (2021) 229:48–54. doi: 10.1016/j.imlet.2020.11.005

48. Al-Ashmawy GMZ. "Dendritic cell subsets, maturation and function. ," *InTech* (2018). doi: 10.5772/intechopen.79926

49. Kim T-G, Kim DS, Kim H-P, Lee M-G. The pathophysiological role of dendritic cell subsets in psoriasis. *BMB Rep* (2014) 47:60. doi: 10.5483/BMBRep.2014.47.2.014

50. Mehta H, Mashiko S, Angsana J, Rubio M, Hsieh Y-CM, Maari C, et al. Differential Changes in Inflammatory Mononuclear Phagocyte and T-Cell Profiles within Psoriatic Skin during Treatment with Guselkumab vs. *Secukinumab. J Invest Dermatol* (2021) 141:1707–1718.e9. doi: 10.1016/j.jid.2021.01.005

51. Chu C-C, Ali N, Karagiannis P, Di Meglio P, Skowera A, Napolitano L, et al. Resident CD141 (BDCA3)+ dendritic cells in human skin produce IL-10 and induce regulatory T cells that suppress skin inflammation. *J Exp Med* (2012) 209:935–45. doi: 10.1084/jem.20112583

52. Uto T, Fukaya T, Takagi H, Arimura K, Nakamura T, Kojima N, et al. Clec4A4 is a regulatory receptor for dendritic cells that impairs inflammation and T-cell immunity. *Nat Commun* (2016) 7:1–15. doi: 10.1038/ncomms11273

53. Bakdash G, Buschow SI, Gorris MAJ, Halilovic A, Hato SV, Sköld AE, et al. Expansion of a BDCA1+CD14+ Myeloid cell population in melanoma patients may attenuate the efficacy of dendritic cell vaccines. *Cancer Res* (2016) 76:4332–46. doi: 10.1158/0008-5472.CAN-15-1695

54. Heger L, Hofer TP, Bigley V, de Vries IJM, Dalod M, Dudziak D, et al. Subsets of CD1c+ DCs: dendritic cell versus monocyte lineage. *Front Immunol* (2020) 11:559166. doi: 10.3389/fimmu.2020.559166

55. Kim J, Moreno A, Krueger JG. The imbalance between Type 17 T-cells and regulatory immune cell subsets in psoriasis vulgaris. *Front Immunol* (2022) 13:1005115. doi: 10.3389/fimmu.2022.1005115

56. Maggi L, Santarlasci V, Capone M, Peired A, Frosali F, Crome SQ, et al. CD161 is a marker of all human IL-17-producing T-cell subsets and is induced by RORC. *Eur J Immunol* (2010) 40:2174–81. doi: 10.1002/eji.200940257

57. Peternel S, Kastelan M. Immunopathogenesis of psoriasis: focus on natural killer T cells. *J Eur Acad Dermatol Venereol* (2009) 23:1123–7. doi: 10.1111/j.1468-3083.2009.03292.x

58. Cameron AL, Kirby B, Fei W, Griffiths CE. Natural killer and natural killer-T cells in psoriasis. *Arch Dermatol Res* (2002) 294:363–9. doi: 10.1007/s00403-002-0349-4

59. Curry JL, Qin J-Z, Robinson J, Nickoloff BJ. Reactivity of resident immunocytes in normal and prepsoriatic skin using an ex vivo skin-explant model system. *Arch Pathol Lab Med* (2003) 127:289–96. doi: 10.5858/2003-127-0289-RORIIN

60. Young NT, Waller ECP, Patel R, Roghanian A, Austyn JM, Trowsdale J. The inhibitory receptor LILRB1 modulates the differentiation and regulatory potential of human dendritic cells. *Blood* (2008) 111:3090–6. doi: 10.1182/blood-2007-05-089771

61. Guttman-Yassky E, Zhou L, Krueger JG. The skin as an immune organ: Tolerance versus effector responses and applications to food allergy and hypersensitivity reactions. *J Allergy Clin Immunol* (2019) 144:362–74. doi: 10.1016/j.jaci.2019.03.021

62. Zimmerman KD, Espeland MA, Langefeld CD. A practical solution to pseudoreplication bias in single-cell studies. *Nat Commun* (2021) 12:738. doi: 10.1038/s41467-021-21038-1

63. Murphy AE, Skene NG. A balanced measure shows superior performance of pseudobulk methods in single-cell RNA-sequencing analysis. *Nat Commun* (2022) 13:7851. doi: 10.1038/s41467-022-35519-4

64. Gagnon J, Pi L, Ryals M, Wan Q, Hu W, Ouyang Z, et al. Recommendations of scRNA-seq differential gene expression analysis based on comprehensive benchmarking. *Life* (2022) 12:850. doi: 10.3390/life12060850

65. Hou W, Ji Z, Ji H, Hicks SC. A systematic evaluation of single-cell RNA-sequencing imputation methods. *Genome Biol* (2020) 21:218. doi: 10.1186/s13059-020-02132-x

66. Vallejos CA, Richardson S, Marioni JC. Beyond comparisons of means: understanding changes in gene expression at the single-cell level. *Genome Biol* (2016) 17:70. doi: 10.1186/s13059-016-0930-3

67. Mou T, Deng W, Gu F, Pawitan Y, Vu TN. Reproducibility of methods to detect differentially expressed genes from single-cell RNA sequencing. *Front Genet* (2019) 10:1331. doi: 10.3389/fgene.2019.01331

68. Squair JW, Gautier M, Kathe C, Anderson MA, James ND, Hutson TH, et al. Confronting false discoveries in single-cell differential expression. *Nat Commun* (2021) 12:5692. doi: 10.1038/s41467-021-25960-2

69. Visvanathan S, Baum P, Vinisko R, Schmid R, Flack M, Lalovic B, et al. Psoriatic skin molecular and histopathologic profiles after treatment with risankizumab versus ustekinumab. *J Allergy Clin Immunol* (2019) 143:2158–69. doi: 10.1016/j.jaci.2018.11.042

frontiers | Frontiers in Immunology

TYPE Original Research
PUBLISHED 20 September 2023
DOI 10.3389/fimmu.2023.1266359

C-type lectin receptor expression is a hallmark of neutrophils infiltrating the skin in epidermolysis bullosa acquisita

Christian F. Guerrero-Juarez[1,2†], Paul Schilf[3†], Jing Li[2], Maria Paula Zappia[4], Lei Bao[3], Payal M. Patel[2,5], Jenny Gieseler-Tillmann[3], Sripriya Murthy[3], Connor Cole[2], Maria Sverdlov[6], Maxim V. Frolov[4], Takashi Hashimoto[7], Norito Ishii[8], Thomas Rülicke[9], Katja Bieber[3,10], Ralf J. Ludwig[3,10], Christian D. Sadik[3‡] and Kyle T. Amber[2,11*‡]

[1]Carle Illinois College of Medicine, University of Illinois, Urbana-Champaign, Urbana, IL, United States, [2]Department of Dermatology, Rush University Medical Center, Chicago, IL, United States, [3]Department of Dermatology, Allergy, and Venereology, University of Lübeck, Lübeck, Germany, [4]Department of Biochemistry and Molecular Genetics, University of Illinois at Chicago, Chicago, IL, United States, [5]Department of Dermatology, Massachusetts General Hospital, Boston, MA, United States, [6]Research Histology Core, University of Illinois at Chicago, Chicago, IL, United States, [7]Department of Dermatology, Osaka Metropolitan University Graduate School of Medicine, Osaka, Japan, [8]Department of Dermatology, Kurume University School of Medicine, and Kurume University Institute of Cutaneous Cell Biology, Kurume, Japan, [9]Department of Biomedical Sciences and Ludwig Boltzmann Institute for Hematology and Oncology, University of Veterinary Medicine Vienna, Vienna, Austria, [10]Lübeck Institute of Experimental Dermatology, University of Lübeck, Lübeck, Germany, [11]Department of Internal Medicine, Rush University Medical Center, Chicago, IL, United States

EDITED BY
Shiang-Jong Tzeng,
National Taiwan University, Taiwan

REVIEWED BY
Wendy B. Bollag,
Augusta University, United States
Christoph Hudemann,
Philipps-University Marburg, Germany

*CORRESPONDENCE
Kyle T. Amber
kyle_amber@rush.edu

[†] These authors have contributed equally to this work

[‡] These authors have contributed equally to this work

RECEIVED 24 July 2023
ACCEPTED 31 August 2023
PUBLISHED 20 September 2023

CITATION
Guerrero-Juarez CF, Schilf P, Li J, Zappia MP, Bao L, Patel PM, Gieseler-Tillmann J, Murthy S, Cole C, Sverdlov M, Frolov MV, Hashimoto T, Ishii N, Rülicke T, Bieber K, Ludwig RJ, Sadik CD and Amber KT (2023) C-type lectin receptor expression is a hallmark of neutrophils infiltrating the skin in epidermolysis bullosa acquisita. *Front. Immunol.* 14:1266359. doi: 10.3389/fimmu.2023.1266359

Introduction: Inflammatory epidermolysis bullosa acquisita (EBA) is characterized by a neutrophilic response to anti-type VII collagen (COL7) antibodies resulting in the development of skin inflammation and blistering. The antibody transfer model of EBA closely mirrors this EBA phenotype.

Methods: To better understand the changes induced in neutrophils upon recruitment from peripheral blood into lesional skin in EBA, we performed single-cell RNA-sequencing of whole blood and skin dissociate to capture minimally perturbed neutrophils and characterize their transcriptome.

Results: Through this approach, we identified clear distinctions between circulating activated neutrophils and intradermal neutrophils. Most strikingly, the gene expression of multiple C-type lectin receptors, which have previously been reported to orchestrate host defense against fungi and select bacteria, were markedly dysregulated. After confirming the upregulation of *Clec4n*, *Clec4d*, and *Clec4e* in experimental EBA as well as in lesional skin from patients with inflammatory EBA, we performed functional studies in globally deficient *Clec4e*$^{-/-}$ and *Clec4d*$^{-/-}$ mice as well as in neutrophil-specific *Clec4n*$^{-/-}$ mice. Deficiency in these genes did not reduce disease in the EBA model.

Discussion: Collectively, our results suggest that while the upregulation of *Clec4n*, *Clec4d*, and *Clec4e* is a hallmark of activated dermal neutrophil populations, their individual contribution to the pathogenesis of EBA is dispensable.

KEYWORDS

epidermolysis bullosa acquisita, pemphigoid, neutrophil, single cell RNA seq, C-type lectin receptor (CLRs)

Introduction

Epidermolysis bullosa acquisita (EBA) is a rare chronic skin condition caused by autoantibodies to type VII collagen (COL7). Within EBA, there are several distinct clinical phenotypes (1, 2). The inflammatory (bullous pemphigoid-like) phenotype is characterized by pruritis, dermatitis, and bullae. Histologically, inflammatory EBA is characterized by an abundance of neutrophils that release, among others, reactive oxygen species (ROS), leukotriene B_4 (LTB_4), and proteases at the cutaneous basement membrane zone, resulting in skin blistering (3–7). Neutrophils are the most abundant leukocyte in human blood. Circulating neutrophils demonstrate limited antimicrobial activity (8). However, after priming with various molecules, such as proinflammatory cytokines and chemokines, as well as microbial products, neutrophils gain improved phagocytic capacity and ROS production, and demonstrate a distinct surface phenotype (9, 10). CD54, dectin-2, and IL-1β expression is acquired by neutrophils during the late phase of priming as they prepare for migration to inflammatory sites (11). Dectin-2 (CLEC6A/CLEC4N) belongs to the C-type lectin-like family of receptors (CTLR) (12), a family of transmembrane pattern recognition receptors expressed on myeloid cells. These CTLRs recognize pathogen-associated molecular patterns as well as certain modified self-antigens, such as damage-associated molecular patterns released from dead cells.

While neutrophil priming was previously thought to occur in the absence of transcription or translation, several studies have refuted this notion (11). Recent technological advances have allowed detection of neutrophil transcriptomes in spite of their low RNA content, revealing their heterogeneity in the blood and in host defense (13). Yet, the distinction between skin-infiltrating versus blood neutrophils remains largely unknown. While several phenotypic neutrophil activation markers have been identified, it is likely that these skin-infiltrating neutrophils have a distinct phenotype from blood and even activated blood neutrophils, as has been shown in other tissues (14).

As neutrophils play a central role in innate immunity, the concept of global therapeutic inhibition of neutrophils would be associated with significant potential side effects. However, targeting markers present only on neutrophils contributing towards disease pathology would potentially bypass this risk. Aside from identifying targetable surface markers on neutrophils, identification of intradermal function is of great importance in disease, as they may contribute to local inflammation. In psoriasis, for example, neutrophils are a source of IL-17 (15).

The identification of novel disease-specific neutrophil markers is complicated, among others, by the fact that neutrophils are sensitive cells, susceptible to both swift activation and apoptosis in response to manipulation. To identify characteristic markers of cutaneous neutrophils in EBA, we performed single-cell RNA-sequencing (scRNA-seq) on unsorted blood and skin from mice in the antibody transfer model of EBA. By minimizing enrichment steps and manipulation time, this approach permitted us to capture viable neutrophils, allowing bioinformatic analysis of neutrophil activation from blood to skin.

Materials and methods

Animal experiments

Animal experiments were approved by the Animal Care and Use Committee at the Rush University Medical Center (IACUC No 20-079) or the state government of Schleswig-Holstein (Protocol 119-10/17), depending on where the experiments were conducted. All experiments were performed by certified personnel.

Human samples and ethics statement

Tissue from five patients with confirmed inflammatory EBA, defined as a neutrophilic inflammatory infiltrate, positive direct immunofluorescence, and positive dermal side indirect immunofluorescence with corresponding anti-COL7 IgG, was retrospectively collected. All patients involved in this study provided written informed consent. All experiments with human samples were approved by the ethical committee of the Rush University Medical Center (IRB No. 20121406) and were performed in accordance with the Declaration of Helsinki.

Abbreviations: AUC, Area under curve; BSA, Body surface area; CTLR, C-type lectin receptor; EBA, Epidermolysis bullosa acquisita; FFPE, Formalin-fixed paraffin-embedded; PMN, Polymorphonuclear cell; scRNA-seq, Single-cell RNA-sequencing; UMAP, Uniform Manifold Approximation and Projection.

Mice

C57BL6/J were purchased from Jackson Laboratories (Bar Harbor, ME, USA) (JAX stock 000664). Sperm of C57BL/6-*Clec4d*$^{tm1.1Cfg/Mmucd}$ (*Clec4d*$^{-/-}$; MMRRC stock: 031935-UCD) and C57BL/6-*Clec4e*$^{tm1.1Cfg/Mmucd}$ (*Clec4e*$^{-/-}$) mice (MMRRC stock 031936-UCD), designated with the MMRCR stock numbers 031935-UCD and 031936-UCD, respectively, were purchased from the Mutant Mouse Research and Resource Center (MMRRC; Davis, CA, USA). The sperm was used for *in vitro* fertilization. The heterozygous progeny was used to breed *Clec4d*$^{-/-}$ and *Clec4e*$^{-/-}$ mice and their respective wild-type littermates. *MRP8-Cre-ires/GFP* (MRP8-Cre) mice were obtained from the Jackson Laboratory (Bar Harbor, ME, USA). A conditional knockout of *Clec4n* was generated using *Clec4n*$^{tm2a(KOMP)Wtsi}$ embryonic stem (ES) cells acquired from the KOMP Repository (Davis, CA, USA). Using the fully verified and karyotyped C57BL/6N ES cells, chimeric founder mice were generated by microinjection into BALB/c blastocysts. The resulting mice with the “knockout first allele” were crossed with a C57BL/6N-Tg(CAG-Flpe) deleter mouse to remove the selection cassette and create the conditional *Clec4n*^{tm1c} allele, hereafter referred to as *Clec4n*^{fl} allele. Polymorphonuclear neutrophil (PMN)-specific *Clec4n*$^{-/-}$ (*Clec4n*$^{\Delta PMN}$) mice were generated by crossing homozygous *Clec4n*$^{fl/fl}$ with MRP8-Cre mice inducing an MRP8 promotor-driven Cre recombination excision event during neutrophil differentiation of precursors. To confirm the gene knockout in neutrophils, bone marrow neutrophils were isolated using the Neutrophil Isolation Kit (Miltenyi, Teterow, Germany), and their RNA was isolated using the RNA Mini Kit (Analytik Jena AG, Jena, Germany). cDNA was generated using the Thermo Scientific Revert Aid First Strand cDNA Synthesis Kit (Thermo Fisher Scientific, Bremen, Germany). cDNA was used for quantitative PCR using the SYBR™ Select Mastermix (Thermo Fisher Scientific, Bremen, Germany). Data were acquired using the RealPlex (Eppendorf, Hamburg, Germany) cycler (data not shown).

Generation of COL7 ^{vWFA2}

Recombinant murine von Willebrand factor A-like domain 2 (vWFA2) of the NC1 domain of collagen 7 (aa1048-1238) was produced, as previously described (16, 17).

Development of anti-murine COL7^{vWFA2} IgG

New Zealand white rabbits were immunized with COL7^{vWFA2} as previously described (18). IgG was purified from rabbit serum using Protein G Sepharose Fast Flow affinity column chromatography (Amersham Biosciences, Freiburg, Germany) as previously described (18). Reactivity of IgG fractions was analyzed by the immunofluorescence microscopy on murine skin. Concentrations of purified rabbit IgG were measured at 280 nm by a spectrophotometer. Total rabbit IgG underwent an additional purification step of antigen affinity purification using COL7^{vWFA2} coupled Affi-Gel 10 (Bio-Rad, Munich, Germany) as previously described (19).

Induction of experimental EBA

Mice were housed under specific pathogen-free conditions at Rush University (Chicago, IL, USA) or at the University of Lübeck (Lübeck, Schleswig-Holstein, Germany) and were provided standard mouse chow and acidified drinking water *ad libitum*. Mice were conditioned at least 2 weeks prior to experiments and were under 12 h:12 h light/dark cycles. Sex-matched mice, age 6–12 weeks were used for the experiments. For transcriptomic analyses, antibody transfer EBA was performed, as previously described (17). Affinity-purified anti-COL7^{vWFA2} IgG (200 μg) was injected intraperitoneally thrice weekly for 2 weeks. In experiments examining the contribution of Dectin-2, Dectin-3, and Mincle to experimental EBA, disease was induced and evaluated, as previously described (4, 20). Briefly, New Zealand rabbits were immunized against three epitopes of type VII collagen. IgG directed to the epitope C (anti-COL7c) was affinity purified, and 50 μg of anti-COL7c was injected subcutaneously on days 0, 2, and 4 of the experiment. The percentage of the total body surface area affected by skin lesions (erythema, blisters, erosions, crusts, or alopecia) was determined by an investigator blinded to the experimental conditions. All clinical examinations and bleedings were performed under anesthesia.

Histology and immunofluorescence

For mouse tissue, additional perilesional tissue from previous passive transfer experiments and optimizations were used to minimize animal numbers. Hematoxylin and eosin stains were performed using standard protocols. For both human and mouse, FFPE blocks were sectioned routinely and stained with the following antibodies: CLE4D (MBS9607710, rabbit polyclonal, Mybiosource, San Diego, CA, USA), CLEC4E (BS08541R, rabbit polyclonal, Bioss, Woburn, Massachusetts, USA), and CLEC4N (clone IMG3D1, ab107572, mouse IgG3 monoclonal, Abcam, Boston, Massachusetts, USA). Human neutrophils were stained for MPO (AF3667, goat polyclonal, R&D Systems, Minneapolis, Minnesota, USA), while mouse samples were stained for Ly6G (clone RB6-8C5, SC-53515, rat monoclonal IgG2b, Santa Cruz, Dallas, Texas). Secondary antibodies and DAPI counterstain were purchased from ThermoFisher (Rockford, IL, USA). Mouse direct immunofluorescence was performed as previously described, using anti-rabbit secondary antibody to confirm successful passive transfer (17). All slides were immediately photographed following staining using an Evos FL microscope (ThermoFisher, Rockford, IL, USA). The frequency of dual-positive cells was quantified in ImageJ v1.52 (Bethesda, Maryland, USA)

Flow cytometry

Surface antigen staining was performed according to standard flow cytometry procedures. The following antibodies and reagents were used: Zombie aqua viability stain, anti-Ly6G (clone 1A8, 127628, Rat IgG2a), anti-CD45 (clone 30-F11, 103151, Rat IgG2b), and anti-CD11b (clone M1/70, 101243, Rat IgG2b), all of which were purchased from BioLegend (San Diego, CA, USA). Anti-CLEC4D (clone MA5-24152, mouse IgG2b) was purchased from ThermoFisher (Rockford, IL, USA) and conjugated with APC using the Lightning-Link APC Conjugation Kit (Abcam, Boston, Massachusetts, USA). Recombinant anti-CLEC4N targeting the extracellular domain (50267-R001, Rabbit IgG, Sino Biological, Wayne, PA, USA), was conjugated with PE using the Lightning-Link PE Conjugation Kit (Abcam, Boston, Massachusetts, USA) and anti-CLEC4E (BS-8541R, Rabbit polyclonal, ThermoFisher, Rockford, IL, USA), was conjugated with Alexafluor-488 using the Lightning-Link Alexafluor488 Conjugation Kit (Abcam, Boston, Massachusetts, USA). Flow cytometry was performed on an LSRFortessa (BD Biosciences, San Jose, CA, USA), using compensation beads (BioLegend, San Diego, CA, USA) and FACSDiva software (BD Biosciences, San Jose, CA, USA). Gating was performed by removing doublets and dead cells, followed by use of fluorescent minus one control. Flow cytometry data were analyzed using FCS Express 7 Plus software (*De Novo* Software, Pasadena, CA, USA).

Tissue harvesting for single-cell RNA-sequencing

Blood was collected by retrobulbar bleeding from anesthetized mice, and immediately followed by RBC lysis (BioLegend, San Diego, CA, USA). Lesional (ear) skin from anesthetized mice was harvested by punch biopsies and enzymatically digested using the whole skin digestion kit (Miltenyi, Auburn, CA, USA) per manufacturer instructions with minor modifications. Following addition of enzymes, samples were incubated in a water bath at 37°C for 2 h and shaken every 15 min. Mechanical dissociation by pipetting was only performed at the end of the incubation. Cells were then filtered using a 70-µm filter, centrifuged at 300*g* for 10 min at 4°C, washed and resuspended in 0.04% BSA/HBSS (ThermoFisher, Rockford, IL, USA). Cell viability was immediately assessed by trypan blue (ThermoFisher, Rockford, IL, USA). Single-cell suspensions of 1,000 cells/µL were run into the chromium Controller (10x Genomics, Pleasanton, CA, USA) to encapsulate 5,000 and 10,000 cells for blood and skin samples, respectively. Ambion RNase inhibitor (Invitrogen, Waltham, Massachusetts, USA) was added to the master mix. Samples were processed using the Chromium Single Cell 3′ GEM, Library & Gel Bead Kit v3 (10x genomics, Pleasanton, CA, USA) per manufacturer's instructions. Library QC was performed using the Agilent Tape station. Sequencing was performed using two NovaSeq 6000 SP lanes (Illumina, San Diego, CA, USA). Cell capture, RT, library preparation, and sequencing were performed at the University of Illinois at Chicago.

Single-cell RNA-sequencing and bioinformatics

Raw FASTQ reads were mapped to mouse mm10 reference genome (GRCm38.93.dna/GRCm38.93.gtf) using Cell Ranger Version 3.0.0. Web summary alignment metrics are provided in Supplementary Table 3.

Doublet/multiplet simulation and low-quality cell pruning

Raw, digitized count matrices were pre-processed and doublets/multiplets were simulated using Single-Cell Remover of Doublets (Scrublet) (21) (version 0.2.1) with standard parameters enabled. Putative singlets were filtered in Seurat to remove low-quality cells and kept for downstream analysis if and only if they met the following user-defined, collective quality control metrics criteria: (a) 350 < genes/cell < 5,000, (b) cells contained no more than 10% mitochondrial gene expression, and (c) cells were not defined as outliers (22).

Anchoring, integration, and downstream analysis

We performed anchoring and integration of pathogenic IgG or non-pathogenic IgG-treated mouse blood or pathogenic IgG or non-pathogenic IgG-treated mouse skin datasets using the Seurat package (Version 3.2.2, R Studio version 3.6.1) (23) as suggested by the developer. Briefly, Seurat objects were created using Scrublet-pre-processed individual, raw digitized count matrices and merged. Individual gene expression digital matrices were normalized, and the top 2,000 variable genes/features were identified. Integration anchors were identified using the dimensions set to 30, and datasets were integrated with dimensions set to 30. The integrated object was scaled, and significant principal components used for clustering and finding neighbors were identified using a combination of statistical and heuristic methods. Neighbors and clusters were then identified with dimensions specified by user and visualized using Uniform Manifold Approximation and Projection (UMAP). Putative cell identities were identified based on differential gene expression profiles (cluster markers) (log fold change of 25% with a minimum of 25% of cells expressing such gene in either one cluster). Genes were log-normalized and visualized as two-dimensional feature plots or bubble plots.

Differential gene expression analysis

Differentially expressed genes between cell types across treatments were calculated with Seurat. Differentially expressed genes for a particular comparison were filtered using a p-adjusted threshold of 0.05 and a Log_2 fold-change of 0.58 or greater in either direction.

Gene class and GO analysis

Differentially expressed genes were used to calculate Gene Ontologies (GOs). Manual curation of GOs was performed using Enrichr (24) and visualized as bubble plots. A list of significant GOs (p-adjusted < 0.05) is included in Supplementary Table 4.

Marker gene module scoring

Aggregate, composite gene scores were assigned to neutrophils using the *AddModuleScore* function in Seurat. This *"Neutrophil aggregate score"* was defined by a core set of known neutrophil-associated marker genes, including *S100a8*, *S100a9*, and *Ly6g*. Aggregate, composite gene scores were log-normalized and visualized as two-dimensional feature plots.

Pseudotime analysis

Pseudo-ordering of individual cells was performed using Monocle2 (Version 2.10.1) (25). Briefly, neutrophils were bioinformatically gated in Seurat and a *cellDataSet* object was created in Monocle2. Subclustered cells were ordered based on variable features and dimensionality reduction was performed with the *reduction method = 'DDRTree'* argument enabled and then ordered. To identify pseudotime-dependent gene expression changes in neutrophils in the putative blood–skin transition, we applied the single-cell Energy path (scEpath; Version 1; MATLAB Version 9.5) (26) algorithm on a subset of Monocle2-ordered neutrophils. To identify statistically significant pseudotime-dependent gene changes, we compared the standard deviation of the observed smoothed expressions with a set of similarly permuted expressions by randomly permuting the cell order (i.e., 100 permutations) as suggested by the developer. We considered all genes with a standard deviation greater than 0.01 and a Bonferroni-corrected p-value below a significance level $\alpha = 0.05$ to be pseudotime-dependent. To analyze pseudotime-dependent mouse transcription factors, we used genes annotated in the Animal Transcription Factor Database (AnimalTFDB 3.0) (27) in scEpath. Pseudotime-dependent genes were represented and visualized using a rolling wave plot with user-defined optimal K clusters.

Statistical analyses

Percentages of CLEC4-positive neutrophils between blood in EBA versus control or EBA blood versus skin were determined by log-transformation of the percentage of dually positive cells, followed by Student's t-test. Comparisons of the body surface area affected by skin lesions were performed by two-way ANOVA using GraphPad Prism 9 (GraphPad, San Diego, CA, USA), and comparisons of the area under the curve of the affected body surface area over time were performed using Student's t-test. All tests were two sided with a $p < 0.05$. Given the relatively few numbers of comparisons and lack of statistically significant results, correction for multiplicity was not performed. All data are reported as mean ± SEM.

Results

A single-cell repertoire of whole blood and lesional skin in experimental EBA

Mice were injected thrice weekly for 2 weeks with pathogenic rabbit anti-mouse antigen affinity-purified COL7$^{\mathrm{vWFA2}}$ IgG or with non-pathogenic rabbit IgG, as previously described (17). As expected, the group treated with pathogenic IgG consequently developed a characteristic disease phenotype with positive direct immunofluorescence against the basement membrane zone. We then performed scRNA-seq on unsorted cells from RBC-lysed blood (Figure 1A) or ear skin (Figure 2A) in experimental EBA mice or controls at day 14. Following doublet removal and quality control filtering (Supplementary Figure 1), 7,143 cells ($k_{\mathrm{EBA}} = 2{,}878$ vs. $k_{\mathrm{IgG}} = 4{,}265$) were anchored and integrated and included in our blood analysis (Figures 1B, C), and 8,173 cells ($k_{\mathrm{EBA}} = 3{,}445$ vs. $k_{\mathrm{IgG}} = 4{,}728$) in our skin analysis (Figures 2B, C).

Assessment of immune cell heterogeneity in experimental EBA reveals a signature-activated neutrophil transcriptome

Unsupervised clustering of blood cells was performed with Seurat (28), revealing eight distinct clusters. Using differentially expressed gene signatures, we assigned clusters based on their putative identities and hierarchical similarities. As expected, these clusters were primarily composed of immune cells (Figures 1C, D), of which lymphocytes were most abundant followed by neutrophils (Supplementary Figure 2). We next compared the ratio of immune cells per cluster post-normalization between the pathogenic IgG and the non-pathogenic IgG-treated groups to identify shifts in immune populations because of disease. Neutrophils and myeloid cells appeared in larger amounts in samples from pathogenic IgG-treated mice relative to non-pathogenic IgG-treated mice (Supplementary Figure 2). Putative neutrophils were identified based on an aggregate, composite gene score including *S100a8*, *S100a9*, and *Ly6g*. Notably, two-dimensional UMAP demonstrates an apparent neutrophil activation in EBA samples that is absent in IgG control samples, seen in an expanding population emanating from the basal neutrophil populations (Figure 1E). Bioinformatic gating was subsequently performed to isolate neutrophils based on these putative markers, with resolution decreased to consider neutrophils as a single, granular population for each treatment condition. Wilcoxon Rank Sum Test revealed 148 upregulated and 375 downregulated genes between neutrophils from the pathogenic IgG and the non-pathogenic IgG-treated groups, defined as >0.25 fold-change difference, and a p-adjusted < 0.05 (Supplementary Table 1).

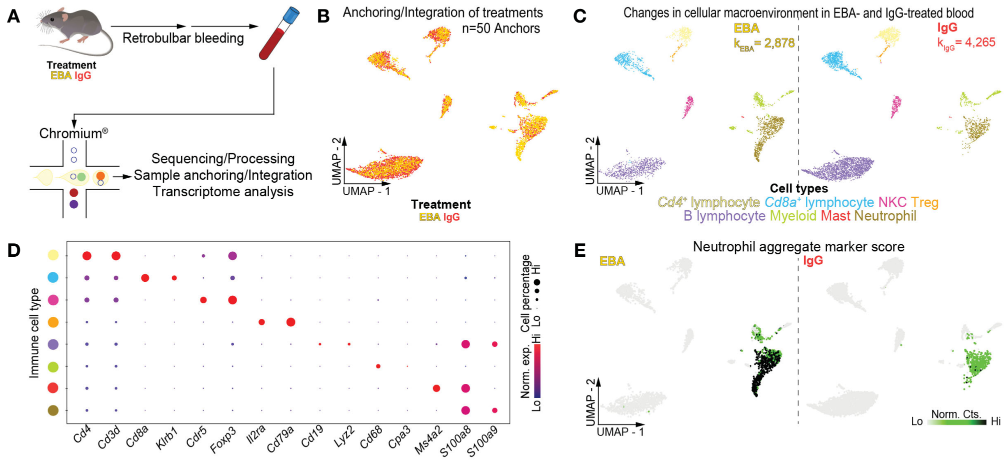

FIGURE 1
Single-cell transcriptome of mouse blood in experimental EBA. **(A)** Schematic of blood cell isolation, processing, and capture by droplet-based device, 3′-scRNA-seq, and downstream analyses. **(B)** Anchoring of EBA or control mouse leukocytes into a single object and visualized in two-dimensional UMAP space. **(C)** Clustering and neighbor identification of anchored datasets. Eight putative immune cell populations were identified and color coded. Putative cluster identity based on *bona fide* marker gene expression is defined on the bottom. **(D)** Dot plot of key markers of each immune population with Figure 1C. **(E)** Two-dimensional feature plot showing expression of aggregate, composite neutrophil gene score. Light green—low, black—high gene expression based on normalized counts. Data shown are from n = 3 pooled biologic replicates per condition. EBA, epidermolysis bullosa acquisita; IgG, immunoglobulin G; UMAP, Uniform Manifold Approximation and Projection; NKC, natural killer cell; Treg, regulatory T cell; Norm. exp., normalized expression; Lo, low; Hi, high; Norm, Cts, normalized counts.

Assessment of cellular heterogeneity in experimental EBA skin identifies the transcriptome of a cutaneous neutrophil population

We next characterized the cutaneous transcriptome in active lesions, with an emphasis on capturing viable lesional-skin neutrophils. Given neutrophil fragility following skin dissociation and flow sorting, dead cell depletion, or alternative dissociation protocols (unpublished), we capitalized on our scRNA-seq workflow to minimize such manipulation. Thus, following dissociation, whole skin dissociates were immediately processed for single-cell capture. Viability threshold of >80% was set without dead cell depletion to minimize dead cell background signal but allow capture of viable neutrophils. Using differentially expressed gene signatures, we assigned clusters based on their putative identities and hierarchical similarities as before (Figure 2D, Supplementary Table 2). Use of our putative neutrophil aggregate marker score highlighted a cutaneous neutrophil population in diseased but not IgG control skin (Figure 2E).

Trajectory analysis reveals activation of neutrophils from blood to lesional skin

To better understand the trajectory of neutrophil activation, whole blood and skin neutrophils were combined into a single object using bioinformatic gating. Cells were then aligned in pseudotime using Monocle2 (25), with pseudotime-dependent genes identified in scEpath (26). Trajectory analysis revealed pseudo-infiltration from activated blood to intralesional neutrophils (Figures 2H, I). Control blood, EBA blood, and EBA skin each exhibited unique transcriptomes, of which the top 10 differentially expressed genes between each comparison are shown (Figure 2F). Gene ontology analyses with Enrichr (24) of the activated and cutaneous neutrophils versus basal neutrophils revealed increased neutrophil degranulation in blood and enhanced cytokine signaling in the skin (Figure 2G). While several genes demonstrated pseudotemporal activation from blood to skin, genes for CTRLs collectively displayed a clear pattern of regulation with several stimulatory CTLRs upregulated and inhibitory CTLRs downregulated (Figure 2J; Supplementary Figure 3). This intriguing finding prompted us to investigate these markers and their functional significance in more detail.

Validation of Dectin-2, Dectin-3, and Mincle expression on neutrophils

Next, we characterized the protein expression levels of Dectin-3, Mincle, and Dectin-2, the proteins encoded by *Clec4d*, *Clec4e*, and *Clec4n*, respectively, on neutrophils. To this end, skin sections from mice with EBA were stained for Ly6G and either Dectin-3, Mincle, or Dectin-2 revealing co-expression in the skin (Figure 3B). To distinguish whether this activation occurred in the blood or in the skin, we performed flow cytometry on blood from mice treated with COL7 antibodies or corresponding isotype controls. As previously described (17), the frequency of $CD45^+Ly6G^+$ neutrophils increased significantly in the EBA compared to the control group (Figure 3A). Dectin-2 was highly expressed in both basal and activated blood neutrophils (>95%), while much lower levels of Dectin-3 and Mincle were detected. There was no significant difference between

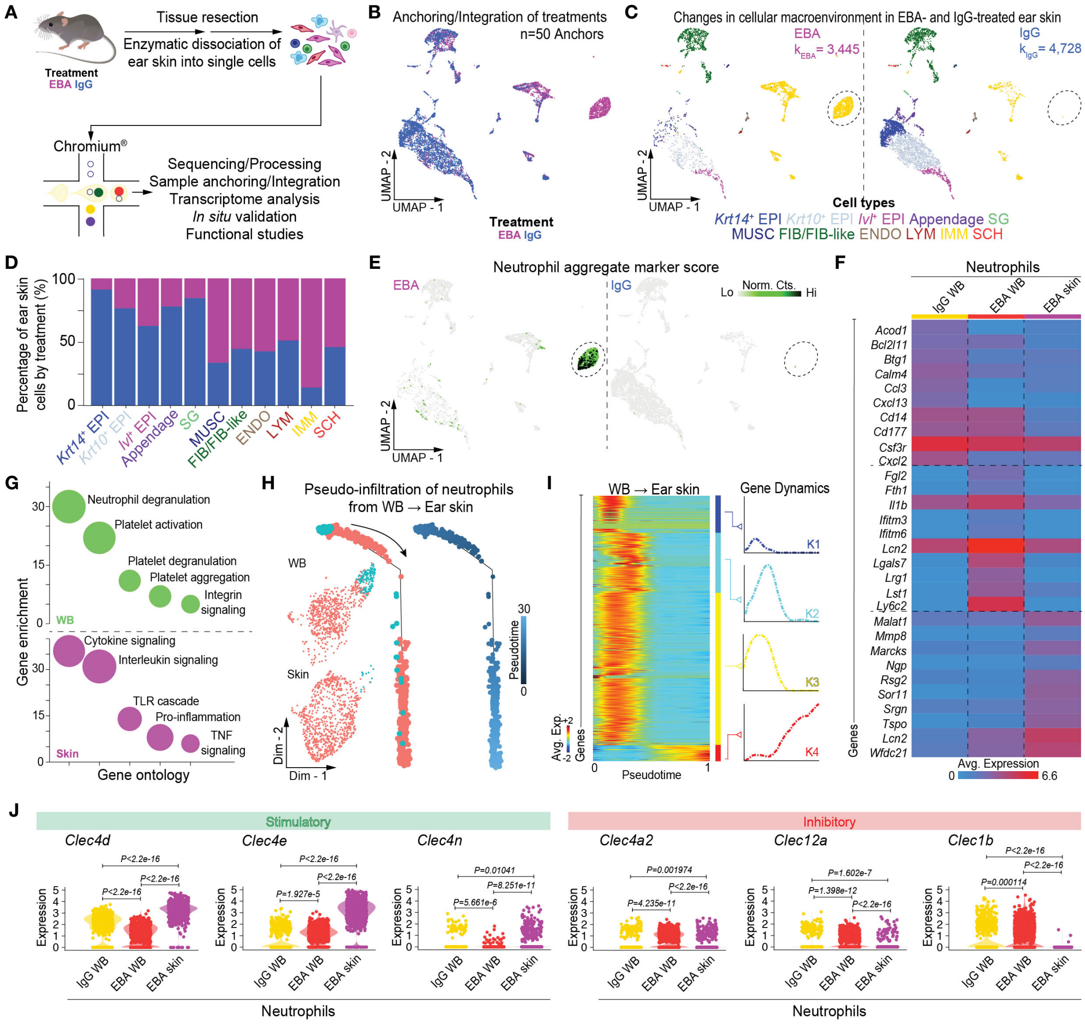

FIGURE 2

Single-cell transcriptome profiling of skin lesions in experimental EBA. **(A)** Schematic of ear skin cell isolation workflow. **(B)** Anchoring of skin cells from EBA or control mice into a single object and visualized in two-dimensional UMAP space. **(C)** Clustering and neighbor identification of anchored datasets. Eleven putative cell populations were identified and color coded. Putative cluster identity based on *bona fide* marker gene expression is defined on the bottom. Major cellular identities of recovered cells reveal a unique population of immune cells in the EBA relative to control group (circled). **(D)** Relative frequency of putative cellular identities of each cluster in EBA (magenta) and IgG control groups (blue). Cells from the EBA group contributed to a far greater number of immune cells, while a greater frequency of keratinocytes were recovered from the control group as expected. **(E)** Two-dimensional feature plot showing expression of aggregate, composite neutrophil gene score demonstrates the immune population unique to EBA skin to be neutrophils. Light green—low, black—high gene expression based on normalized counts. Data shown are from n = 3 pooled biologic replicates per condition. **(F)** Heatmap of differentially expressed genes between neutrophils from the skin and whole blood (LogF.C. = 0.25x, 25% cell/cluster, Wilcoxon Rank Sum Test $p < 0.05$). The top 10 upregulated genes from the following three comparisons are shown: control blood neutrophils versus EBA blood neutrophils; EBA blood neutrophils versus control blood neutrophils; and EBA skin neutrophils versus all blood neutrophils (control and EBA). **(G)** Gene ontology for biological process of differentially expressed genes (LogF.C. = 0.25x, 25% cell/cluster, Wilcoxon Rank Sum Test $p < 0.05$) in the cutaneous and activated neutrophil population respectively versus basal neutrophils. **(H)** Trajectory analysis in pseudotime depicting a pseudo-infiltration of neutrophils from blood into ear skin. **(I)** Rolling wave plot of pseudotemporal total gene (k=4) expression. Pseudotemporal gene expression is based on normalized counts. Blue—downregulated genes; Red—upregulated genes. **(J)** Violin plots demonstrate a relative increase in stimulator CTLR gene expression and decrease in inhibitory CTRL in EBA skin relative to blood neutrophils. EBA, epidermolysis bullosa acquisita; IgG, immunoglobulin G; UMAP, Uniform Manifold Approximation and Projection; EPI, epithelium; SG, sebaceous gland; MUSC, muscle; FIB/FIB-like, fibroblast/fibroblast-like; ENDO, endothelial; LYM, lymphatic; IMM, immune; SCH, Schwann; Norm. exp., normalized expression; WB, whole blood; Avg. Exp., average expression; Lo, low; Hi, high; Norm, Cts, normalized counts.

control and EBA neutrophils (Figure 3C) The percentage of neutrophils expressing Mincle and Dectin-3 was significantly increased in the skin relative to blood neutrophils ($p < 0.001$). We next sought to confirm the expression of these three CLTRs in human EBA patients by assessing formalin-fixed paraffin-embedded (FFPE) sections retrospectively. These sections were co-stained for myeloperoxidase (MPO) and either Dectin-2, Dectin-3, or Mincle. Skin neutrophils from patients with inflammatory EBA demonstrated consistent co-expression of Dectin-2, Dectin-3, and Mincle (Figure 3D). MPO-positive cells were uniformly positive for each CTLR. CTLRs were also detectable in few MPO-negative cells with a mononuclear morphology.

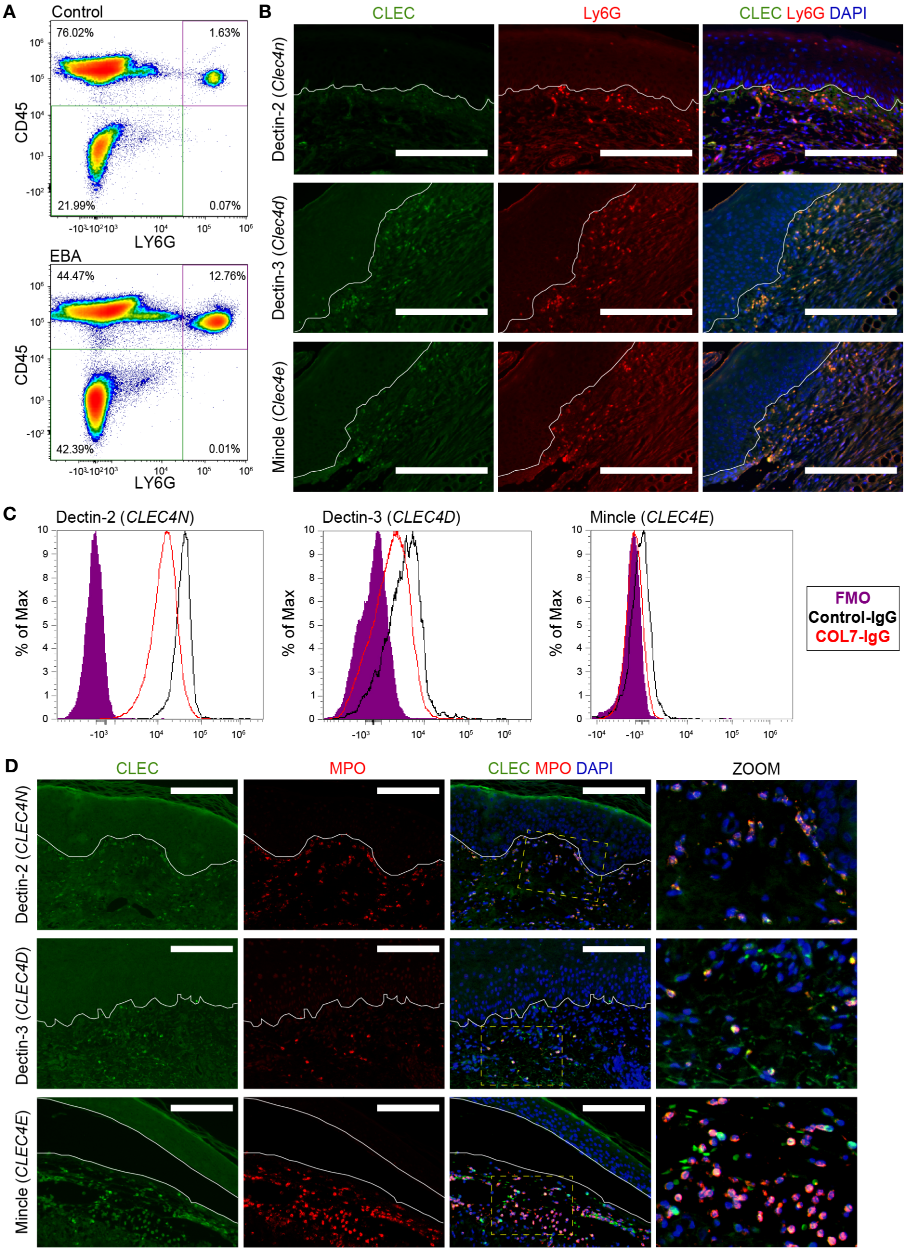

FIGURE 3
Expression of CLEC4 markers in human and experimental EBA neutrophils. **(A)** Flow cytometry of blood demonstrates an increased percentage of Ly6G$^+$CD45$^+$ cells in EBA relative to control mice. **(B)** Immunofluorescent staining of FFPE from mice with EBA reveals co-expression of Ly6G (green) and CLEC4 markers (red) overlaid with DAPI. Dectin-2, Dectin-3, and Mincle are expressed on a majority of neutrophils in experimental EBA. **(C)** Flow cytometry of blood neutrophils demonstrates that CLEC4N and CLEC4D are expressed on both control and EBA neutrophils, while CLEC4E is expressed only on a small number of neutrophils in both EBA and control mice (n = 3–4). **(D)** Immunofluorescent staining of FFPE from patients with inflammatory EBA demonstrates expression of CLEC4N/D/E (green) on MPO+ cells (red). Notes: Epidermis and dermis are demarcated by a white line. The inset demonstrates characteristic nuclear morphology of neutrophils on dually stained cells. Images from mouse tissue are representative of n = 10 from three independent experiments. Flow cytometry density plots are shown of a single biologic replicate and are representative of n = 3–4 mice. Images shown from patients with inflammatory EBA are representative of n = 5. Scale bars, 300 µm **(B)**; 300 µm **(D)**. EBA, epidermolysis bullosa acquisita; IgG, immunoglobulin G; FMO, fluorescent minus one.

Genetic deficiency in *Clec4d* and *Clec4e* and neutrophil-specific deficiency in *Clec4n* do not alter the course of EBA

We analyzed the functional significance of Dectin-3, Mincle, and Dectin-2 in EBA. To this end, we examined the course of EBA in globally genetically deficient *Clec4d*$^{-/-}$ and *Clec4e*$^{-/-}$ mice as well as in neutrophil-specific *Clec4n*$^{-/-}$ mice. The latter were generated by breeding *Clec4n*$^{fl/fl}$ with *Mrp8*$^{+/Cre}$ mice. The clinical course of skin inflammation as well as the histopathology of skin lesions were analyzed, as described in the *Materials and methods* section. Genetic deficiency of each CTLR did not change the course of disease at the clinical or the histopathological level (Figure 4).

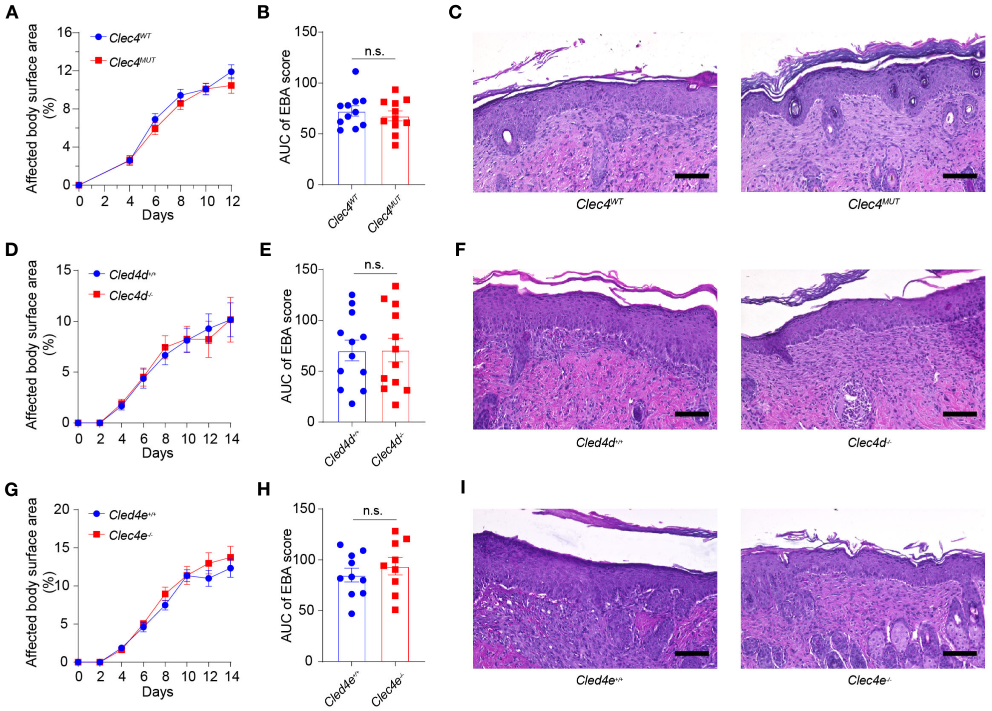

FIGURE 4
Genetic deficiency in *Clec4d*, *Clec4e*, and *Clec4n* in experimental EBA. **(A)** Affected Body Surface Area (BSA; clinical score) in antibody transfer-induced EBA in neutrophil-specific *Clec4n* ($Clec4n^{\Delta PMN}$) mutant mice). **(B)** Area under the curve analysis (AUC) of BSA over time. **(C)** Representative histology of $\text{CLEC4}^{\text{MUT}}$ and CLEC4^{WT} following 2 weeks of antibody transfer reveals comparable inflammatory infiltrate. Similar findings are noted in the **(D)** BSA, **(E)** AUC, and **(F)** histology of $Clec4d^{-/-}$ vs. $Clec4e^{+/+}$ WT, as well as **(G)** BSA **(H)** AUC, and **(I)** histology of $Clec4e^{-/-}$ vs. $Clec4e^{+/+}$ WT. All results are presented as mean ± SEM. Data were merged from two to three independent experiments (*n* = 10–11 mice/group). **(A, D, G)** were analyzed by two-way ANOVA; **(B, E, H)** were analyzed by Student's *t*-test. EBA, epidermolysis bullosa acquisita; BSA, body surface area; IgG, immunoglobulin G; AUC, area under the curve; n.s., not significant.

Discussion

In recent years, evidence has accumulated that neutrophils are plastic cells phenotypically adapting to inflammatory conditions much more than previously anticipated and thus, at least temporarily, becoming a more heterogenous cell population. Understanding the plasticity and heterogeneity of neutrophils under inflammatory conditions is presumably key to elucidate the role of neutrophils in the pathogenesis of disease. Furthermore, they may offer the opportunity for therapeutic interventions specifically targeting those neutrophil subpopulations and functions driving disease.

Our knowledge of neutrophil heterogeneity is, however, still scarce, and predominantly generated from models of infectious diseases instead of sterile chronic inflammatory diseases. The latter, which include autoimmune diseases, are still mostly treated with immunosuppressive strategies associated with significant adverse events, particularly a high susceptibility to infections. They may therefore benefit the most from novel approaches specifically targeting pathogenic neutrophil subpopulations. The development of such approaches requires in-depth knowledge of neutrophil phenotypes under specific disease conditions. Our study reveals that in EBA, as a prototypical example of an organ-specific autoimmune disease affecting the skin, neutrophils significantly change their phenotype both at the transcriptional and protein level. These changes proceed both in the peripheral blood and in the skin, suggesting that both systemic and local signals initiate these shifts in the transcriptome.

Importantly, these findings lay the path to specifically target neutrophils responding to molecular signals derived from site of emerging peripheral sterile tissue inflammation. These strategies may, e.g., either inhibit select effector or regulatory functions or exploit cell surface markers unique among neutrophils for the pathogenic subpopulations for targeted cell depletion. In addition, the changes in the transcriptome of neutrophils in the peripheral blood may be of interest for the development of new biomarkers for the early detection of emerging tissue inflammation in autoimmune and other sterile inflammatory diseases.

A most striking difference between neutrophils in the peripheral blood and in lesional skin was the induction of the three stimulatory CTLRs, i.e., Dectin-2, Dectin-3, and Mincle. All three receptors were also expressed on neutrophils in lesional skin from EBA patients, suggesting that our mouse model faithfully reflects an aspect of the human situation. Collectively, these findings highlight these CTLRs as markers for activated neutrophils in lesional skin in EBA. They are in line and extend the findings of Yao et al. (11), which uncovered that Dectin-2 is upregulated on murine neutrophils upon migration into peripheral tissues. CTLRs play a critical role in host defense against fungal and bacterial pathogens. Dectin-2, for example, regulates Th17 responses to histoplasmosis and coccidioidomycosis and plays a protective role in streptococcal immunity (29–31). Dectin-2 additionally regulates ROS production and NADPH oxidase-independent NETosis in *Candida* infection (32–34). Mincle has a critical function in mycobacterial immunity (35). Dectin-2 and Mincle represent pattern recognition receptors, binding to polysaccharide moieties and resulting in activation of CARD9 and the Myd88 signaling cascade (36, 37). Dectin-3 has additionally a crucial role in mycobacterial immunity as well as in Gram-negative lung infections (38, 39). More recently, CTLRs have also been implicated in the pathogenesis of certain types of sterile tissue inflammation. For example, blockade of Mincle and Dectin-1 binding decreases murine neutrophil cytotoxicity towards tumor cells by inhibiting binding of CTLRs with nidogen-1 (40). Inhibition of Dectin-2 additionally confers resistance to house dust mite airway inflammation with decreased neutrophil influx (41). Dectin-2 can also regulate Th2 immunity through the generation of cysteinyl leukotrienes (42).

In our EBA mouse model, Dectin-2, Dectin-3, and Mincle were upregulated on neutrophils but genetic deficiency in mice for one or the other receptor did not alter the course of skin inflammation. This finding indicates that none of the receptors play a critical, non-redundant role in the regulation of neutrophil activities in EBA. However, as all three receptors were upregulated, we still cannot exclude that they might play a significant redundant role in this process. While neutrophil activation in experimental EBA occurs in a Syk-dependent manner (43), activation appears to occur through a different pathway than CTLR coupling with Syk kinase (44). The upregulation of multiple CTLR likely represents a conserved host response initiated by molecular signals shared by both microbial and sterile tissue inflammation rather than a disease-specific neutrophil phenotype. It is plausible that neutrophils recruited to barrier organs start expressing receptors, allowing the detection of a broad spectrum of pathogens, especially fungi and bacteria. We additionally identified a decrease in the inhibitory CTLRs *Clec4a2*, *Clec12a*, and particularly *Clec1b* (also known as CLEC-2) (45, 46). It is possible that the loss of inhibitory CTLRs may be the contributing factor towards the inflammatory response seen with antibody transfer. For example, Clec1b deficiency has been linked to systemic edema (46). Further mechanistic studies would provide insight into the role of inhibitory CTLRs.

In summary, we demonstrate the transformation of the neutrophil transcriptome from blood to blister in a well-characterized model of EBA. While we have demonstrated that Dectin-2, Dectin-3, and Mincle are most notable on skin-infiltrating neutrophils, our knockout models suggest that they do not individually contribute to the pathogenic role of neutrophils in EBA.

Data availability statement

The datasets presented in this study can be found in online repositories. The names of the repository/repositories and accession number(s) can be found below: https://www.ncbi.nlm.nih.gov/geo/query/GSE231971.

Ethics statement

The studies involving humans were approved by Rush University Medical Center. The studies were conducted in accordance with the local legislation and institutional requirements. The participants provided their written informed consent to participate in this study. The animal study was approved by Rush University Medical Center (IACUC No 20-079) or the state government of Schleswig-Holstein. The study was conducted in accordance with the local legislation and institutional requirements.

Author contributions

CG-J: Formal Analysis, Methodology, Visualization, Writing – original draft, Writing – review & editing, Data curation. PS: Investigation, Visualization, Writing – review & editing. JL: Investigation, Writing – review & editing. MZ: Investigation, Methodology, Writing – review & editing. LB: Investigation, Writing – review & editing. PP: Investigation, Writing – review & editing. JG-T: Investigation, Validation, Writing – review & editing. SM: Funding acquisition, Investigation, Writing – review & editing. CC: Investigation, Writing – review & editing. MS: Investigation, Methodology, Writing – review & editing. MF: Resources, Writing – review & editing. TH: Resources, Writing – review & editing. NI: Resources, Writing – review & editing. TR: Investigation, Resources, Writing – review & editing. KB: Resources, Writing – review & editing. RL: Resources, Writing – review & editing. CS: Writing – original draft, Writing – review & editing. KA: Conceptualization, Formal Analysis, Methodology, Project administration, Resources, Supervision, Validation, Visualization, Writing – original draft, Writing – review & editing.

Funding

The authors declare financial support was received for the research, authorship, and/or publication of this article. KA is supported in part by the Office of Research Infrastructure Programs of the National Institute of Health (R21OD030057). RL is supported in part by Cluster of Excellence Precision Medicine in Chronic Inflammation (EXC 2167) and the Collaborative Research Center Pathomechanisms of Antibody-mediated Autoimmunity (SFB 1526), from both the Deutsche Forschungsgemeinschaft and the Schleswig-Holstein Excellence-Chair Program from the State of Schleswig Holstein.

Acknowledgments

Part of this work was presented as an abstract at the 2023 International Society of Investigative Dermatology meeting in Tokyo, Japan. We thank Lill Kristin Andersen and Tina Berthaler for their contribution to ES cell culture and mouse production. Histology services were provided by the Research

Resources Center–Research Histology and Tissue Imaging Core at the University of Illinois at Chicago established with the support of the Vice Chancellor of Research.

Conflict of interest

KA has served as a consultant for AstraZeneca, Argenx, and Akari Therapeutics. KA has received research funding from AstraZeneca, Argenx, and Kabafusion. RL has received honoraria for speaking or consulting or has obtained research grants from Novartis, Lilly, Bayer, Dompe, Synthon, Pharmaxis, CSL, Argen-X, and Incyte during the last 3 years.

The remaining authors declare that the research was conducted in the absence of any commercial or financial relationships that could be construed as a potential conflict of interest.

The author(s) declared that they were an editorial board member of Frontiers, at the time of submission. This had no impact on the peer review process and the final decision.

Publisher's note

Supplementary material

The Supplementary Material for this article can be found online at: https://www.frontiersin.org/articles/10.3389/fimmu.2023.1266359/full#supplementary-material

SUPPLEMENTARY FIGURE 1

Quality control metrics of scRNA-seq data from blood and ear skin. (Left) Probability density scores showing putative doublets/multiplets demarcated at the bimodal distribution of cells' doublet score. (Middle) Doublets/multiplets were projected on two-dimensional UMAPs and colored black. Singlets were then processed for quality control filtering. Singlets with abnormal gene numbers (350 > genes/cell < 5,000), high mitochondrial gene percentage (<10%), and outliers were removed. Viable singlets were used for downstream query and comparative analyses. (Right) Violin plots showing distribution of features and counts expression levels, and mitochondrial gene percentage in viable singlets used for downstream analyses. EBA, epidermolysis bullosa acquisita; IgG, immunoglobulin G; UMAP, Uniform Manifold Approximation and Projection; WBC, whole blood cells; QC, quality control.

SUPPLEMENTARY FIGURE 2

Immune populations in whole blood. **(A)** Relative percentage of immune cells in EBA (red) and control treatment (yellow), demonstrate a relative increase in immune cells in neutrophils, mast, and myeloid cells in EBA. Percentage of immune cells in EBA **(B)** and control-IgG injections **(C)** demonstrates shift from lymphocytes to myeloid cells in EBA. EBA, epidermolysis bullosa acquisita; IgG, immunoglobulin G; WB, whole blood; NKC, natural killer cell; Treg, regulatory T cell.

SUPPLEMENTARY FIGURE 3

Expression of CLEC genes on gated neutrophils in experimental EBA blood neutrophils. Two-dimensional feature plots showing expression of CLEC genes, including Clec4d, Clec4e, Clec4n, Clec4a2, Clec12a, and Clec1b in EBA skin versus EBA blood versus IgG control ear, blood, and skin neutrophils. Data are shown as a function of total bioinformatically gated, S100a8+, S100a9+, and Ly6g+ neutrophil cells on skin (left) and of gated neutrophils (right). Gray Light green, low normalized gene expression based on normalized counts; black, high normalized gene expression based on normalized counts. EBA, epidermolysis bullosa acquisita; IgG, immunoglobulin G; UMAP, Uniform Manifold Approximation and Projection; Lo, low; Hi, high; Norm, Cts, normalized counts.

SUPPLEMENTARY TABLE 1

Differentially expressed genes between EBA and control blood neutrophils.

SUPPLEMENTARY TABLE 2

Differentially expressed genes between lesional and blood neutrophils in experimental EBA.

SUPPLEMENTARY TABLE 3

Summary alignment metrics for each group.

SUPPLEMENTARY TABLE 4

List of significant gene ontology findings for neutrophils.

References

1. Kridin K, Kneiber D, Kowalski EH, Valdebran M, Amber KT. Epidermolysis bullosa acquisita: A comprehensive review. *Autoimmun Rev* (2019) 18:786–95. doi: 10.1016/j.autrev.2019.06.007

2. Koga H, Prost-Squarcioni C, Iwata H, Jonkman MF, Ludwig RJ, Bieber K. Epidermolysis Bullosa acquisita: the 2019 update. *Front Med (Lausanne)* (2018) 5:362. doi: 10.3389/fmed.2018.00362

3. Sezin T, Krajewski M, Wutkowski A, Mousavi S, Chakievska L, Bieber K, et al. The leukotriene B4 and its receptor BLT1 act as critical drivers of neutrophil recruitment in murine bullous pemphigoid-like epidermolysis Bullosa acquisita. *J Invest Dermatol* (2017) 137:1104–13. doi: 10.1016/j.jid.2016.12.021

4. Sezin T, Murthy S, Attah C, Seutter M, Holtsche MM, Hammers CM, et al. Dual inhibition of complement factor 5 and leukotriene B4 synergistically suppresses murine pemphigoid disease. *JCI Insight* (2019) 4(15):e128239. doi: 10.1172/jci.insight.128239

5. Sadik CD, Miyabe Y, Sezin T, Luster AD. The critical role of C5a as an initiator of neutrophil-mediated autoimmune inflammation of the joint and skin. *Semin Immunol* (2018) 37:21–9. doi: 10.1016/j.smim.2018.03.002

6. Sadik CD, Schmidt E, Zillikens D, Hashimoto T. Recent progresses and perspectives in autoimmune bullous diseases. *J Allergy Clin Immunol* (2020) 145:1145–7. doi: 10.1016/j.jaci.2020.02.020

7. Chiriac MT, Roesler J, Sindrilaru A, Scharffetter-Kochanek K, Zillikens D, Sitaru C. NADPH oxidase is required for neutrophil-dependent autoantibody-induced tissue damage. *J Pathol* (2007) 212:56–65. doi: 10.1002/path.2157

8. Wright HL, Moots RJ, Bucknall RC, Edwards SW. Neutrophil function in inflammation and inflammatory diseases. *Rheumatol (Oxford)* (2010) 49:1618–31. doi: 10.1093/rheumatology/keq045

9. Marchi LF, Sesti-Costa R, Ignacchiti MD, Chedraoui-Silva S, Mantovani B. *In vitro* activation of mouse neutrophils by recombinant human interferon-gamma: increased phagocytosis and release of reactive oxygen species and pro-inflammatory cytokines. *Int Immunopharmacol* (2014) 18:228–35. doi: 10.1016/j.intimp.2013.12.010

10. Condliffe AM, Kitchen E, Chilvers ER. Neutrophil priming: pathophysiological consequences and underlying mechanisms. *Clin Sci (Lond)* (1998) 94:461–71. doi: 10.1042/cs0940461

11. Yao Y, Matsushima H, Ohtola JA, Geng S, Lu R, Takashima A. Neutrophil priming occurs in a sequential manner and can be visualized in living animals by monitoring IL-1beta promoter activation. *J Immunol* (2015) 194:1211–24. doi: 10.4049/jimmunol.1402018

12. Drouin M, Saenz J, Chiffoleau E. C-type lectin-like receptors: head or tail in cell death immunity. *Front Immunol* (2020) 11:251. doi: 10.3389/fimmu.2020.00251

13. Xie X, Shi Q, Wu P, Zhang X, Kambara H, Su J, et al. Single-cell transcriptome profiling reveals neutrophil heterogeneity in homeostasis and infection. *Nat Immunol* (2020) 21:1119–33. doi: 10.1038/s41590-020-0736-z

14. Hu J, Huang Z, Yu M, Zhang P, Xia Z, Gao C. Caspase-8 activation in neutrophils facilitates autoimmune kidney vasculitis through regulating CD4(+) effector memory T cells. *Front Immunol* (2022) 13:1038134. doi: 10.3389/fimmu.2022.1038134

15. Dyring-Andersen B, Honore TV, Madelung A, Bzorek M, Simonsen S, Clemmensen SN, et al. Interleukin (IL)-17A and IL-22-producing neutrophils in psoriatic skin. *Br J Dermatol* (2017) 177:e321–e2. doi: 10.1111/bjd.15533

16. Leineweber S, Schonig S, Seeger K. Insight into interactions of the von-Willebrand-factor-A-like domain 2 with the FNIII-like domain 9 of collagen VII by NMR and SPR. *FEBS Lett* (2011) 585:1748–52. doi: 10.1016/j.febslet.2011.04.071

17. Kasprick A, Bieber K, Ludwig RJ. Drug discovery for pemphigoid diseases. *Curr Protoc Pharmacol* (2019) 84:e55. doi: 10.1002/cpph.55

18. Iwata H, Witte M, Samavedam UK, Gupta Y, Shimizu A, Ishiko A, et al. Radiosensitive hematopoietic cells determine the extent of skin inflammation in experimental epidermolysis Bullosa acquisita. *J Immunol* (2015) 195:1945–54. doi: 10.4049/jimmunol.1501003

19. Bieber K, Witte M, Sun S, Hundt JE, Kalies K, Dräger S, et al. T cells mediate autoantibody-induced cutaneous inflammation and blistering in epidermolysis bullosa acquisita. *Sci Rep* (2016) 6:38357. doi: 10.1038/srep38357

20. Schilf P, Künstner A, Olbrich M, WasChina S, Fuchs B, Galuska CE, et al. A mitochondrial polymorphism alters immune cell metabolism and protects mice from skin inflammation. *Int J Mol Sci* (2021) 22(3):1006. doi: 10.3390/ijms22031006

21. Wolock SL, Lopez R, Klein AM. Scrublet: computational identification of cell doublets in single-cell transcriptomic data. *Cell Syst* (2019) 8:281–91.e9. doi: 10.1016/j.cels.2018.11.005

22. Fan J, Salathia N, Liu R, Kaeser GE, Yung YC, Herman JL, et al. Characterizing transcriptional heterogeneity through pathway and gene set overdispersion analysis. *Nat Methods* (2016) 13:241–4. doi: 10.1038/nmeth.3734

23. Stuart T, Butler A, Hoffman P, Hafemeister C, Papalexi E, Mauck WM, et al. Comprehensive integration of single-cell data. *Cell* (2019) 177:1888–902.e21. doi: 10.1016/j.cell.2019.05.031

24. Kuleshov MV, Jones MR, Rouillard AD, Fernandez NF, Duan Q, Wang Z, et al. Enrichr: a comprehensive gene set enrichment analysis web server 2016 update. *Nucleic Acids Res* (2016) 44:W90–7. doi: 10.1093/nar/gkw377

25. Qiu X, Mao Q, Tang Y, Wang L, Chawla R, Pliner HA, et al. Reversed graph embedding resolves complex single-cell trajectories. *Nat Methods* (2017) 14:979–82. doi: 10.1038/nmeth.4402

26. Jin S, MacLean AL, Peng T, Nie Q. scEpath: energy landscape-based inference of transition probabilities and cellular trajectories from single-cell transcriptomic data. *Bioinformatics* (2018) 34:2077–86. doi: 10.1093/bioinformatics/bty058

27. Hu H, Miao YR, Jia LH, Yu QY, Zhang Q, Guo AY. AnimalTFDB 3.0: a comprehensive resource for annotation and prediction of animal transcription factors. *Nucleic Acids Res* (2019) 47:D33–D8. doi: 10.1093/nar/gky822

28. Butler A, Hoffman P, Smibert P, Papalexi E, Satija R. Integrating single-cell transcriptomic data across different conditions, technologies, and species. *Nat Biotechnol* (2018) 36:411–20. doi: 10.1038/nbt.4096

29. Puerta-Arias JD, Mejia SP, Gonzalez A. The role of the interleukin-17 axis and neutrophils in the pathogenesis of endemic and systemic mycoses. *Front Cell Infect Microbiol* (2020) 10:595301. doi: 10.3389/fcimb.2020.595301

30. Taylor PR, Roy S, Leal SM Jr., Sun Y, Howell SJ, Cobb BA, et al. Activation of neutrophils by autocrine IL-17A-IL-17RC interactions during fungal infection is regulated by IL-6, IL-23, RORgammat and dectin-2. *Nat Immunol* (2014) 15:143–51. doi: 10.1038/ni.2797

31. Akahori Y, Miyasaka T, Toyama M, Matsumoto I, Miyahara A, Zong T, et al. Dectin-2-dependent host defense in mice infected with serotype 3 Streptococcus pneumoniae. *BMC Immunol* (2016) 17:1. doi: 10.1186/s12865-015-0139-3

32. Ifrim DC, Bain JM, Reid DM, Oosting M, Verschueren I, Gow NA, et al. Role of Dectin-2 for host defense against systemic infection with Candida glabrata. *Infect Immun* (2014) 82:1064–73. doi: 10.1128/IAI.01189-13

33. Wu SY, Weng CL, Jheng MJ, Kan HW, Hsieh ST, Liu FT, et al. Candida albicans triggers NADPH oxidase-independent neutrophil extracellular traps through dectin-2. *PloS Pathog* (2019) 15:e1008096. doi: 10.1371/journal.ppat.1008096

34. Wu SY, Wu-Hsieh BA. Neutrophil extracellular trap killing assay of Candida albicans. *Bio Protoc* (2020) 10:e3716. doi: 10.21769/BioProtoc.3716

35. Lu X, Nagata M, Yamasaki S. Mincle: 20 years of a versatile sensor of insults. *Int Immunol* (2018) 30:233–9. doi: 10.1093/intimm/dxy028

36. Drummond RA, Saijo S, Iwakura Y, Brown GD. The role of Syk/CARD9 coupled C-type lectins in antifungal immunity. *Eur J Immunol* (2011) 41:276–81. doi: 10.1002/eji.201041252

37. Loures FV, Pina A, Felonato M, Feriotti C, de Araujo EF, Calich VL. MyD88 signaling is required for efficient innate and adaptive immune responses to Paracoccidioides brasiliensis infection. *Infect Immun* (2011) 79:2470–80. doi: 10.1128/IAI.00375-10

38. Wilson GJ, Marakalala MJ, Hoving JC, van Laarhoven A, Drummond RA, Kerscher B, et al. The C-type lectin receptor CLECSF8/CLEC4D is a key component of anti-mycobacterial immunity. *Cell Host Microbe* (2015) 17:252–9. doi: 10.1016/j.chom.2015.01.004

39. Steichen AL, Binstock BJ, Mishra BB, Sharma J. C-type lectin receptor Clec4d plays a protective role in resolution of Gram-negative pneumonia. *J Leukoc Biol* (2013) 94:393–8. doi: 10.1189/jlb.1212622

40. Sionov RV, Lamagna C, Granot Z. Recognition of Tumor nidogen-1 by neutrophil C-type lectin receptors. *Biomedicines* (2022) 10(4):908. doi: 10.10.3390/biomedicines10040908

41. Clarke DL, Davis NH, Campion CL, Foster ML, Heasman SC, Lewis AR, et al. Dectin-2 sensing of house dust mite is critical for the initiation of airway inflammation. *Mucosal Immunol* (2014) 7:558–67. doi: 10.1038/mi.2013.74

42. Barrett NA, Rahman OM, Fernandez JM, Parsons MW, Xing W, Austen KF, et al. Dectin-2 mediates Th2 immunity through the generation of cysteinyl leukotrienes. *J Exp Med* (2011) 208:593–604. doi: 10.1084/jem.20100793

43. Samavedam UK, Mitschker N, Kasprick A, Bieber K, Schmidt E, Laskay T, et al. Whole-genome expression profiling in skin reveals SYK as a key regulator of inflammation in experimental epidermolysis Bullosa acquisita. *Front Immunol* (2018) 9:249. doi: 10.3389/fimmu.2018.00249

44. Chiffoleau E. C-type lectin-like receptors as emerging orchestrators of sterile inflammation represent potential therapeutic targets. *Front Immunol* (2018) 9:227. doi: 10.3389/fimmu.2018.00227

45. Redelinghuys P, Brown GD. Inhibitory C-type lectin receptors in myeloid cells. *Immunol Lett* (2011) 136:1–12. doi: 10.1016/j.imlet.2010.10.005

46. Bénézech C, Nayar S, Finney BA, Withers DR, Lowe K, Desanti GE, et al. CLEC-2 is required for development and maintenance of lymph nodes. *Blood* (2014) 123:3200–7. doi: 10.1182/blood-2013-03-489286

frontiers | Frontiers in Immunology

TYPE Original Research
PUBLISHED 26 September 2023
DOI 10.3389/fimmu.2023.1265517

EDITED BY
Shiang-Jong Tzeng,
National Taiwan University, Taiwan

REVIEWED BY
Yale Liu,
The Second Affiliated Hospital of Xi'an
Jiaotong University, China
Xiaoming Yang,
University of South Carolina, United States

*CORRESPONDENCE
Yuzhen Li
✉ lyzdermatology@163.com
Yizhou Hu
✉ yizhou.hu@ki.se

†These authors have contributed equally to this work

RECEIVED 23 July 2023
ACCEPTED 11 September 2023
PUBLISHED 26 September 2023

CITATION
Gao Y, Na M, Yao X, Li C, Li L, Yang G, Li Y and Hu Y (2023) Integrative single-cell transcriptomic investigation unveils long non-coding RNAs associated with localized cellular inflammation in psoriasis.
Front. Immunol. 14:1265517.
doi: 10.3389/fimmu.2023.1265517

Integrative single-cell transcriptomic investigation unveils long non-coding RNAs associated with localized cellular inflammation in psoriasis

Yuge Gao[1†], Mengxue Na[1†], Xinyu Yao[2†], Chao Li[1], Li Li[3], Guangyu Yang[1], Yuzhen Li[1*] and Yizhou Hu[4*]

[1]Department of Dermatology, The Second Affiliated Hospital of Harbin Medical University, Harbin, China, [2]Department of Dermatology, Peking University First Hospital, Beijing, China, [3]Department of Oncology, The Second Affiliated Hospital of Harbin Medical University, Harbin, China, [4]Department of Medical Biochemistry and Biophysics, Karolinska Institute, Stockholm, Sweden

Psoriasis is a complex, chronic autoimmune disorder predominantly affecting the skin. Accumulating evidence underscores the critical role of localized cellular inflammation in the development and persistence of psoriatic skin lesions, involving cell types such as keratinocytes, mesenchymal cells, and Schwann cells. However, the underlying mechanisms remain largely unexplored. Long non-coding RNAs (lncRNAs), known to regulate gene expression across various cellular processes, have been particularly implicated in immune regulation. We utilized our neural-network learning pipeline to integrate 106,675 cells from healthy human skin and 79,887 cells from psoriatic human skin. This formed the most extensive cell transcriptomic atlas of human psoriatic skin to date. The robustness of our reclassified cell-types, representing full-layer zonation in human skin, was affirmed through neural-network learning-based cross-validation. We then developed a publicly available website to present this integrated dataset. We carried out analysis for differentially expressed lncRNAs, co-regulated gene patterns, and GO-bioprocess enrichment, enabling us to pinpoint lncRNAs that modulate localized cellular inflammation in psoriasis at the single-cell level. Subsequent experimental validation with skin cell lines and primary cells from psoriatic skin confirmed these lncRNAs' functional role in localized cellular inflammation. Our study provides a comprehensive cell transcriptomic atlas of full-layer human skin in both healthy and psoriatic conditions, unveiling a new regulatory mechanism that governs localized cellular inflammation in psoriasis and highlights the therapeutic potential of lncRNAs in this disease's management.

KEYWORDS

psoriasis, lncRNA, single cell, skin, transcriptomic atlas, localized inflammation

Introduction

Psoriasis is a genetically related, immune-mediated chronic inflammatory systemic disease characterized by skin manifestations, with a prevalence rate of approximately 2% to 3% worldwide, leading a significant burden of disease (1). Psoriasis can cause skin redness, swelling, scales, and other systems such as joints, blood vessels, and intestines, and relate to the occurrence of metabolic diseases such as diabetes.

An increasing number of cell subtypes have been implied to contribute to psoriasis pathogenesis. These cell subtypes interact and form a complicated regulatory network, impacting one another in numerous ways. Key genetic loci within skin-resident cell types can directly affect non-immune cell immune regulation, resulting in localized skin cell inflammation (2). This persistent inflammatory state, either directly or indirectly, contributes to psoriasis onset. Therefore, the localized inflammation in the skin is a distinct hallmark of psoriasis. Despite substantial strides in understanding the underlying mechanisms of psoriasis, effective treatments specifically addressing the localized inflammation seen in psoriatic skin are yet to be discovered. Notably, the epigenetic regulatory mechanisms governing inflammation within resident skin cells remain largely elusive.

Non-coding RNAs (ncRNAs), a class of RNA molecules that do not encode proteins, have emerged as critical regulators of gene expression, and aberrant ncRNA expression has been implicated in various diseases, including psoriasis (3). Among ncRNAs, long non-coding RNAs (lncRNAs) have garnered considerable attention for their diverse functions in regulating gene expression, ranging from transcriptional and post-transcriptional regulation to epigenetic modulation. Recent studies have shown that lncRNAs can modulate various cellular processes involved in inflammation and immune regulation, suggesting a potential role for lncRNAs in psoriasis pathogenesis (4, 5).

The advent of single-cell transcriptomics has revolutionized the field of genomics, enabling the study of gene expression at the resolution of individual cells. It can define cell subpopulations with potential therapeutic targets and characterize the specific responses of cell subpopulations to drugs or other stimuli (6). In the context of psoriasis, single-cell transcriptomic (scRNAseq) datasets generated from different research groups have revealed the cellular diversity of psoriasis lesions and identified novel cell populations involved in the pathogenesis of psoriasis (2, 7, 8). scRNAseq can discover new cell subpopulations and evaluate organ- or tissue-specific transcriptomic features of keratinocytes (KCs), fibroblasts, endothelial cells, and immune cells that are involved in inflammation or infiltration, elucidating the functional heterogeneity of cells in psoriasis. It is also used to analyze cell distribution and cell-to-cell communication, providing new clues to the complex interactions between components involved in disease response (9). However, the data batch exists across these datasets, obstacle the skin cell classification and the accuracy of exploring the underlying pathogenesis of psoriatic skin.

In this study, we employed our neural-network learning pipeline to integrate 106,675 cells from healthy human skin and 79,887 cells from psoriatic human skin. This integration resulted in the most comprehensive cell transcriptomic atlas of human psoriatic skin so far. Cross-validation, grounded on neural-network learning, affirmed the validity of our reclassified cell-types, portraying full-layer zonation in human skin. We also launched a publicly accessible website featuring this consolidated dataset (https://yz-studio.shinyapps.io/psoriaticskincellatlas2/). Furthermore, this study pioneers the use of single-cell transcriptomics of entire skin tissue to pinpoint lncRNAs that modulate localized inflammation in psoriasis at the cellular level. We profiled transcriptomes of individual cells isolated from psoriatic lesions and healthy skin, identifying novel differentially expressed lncRNAs involved in localized inflammation. These lncRNAs, previously not associated with psoriasis, constitute promising candidates for future research and therapeutic development. Our study furnishes novel insights into the regulatory mechanisms at the heart of psoriasis pathogenesis, and underscores the power of single-cell transcriptomics in discerning disease-relevant cell populations and molecular targets.

Materials and methods

Single-cell data analysis

The single-cell data analysis was described in our previous study (10, 11), including neural network learning and visualization, differential gene expression in each cell-type, GO enrichment. Most analysis tools have been integrated in the toolkit scCAMEL with tutorials online: https://sccamel.readthedocs.io/. The website representing our integrated cell atlas were constructed by using Shinny apps. To strike a balance between accuracy and efficient website navigation, we downsampled the cell number to maximum 300 for each cell type (12), under each condition, and for each donor. This resulted in a total of 49,237 cells available for website visualization.

Improved SWAPLINE integration and projection

We enhanced the SWAPLINE package by augmenting its adaptability during dataset integration and projection, thus generating an updated version, as detailed in our recent publication (10, 11). Briefly, we utilized an interpretable neural network for training each dataset and predicting all other datasets. The probabilistic scores derived from both trained and predicted datasets form the latent space for subsequent analysis. Using this approach, we successfully integrated a healthy skin reference dataset and reclassify the cell types to reflect the full-layer skin zonation. The improved SWAPLINE and the integration case study will be published separately.

For projecting human healthy and psoriatic skin datasets in this study, we computed the probabilistic score for each cell within each query dataset in the trained reference datasets, building the latent space for label transfer analysis in nearest neighbor model. At the same time, gene expression normalization and denoising were carried out using an interpretable learning nearest neighbor model. Feature weights for each reference cell type were estimated using the DeepLift algorithm in the Captum package for PyTorch. The gene expression for each cell, either learned or predicted in a trained reference dataset, was inferred through matrix multiplication of the feature weights and cell-type probabilistic scores. In the end, the gene-cell expression matrix was computed by averaging non-empty values across all datasets. Therefore, with a ready-built reference skin cell transcriptomic atlas, we successfully project the healthy and psoriatic skin cells from three public datasets, recovered the expression of most protein-coding genes and lncRNAs (2, 8, 9).

Sample collection and ethics approval

This experiment recruited volunteers with diagnosed psoriasis and healthy controls, all of whom signed an informed consent form and underwent ethical review declaration. Typical lesion sites on the trunk were selected, and after disinfection, full-thickness skin samples were surgically excised and excess subcutaneous tissue and fat were removed. Cell digestion solution was prepared in RPMI 1640 10% FBS medium with collagenase IV (VETEC, USA) 200 U/ml and DNase I (Solarbio, CHN) 200 μg/ml at appropriate concentrations. The tissue was minced and digested overnight in a 37°C, 5% CO2 incubator. The resulting single-cell suspension was obtained after centrifugation and filtration and was used for flow cytometry cell sorting.

Flow cytometry

For the flow cytometric analysis sorting, skin cells were sorting according to Propidium Iodide (Biosharp, China). The PI-negative cells were immunolabeled with *IL-20RB* Polyclonal antibody (Proteintech, USA), then immunolabeled with Goat Anti Rabbit IgG(H&L)-Alexa Fluor 488 and PE anti-human *CD140b* (*PDGFRB*) Antibody (Biolegend, USA). *IL20RB*-positive and *PDGFRB*-positive cells were collected on Beckman MoFloXDP for RT-qPCR analysis of gene expression levels, the result was analyzed by FlowJo.

For flow cytometry, live DCs were immunolabeled with APC-CY7-livedead (Thermo Fisher Scientific, Massachusetts, USA), Brilliant Violet 605™ anti-mouse *CD11C* (BioLegend, CA), PE anti-mouse *CD80* (Thermo Fisher Scientific), FITC anti-mouse *CD86* (Thermo Fisher Scientific) at 4°C for 30 min. All cells were detected on Beckman Cytoflex LX and the result was analyzed by FlowJo.

RT-qPCR

Dispersed cell suspensions or cell samples were extracted with TRIzol (Invitrogen, Australia) to obtain total RNA. All-in-one First Strand cDNA Synthesis Kit (Seven, CHN) was used to prepare the DNA library. The reaction was terminated by incubating at 85°C for 5 seconds. Quantitative real-time PCR was performed using the 2× SYBR Green kit (Seven, CHN) on a fluorescence quantitative PCR detection system (Hangzhou Bori, CHN). The reaction was performed according to the manufacturer's instructions. Relative gene expression was calculated using the 2-ΔΔCT method. All experiments were repeated three times.

Primer sequence as follows: *SNHG9* human F: GACTGCAGACCCCTAACCTT; R: ACCCGCATGCAGTGAGTTA. *CALML3-AS1* human F: TGCAGTGTCACTCTGGAAGC; R: CACTGTCTCAGGCCAGGTTT. *CARMN* human F: AGGAGAGCAACGGCTGTAAC; R: TCTCTGACATCAGCATGGCG. *GAPDH* human F: CATGTTCGTCATGGGTGTGAA; R: GGCATGGACTGTGGTCATGAG. *CXCL8* human F: TTTTGCCAAGGAGTGCTAAAGA; *CXCL8* human R: AACCCTCTGCACCCAGTTTTC. *CCL20* human F: TGCTGTACCAAGAGTTTGCTC; *CCL20* human R: CGCACACAGACAACTTTTTCTTT. *IL-17B* human F: AGCCCCAAAAGCAAGAGGAA; *IL-17B* human R: TGCGGGCATACGGTTTCATC. *IL-1B* human F: ATGATGGCTTATTACAGTGGCAA; *IL-1B* human R: GTCGGAGATTCGTAGCTGGA. *IL6* human F: ACTCACCTCTTCAGAACGAATTG; *IL6* human R: CCATCTTTGGAAGGTTCAGGTTG.

Cell culture and RNA interference

HACAT cells were cultured in DMEM medium containing 10% fetal bovine serum. HSF cells were cultured in F12 medium containing 10% fetal bovine serum. siRNAs were used to silence *SNHG9/CALML3-AS1* in the HACAT cell line and *CARMN* in the HSF, transfected with Lipo8000 transfection reagents (Beyotime, CHN) following the product manual, with cells treated with blank siRNA serving as negative controls. Cells were stimulated with recombinant human TNF-α protein (Abcam) 50ng/ml to simulate localized inflammation.

siRNA sequences targeting the lncRNA as follow: *CALML3-AS1-Homo-2405*: GGUGUUCCUCGCAUGACUUTT; AAGUCAUGCGAGGAACACCTT. *CARMN-Homo-899*: CCUGUGCUCUGUGACAAUATT; UAUUGUCACAGAGCACAGGTT. *SNHG9-Homo-78*: CCCGAAGAGUGGCUAUAAATT; UUUAUAGCCACUCUUCGGGTT.

Co-culture of skin resident cells and dendritic cells

pDCs purchased from ATCC, and were cultured in 1640 medium containing 10% fetal bovine serum, 1% penicillin/streptomycin, 10ng/ml recombinant human IL-4 protein, and 20ng/ml granulocyte-macrophage colony-stimulating factor (GM-CSF) under 37°C and 5% CO2 for 7 days. After washing and collecting the cells, they were mixed with dendritic cells and cultured overnight in 1640 medium containing 10% fetal bovine serum under 37°C and 5% CO2. Dendritic cells were labeled with

CD11C, and CD80 and CD86 were used as activation markers. Flow cytometry was used to detect the cells, and the proportion of CD80 and CD86 positive cells in CD11C positive dendritic cells was calculated to evaluate the degree of DCs activation by skin-resident cells in different groups.

Statistical analysis

Statistical analysis was performed by GraphPad Prism 9 software. All the data values were presented as means ± SEM. The statistical significance was assessed by Student's unpaired two taied t test for the two-group comparison. Each experiment was repeated at least three times. $P < 0.05$ was considered statistically significant ($*P < 0.05$, $**P < 0.01$, $***P < 0.001$, $****P < 0.0001$).

Results

Neural-network learning based integrative analysis constructs the cell transcriptomic atlas of psoriatic skin

By employing our recently developed interpretable neural-network analysis toolkit, we successfully integrated 106,675 cells from healthy human skin and 79,887 cells from psoriatic human skin across three public datasets (2, 7, 8). Through this, we construct the largest transcriptomic cell atlas of human psoriatic skin to date.

To make an insight further into the role of localized inflammation in resident skin cells during psoriasis, we performed an extensive clustering of epidermal and mesenchymal cells, revealing 21 main skin cell subtypes (Figures 1A, B). Employing interpretable learning, we recovered over 30,000 features of protein coding genes and lncRNAs, and assessed the marker genes for each cell type (Figure 1C). Various cell types and subtypes were defined by distinct markers. *CLDN5* and *PECAM1* distinguished two types of endothelial cells, with lymphatic endothelial cells (Endo_Endo-Lymph) highly expressing *TFF3* and *MMRN1*, and regular endothelial cells expressing *CD34* and *EMCN*. Nine epidermal cell subtypes were identified following skin cell zonation, and we observed a gradient change in marker genes (*KRT14*, *KRT5*, *SBSN*, *CALML5*, *GRHL1*, *TGM3*) from basal layers to granular layers, including basal cell (EpD_KRT1_Basal), basal-spinous intermedia cell (EpD_KRT3_earlySpinous), differentiating spinous-granular cell (EpD_KRT4_diffSpinous), granular cell (EpD_ERT5_Granular), and a few cells of basal-granular intermedia cell type (EpD_KRT6_BasalGranular). Inflammatory basal cell (EpD_KRT2_Basalinflammatory) were branched out from basal cell types due to the high expression of immune driver genes like *JUNB* and *JUND*. Our machine learning strategy also identified a small group of cells similar to hair follicle cells (EpD_HF_HairFollicle), but we could not identify any specific markers for this cell type due to the limited cell number.

We identified six mesenchymal cell subtypes, which could be classified into either *PDGFRA*-high/*PDGFRB*-low fibroblasts or *PDGFRB*-high/*PDGFRA*-low perivascular mural cells. Fibroblast cell types include fibroblast dermal papillae (Mes_FibroDS, labeled by *COL11A1*, *TNN*), inflammatory fibroblast (Mes_FibroInflammatory, labeled by *CXCL12*, *IGFBP7*), Papillary fibroblast (Mes_FibroPapillary, labeled by *COL13A1*-high/*COL18A1*-high), and Reticular fibroblast (Mes_FibroReticular, labeled by *COL13A1*-low/*COL18A1*-high). Perivascular mural cells include two main types: Mes_PeriV (*ACTA2*-high/*TAGLN*-high), and Mes_PeriVInflammatory (*STAT3*-high/*CCL2*-high). Immune cells comprised two main subtypes: lymphocytes (Imm_Lymphocyte, labeled by *PTPRC*-high/*HCST*-high) and

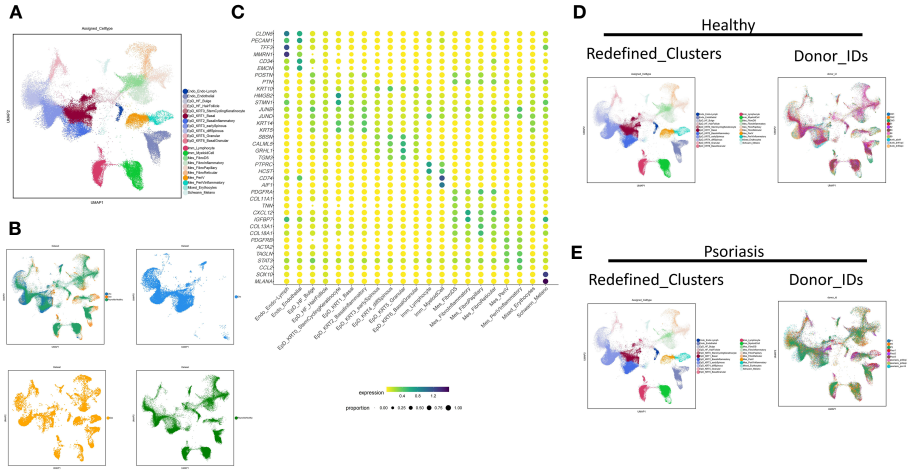

FIGURE 1
Neural-network learning based integrative analysis constructs the cell transcriptomic atlas of psoriatic skin. **(A, B)** UMAP visualization of the integrated cell transcriptomic atlas of human healthy and psoriatic skin. Each cell marked by ".", colored by cluster names **(A)**. Original datasets are colored in an integrated visualization and separated visualization **(B)**. **(C)** Normalized gene expression defining each cell type of human healthy and psoriatic skin. Blue-to-red color gradient and dot size from small to large represent expression level and cell percent from low to high. **(D, E)** UMAP visualization of the integrated cell transcriptomic atlas of human healthy **(D)** and psoriatic skin **(E)**. Each cell marked by ".", colored by cluster names at the left side. Each donor colored at the right side.

myeloid cells (Imm_MyeloidCell, *CD74*-high/*AIF1*-high). Lastly, Schwann cells and melanocytes were grouped together as Schwann_Melano (*SOX10*, *MLANA*), and erythrocytes and a few undefined cells were categorized as Mixed_Erythrocytes with no typical maker genes.

The distribution of these cell subtypes was consistent across different datasets, indicating the reliability of the classification (Figure 1B). Furthermore, we visualized the cell clustering and individual distribution in both healthy and psoriatic skin, and the results were consistent with our clustering definitions (Figures 1D, E).

The robustness of our current skin cell classification

Next, we examined the robustness of our redefined clusters. Firstly, we compared the redefined cell subgroups with the previous cell classifications of our published dataset (2). We found that the new epidermal and mesenchymal cell subtypes were more specific, while all cell subtypes remained consistent with the previous findings (Figure 2A). Furthermore, we employed the machine learning to evaluate the assignment accuracy under the condition of current cell-type classification and observed more than 90% accuracy in our defined cell-types under both healthy and psoriasis condition (Figures 2B, C). We used this ready-built learning model to predict the other two datasets involved in our study (Figures 2D, E), and all defined cell-types were correctly predicted except two cell-types (EpD_HF_HairFollicle and EpD_KRT6_BasalGranular) (7, 8). Both of these two cell-types are more specific to mouse hair skin, and rarely observed in human skin (data will be published separately). Interestingly, our redefined cell-types also correctly recognized the layer zonation that confirmed that Cho dataset (7) is only from human epidermis.

The differential expression of lncRNAs in each cell-type between health and psoriatic skin

Through further analysis and experimental validation, our previous study uncovered that several subtypes of skin resident cells from epidermal and mesenchymal origins can participate in localized inflammation through alternative immune pathways and contribute to the development of psoriasis (2). To further study the differential expression and function of long non-coding RNAs in psoriasis at the single-cell level, we analyzed the expression of lncRNAs in all cell subgroups from our integrated psoriasis skin cell atlas and identified all lncRNAs that were specifically upregulated or downregulated in each skin cell type during the disease state. All lncRNAs identified are presented in SI_Table 1.

To expand upon the differential expression patterns of lncRNAs, we meticulously parsed our dataset to focus on individual cell subtypes of epidermal and mesenchymal cells, particularly under psoriasis conditions, as detailed in SI_Table 1. From this analysis, we have earmarked highly specific marker genes within the epidermal and mesenchymal cell clusters, setting them aside for deeper exploration in forthcoming experiments.

Through this analysis, we pinpointed pronounced fluctuations in the expression of *SNHG9* in an array of epidermal cell subtypes, including EpD_Basal2, EpD_Basal3, EpD_Corneum, EpD_Foli, EpD_Granular-spinous, EpD_Granular, and EpD_Spinous. In addition, our scrutiny unveiled distinct expression variations in *CALML3-AS1* within the EpD_Basal1 cell subtype, coupled with

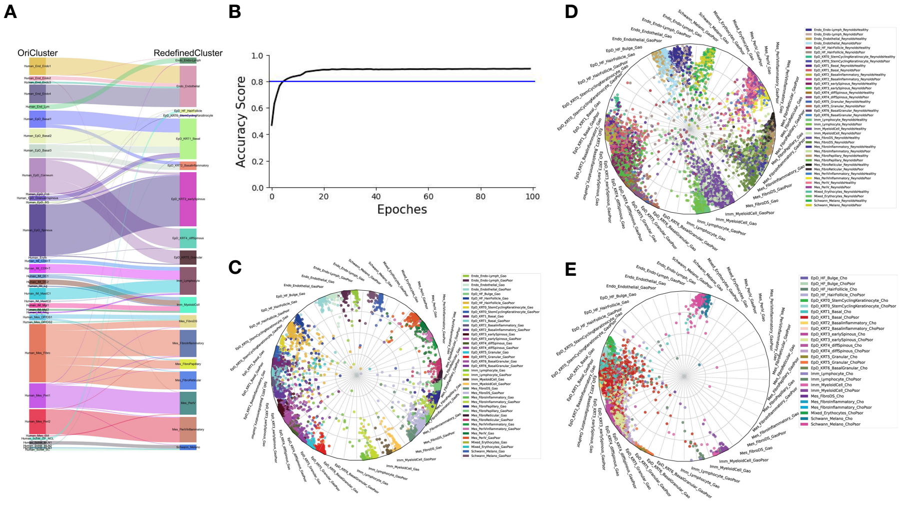

FIGURE 2
The robustness of our current skin cell classification. **(A)** Sankey plot visualization of the cell-type assignment between our original cell-types (left) and the currently redefined cell-types (right). Sankey flows between left and right are colored by the original cell-types. **(B)** Learning curve (Black) indicates the classification accuracy, blue line indication the threshold of 80% accuracy. **(C–E)** Radar plot visualization of the cell-type scores of skin cells from Gao dataset **(C)**, Reynold dataset **(D)** and Cheng/Cho dataset **(E)** in relation to the trained reference cell types (Gao dataset). Color coding based on cell types (left) as shown at the right side. The position of each dot indicates the cell-type score between that cell and the trained reference cell types, which are indicated outside each wheel bend.

marked differentiation in the expression of *CARMN* in mesenchymal clusters, namely Mes_DP-DS1 and Mes_Fibro.

To experimental validate the immunoregulatory potential of cell-type specific lncRNAs, we selected three lncRNAs (*SNHG9*, *CALML3-AS1*, and *CARMN*), and in silico examined their expression levels in different cell clusters under healthy and psoriasis conditions (Figures 3A, B). We found that *SNHG9* exhibited significantly higher expression in the EpD_KRT0_StemCyclingKeratinocyte, EpD_KRT1_Basal, EpD_KRT2_ Basalinflammatory and EpD_ KRT3_earlySpinous clusters in psoriasis skin. *CALML3-AS1* showed increased expression in the EpD_HF_HairFollicle, EpD_ KRT0_StemCyclingKeratinocyte, EpD_KRT1_Basal, EpD_KRT2_ Basalinflammatory, EpD_KRT3_earlySpinous, EpD_KRT4_ diffSpinous, EpD_KRT5_Granular and EpD_KRT6_BasalGranular clusters in both normal and psoriasis skin, with significant upregulation observed in psoriasis. *CARMN* demonstrated elevated and significant expression in EpD_KRT2_ Basalinflammatory, EpD_KRT3_earlySpinous, EpD_KRT4_diffSpinous, Mes_ PeriVInflammatory and Mes_PeriV clusters in both normal and psoriasis skin (Figure 4A). For detailed expression patterns of all lncRNAs in different cell clusters, please refer to SI_Table 1.

Experimental validation of the expression change of lncRNAs *SNHG9*, *CALML3-AS1* and *CARMN* in psoriatic skin

To further confirm the expression patterns and potential functions of these lncRNAs in psoriasis and healthy skin cell subtypes, we performed the following experiments. First, we collected full-thickness skin tissue from patients with moderate to severe psoriasis and healthy volunteers, respectively, and obtained cell suspensions after digestion and dissociation. Then, we sorted the cells according to their cell type maker genes by flow cytometry (Figure 4B). *IL20RB* was used as a marker for epidermal cells, and *PDGFRB* was used as a marker for mesenchymal-derived cells. It has been previously validated that *IL20RB* and *PDGFRB* can be used as markers for epidermal and dermal mesenchymal cells, respectively, which is consistent with the single-cell RNA sequencing results in our experiment (13–15). We then used fluorescent quantitative PCR to detect the expression of specific lncRNAs in sorted epidermal and mesenchymal-derived cells. We found that in clinical skin samples, the expression levels of *SNHG9*, *CALML3-AS1* in epidermal cell types were significantly higher in

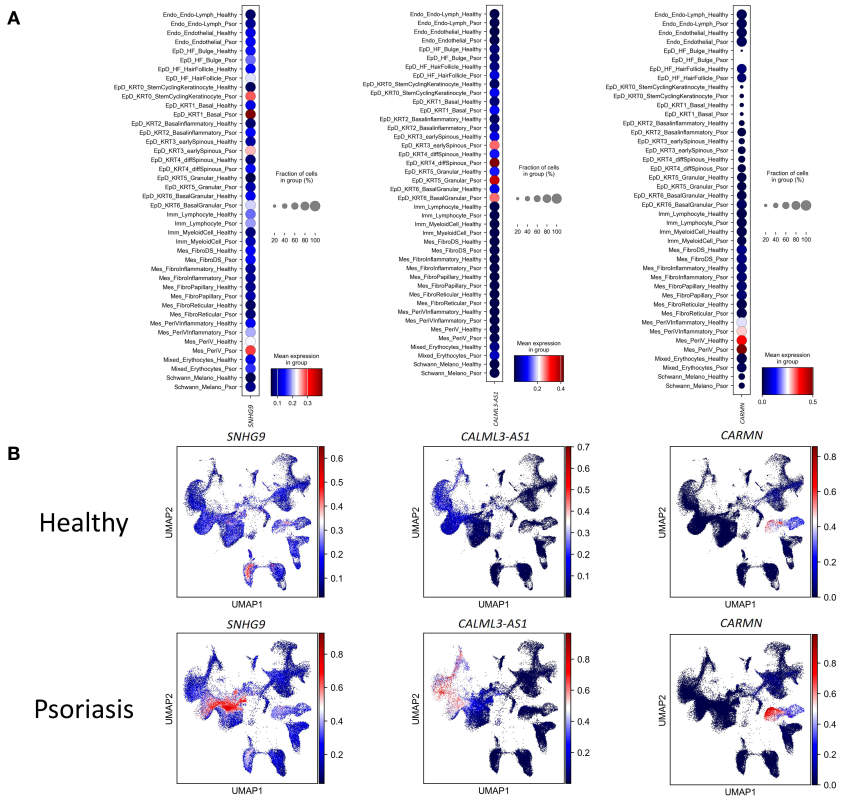

FIGURE 3
The differential expression of lncRNAs in each cell-type between health and psoriatic skin. **(A)** Normalized gene expression defining each cell type of human healthy and psoriatic skin. Blue-to-red color gradient and dot size from small to large represent expression level and cell percent from low to high. **(B)** UMAP visualization of comparing the lncRNAs' expression between human healthy and psoriatic skin. LncRNA names are listed at the top of each sub plot. Blue-to-red color gradient represent expression level.

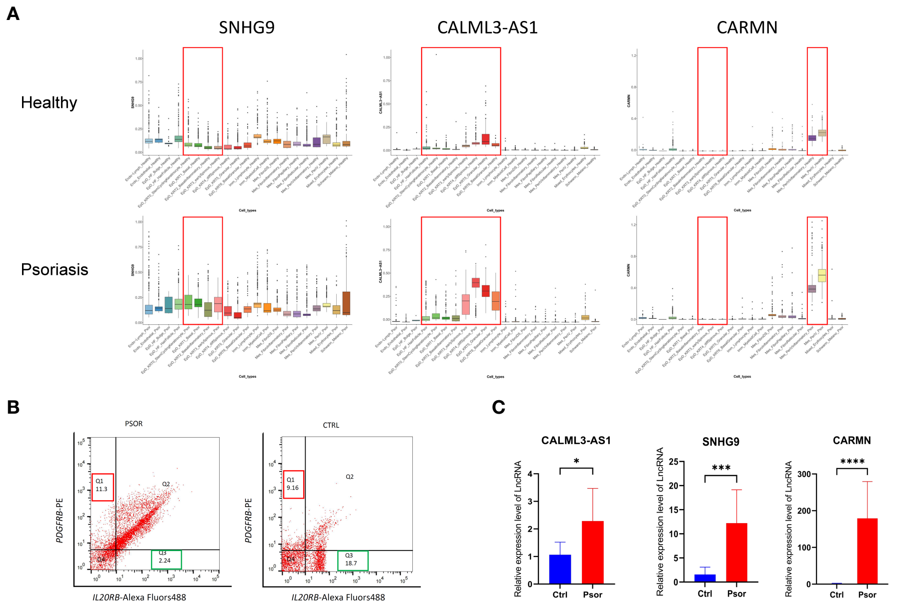

FIGURE 4

Experimental validation of the expression changes of lncRNAs *SNHG9, CALML3-AS1* and *CARMN* in psoriatic skin. **(A)** Box plot visualization of the expression change of lncRNAs *SNHG9, CALML3-AS1* and *CARMN* between health and psoriatic skin. lncRNA names are listed at the top of each plot, and the cell types with significantly altered lncRNA expression are highlighted with red box. **(B)** Representative images of flow cytometry sorting showing *PDGFRB*-positive mesenchymal cells (Q1 region) and *IL20RB*-positive epidermal cells (Q3 region) isolated from psoriasis and healthy control skin tissues. The numerical values within the boxes indicate the percentage of cells in each cell population (%). **(C)** Relative expression levels of lncRNAs *SNHG9, CALML3-AS1*, and *CARMN* in their respective cell types from psoriasis and healthy skin tissues. *$P < 0.05$, ***$P < 0.001$, ****$P < 0.0001$, t-test, n = 3 (mean ± SD).

psoriasis than in the healthy group. Similarly, the expression of *CARMN* in psoriatic mesenchymal-derived cell types was higher than in the healthy group. All results showed significant differences, as shown in the Figure 4C.

Cell-specific lncRNAs *SNHG9*, *CALML3-AS1* and *CARMN* regulate localized inflammatory responses in skin resident cell clusters

Psoriasis is characterized by inflammation in the epidermis and dermis, and the regulation of localized inflammatory responses in epidermal and dermal cells by lncRNAs is of great importance for disease occurrence. EpD cells and Mes cells, as important resident cells in the epidermis and dermis, have been extensively studied and shown to play crucial roles in inflammation in psoriasis. Here, we further demonstrate the regulatory effects of *SNHG9*, *CALML3-AS1* and *CARMN* on the inflammatory responses of their respective cell types.

To further investigate the mechanisms of action of these cell subtype-specific expressed lncRNAs in psoriasis, we performed correlated genes analysis of *SNHG9*, *CALML3-AS1*, *CARMN* and GO enrichment analysis on the integrated single-cell data. We found that *SNHG9* and *CALML3-AS1* correspond to a high coexpression ratio with *NFKB1* and *STAT3* in the EpD cell clusters. *CARMN* correspond to a high co expression ratio with *NFLB1*, *STAT3*, *STAT5B*, and *STAT6* in Mes_PeriVInflammatory and Mes_PeriV clusters. The coexpression of lncRNAs and genes detail was showed in SI_Table 2. NF-kappa B (nuclear factor-kappa B) is a rapidly acting primary transcription factor found in all cell types. It is involved in cellular responses to stimuli such as cytokines and stress and plays a key role in regulating the immunological response to infections (16, 17). STATs (signal transducers and activators of transcription) are a family of seven transcription factors that form part of the JAK-STAT signaling cascade, which serves as the basis for the signal transduction mechanism of many cytokine receptors (18). STATs are activated by phosphorylation by JAKs. *STAT3*, in particular, has been implicated in several autoimmune diseases, including psoriasis (19, 20).

GO enrichment analysis revealed that these three lncRNAs are associated with biological processes related to excessive proliferation and inflammation observed in psoriasis skin in their respective cell clusters. The results of GO enrichment analysis are detailed in SI_Tables 3–5. Specifically, *SNHG9* in EpD cells is involved in leukocyte migration. *CALML3-AS1* in EpD cells functions in the activation of immune response, regulation of lymphocyte activation, regulation of leukocyte cell-cell adhesion,

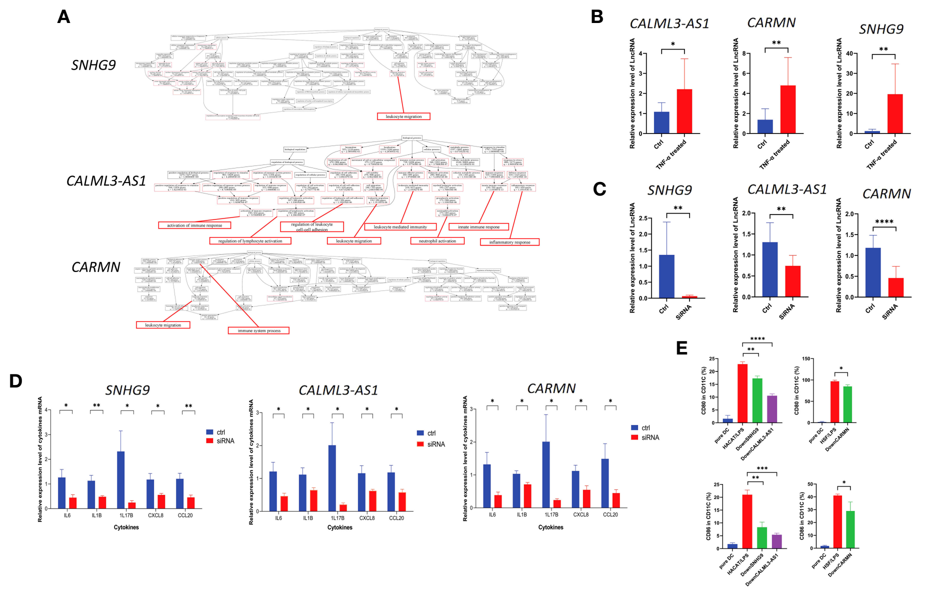

FIGURE 5
lncRNAs *SNHG9*, *CALML3-AS1*, and *CARMN* exhibit immune regulatory functions in skin-resident cell types. **(A)** GO enrichment analysis of *SNHG9*, *CALML3-AS1*, and *CARMN* on the integrated single-cell data. Immune-related functions are highlighted in red. **(B)** Relative expression levels of lncRNAs *SNHG9*, *CALML3-AS1* (in HACAT), and *CARMN* (in HSF) before and after treatment with TNF-α in cell lines. **(C)** Relative expression levels of lncRNAs *SNHG9*, *CALML3-AS1* (in HACAT), and *CARMN* (in HSF) before and after RNA interference in cell lines. **(D)** Relative expression levels of various cytokine mRNAs in cell lines from the TNF-α-treated group and the RNA interference group compared to the control group. **(E)** Flow cytometry analysis of *CD11C*-positive dendritic cells co-cultured with cell lines from the RNA interference group and the control group, showing the percentage of *CD80* and *CD86*-positive cells (%). *P < 0.05, **P < 0.01, ***P < 0.001, ****P < 0.0001, t-test, n = 3 (mean ± SD).

leukocyte migration, leukocyte mediated immunity, neutrophil activation, innate immune response, and inflammatory response. *CARMN* in Mes cell population is associated with lymphocyte migration and immune system process (Figure 5A). These biological processes indicate that *SNHG9*, *CALML3-AS1*, and *CARMN* have immune-related functions in their respective cell clusters. To further validate their roles in psoriasis, functional experiments were performed on these lncRNAs in cell lines.

Numerous studies have confirmed TNF-α as one of the key pathogenic cytokines in psoriasis and extensively used for inducing inflammatory conditions in epidermal cell lines (21–24). TNF-α can activate myeloid dendritic cells, induce epidermal proliferation and incomplete keratinization, and release host defense proteins and chemokines such as *CCL20* and *CXCL8*, leading to local skin thickening and inflammatory reactions that sustain the psoriatic phenotype (25–27). *IL1B* and *IL6* are potent pro-inflammatory cytokines that can induce Th1 generation of *IFNG* and synergistically promote inflammation and angiogenesis along with TNF-α (28–31). Our previous results have confirmed the involvement of *IL17B* in localized inflammation in psoriatic skin (2). Based on these experimental foundations, we treated HACAT and HSF cell lines with exogenous TNF-α to simulate the localized inflammatory response of epidermal and mesenchymal-derived cells in psoriasis, and analyzed the levels of *CXCL8*, *CCL20*, *IL1B*, *IL6*, and *IL17B* expression to assess the extent and status of inflammation.

We treated the immortalized human epidermal cell line HACAT and human dermal fibroblast cell line HSF with TNF-α and examined the expression levels of the aforementioned lncRNAs under inflammatory conditions. We found that after TNF-α treatment, the expression of *SNHG9*, *CALML3-AS1* in HACAT, and *CARMN* in HSF were all significantly upregulated compared to the control group, and all results showed statistical significance (P < 0.05) (Figure 5B). This finding is consistent with the expression results observed in the integrated atlas dataset of psoriatic skin and cell subtypes extracted from tissues, indicating elevated expression of *SNHG9*, *CALML3-AS1* and *CARMN* under localized inflammatory conditions in the skin.

Next, we further investigated the role of these lncRNAs in the TNF-α-induced inflammatory response in HACAT and HSF cell lines. RNA interference was used to knockdown the expression of *SNHG9*, *CALML3-AS1* in the epidermal HACAT cell line, and *CARMN* in the mesenchymal HSF cell line, respectively. qPCR analysis demonstrated that the expression of these lncRNAs in both the HACAT and HSF cell lines was significantly lower in the siRNA group compared to the control group, confirming successful interference, as shown in the Figure 5C.

Following TNF-α treatment of the successfully knocked-down lncRNA cell lines, we evaluated the mRNA expression levels of the inflammatory factors *CXCL8*, *CCL20*, *IL1B*, *IL6*, and *IL17B* using qPCR. We observed that, after lncRNA knockdown, the expression levels of TNF-α-induced *CXCL8*, *CCL20*, *IL1B*, *IL6*, and *IL17B* were all lower than those in the control group, and all results showed statistical significance (P < 0.05) (Figure 5D). Based on the above results, we can infer that these lncRNAs have the ability to regulate the localized inflammatory response in both epidermal and mesenchymal cell lines induced by TNF-α. Knocking down these lncRNAs leads to a reduction in the production of inflammatory factors induced by TNF-α.

LncRNA *SNHG9*, *CALML3-AS1*, and *CARMN* can regulate the activation ability of corresponding skin cell types on dendritic cells

Dendritic cells (DCs) play a crucial role as upstream initiating cells in the localized inflammatory response in the skin, and their activation is essential for the pathogenesis of psoriasis, which is considered a key link in both the initiation and the maintenance phases of psoriasis (32). Based on previous sequencing results, we selected cell types expressing lncRNAs *SNHG9*, *CALML3-AS1*, and *CARMN*. After silencing lncRNA *SNHG9* and *CALML3-AS1* in the HACAT cell line, we co-cultured it with primary dendritic cells.

Here, we used *CD11C* as a marker to identify dendritic cells. *CD11C*, as a classical marker for dendritic cells, has been widely employed in research studies (33). The expression of *CD80*/*CD86* stimulatory molecules on dendritic cells can indicate their activation and their ability to initiate and regulate immune responses. We found that the levels of *CD80* and *CD86* expressed by dendritic cells induced by the epidermal cell line after lipopolysaccharide (LPS) 50ng/ml stimulation were regulated by *SNHG9* and *CALML3-AS1*, respectively. Specifically, interfering with the expression of *SNHG9* and *CALML3-AS1* in epidermal cells resulted in a decrease in the activation ratio of dendritic cells. We first used flow cytometry to measure the frequency of *CD80*/*CD86* in *CD11C*, which represents the activation level of dendritic cells, in primary dendritic cells before co-culture. We observed that untreated *CD11C*-positive dendritic cells exhibited a low proportion of *CD80*/*CD86*-positive cells, indicating that these dendritic cells were in an inactivated state.

To simulate the localized inflammation state in psoriasis, we treated HACAT and HSF cells with LPS respectively and then co-cultured them with dendritic cells. Flow cytometry was performed to assess the proportions of *CD80* and *CD86*-positive cells in *CD11C*-positive dendritic cells. This analysis allowed us to evaluate the activation level of dendritic cells and assess the extent of localized inflammation induced by skin-resident cells. Following siRNA-mediated knockdown of *SNHG9*, *CALML3-AS1* in HACAT cells, and *CARMN* in HSF cells, we repeated the aforementioned experiments. By measuring the activation level of dendritic cells, we analyzed the impact of *SNHG9*, *CALML3-AS1*, and *CARMN* on localized inflammation in skin cells. We observed a significant decrease in the proportion of *CD80* and *CD86*-positive cells in *CD11C*-positive dendritic cells upon knockdown of *SNHG9*, *CALML3-AS1* in HACAT cells, and *CARMN* in HSF cells, indicating an attenuation of dendritic cell activation (Figure 5E). These results suggest that lncRNAs *SNHG9*, *CALML3-AS1*, and *CARMN* in skin tissues can regulate the activation ability of respective cell types on dendritic cells. Interfering with the expression of these lncRNAs can inhibit the activation of dendritic cells, which may have potential regulatory effects on localized inflammation in psoriasis.

Discussion

Psoriasis, characterized by excessive proliferation and abnormal differentiation of epidermal cells, involves a complex regulatory network with various cellular and molecular players. Even after the remission of clinical symptoms, psoriasis can relapse due to continued inflammatory reactions from certain skin-resident cells. This localized inflammation operates in tandem with known psoriasis immune pathways, causing a secondary immune response that prolongs skin inflammation (34). While biologics targeting IL-23, IL-17A, and TNF-α have shown effectiveness, discontinuation of treatment often leads to disease recurrence. This points towards the potential of localized skin inflammation, possibly fueled by epigenetic regulation within skin-resident cells, as an independent mechanism contributing to the persistence of the disease.

The advent of scRNAseq technology allows the uncovering of rare cell subpopulations playing significant roles in psoriasis, extending our understanding beyond the traditional classification boundaries of the epidermis and dermis (35–39). Thanks to scRNAseq, a variety of single-cell atlases such as the Human Cell Atlas and Tabula Muris have been established. These atlases, comprising samples from different tissues, laboratories, and experimental conditions, inevitably carry batch effects. Therefore, the development of integration methods to overcome these batch effects has become a priority in recent years. By meticulously merging 106,675 cells from healthy human skin and 79,887 cells from psoriatic human skin, we have crafted the most detailed and expansive transcriptomic cell atlas of human psoriatic skin to date, distinctly surpassing the boundaries set by previous datasets. The core strength of our study lies in the sophisticated integration of a sizable cell atlas facilitated by our neural-network learning pipeline. This integrated approach mitigates the batch effects that have been a persistent challenge in other datasets and enhances the accuracy and depth of skin cell classification, thus uncovering the underlying mechanisms of psoriatic skin pathogenesis. Furthermore, our pioneering approach in employing interpretable learning enabled us to mine over 30,000 features of protein-coding genes and lncRNAs, setting a new benchmark in the depth and breadth of cellular analysis, distinguishing our dataset as a markedly superior tool in the quest to unravel the mysteries of psoriasis.

Our approach has spotlighted a rich diversity of skin cell subtypes, accentuating the finer nuances that govern the complex dynamics of psoriasis. The robustness and specificity in our newly defined epidermal and mesenchymal cell subtypes are a testament to our integrated dataset's heightened accuracy and reliability, distinctly setting it apart from earlier studies. Notably, our methodology demonstrated an accuracy exceeding 90%, showcasing our significant advancements in cell classification and underscoring the potential to venture deeper into uncharted territories of cellular dynamics in psoriasis.

Beyond identifying cellular subtypes, our study has honed in on the critical role of long non-coding RNAs (lncRNAs) in modulating localized inflammation in psoriasis. This focus, previously underexplored, now opens up a new frontier for research and therapeutic development, underscoring the advantage of our integrated approach in spotlighting promising candidates for further investigation.

As we advance, we remain responsible to unravel the regulatory mechanisms underlying psoriasis pathogenesis. Our consolidated dataset is a novel and powerful resource that promises to catalyze the next wave of breakthroughs in this field. Moreover, the public online accessibility of our dataset ensures that it serves as a collaborative platform, promoting further innovation and discoveries in psoriasis research.

In our previous report, we demonstrated that local resident cells, including epidermal cells and mesenchymal cells, display an immune-priming profile that amplifies inflammation in psoriatic skin (2). As a key player in this network, epidermal cells are impacted by multiple factors including genetics, cytokines, receptors, metabolism, cell signaling pathways, transcription factors, non-coding RNAs, antimicrobial peptides, and diverse functional proteins (40). These factors collectively contribute to the onset and progression of psoriasis. In concert with mesenchymal-derived fibroblasts and endothelial cells, Epidermal cells instigate tissue remodeling through endothelial cell activation and proliferation, as well as extracellular matrix deposition (41, 42). Recent studies have also found that inhibitors of glucose transporter 1 (Glut1), pyruvate kinase M2 (PKM2), and 2-deoxy-D-glucose (2DG) can alleviate the severity of psoriasis-like skin inflammation (43–45).

Mesenchymal cells are widely present in connective tissues, as well as in the skin and subcutaneous tissues, including dermal fibroblasts and pericytes in the dermis, and adipocytes in subcutaneous tissues (46, 47). Dermal fibroblasts, once activated, have the potential to play an important role in the development of psoriasis. They can be recruited to skin tissue that is damaged, inflamed, or healing, and they can activate immune cells and modulate inflammation levels. In addition, activated fibroblasts are capable of secreting cytokines, leading to excessive proliferation of keratinocytes, a crucial factor in the progression of psoriasis (46, 48).

Furthermore, immune cells, especially dendritic cells, play pivotal roles in both the initiation and maintenance phases of psoriasis (32, 41). DCs, activated by epidermal cells, release inflammatory cytokines such as TNF-α, IL-12, and IL-23, which further activate Th1 and Th17 cells. These immune cells then secrete additional inflammatory cytokines, forming a positive feedback loop that exacerbates psoriasis-associated inflammation and epidermal hyperproliferation (40, 49).

Emerging evidence points towards long non-coding RNAs (lncRNAs) as critical epigenetic regulators in psoriasis (49–51). Through high-throughput sequencing, numerous differentially expressed lncRNAs have been identified in psoriasis skin tissues, indicating their crucial roles in psoriasis pathogenesis (52–57). Yet, previous RNA sequencing largely focused on cell types with the largest changes in psoriasis, leading to an underrepresentation of other important cell subtypes.

Through this integrated dataset, we identify differentially expressed lncRNAs in cell subtypes implicated in psoriasis and experimentally validate the functions of lncRNAs *SNHG9*, *CALML3-AS1* in epidermal cells, and *CARMN* in mesenchymal cells. At present, study on these lncRNAs is very limited, and the mechanism by which they participate in regulating immune function is still unclear. *SNHG9*, affiliated with the lncRNA class, is an RNA gene that is currently believed to promote the proliferation of various types of tumor cells through multiple pathways, including phosphatidylinositol binding, inhibition of autophagy, and participation in methylation regulation (58–60). *SNHG9* secreted by adipocyte-derived exosomes can alleviate inflammation and endothelial cell apoptosis by inhibiting *TRADD* expression (61). However, it is unclear whether this anti-endothelial cell apoptosis property is related to the microvascular endothelial proliferation observed in psoriasis. Existing research on the *CALML3-AS1* is relatively sparse, and the principal focus of existing studies is cancer biology. Current hypotheses suggest that *CALML3-AS1* may exert a regulatory influence on tumorigenesis via mechanisms that may include functioning as a molecular sponge for microRNAs or operating as a transcriptional regulator (62). *CARMN* plays a role in smooth muscle-related diseases and tumors. *CARMN* can maintain a contractile phenotype by binding to myosin (17). *CARMN* in smooth muscle cells regulates cell plasticity and atherosclerosis by interacting with serum response factors (63), and its deficiency can accelerate atherosclerosis progression (64). We sorted epidermal and mesenchymal cell types from the skin tissues of patients with psoriasis and healthy volunteers, and verified that these lncRNAs were significantly increased in the corresponding cell types under disease conditions compared to healthy controls. They have been confirmed to have immune function through *in vitro* cell experiments, silencing these lncRNAs in skin resident cell clusters can attenuate the expression of inflammatory cytokines and inhibit dendritic cell activation under inflammatory conditions, suggesting a potential therapeutic strategy to reduce localized inflammation in psoriasis. This research provides valuable insights into the development of psoriasis at the single-cell level and indicates potential targets for therapeutic interventions.

Data availability statement

The original contributions presented in the study are included in the article/Supplementary Material. Further inquiries can be directed to the corresponding authors.

Ethics statement

The studies involving humans were approved by The Second Affiliated Hospital of Harbin Medical University. The studies were conducted in accordance with the local legislation and institutional requirements. The participants provided their written informed consent to participate in this study.

Author contributions

YG: Data curation, Methodology, Validation, Writing – original draft, Writing – review & editing. MN: Investigation, Methodology, Project administration, Writing – original draft. XY: Methodology, Investigation, Writing – original draft. CL: Methodology, Writing – original draft, Formal Analysis, Project administration. LL: Methodology, Project administration, Resources, Writing – original draft. GY: Formal Analysis, Project administration, Resources, Writing – original draft. YL: Conceptualization, Funding acquisition, Writing – review & editing. YH: Conceptualization, Investigation, Writing – review & editing.

Funding

The authors declare financial support was received for the research, authorship, and/or publication of this article. This study was supported by the National Natural Science Foundation of China (No. 81972925), Heilongjiang Postdoctoral Research Fund (No. LBH-Z21174). Swedish Society for Medical Research (SSMF) fellowship, Åke Wiberg research grant, and Karolinska Institute research grant to YH.

Acknowledgments

We thank Science for Life Laboratory, the National Genomics Infrastructure funded by the Swedish Research Council, and Uppsala Multidisciplinary Center for Advanced Computational Science for access to the UPPMAX computational infrastructure.

Conflict of interest

The authors declare that the research was conducted in the absence of any commercial or financial relationships that could be construed as a potential conflict of interest.

Publisher's note

Supplementary material

The Supplementary Material for this article can be found online at: https://www.frontiersin.org/articles/10.3389/fimmu.2023.1265517/full#supplementary-material

References

1. Disease GBD, Injury I and Prevalence C. Global, regional, and national incidence, prevalence, and years lived with disability for 354 diseases and injuries for 195 countries and territories, 1990-2017: a systematic analysis for the Global Burden of Disease Study 2017. *Lancet* (2018) 392(10159):1789–858. doi: 10.1016/S0140-6736(18)32279-7

2. Gao Y, Yao X, Zhai Y, Li L, Li H, Sun X, et al. Single cell transcriptional zonation of human psoriasis skin identifies an alternative immunoregulatory axis conducted by skin resident cells. *Cell Death Dis* (2021) 12(5):450. doi: 10.1038/s41419-021-03724-6

3. Kumar D, Sahoo SS, Chauss D, Kazemian M, Afzali B. Non-coding RNAs in immunoregulation and autoimmunity: Technological advances and critical limitations. *J Autoimmun* (2023) 134:102982. doi: 10.1016/j.jaut.2022.102982

4. Tang L, Liang Y, Xie H, Yang X, Zheng G. Long non-coding RNAs in cutaneous biology and proliferative skin diseases: Advances and perspectives. *Cell Prolif* (2020) 53 (1):e12698. doi: 10.1111/cpr.12698

5. Zeng C, Tsoi LC, Gudjonsson JE. Dysregulated epigenetic modifications in psoriasis. *Exp Dermatol* (2021) 30(8):1156–66. doi: 10.1111/exd.14332

6. Hedlund E, Deng Q. Single-cell RNA sequencing: Technical advancements and biological applications. *Mol Aspects Med* (2018) 59:36–46. doi: 10.1016/j.mam.2017.07.003

7. Cheng JB, Sedgewick AJ, Finnegan AI, Harirchian P, Lee J, Kwon S, et al. Transcriptional programming of normal and inflamed human epidermis at single-cell resolution. *Cell Rep* (2018) 25(4):871–83. doi: 10.1016/j.celrep.2018.09.006

8. Reynolds G, Vegh P, Fletcher J, Poyner EFM, Stephenson E, Goh I, et al. Developmental cell programs are co-opted in inflammatory skin disease. *Science* (2021) 371(6527):eaba6500. doi: 10.1126/science.aba6500

9. Xia D, Wang Y, Xiao Y, Li W. Applications of single-cell RNA sequencing in atopic dermatitis and psoriasis. *Front Immunol* (2022) 13:1038744. doi: 10.3389/fimmu.2022.1038744

10. Hu Y, Jiang Y, Behnan J, Ribeiro MM, Kalantzi C, Zhang MD, et al. Neural network learning defines glioblastoma features to be of neural crest perivascular or radial glia lineages. *Sci Adv* (2022) 8(23):eabm6340. doi: 10.1126/sciadv.abm6340

11. Yu H, Usoskin D, Nagi SS, Hu Y, Kupari J, Bouchatta O, et al. Single-soma deep RNA sequencing of human DRG neurons reveals novel molecular and cellular mechanisms underlying somatosensation. *bioRxiv* [Preprint] (2023) 2023.03.17.533207. doi: 10.2139/ssrn.4399558

12. Stuart T, Butler A, Hoffman P, Hafemeister C, Papalexi E, Mauck WM 3rd, et al. Comprehensive integration of single-cell data. *Cell* (2019) 177(7):1888–902.e21. doi: 10.1016/j.cell.2019.05.031

13. Kirkwood PM, Gibson DA, Smith JR, Wilson-Kanamori JR, Kelepouri O, Esnal-Zufiaurre A, et al. Single-cell RNA sequencing redefines the mesenchymal cell landscape of mouse endometrium. *FASEB J* (2021) 35(4):e21285. doi: 10.1096/fj.202002123R

14. Smyth LCD, Rustenhoven J, Scotter EL, Schweder P, Faull RLM, Park TIH, et al. Markers for human brain pericytes and smooth muscle cells. *J Chem Neuroanat* (2018) 92:48–60. doi: 10.1016/j.jchemneu.2018.06.001

15. Reemann P, Reimann E, Suutre S, Paavo M, Loite U, Porosaar O, et al. Expression of class II cytokine genes in children's skin. *Acta Derm Venereol* (2014) 94(4):386–92. doi: 10.2340/00015555-1717

16. Hayden MS, Ghosh S. NF-kappaB in immunobiology. *Cell Res* (2011) 21(2):223–44. doi: 10.1038/cr.2011.13

17. Poma P. NF-kappaB and disease. *Int J Mol Sci* (2020) 21(23):9181. doi: 10.3390/ijms21239181

18. Stark GR, Cheon H, Wang Y. Responses to cytokines and interferons that depend upon JAKs and STATs. *Cold Spring Harb Perspect Biol* (2018) 10(1):a028555. doi: 10.1101/cshperspect.a028555

19. Platanitis E, Decker T. Regulatory networks involving STATs, IRFs, and NFkappaB in inflammation. *Front Immunol* (2018) 9:2542. doi: 10.3389/fimmu.2018.02542

20. Banerjee S, Biehl A, Gadina M, Hasni S, Schwartz DM. JAK-STAT signaling as a target for inflammatory and autoimmune diseases: current and future prospects. *Drugs* (2017) 77(5):521–46. doi: 10.1007/s40265-017-0701-9

21. Lee H, Lee DH, Oh JH, Chung JH. Skullcapflavone II suppresses TNF-alpha/IFN-gamma-induced TARC, MDC, and CTSS production in haCaT cells. *Int J Mol Sci* (2021) 22(12):6428. doi: 10.3390/ijms22126428

22. Gao J, Chen F, Fang H, Mi J, Qi Q, Yang M. Daphnetin inhibits proliferation and inflammatory response in human HaCaT keratinocytes and ameliorates imiquimod-induced psoriasis-like skin lesion in mice. *Biol Res* (2020) 53(1):48. doi: 10.1186/s40659-020-00316-0

23. Jayasinghe AMK, Kirindage K, Fernando IPS, Han EJ, Oh GW, Jung WK, et al. Fucoidan isolated from sargassum confusum suppresses inflammatory responses and oxidative stress in TNF-alpha/IFN-gamma- stimulated haCaT keratinocytes by activating nrf2/HO-1 signaling pathway. *Mar Drugs* (2022) 20(2):117. doi: 10.3390/md20020117

24. Wikan N, Hankittichai P, Thaklaewphan P, Potikanond S, Nimlamool W. Oxyresveratrol inhibits TNF-alpha-stimulated cell proliferation in human immortalized keratinocytes (HaCaT) by suppressing AKT activation. *Pharmaceutics* (2021) 14(1):63. doi: 10.3390/pharmaceutics14010063

25. Gupta RK, Gracias DT, Figueroa DS, Miki H, Miller J, Fung K, et al. TWEAK functions with TNF and IL-17 on keratinocytes and is a potential target for psoriasis therapy. *Sci Immunol* (2021) 6(65):eabi8823. doi: 10.1126/sciimmunol.abi8823

26. Elnabawi YA, Garshick MS, Tawil M, Barrett TJ, Fisher EA, Lo Sicco K, et al. CCL20 in psoriasis: A potential biomarker of disease severity, inflammation, and impaired vascular health. *J Am Acad Dermatol* (2021) 84(4):913–20. doi: 10.1016/j.jaad.2020.10.094

27. Patel AB, Tsilioni I, Weng Z, Theoharides TC. TNF stimulates IL-6, CXCL8 and VEGF secretion from human keratinocytes via activation of mTOR, inhibited by tetramethoxyluteolin. *Exp Dermatol* (2018) 27(2):135–43. doi: 10.1111/exd.13461

28. LaRock CN, Todd J, LaRock DL, Olson J, O'Donoghue AJ, Robertson AA, et al. IL-1beta is an innate immune sensor of microbial proteolysis. *Sci Immunol* (2016) 1(2):eaah3539. doi: 10.1126/sciimmunol.aah3539

29. Pyrillou K, Burzynski LC, Clarke MCH. Alternative pathways of IL-1 activation, and its role in health and disease. *Front Immunol* (2020) 11:613170. doi: 10.3389/fimmu.2020.613170

30. Landskron G, de la Fuente M, Thuwajit P, Thuwajit C, Hermoso MA. Chronic inflammation and cytokines in the tumor microenvironment. *J Immunol Res* (2014) 2014:149185. doi: 10.1155/2014/149185

31. Murakami M, Kamimura D, Hirano T. Pleiotropy and specificity: insights from the interleukin 6 family of cytokines. *Immunity* (2019) 50(4):812–31. doi: 10.1016/j.immuni.2019.03.027

32. Kamata M, Tada Y. Dendritic cells and macrophages in the pathogenesis of psoriasis. *Front Immunol* (2022) 13:941071. doi: 10.3389/fimmu.2022.941071

33. Singh-Jasuja H, Thiolat A, Ribon M, Boissier MC, Bessis N, Rammensee HG, et al. The mouse dendritic cell marker CD11c is down-regulated upon cell activation through Toll-like receptor triggering. *Immunobiology* (2013) 218(1):28–39. doi: 10.1016/j.imbio.2012.01.021

34. Chen L, Shen Z. Tissue-resident memory T cells and their biological characteristics in the recurrence of inflammatory skin disorders. *Cell Mol Immunol* (2020) 17(1):64–75. doi: 10.1038/s41423-019-0291-4

35. Liu J, Chang HW, Huang ZM, Nakamura M, Sekhon S, Ahn R, et al. Single-cell RNA sequencing of psoriatic skin identifies pathogenic Tc17 cell subsets and reveals distinctions between CD8(+) T cells in autoimmunity and cancer. *J Allergy Clin Immunol* (2021) 147(6):2370–80. doi: 10.1016/j.jaci.2020.11.028

36. Penkava F, Velasco-Herrera MDC, Young MD, Yager N, Nwosu LN, Pratt AG, et al. Single-cell sequencing reveals clonal expansions of pro-inflammatory synovial CD8 T cells expressing tissue-homing receptors in psoriatic arthritis. *Nat Commun* (2020) 11(1):4767. doi: 10.1038/s41467-020-18513-6

37. Hughes TK, Wadsworth MH 2nd, Gierahn TM, Do T, Weiss D, Andrade PR, et al. Second-strand synthesis-based massively parallel scRNA-seq reveals cellular states and molecular features of human inflammatory skin pathologies. *Immunity* (2020) 53 (4):878–94 e7. doi: 10.1016/j.immuni.2020.09.015

38. Kashem SW, Haniffa M, Kaplan DH. Antigen-presenting cells in the skin. *Annu Rev Immunol* (2017) 35:469–99. doi: 10.1146/annurev-immunol-051116-052215

39. Bielecki P, Riesenfeld SJ, Hutter JC, Torlai Triglia E, Kowalczyk MS, Ricardo-Gonzalez RR, et al. Skin-resident innate lymphoid cells converge on a pathogenic effector state. *Nature* (2021) 592(7852):128–32. doi: 10.1038/s41586-021-03188-w

40. Zhou X, Chen Y, Cui L, Shi Y, Guo C. Advances in the pathogenesis of psoriasis: from keratinocyte perspective. *Cell Death Dis* (2022) 13(1):81. doi: 10.1038/s41419-022-04523-3

41. Griffiths CEM, Armstrong AW, Gudjonsson JE, Barker J. Psoriasis. *Lancet* (2021) 397(10281):1301–15. doi: 10.1016/S0140-6736(20)32549-6

42. Deng Y, Chang C, Lu Q. The inflammatory response in psoriasis: a comprehensive review. *Clin Rev Allergy Immunol* (2016) 50(3):377–89. doi: 10.1007/s12016-016-8535-x

43. Huang X, Chen J, Zeng W, Wu X, Chen M, Chen X. Membrane-enriched solute carrier family 2 member 1 (SLC2A1/GLUT1) in psoriatic keratinocytes confers sensitivity to 2-deoxy-D-glucose (2-DG) treatment. *Exp Dermatol* (2019) 28(2):198–201. doi: 10.1111/exd.13850

44. Zhang Z, Zi Z, Lee EE, Zhao J, Contreras DC, South AP, et al. Differential glucose requirement in skin homeostasis and injury identifies a therapeutic target for psoriasis. *Nat Med* (2018) 24(5):617–27. doi: 10.1038/s41591-018-0003-0

45. Liu YZ, Xu MY, Dai XY, Yan L, Li L, Zhu RZ, et al. Pyruvate kinase M2 mediates glycolysis contributes to psoriasis by promoting keratinocyte proliferation. *Front Pharmacol* (2021) 12:765790. doi: 10.3389/fphar.2021.765790

46. Koliaraki V, Prados A, Armaka M, Kollias G. The mesenchymal context in inflammation, immunity and cancer. *Nat Immunol* (2020) 21(9):974–82. doi: 10.1038/s41590-020-0741-2

47. Xue K, Shao S, Fang H, Ma L, Li C, Lu Z, et al. Adipocyte-derived CTRP3 exhibits anti-inflammatory effects via LAMP1-STAT3 axis in psoriasis. *J Invest Dermatol* (2022) 142(5):1349–59.e8. doi: 10.1016/j.jid.2021.09.027

48. Dakin SG, Buckley CD, Al-Mossawi MH, Hedley R, Martinez FO, Wheway K, et al. Persistent stromal fibroblast activation is present in chronic tendinopathy. *Arthritis Res Ther* (2017) 19(1):16. doi: 10.1186/s13075-016-1218-4

49. Dopytalska K, Ciechanowicz P, Wiszniewski K, Szymanska E, Walecka I. The role of epigenetic factors in psoriasis. *Int J Mol Sci* (2021) 22(17):9294. doi: 10.3390/ijms22179294

50. Hawkes JE, Nguyen GH, Fujita M, Florell SR, Callis Duffin K, Krueger GG, et al. microRNAs in psoriasis. *J Invest Dermatol* (2016) 136(2):365–71. doi: 10.1038/JID.2015.409

51. Domingo S, Sole C, Moline T, Ferrer B, Cortes-Hernandez J. MicroRNAs in several cutaneous autoimmune diseases: psoriasis, cutaneous lupus erythematosus and atopic dermatitis. *Cells* (2020) 9(12):2656. doi: 10.3390/cells9122656

52. Song JK, Yin SY, Li W, Li XD, Luo Y, Luo Y, et al. An update on the role of long non-coding RNAs in psoriasis. *Chin Med J (Engl)* (2020) 134(4):379–89. doi: 10.1097/CM9.0000000000001243

53. Sonkoly E, Bata-Csorgo Z, Pivarcsi A, Polyanka H, Kenderessy-Szabo A, Molnar G, et al. Identification and characterization of a novel, psoriasis susceptibility-related noncoding RNA gene, PRINS. *J Biol Chem* (2005) 280(25):24159–67. doi: 10.1074/jbc.M501704200

54. Qiao M, Li R, Zhao X, Yan J, Sun Q. Up-regulated lncRNA-MSX2P1 promotes the growth of IL-22-stimulated keratinocytes by inhibiting miR-6731-5p and activating S100A7. *Exp Cell Res* (2018) 363(2):243–54. doi: 10.1016/j.yexcr.2018.01.014

55. Tsoi LC, Iyer MK, Stuart PE, Swindell WR, Gudjonsson JE, Tejasvi T, et al. Analysis of long non-coding RNAs highlights tissue-specific expression patterns and epigenetic profiles in normal and psoriatic skin. *Genome Biol* (2015) 16(1):24. doi: 10.1186/s13059-014-0570-4

56. Tang ZL, Zhang K, Lv SC, Xu GW, Zhang JF, Jia HY. LncRNA MEG3 suppresses PI3K/AKT/mTOR signalling pathway to enhance autophagy and inhibit inflammation in TNF-alpha-treated keratinocytes and psoriatic mice. *Cytokine* (2021) 148:155657. doi: 10.1016/j.cyto.2021.155657

57. Jia HY, Zhang K, Lu WJ, Xu GW, Zhang JF, Tang ZL. LncRNA MEG3 influences the proliferation and apoptosis of psoriasis epidermal cells by targeting miR-21/caspase-8. *BMC Mol Cell Biol* (2019) 20(1):46. doi: 10.1186/s12860-019-0229-9

58. Li RH, Tian T, Ge QW, He XY, Shi CY, Li JH, et al. A phosphatidic acid-binding lncRNA SNHG9 facilitates LATS1 liquid-liquid phase separation to promote oncogenic YAP signaling. *Cell Res* (2021) 31(10):1088–105. doi: 10.1038/s41422-021-00530-9

59. Wen D, Liu WL, Lu ZW, Cao YM, Ji QH, Wei WJ. SNHG9, a papillary thyroid cancer cell exosome-enriched lncRNA, inhibits cell autophagy and promotes cell apoptosis of normal thyroid epithelial cell nthy-ori-3 through YBOX3/P21 pathway. *Front Oncol* (2021) 11:647034. doi: 10.3389/fonc.2021.647034

60. Ye S, Ni Y. lncRNA SNHG9 promotes cell proliferation, migration, and invasion in human hepatocellular carcinoma cells by increasing GSTP1 methylation, as revealed by CRISPR-dCas9. *Front Mol Biosci* (2021) 8:649976. doi: 10.3389/fmolb.2021.649976

61. Song Y, Li H, Ren X, Li H, Feng C. SNHG9, delivered by adipocyte-derived exosomes, alleviates inflammation and apoptosis of endothelial cells through suppressing TRADD expression. *Eur J Pharmacol* (2020) 872:172977. doi: 10.1016/j.ejphar.2020.172977

62. Zhang X, Zhang X, Jia Q, Li H, Ma R, Yang G, et al. LncRNA CALML3-AS1 suppresses papillary thyroid cancer progression via sponging miR-20a-5p/RBM38 axis. *BMC Cancer* (2022) 22(1):344. doi: 10.1186/s12885-022-09360-3

63. Ni H, Haemmig S, Deng Y, Chen J, Simion V, Yang D, et al. A smooth muscle cell-enriched long noncoding RNA regulates cell plasticity and atherosclerosis by interacting with serum response factor. *Arterioscler Thromb Vasc Biol* (2021) 41 (9):2399–416. doi: 10.1161/ATVBAHA.120.315911

64. Vacante F, Rodor J, Lalwani MK, Mahmoud AD, Bennett M, De Pace AL, et al. CARMN loss regulates smooth muscle cells and accelerates atherosclerosis in mice. *Circ Res* (2021) 128(9):1258–75. doi: 10.1161/CIRCRESAHA.120.318688

frontiers | Frontiers in Immunology

TYPE Original Research
PUBLISHED 17 November 2023
DOI 10.3389/fimmu.2023.1279439

Single cell transcriptome analyses reveal the roles of B cells in fructose-induced hypertension

Cheong-Wun Kim[1], Sung Yong Joo[2], Boa Kim[3], Jee Young Kim[1], Sungmin Jang[1], Shiang-Jong Tzeng[4]*, Sang Jin Lee[5]*, Myunghoo Kim[2]* and Inkyeom Kim[1]*

[1]Department of Pharmacology, BK21 Plus Kyungpook National University (KNU) Biomedical Convergence Program, Cardiovascular Research Institute, School of Medicine, Kyungpook National University, Daegu, Republic of Korea, [2]Department of Animal Science, Pusan National University, Miryang, Republic of Korea, [3]Cardiovascular Research Institute, School of Medicine, Kyungpook National University, Daegu, Republic of Korea, [4]Graduate Institute of Pharmacology, College of Medicine, National Taiwan University, Taipei, Taiwan, [5]Division of Rheumatology, Cardiovascular Research Institute, School of Medicine, Kyungpook National University, Daegu, Republic of Korea

EDITED BY
Jun Yu,
Temple University, United States

REVIEWED BY
Chuanming Xu,
Jiangxi University of Traditional Chinese Medicine, China
Shigeru Tanaka,
Chiba University, Japan

*CORRESPONDENCE
Shiang-Jong Tzeng
✉ sjtzeng@ntu.edu.tw
Sang Jin Lee
✉ dream1331@knu.ac.kr
Myunghoo Kim
✉ kimmhmm3@gmail.com
Inkyeom Kim
✉ inkim@knu.ac.kr

RECEIVED 18 August 2023
ACCEPTED 31 October 2023
PUBLISHED 17 November 2023

CITATION
Kim C-W, Joo SY, Kim B, Kim JY, Jang S, Tzeng S-J, Lee SJ, Kim M and Kim I (2023) Single cell transcriptome analyses reveal the roles of B cells in fructose-induced hypertension. *Front. Immunol.* 14:1279439. doi: 10.3389/fimmu.2023.1279439

Rationale: While the immune system plays a crucial role in the development of hypertension, the specific contributions of distinct immune cell populations remain incompletely understood. The emergence of single-cell RNA-sequencing (scRNA-seq) technology enables us to analyze the transcriptomes of individual immune cells and to assess the significance of each immune cell type in hypertension development.

Objective: We aimed to investigate the hypothesis that B cells play a crucial role in the development of fructose-induced hypertension.

Methods and Results: Eight-week-old Dahl salt-sensitive (SS) male rats were divided into two groups and given either tap water (TW) or a 20% fructose solution (HFS) for 4 weeks. Systolic blood pressure was measured using the tail-cuff method. ScRNA-seq analysis was performed on lamina propria cells (LPs) and peripheral blood mononuclear cells (PBMCs) obtained from SS rats subjected to either TW or HFS. The HFS treatment induced hypertension in the SS rats. The analysis revealed 27 clusters in LPs and 28 clusters in PBMCs, allowing for the identification and characterization of various immune cell types within each cluster. Specifically, B cells and follicular helper T (Tfh) cells were prominent in LPs, while B cells and M1 macrophages dominated PBMCs in the HFS group. Moreover, the HFS treatment triggered an increase in the number of B cells in both LPs and PBMCs, accompanied by activation of the interferon pathway.

Conclusions: The significant involvement of B cells in intestinal and PBMC responses indicates their pivotal contribution to the development of hypertension. This finding suggests that targeting B cells could be a potential strategy to mitigate high blood pressure in fructose-induced hypertension.

Moreover, the simultaneous increase in follicular B cells and Tfh cells in LPs, along with the upregulation of interferon pathway genes in B cells, underscores a potential autoimmune factor contributing to the pathogenesis of fructose-induced hypertension in the intestine.

KEYWORDS

single-cell RNA-sequencing, immunity, hypertension, B cell, interferon pathway

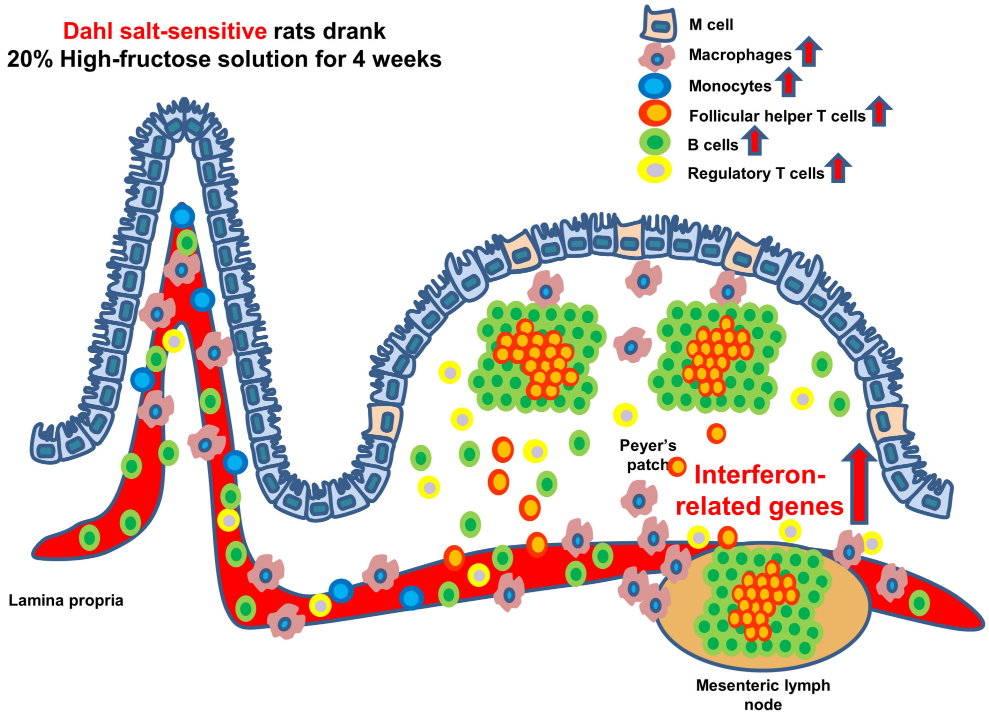

GRAPHICAL ABSTRACT

1 Introduction

The consumption of a high-fructose solution (HFS) is associated with an increase in blood pressure. Furthermore, combining a high-fructose with a high-salt diet induces salt-sensitive hypertension. These processes involve the activation of the renin-angiotensin-aldosterone system, changes in gut microbiota, increased sympathetic nervous system activity, enhanced reactive oxygen species (ROS), an increase in uric acid levels mediated by fructokinase, which leads to an upregulation of ion channels like Na$^+$ -H$^+$ exchanger 3 and Na$^+$ -K$^+$ -2Cl$^-$ cotransporter (1).

The immune system plays a crucial role in the pathogenesis of hypertension (2, 3). The hallmarks of hypertension include the infiltration of innate and adaptive immune cells into perivascular fat, kidney, and myocardium, accompanied by elevated levels of cytokines, chemokines, adhesion molecules, and ROS. Studies using knock-in and knock-out mouse models have demonstrated the involvement of macrophages, monocytes, B cells, and T cells in hypertension (2). Moreover, excess fructose intake induces the secretion of pro-inflammatory cytokines, such as interleukin-6 (IL-6), tumor necrosis factor-α (TNF-α), and plasminogen activator inhibitor-1 (PAI-1) (4). Previous research has shown that administering a high-fructose diet induces the expression of serum/glucocorticoid-regulated kinase 1 (SGK1). In consequence, the induction of SGK1 expression leads to the phosphorylation of forkhead box O 1/3. As a result, this suppresses the expression of the

---

Abbreviations: SS, Dahl salt-sensitive; TW, tap water; HFS, high-fructose solution; Th, helper T; Tfh, follicular helper T cells; Treg, regulatory T cells; LPs, lamina propria cells; PBMCs, peripheral blood mononuclear cells; UMAP, Uniform Manifold Approximation and Projection; GSEA, Gene Set Enrichment Assay; NES, normalized enrichment score.

master transcription factor forkhead box P3 (FoxP3) in regulatory T (Treg) cells and activates T helper 17 (Th17) cells to secrete IL23, further contributing to development of hypertension (5, 6).

The gastrointestinal (GI) tract, which is the largest mucosal tissue in both humans and animals, comprise epithelial, immunological, and vascular barriers and hosts a diverse community of gut microorganism (7, 8). The GI tract is continuously exposed to antigenic stimuli, and the epithelial layer and the lamina propria play crucial roles in immune responses. In particular, the lamina propria contains various immune cells, including cytotoxic T cells, B cells, Th cells, eosinophils, dendritic cells (DCs), and macrophages, which are key effector cells of the immune response. Furthermore, the intestinal immune cells are organized to form gut-associated lymphoid tissue, which comprise lymphoid structures such as Peyer's patches, lymphoid follicles, and mesenteric lymph nodes (7, 9, 10). These organized structures regulate responses to both self and non-self-antigens. Dysregulated immune responses can lead to conditions such as food allergies and inflammatory bowel disease (7, 11).

Mounting evidence highlights the substantial involvement of the gut microbiome in the development and progression of hypertension, which is mediated by interactions with immune cells (12). Moreover, this link between the gut microbiome and hypertension is not limited to specific species (13). A study involving both mice and humans has found that a high-salt diet leads to a reduction in *Lactobacillus* spp. levels and an increase in blood pressure. Notably, the significance of using pro-biotic lactobacillus treatment should be emphasized, as it can suppress Th17 cells and ameliorate salt-sensitive hypertension (13, 14).

B cells recognize antigens and interact with Tfh cells, subsequently releasing cytokines that drive their differentiation into plasma cells responsible for antibody production (15). In murine models, the interaction between follicular helper T (Tfh) cells and germinal center (GC) B cells promotes the selection of B cells with the highest affinity for antigens through the expressions of CD40L, inducible T cell costimulatory (ICOS), and B cell activating factor (BAFF). However, B-cell immune responses extend beyond the GC environment. Extra-follicular B cell responses serve as early antibody sources during infection, maintaining elevated levels of G protein-coupled receptor 183 (GPR183) to avoid the GC milieu and increasing CXCR4 expression to facilitate their migration to lymph nodes (16–18). Dysregulation of GC and extra-follicular responses can result in the production of autoantibodies against self-antigens, contributing to the development of autoimmune diseases such as lupus and rheumatoid arthritis (17, 19).

While T cells have been well-recognized for their crucial role in the pathophysiology of hypertension, research into the connection between B cells and hypertension remains limited (20). Mice with simultaneous knockout of both T cells and B cells exhibit a blunted hypertensive response to angiotensin II (Ang II) stimulation. Interestingly, when wild type (WT) T cells and B cells are transplanted into the T cell-deficient and B cell-deficient mice, respectively, only the T cell transplantation exhibits a restoration of the hypertensive response to Ang II (21). However, depletion of B cells using anti-CD20 antibody and knocking out BAFF-receptor (BAFF-R) in mice result in a reduced increase in blood pressure induced by Ang II compared to WT mice. Furthermore, when WT B cells are transplanted into mice lacking BAFF-R, the hypertensive response is restored upon Ang II infusion (22).

In this study, we aimed to elucidate the immunological mechanisms underlying the development of hypertension induced by HFS in Dahl salt-sensitive (SS) rats. We performed single-cell RNA sequencing (scRNA-seq) on peripheral blood mononuclear cells (PBMCs) and lamina propria cells (LPs) isolated from SS rats receiving HFS (hereafter, "HFS group"). Our findings indicate an enlarged B cell population in the HFS group compared to the tap water (TW) group. Furthermore, our analysis using Gene Set Enrichment Assay (GSEA) and Differentially Expressed genes (DEGs) revealed a significant increase in interferon-related genes within B cells of the HFS group compared to the WT group.

2 Materials and methods

2.1 Animals

The *in vivo* experiments were conducted with the approval of the Kyungpook National University Institutional Review Board (Approval No. 2022-0456), following the guidelines outlined in the National Institutes of Health Guide for the Care and Use of Laboratory Animals. The study design aimed to minimize the number of animals used and to reduce the suffering of the experimental animals. Six-week-old Dahl-Iwai salt-sensitive (SS, DIS/EisSlc) male rats were purchased from Japan SLC, Inc (Hamamatsu, Shizoka, Japan). The rats had free access to a chow diet containing 0.4% NaCl (SAFE® D 40, Paris, France) for one week to acclimate and were trained weekly for tail-cuff plethysmography. Subsequently, they were randomly assigned to either the high-fructose solution (HFS; 20% D-fructose; MB-F4695, Kisanbio, Korea) or tap water (TW) group for 4 weeks. The rats were anesthetized with sodium pentobarbital (50 mg/kg intraperitoneally) for euthanization, followed by the collection of tissues and PBMCs.

2.2 Blood pressure measurements

We measured the systolic blood pressure (SBP) of the SS rats using the tail-cuff method. The SS rats were placed on a hot plate (35°C) in a restraining device for 10 minutes. A cuff with a pneumatic pulse sensor was then attached to their tails. The CODA system (Kent Scientific Corporation, Torrington, CT, U.S.A.) was used to record blood pressure levels. To calculate the average blood pressure, at least five consecutive readings were obtained from each rat.

2.3 Isolation of LPs

LPs were isolated as described by Joo et al. (23). Briefly, jejunum tissues were cut into 0.5-cm pieces and washed with phosphate-buffered saline (PBS) containing 10 mM 4-[2-hydroxyethyl]-1-

piperazineethanesulfonic acid (HEPES), 1 mM DL-dithiothreitol (DTT), and 30 mM ethylene-diamine-tetra acetic acid (EDTA; all from Thermo Fisher Scientific, Waltham, WA, U.S.A.) at 37°C for 10 minutes. Subsequently, the tissue samples underwent another wash in PBS containing 10 mM HEPES and 30 mM EDTA at 37°C for 10 minutes. After the wash, the tissues were transferred into 5 mL of RPMI 1640 (Gibco, Carlsbad, CA, U.S.A.) containing 10% fetal bovine serum (FBS) and inverted for 2 minutes. Following this step, the tissues were digested in RPMI 1640 containing 10% FBS with 0.5 mg/ml collagenase VIII (Sigma-Aldrich, St. Louis, MO, U.S.A.) at 37°C for 1 hour. After the digestion, isolated cells were applied to Percoll (GE Healthcare, Chicago, IL, U.S.A.) gradient centrifugation. LP samples were obtained after the removal of Peyer's patches.

2.4 Isolation of PBMCs

Peripheral blood was collected from each rat, and PBMCs were isolated using Ficoll-Paque Plus® gradient centrifugation (GE Healthcare, Chicago, IL, U.S.A.). The isolated PBMCs were washed with PBS and stored at room temperature for subsequent experiments.

2.5 Single-cell RNA library preparation and sequencing

The single-cell RNA library preparation and sequencing were performed by E-Biogen Inc. (Seoul, South Korea). The sequencing was conducted using the Nova-Seq 600 platform in a paired-end 100bp format, with 5000 cells sampled per sample. The library preparation method employed was the 10x Genomics Next Gem technology.

2.6 LPs and PBMCs clustering and annotation

We conducted the analysis using the filtered Cell Ranger files obtained from E-Biogen. The clustering of LPs and PBMCs was performed using the Seurat R Package (Seurat 4.4.0 version, https://satijalab.org/seurat/), a clustering tool developed for the merged matrix for scRNA-seq data. Potential doublets and low-quality cells (less than 200 genes or more than 10% of mitochondrial expression) were filtered out based on gene expression. The data were then normalized and combined. Variable genes were identified using the Seurat function "FindVariableGenes". The previously identified variable genes were used for principal component analysis (PCA) to reduce the data dimensions. Subsequently, 30 principal components were utilized in the Uniform Manifold Approximation and Projection (UMAP) algorithm to further reduce the dimensions based on the neighborhood relationship. In the first round (pre-clustering; resolution = 0.8), major cell types were identified. In the second round (sub-clustering; resolution = 0.2), T cell or B cell subsets were further subdivided using specific signature genes. Gene expression was visualized using DotPlot, FeaturePlot, and VlnPlot functions from the Seurat package's guidelines. Volcano plots were generated using the R package EnhancedVolcanoPlot.

2.7 Gene set enrichment assay

To explore the potential roles of B cells in both LPs and PBMCs, we utilized the Molecular Signature Database (MSigDB) and conducted GSEA. Data were analyzed using Seurat, dplyr, presto, msigdbr, fgsea, tibble, tidyverse, and data.table package in R. This analysis involved calculating a normalized enrichment score (NES), and was performed focusing on the most significant hallmark genes. GSEA results were visualized to identify functional or pathway differences. We used *Rattus norvegicus* as the species and categorized the results into the "H" category to specifically identify hallmark pathways in the HFS group.

2.8 Statistics

Blood pressure values were presented as the mean ± standard error of mean (SEM). Statistical analyses were performed using GraphPad Prism 7 (GraphPad Software, San Diego, CA, U.S.A.), and significance was determined with a p value of lower than 0.05. The Vlnplot of interferon-related genes was evaluated for significance using the Wilcoxon signed rank test.

3 Results

3.1 High-fructose intake increased blood pressure in SS rats

To determine the effect of a high-fructose solution on blood pressure, we conducted weekly measurements of systolic blood pressure (SBP) in SS rats over a 4-week period. The rats were divided into two groups: one group receiving tap water (TW) and the other receiving a 20% high-fructose solution (HFS). The results showed a significant increase in SBP and mean blood pressure in the HFS group for 4 weeks, but no significant change was observed in the TW group (Figures 1A and S1B). There were no significant differences in diastolic blood pressure, heart rate, calorie intake, body weight, and water intake between the groups (Figures 1B, C, S1A, S1C, S2). However, the HFS group exhibited a decrease in food intake (Figure 1D).

3.2 Landscape of major cell types in LPs of TW and HFS group

We performed scRNA-seq on PBMCs (n = 3) and LPs (n = 4) obtained from the TW and HFS groups (Figure 2A). The datasets from these groups were combined for further analysis. After quality control, we successfully processed an average of 3445 cells and 3481 cells in the LPs of the TW and HFS groups, respectively. The major

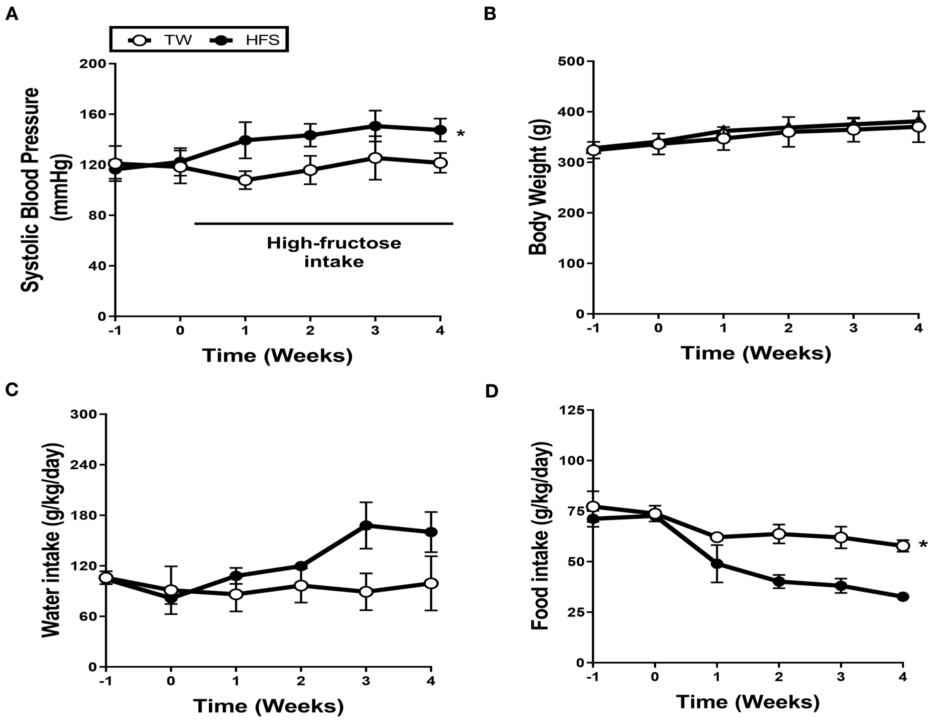

FIGURE 1
High-fructose intake induced hypertension. Dahl salt-sensitive (SS) rats were given either 20% high-fructose solution (HFS) or tap water (TW) for 4 weeks. **(A)** The HFS significantly increased systolic blood pressure (SBP). **(B, C)** There were no significant differences observed in body weight and water intake. **(D)** Conversely, the HFS group exhibited a notable reduction in food intake. The graph represents the mean ± SEM of eight independent experiments. The statistical analysis involved conducting a repeated measures ANOVA followed by Tukey's *post-hoc* multiple comparisons test. The asterisk (*) indicates statistical significance ($p < 0.05$) compared to the TW group. The study was conducted with a sample size of n = 4.

cell types were classified and identified as B cells, helper T (Th) cells, cytotoxic T cells, natural killer (NK) cells, and macrophages. These cell types were visualized using a UMAP plot (Figure 2B), with their identification based on specific marker genes. B cells were characterized by the marker genes *Cd19*, *Cd79a*, and *Cd79b*, while Th cells were distinguished by *Cd3d*, *Cd3e*, and *Cd3g*. Cytotoxic T cells were marked by *Cd3d*, *Cd3g*, and *Cd8a*, NK cells by *Cd8a*, *Nkg7*, and *Klrd1*, and macrophages by *Cd14*, *Cd68*, *Cd86*, and *Cd163*. These cell types and their corresponding marker genes were visualized through dot plots and feature plots (Figures 2C, D). A comparison of UMAP plots between the groups highlighted a greater abundance of B cell clusters in the HFS group compared to the TW group (Figure 2E). This observation was further corroborated through a bar graph, illustrating the increased proportion of B cells in the HFS group compared to the TW group (Figures 2F, G).

3.3 Increased follicular helper T cells in the T cell subsets of LPs from the HFS group

To explore the diversity of T cell subsets within the major LP clusters, we conducted sub-clustering with a focus on the Th cell and cytotoxic T cell clusters. As a result, T cell subsets, including Th1, Th17, Tfh, Treg, and cytotoxic T cells, were identified. The identification of T cell subsets was based on specific marker genes. Th1 cells were identified by *Ccr5*, *Cxcr3*, *Stat4*, and *Tbx21*. Th17 cells were defined by *Ccr6*, *Il23r*, *Il17a*, and *Il17f*. Tfh cells were delineated by *Cxcr5*, *Il6r*, and *Stat3*. Treg cells were categorized using *Il2ra*, *Ctla4*, and *Foxp3*. Cytotoxic T cells were pinpointed through *Cd8a*, *Gzmm*, and *Nkg7*. These T cell subsets, along with their characteristic marker genes, were visually presented through a dot plot and feature plots (Figures 3A and S3). Visualization of these T cell subsets were achieved through UMAP plots, and a comparison between the two groups revealed a higher presence of Tfh cells in the HFS group (Figure 3B). This observation was further supported by the bar graph, which displayed a higher proportion of Tfh cells within LPs from the HFS group compared to the TW group (Figures 3C, D).

3.4 Elevated levels of follicular B cells in the B cell subsets of LPs from the HFS group

Our exploration of B cell diversity within the major LP clusters involved sub-clustering, focusing particularly on the B cell clusters. By referencing established works (24–26), we conducted the annotation of B cell subsets and identified distinct B cell subsets: follicular B, memory B, Naïve B, regulatory B (Breg), immature B, and plasma cells. The B cell subsets were further visualized using UMAP plots. The characterization of B cell subsets was based on specific marker genes. Follicular B cells were classified by their high expression of *Cxcr5*, *Cd24*, and *Cd38*. Memory B cells were

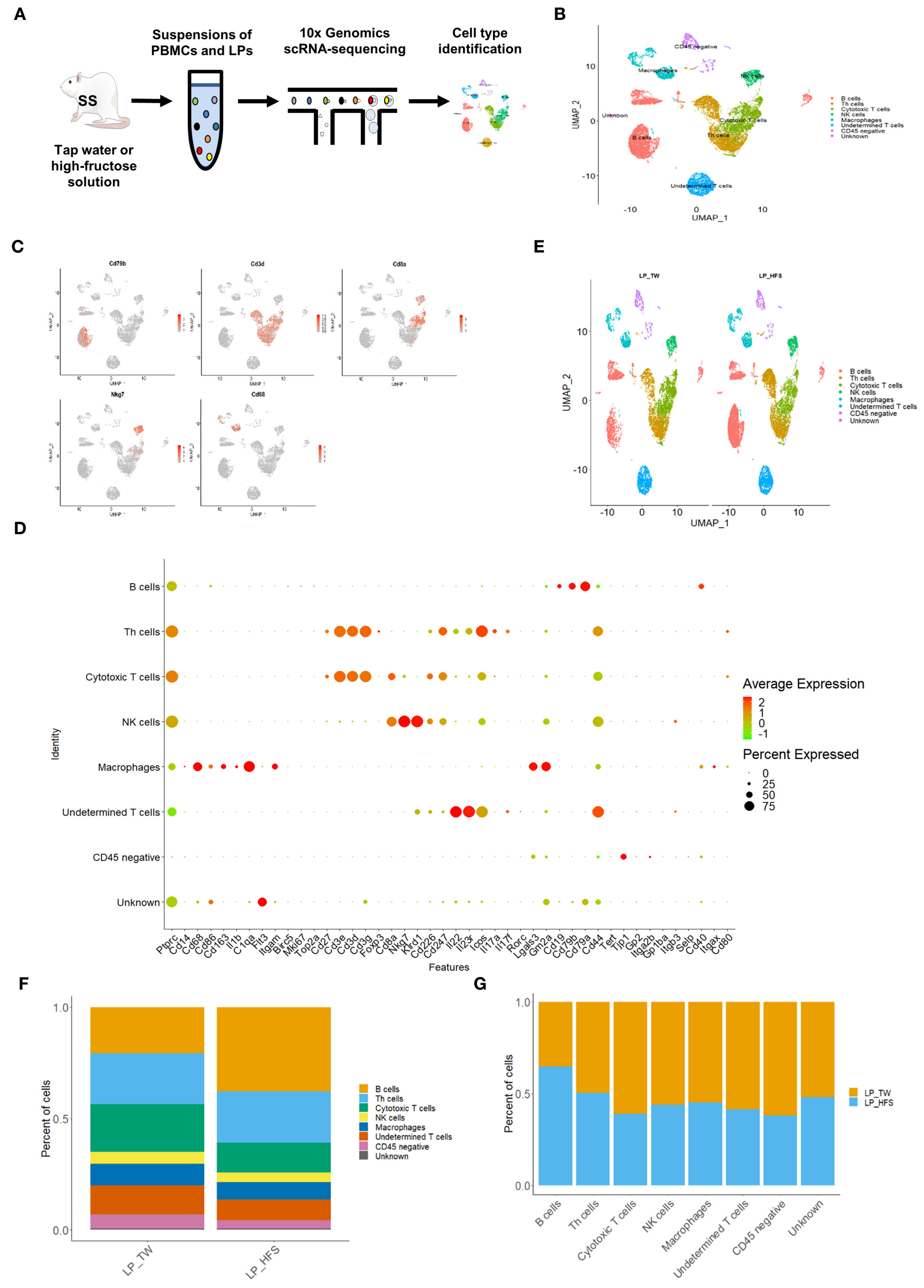

FIGURE 2
High-fructose intake increased B cells within the lamina propria cells (LPs). **(A)** Schematic representation of the experimental strategy. **(B)** The UMAP plot of LPs revealed five major immune cell types, along with CD45 (protein tyrosine phosphatase receptor type C; *Ptprc*)-negative cells, undetermined T cells, and unknown cell types. **(C)** The feature plots demonstrate pronounced expression of *CD68* in macrophages, *Nkg7* in NK cells, *Cd3d* in Th cells, *Cd8a* in cytotoxic T cells, and *Cd79b* in B cells. **(D)** The dot plot of selected marker genes for each cell type. The size of dots represents the percentage of gene expression in each cell subset, while the color of dots indicates the expression levels. **(E)** The HFS group showed an increase in B cells (in red) compared to the TW group. The UMAP plots compare the distribution of the cell types across the TW and HFS groups. **(F, G)** The proportion of B cells was notably higher in the HFS group than in the TW group. **(F)** Depiction of the cell type proportions in each group. **(G)** The relative quantification of each cell type between the two groups.

identified based on their high expression of *Cd27* and *Cd38*. Naïve B cells were recognized by their high expression of *Cxcr5* and *Cd24*, accompanied by low expression of *Cd38*. Breg cells were identified through their high expression of *Cd24* and *Cd38*. Immature B cells were identified by their high expression of *Ybx3* and *Cd38*. Plasma cells were categorized by their high expression of *Sdc1* and *Ighm*, coupled with low expression of *Ptprc* and *Cd24*. These B cell subsets, along with their associated marker genes, were visually presented

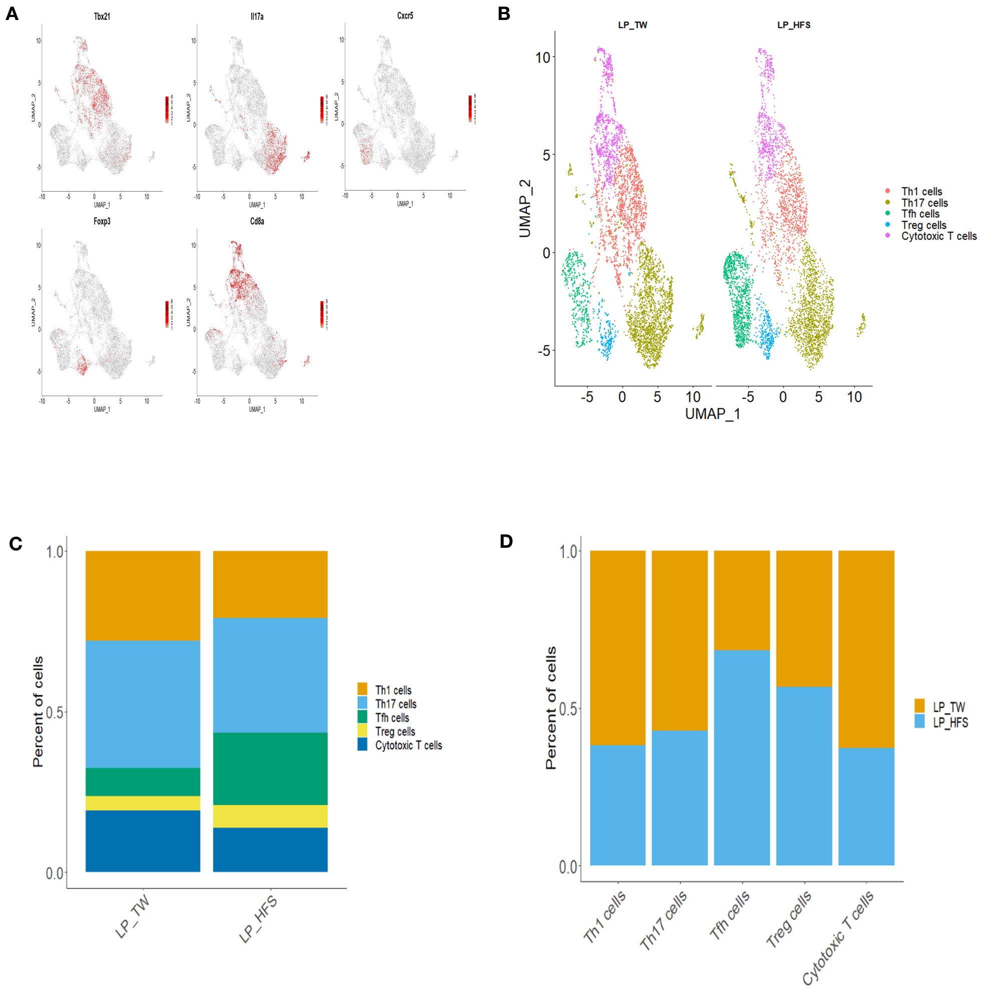

FIGURE 3
High-fructose intake increased the follicular helper T cell subset in LPs. **(A, B)** The HFS group displayed an increased presence of Tfh cells (in green) compared to the TW group. **(A)** The feature plots demonstrate high expression of *Tbx21* in Th1 cells, *Cxcr5* in Tfh cells, *Il17a* in Th17 cells, *Foxp3* in Treg cells, and *Cd8a* in cytotoxic T cells. **(C, D)** The proportion of Tfh and regulatory T (Treg) cells was higher in the HFS group compared to the TW group. **(B)** The UMAP plot enables a visual comparison of the distribution of T cell subsets between the TW and HFS groups. **(C)** Depiction of the proportions of T cell subsets in each group. **(D)** The relative amount of each T cell subset between the two groups.

through a dot plot and feature plots (Figures 4A and S4). A comparative analysis of these B cell subsets between the two groups revealed a higher abundance of follicular B cells in the HFS group (Figure 4B). This trend was supported by a bar graph, which showed a higher proportion of follicular B cells in LPs from the HFS group compared to the TW group (Figures 4C, D).

3.5 Landscape of major cell types from PBMCs of TW and HFS group

We analyzed scRNA-seq datasets from PBMCs of the TW and HFS groups. Subsequently, these datasets were merged for comprehensive scrutiny. Following rigorous quality control measures, an average of 5255 cells in the TW group and 5886 cells in the HFS group were successfully acquired within the PBMCs. Among these, major cell types were identified and classified as B cells, Th cells, cytotoxic T cells, NK cells, macrophages, and monocytes. B cells were identified using *Cd19*, *Cd79a*, and *Cd79b*. Th cells were confirmed using *Cd3d*, *Cd3e*, and *Cd3g*. Cytotoxic T cells were validated through *Cd3d*, *Cd3g*, and *Cd8a*. NK cells were pinpointed using *Cd8a*, *Nkg7*, and *Klrd1*. Macrophages and monocytes were precisely identified using *Cd14*, *Cd68*, *Cd86*, and *Lgals3*, *Gm2a*, *Itgam*, respectively. This comprehensive categorization was visually presented in a dot plot (Figure 5A). These cell types were visualized using bar plots (Figures 5B, C), and their identification was based on specific marker genes.

To further explore T cell and B cell subsets, we visualized them through UMAP plots. The classification of T cell subsets included undifferentiated T cells, cytotoxic T cells, Tfh cells, and Treg cells. These distinctions were made based on specific marker genes. Cytotoxic T cells were defined by *Cd8a*, *Cd8b*, *Gzmm*, and *Nkg7*. Tfh cells were identified using *Cxcr5*, *Icos*, and *Il6r*. Treg cells were identified using *Il2ra*, *Ctla4*, and *Foxp3*. The results of this comprehensive categorization were summarized in a dot plot

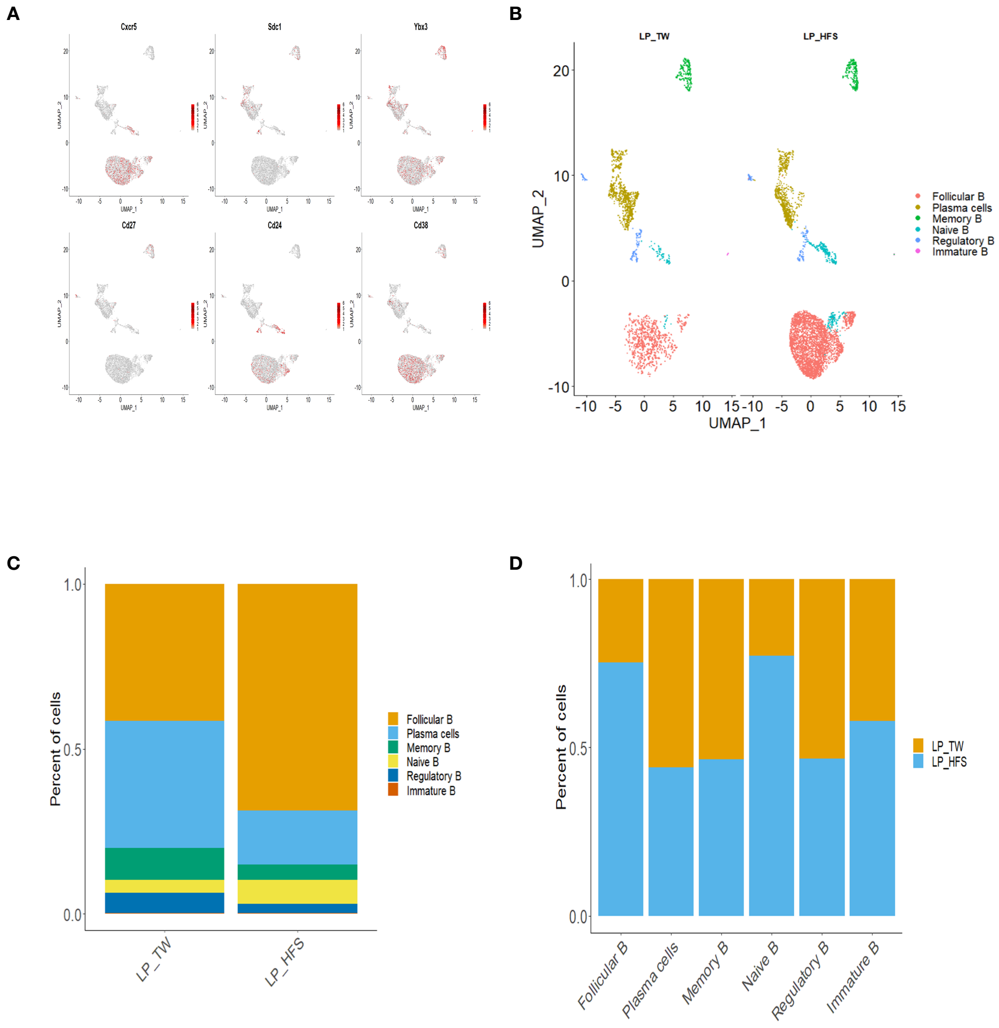

FIGURE 4
High-fructose intake increased the follicular B cell subset in LPs. **(A, B)** The HFS group exhibited an increase in follicular B cells compared to the TW group. **(A)** The feature plots demonstrate high expression of *Cxcr5* and *Cd38* in follicular B cells, *Sdc1* in plasma cells, *Ybx3* in immature B cells, *Cd27* in memory B cells, *Cd24* and *Sdc1* in regulatory B cells, and *Cd24* in naïve B cells, with low expression of *Cd38*. **(B)** The UMAP plot compares the distribution of B cell subsets across the TW and HFS groups. **(C, D)** The proportion of follicular B cells was higher in the HFS group than in the TW group. **(C)** The proportion of B cell subsets in each group. **(D)** The relative amount of each B cell subset between the two groups.

(Figure S5A). Similarly, B cell subsets exhibited a wide range of diversity, including plasma cells, Breg cells, naïve B cells, follicular B cells, mature B cells, memory B cells, immature B cells, and pre B cells. The identification of these subsets was based on distinct marker genes. Breg cells were identified by their high expression of *Cd19*, *Cd24*, *Ms4a1*, and *Cd38*. Mature B cells were classified by their high expression of *Cd19* and *Pax5*, with low expression of *CD79a*. Follicular B cells exhibited high expression of *Cxcr5* and *Cd19*, coupled with low expression of *Cd27*. Immature B cells were recognized by their high expression of *Ybx3* and *Cd38*. Memory B cells were classified based on high expression of *Cd27* and *Cd38*. Plasma cells were distinguished by their high expression of *Sdc1* and *Ighm*, alongside low expression of *Ptprc* and *Cd24*. Pre B cells were identified based on their high expression of *Cd19* and low expression of *Ms4a1*. The diversity of B cells was illustrated in a dot plot (Figure S6). Further investigation of UMAP plots and bar plots between the two groups in PBMCs revealed a noteworthy trend: within T cell subsets, the HFS group exhibited a higher abundance of Treg cells, while nearly all B cells in the HFS group displayed a greater prevalence (Figures 5D-G and S5B, S5C).

3.6 Activation of the interferon signaling pathway in B cells of PBMCs and LPs from the HFS group

To elucidate the differences between the TW and HFS groups, we conducted gene set enrichment analysis (GSEA) on B cells. The GSEA results unveiled the upregulation of hallmark pathways "INTERFERON_ALPHA_RESPONSE" and "INTERFERON_GAMMA_RESPONSE" in B cells from the HFS group (Figures 6A, B). In addition, Differentially Expressed Genes

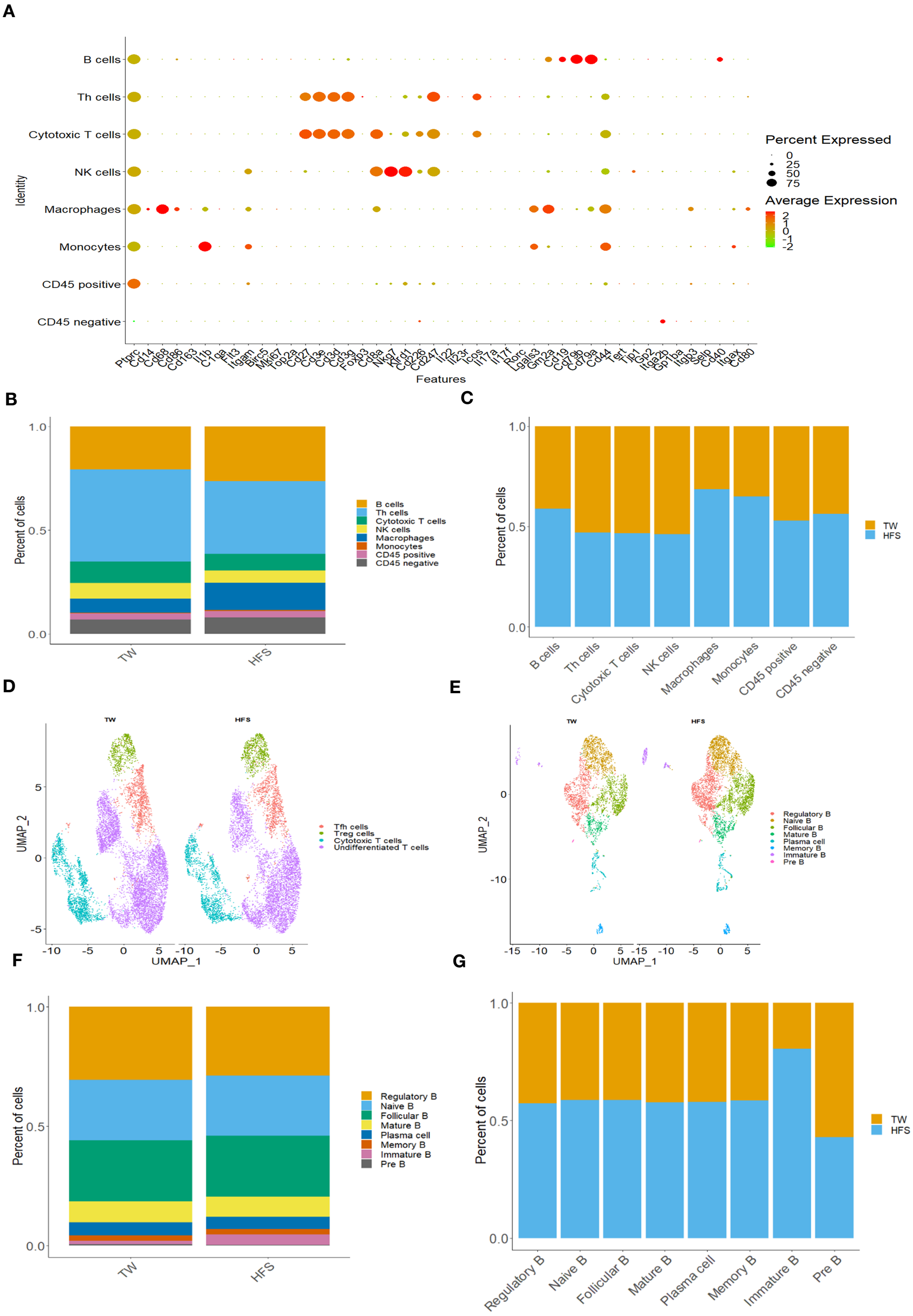

FIGURE 5
High-fructose intake increased B cells, monocytes, and macrophages within peripheral blood mononuclear cells (PBMCs). **(A-C)** The HFS group exhibited an increase in B cells, macrophages, and monocytes compared to the TW group. **(A)** The dot plot of selected marker genes for each cell type. Dot size indicates the percentage of each gene expressed in each cell type, while dot color indicates expression levels. **(B)** The proportion of cell types in each group. **(C)** The relative amount of each cell type between the two groups. **(D)** The UMAP plot compares the distribution of the T cell subsets across the TW and HFS groups. **(E-G)** HFS increased almost all B cell subsets in HFS group compared to TW group in PBMCs. **(E)** The UMAP plot compares the B cell subsets distribution across TW and HFS groups. **(F)** The proportion of B cell subsets in each group. **(G)** The relative amount of each B cell subtype between the two groups.

(DEGs) analysis was performed on T cells and B cells to investigate the gene expression differences between the TW and HFS groups. The enhanced volcano plots unveiled elevated expression of ISGs, in the enhanced volcano plots of T cells from both the TW and HFS groups, genes associated with Treg cells and ISGs, such as *Foxp3* and *Ifitm1*, exhibited higher expression in PBMCs. Furthermore, in B cells, such as *Ifi30*, *Mx1*, and *Mx2* were found to be increased (Figures S7A, S7B). Moreover, genes related to Treg and Tfh cells that were found to be increased in LPs included *Icos* and *Foxp3*, and genes such as *Ifitm1* and *Ifitm3* in B cells were also increased in the

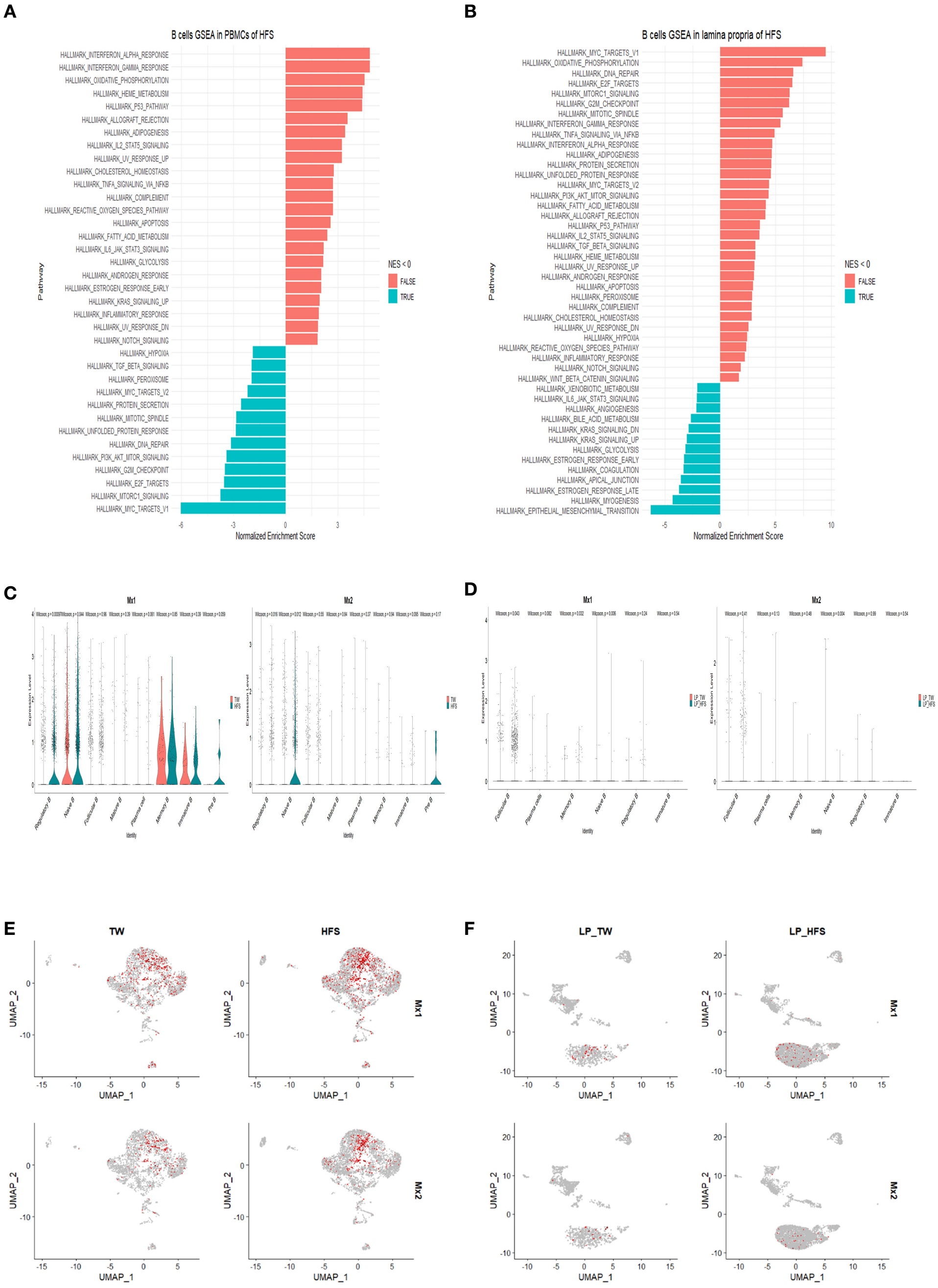

FIGURE 6

High-fructose intake upregulated the expression of interferon-related genes in B cells found in PBMCs and LPs. **(A, B)** The hallmark pathways, including "INTERFERON_ALPHA_RESPONSE" and "INTERFERON_GAMMA_RESPONSE", were upregulated in B cells from the HFS group. **(A)** Utilizing gene set enrichment analysis (GSEA) and normalized enrichment score (NES), enriched hallmark gene sets in B cells from PBMCs of the HFS group were identified compared to the TW group. **(B)** Similarly, GSEA and NES were applied to identify enriched hallmark gene sets in B cells from LPs from the HFS group compared to the TW group. Gene sets with a NES < 0 are shown as leftward bars (in blue), whereas gene sets with NES > 0 are shown as rightward bars (in red). **(C-F)** Notably, the expression of ISGs was increased in B cell subsets of both PBMCs and LPs from the HFS group compared to the TW group. **(C)** The violin plots display the ISG expression, including *myxovirus resistance-1* (*Mx1*) and *myxovirus resistance-2* (*Mx2*), within each B cell subset of PBMCs. The TW group is depicted in red and the HFS group in blue on the vln plots. **(D)** The violin plots display the expression of ISGs such as *Mx1* and *Mx2* within each B cell subset of LPs. The TW group is depicted in red and the HFS group in blue on the vln plots. **(E)** The feature plots illustrate the expression of ISGs such as *Mx1* and *Mx2* within each B cell subset of PBMCs. **(F)** The feature plots illustrate the expression of ISGs such as *Mx1* and *Mx2* within each B cell subset of LPs.

HFS group compared to the TW group (Figures S7C, S7D). Comparative analysis of B cell clusters from PBMCs and LPs using violin (vln) plots reveled distinct expression of IFN-stimulated genes (ISGs). Specifically, in PBMCs, *Mx1* showed significantly elevated expression in Breg, while *Mx2* was significantly upregulated in Breg and naïve B in the HFS group. In LPs, *Mx1* showed significantly elevated expression in follicular B cells in the HFS group (Figures 6C, D). These observations were further supported by the feature plots, which depicted an increased proportion of ISGs in B cells of both PBMCs and LPs from the HFS group (Figures 6E, F). When comparing the expression levels of other interferon-related genes using vln plots in T cell subsets of PBMCs, we observed elevated *Ifnar2 and Ifngr1* were significantly upregulated in Tfh cells of PBMCs from the HFS group (Figure S8). In B cells, *Ifi30* and *Ifngr1* were significantly upregulated in plasma cells, and *Ifngr1* showed significantly elevated expression in follicular B cells of PBMCs from the HFS group compared to the TW group (Figure S9). Moreover, further analysis of the interferon-related genes in the T cell subsets of LPs revealed that *Irf1, Ifi30, Ifitm1, Ifnar1, and Ifngr2* were significantly upregulated in Tfh cells in the HFS group (Figure S10). In B cells, *Irf1, Stat2, Ifi30, Ifngr1, Ifngr2, Ifnar1* and *Ifnar2* were significantly upregulated in follicular B cells of LPs from the HFS group compared to the TW group (Figure S11). Furthermore, a significant increase in *IFN-γ* was observed in Th1 cells from LPs with HFS (Figure S12). These results collectively suggest a comprehensive activation of interferon-related genes in B cells from PBMCs and LPs in the context of hypertension induced by HFS.

4 Discussion

In this study, we provide evidence that HFS leads to an increase in blood pressure, linked to the activation of the IFN signaling pathway in B cells within both LPs and PBMCs. Notably, we observed that the administration of HFS led to an augmented population of B cells among the major cell types in both LPs and PBMCs. Moreover, our investigation uncovered distinct subsets within T cells and B cells: Tfh and Treg cells exhibited an increase within T cell subsets, while follicular B cells showed an elevation in B cell subsets from LPs in the HFS group. Moreover, Treg cells demonstrated an increase in T cell subsets, and B cells (excluding pre B cells) were elevated in B cell subsets from PBMCs in the HFS group.

Our findings indicate that HFS increases SBP through the activation of both the type I and type II IFN signaling pathways in B cells derived from both LPs and PBMCs. The IFN family consists of two main classes: type I IFNs (IFN-α, β, δ, ϵ, κ, τ, and ω), and type II IFN (IFN-γ) (27, 28). Type I IFNs are produced by various cell types. For instance, IFN-α is produced by plasmacytoid DCs, while IFN-β originates from fibroblasts, epithelial cells, macrophages, and monocytes (29, 30). Recent studies have reported that B cells can autonomously produce IFN-α and IFN-β (31, 32). Interestingly, type I IFN has been associated with pulmonary arterial hypertension (PAH) and autoimmune diseases in both humans and mice (33, 34). On the other hand, the predominant producers of type II IFN are Th1 cells, cytotoxic T cells, and NK cells (35, 36), and this cytokine has been associated with the development of hypertension. Intriguingly, the absence of IFN-γ has been shown to result in a blunted increase in SBP in animal models of hypertension induced by Ang II or deoxycorticosterone acetate (DOCA) in combination with salt (37, 38). Previous studies have demonstrated that B cells also secrete both types of IFNs as well as various cytokines (36, 39, 40). Furthermore, both type I and type II IFNs induce the expression of ISGs, which possess diverse immunomodulatory activities and are associated with hypertension (41). Among the ISGs, *Ifi30*, derived from DEGs of monocytes and macrophages, has been correlated with hypertension in patients with abdominal aortic aneurism or intracranial aneurism (42). The upregulation of the *Mx1* and *Mx2* genes has also been linked to inherited stress-induced arterial hypertension in rats (43).

We have observed an increase in Tfh cells in the LPs of the HFS group. These Tfh cells play a crucial role in assisting B cells, particularly follicular B cells, within germinal center (GC) reactions. GC reactions are important for effective immune responses against invading pathogens, but the dysregulation of Tfh cells has been implicated in various autoimmune diseases, inflammatory conditions, and B cell-related malignancies (19). Furthermore, Tfh cells have been linked to the development of hypertension (44, 45). Tfh cells are recognized for their secretion of IL-21, which fosters the activation of GC B cells within secondary or tertiary lymphoid organs. The IL-21 derived from Tfh cells plays a critical role in processes such as immunoglobulin (Ig) class switching and the generation of high-affinity antibodies by GC B cells (46, 47). Notably, when Ang II is administered into IL-21 knockout mice versus WT mice, IL-21 deficiency is associated with lower blood pressure, diminished vascular and end-organ damage, and reduced levels of IL-17A and IFN-γ compared to WT mice. Moreover, the neutralization of IL-21 results in decreased blood pressure, alleviation of vascular inflammation, and improvement in endothelial dysfunction. Importantly, human subjects with hypertension exhibit higher levels of IL-21 in their PBMCs compared to individuals with normal blood pressure (46).

Our research demonstrates that the consumption of HFS leads to an increase in B cells in both LPs and PBMCs. Recent evidence underscores the potential contribution of B cells in the development and progression of hypertension and vascular injury. The infusion of Ang II has revealed a surge in activated B cells and plasma cells. Moreover, studies using mice lacking the B cell activating factor receptor (BAFF-R) have shown prevention of blood pressure elevation and a reduction in aortic macrophage infiltration. Remarkably, the adoptive transfer of B cells from WT mice into those lacking BAFF-R reinstates their susceptibility to hypertension. Notably, the depletion of B cells by anti-CD20 antibodies in combination with Ang II administration results in a significant decrease in blood pressure (22). Furthermore, mice deficient in the B cell transcription factor c-myb, which is essential for the development of mature B cells, exhibit lower blood pressure compared to their WT littermates (48).

Hence, when implementing a high-fructose diet, blood pressure elevates through non-immune mechanisms. Subsequently, the activation of macrophages and DC cells is induced by specific antigens associated with hypertension, including neo-antigens and damage associated molecular patterns (DAMPs). These activated immune cells then proceed to stimulate T cells in the spleen, which, in turn, activate B cells to produce auto-antibodies. Consequently, this process leads to more extensive damage to various tissues such as blood vessels, kidneys, and the heart, ultimately progressing into more severe hypertension (49). Furthermore, a high-fructose diet may induce changes in gut microbiota composition, potentially activating B cells. For example, in a systemic sclerosis mouse model, when a high-fructose diet was administered for 4 and 12 weeks, *Bifidobacterium pseudomonas* and *Muribacterium intestinale* species in the gut microbiota decreased while *Olsenella timonensis* and *Desulfovibrio vulgaris* species increased. Subsequently, we observed a trend of increased B cells and Treg cells in the ileum 4 weeks after the high-fructose diet (50). Another example can be seen in non-alcoholic steatohepatitis (NASH), where a 20-week high-fructose diet resulted in the significant accumulation of pro-inflammatory B cells in the liver. This was attributed to factors induced by changes in gut microbiota (51). Consequently, we speculate, based on our experimental findings, that alterations in gut microbiota composition due to a high-fructose diet may activate B cells, potentially impacting not only systemic sclerosis and non-alcoholic fatty liver disease (NAFLD), but also hypertension.

Our study reveals a notable increase in the Treg population in both LPs and PBMCs from the HFS group. Treg cells not only play a crucial role as key regulators of inflammation but also have a dual role in maintaining self-tolerance and protecting against autoimmune diseases. The stability and function of the Treg cell lineage rely on the signaling mediated by the transcription factor Foxp3 (52, 53). These cells employ diverse mechanisms to suppress antigen presentation, including the induction of IL-10 expression as well as the inhibition of DC maturation (54, 55). Moreover, Treg cells control T cell proliferation and differentiation through upregulation of the expression of granzyme B and CD73, while simultaneously dampening the production of multiple cytokines such as IL-2, IFN-γ, and TNF-α (56). Previous investigations have reported the role of Treg cells in inhibiting B cell activity, both *in vitro* and *in vivo*, through mechanisms that depend on cellular contact (57, 58). Other studies have suggested that B cells are essential for the proliferation and expansion of not only antigen-primed effector Th cells but also Treg cells (40, 59, 60). Based on our findings, it is reasonable to propose that the observed augmentation in Treg cells could serve as a compensatory response aimed at counterbalancing the effects of B cells in LPs and PBMCs. The elevated expression of IFNs and ISGs within these B cells implies a connection to immune regulatory processes, potentially associated with autoimmunity. This aligns with recent evidence highlighting the connection between inflammation, autoimmunity, and the development of hypertension (34).

In our previous findings, the application of an HFS induced an imbalance in SGK1-Foxo1/3 signaling. Th17 cells increased in PBMCs and the spleen of Dahl salt-sensitive rats, while the Treg cells remained unaffected (6). However, upon verification through scRNA-Seq data, we observed that in the LP, there was no significant difference in the expression of SGK1 and Foxo1/3 when a HFS was applied. Th17 cells exhibited a tendency to decrease as compared to the WT. Although we were unable to pinpoint the exact causes, it is speculated that Th17 cells play a minimal role in the LP when hypertension occurs. This is likely due to tissue and environmental characteristics. For example, in previous studies, it has been well-documented that in rodent models, when $CD8^+$ T cells are transferred or high-salt diets are administered, $CD8^+$ T cells become established in the kidneys, contributing to the induction of hypertension (61). Moreover, when mice with knockout of IFN-γ, a cytokine secreted by $CD8^+$ T cells, were subjected to DOCA-salt treatment, they showed lower blood pressure as compared to WT mice. Additionally, there was a reduced presence of $CD8^+$ T cells in the kidneys (38). This evidence strongly supports the association of $CD8^+$ T cells with the development of hypertension in the kidneys. However, a study examining the relationship between hypertension history and the gut in humans revealed a reduction in $CD8^+$ T cells in the intestines of individuals with hypertension as compared to those with healthy intestines (62).

In summary, our study demonstrates that high fructose intake leads to an increase in blood pressure. This increase is driven by the activation of the IFN signaling pathway in B cells in both LPs and PBMCs. These findings suggest that targeting B cells could be a potential intervention strategy to reduce blood pressure in individuals with fructose-induced hypertension.

Data availability statement

The data presented in the study are deposited in the NCBI Sequencing Read Archive database, accession number PRJNA1013706, at the following link: http://www.ncbi.nlm.nih.gov/sra/?term=PRJNA1013706.

Ethics statement

The animal study was approved by Kyungpook National University Institutional Review Board. The study was conducted in accordance with the local legislation and institutional requirements.

Author contributions

C-WK: Data curation, Formal Analysis, Investigation, Methodology, Validation, Visualization, Writing – original draft. SJ: Investigation, Methodology, Writing – review & editing. BK: Investigation, Writing – review & editing. JK: Investigation, Writing – review & editing. SJ: Investigation, Writing – review & editing. S-JT: Writing – review & editing. SL: Writing – review & editing, Data curation. MK: Writing – review & editing, Data curation. IK: Conceptualization, Funding acquisition, Project administration, Supervision, Writing – review & editing, Data curation.

Funding

The author(s) declare financial support was received for the research, authorship, and/or publication of this article. This research was supported by the Basic Science Research Program through the National Research Foundation of Korea (NRF), funded by the Ministry of Education, Science and Technology (NRF-2021R1A2B5B02001763, and 2021R1A4A1021617).

Conflict of interest

The authors declare that the research was conducted in the absence of any commercial or financial relationships that could be construed as a potential conflict of interest.

Publisher's note

All claims expressed in this article are solely those of the authors and do not necessarily represent those of their affiliated organizations, or those of the publisher, the editors and the reviewers. Any product that may be evaluated in this article, or claim that may be made by its manufacturer, is not guaranteed or endorsed by the publisher.

Supplementary material

The Supplementary Material for this article can be found online at: https://www.frontiersin.org/articles/10.3389/fimmu.2023.1279439/full#supplementary-material

References

1. Xu C, Yu J. Pathophysiological mechanisms of hypertension development induced by fructose consumption. *Food Funct* (2022) 13(4):1702–17. doi: 10.1039/d1fo03381f

2. Caillon A, Paradis P, Schiffrin EL. Role of immune cells in hypertension. *Br J Pharmacol* (2019) 176(12):1818–28. doi: 10.1111/bph.14427

3. Zhang Z, Zhao L, Zhou X, Meng X, Zhou X. Role of inflammation, immunity, and oxidative stress in hypertension: new insights and potential therapeutic targets. *Front Immunol* (2022) 13:1098725. doi: 10.3389/fimmu.2022.1098725

4. Zhang DM, Jiao RQ, Kong LD. High dietary fructose: direct or indirect dangerous factors disturbing tissue and organ functions. *Nutrients* (2017) 9(4):335. doi: 10.3390/nu9040335

5. Yoo S, Ahn H, Park YK. High dietary fructose intake on cardiovascular disease related parameters in growing rats. *Nutrients* (2016) 9(1):11. doi: 10.3390/nu9010011

6. Lee E, Kim N, Kang J, Yoon S, Lee HA, Jung H, et al. Activated pathogenic th17 lymphocytes induce hypertension following high-fructose intake in dahl salt-sensitive but not dahl salt-resistant rats. *Dis Model Mech* (2020) 13(5):dmm044107. doi: 10.1242/dmm.044107

7. Di Sabatino A, Santacroce G, Rossi CM, Broglio G, Lenti MV. Role of mucosal immunity and epithelial-vascular barrier in modulating gut homeostasis. *Intern Emerg Med* (2023) 18(6):1635–46. doi: 10.1007/s11739-023-03329-1

8. Sardinha-Silva A, Alves-Ferreira EVC, Grigg ME. Intestinal immune responses to commensal and pathogenic protozoa. *Front Immunol* (2022) 13:963723. doi: 10.3389/fimmu.2022.963723

9. Montalban-Arques A, Chaparro M, Gisbert JP, Bernardo D. The innate immune system in the gastrointestinal tract: role of intraepithelial lymphocytes and lamina propria innate lymphoid cells in intestinal inflammation. *Inflammation Bowel Dis* (2018) 24(8):1649–59. doi: 10.1093/ibd/izy177

10. McDermott AJ, Huffnagle GB. The microbiome and regulation of mucosal immunity. *Immunology* (2014) 142(1):24–31. doi: 10.1111/imm.12231

11. Groschwitz KR, Hogan SP. Intestinal barrier function: molecular regulation and disease pathogenesis. *J Allergy Clin Immunol* (2009) 124(1):3–20; quiz 1-2. doi: 10.1016/j.jaci.2009.05.038

12. Battson ML, Lee DM, Weir TL, Gentile CL. The gut microbiota as a novel regulator of cardiovascular function and disease. *J Nutr Biochem* (2018) 56:1–15. doi: 10.1016/j.jnutbio.2017.12.010

13. Avery EG, Bartolomaeus H, Maifeld A, Marko L, Wiig H, Wilck N, et al. The gut microbiome in hypertension: recent advances and future perspectives. *Circ Res* (2021) 128(7):934–50. doi: 10.1161/CIRCRESAHA.121.318065

14. Wilck N, Matus MG, Kearney SM, Olesen SW, Forslund K, Bartolomaeus H, et al. Salt-responsive gut commensal modulates T(H)17 axis and disease. *Nature* (2017) 551(7682):585–9. doi: 10.1038/nature24628

15. Sabatino JJ Jr., Probstel AK, Zamvil SS. B cells in autoimmune and neurodegenerative central nervous system diseases. *Nat Rev Neurosci* (2019) 20(12):728–45. doi: 10.1038/s41583-019-0233-2

16. Kelly LM, Pereira JP, Yi T, Xu Y, Cyster JG. Ebi2 guides serial movements of activated B cells and ligand activity is detectable in lymphoid and nonlymphoid tissues. *J Immunol* (2011) 187(6):3026–32. doi: 10.4049/jimmunol.1101262

17. Lee DSW, Rojas OL, Gommerman JL. B cell depletion therapies in autoimmune disease: advances and mechanistic insights. *Nat Rev Drug Discovery* (2021) 20(3):179–99. doi: 10.1038/s41573-020-00092-2

18. Gatto D, Paus D, Basten A, Mackay CR, Brink R. Guidance of B cells by the orphan G protein-coupled receptor ebi2 shapes humoral immune responses. *Immunity* (2009) 31(2):259–69. doi: 10.1016/j.immuni.2009.06.016

19. Qin L, Waseem TC, Sahoo A, Bieerkehazhi S, Zhou H, Galkina EV, et al. Insights into the molecular mechanisms of T follicular helper-mediated immunity and pathology. *Front Immunol* (2018) 9:1884. doi: 10.3389/fimmu.2018.01884

20. Chen Y, Dale BL, Alexander MR, Xiao L, Ao M, Pandey AK, et al. Class switching and high-affinity immunoglobulin G production by B cells is dispensable for the development of hypertension in mice. *Cardiovasc Res* (2021) 117(4):1217–28. doi: 10.1093/cvr/cvaa187

21. Guzik TJ, Hoch NE, Brown KA, McCann LA, Rahman A, Dikalov S, et al. Role of the T cell in the genesis of angiotensin ii induced hypertension and vascular dysfunction. *J Exp Med* (2007) 204(10):2449–60. doi: 10.1084/jem.20070657

22. Chan CT, Sobey CG, Lieu M, Ferens D, Kett MM, Diep H, et al. Obligatory role for B cells in the development of angiotensin ii-dependent hypertension. *Hypertension* (2015) 66(5):1023–33. doi: 10.1161/HYPERTENSIONAHA.115.05779

23. Joo SS, Yoon JH, Jung JY, Joo SY, An SH, Ban BC, et al. The modulatory effects of lacticaseibacillus paracasei strain nsmj56 on gut immunity and microbiome in early-age broiler chickens. *Anim (Basel)* (2022) 12(23):3413. doi: 10.3390/ani12233413

24. Patel AM, Liu YS, Davies SP, Brown RM, Kelly DA, Scheel-Toellner D, et al. The role of B cells in adult and paediatric liver injury. *Front Immunol* (2021) 12:729143. doi: 10.3389/fimmu.2021.729143

25. Morgan D, Tergaonkar V. Unraveling B cell trajectories at single cell resolution. *Trends Immunol* (2022) 43(3):210–29. doi: 10.1016/j.it.2022.01.003

26. Qian J, Gao Y, Lai Y, Ye Z, Yao Y, Ding K, et al. Single-cell rna sequencing of peripheral blood mononuclear cells from acute myocardial infarction. *Front Immunol* (2022) 13:908815. doi: 10.3389/fimmu.2022.908815

27. Lee AJ, Ashkar AA. The dual nature of type I and type ii interferons. *Front Immunol* (2018) 9:2061. doi: 10.3389/fimmu.2018.02061

28. Platanias LC. Mechanisms of type-I- and type-ii-interferon-mediated signalling. *Nat Rev Immunol* (2005) 5(5):375–86. doi: 10.1038/nri1604

29. Muskardin TLW, Niewold TB. Type I interferon in rheumatic diseases. *Nat Rev Rheumatol* (2018) 14(4):214–28. doi: 10.1038/nrrheum.2018.31

30. Ivashkiv LB, Donlin LT. Regulation of type I interferon responses. *Nat Rev Immunol* (2014) 14(1):36–49. doi: 10.1038/nri3581

31. Ward JM, Ratliff ML, Dozmorov MG, Wiley G, Guthridge JM, Gaffney PM, et al. Human effector B lymphocytes express arid3a and secrete interferon alpha. *J Autoimmun* (2016) 75:130–40. doi: 10.1016/j.jaut.2016.08.003

32. Benard A, Sakwa I, Schierloh P, Colom A, Mercier I, Tailleux L, et al. B cells producing type I ifn modulate macrophage polarization in tuberculosis. *Am J Respir Crit Care Med* (2018) 197(6):801–13. doi: 10.1164/rccm.201707-1475OC

33. George PM, Oliver E, Dorfmuller P, Dubois OD, Reed DM, Kirkby NS, et al. Evidence for the involvement of type I interferon in pulmonary arterial hypertension. *Circ Res* (2014) 114(4):677–88. doi: 10.1161/CIRCRESAHA.114.302221

34. Chasset F, Dayer JM, Chizzolini C. Type I interferons in systemic autoimmune diseases: distinguishing between afferent and efferent functions for precision medicine and individualized treatment. *Front Pharmacol* (2021) 12:633821. doi: 10.3389/fphar.2021.633821

35. Han L, Tu S, Shen P, Yan J, Huang Y, Ba X, et al. A comprehensive transcriptomic analysis of alternate interferon signaling pathways in peripheral blood mononuclear cells in rheumatoid arthritis. *Aging (Albany NY)* (2021) 13(16):20511–33. doi: 10.18632/aging.203432

36. Schroder K, Hertzog PJ, Ravasi T, Hume DA. Interferon-gamma: an overview of signals, mechanisms and functions. *J Leukoc Biol* (2004) 75(2):163–89. doi: 10.1189/jlb.0603252

37. Kamat NV, Thabet SR, Xiao L, Saleh MA, Kirabo A, Madhur MS, et al. Renal transporter activation during angiotensin-ii hypertension is blunted in interferon-gamma-/- and interleukin-17a-/- mice. *Hypertension* (2015) 65(3):569–76. doi: 10.1161/HYPERTENSIONAHA.114.04975

38. Benson LN, Liu Y, Wang X, Xiong Y, Rhee SW, Guo Y, et al. The ifngamma-pdl1 pathway enhances cd8t-dct interaction to promote hypertension. *Circ Res* (2022) 130(10):1550–64. doi: 10.1161/CIRCRESAHA.121.320373

39. Akkaya M, Akkaya B, Miozzo P, Rawat M, Pena M, Sheehan PW, et al. B cells produce type 1 ifns in response to the tlr9 agonist cpg-a conjugated to cationic lipids. *J Immunol* (2017) 199(3):931–40. doi: 10.4049/jimmunol.1700348

40. Saze Z, Schuler PJ, Hong CS, Cheng D, Jackson EK, Whiteside TL. Adenosine production by human B cells and B cell-mediated suppression of activated T cells. *Blood* (2013) 122(1):9–18. doi: 10.1182/blood-2013-02-482406

41. Liu SY, Sanchez DJ, Aliyari R, Lu S, Cheng G. Systematic identification of type I and type ii interferon-induced antiviral factors. *Proc Natl Acad Sci U.S.A.* (2012) 109 (11):4239–44. doi: 10.1073/pnas.1114981109

42. Li Y, Zhang Z, Liu D. Intracranial aneurysms induced by runx1 through regulation of nfkb1 in patients with hypertension-an integrated analysis based on multiple datasets and algorithms. *Front Neurol* (2022) 13:877801. doi: 10.3389/fneur.2022.877801

43. Redina OE, Smolenskaya SE, Fedoseeva LA, Markel AL. [Differentially expressed genes in the locus associated with relative kidney weight and resting blood pressure in hypertensive rats of the isiah strain]. *Mol Biol (Mosk)* (2016) 50(6):944–52. doi: 10.7868/S0026898416050141

44. Spolski R, Leonard WJ. Interleukin-21: A double-edged sword with therapeutic potential. *Nat Rev Drug Discovery* (2014) 13(5):379–95. doi: 10.1038/nrd4296

45. Ozaki K, Spolski R, Feng CG, Qi CF, Cheng J, Sher A, et al. A critical role for il-21 in regulating immunoglobulin production. *Science* (2002) 298(5598):1630–4. doi: 10.1126/science.1077002

46. Dale BL, Pandey AK, Chen YH, Smart CD, Laroumanie F, Ao MF, et al. Critics role of il-21 and T follicular helper cells in hypertension and vascular dysfunction. *JCI Insight* (2019) 4(11):e129278. doi: 10.1172/jci.insight.129278

47. Ettinger R, Sims GP, Fairhurst AM, Robbins R, da Silva YS, Spolski R, et al. Il-21 induces differentiation of human naive and memory B cells into antibody-secreting plasma cells. *J Immunol* (2005) 175(12):7867–79. doi: 10.4049/jimmunol.175.12.7867

48. Dingwell LS, Shikatani EA, Besla R, Levy AS, Dinh DD, Momen A, et al. B-cell deficiency lowers blood pressure in mice. *Hypertension* (2019) 73(3):561–70. doi: 10.1161/HYPERTENSIONAHA.118.11828

49. Drummond GR, Vinh A, Guzik TJ, Sobey CG. Immune mechanisms of hypertension. *Nat Rev Immunol* (2019) 19(8):517–32. doi: 10.1038/s41577-019-0160-5

50. Peterson SR, Ali S, Shrode RL, Mangalam AK. Effect of a fructose-rich diet on gut microbiota and immunomodulation: potential factors for multiple sclerosis. *Immunohorizons* (2023) 7(3):213–27. doi: 10.4049/immunohorizons.2300008

51. Barrow F, Khan S, Fredrickson G, Wang H, Dietsche K, Parthiban P, et al. Microbiota-driven activation of intrahepatic B cells aggravates nash through innate and adaptive signaling. *Hepatology* (2021) 74(2):704–22. doi: 10.1002/hep.31755

52. Shevach EM, Thornton AM. Ttregs, ptregs, and itregs: similarities and differences. *Immunol Rev* (2014) 259(1):88–102. doi: 10.1111/imr.12160

53. Tian W, Jiang SY, Jiang X, Tamosiuniene R, Kim D, Guan T, et al. The role of regulatory T cells in pulmonary arterial hypertension. *Front Immunol* (2021) 12:684657. doi: 10.3389/fimmu.2021.684657

54. Mittal SK, Cho KJ, Ishido S, Roche PA. Interleukin 10 (Il-10)-mediated immunosuppression: march-I induction regulates antigen presentation by macrophages but not dendritic cells. *J Biol Chem* (2015) 290(45):27158–67. doi: 10.1074/jbc.M115.682708

55. Mittal SK, Roche PA. Suppression of antigen presentation by il-10. *Curr Opin Immunol* (2015) 34:22–7. doi: 10.1016/j.coi.2014.12.009

56. Qiu H, He Y, Ouyang F, Jiang P, Guo S, Guo Y. The role of regulatory T cells in pulmonary arterial hypertension. *J Am Heart Assoc* (2019) 8(23):e014201. doi: 10.1161/JAHA.119.014201

57. Iikuni N, Lourenco EV, Hahn BH, La Cava A. Cutting edge: regulatory T cells directly suppress B cells in systemic lupus erythematosus. *J Immunol* (2009) 183 (3):1518–22. doi: 10.4049/jimmunol.0901163

58. Lim HW, Hillsamer P, Banham AH, Kim CH. Cutting edge: direct suppression of B cells by cd4+ Cd25+ Regulatory T cells. *J Immunol* (2005) 175(7):4180–3. doi: 10.4049/jimmunol.175.7.4180

59. Chen LC, Delgado JC, Jensen PE, Chen X. Direct expansion of human allospecific foxp3+Cd4+ Regulatory T cells with allogeneic B cells for therapeutic application. *J Immunol* (2009) 183(6):4094–102. doi: 10.4049/jimmunol.0901081

60. Tu W, Lau YL, Zheng J, Liu Y, Chan PL, Mao H, et al. Efficient generation of human alloantigen-specific cd4+ Regulatory T cells from naive precursors by cd40-activated B cells. *Blood* (2008) 112(6):2554–62. doi: 10.1182/blood-2008-04-152041

61. Liu Y, Rafferty TM, Rhee SW, Webber JS, Song L, Ko B, et al. Cd8(+) T cells stimulate na-cl co-transporter ncc in distal convoluted tubules leading to salt-sensitive hypertension. *Nat Commun* (2017) 8:14037. doi: 10.1038/ncomms14037

62. Hickey JW, Becker WR, Nevins SA, Horning A, Perez AE, Zhu C, et al. Organization of the human intestine at single-cell resolution. *Nature* (2023) 619 (7970):572–84. doi: 10.1038/s41586-023-05915-x

Frontiers in Immunology

TYPE Original Research
PUBLISHED 14 December 2023
DOI 10.3389/fimmu.2023.1282770

OPEN ACCESS

EDITED BY
InKyeom Kim,
Kyungpook National University, Republic of Korea

REVIEWED BY
Jens Geginat,
University of Milan, Italy
Cheong-Wun Kim,
Kyungpook National University, Republic of Korea

*CORRESPONDENCE
Peter E. Lipsky
✉ peterlipsky@comcast.net
Xin M. Luo
✉ xinluo@vt.edu

†These authors have contributed equally to this work

RECEIVED 24 August 2023
ACCEPTED 29 November 2023
PUBLISHED 14 December 2023

CITATION
Daamen AR, Alajoleen RM, Grammer AC, Luo XM and Lipsky PE (2023) Single-cell RNA sequencing analysis reveals the heterogeneity of IL-10 producing regulatory B cells in lupus-prone mice.
Front. Immunol. 14:1282770.
doi: 10.3389/fimmu.2023.1282770

Single-cell RNA sequencing analysis reveals the heterogeneity of IL-10 producing regulatory B cells in lupus-prone mice

Andrea R. Daamen[1†], Razan M. Alajoleen[2†], Amrie C. Grammer[1], Xin M. Luo[2*] and Peter E. Lipsky[1*]

[1]AMPEL BioSolutions LLC and the RILITE Research Institute, Charlottesville, VA, United States, [2]Department of Biomedical Sciences and Pathology, Virginia-Maryland College of Veterinary Medicine, Virginia Tech, Blacksburg, VA, United States

Introduction: B cells can have both pathogenic and protective roles in autoimmune diseases, including systemic lupus erythematosus (SLE). Deficiencies in the number or immunosuppressive function of IL-10 producing regulatory B cells (Bregs) can cause exacerbated autoimmune inflammation. However, the exact role of Bregs in lupus pathogenesis has not been elucidated.

Methods: We carried out gene expression analysis by scRNA-seq to characterize differences in splenic Breg subsets and molecular profiles through stages of disease progression in lupus-prone mice. Transcriptome-based changes in Bregs from mice with active disease were confirmed by phenotypic analysis.

Results: We found that a loss of marginal zone (MZ) lineage Bregs, an increase in plasmablast/plasma cell (PB-PC) lineage Bregs, and overall increases in inflammatory gene signatures were characteristic of active disease as compared to Bregs from the pre-disease stage. However, the frequencies of both MZ Bregs and PB-PCs expressing IL-10 were significantly decreased in active-disease mice.

Conclusion: Overall, we have identified changes to the repertoire and transcriptional landscape of Breg subsets associated with active disease that provide insights into the role of Bregs in lupus pathogenesis. These results could inform the design of Breg-targeted therapies and interventions to restore Breg suppressive function in autoimmunity.

KEYWORDS

lupus, Breg, single-cell, transcriptomics, bioinformatics

Introduction

B cells are typically thought of as positive effectors of autoimmunity through the production of autoantibodies and inflammatory cytokines. However, subsets of B cells generally characterized by the production of interleukin-10 (IL-10) and broadly labeled regulatory B cells (Bregs) can also function as negative regulators of the immune response (1). Multiple populations of suppressive B cells have been described and defined by the expression of a variety of B-lineage and context-dependent markers (2), including transitional 2-marginal zone precursors (T2-MZP) (3), mature MZ B cells (4, 5), TIM-1 B cells (6), Plasmablasts (PBs) (7), Plasma Cells (PCs) (8), and B1a B cells (9). The immunosuppressive function of Bregs is primarily mediated by inhibition of T cell activation and pro-inflammatory responses (10). This may occur through direct or indirect mechanisms, including production of anti-inflammatory cytokines such as IL-10, IL-35, and transforming growth factor receptor β (TGF-β), inhibition through cognate interactions with pro-inflammatory immune cells, or by promoting Treg cell differentiation (11). Notably, the absence or loss of Bregs has been associated with increased inflammation in mice with a variety of autoimmune disorders, including experimental autoimmune encephalomyelitis (EAE) (12–14), ulcerative colitis (UC) (15, 16), collagen-induced arthritis (3), and SLE (17, 18). Despite evidence of an important role for suppressive B cells in modulating aberrant immune responses, however, their origins and regulatory mechanisms are poorly understood.

The important role of B cell regulatory function for maintaining immune tolerance has driven research on Bregs and their potential as targets for treatment of various autoimmune diseases, including SLE (19). However, deciphering the exact role of Bregs in SLE pathogenesis has been complicated by heterogeneity in lupus patients and Breg subsets described in the context of each study. Multiple studies have found increased serum IL-10 levels as well as increased numbers of circulating Bregs in SLE patients (20–22). However, others have described decreased Bregs in specific cohorts of SLE patients, including those with active lupus nephritis (LN) (23) and decreases in individual marker-defined Breg subsets (24, 25) indicating that specific Breg populations may be important for counteracting specific manifestations of SLE pathogenesis. Even when Bregs are present in sufficient numbers in SLE patients, they appear to be functionally impaired suggesting that defects in Breg-mediated suppression may contribute to autoimmunity (26–28). Thus, many questions remain as to the role of Bregs in SLE, including how specific Breg populations function in the context of autoimmunity and how this may be exploited to inform better treatment of SLE patients.

In previous work, we utilized the autoimmune-prone MRL/Mp-*Fas*^{lpr} (MRL/*lpr*) mouse strain, which spontaneously develops lupus-like disease, to investigate the role of gut microbiota in autoimmunity (29, 30). Interestingly, early treatment with the antibiotic vancomycin before disease onset exacerbated disease pathogenesis and concomitantly lead to reduced numbers of splenic Bregs as well as decreased circulating IL-10 and IL-35. Moreover, adoptive transfer of Bregs pre-disease improved disease pathology, whereas transfer during active disease was not protective (30). This result emphasizes the importance of Bregs in preventing autoimmunity, but also suggests that these effects are disease-context dependent.

Here, we used a combination of phenotypic and single-cell transcriptional analysis of MRL/*lpr* mice as a model to examine the role of Bregs and heterogeneity of Breg subsets generated from mice at different stages of lupus disease progression. We identified deficiencies in the overall number of IL-10^{+} Bregs as well as differences in the proportion and transcriptional profiles of specific Breg subsets derived from mice with active disease as compared to mice before disease onset. This result suggests that not only deficiencies in Bregs as a whole, but alterations to the repertoire of Bregs may play a critical role in lupus pathogenesis and that enhancing the function of specific Breg subsets could be exploited to restore Breg-mediated suppression in the context of autoimmunity.

Materials and methods

Mice

MRL/*lpr* mice (MRL/Mp-*Fas*^{lpr}, stock number 000485) were purchased from The Jackson Laboratory (Bar Harbor, ME) and kept in a pathogen-free facility per the requirements of Virginia Tech's Institutional Animal Care and Use Committee (IACUC). Female MRL/*lpr* mice aged six weeks were used to represent the pre-disease stage and female MRL/*lpr* mice aged ten weeks were used to represent the active disease stage. Only female mice were used as these mice get earlier and more severe disease as compared to male mice in a manner similar to human patients with lupus and other autoimmune diseases.

Flow cytometry

Spleens were collected and pressed through 70-µm cell strainers with complete medium (RPMI 1640, 10% fetal bovine serum, 1 mM sodium pyruvate, 1% 100 MEM non-essential amino acids, 10 mM HEPES, 55 mM 2-mercaptoethanol, 2 mM L-glutamine, 100 U/ml penicillin-streptomycin, all from Life Technologies, Grand Island, NY). Red blood cells (RBCs) were excluded using previously published methods (30). Single-cell suspensions were stimulated for 24 hours with 10 µg/ml LPS, followed by 5 hours of 50 ng/ml PMA and 500 ng/ml ionomycin, blocked for 10 minutes on ice with the Fc receptor block anti-CD16/32 (eBioscience), then stained for 15 minutes in the dark with fluorochrome-conjugated antibodies and analyzed with a BD FACS Aria II flow cytometer (BD Biosciences, San Jose, CA). Foxp3 Fixation/Permeabilization kit (eBioscience) was used for intracellular staining. To exclude dead cells, a Zombie Aqua fixable viability kit (Biolegend) was used. The following monoclonal anti-mouse antibodies were used in this study: AF700 or APC conjugated anti-CD19 diluted 1:800, PE-Cy7 conjugated anti-CD23 diluted 1:60, APC-Cy7 conjugated anti-CD21 diluted 1:80, FITC conjugated anti-CD24 diluted 1:200, PE conjugated anti-IL-10 diluted 1:80, BV711 conjugated anti-CD138 diluted 1:800, and APC conjugated anti-IgH (μ chain) diluted 1:800 (BioLegend).

Cell preparation for analysis of Breg populations and IL-10 production

Enriched B cells were stimulated for 24 hours with 10 μg/ml LPS, followed by 5 hours of 50 ng/ml PMA and 500 ng/ml ionomycin. Stimulated cells were labeled with Miltenyi Biotec's Regulatory B Cell Catch Reagent and incubated for 45 minutes. After removing the supernatant, the cells were resuspended in buffer and labeled with Regulatory B Cell Detection Antibody. Anti-PE microbeads were mixed into the cell suspension before magnetic separation on LS columns (Miltenyi Biotec) to capture IL-10 secreting Breg cells through positive selection.

Cell preparation for single-cell RNA-seq

The splenocytes of three pre-disease female MRL/*lpr* mice were pooled into each of two samples (a total of 6 pre-disease mice) and the splenocytes of two active-disease female MRL/*lpr* mice were pooled into each of two samples (a total of 4 active-disease mice). Cells were stimulated for 24 hours with 10 μg/ml LPS, followed by 5 hours of 50 ng/ml PMA and 500 ng/ml ionomycin. IL-10 producing B cells were isolated using the Mouse Regulatory B Cell Isolation Kit purchased from Miltenyi Biotec (Gladbach, Germany) following the manufacturer's protocol. In summary, single cell suspensions from spleens were enriched using the Regulatory B cell Biotin-Antibody cocktail, followed by the addition of Anti-Biotin MicroBeads and magnetic separation on LD Columns (Miltenyi Biotec).

Single-cell RNA-seq

Single-cell RNA-seq was performed using 10X Genomics' Chromium Single Cell 3′ V3.1 chemistry (Dual index). The experiment was designed to target 1,000 cells. Gel-Bead in Emulsions (GEMs) were made and the RT reaction was carried out in the Nexus GX2 PCR instrument (Eppendorf). Post-GEM RT-cleanup was used to obtain barcoded cDNA from the GEMs, which was then amplified for 12 cycles. According to the manufacturer's protocol, amplified cDNA was subjected to enzymatic fragmentation, end-repair, A tailing, adaptor ligation, and 10X specific sample indexing. Bioanalyzer analysis was used to determine the quality and quantity of libraries. Following that, libraries were pooled and sequenced on the Illumina HiSeq platform (Novogene).

Single-cell RNA-seq sample pre-processing, clustering, and dimensionality reduction

Sequencing reads were processed with 10x Genomics Cell Ranger software (v 7.0.1) using the standard pipeline. FASTQ files were generated and demultiplexed with the cellranger mkfastq command. Read alignment to mouse reference genome mm10 and gene quantification were carried out with cellranger count. Downstream analysis of output count, gene/feature, and barcode matrices was done using the R/BioConductor package Seurat (v 4.2.0). Quality control analysis was carried out to filter for high-quality cells with unique molecular identifier (UMI) counts per cell > 1000, genes per cell > 1000, $\log_{10}$ genes per UMI < 0.75, and ratio of cell reads from mitochondrial genes < 0.1 (all thresholds were set using empirical distributions). Doublet discrimination was carried out on filtered samples using DoubletFinder (v 2.0.3) and predicted doublets were removed for downstream analysis. Cell cycle scores were calculated using the CellCycleScoring function to ensure that cell cycle phase was not a significant source of variation in the data. Filtered datasets were split into Seurat objects corresponding to each cohort (pre-disease and active-disease) and count normalization and variance stabilization was carried out for each object using the SCTransform function. Integrated analysis was performed using the most highly variable shared genes to identify analogous populations and facilitate direct comparison of differential gene expression (DEG) between cohorts. Cell clustering was performed with Seurat using the top 15 principal components (PCs) as determined by the elbow method with a cluster resolution of 0.8 for separate cohort analysis and resolution of 0.4 for integrated analysis. Clusters were visualized with the Uniform Manifold Approximation and Projection (UMAP) method. Cluster markers were identified using the FindAllMarkers function with logfc.threshold of 0.5 for separate cohort clusters and of 0.25 for integrated clusters. DEGs in active-disease cells from integrated clusters were identified using the FindMarkers function with the Wilcoxon rank sum test. DEGs with p<0.05 were considered statistically significant.

Single-cell cluster annotation

Single-cell clusters were annotated based on enrichment of cluster marker genes with pre-defined Breg subset and immune/cellular pathway gene sets listed in Supplementary Table 1. Curated gene sets were generated based on a combination of literature mining, Mouse Genome Informatics (MGI) gene ontology (GO) terms, and immune cell-specific expression compiled from the Immunological Genome Project Consortium (ImmGen). Enrichment statistics for overlap of cluster markers with curated gene sets were calculated by a two-sided Fisher's Exact Test in R using the function fisher.test(). Enrichments with p<0.05 were considered statistically significant. The unannotated clusters, representing populations with cluster-defining marker genes that were not informative in identifying specific Breg subsets, were removed from downstream analyses.

Ingenuity pathway analysis

The canonical pathway function of IPA core analysis (Qiagen) was used as an independent method of annotated differentially expressed genes (DEGs) between active-disease and pre-disease IL-10^+ B cells within integrated single-cell clusters. Overlap p-values of $p<0.05$ were considered statistically significant.

Single-cell pseudotime trajectory analysis

Trajectory analysis was carried out to estimate developmental relationships between the Seurat-generated IL-10^+ B cell clusters from pre-disease and active-disease MRL/*lpr* mice using the R/Bioconductor package Monocle 3 (v 1.3.1). Trajectories were constructed using the learn_graph() function and cells were ordered in pseudotime using the $\mathrm{IgD}^{\mathrm{mid}}$ Naïve B Cell cluster (cluster 6) as the root cluster for pre-disease cells and the Naïve B Cell Cluster (cluster 2) as the root cluster for active-disease cells. Cells were visualized based on pseudotime in a trajectory heatmap using the plot_cells() function and displayed as boxplots depicting the range of pseudotime values for each cluster using ggplot().

Gene set variation analysis (GSVA)

Gene sets used as input for GSVA are listed in Supplementary Table 1. The R/Bioconductor package GSVA (31) (v1.36.3) was used as a non-parametric method to estimate variation in enrichment of these gene sets in publicly available microarray data from isolated murine $\mathrm{CD138}^+$ PB-PCs (GSE103458) as previously described (32).

Statistical analysis

Enrichment statistics (p-values and odds ratios) for the overlap of single-cell cluster markers and pre-defined gene sets were calculated using a two-sided Fisher's Exact Test in R with confidence level of 0.95. Statistical tests and graphs comparing GSVA enrichment scores for isolated $\mathrm{CD138}^+$ IL-10^+ and IL-10^- cells were calculated using an unpaired, two-sided Welch's t-test in GraphPad Prism (v9.3.1).

Study approval

The study was approved by the Virginia Tech IACUC under protocol number 21-003.

Results

Bregs are numerically and functionally impaired in lupus-prone mice with active disease

To investigate the role of regulatory B cells (Bregs) in the establishment and progression of disease in MRL/*lpr* mice, we chose to focus on differences in the number and suppressive function of Bregs generated from mice at two disease stages: before disease onset (pre-disease; 6-8 weeks) and after establishment of autoimmunity (active-disease; 10-12 weeks). Therefore, splenic B cells were isolated from pre-disease and active-disease mice, stimulated with 10 µg/ml LPS for 24 h followed by 5 h of 50 ng/ml PMA and 500 ng/ml ionomycin and the numbers of IL-10^+ B cells and IL-10 production were assessed. The frequency of splenic IL-10^+ B cells was significantly decreased in mice with active disease as compared to the pre-disease stage (Figure 1A). In addition, levels of serum IL-10 were significantly decreased in active-disease mice (Figure 1B). To identify potential deficiencies in IL-10 mediated Breg suppression during the active-disease stage, levels of IL-10 were assessed in the supernatant of *in vitro* stimulated splenic B cells. As with total serum IL-10 levels, production of IL-10 by B cells from mice with active disease was also significantly reduced (Figure 1C). Overall, these results indicate that the development of autoimmunity in lupus-prone mice is accompanied by both numerical and functional defects in regulatory B cells.

scRNA-seq analysis identifies Breg cell subsets in lupus-prone mice at the pre-disease stage

To define variations in Bregs from lupus-prone mice at different stages of disease progression, we carried out single-cell RNA sequencing (scRNA-seq) on IL-10^+ $\mathrm{CD19}^+$ B cells generated from spleens of female MRL/*lpr* mice at the pre-disease stage (6-8 weeks old) or active-disease stage (10-12 weeks old). To account for the increased expansion of splenic B cells in active-disease mice, IL-10^+ B cells were pooled from 3 pre-disease mice or 2 active-disease mice per sample to yield approximately 10,000 total cells in duplicate for each disease cohort. Quality control and doublet discrimination were carried out separately on each sample before singlets from each disease stage were combined to yield a final total of 12,130 pre-disease and 13,895 active-disease cells retained for downstream analyses.

Initially, pre-disease and active-disease cells were evaluated separately to identify groups of Breg cells with shared transcriptional profiles from lupus-prone mice at each stage of disease progression. IL-10^+ B cells from pre-disease mice formed 12 cell clusters (Figure 2A), that were annotated based on enrichment of cluster-defining gene markers in pre-defined gene sets representative of previously identified Breg subsets, cellular processes, and inflammatory pathways Supplementary Table 1. As a result, we identified that 7 of the 12 clusters had significant cluster marker overlaps with Breg subset genes indicating that these clusters represented transcriptionally distinct subpopulations of IL-10^+ B cells from pre-disease lupus mice (Figure 2B). These clusters were selected for further investigation and unannotated clusters, in which cluster markers were not informative in defining Breg subsets, were removed. The combined cell type and pathway gene set enrichments and key cluster marker genes were then used to label each annotated Breg subpopulation (Figure 2C; Supplementary Figure 1). The highest proportion of annotated

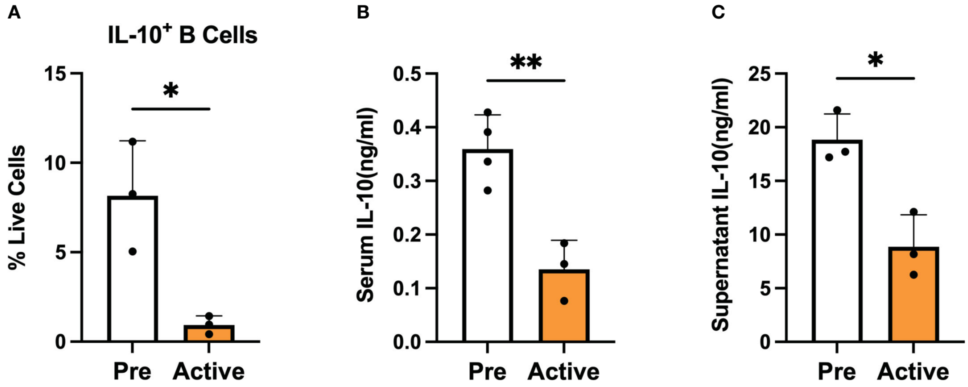

FIGURE 1
Bregs are numerically and functionally impaired in lupus-prone mice with active disease. Female MRL/*lpr* mice were assessed at the pre-disease (6-8 weeks) and active-disease (10-12 weeks) stages. Splenic IL-10 producing B cells were generated by stimulation with 10 µg/ml LPS for 24 h followed by 5 h of 50 ng/ml PMA and 500 ng/ml ionomycin. **(A)** Percentage of splenic IL-10 producing B cells. **(B)** Serum level of IL-10. **(C)** Supernatant level of IL-10 from stimulated splenic B cells. **p* < 0.05, ** *p* < 0.01.

Breg cells (11.94%) in cluster 3 were designated as Plasmablasts (PBs) by enrichment of the Plasmablast/Plasma Cell (PB-PC), Ig Chain, Pro-Cell Cycle, and UPR & Stress gene sets, including increased expression of *Irf4, Prdm1, Ighm, Il10*, and *Ebi3*. Two populations in clusters 4 and 6 of pre-disease cells were representative of naïve B cells, although they also manifested enrichment of the Activated B Cell gene set and increased expression of *Ighd* relative to other clusters. As cluster 4 had the highest *Ighd* expression, these cells were designated IgD^{high} Naïve B Cells and cluster 6 cells as IgD^{mid} Naïve B Cells. Pre-disease Bregs in cluster 5 were enriched for markers of T2-MZP/MZ B Cells, including *Cd24a* as well as metabolic pathway genes involved in Glycolysis and Mitochondrial Oxidative Phosphorylation (OxPhos). Cluster 7 cells were enriched for gene sets for PB-PCs (*Mzb1, Xbp1, Prdm1*), Ig Chains (*Ighm, Ighg3*), MHC Class II, N- and O-linked Glycosylation, and UPR & Stress indicative of a mixed population of PBs and class-switched PCs. Interestingly, this cluster was also enriched for the Phagocytosis gene set and thus was designated as the Phagocytic PB-PC subset. Because of the high expression of *Havcr1* as compared to other clusters, cluster 8 cells were labeled TIM-1 B Cells. Finally, the lowest proportion of annotated Bregs in pre-disease mice was a population of activated B cells that expressed the highest levels of *Il10* as compared to other clusters in conjunction with other anti-inflammatory molecules, including *Ebi3, Cd274* encoding PD-L1, *Siglecg*, and *Cd300lf* and, therefore, was designated Suppressive B Cells.

Transcriptionally-defined IL-10$^+$ B cell subsets are altered in lupus-prone mice with active disease

Single-cell gene expression profiles of IL-10$^+$ B cells from active-disease mice exhibited a distinct spatial pattern from pre-disease mice that resulted in 14 clusters of cells in similar molecular states (Figure 3A), 8 of which were enriched for pre-defined B cell subset markers (Figure 3B). Overall, cluster enrichments in active disease reflected a heightened inflammatory state with an increased number of clusters enriched for Type I/II IFN signature genes with or without enrichment of TNF signature genes as compared to pre-disease mice (Figure 3B). Cluster annotations for Breg cells from active-disease mice also exhibited key variations from pre-disease mice indicative of the more pro-inflammatory environment present during active autoimmunity (Figure 3C; Supplementary Figure 2). Several of the Breg clusters found in pre-disease mice were also present during active disease, but in differing proportions of the total analyzed population, and we found key variations in markers defining these subsets. Unlike in pre-disease mice, the Naïve B Cell cluster of active-disease cells expressing *Ighd* (cluster 2) was confined to one cluster and represented the greatest proportion of total Bregs (14.84%). The Breg cluster enriched for the PB-PC and Phagocytosis gene signatures (cluster 3) was present at a greater percentage (13.61%) in active-disease as compared to pre-disease (4.89%) mice and unlike in pre-disease mice, appeared to be a pre-class switched population expressing *Ighm* and was also the lone active-disease cluster with *Cd274* as a significant cluster marker. The TIM-1 B Cell cluster (cluster 6) was more highly represented in active-disease mice (6.51%) whereas the T2-MZP Cell cluster (cluster 8) was less represented (3.30%) and appeared more skewed to a MZP population through increased expression of *Cd23a* as compared to other clusters.

Two clusters unique to IL-10$^+$ cells from active-disease mice were annotated with GC B Cell (cluster 9) and/or PC markers (cluster 11). Cluster 9 cells were identified as GC B Cells/PCs because of expression of *Rgs13* as well as *Igha* and *Ighg1* and cluster 11 cells were labeled PCs because of expression of *Sdc1, Ighm, Igha*, and *Ighg2b/c*. This was particularly notable as in pre-disease mice the only cells with evidence of class-switching were found in the Phagocytic PB-PC cluster and expressed *Ighg3*. The final two cell marker-annotated clusters of active-disease Bregs (cluster 7 and cluster 11) were characterized by expression of unique inflammatory signatures and markers. Cluster 7 was enriched for

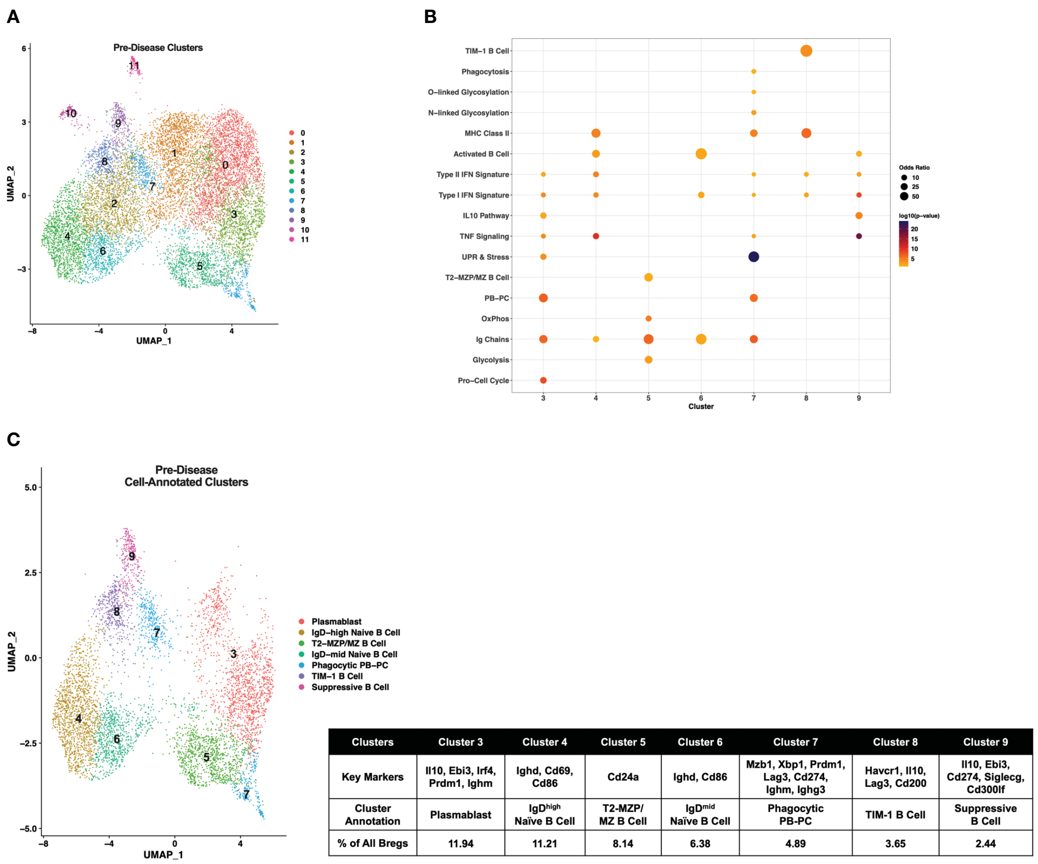

Clusters	Cluster 3	Cluster 4	Cluster 5	Cluster 6	Cluster 7	Cluster 8	Cluster 9
Key Markers	Il10, Ebi3, Irf4, Prdm1, Ighm	Ighd, Cd69, Cd86	Cd24a	Ighd, Cd86	Mzb1, Xbp1, Prdm1, Lag3, Cd274, Ighm, Ighg3	Havcr1, Il10, Lag3, Cd200	Il10, Ebi3, Cd274, Siglecg, Cd300lf
Cluster Annotation	Plasmablast	IgD^{high} Naïve B Cell	T2-MZP/ MZ B Cell	IgD^{mid} Naïve B Cell	Phagocytic PB-PC	TIM-1 B Cell	Suppressive B Cell
% of All Bregs	11.94	11.21	8.14	6.38	4.89	3.65	2.44

FIGURE 2

Single-cell transcriptional analysis identifies subsets of IL-10$^+$ Bregs from lupus-prone mice prior to disease onset. Splenic IL-10 producing B cells (Bregs) were generated from pre-disease female MRL/*lpr* mice and analyzed by single-cell RNA-seq. **(A)** UMAP plot showing 12 clusters of pre-disease Bregs. **(B)** Bubbleplot depicting the overlap of pre-disease Breg cluster markers with pre-defined cell type and pathway gene sets. **(C)** Annotation of 7 pre-disease clusters that had significant overlap of cluster marker genes with Breg subset gene sets. Key markers used to define each cluster annotation and percentage of cells in each cluster out of total Bregs are displayed.

the IL-10 Pathway and TNF Signaling gene signatures and had increased expression of *Tnfrsf13b* encoding the B cell survival factor receptor TACI and thus was designated as the TNF/TACI B cell cluster. Finally, cluster 11 represented a minor outlier population (0.31%) of innate-like B1a cells expressing *Cd5, Itgam*, and *Gzmb* and enriched for the Pattern Recognition Receptor (PRR) and UPR & Stress gene signatures. Thus, gene expression-derived Breg subsets from lupus-prone mice with active disease were more represented by PB-PC populations than in pre-disease mice and had a lower proportion of MZ-like cells expressing markers indicative of a more naïve developmental stage.

Single-cell trajectory analysis suggests developmental relationships among Breg subsets from lupus-prone mice at pre-disease and active-disease stages

Breg cells are generally defined by expression of IL-10, but it is unclear how Bregs are induced and whether or how Breg subsets are developmentally linked (1). In addition, it is not known how Breg development or differentiation may be altered in the context of autoimmunity. To investigate the relationships among Breg subsets and to compare differences in populations identified at different stages of disease progression in lupus-prone mice, we carried out single-cell trajectory analysis to order IL-10$^+$ B cells in pseudotime based on changes in gene expression (Figure 4A). Initially, we noted the increase in overall complexity of cellular trajectories between active-disease as compared to pre-disease cells which could arise from the greater variety of inflammatory stimuli inducing B cell production of IL-10. Because of the critical role of autoantibody producing PCs in lupus disease pathology, Breg subsets from pre-disease and active-disease mice were divided into PB-PC and non-PB-PC annotated clusters. Learned trajectories for each group of clusters were created and rooted in the Naïve B cell cluster as we predicted this subset to be the least developmentally advanced B cell population at each disease stage. Then other clusters were ordered by relative pseudotime distance along the trajectory from the root population and displayed as heatmaps detailing the trajectory paths and boxplots depicting the range of pseudotime encompassed by each Breg cluster. From pre-disease mice, the PB-PC annotated clusters followed three branching trajectories stemming from the

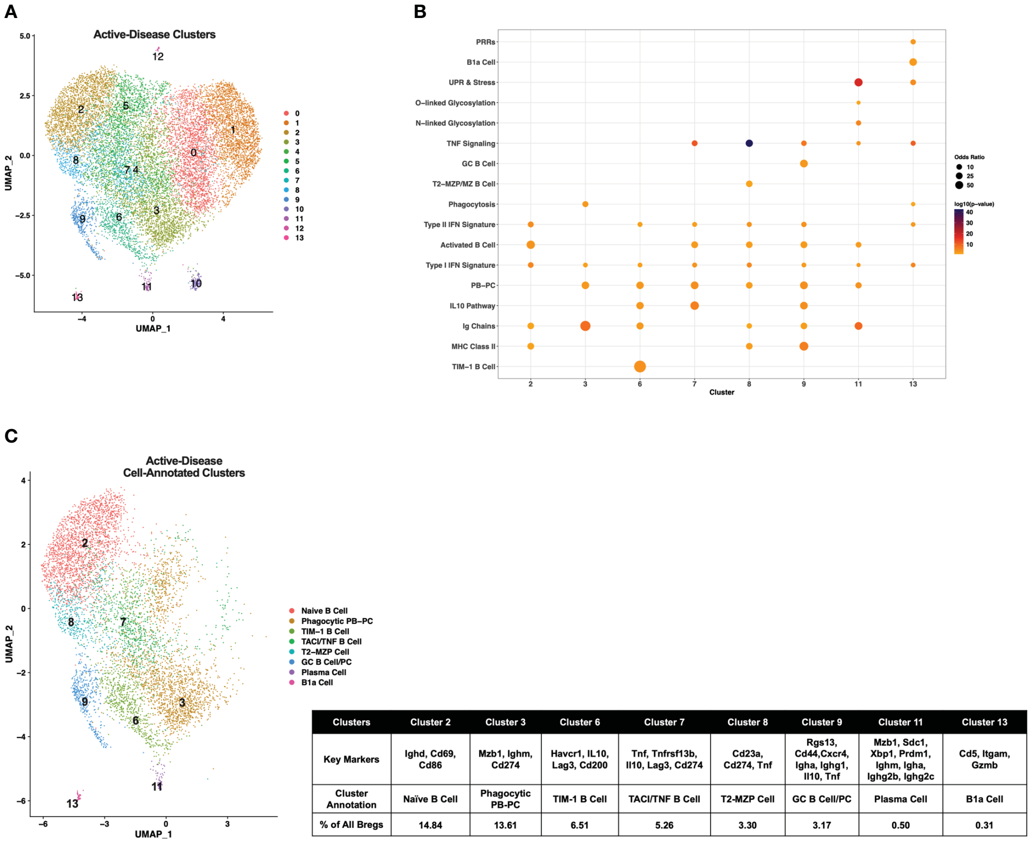

Clusters	Cluster 2	Cluster 3	Cluster 6	Cluster 7	Cluster 8	Cluster 9	Cluster 11	Cluster 13
Key Markers	Ighd, Cd69, Cd86	Mzb1, Ighm, Cd274	Havcr1, IL10, Lag3, Cd200	Tnf, Tnfrsf13b, Il10, Lag3, Cd274	Cd23a, Cd274, Tnf	Rgs13, Cd44,Cxcr4, Igha, Ighg1, Il10, Tnf	Mzb1, Sdc1, Xbp1, Prdm1, Ighm, Igha, Ighg2b, Ighg2c	Cd5, Itgam, Gzmb
Cluster Annotation	Naïve B Cell	Phagocytic PB-PC	TIM-1 B Cell	TACI/TNF B Cell	T2-MZP Cell	GC B Cell/PC	Plasma Cell	B1a Cell
% of All Bregs	14.84	13.61	6.51	5.26	3.30	3.17	0.50	0.31

FIGURE 3
Single-cell analysis reveals differences in transcriptional profiles IL-10$^+$ Bregs present in mice with ongoing autoimmune inflammation. Splenic Bregs were generated from active-disease female MRL/*lpr* mice and analyzed by single-cell RNA-seq. **(A)** UMAP plot showing 14 clusters of active-disease Bregs. **(B)** Bubbleplot depicting the overlap of active-disease Breg cluster markers with pre-defined cell type and pathway gene sets. **(C)** Annotation of 8 active-disease clusters that had significant overlap of cluster marker genes with Breg subset gene sets. Key markers used to define each cluster annotation and percentage of cells in each cluster out of total Bregs are displayed.

Naïve B cell cluster (Figure 4B). The Phagocytic PB-PC population exhibited a wide pseudotime range that was split into two groups, one of less differentiated cells likely representing PBs and one of highly differentiated cells likely representing class-switched PCs. In contrast, the PB cluster from pre-disease appeared to be in an intermediate developmental state between the two subsets of Phagocytic PB-PC cells. The Non-PB-PC pre-disease clusters followed two distinct developmental trajectories stemming from the IgD^{mid} Naïve B Cell cluster (Figure 4C). Along one trajectory were the T2-MZP/MZ B cells, which represented a range of pseudotimes representing the differentiation from a precursor population to a mature IL-10$^+$ MZ B cell. Along the second trajectory, the TIM-1 B cell cluster appeared to be more proximal in pseudotime to naïve cells as compared to the Suppressive B cell population which was the furthest cluster along the pseudotime trajectory in pre-disease mice.

Single cell trajectory analysis of IL-10$^+$ B cells from mice with active disease revealed notable differences in Breg developmental states as compared to pre-disease mice. Notably, trajectories in active-disease mice were much more complex. Anchored in the Naïve B Cell cluster, PB-PC annotated clusters formed two branching trajectories (Figure 4D). Similar to pre-disease mice, the Phagocytic PB-PC population of active-disease cells was divided into a less differentiated, early subpopulation representing PBs and a more differentiated, late subpopulation representing PCs. However, unlike pre-disease mice, we also observed a second trajectory of GC B cells and class-switched PCs indicative of a robust and ongoing production of autoantibody producing cells during the height of disease activity. Trajectory analysis of Non-PB-PC, active-disease IL-10$^+$ B cells was carried out to predict the developmental pathways of other unique Breg subets present in mice with ongoing disease pathology (Figure 4E). Interestingly, as suggested by the differences in cluster marker expression, the T2-MZP cell cluster in active-disease mice appeared to be a less differentiated population nearly identical to the Naïve B cell cluster in pseudotime and with no indication of a more developed population of MZ B cells as observed in pre-disease mice. More advanced populations in pseudotime exhibited a split trajectory between the TACI/TNF B cell cluster and the TIM-1 B cell cluster that included cells with a wide pseudotime range indicative of within-cluster heterogeneity in

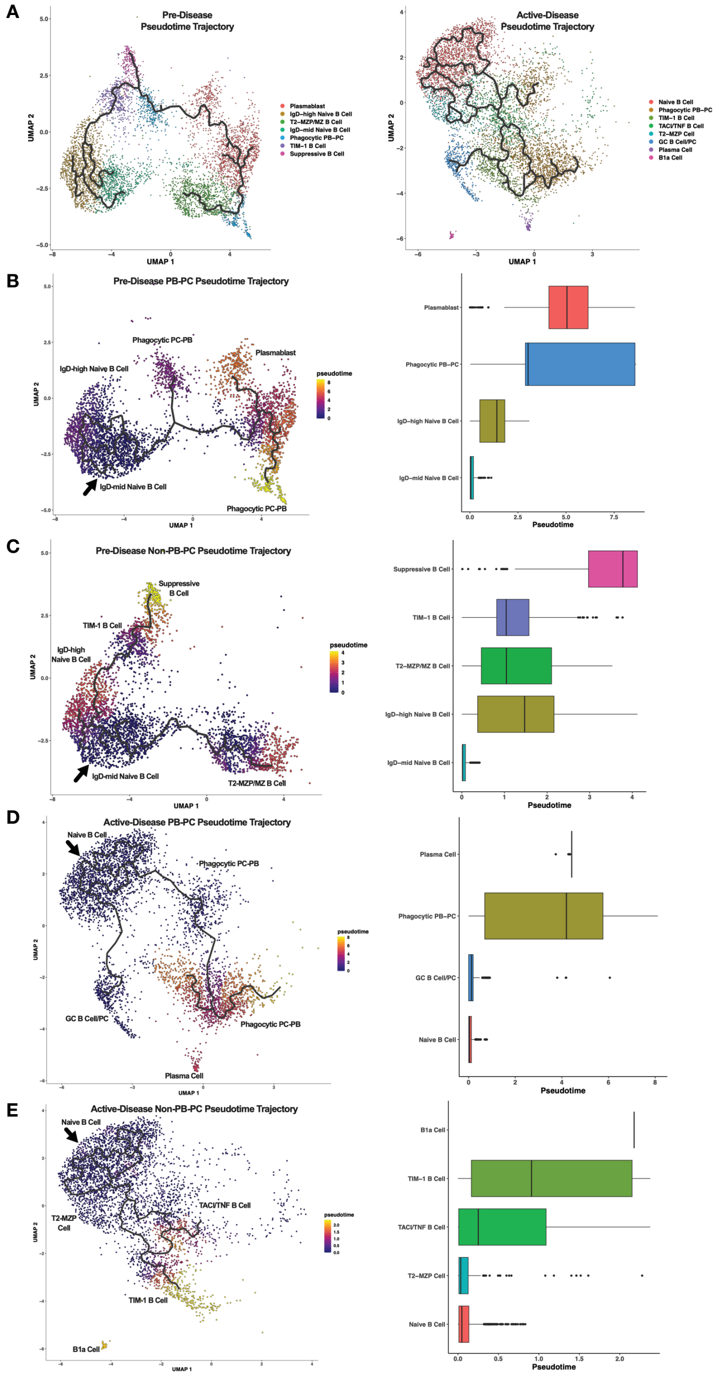

FIGURE 4
Trajectory analysis reveals relationships between Breg subsets from lupus-prone mice at pre-disease and active-disease stages. Breg subset marker-annotated single-cell clusters from pre-disease and active-disease mice were ordered in pseudotime using Monocle 3. **(A)** Trajectory plots of pre-disease and active-disease Breg clusters. **(B, C)** Trajectory mapping of pre-disease plasmablast/plasma cell (PB-PC) and non-PB-PC annotated clusters. Clusters were ordered in pseudotime distance originating from the IgD-mid Naïve B Cell annotated cluster. **(D, E)** Trajectory mapping of active-disease PB-PC and non-PB-PC annotated clusters. Clusters were ordered in pseudotime distance originating from the Naïve B Cell annotated cluster. Boxplots show the pseudotime range of each Breg cluster in relation to the root cluster.

gene expression profiles. Finally, the outlier cluster of B1a cells, unique to active-disease mice, was the most advanced in pseudotime as compared to the naïve population and appeared to be developmentally distinct and unlinked to the developmental trajectory of other Breg subsets. Thus, pseudotime trajectory analysis of IL-10^+ B cells from lupus-prone mice revealed multiple pathways leading to the development of transcriptionally diverse Breg subsets present at different stages of disease progression.

Integrated single-cell analysis of pre-disease and active-disease lupus-prone mice identifies stage-dependent alterations in IL-10^{+} B cell populations

To compare IL-10^{+} B cells generated from lupus-prone MRL/*lpr* mice at different stages of disease progression directly, scRNA-seq datasets of pre-disease and active-disease cells were integrated and co-clustered based on shared sources of transcriptional variation (Figure 5A). With this approach, each integrated cluster represents a population of Breg cells in a shared biological state between pre-disease and active-disease mice. Then, cluster markers were identified separately from pre-disease and active-disease cells within each integrated cluster in order to highlight differences in co-clustered Breg cells generated from each disease stage, and used to assign Breg subset annotations. Integrated cluster markers derived from pre-disease cells identified 6 clusters with significant marker overlaps with pre-defined Breg subset genes and cellular pathways that were used to assign each cluster identity (Figures 5B, C. The highest proportion of pre-disease cells (19.65%) in cluster 0 represented Naïve B cells with expression of *Ighd*, the Activated B Cell markers *Cd69* and *Cd86*, and MHC Class II genes *H2-Aa* and *H2-Ab1* (Figure 5C; Supplementary Figure 3). Cluster 3 contained 11.76% of pre-disease Bregs and was designated the Suppressive B Cell cluster as these cells expressed the highest levels of *Il10* and, interestingly, were also enriched for the Lipid Metabolism gene set, including high expression of *Apoe*. The PB annotated cluster (cluster 4) consisted of 15.78% of pre-disease cells and was designate PB based on enrichment of the PB-PC (*Mzb1, Xbp1, Prdm1, Ms4a1*) and Ig Chains (*Ighm*) gene sets. Pre-disease Bregs in cluster 6 (2.37%) represented T2-MZP/MZ B cells with high expression of *Cd24a* and were also highly enriched for Pro-Cell Cycle genes. The final two cell-annotated integrated clusters represented minor populations of pre-disease Bregs including 0.66% of cells in cluster 8 annotated as PCs and the outlier population of B1a cells (0.11%) in cluster 10. Pre-disease PCs were enriched for Activated B cell (*Cd28*), PB-PC (*Mzb1, Xbp1, Prdm1, Cd274*), Ig Chains (*Ighm, Ighg1, Ighg2b, Ighg2c*), N-linked glycosylation, and UPR & Stress gene sets, whereas pre-disease B1a cells were marked by high expression of the pro-inflammatory markers *Itgam, C3, Ifng, Il1b*, and *Gzmb*.

Integrated cluster marker enrichment analysis and annotation of active-disease IL-10^{+} B cells resulted in shared labels for the 6 clusters of pre-disease cells, but with key differences in the proportion of total cells and marker genes in each cluster (Figures 5D, E). The Naïve B cell cluster (cluster 0) consisted of a similar proportion of total active-disease cells (20.54%) as compared to pre-disease cells and was still characterized by enrichment of the Activated B cell markers *Cd69* and *Ighd*, but unlike pre-disease Naïve B cells, active-disease B cells were not enriched for MHC Class II genes. Active-disease Suppressive B cells in cluster 3 shared representative cluster markers with pre-disease cells, but contained a higher proportion of total cells (20% *vs.* 11.76%). In contrast, a lower proportion of active-disease cells were PBs in cluster 4 and further differed from analogous pre-disease cells through enrichment of MHC Class II genes (*H2-Aa, H2-Eb1*), markers of the Naïve B cell cluster of pre-disease cells. A lower proportion of active-disease cells as compared to pre-disease cells were found in the T2-MZP/MZ B cell annotated cluster (cluster 6, 0.55% *vs.* 2.37%) and active-disease cells in this cluster also uniquely expressed marker genes *Stat1* and *Il6*. The PC cluster of active-disease Bregs in cluster 8 was a modestly smaller proportion of total cells than in pre-disease (0.47% *vs.* 0.66%) and exhibited differences in expression of class-switched Ig Chain genes, including *Igha* in place of *Ighg1* on pre-disease cells and were not enriched for expression of *Cd274.* In contrast, the B1a cell-annotated cluster 10 represented a larger proportion of total active-disease cells (0.29% *vs.* 0.11%) and further differed in expression of *Fasl* as a cluster marker.

We also noted that a new, cell-annotated, integrated cluster emerged from active-disease IL-10^{+} B cells that was not observed in pre-disease mice. Active-disease Bregs in cluster 5 exhibited increased expression of Activated B cell markers as compared to other clusters and were further distinguished by enrichment of the PB-PC and TNF Signaling gene sets (Figure 5E; Supplementary Figure 4). Key marker genes defining this cluster included increased expression of *Tnf* and *Tnfrsf13b* encoding TACI and thus this cluster was designated the TACI/TNF B cell cluster. Overall, integrated clustering and separate cluster marker identification of pre-disease and active-disease IL-10^{+} B cells in similar biological states revealed key variations in analogous populations of regulatory B cells through disease progression in lupus-prone mice.

Transcriptomic comparison of integrated single cell datasets reveals pathologic inflammatory gene signatures associated with IL-10^{+} B cells from active-disease mice

To evaluate differences in gene expression profiles between co-clustered populations of pre-disease and active-disease IL-10^{+} B cells, we identified differentially expressed genes (DEGs) in active-disease Bregs as compared to their pre-disease counterparts within the same integrated cluster. For this analysis, we focused on 4 of the 6 clusters found in both active-disease and pre-disease mice. These included cluster 4 PBs, cluster 5 TACI/TNF B cells, cluster 6 T2-MZP/MZ B cells, and cluster 8 PCs. For each cluster, up and down-regulated genes in active-disease cells were used as input for Ingenuity Pathway Analysis (IPA) to identify significant overlaps with canonical pathways (Figure 5F). As a whole, we found that active-disease Bregs exhibited increased expression of genes involved in inflammatory and stress response pathways and decreased expression of genes involved in cell cycle and DNA repair pathways. Specifically, in cluster 4 PBs from mice with active disease, up-regulated DEGs were enriched for TREM1 Signaling, Th1 response, IL-6 signaling, and phospholipid synthesis, whereas down-regulated DEGs were enriched for cell cycle regulation and DNA damage response pathways (Figure 5F). Active-disease cells in the TACI/TNF cluster (cluster 5) manifested increased expression of several immune activation pathways and pro-inflammatory signaling pathways through CD40, IL-6, TNFR2,

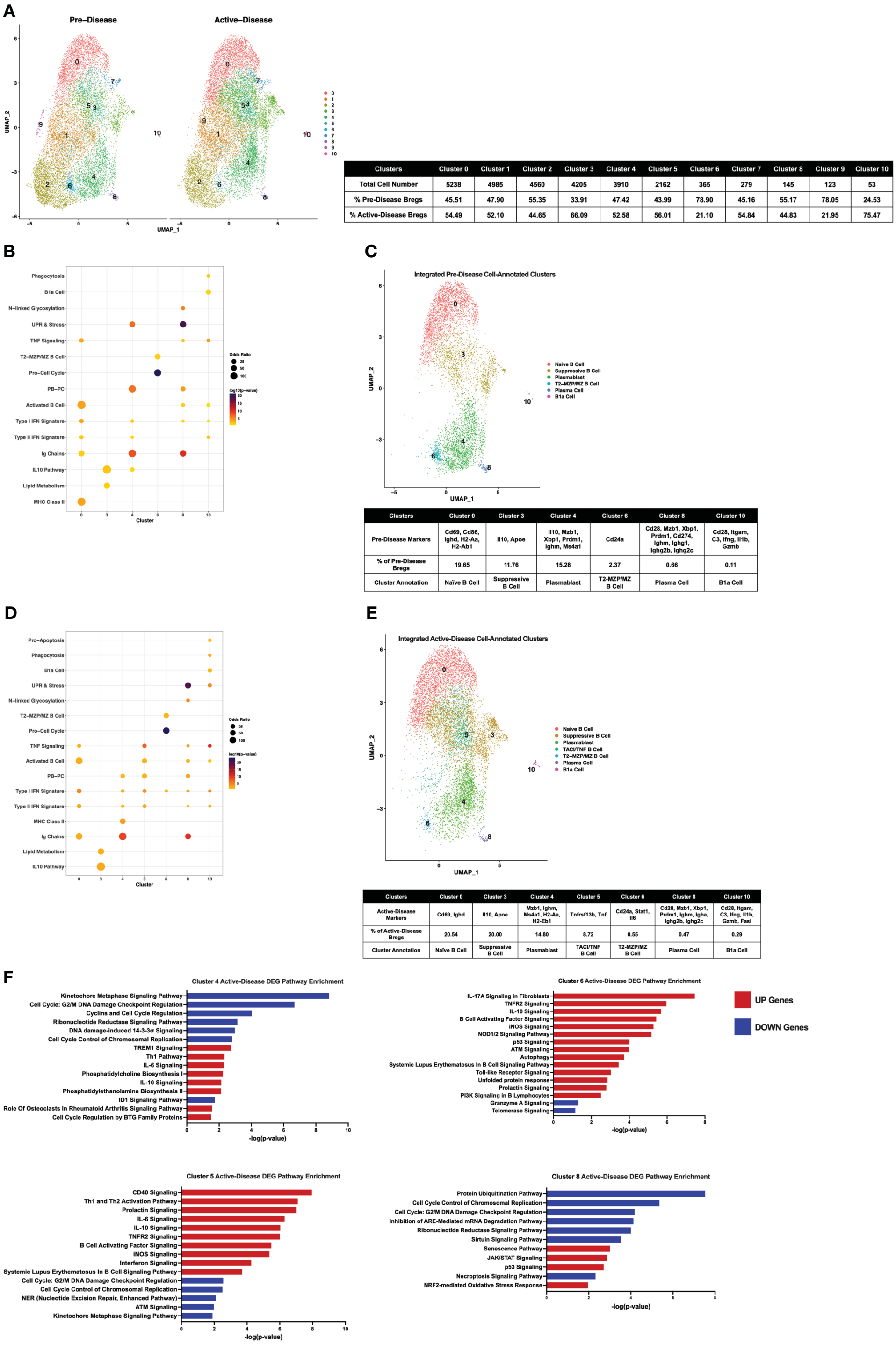

Clusters	Cluster 0	Cluster 1	Cluster 2	Cluster 3	Cluster 4	Cluster 5	Cluster 6	Cluster 7	Cluster 8	Cluster 9	Cluster 10
Total Cell Number	5238	4985	4560	4205	3910	2162	365	279	145	123	53
% Pre-Disease Bregs	45.51	47.90	55.35	33.91	47.42	43.99	78.90	45.16	55.17	78.05	24.53
% Active-Disease Bregs	54.49	52.10	44.65	66.09	52.58	56.01	21.10	54.84	44.83	21.95	75.47

Clusters	Cluster 0	Cluster 3	Cluster 4	Cluster 6	Cluster 8	Cluster 10
Pre-Disease Markers	Cd69, Cd86, Ighd, H2-Aa, H2-Ab1	Il10, Apoe	Il10, Mzb1, Xbp1, Prdm1, Ighm, Ms4a1	Cd24a	Cd28, Mzb1, Xbp1, Prdm1, Cd274, Ighm, Ighg1, Ighg2b, Ighg2c	Cd28, Itgam, C3, Ifng, Il1b, Gzmb
% of Pre-Disease Bregs	19.65	11.76	15.28	2.37	0.66	0.11
Cluster Annotation	Naïve B Cell	Suppressive B Cell	Plasmablast	T2-MZP/MZ B Cell	Plasma Cell	B1a Cell

Clusters	Cluster 0	Cluster 3	Cluster 4	Cluster 5	Cluster 6	Cluster 8	Cluster 10
Active-Disease Markers	Cd69, Ighd	Il10, Apoe	Mzb1, Ighm, Ms4a1, H2-Aa, H2-Eb1	Tnfrsf13b, Tnf	Cd24a, Stat1, Il6	Cd28, Mzb1, Xbp1, Prdm1, Ighm, Igha, Ighg2b, Ighg2c	Cd28, Itgam, C3, Ifng, Il1b, Gzmb, Fasl
% of Active-Disease Bregs	20.54	20.00	14.80	8.72	0.55	0.47	0.29
Cluster Annotation	Naïve B Cell	Suppressive B Cell	Plasmablast	TACI/TNF B Cell	T2-MZP/MZ B Cell	Plasma Cell	B1a Cell

FIGURE 5

Single-cell integration compares analogous Breg subsets present through stages of disease progression in lupus-prone mice. Single-cell datasets of Bregs from pre-disease and active-disease mice were integrated and co-clustered to facilitate comparison of cells with shared biological states. **(A)** Split UMAP plots of 11 integrated clusters of pre-disease and active-disease Bregs. **(B, D)** Bubbleplots depicting the overlap of integrated pre-disease **(B)** and active-disease **(D)** Breg clusters with pre-defined cell type and pathway gene sets. **(C, E)** Annotation of 6 pre-disease **(C)** and 7 active-disease **(E)** integrated clusters exhibiting significant overlap of cluster marker genes with Breg subset gene sets. Key markers used to define each cluster annotation and percentage of cells in each cluster out of total Bregs are displayed. **(F)** IPA canonical pathway analysis of differentially expressed genes in active-disease Bregs as compared to pre-disease Bregs from selected integrated single-cell clusters.

B Cell Activating Factor, iNOS, and IFN. Like the PB cluster, active-disease cells in the TACI/TNF cluster had decreased expression of genes involved in DNA damage repair and cell cycle arrest pathways. In addition to inflammatory mediator signaling pathways, DEGs in active-disease cells in the T2-MZP/MZ B cell cluster (cluster 6) were indicative of cellular dysfunction and stress with involvement in pathways including autophagy, the unfolded protein response, p53 signaling, and telomerase signaling. Finally, DEGs from cluster 8 PCs were largely decreased in active-disease mice and were enriched for pathways related to cell cycle checkpoint control and metabolic regulation, including protein ubiquitination, mRNA degradation, and sirtuin signaling. Conversely, upregulated genes in active-disease cluster 8 PCs were involved in cellular senescence and the oxidative stress response (Figure 5F). Notably, we found that expression of *Il10* and IL-10 Signaling Pathway genes were consistently upregulated in active-disease Bregs from all clusters (Supplementary Figure 5), indicating that pathologic autoimmunity in these mice was not related to a deficiency in expression of *Il10* transcript, but rather a separate source of regulatory dysfunction. Thus, DEGs from IL-10^{+} B cells in the context of active autoimmunity were indicative of response to a heightened inflammatory environment resulting in immune activation and exposure to intra- and extra-cellular stressors that could affect the ability of these cells to function as immune regulators.

Validation of transcriptionally defined alterations to the landscape of Breg subsets in lupus-prone mice with active disease

To confirm the changes we observed in representation of specific Breg subsets using single-cell gene expression analysis, we carried out flow cytometric staining of splenic IL-10^{+} B cells from MRL/*lpr* mice at the pre-disease or active-disease stages. We focused on changes in the proportion of MZ and PB-PC lineage cells, as these populations showed the greatest difference based on expression of canonical marker genes. Notably, both T2-MZP (CD19^{+}IL10^{+}CD21^{+}CD24^{hi}IgM^{+}CD23^{+}) and MZ B cells (CD19^{+}IL10^{+}CD21^{+}CD24^{hi}IgM^{+}CD23^{-}) were significantly decreased in the spleens of active-disease as compared to pre-disease mice (Figure 6A; Supplementary Figure 6). In contrast, we observed significant increases in the proportion of splenic PBs (CD19^{+}CD138^{+}) and PCs (CD19^{-}CD138^{+}) in active-disease mice (Figure 6B; Supplementary Figure 6). Both of these results were in line with differences in the proportion of cells expressing a T2/MZP/MZ B cell or PB-PC gene signature as determined by scRNA-seq. However, despite increases in total PB-PCs in active-disease mice, the percentage of both PBs and PCs expressing IL-10 was significantly decreased (Figure 6C; Supplementary Figure 6). This result suggests that the the imbalance between pathogenic and

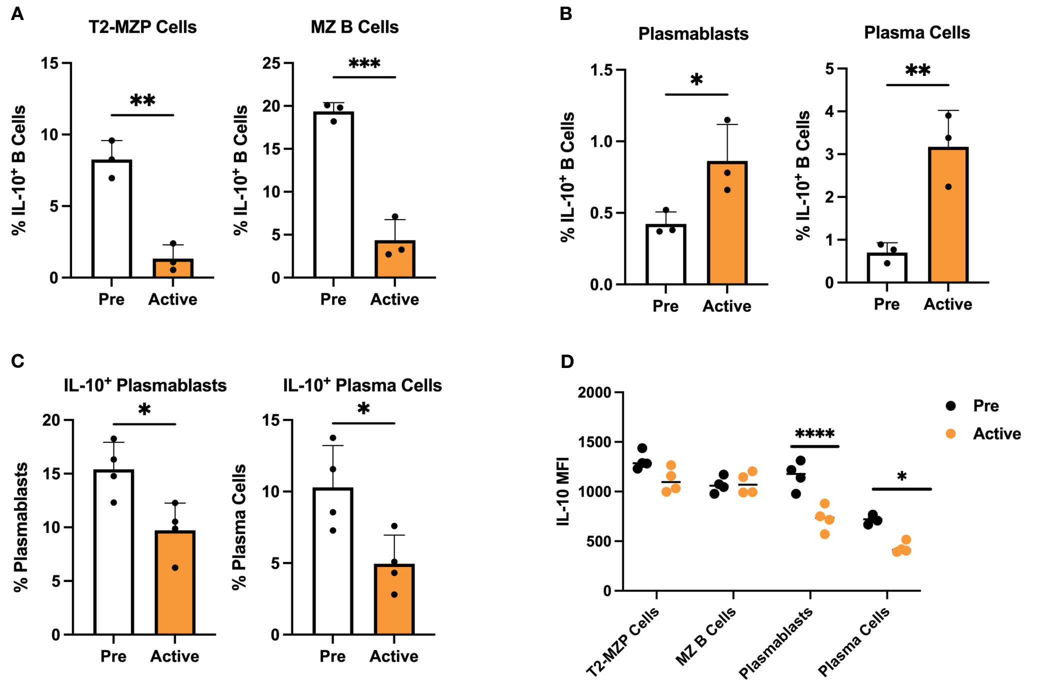

FIGURE 6
Transcriptionally defined disease-dependent alterations to Breg subsets are confirmed in lupus-prone mice. Splenic Breg subsets generated from female MRL/*lpr* mice were assessed at the pre-disease (6-8 weeks) and active-disease (10-12 weeks) stages. **(A)** Percentage of T2-MZP cells and MZ B cells from total IL-10^{+} cells. **(B)** Percentage of PBs and PCs from total IL-10^{+} cells. **(C)** Percentage of IL-10 producing PBs and IL-10 producing PCs from total PBs and total PCs. **(D)** Mean fluorescence intensity (MFI) of IL-10 expression from splenic Breg subsets in A-C. *$p < 0.05$, **$p < 0.01$, ***$p < 0.001$, ****$p < 0.0001$.

regulatory, IL-10 producing PB-PCs contributes to the progression of autoimmune disease in lupus-prone mice.

Our initial measurement of serum IL-10 and IL-10 produced by activated IL-10^+ B cells indicated that both were significantly decreased in lupus-prone mice with active disease. However, expression of *Il10* and IL-10 signaling pathway transcripts were consistently upregulated in active-disease Bregs from integrated single cell clusters. To investigate this further, we carried out intracellular staining for IL-10 in isolated MZ and PB-PC lineage B cells from pre-disease and active-disease mice (Figure 6D). As a result, we found no difference in mean fluorescent intensity (MFI) of IL-10 in T2-MZP or MZ B cells based on disease stage. However, in line with the decreased secreted IL-10 from total splenic Bregs, both PBs and PCs from active-disease mice expressed significantly reduced levels of intracellular IL-10. Therefore, this result demonstrates that the dominant populations of IL-10 producing B cells present in active-disease mice also display the greatest evidence of deficiency in IL-10 mediated immunoregulation.

To explore the differences in IL-10 producing PB-PCs from mice with active lupus that could render these cells unable to suppress autoimmunity effectively, we sought to establish a baseline of gene signatures expressed by Bregs from the PB-PC lineage in a normal immune response. To achieve this, we analyzed publicly available bulk gene expression data from a population of IL-10 producing PB-PCs induced in response to bacterial infection (33). These cells were initially characterized as CD138$^+$IL10$^+$ cells that exhibited increased expression of the inhibitory receptors LAG3, CD200, PD-L1, and PD-L2 as compared to CD138$^+$IL10$^-$ cells and were the predominant source of IL-10 produced in response to infection. Our analysis of these mice confirmed that $\log_2$ gene expression of *Lag3* and *Cd274* were significantly increased in CD138$^+$IL10$^+$ cells (Figure 7A). Interestingly, we found similar populations of IL-10 producing cells from scRNA-seq of lupus-prone mice as these markers were expressed by the Phagocytic PB-PC and TIM-1 B Cell populations from pre-disease mice and the TACI/TNF B Cell and TIM-1 B Cell populations from active-disease mice. Next, to characterize the immune profiles of CD138$^+$IL10$^+$ PB-PCs induced in a normal response to infection, we carried out gene set variation analysis (GSVA) with pre-defined gene sets comprising cellular and inflammatory pathways (Figure 7B). As a result, we found that CD138$^+$IL10$^+$ cells were de-enriched for inflammatory signatures of Type I IFN, Type II IFN, and MHC Class II and also exhibited decreased enrichment of proliferation and metabolism-related signatures as compared to CD138$^+$IL10$^-$ cells. Notably, this was in contrast to gene expression profiles of IL10-producing PB-PCs from lupus-prone mice, which were enriched for pro-inflammatory gene signatures and thus appeared more like IL10$^-$ cells from mice post-infection. This result suggested that differences in Breg induction in the context of autoimmunity as compared to a normal immune response may alter the anti-inflammatory nature of IL-10 producing cells. Overall, we have demonstrated that disease stage-dependent differences in the single-cell transcriptional profiles of IL-10$^+$ B cells directly translate to differences in the proportion of these subsets present in lupus-prone mice and that this likely contributes to their inability to control the onset or severity of autoimmunity.

Discussion

Deficiencies in number and/or function of IL-10 producing, suppressive B cells or Bregs have been found both in mouse models of SLE and human SLE patients suggesting an important role for Bregs in controlling autoimmunity (34). However, because of the heterogeneity in subset markers and mechanisms of suppression, it remains unclear how Bregs are phenotypically and functionally altered in lupus and how this contributes to disease pathology. In this study, we utilized single-cell RNA sequencing to identify disease stage-dependent changes to the transcriptional profiles of Bregs generated from lupus-prone mice that were further validated by phenotypic analyses. As a result we have identified specific Breg subsets and inflammatory gene signatures associated with active disease that provide insights into the role of Bregs in lupus pathogenesis.

Our past work revealed that Bregs isolated from lupus-prone MRL/*lpr* mice before disease onset, but not Bregs from mice with active disease, were able to attenuate autoimmunity suggesting that active-disease Bregs were functionally impaired (30). In the present work, we confirmed that numbers of Bregs, levels of total serum IL-10, and production of IL-10 by Bregs induced from mice with active disease were all significantly decreased as compared to pre-disease mice. This result is in line with numerous studies that have demonstrated associations between numerical and functional impairment of Bregs and increased risk for development or enhanced severity of murine models of autoimmune disease (13, 14, 17, 28). However, these studies did not investigate the relative roles of different subsets of Bregs and their contributions to controlling or exacerbating disease.

We previously demonstrated the utility of gene expression analysis by bulk RNA-seq to construct immune profiles of lupus-prone mice and directly translated these results to human lupus patients (32, 35). Single-cell sequencing technology offers an advantage over bulk sequencing when studying rare cell populations or identifying and comparing subsets of select cell populations, such as Bregs (36). A previous study carried out scRNA-seq to characterize Bregs in different murine organs, but did not isolate IL-10 producing cells before sequencing and instead relied on marker genes to separate Bregs from total B cells (37). Previous studies have also used scRNA-seq to profile the heterogeneity in cell populations derived from blood and tissues of lupus mouse models and human lupus patients (38–41). Here we report the first study that employs the unique advantages of single-cell sequencing technology to demystify the heterogeneity in Breg subsets present in lupus-prone mice before disease onset and in the context of active autoimmune disease.

Overall, scRNA-seq revealed that IL-10 producing B cells generated from lupus-prone mice at the active-disease stage exhibited unique spatial transcriptomic profiles as compared to cells from mice before disease onset that reflected a heightened pro-inflammatory environment and evidence of increased activation of cell stress response pathways. The most striking differences we found in the distribution of Breg subsets from active-disease mice were decreased representation of MZ B cell subsets and increased representation of PB-PC subsets as compared to pre-disease mice.

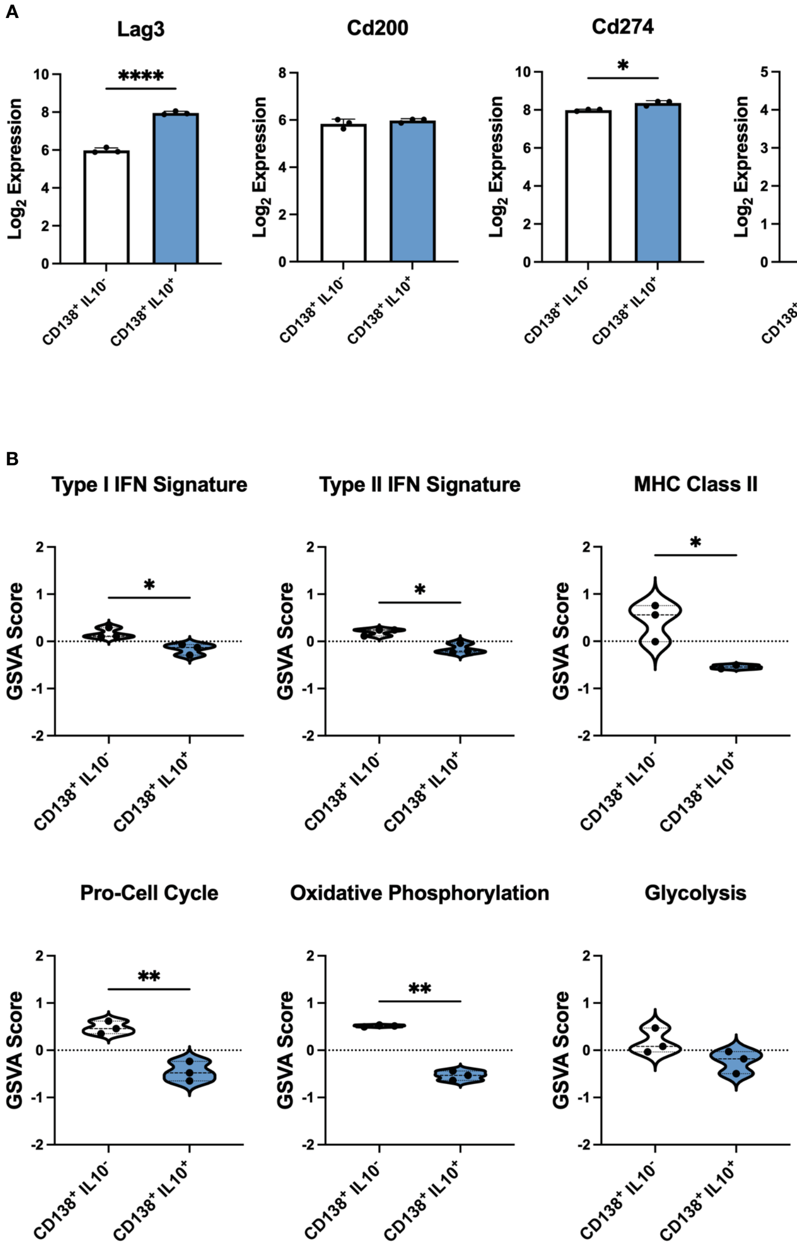

FIGURE 7
IL-10 producing PB-PCs induced by infection differ in inflammatory gene expression from those derived from autoimmune mice. Gene expression analysis by bulk RNA-seq of splenic $CD138^+IL10^-$ and $CD138^+IL10^+$ cells isolated from mice 24 hours after bacterial infection. **(A)** Log_2 expression values of selected inhibitory receptor genes. **(B)** Gene set variation analysis (GSVA) comparing enrichment of inflammatory and cellular pathway gene sets between $IL10^-$ and $IL10^+$ PB-PCs from infected mice. *$p < 0.05$, ** $p < 0.01$, **** $p < 0.0001$.

MZ B cells are innate-like cells that typically retain poly-reactive/ self-reactive B cell receptors (BCRs), rapidly produce natural antibodies, and participate in clearance of pathogens and cellular debris (42). Exposure to apoptotic cells can induce MZ B cells to secrete IL-10 and take on regulatory functions, such that IL-10 producing T2-MZP and MZ B cells have been shown to have a protective role in murine models of collagen-induced arthritis (3, 5, 43). The increased proportion of Bregs of the MZ lineage generated from lupus-prone mice before disease onset raises a few interesting possibilities. Because of the innate-like nature of MZ B cells and their roles in the rapid immune response to pathogens, it is not surprising that MZ lineage cells would also be among the first Breg subsets to be induced in response to early autoimmune stimuli. Then, the decreased capacity to induce production of IL-10 producing MZ B cells as disease progresses could be caused by exposure to increasing inflammation that would promote egress of MZ-lineage Bregs to the periphery and/or the expansion of autoreactive PB-PC subsets in the spleen. Importantly, our observation that B cells from active-disease mice exhibited decreased numbers but not decreased IL-10 production by MZ B cell subsets as compared to pre-disease mice suggests that this subset may be particularly important to control autoimmune disease pathogenesis in this model.

B cells of the PB-PC lineage have also been attributed with regulatory function through production of IL-10 and IL-35 and suppression of pro-inflammatory and autoinflammatory responses (7, 44). Importantly, PB-PCs do not inherently produce IL-10 at steady state, but they may be induced to produce IL-10 by inflammatory environments present during infection or disease (45). It has also been noted that splenic B10 cells are capable of differentiation into antibody-secreting cells (ASCs) after *in vitro* or *in vivo* stimulation (46). Thus, in addition to their well-established contribution to lupus pathogenesis through the production of autoantibodies, PB-PCs also have the capacity to act as suppressors of autoimmunity although the origins and functions of IL-10 producing PB-PCs in SLE patients or lupus-prone mice have not been elucidated.

The MRL/*lpr* lupus-prone mouse strain is characterized by elevated lymphoproliferation, including the outgrowth of PB-PCs (47), and in line with this, we observed an increased percentage of IL-10 producing PB-PCs induced from B cells originating from the autoinflammatory environment present during active disease. However, evidence from our work and others would suggest that these Bregs are more inflammatory in nature and ineffective mediators of immunosuppression. Single-cell transcriptional analysis revealed that PB-PCs from active-disease mice exhibited increased expression of inflammatory pathway genes, which differed from IL-10 producing PB-PCs induced in a normal immune response to bacterial infection (33). We also found greater evidence of terminally differentiated, class-switched PC generation including the presence of a Breg cluster expressing GC B cell markers in active-disease but not pre-disease mice, a finding that supports the conclusion that a population of IL-10 producing PCs was increased within the Breg population in active disease. Even though the percentage of IL-10 producing PCs was increased in the Breg population, the fraction of total PCs that produced IL-10 was significantly decreased in active disease, consistent with the conclusion that the onset of autoimmunity in MRL/*lpr* mice was associated with an expansion of PCs but a decrease in differentiation toward the Breg phenotype in this population. This could contribute to an imbalance in the ratio of pro-inflammatory and regulatory influences and lead to the progression from the pre-disease to active-disease stage. Regarding the regulatory function of active-disease PB-PCs, we found no evidence for defective *Il10* transcription, but did observe decreased IL-10 MFI in PB-PCs from active-disease mice suggesting that they may transcribe *Il10* but not produce IL-10 protein (48). This could be because of defects in IL-10 translation, deficiencies in positive signals needed for IL-10 secretion, or improper negative regulation of IL-10. It is also possible that PB-PCs from active-disease mice are ineffective at immunosuppression because of improper localization and, thus, not positioned to interact with and suppress autoreactive T cells.

This study provides insights into differences in IL-10 producing B cells generated from lupus-prone mice before disease onset and in the context of active autoimmune inflammation. However, there are limitations to the study design that might narrow the interpretation of these results. Because of the low numbers of endogenous splenic Bregs, in particular in an environment with low inflammatory stimuli, we chose to boost the overall numbers of IL-10 producing cells for use in downstream analyses through *in vitro* stimulation. Thus, the populations of Bregs identified by single-cell sequencing are not a definitive survey of Breg development *in vivo*, but rather are indicative of the potential landscape of Breg subsets that may develop through the course of disease progression. In addition, due to our focus on changes to IL-10 producing B cells, we cannot identify potential relationships between changes to the composition of Bregs and changes to the total B cell population in the spleen that occur in the context of active disease. Therefore, this work represents compelling justification for future studies utilizing larger numbers of IL-10$^+$ cells analyzed *ex vivo*. Furthermore, analysis of Bregs from lupus-prone mice could then serve as references for analogous Breg populations derived from human lupus patients.

The role of Bregs in the suppression of autoimmune inflammation and impaired functionality in SLE patients emphasizes the importance of improving our understanding of the heterogeneity of Breg subsets and how changes to Breg subset composition and function could impact lupus pathogenesis. We have utilized scRNA-seq to transcriptionally profile Bregs present at different disease stages in lupus-prone MRL/*lpr* mice and identified Breg subsets associated with increased inflammatory gene signatures specific to mice with active disease. Future studies are needed to investigate the functional competence and localization of IL-10$^+$ Bregs, and in particular Bregs from the MZ B cell and PB-PC lineages, from pre-disease and active-disease mice to further elucidate their contributions to disease onset and progression. This work may better inform investigation of Breg subsets and functional capacity in human lupus patients and support the development of therapies targeting deficiencies in Breg-mediated regulation to improve clinical outcomes of autoimmune pathology.

Data availability statement

The data presented in the study are deposited in the NCBI GEO repository, accession numbers GSE242200 and GSE103458.

Ethics statement

The animal study was approved by Virginia Tech Institutional Animal Care and Use Committee. The study was conducted in accordance with the local legislation and institutional requirements.

Author contributions

AD: Conceptualization, Formal Analysis, Investigation, Methodology, Software, Visualization, Writing – original draft, Writing – review & editing. RA: Conceptualization, Formal Analysis, Investigation, Methodology, Visualization, Writing – review & editing. AG: Funding acquisition, Project

administration, Supervision, Writing – review & editing. XL: Conceptualization, Funding acquisition, Methodology, Project administration, Resources, Supervision, Writing – review & editing. PL: Conceptualization, Funding acquisition, Methodology, Project administration, Resources, Supervision, Writing – review & editing.

Funding

The author(s) declare financial support was received for the research, authorship, and/or publication of this article. NIH/NIAMS grants 1R01AR073240 and 1R21AI156197 (XL). RILITE Foundation (AG, PL)

Acknowledgments

We thank Mellissa Makris from the Virginia Tech flow cytometry core facility and the Virginia Tech Genomic Sequencing Center. We thank members of the Luo lab at Virginia Tech and colleagues at AMPEL BioSolutions for providing their scientific insights through the development of this project.

Conflict of interest

Authors AD, AG, and PL were employed by the company AMPEL BioSolutions LLC.

The remaining authors declare that the research was conducted in the absence of any commercial or financial relationships that could be construed as a potential conflict of interest.

Publisher's note

Supplementary material

The Supplementary Material for this article can be found online at: https://www.frontiersin.org/articles/10.3389/fimmu.2023.1282770/full#supplementary-material

References

1. Rosser EC, Mauri C. Regulatory B cells: origin, phenotype, and function. *Immunity* (2015) 42:607–12. doi: 10.1016/j.immuni.2015.04.005

2. Mauri C, Menon M. The expanding family of regulatory B cells. *Int Immunol* (2015) 27:479–86. doi: 10.1093/intimm/dxv038

3. Evans JG, Chavez-Rueda KA, Eddaoudi A, Meyer-Bahlburg A, Rawlings DJ, Ehrenstein MR, et al. Novel suppressive function of transitional 2 B cells in experimental arthritis. *J Immunol* (2007) 178:7868–78. doi: 10.4049/jimmunol.178.12.7868

4. Lenert P, Brummel R, Field EH, Ashman RF. TLR-9 activation of marginal zone B cells in lupus mice regulates immunity through increased IL-10 production. *J Clin Immunol* (2005) 25:29–40. doi: 10.1007/s10875-005-0355-6

5. Huber K, Sármay G, Kövesdi D. MZ B cells migrate in a T-bet dependent manner and might contribute to the remission of collagen-induced arthritis by the secretion of IL-10. *Eur J Immunol* (2016) 46:2239–46. doi: 10.1002/eji.201546248

6. Ding Q, Yeung M, Camirand G, Zeng Q, Akiba H, Yagita H, et al. Regulatory B cells are identified by expression of TIM-1 and can be induced through TIM-1 ligation to promote tolerance in mice. *J Clin Invest* (2011) 121:3645–56. doi: 10.1172/JCI46274

7. Matsumoto M, Baba A, Yokota T, Nishikawa H, Ohkawa Y, Kayama H, et al. Interleukin-10-producing plasmablasts exert regulatory function in autoimmune inflammation. *Immunity* (2014) 41:1040–51. doi: 10.1016/j.immuni.2014.10.016

8. Fillatreau S. Natural regulatory plasma cells. *Curr Opin Immunol* (2018) 55:62–6. doi: 10.1016/j.coi.2018.09.012

9. Hsu L-H, Li K-P, Chu K-H, Chiang BL. A B-1a cell subset induces Foxp3(-) T cells with regulatory activity through an IL-10-independent pathway. *Cell Mol Immunol* (2015) 12:354–65. doi: 10.1038/cmi.2014.56

10. DiLillo DJ, Matsushita T, Tedder TF. B10 cells and regulatory B cells balance immune responses during inflammation, autoimmunity, and cancer. *Ann N Y Acad Sci* (2010) 1183:38–57. doi: 10.1111/j.1749-6632.2009.05137.x

11. Catalán D, Mansilla MA, Ferrier A, Soto L, Oleinika K, Aguillón JC, et al. Immunosuppressive mechanisms of regulatory B cells. *Front Immunol* (2021) 12:611795. doi: 10.3389/fimmu.2021.611795

12. Wolf SD, Dittel BN, Hardardottir F, Janeway CA. Experimental autoimmune encephalomyelitis induction in genetically B cell-deficient mice. *J Exp Med* (1996) 184:2271–8. doi: 10.1084/jem.184.6.2271

13. Fillatreau S, Sweenie CH, McGeachy MJ, Gray D, Anderton SM. B cells regulate autoimmunity by provision of IL-10. *Nat Immunol* (2002) 3:944–50. doi: 10.1038/ni833

14. Matsushita T, Yanaba K, Bouaziz JD, Fujimoto M, Tedder TF. Regulatory B cells inhibit EAE initiation in mice while other B cells promote disease progression. *J Clin Invest* (2008) 118:3420–30. doi: 10.1172/JCI36030

15. Mizoguchi A, Mizoguchi E, Smith RN, Preffer FI, Bhan AK. Suppressive role of B cells in chronic colitis of T cell receptor alpha mutant mice. *J Exp Med* (1997) 186:1749–56. doi: 10.1084/jem.186.10.1749

16. Mizoguchi A, Mizoguchi E, Takedatsu H, Blumberg RS, Bhan AK. Chronic intestinal inflammatory condition generates IL-10-producing regulatory B cell subset characterized by CD1d upregulation. *Immunity* (2002) 16:219–30. doi: 10.1016/S1074-7613(02)00274-1

17. Watanabe R, Ishiura N, Nakashima H, Kuwano Y, Okochi H, Tamaki K, et al. Regulatory B cells (B10 cells) have a suppressive role in murine lupus: CD19 and B10 cell deficiency exacerbates systemic autoimmunity. *J Immunol* (2010) 184:4801–9. doi: 10.4049/jimmunol.0902385

18. Haas KM, Watanabe R, Matsushita T, Nakashima H, Ishiura N, Okochi H, et al. Protective and pathogenic roles for B cells during systemic autoimmunity in NZB/W F1 mice. *J Immunol* (2010) 184:4789–800. doi: 10.4049/jimmunol.0902391

19. Mauri C, Menon M. Human regulatory B cells in health and disease: Therapeutic potential. *J Clin Invest* (2017) 127:772–9. doi: 10.1172/JCI85113

20. Park YB, Lee SK, Kim DS, Lee J, Lee CH, Song CH. Elevated interleukin-10 levels correlated with disease activity in systemic lupus erythematosus. *Clin Exp Rheumatol* (1998) 16:283–8.

21. Iwata Y, Matsushita T, Horikawa M, Dilillo DJ, Yanaba K, Venturi GM, et al. Characterization of a rare IL-10-competent B-cell subset in humans that parallels mouse regulatory B10 cells. *Blood* (2011) 117:530–41. doi: 10.1182/blood-2010-07-294249

22. Wang T, Li Z, Li X, Chen L, Zhao H, Jiang C, et al. Expression of CD19+CD24highCD38high B cells, IL-10 and IL-10R in peripheral blood from patients with systemic lupus erythematosus. *Mol Med Rep* (2017) 16:6326–33. doi: 10.3892/mmr.2017.7381

23. Heinemann K, Wilde B, Hoerning A, Tebbe B, Kribben A, Witzke O, et al. Decreased IL-10(+) regulatory B cells (Bregs) in lupus nephritis patients. *Scand J Rheumatol* (2016) 45:312–6. doi: 10.3109/03009742.2015.1126346

24. Jin L, Weiqian C, Lihuan Y. Peripheral CD24hiCD27+CD19+B cells subset as a potential biomarker in naïve systemic lupus erythematosus. *Int J Rheum Dis* (2013) 16:698–708. doi: 10.1111/1756-185X.12229

25. Xiong H, Tang Z, Xu Y, Shi Z, Guo Z, Liu X, et al. CD19+CD24highCD27+ B cell and interleukin 35 as potential biomarkers of disease activity in systemic lupus erythematosus patients. *Adv Rheumatol* (2022) 62:48. doi: 10.1186/s42358-022-00279-8

26. Blair PA, Noreña LY, Flores-Borja F, Rawlings DJ, Isenberg DA, Ehrenstein MR, et al. CD19+CD24hiCD38hi B cells exhibit regulatory capacity in healthy individuals but are functionally impaired in systemic lupus erythematosus patients. *Immunity* (2010) 32:129–40. doi: 10.1016/j.immuni.2009.11.009

27. Gao N, Dresel J, Eckstein V, Gellert R, Störch H, Venigalla RKC, et al. Impaired suppressive capacity of activation-induced regulatory B cells in systemic lupus erythematosus. *Arthritis Rheumatol (Hoboken NJ)* (2014) 66:2849–61. doi: 10.1002/art.38742

28. Sim JH, Kim HR, Chang SH, Kim IJ, Lipsky PE, Lee J. Autoregulatory function of interleukin-10-producing pre-naïve B cells is defective in systemic lupus erythematosus. *Arthritis Res Ther* (2015) 17:1–15. doi: 10.1186/s13075-015-0687-1

29. Luo XM, Edwards MR, Mu Q, Yu Y, Vieson MD, Reilly CM, et al. Gut microbiota in human systemic lupus erythematosus and a mouse model of lupus. *Appl Environ Microbiol* (2018) 84:1–10. doi: 10.1128/AEM.02288-17

30. Mu Q, Edwards MR, Swartwout BK, Cabana Puig X, Mao J, Zhu J, et al. Gut microbiota and bacterial DNA suppress autoimmunity by stimulating regulatory B cells in a murine model of lupus. *Front Immunol* (2020) 11:593353. doi: 10.3389/fimmu.2020.593353

31. Hänzelmann S, Castelo R, Guinney J. GSVA: gene set variation analysis for microarray and RNA-Seq data. *BMC Bioinf* (2013) 14:7. doi: 10.1186/1471-2105-14-7

32. Daamen AR, Wang H, Bachali P, Shen N, Kingsmore KM, Robl RD, et al. Molecular mechanisms governing the progression of nephritis in lupus prone mice and human lupus patients. *Front Immunol* (2023) 14:1147526. doi: 10.3389/fimmu.2023.1147526

33. Lino AC, Dang VD, Lampropoulou V, Welle A, Joedicke J, Pohar J, et al. LAG-3 inhibitory receptor expression identifies immunosuppressive natural regulatory plasma cells. *Immunity* (2018) 49:120–133.e9. doi: 10.1016/j.immuni.2018.06.007

34. Yang M, Rui K, Wang S, Lu L. Regulatory B cells in autoimmune diseases. *Cell Mol Immunol* (2013) 10:122–32. doi: 10.1038/cmi.2012.60

35. Ren J, Catalina MD, Eden K, Liao X, Read KA, Luo X, et al. Selective histone deacetylase 6 inhibition normalizes b cell activation and germinal center formation in a model of systemic lupus erythematosus. *Front Immunol* (2019) 10:2512. doi: 10.3389/fimmu.2019.02512

36. Hwang B, Lee JH, Bang D. Single-cell RNA sequencing technologies and bioinformatics pipelines. *Exp Mol Med* (2018) 50:1–14. doi: 10.1038/s12276-018-0071-8

37. Yang S-Y, Long J, Huang M-X, Luo P-Y, Bian Z-H, Xu Y-F, et al. Characterization of organ-specific regulatory B cells using single-cell RNA sequencing. *Front Immunol* (2021) 12:711980. doi: 10.3389/fimmu.2021.711980

38. Nehar-Belaid D, Hong S, Marches R, Chen G, Bolisetty M, Baisch J, et al. Mapping systemic lupus erythematosus heterogeneity at the single-cell level. *Nat Immunol* (2020) 21:1094–106. doi: 10.1038/s41590-020-0743-0

39. Perez RK, Gordon MG, Subramaniam M, Kim MC, Hartoularos GC, Targ S, et al. Single-cell RNA-seq reveals cell type-specific molecular and genetic associations to lupus. *Science* (2022) 376(6589):eabf1970. doi: 10.1126/science.abf1970

40. Smita S, Chikina M, Shlomchik MJ, Tilstra JS. Heterogeneity and clonality of kidney-infiltrating T cells in murine lupus nephritis. *JCI Insight* (2022) 7:1–18. doi: 10.1172/jci.insight.156048

41. Akama-Garren EH, Carroll MC. Lupus susceptibility loci predispose mice to clonal lymphocytic responses and myeloid expansion. *J Immunol* (2022) 208:2403–24. doi: 10.4049/jimmunol.2200098

42. Palm A-KE, Kleinau S. Marginal zone B cells: From housekeeping function to autoimmunity? *J Autoimmun* (2021) 119:102627. doi: 10.1016/j.jaut.2021.102627

43. Gray M, Miles K, Salter D, Gray D, Savill J. Apoptotic cells protect mice from autoimmune inflammation by the induction of regulatory B cells. *Proc Natl Acad Sci U.S.A.* (2007) 104:14080–5. doi: 10.1073/pnas.0700326104

44. Shen P, Roch T, Lampropoulou V, O'Connor RA, Stervbo U, Hilgenberg E, et al. IL-35-producing B cells are critical regulators of immunity during autoimmune and infectious diseases. *Nature* (2014) 507:366–70. doi: 10.1038/nature12979

45. Fillatreau S. Regulatory functions of B cells and regulatory plasma cells. *BioMed J* (2019) 42:233–42. doi: 10.1016/j.bj.2019.05.008

46. Maseda D, Smith SH, DiLillo DJ, Bryant JM, Candando KM, Weaver CT, et al. Regulatory B10 cells differentiate into antibody-secreting cells after transient IL-10 production. *vivo. J Immunol* (2012) 188:1036–48. doi: 10.4049/jimmunol.1102500

47. Cohen PL, Eisenberg RA. Lpr and gld: single gene models of systemic autoimmunity and lymphoproliferative disease. *Annu Rev Immunol* (1991) 9:243–69. doi: 10.1146/annurev.iy.09.040191.001331

48. Tone M, Powell MJ, Tone Y, Thompson SA, Waldmann H. IL-10 gene expression is controlled by the transcription factors Sp1 and Sp3. *J Immunol* (2000) 165:286–91. doi: 10.4049/jimmunol.165.1.286

frontiers | Frontiers in Immunology

TYPE Original Research
PUBLISHED 25 April 2024
DOI 10.3389/fimmu.2024.1376933

Comparative single-cell multiplex immunophenotyping of therapy-naive patients with rheumatoid arthritis, systemic sclerosis, and systemic lupus erythematosus shed light on disease-specific composition of the peripheral immune system

József Á. Balog[1,2], Ágnes Zvara[1,2], Vivien Bukovinszki[3], László G. Puskás[1,2], Attila Balog[3*†] and Gábor J. Szebeni[1,2,4,5*†]

[1]Laboratory of Functional Genomics, Institute of Genetics, HUN-REN Biological Research Centre, Szeged, Hungary, [2]Core Facility, HUN-REN Biological Research Centre, Szeged, Hungary, [3]Department of Rheumatology and Immunology, Faculty of Medicine, Albert Szent-Gyorgyi Health Centre, University of Szeged, Szeged, Hungary, [4]Department of Internal Medicine, Hematology Centre, Faculty of Medicine University of Szeged, Szeged, Hungary, [5]Astridbio Technologies Ltd., Szeged, Hungary

Introduction: Systemic autoimmune diseases (SADs) are a significant burden on the healthcare system. Understanding the complexity of the peripheral immunophenotype in SADs may facilitate the differential diagnosis and identification of potential therapeutic targets.

Methods: Single-cell mass cytometric immunophenotyping was performed on peripheral blood mononuclear cells (PBMCs) from healthy controls (HCs) and therapy-naive patients with rheumatoid arthritis (RA), progressive systemic sclerosis (SSc), and systemic lupus erythematosus (SLE). Immunophenotyping was performed on 15,387,165 CD45$^+$ live single cells from 52 participants (13 cases/group), using an antibody panel to detect 34 markers.

Results: Using the t-SNE (t-distributed stochastic neighbor embedding) algorithm, the following 17 main immune cell types were determined: CD4$^+$/CD57$^-$ T cells, CD4$^+$/CD57$^+$ T cells, CD8$^+$/CD161$^-$ T cells, CD8$^+$/CD161$^+$/CD28$^+$ T cells, CD8^{dim} T cells, CD3$^+$/CD4$^-$/CD8$^-$ T cells, TCRγ/δ T cells, CD4$^+$ NKT cells, CD8$^+$ NKT cells, classic NK cells, CD56^{dim}/CD98^{dim} cells, B cells, plasmablasts, monocytes, CD11cdim/CD172dim cells, myeloid dendritic cells (mDCs), and plasmacytoid dendritic cells (pDCs). Seven of the 17 main cell types exhibited statistically significant frequencies in the investigated groups. The expression levels of the 34 markers in the main populations were compared between HCs and SADs. In summary, 59 scatter plots showed significant differences in the expression intensities between at least two groups. Next, each immune cell population was divided into subpopulations (metaclusters) using the FlowSOM (self-organizing map) algorithm. Finally, 121 metaclusters (MCs) of the 10 main

OPEN ACCESS

EDITED BY
Shiang-Jong Tzeng,
National Taiwan University, Taiwan

REVIEWED BY
Michelle Delano Catalina,
AbbVie, United States
Tinhinane Fali,
Institut National de la Santé et de la
Recherche Médicale (INSERM), France

*CORRESPONDENCE
Attila Balog
balog.attila@med.u-szeged.hu
Gábor J. Szebeni
szebeni.gabor@brc.hu

†These authors have contributed equally to this work and share senior authorship

RECEIVED 26 January 2024
ACCEPTED 03 April 2024
PUBLISHED 25 April 2024

CITATION
Balog JÁ, Zvara Á, Bukovinszki V, Puskás LG, Balog A and Szebeni GJ (2024) Comparative single-cell multiplex immunophenotyping of therapy-naive patients with rheumatoid arthritis, systemic sclerosis, and systemic lupus erythematosus shed light on disease-specific composition of the peripheral immune system. *Front. Immunol.* 15:1376933. doi: 10.3389/fimmu.2024.1376933

immune cell populations were found to have significant differences to classify diseases. The single-cell T-cell heterogeneity represented 64MCs based on the expression of 34 markers, and the frequency of 23 MCs differed significantly between at least twoconditions. The CD3^{-} non-T-cell compartment contained 57 MCs with 17 MCs differentiating at least two investigated groups. In summary, we are the first to demonstrate the complexity of the immunophenotype of 34 markers over 15 million single cells in HCs vs. therapy-naive patients with RA, SSc, and SLE. Disease specific population frequencies or expression patterns of peripheral immune cells provide a single-cell data resource to the scientific community.

KEYWORDS

rheumatoid arthritis, progressive systemic sclerosis, systemic lupus erythematosus, mass cytometry, autoimmunity

1 Introduction

Inflammatory, rheumatic, and systemic autoimmune diseases collectively contribute to a significant burden on healthcare systems. Treatments are only partially effective, and disease severity and therapeutic responses in individual patients are unpredictable. The complexity of systemic autoimmune disease (SAD) etiology, an incomplete list of causative agents, environmental factors, and polygenetic predispositions make both the diagnosis and clinical management of these pathologies difficult (1). The known fundamentals of the pathological mechanisms of these SADs are beyond the scope of our study; however, the latest findings have been reviewed elsewhere for rheumatoid arthritis (RA) (2), systemic sclerosis (SSc) (3), and systemic lupus erythematosus (SLE) (4). The differential diagnosis of spectrum disorders, such as SADs with similar signs and symptoms, including RA, SSc, and SLE, remains a major challenge for clinicians. The progression of these diseases is unpredictable, and if any damage is fatal or chronic, it can lead to a substantial combined impact on premature mortality (5, 6). Therefore, early diagnosis of SADs is highly important before irreversible damage to several organs, such as the joints, kidneys, and lungs, which are frequently involved in autoimmune attacks, develops. The introduction of disease-modifying antirheumatic drugs (DMARDs) with the high importance of biological DMARDs (bDMARDs) and the advent of targeted inhibitors have reached a breakthrough, leading to disease stabilization and improved quality of life (7–9). However, a lack of treatment response occurs in severe cases or therapeutic resistance can develop (10–12). Therefore, stratifying patients with clinically heterogeneous diseases, such as SADs, has become a novel approach to understanding the complexity of imbalances in immune homeostasis, molecular profiling, and the integration of multi-omics data. Analyzing the immunophenotype in early, untreated SADs may provide information for precision medicine approaches and may suggest diverse underlying pathology leading to similar phenotype. Mass cytometry has been used earlier studying a wide list of human spectrum diseases with deep insight into the heterogeneity of the immunophenotype (13, 14). In line with this assumption, the complex immunophenotyping of SADs can facilitate the prediction of the severity of the disease and therapeutic response, in addition to suggestions for future precision medicine. Mulhearn et al. reviewed the potential of peripheral blood immunophenotyping to predict therapeutic outcomes in response to biologics in RA (15). Papadimitriou et al. summarized the link between the innate and adaptive arms of the immune system in the pathological mechanisms of SSc in the context of the currently available treatment regimen (16). Nagafuchi et al. and Nakayamada et al. recently reviewed the influence of immunophenotyping on therapeutic strategy planning for SLE (17, 18).

The multiparametric immunophenotyping of peripheral immunity may assist in better understanding the pathobiology of SADs because the heterogeneity of inherent and external factors can influence the pathological mechanism and therapeutic response (19). An earlier immunophenotyping study published by Nagafuchi et al. reported a link between the HLA-DRB1 genotype and a higher frequency of peripheral memory CXCR4^{+}CD4^{+} T cells in patients with RA (20). Furthermore, a multidimensional analysis of the peripheral immunophenotype of 311 patients with RA revealed that the expansion of effector memory follicular helper T cells (Tfh) correlated with disease activity (21). Bader et al. analyzed the peripheral blood of 20 therapy-naive RA patients using a 23-marker mass cytometry (CyTOF) antibody panel and reported the following markers: p-p38, IkBa, p-cJun, p-NFkB, and CD86 in the cells of both the myeloid innate and adaptive branches (memory CD4^{+} T cells) of the immune system as potential markers for discriminating patients with RA from healthy donors (22). Koppejan et al. used a 36-marker

CyTOF panel for the immunophenotyping of treatment-naive patients with early ACPA$^+$ (anti-citrullinated protein antibodies) and ACPA-RA and found a reduced frequency of CD62L$^+$ basophils in patients with ACPA-RA (23).

Immunophenotyping of 20 systemic sclerosis cases using a 36-marker CyTOF panel revealed 18 significant alterations in peripheral blood mononuclear cells (PBMCs), highlighting the involvement of CD4$^+$, CD8$^+$, mucosal-associated invariant T cells, and B-cell subsets in pathogenic chronic inflammation (24). In a mass cytometric study by Kroef et al., hierarchical clustering of PBMCs from 88 patients with SSc was performed using a 34-marker antibody panel. They found altered cell populations in four clusters: cluster 1 (n = 16) with high CD16$^+$ monocytes and low memory B-cell subsets, cluster 2 (n = 25) with increased classical monocytes, cluster 3 (n = 8) with higher memory B-cell counts, and cluster 4 (n = 37) with lower circulating classical monocyte counts (25). Multiparametric flow cytometric investigation of 88 patients with early SSc showed a decrease in CD8$^+$ T cells and an expansion of CD28$^-$ and CD319$^+$ within the CD4$^+$ subset in the SSc group compared with HCs (26). Agarbati et al. analyzed 46 patients with SSc using an eight-color FACS panel and showed a higher ratio of CD38$^+$ T cells and CD4$^+$CD25$^+$FOXP3$^+$ regulatory T cells in patients with SSc (27). Agarbati et al. also investigated the humoral arm of the adaptive immune system in SSc and found a higher frequency of CD24^{high}CD19$^+$CD38^{high} regulatory B cells, more circulating CD38^{high}CD27$^+$ plasmablasts, and peripheral CD138$^+$CD38^{high} plasma cells than in HCs (27).

An early immunophenotyping study revealed reduced expression of CD3$^+$ and CD4$^+$ T-cell markers and increased expression of CD8$^+$ cytotoxic T-cell and CD20$^+$ B-cell markers in SLE based on traditional flow cytometry of 21 SLE patients vs. HCs (28). Later, Perry et al. showed a higher ratio of CD38$^+$HLA-DR$^+$ T cells in SLE in a flow cytometric study analyzing samples from 35 patients with SLE compared with samples from HCs (29). Lee et al. also used traditional flow cytometry to compare the peripheral immune signatures of 13 patients with SLE and nine HCs. They found 29 immune subsets discriminating SLE from HCs, with the emphasis on lower DC and NK cell ratios in SLE, but elevated CD8$^+$ NK Treg cells in lupus (30). Recently, Sasaki et al. published the most comprehensive immunophenotyping of lupus in nine early and 15 established SLE patients compared with controls using two CyTOF panels measuring 38–39 parameters. Their key findings were an increased frequency of ICOS$^+$Ki-67$^+$CD8$^+$ T cells, Ki-67$^+$ regulatory T cells, CD19^{intermediate}Ki-67^{high} plasmablasts, and PU.1^{high}Ki-67^{high} monocytes in patients with early SLE (31).

In this study, single-cell mass cytometric immunophenotyping of over 15 million single cells was performed on PBMC samples of healthy controls (HCs, n = 13) and therapy-naive patients with RA (n = 13), SSc (n = 13), and SLE (n = 13) using an antibody panel detecting 34 markers. DMARDs can influence the peripheral immunophenotype. Therefore, we enrolled therapy-naive patients, which makes this study unique in the field of clinical rheumatology. Our aim was to decipher the complex alterations in the peripheral immunity in SADs and to reveal disturbances in immune homeostasis that may contribute to our understanding of the specific pathobiology of RA, SSc, or SLE.

2 Materials and methods

2.1 Human participants

Patients were recruited during visits to the Department of Rheumatology and Immunology at the University of Szeged. Healthy controls were voluntary staff members of the BRC or the University of Szeged. The participants were informed of the research by a physician. Written informed consent was obtained from all the participants, and the study was reviewed and approved by the independent ethics committee of the university. Details regarding the study design and handling of biological materials were submitted to the Human Investigation Review Board of the University of Szeged under the 149/2019-SZTE Project Identification code. Laboratory studies and interpretations were performed on coded samples with personal and diagnostic identifiers removed. The study adhered to the principles of the most recent revision of the Declaration of Helsinki.

2.2 Study design

Multiplex protein analysis of 52 drug-naive patients with SADs [RA (n = 13; median: 57 years; range: 29–73 years; Supplementary Table 1), SSc (n = 13; median age: 63 years; range: 29–75 years; Supplementary Table 2), and SLE (n = 13; median: 50 years; range: 20–72 years; Supplementary Table 3) patients and age- and sex-matched healthy controls (n = 13; median: 54 years; range: 22–77 years) was performed. We enrolled newly diagnosed drug-naive patients with RA, SSc, and SLE who had not received antirheumatic treatment, including non-steroidal anti-inflammatory drugs (NSAIDs), DMARDs, or glucocorticoids, until the time of blood sampling. Patients with RA were diagnosed according to the latest American College of Rheumatology/European League Against Rheumatism criteria (32) (Supplementary Table 1). Thirteen newly diagnosed patients who fulfilled the criteria proposed by the 2013 American College of Rheumatology/European League Against Rheumatism classification criteria for SSc were enrolled (33). Four out of 13 patients were further classified as having limited cutaneous SSc, and nine out of 13 were classified as having diffuse cutaneous scleroderma according to LeRoy et al. (34) (Supplementary Table 2). Patients with SLE who met the 2012 Systemic Lupus Collaborating Clinics (SLICC) criteria and had active, newly diagnosed SLE were considered eligible (35). Several clinical and immunological parameters were assessed at the time of SLE diagnosis (Supplementary Table 3). Healthy controls were age- and sex-matched to patients and had a negative history of rheumatic symptoms and negative status upon detailed physical and laboratory examinations. No comorbidities were detected in the patients or controls that could have influenced our investigation, nor did they take any medication that could have interfered with the measurements.

2.3 PBMC isolation

PBMCs were isolated as previously described (36). Briefly, after the collection of 20 ml of blood in an EDTA vacutainer (Becton

Dickinson, Franklin Lakes, New Jersey, USA), PBMCs were purified using Leucosep tubes (Greiner Bio-One, Austria) according to the manufacturer's instructions. If the pellet was light red, 2 ml of ACK Lysing Buffer (ACK) was added at room temperature (RT, 20°C) for 2 min. Samples were washed twice with 10 ml of PBS, and cell count and viability were checked using Trypan Blue. PBMCs were cryopreserved in stocks of 4×10^6 cells in 1 ml of FCS (Euroclone, Milano, Italy) supplemented with 1:10 DMSO (Merck, Darmstadt, Germany) [v/v] in liquid nitrogen.

2.4 Cell preparation

Cells were processed for CyTOF as described previously by our group with minor modifications (37). Briefly, cryotubes were thawed in a 37°C water bath for 2 min, and cells were transferred into 14 ml of cRPMI at 37°C and centrifuged at 350*g* for 6 min at room temperature (RT). PBMCs were washed once more with 10 ml of cRPMI, cells were counted, and viability was determined by Trypan Blue exclusion. PBMCs including up to $2–3 \times 10^6$ cells/sample were plated onto a 96-well repellent plate separately in 200 µl of cRPMI and rested overnight in an incubator with 5% CO_2 at 37°C. The rested cells were collected and washed twice with Maxpar Cell Staining Buffer (MCSB; Fluidigm, now Standard BioTools, South San Francisco, California, USA).

2.5 Barcoding and antibody staining

Mass cytometry was performed as previously described by our group with minor modifications (38, 39). Briefly, cells were resuspended in 50 µl of MCSB supplemented with 1:20 v/v Human TruStain FcX Fc Receptor Blocking Solution (BioLegend, San Diego, California, USA) and incubated at RT for 10 min. Anti-CD45 antibody-based live cell barcoding was performed as described previously by Fish et al. (40). Without the washing step, 50 µl of different metal-tagged (^{89}Y, ^{106}Cd, ^{114}Cd, ^{116}Cd) CD45 antibodies (clone: HI30; Fluidigm) at a final concentration of 1:100 [v/v] per antibody were added separately and incubated at 4°C for 30 min. PBMCs were washed twice with MCSB and 1×10^6 cells from all four samples were pooled into 100 µl of MCSB. Cells were stained with 1:100 [v/v] of five markers, CD32, CD47, CD98, CD172a, and CD335 (Fluidigm), and incubated at RT for 20 min in MCSB. PBMCs were diluted by 200 µl of MCSB and transferred into a single tube of Maxpar Direct Immune Profiling Assay (Fluidigm) and incubated at RT for 30 min. The panel of antibodies used is listed in Supplementary Table 4. Cells were washed twice with MCSB, prefixed with 1 ml of Pierce^{TM} 16% formaldehyde (w/v) (Thermo Fisher Scientific, Waltham, Massachusetts, USA) solution diluted in PBS to 1.6%, and incubated at RT for 10 min. Stained and prefixed cells were centrifuged at 800*g* at RT for 6 min and resuspended in 800 µl of Fix & Perm solution (Fluidigm) supplemented with 1:1,000 [v/v] ^{191}Ir-^{193}Ir DNA intercalator (Fluidigm) for overnight incubation.

2.6 CyTOF data acquisition

CyTOF samples were acquired as described previously by our group with minor modifications (36, 41). Samples were washed three times with MCSB and filtered through a 30-µm CellTrics gravity filter (Sysmex, Görlitz, Germany), and the cell concentration was adjusted to 7×10^5/ml in CAS (cell acquisition solution) for the WB injector. Finally, EQ four-element calibration beads (Fluidigm) were added at a 1:10 ratio [v/v] and acquired using a properly tuned Helios mass cytometer (Fluidigm). From the pooled samples, 1.2×10^6 events (3×10^5/individual PBMC) were collected to identify rare cell subsets. The generated flow cytometry standard (FCS) files were randomized and normalized with the default settings of the internal FCS-processing unit of the CyTOF software (Fluidigm, version:7.0.8493).

2.7 Data processing

The randomized and normalized FCS files were uploaded to the Cytobank Premium analysis platform (Beckman Coulter). Exclusion of normalized beads, dead cells, debris, and doublets and manual debarcoding were performed as described in Supplementary Figures 1, 2. No significant differences in the cell counts between the examined groups were observed. FCS files with CD45-positive living singlets were exported and further analyzed in R. Compensation methodology, FlowSOM clustering, and dimensionality reduction were adapted from Crowell et al. (42). FlowSOM was chosen following the publication of Weber et al. about the unsupervised analysis of CyTOF data (43). Data analysis was performed as described by Nowicka et al. (44). Using the BioConductor CATALYST and FlowCore R packages, the FCS files were integrated, compensated, and transformed. After signal spillover compensation, the CyTOF marker intensities were inverse-hyperbolic sine-transformed (arcsinh) with cofactor 5. For the main population definition, we performed self-organizing map-based method metaclustering on the compensated and transformed files. We identified 17 main different metaclusters as different cell types that were separately subclustered in another round of FlowSOM. High-dimensional reduction and visualization were performed using the (t-SNE) algorithm/method. In total, 300,000 cells and 34 markers were used to create a t-SNE map of the human peripheral immune system. The event numbers in the identified main immune cell populations and in the immune cell-related metaclusters are listed in Supplementary Table 5 for each human subject. The minimum criteria for the cell number for the 17 main immune cell populations was at least 150 cells in each of the 10 subjects from the 13 participants meeting at least one of the conditions (HCs, RA, SSc, or SLE). The minimum criteria for the cell number for the metaclusters to move forward with the analysis was at least 50 cells in each of the 10 subjects from the 13 participants meeting at least one of the conditions (HCs, RA, SSc, or SLE).

2.8 Statistical analysis

Median signal intensities, cell frequencies, and subpopulation frequencies were analyzed using GraphPad Prism 8.0.1. The normality of distributions was tested using the D'Agostino and Pearson test and passed if all the groups' alpha values were <0.05.

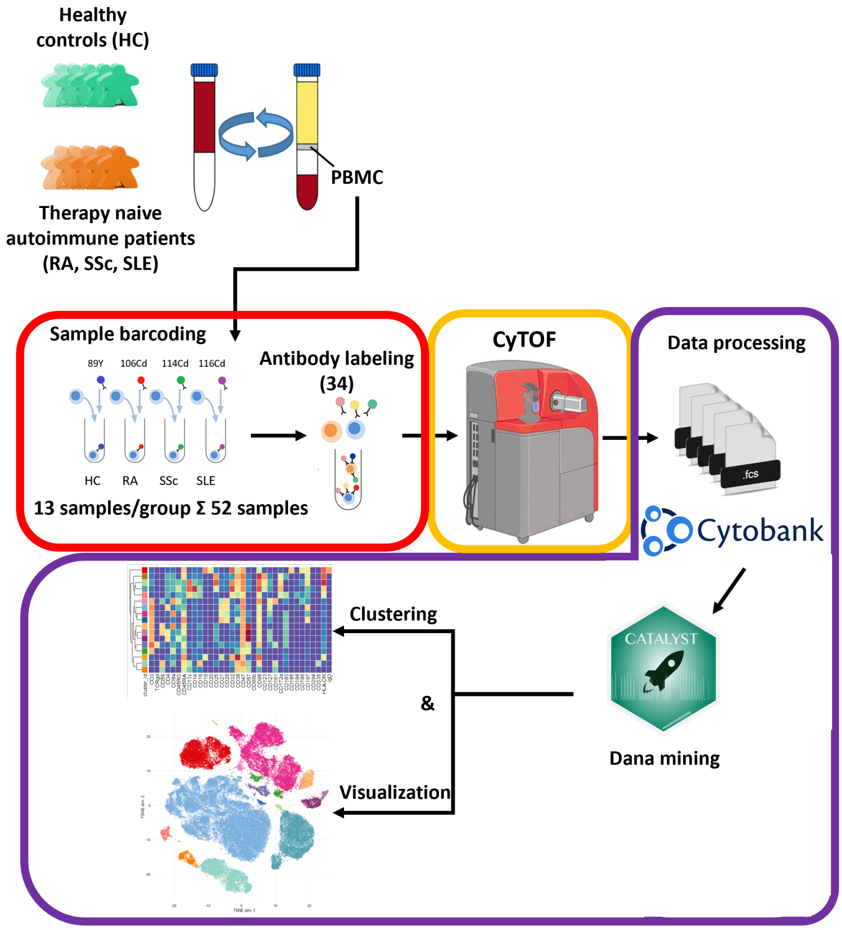

FIGURE 1
Schematic cartoon of the workflow of the study. Thirteen subjects were enrolled per group, namely, therapy-naive RA, SSc, and SLE patients and HCs. The PBMCs were purified from the peripheral blood by Ficoll-density gradient centrifugation. Immunophenotyping was performed using a 34-membered antibody panel optimized for single-cell mass cytometry. The PBMCs of four subjects were labeled separately with anti-CD45 antibodies conjugated with different metal tags. Subsequently, the cells of the four barcoded subjects were stained simultaneously in one tube. The CyTOF was performed by the Helios system. Data analysis was carried out using Cytobank Premium and Catalyst package in R software as described in the *Materials and methods* section.

Normally distributed datasets were compared using ordinary one-way ANOVA or Brown–Forsythe ANOVA when standard deviations were not equal. For non-parametric analysis, the Kruskal–Wallis test was used. All significance tests were corrected for multiple comparisons by controlling the false discovery rate (FDR) using the two-stage Benjamini, Krieger, and Yekutieli approach, with an FDR cutoff of 10%. Differences were considered significant at $p < 0.05$.

3 Results

3.1 Enrollment of therapy-naive SAD patients and the workflow of single-cell immunophenotyping

Our aim was to perform single-cell immunophenotyping of SADs, namely, RA, SSc, SLE, and HCs. For better clarity, a schematic cartoon of the project workflow is summarized in Figure 1. The enrollment of therapy-naive SAD patients allowed unprecedented insight into the early stage of disease development without the masking effect of disease-modifying antirheumatic drugs following therapy.

3.2 Determination and characterization of the 17 main immune populations in HCs and therapy-naive patients with RA, SSC, and SLE

The 34-marker antibody panel for the single-cell mass cytometric investigation and the subsequent FlowSOM analysis identified 17 immune cell types among the 15,387,165 cells from the 52 participants. Visualization of single-cell data delineated the 17 main immune cell populations in the viSNE plots (Figure 2A). The following seven T-cell types were identified: CD4$^+$/CD57$^-$ T cells, CD4$^+$/CD57$^+$ T cells, CD8$^+$/CD161$^-$ T cells, CD8$^+$/CD161$^+$/

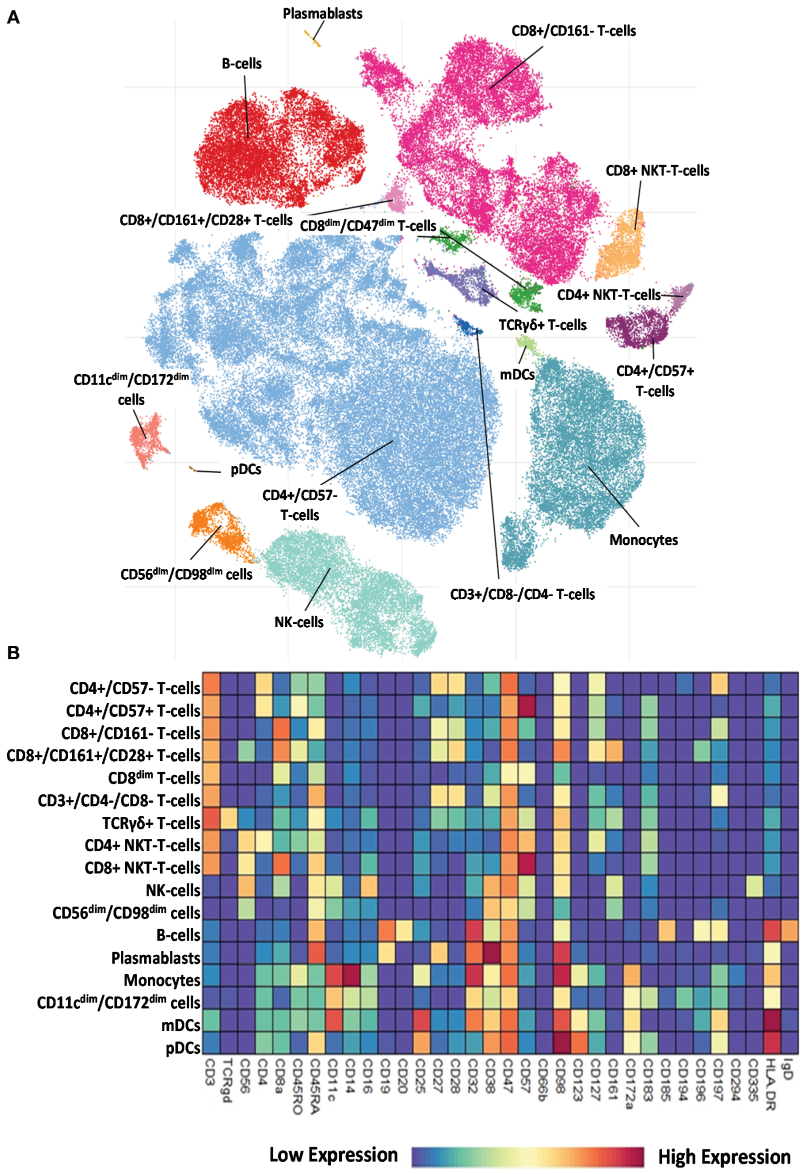

FIGURE 2
Single-cell immunophenotyping of leukocytes using 34 antibodies. **(A)** Representative viSNE diagram of the distribution of 17 main immune subsets with a single-cell resolution. Each dot represents one cell, and the size of one cloud is proportional to the size of that population. For visualization, the algorithm chose 3,000 cells randomly from each of the 52 samples. **(B)** The heatmap of the 17 main immune subsets showing their marker expression profile. Coloration indicates the intensity of the cell surface marker density. Dark red refers to high expression; dark blue refers to low expression.

$CD28^+$ T cells, $CD8^{dim}$ T cells, $CD3^+/CD4^-/CD8^-$ (DN = double negative) T cells, and TCRγ/δ T cells. The following four NK cell types were characterized: $CD4^+$ NKT cells, $CD8^+$ NKT cells, NK cells (classic NK), and $CD56^{dim}/CD98^{dim}$ cells. The following two B-cell types were analyzed: cells and plasmablasts. Three myeloid cell types were studied: monocytes, $CD11c^{dim}/CD172^{dim}$ cells, and myeloid dendritic cells (mDCs). Finally, innate lymphoid plasmacytoid dendritic cells (pDCs) were also involved in patient immunophenotyping. The expression profiles of the 17 immune cell populations for the 34 investigated markers are shown on a heatmap (Figure 2B), where data were aggregated from 52 FCS files (13 participants/group). This expression analysis supplemented the viSNE plot for the discrimination of the 17 immune cell populations, highlighting both common and cell-type-specific marker expression.

Next, we examined the distribution of the identified peripheral immune cell types among the HC, RA, SSc, and SLE groups. Significant differences in the population percentages are shown in Figure 3. Seven populations showed significantly different frequencies: $CD4^+/CD57^+$ T cells, $CD8^+/CD161^+/CD28^+$ T cells, DN T cells, $CD4^+$ NKT cells, $CD56^{dim}/CD98^{dim}$ cells, plasmablasts, and $CD11c^{dim}/CD172a^{dim}$ cells. $CD4^+/CD57^+$ aging T cells showed the lowest frequency in the SLE group (0.402% in SLE vs. 3.089% in SSc or 2.819% in HCs). $CD8^+/CD161^+/CD28^+$ mucosal-associated invariant T cells (MAIT) were at the highest frequency in healthy controls (1.351% in HCs vs. 0.405% in RA, 0.323% in SSc, and 0.286%

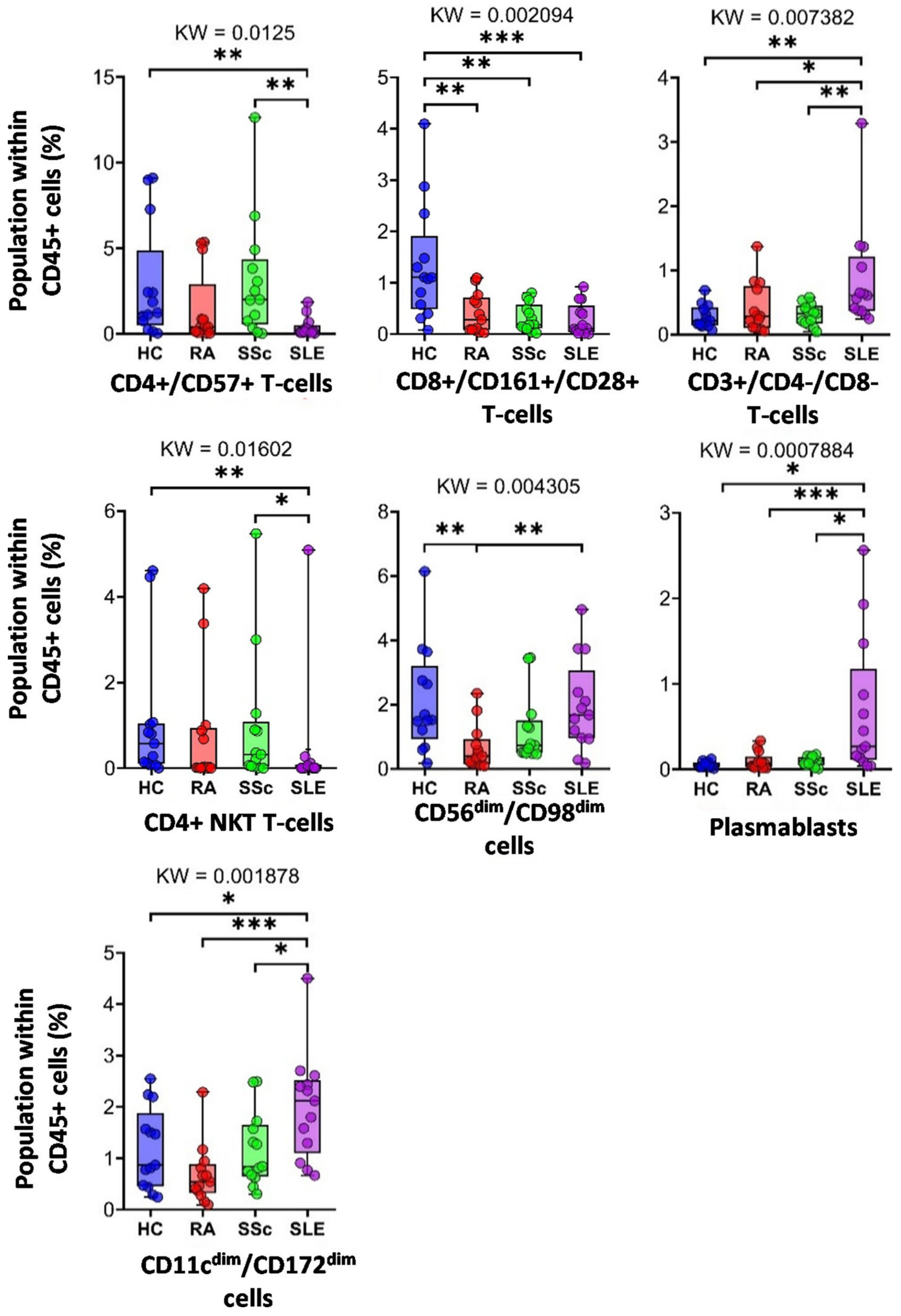

FIGURE 3
The percentage of the main immune subsets within the matured living peripheral CD45$^+$ leukocytes. Only significant changes are shown here, and non-significant differences are illustrated in Supplementary Figure 3. The groups were compared using the Kruskal–Wallis (KW) test, and the results are shown on the top of each column bar. Significance was determined when the *q*-value of the false discovery rate (FDR) was below 0.1 and $p < 0.05$; $^*p < 0.05$, $^{**}p < 0.01$, $^{***}p < 0.001$. The values shown on the column bar from the bottom to the top: lower bar = minimum value, bottom line of the chart = lower quartile (Q1), middle line = median, top line of the chart = upper quartile (Q3), upper bar = maximum value.

in SLE). DN T cells showed the highest incidence in SLE (0.867% in SLE vs. 0.279% in HCs, 0.421% in RA, or 0.307% in SSc). CD4$^+$ NKT cells were significantly decreased in SLE (0.432% in SLE vs. 1.083% in HCs or 0.968% in SSc). CD56^{dim}/CD98^{dim} NK cells were reduced in RA (0.657% in RA vs. 2.133% in HCs or 1.967% in SLE). The percentage of plasmablasts was significantly higher in SLE (0.686% in SLE vs. 0.053% in HCs, 0.101% in RA, or 0.097% in SSc). CD11c^{dim}/CD172^{dim} monocytes (with low expression of CD32, CD47, CD98, and HLA-DR) were also more prevalent in SLE (2.008% in SLE vs. 1.187% in HCs, 0.682% in RA, and 1.178% in SSc). The remaining 10 of the 17 main populations did not show differential distributions among the investigational groups. The distribution of these 10 populations is shown in Supplementary Figure 3.

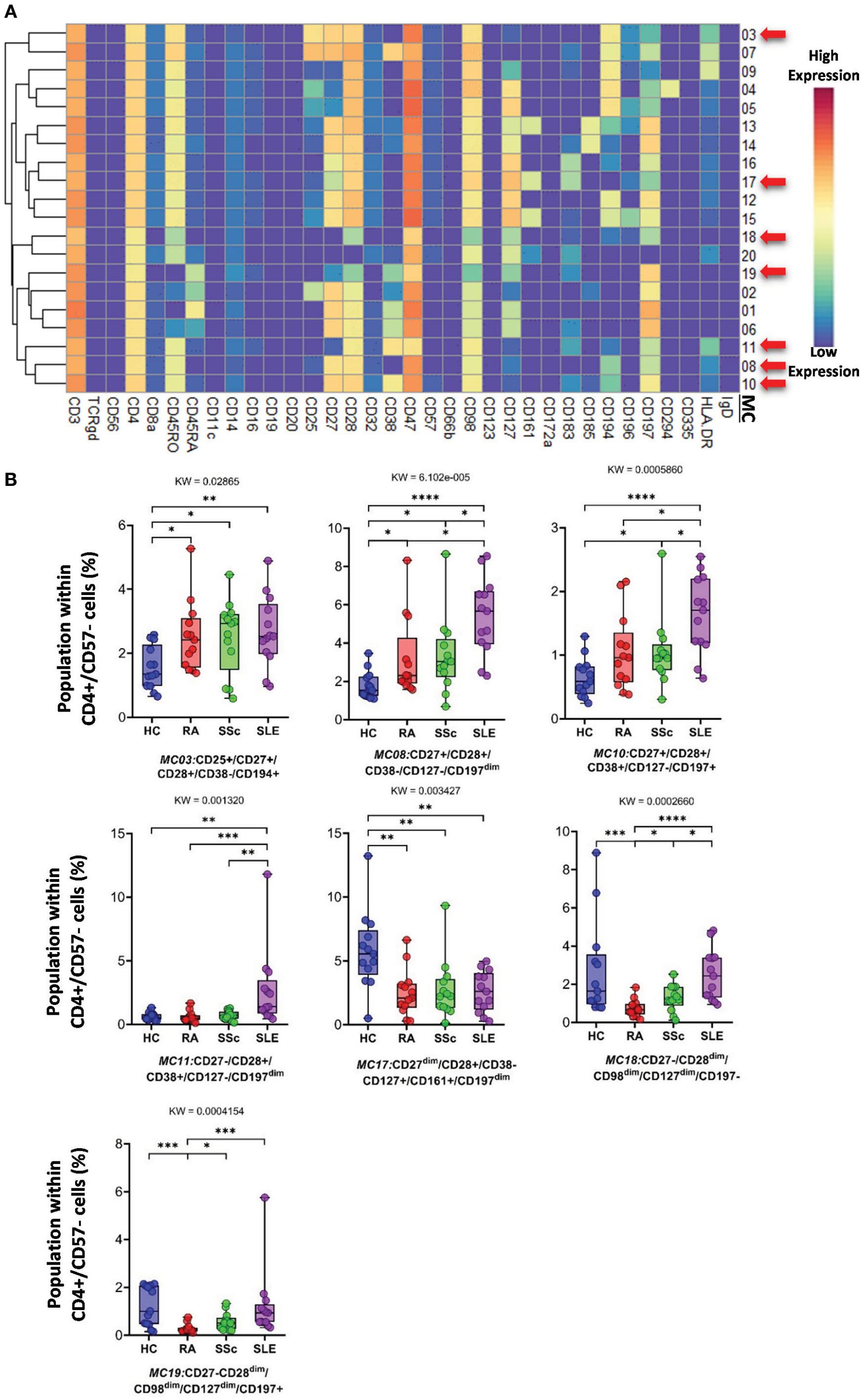

FIGURE 4
The subpopulations of CD4$^+$/CD57$^-$ helper T cells. **(A)** Marker expression heatmap of the CD4$^+$/CD57$^-$ helper T cells divided into 20 MCs by the FlowSOM algorithm. Coloration indicates the intensity of the cell surface marker density. Dark red refers to the highest expression; dark blue refers to the lowest expression. Red arrows highlight the MCs with significant differences among the studied groups. **(B)** Chart diagrams of the MCs with significantly different frequencies among the studied groups. The differences between groups were evaluated using the Kruskal–Wallis (KW) test, and the results are shown on the top of each column bar. Significance was determined when the *q*-value of the false discovery rate (FDR) was below 0.1 and $p < 0.05$; $^*p < 0.05$, $^{**}p < 0.01$, $^{***}p < 0.001$, $^{****}p < 0.0001$. The values shown on the column bar from the bottom to the top: lower bar = minimum value, bottom line of the chart = lower quartile (Q1), middle line = median, top line of the chart = upper quartile (Q3), upper bar = maximum value.

3.3 Disease-specific expression intensities of single-cell mass cytometry data comparing peripheral immune cells in HCs, RA, SSc, and SLE

Characterization of the 34-marker expression of the 17 main populations is shown in the viSNE plots in Supplementary Figure 4. The areas of the t-SNE plots correspond to the main 17 immune subsets, as shown in Figure 2A. Next, the individual expression data (only significant changes among the four groups) were plotted on the scatter plots as follows: $CD4^+/CD57^-$ T cells, $CD4^+/CD57^+$ T cells, $CD8^+/CD161^-$ T cells (Supplementary Figure 5); $CD8^+/CD161^+/CD28^+$ T cells, $CD8^{dim}$ T cells (Supplementary Figure 6); DN T cells (Supplementary Figure 7); TCR γ/δ T cells, $CD4^+$ NKT cells, $CD8^+$ NKT cells (Supplementary Figure 8); NK cells, $CD56^{dim}/CD98^{dim}$ cells (Supplementary Figure 9); B cells and plasmablasts (Supplementary Figure 10); monocytes, $CD11c^{dim}/CD172a^{dim}$ cells (Supplementary Figure 11); and mDCs and pDCs (Supplementary Figure 12).

Here, we highlight the primary differences. Except for helper T cells, CD38 expression in all cell types was higher in at least one autoimmune disease than in HCs. In the case of DN T cells (Supplementary Figure 7), $TCR\gamma/\delta^+$ T cells, $CD8a^+$ NKT cells (Supplementary Figure 8), NK cells (Supplementary Figure 9), and monocytes (Supplementary Figure 11), all three patient groups had significantly higher CD38 expression compared with HCs (in the case of NK cells, there was no significant difference between RA vs. HCs, $p = 0.0681$). The results were similar for the $CD8a^{dim}/CD47^{dim}$ population, with the addition of the SLE group showing significantly higher CD38 expression than the other two patient groups (Supplementary Figure 6). In the case of $CD8a^+/CD161^-$ cytotoxic T cells, the SLE group expressed significantly higher levels of CD38 compared with all the three other groups (Supplementary Figure 5), whereas in the case of mDCs, the difference between HCs and SLE was significant (Supplementary Figure 12). In patients with SLE, in contrast to CD38, CD45RA had the lowest expression in immune cells. We observed a significantly lower expression of CD45RA compared with the HC, RA, and SSc groups in the following cell types: $CD4^+/CD57^+$ T cells (Supplementary Figure 5), $CD8a^{dim}/CD47^{dim}$ T cells (Supplementary Figure 6), $CD56^{dim}/CD98^{dim}$ cells (Supplementary Figure 9), and B cells (Supplementary Figure 10). Comparing HCs vs. SLE, we detected significantly lower expression of CD45RA in $CD8a^+$ NKT cells (Supplementary Figure 10), NK cells (Supplementary Figure 9), and pDCs (Supplementary Figure 12) in the SLE group. There was only one exception: CD45RA expression was higher in SLE and the other two autoimmune patient groups than in HCs in DN T cells (Supplementary Figure 7). In patients with SSc, the expression of the two markers was significantly higher than that in the other three groups: CD57 expression in $CD4^+/CD57^+$ T cells (Supplementary Figure 5) and CD16 expression in NK cells (Supplementary Figure 9). Patients with RA were also differentiated from the other conditions by significantly different expressions as follows: in $CD11c^{dim}/CD172a^{dim}$ cells, the expression of CD32 and CD98 was significantly higher than in the other three groups (Supplementary Figure 11). CD98 expression in $CD56^{dim}/CD98^{dim}$ cells was higher in the RA group than in the other three groups (Supplementary Figure 9). CD47 expression in $CD11c^{dim}/CD172a^{dim}$ cells was significantly higher (Supplementary Figure 11), whereas in $CD8a^+/CD161^+/CD28^+$ T cells, it was significantly lower in patients with RA than in the HC, SSc, and SLE groups (Supplementary Figure 6). The expression of HLA-DR in $TCR\gamma/\delta^+$ T cells (Supplementary Figure 8), B cells (Supplementary Figure 10), and mDCs (Supplementary Figure 12) was also significantly lower in the RA group compared with the other three groups.

Taken together, 59 scatter plots demonstrated significant marker expression differences in the 17 main immune populations differentiating therapy-naive patients with RA, SLE, and SSc from HCs and between the SADs (Supplementary Figures 5–12). However, a detailed explanation of these data is beyond the scope of our research paper; rather, these Supplementary Data provide a resource and repository for the scientific community. Next, the authors preferred to thoroughly analyze and explain the unsupervised FlowSOM data of the subsequent analysis of the cell-type heterogeneity of the 17 main populations, the distribution of metaclusters (subpopulations), and significant differences in their marker expressions.

3.4 Characterization of the specific RA, SSc, and SLE differences in the single-cell immunophenotype of the subpopulations of the 17 main immune cell types of peripheral blood

Analysis of FlowSOM metaclusters of mass cytometry data revealed intracell-type heterogeneity of each main immune cell type in therapy-naive cases of RA, SSc, and SLE vs. HCs. First, the *$CD4^+/CD57^-$ T cells* were divided into 20 subpopulations (MCs = metaclusters), and the heatmap of the marker expression profile of the MCs is shown in Figure 4A. Visualization and a viSNE map of the MCs of $CD4^+/CD57^-$ T cells are shown in Supplementary Figure 13A. The size of the MCs in the viSNE plot is proportional to the number of cells within an MC, and the proximity of the MCs is proportional to the common marker expression profile (Supplementary Figure 13A). The cell density plots highlighted HC and disease-specific MC distribution (Supplementary Figure 13A). Seven MCs (red arrows) showed significant differences within $CD4^+/CD57^-$ T cells (Figures 4A, B, Supplementary Figure 13A). One Treg subpopulation ($CD4^+/CD25^+/CD45RA^-/CD127^-$) and MC03 ($CD25^+CD38^-CD127^-CD194^+$) were the lowest in HCs (HCs: 1.554%; RA: 2.520%; SSc: 2.520%; SLE: 2.675%). One effector memory (T_{EM}) T-cell ($CD45RA^-/CD197^-$) subpopulation, MC08 ($CD4^+/CD27^+/CD28^+/CD38^-/CD127^-/CD197^-$), was the lowest in HCs and the highest in SLE (HCs: 1.797%; RA: 3.156%; SSc: 3.320%; SLE: 5.396%). The MC10 ($CD27^+CD28^+CD38^+CD127^-CD197^+$) and $CD4^+$ central memory (T_{CM}) T-cell ($CD45RA^-CD197^-$) subpopulations were the highest in SLE (HCs: 0.648%; RA: 1.040%; SSc: 1.049%; SLE: 1.634%). The other T_{EM} subpopulation, MC11 ($CD27^-CD28^+CD38^+CD127^-CD197^-$), was also the highest in SLE, highlighting the discrimination from RA and SSc, not only from HCs (HCs: 0.624%; RA: 0.593%; SSc: 0.716%; SLE: 2.675%). MC17

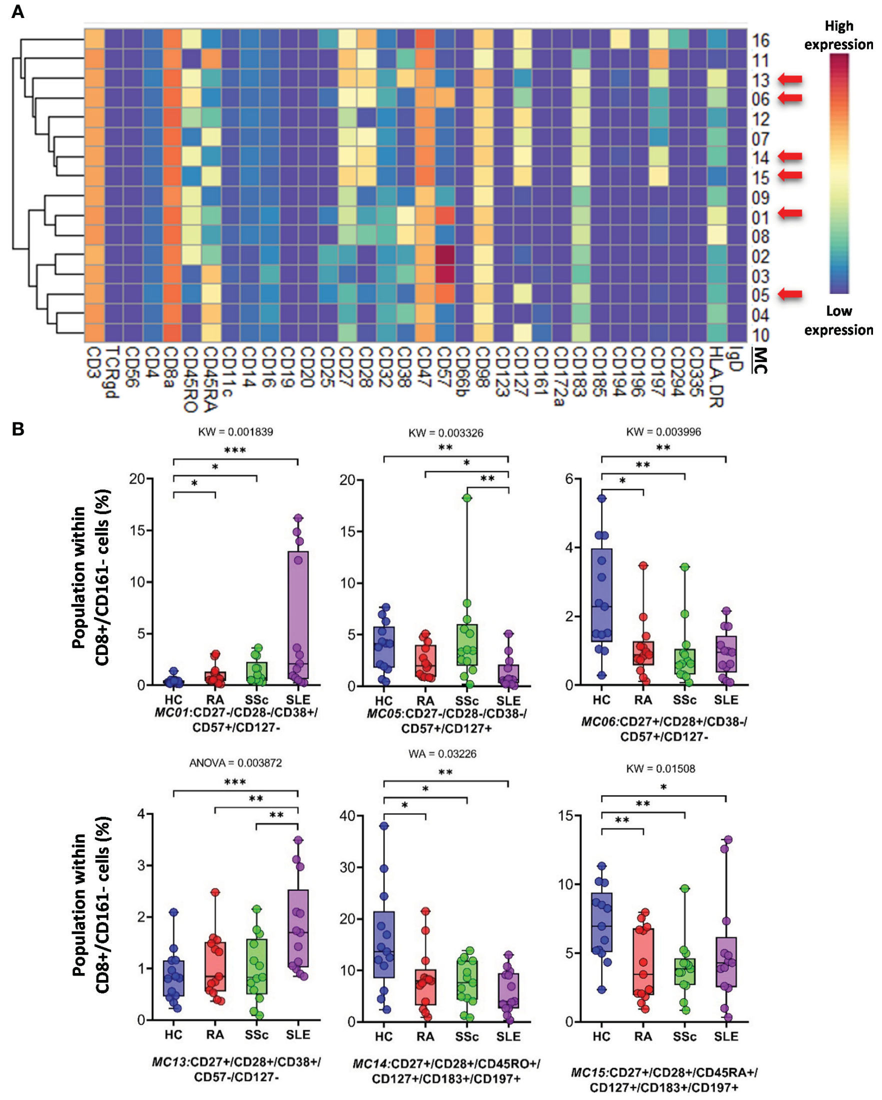

FIGURE 5

The subpopulations of CD8^{+}/CD161^{-} cytotoxic T cells. **(A)** Marker expression heatmap of the CD8^{+}/CD161^{-} helper T cells divided into 16 MCs by the FlowSOM algorithm. Coloration indicates the intensity of the cell surface marker density. Dark red refers to high expression; dark blue refers to low expression. Red arrows highlight the MCs with significant differences among the studied groups. **(B)** Chart diagrams of the MCs with significantly different frequencies among the studied groups. The differences between groups were evaluated using the Kruskal–Wallis (KW) test, Welch-ANOVA (WA), or one-way ANOVA (ANOVA), and the results are shown on the top of each column bar. Significance was determined when the q-value of the false discovery rate (FDR) was below 0.1 and $p < 0.05$; *$p < 0.05$, **$p < 0.01$, ***$p < 0.001$. The values shown on the column bar from the bottom to the top: lower bar = minimum value, bottom line of the chart = lower quartile (Q1), middle line = median, top line of the chart = upper quartile (Q3), upper bar = maximum value.

(CD27^{-}CD28^{+}CD38^{-}CD127^{+}CD161^{+}CD183^{+}CD197^{-}) was elevated in HCs (HCs: 5.793%; RA: 2.523%; SSc: 2.747%; SLE: 2.605%). Two populations (MC18 and MC19) were significantly lower in RA patients with a common lack of CD98, CD28, and CD27, and MC18 (CD27^{-}CD28$^{\text{dim}}$CD98$^{\text{dim}}$CD127^{-}CD197^{-}) was the lowest in RA patients (HCs: 2.718%; RA: 0.749%; SSc: 1.278%; SLE: 2.514%). MC19 differed from MC18 in the expression of the CCR7 receptor (CD27^{-}CD28$^{\text{dim}}$CD98$^{\text{dim}}$CD127^{-}CD197^{+}), which was significantly decreased in RA (HCs: 1.223%; RA: 0.277%; SSc: 0.570%; SLE: 1.227%).

CD8^{+}/CD161^{-} cells were divided into 16 MCs, and six MCs differed significantly from the other three groups (Figure 5A and Supplementary Figure 13B). The expression pattern of CD8^{+}/CD161^{-} MCs is summarized on the heatmap (Figure 5A). The MC01 (CD27^{-}CD28^{-}CD38^{+}CD57^{+}CD127^{-}HLA-DR^{+}) was the highest in SLE (HCs: 0.408%; RA: 1.004%; SSc: 1.300%; SLE: 5.383%). MC05 (CD27^{-}CD28^{-}CD38^{-}CD57^{+}CD127^{+}HLA-DR^{-}), which differed in CD38^{-} and CD127^{+} from MC01, was the lowest in SLE (HCs: 3.803%; RA: 2.407%; SSc: 4.731%; SLE: 1.289%) (Figure 5B). The MC05 is a subpopulation within CD8^{+} $_{\text{TEMRA}}$: CD45RA^{+}CD197^{-} (terminally differentiated effector memory cells re-expressing CD45RA). MC06 (CD27^{+}CD28^{+}CD38^{-}CD57^{+} CD127^{-}HLA-DR^{-}) differed from MC01 and MC05 in terms of CD27^{+}CD28^{+} and CD38^{-}CD127^{-} and showed the highest prevalence in HCs (HCs: 2.492%; RA: 1.083%; SSc: 0.921%; SLE: 0.910%) (Figure 5B; Supplementary Figure 13B). Similar to MC01,

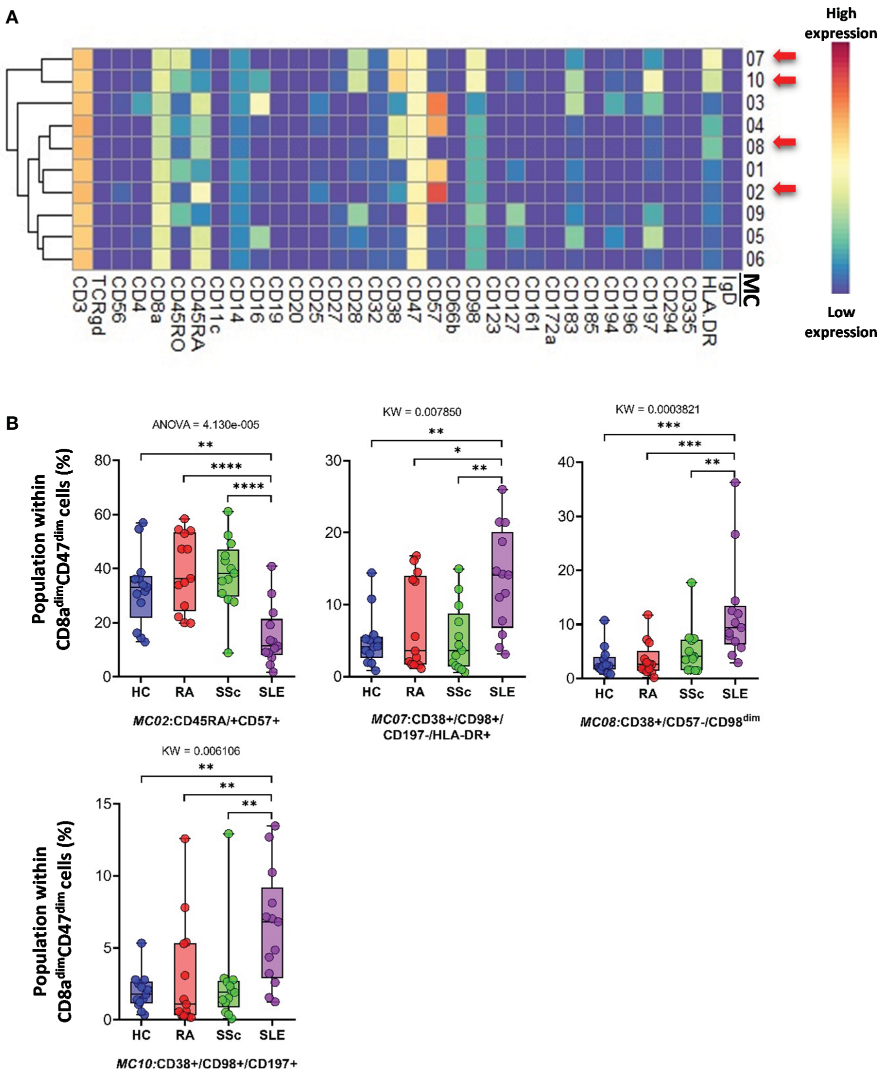

FIGURE 6

The subpopulations of CD8a^{dim}/CD47^{dim} cytotoxic T cells. **(A)** Marker expression heatmap of the CD8a^{dim}/CD47^{dim} helper T cells divided into 10 MCs by the FlowSOM algorithm. Coloration indicates the intensity of the cell surface marker density. Dark red refers to high expression; dark blue refers to low expression. Red arrows highlight the MCs with significant differences among the studied groups. **(B)** Chart diagrams of the MCs with significantly different frequencies among the studied groups. The differences between the groups were evaluated using the Kruskal–Wallis test (KW) or one-way ANOVA (ANOVA), and the results are shown on the top of each column bar. Significance was determined when the q-value of the false discovery rate (FDR) was below 0.1 and $p < 0.05$; *$p < 0.05$, **$p < 0.01$, ***$p < 0.001$, ****$p < 0.0001$. The values shown on the column bar from the bottom to the top: lower bar = minimum value, bottom line of the chart = lower quartile (Q1), middle line = median, top line of the chart = upper quartile (Q3), upper bar = maximum value.

MC13 (CD27^{+}CD28^{+}CD38^{+}CD57^{-}CD127^{-}HLA-DR^{+}) was the highest in SLE (HCs: 0.866%; RA: 1.075%; SSc: 0.991%; SLE: 1.809%): CD27^{+}CD28^{+} and CD57^{-}. MC14 (CD27^{+}CD28^{+}CD45RO^{+}CD127^{+}CD183^{+}CD197^{+}) (HCs: 15.719%; RA: 8.301%; SSc: 7.556%; SLE: 5.911%) and MC15 (CD27^{+}CD28^{+}CD45RA^{+}CD127^{+}CD183^{+}CD197^{+}) were the highest in HCs (HCs: 7.087%; RA: 4.167%; SSc: 3.941%; SLE: 5.065%).

CD8a^{dim}/CD47^{dim} T cells represented 10 MCs, in which four MCs differentiated into HCs and therapy-naive RA, SSC, and SLE. A heatmap of the expression intensities of the 34 markers in CD8a^{dim}/CD47^{dim} T cells is shown in Figure 6A. The viSNE diagram and cell density plots of CD8a^{dim}/CD47^{dim} T cells are shown in Supplementary Figure 13C. MC02 (CD45RA^{+}CD57^{+}) cells in patients with SLE were min. half (or less) than those in the other three groups (HCs: 32.482%; RA: 39.018%; SSc: 38.138%; SLE: 14.912%) (Figure 6B). The other three MCs that dominated in SLE were MC07 (CD38^{+}CD197^{-}HLA-DR^{+}) (HCs: 5.081%; RA: 7.228%; SSc: 5.179%; SLE: 13.378%), MC08 (CD38^{+}CD57^{-}CD197^{-}HLA-DR^{-}) (HCs: 3.209%; RA: 3.461%; SSc: 5.072%; SLE: 12.104%), and MC10 (CD38^{+}CD197^{+}) (HCs: 1.963%; RA: 2.981%; SSc: 2.501%; SLE: 6.404%) (Figure 6B).

CD3^{+}/CD4^{-}/CD8^{-} (DN) T cells were divided into six subpopulations (Figure 7; Supplementary Figure 14A). Red arrows on the expression heatmap indicate MCs that differentiated SADs from each other (Figure 7A). MCs were also observed in the viSNE and cell density plots (Supplementary

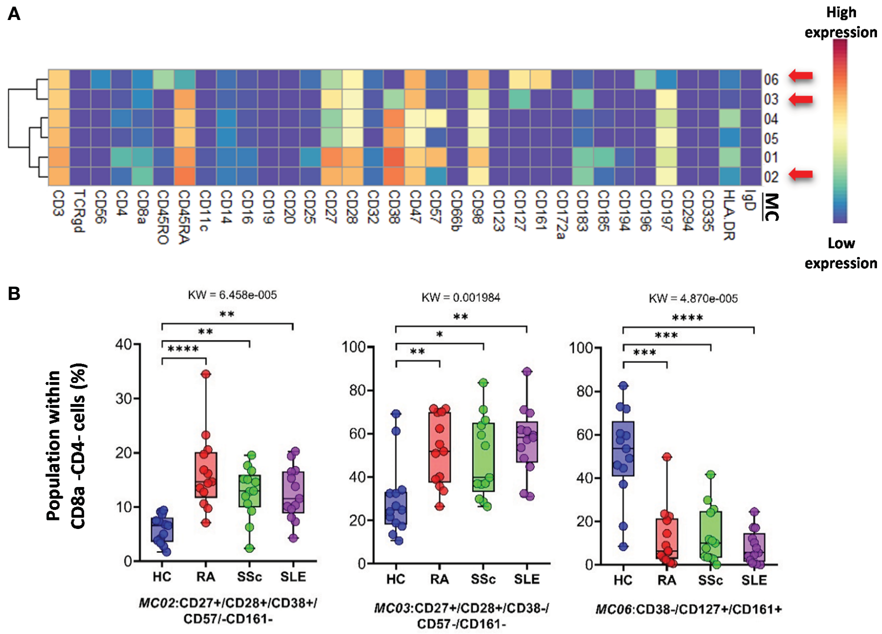

FIGURE 7
The subpopulations of CD8a$^-$/CD4$^-$ cytotoxic T cells. **(A)** Marker expression heatmap of the CD8a$^-$/CD4$^-$ helper T cells divided into six MCs by the FlowSOM algorithm. Coloration is proportional to the intensity of the cell surface marker density. Dark red refers to the highest expression; dark blue refers to no expression. Red arrows highlight the MCs with significant differences among the studied groups. **(B)** Chart diagrams of the MCs with significantly different frequencies among the studied groups. The differences between groups were evaluated using the Kruskal–Wallis test (KW), and the results are shown on the top of each column bar. Significance was determined when the q-value of the false discovery rate (FDR) was below 0.1 and $p < 0.05$; *$p < 0.05$, **$p < 0.01$, ***$p < 0.001$, ****$p < 0.0001$. The values shown on the column bar from the bottom to the top: lower bar = minimum value, bottom line of the chart = lower quartile (Q1), middle line = median, top line of the chart = upper quartile (Q3), upper bar = maximum value.

Figure 14A). MC02 (CD27$^+$CD28$^+$CD38$^+$CD57$^-$CD161$^-$), similar to CD38$^+$CD8 T cells, was the lowest in HCs (HCs: 5.868%; RA: 16.456%; SSc: 12.705%; SLE: 12.568%) (Figure 7B). The CD38$^-$ MC03 (CD27$^+$CD28$^+$CD38$^-$CD57$^-$CD161$^-$), similar to MC02, was also the lowest in HCs (HCs: 29.748%; RA: 52.147%; SSc: 48.745%; SLE: 54.712%). In contrast to MC02 and MC03, MC06 (CD38$^-$CD127$^+$CD161$^+$) was the highest in HCs (HCs: 50.881%; RA: 12.540%; SSc: 13.452%; SLE: 8.154%) (Figure 7B).

The FlowSOM algorithm revealed 12 MCs in the *TCRγ/δ T-cell* compartment. The heatmap of the expression of 34 markers in the TCR γ/δ T-cell population is shown in Figure 8A. The viSNE and cell density plots of the frequency of MCs are shown in Supplementary Figure 14B. One population of naive (CD27$^+$CD45RA$^+$) TCRγ/δ T cells, the MC01 (CD27$^+$CD197$^+$), was the highest in SLE (HCs: 7.254%; RA: 6.665%; SSc: 10.563%; SLE:19.745%) (Figure 8B). One effector memory TCRγ/δ T-cell population was the lowest in HCs (HCs: 3.024%; RA: 8.301%; SSc: 7.405%; SLE: 12.351%). In contrast to MC01, MC12 (CD45RA$^+$CD56$^+$CD57$^+$) was significantly lower in SLE patients (HCs: 11.691%; RA: 12.172%; SSc: 10.995%; SLE: 4.929%).

Classical *CD3$^-$/CD56$^+$ NK cells* represented 14 MCs. Clustering of MCs based on the expression patterns of 34 markers is shown in Figure 9A. The viSNE and cell density plots of the MCs are shown in Supplementary Figure 14C. MC03 (CD38$^-$CD57$^-$CD161$^-$) was almost two times higher in HCs than in RA and SSc and three times higher in HCs than in SLE (HCs: 5.624%; RA: 3.384%; SSc: 2.131%; SLE: 1.379%). MC05 (CD56^{bright}CD45RA$^-$) cells were more than double in the PBMCs of SLE patients compared to those in the other three groups (HCs: 4.559%; RA: 5.354%; SSc: 6.066%; SLE: 12.501%) (Figure 9B). MC07 (CD16$^+$CD38$^+$CD57$^+$CD161$^+$) showed double the frequency in SSc compared with HCs, RA, or SLE (HCs: 11.864%; RA: 11.810%; SSc: 19.294%; SLE: 11.811%). In contrast to MC05, MC10 (CD8a$^+$CD38$^+$CD57$^+$) was the lowest in patients with SLE (HCs: 10.642%; RA: 12.004%; SSc: 13.058%; SLE: 8.152%).

CD56^{dim}/CD98^{dim} NK cells were divided into seven MCs. The expression profiles of the 34 markers are shown in Figure 10A. The viSNE plots of the seven MCs and cell density plots are shown in Supplementary Figure 15A. Only one MC, MC05 (CD16$^+$/CD57$^+$/CD183$^-$), showed a significant difference, and the percentage of cells in MC05 was almost half of that in the HC, RA, and SSc groups (HCs: 4.921%; RA: 4.077%; SSc: 5.249%; SLE: 2.049%).

CD19$^+$ B cells showed high heterogeneity, with 19 identified MCs. Seven MCs differentiated patients with SADs from each other or from HCs. The expression of 34 markers among the 19 MCs is shown in Figure 11A. The viSNE and cell density plots of 19 MCs of conventional peripheral B cells are shown in Supplementary Figure 15B. Two MCs were the lowest in RA, MC02 (CD98^{dim}/CD185$^+$/IgD$^+$) (HCs: 4.320%; RA: 1.871%; SSc: 3.223%; SLE: 5.761%) and MC03 (CD38$^-$/CD98^{dim}/CD185$^-$/IgD$^-$) (HCs: 2.606%; RA: 0.490%; SSc: 0.975%; SLE: 1.662%). The number of MC07 (CD38$^+$/CD196$^+$/IgD$^-$) B cells was significantly higher in the

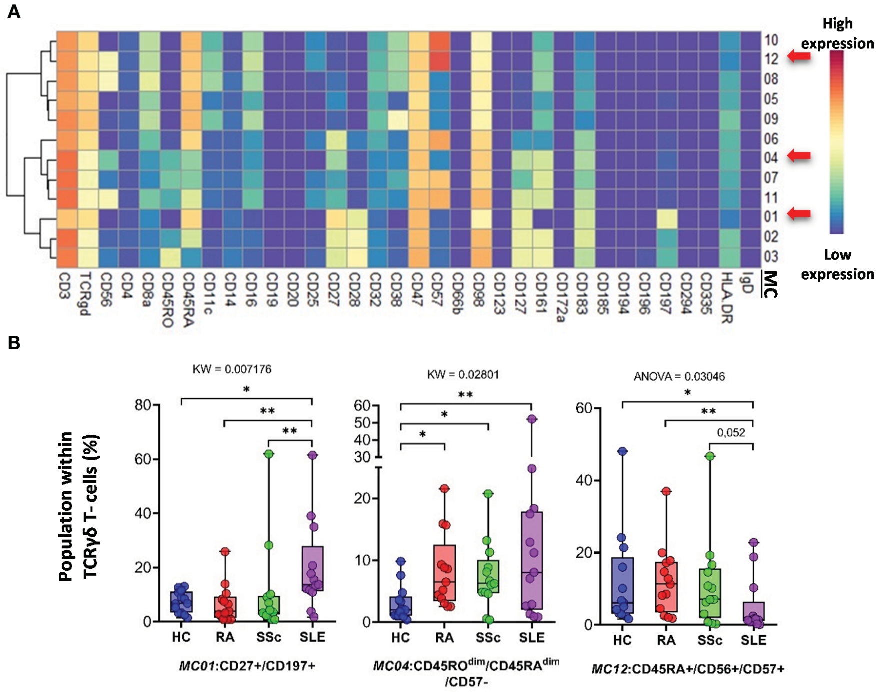

FIGURE 8

The subpopulations of TCRγδ T cells. **(A)** Marker expression heatmap of the TCRγδ T cells divided into 12 MCs by the FlowSOM algorithm. Coloration indicates the intensity of the cell surface marker density. Dark red refers to high expression; dark blue refers to low expression. Red arrows highlight the MCs with significant differences among the studied groups. **(B)** Chart diagrams of the MCs with significantly different frequencies among the studied groups. The differences were evaluated using the Kruskal–Wallis (KW) test or one-way ANOVA (ANOVA), and the results are shown on the top of each column bar. Significance was determined when the q-value of the false discovery rate (FDR) was below 0.1 and $p < 0.05$; *$p < 0.05$, **$p < 0.01$. The values shown on the column bar from the bottom to the top: lower bar = minimum value, bottom line of the chart = lower quartile (Q1), middle line = median, top line of the chart = upper quartile (Q3), upper bar = maximum value.

SLE group (HCs: 0.914%; RA: 0.802%; SSc: 0.988%; SLE: 2.638%) (Figure 11B). The number of MC08 (CD25$^+$/IgD$^+$) B cells was double in HCs than in RA or SSC and three times higher in HCs than in SLE (HCs: 16.239%; RA: 9.337%; SSc: 8.581%; SLE: 5.493%). The two CD11c$^+$ B-cell populations were significantly higher in the SLE group than in the other three groups: MC09 (CD11c$^+$/CD38$^-$/CD185$^-$) (HCs: 0.562%; RA: 0.785%; SSc: 0.571%; SLE: 2.312%) and MC16 (CD11c$^+$/CD183$^+$) (HCs: 0.337%; RA: 0.356%; SSc: 0.364%; SLE: 0.838%). The CD20$^-$/CD25$^+$ MC19 B cells were the highest in HCs (HCs: 2.772%; RA: 0.998%; SSc: 0.897%; SLE: 0.949%).

The *plasmablasts* in the peripheral blood represented two MCs depending on their expression (MC02) or lack of CD27 (MC01) (Figure 12A). The viSNE and cell density plots of plasmablasts are shown in Supplementary Figure 15C. The MC01 (CD27$^-$) was the highest in SLE (HCs: 33.527%; RA: 20.424%; SSc: 26.482%; SLE: 48.871%). In contrast, MC02 (CD27$^+$) was significantly lower in patients with SLE (HCs: 66.472%; RA: 79.575%; SSc: 73.517%; SLE: 51.128%) (Figure 12B).

The *monocytes* were classified into 15 types of MCs using the FlowSOM algorithm (Figure 13A). A heatmap of the expression profiles is shown in Figure 13A. The distribution of MCs in the viSNE and cell density plots is shown in Supplementary Figure 16. One group of classical monocytes (CD14^{++}/CD16$^-$) and MC10 (CD16$^-$CD25$^+$CD127$^-$HLA-DR$^-$) were higher in RA, SSc, and SLE than in HCs (HCs: 3.977%; RA: 8.902%; SSc: 9.207%; SLE: 9.176%) (Figure 13B). Two transitional monocyte populations (CD14^{++}/CD16$^+$) showed a higher percentage of SSc with double frequency than the other three groups: MC11 (CD16$^+$CD25$^+$CD197$^-$) (HCs: 1.369%; RA: 1.101%; SSc: 2.457%; SLE: 0.994%) and MC12 (CD16$^+$CD25$^+$CD197$^+$) (HCs: 1.081%; RA: 0.844%; SSc: 1.786%; SLE: 0.845%).

4 Discussion

To the best of our knowledge, this is the first study to characterize the detailed immunophenotypes of patients with three different newly diagnosed SADs at the same time. Additionally, all patients were investigated before starting immunosuppressive therapy; therefore, we can rule out the potential immuno-modifying effects.

First, the distribution of the main populations within the CD45$^+$ living cells was determined and compared among the investigated groups. The seven main cell types showed significant differences (Figure 3). Among the main immune populations, CD4$^-$/CD8$^-$ double-negative (DN) T cells, plasmablasts, and CD11c^{dim}/CD172a^{dim} cells showed a significantly higher average population percentage in patients with SLE than in all the other groups. No publications are available on the CD11c^{dim}/CD172a^{dim} in the context of SLE. In contrast, CD4$^+$/CD57$^+$ T cells and CD4$^+$ NKT

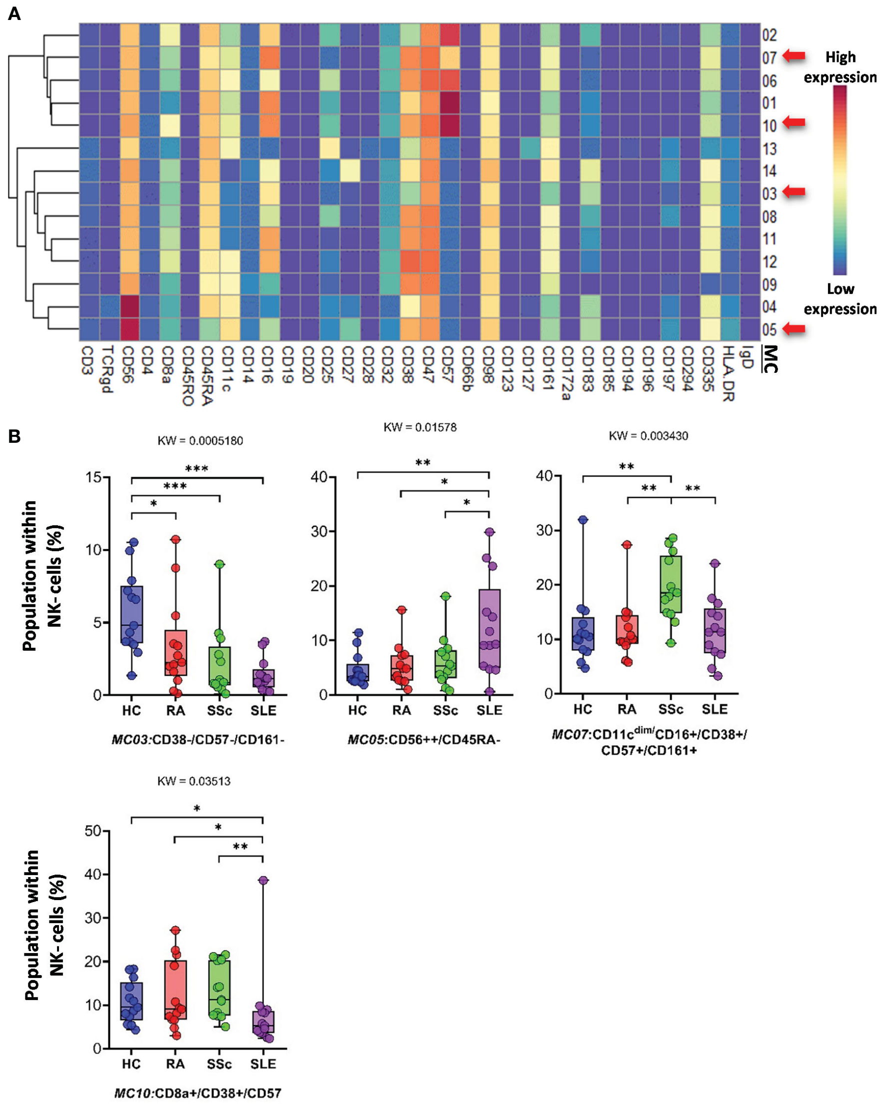

FIGURE 9
The subpopulations of NK cells. **(A)** Marker expression heatmap of the NK cells divided into 14 MCs by the FlowSOM algorithm. Coloration indicates the intensity of the cell surface marker density. Dark red refers to high expression; dark blue refers to low expression. Red arrows highlight the MCs with significant differences among the studied groups. **(B)** Chart diagrams of the MCs with significantly different frequencies among the studied groups. The differences between groups were evaluated using the Kruskal–Wallis (KW) test, and the results are shown on the top of each column bar. Significance was determined when the q-value of the false discovery rate (FDR) was below 0.1 and $p < 0.05$; $^{*}p < 0.05$, $^{**}p < 0.01$, $^{***}p < 0.001$. The values shown on the column bar from the bottom to the top: lower bar = minimum value, bottom line of the chart = lower quartile (Q1), middle line = median, top line of the chart = upper quartile (Q3), upper bar = maximum value.

cells were present in significantly lower numbers in patients with SLE than in healthy controls and the SSc group. The average population of CD8$^+$/CD161$^+$/CD28$^+$ cytotoxic T cells was significantly higher in healthy individuals than in patients with SADs. Two populations were identified, CD8a^{dim}/CD47^{dim} and CD56^{dim}/CD98^{dim}, with the mean population percentages within CD45$^+$ single cells being the lowest in the RA group. In the case of the CD56^{dim}/CD98^{dim} population, the difference was significant compared with the SLE and HC groups. This observation is also considered novel.

Second, the expression levels of the 34 markers in the main populations were compared between the groups. In summary, 59 scatter plots showed significant differences between at least two groups (Supplementary Figures 4–12). The most potent marker is cyclic ADP-ribose hydrolase (CD38). It was highly expressed in a variety of immune cells in all three therapy-naive patient groups compared with HCs: DN T cells, TCRγ/δ$^+$ T cells, CD8a$^+$ NKT cells, NK cells, and monocytes. Similarly, the CD8a^{dim}/CD47^{dim} population in the SLE group showed significantly higher CD38 expression than those in the RA and SSc groups. CD38 expression was also significantly higher in CD8a$^+$/CD161$^-$ cytotoxic T cells in the SLE group than in the other groups. CD38 as a targeted therapy (daratumumab) has been approved for multiple myeloma, but it has also been suggested for SADs, particularly SLE, where plasma cells do not express CD20, leading to rituximab resistance; however, they highly express the CD38 (Figure 12A) (45–47).

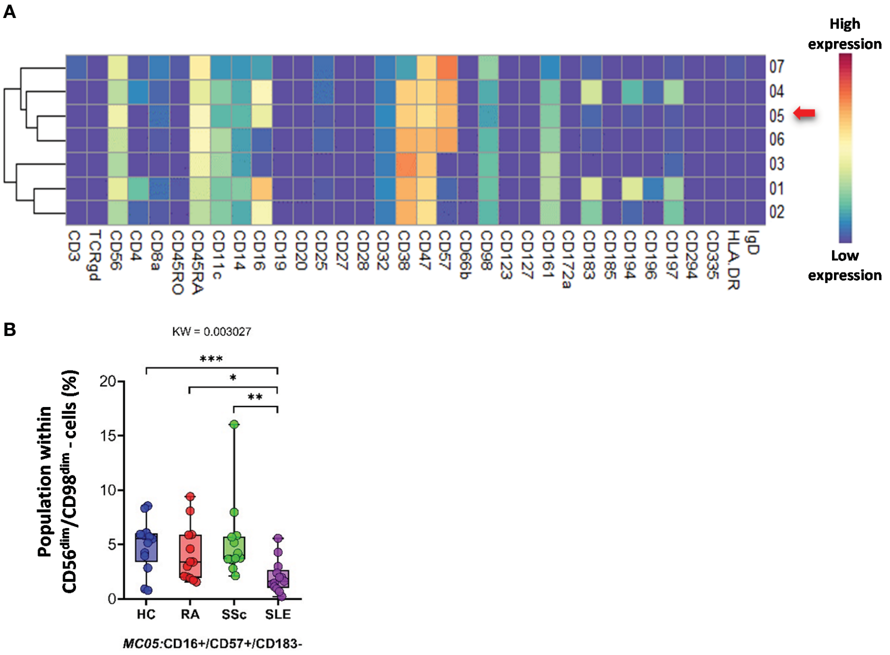

FIGURE 10
The subpopulations of CD56^{dim}/CD98^{dim} cells. **(A)** Marker expression heatmap of the CD56^{dim}/CD98^{dim} cells divided into seven MCs by the FlowSOM algorithm. Coloration indicates the intensity of the cell surface marker density. Dark red refers to high expression; dark blue refers to low expression. Red arrows highlight the MCs with significant differences among the studied groups. **(B)** Chart diagrams of the MCs with significantly different frequencies among the studied groups. The differences between the groups were evaluated using the Kruskal–Wallis (KW) test, and the results are shown on the top of each column bar. Significance was determined when the q-value of the false discovery rate (FDR) was below 0.1 and $p < 0.05$; $^*p < 0.05$, $^{**}p < 0.01$, $^{***}p < 0.001$. The values shown on the column bar from the bottom to the top: lower bar = minimum value, bottom line of the chart = lower quartile (Q1), middle line = median, top line of the chart = upper quartile (Q3), upper bar = maximum value.

Third, each immune cell population was divided into subpopulations (MCs) using the FlowSOM algorithm (Figures 4–13; Supplementary Figures 13–16). Subpopulation percentages were compared among the populations in different groups. We identified 121 MCs from 10 major immune cell populations. In addition, T cells were classified into 64 MCs based on the expression of 34 markers. Twenty-three T-cell subpopulations were found with significantly different percentages between at least two groups (Figures 4–8). Tregs are known to be present at lower frequencies in HCs than in the SSc group (48, 49), and we identified a subpopulation of Tregs (MC03: CD25$^+$CD38$^-$CD127$^-$CD194$^+$) within CD4$^+$CD57$^-$ T cells with a decreased ratio in HCs. Burnst et al. reported elevated expression of CD38 in effector memory CD4$^+$ T cells (50). We identified two CD4$^+$ T$_{EM}$ which were present in higher percentages in SLE: CD38 negative (MC08: CD45RA$^-$CD4$^+$CD27$^+$CD28$^+$CD38$^-$CD127$^-$CD197$^-$) and CD38 positive (MC11: CD45RA$^-$CD4$^+$CD27$^-$CD28$^+$CD38$^+$CD127$^-$CD197$^-$), differentiating SLE from therapy-naive RA and SSc. Lima et al. reported that CD38$^+$HLA-DR$^+$ cytotoxic T cells were elevated in patients with SLE (51). We demonstrated that the MC01 (CD27$^-$CD28$^-$CD38$^+$CD57$^+$CD127$^-$HLA-DR$^+$) population in CD8$^+$CD161$^-$ T cells was the best in differentiating SLE from RA and SSc. Comte et al. did not observe differences in the ratio of CD8$^+$ T$_{EMRA}$ (CD45RA$^+$CD197$^-$) between HCs and patients with SLE (52). In contrast, we demonstrated that one subpopulation of CD8$^+$ T$_{EMRA}$, the MC05 (CD27$^-$CD28$^-$CD38$^-$CD57$^+$CD127$^+$), was the lowest in SLE compared with HCs, RA, and SSc. Yuan et al. showed a higher percentage of naive CD8$^+$ T cells in HCs vs. SLE (53). In addition, the highest percentage of naive CD8$^+$ T-cell subpopulation was found in HCs, whereas MC15 (CD27$^+$CD28$^+$CD45RA$^+$CD45RO$^-$CD127$^+$CD183$^+$CD197$^+$) was higher in HCs than in SADs. Cho et al. reported that DN MAIT cells were more prevalent in HCs than in patients with RA and SLE (54). Our results also confirmed a lower ratio of MC06 DN T cells (CD38$^-$CD127$^+$CD161$^+$) in patients with SLE. The unequivocal role of TCRγ/δ T cells in the pathogenesis of SADs has been described recently (55, 56). We identified three subpopulations of TCRγ/δ T cells differentiating SLE from HCs, RA, and SSc. Two of these were significantly higher in SLE (MC01: CD27$^+$CD197) (MC04: CD45RO^{dim}CD45RA^{dim}CD57$^-$), and one was significantly lower in SLE (MC12: CD45RA$^+$CD56$^+$CD57$^+$).

Subsequently, 57 subpopulations (MCs) of non-T-cell compartments were demonstrated in CD3$^-$ cells; among these, 17 populations showed significantly different subpopulation percentages between at least two investigated groups (Figures 9–13). A lower proportion of CD56$^+$ NK cells has been reported in patients with RA and SLE (57, 58). In line with this, we identified one subpopulation of NK cells, MC03 (CD38$^-$CD57$^-$CD161$^-$), with the highest percentage in HCs. Schepis et al. reported an increased frequency of CD56^{bright}CD16$^-$ NK cells in patients with SLE compared to HCs (59). Based on our study, the number of MC05 (CD56^{bright}CD45RA$^-$CD16^{low}) cells was the highest in SLE. In

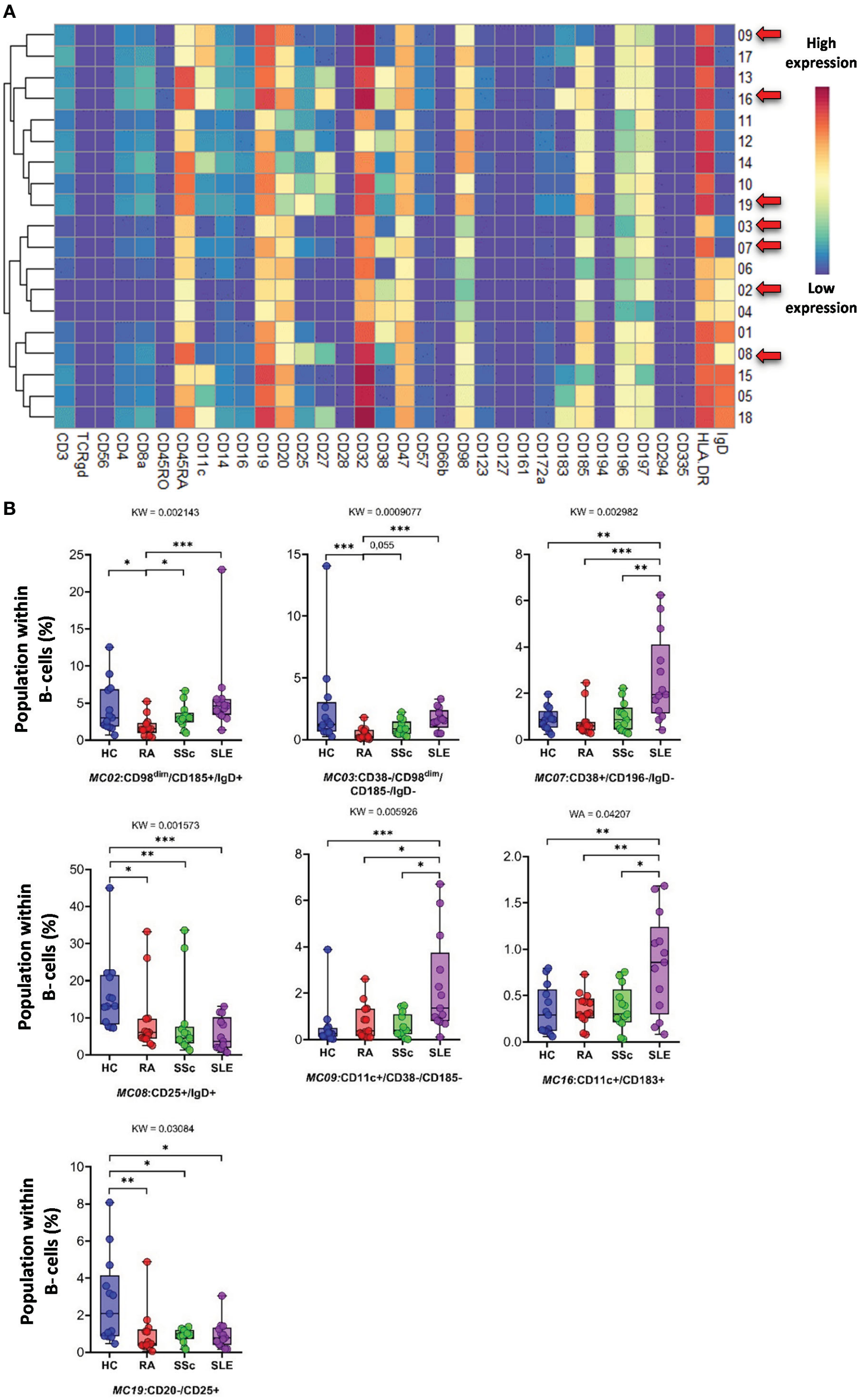

FIGURE 11
The subpopulations of B cells. **(A)** Marker expression heatmap of the B cells divided into 19 MCs by the FlowSOM algorithm. Coloration indicates the intensity of the cell surface marker density. Dark red refers to high expression; dark blue refers to low expression. Red arrows highlight the MCs with significant differences among the studied groups. **(B)** Chart diagrams of the MCs with significantly different frequencies among the studied groups. The differences among the groups were evaluated using the Kruskal–Wallis (KW) test, and the results are shown on the top of each column bar. Significance was determined when the *q*-value of the false discovery rate (FDR) was below 0.1 and $p < 0.05$; $^{*}p < 0.05$, $^{**}p < 0.01$, $^{***}p < 0.001$. The values shown on the column bar from the bottom to the top: lower bar = minimum value, bottom line of the chart = lower quartile (Q1), middle line = median, top line of the chart = upper quartile (Q3), upper bar = maximum value.

contrast to MC05, the MC10 (CD8a^{+}CD38^{+}CD57^{+}) NK cell population was the lowest in patients with SLE. A lower ratio of CD56^{+}CD57^{+} NK cells in SLE compared to HCs was reported previously by Lu et al. (60); however, our data also included comparisons with RA and SSc. We identified a subpopulation of CD56^{dim}/CD98^{dim} MC05 (CD16^{+}/CD57^{+}/CD183^{-}) cells with a significant decrease in SLE, but there is a lack of data on these cells in the context of SADs. Amu et al. showed that

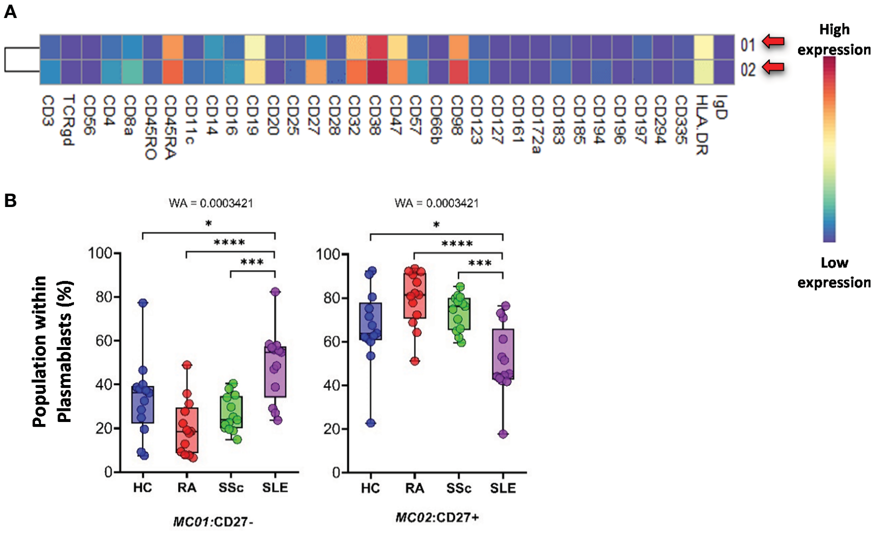

FIGURE 12
The subpopulations of plasmablasts. **(A)** Marker expression heatmap of the plasmablasts divided into two MCs by the FlowSOM algorithm. Coloration indicates the intensity of the cell surface marker density. Dark red refers to high expression; dark blue refers to low expression. Red arrows highlight the MCs with significant differences among the studied groups. **(B)** Chart diagrams of the MCs with significantly different frequencies among the studied groups. The differences between the groups were evaluated using the Welch-ANOVA test (WA), and the results are shown on the top of each column bar. Significance was determined when the q-value of the false discovery rate (FDR) was below 0.1 and $p < 0.05$; *$p < 0.05$, ***$p < 0.001$, ****$p < 0.0001$. The values shown on the column bar from the bottom to the top: lower bar = minimum value, bottom line of the chart = lower quartile (Q1), middle line = median, top line of the chart = upper quartile (Q3), upper bar = maximum value.

CD25$^+$CD20$^+$CD27$^+$ B cells were the lowest in patients with SLE compared with HCs (61). Our results also supported the lowest percentage of MC08 (CD25$^+$CD20$^+$CD27$^+$IgD$^+$) B cells in SLE compared with that in HCs, RA, and SSc. Rincon-Arevalo et al. reported an increased proportion of CD11c$^+$ B cells in patients with SLE (62). Additionally, we differentiated two CD11c subsets of B cells with the highest frequency in SLE: MC09 (CD11c$^+$CD38$^-$CD185$^-$) and MC16 (CD11c$^+$CD183$^+$). B cells expressing CD11c and lacking CD21 expression (age-associated B cells = ABCs) are reported as an increasing population in SLE (63). Indeed, our MC16 population expresses CD11c, but we highlighted the co-expression of CD183 (or panel missed CD21), which differentiates it from the ABCs. The M16 B-cell population (IgD$^-$CD27$^+$) is different also from the double-negative IGD$^-$CD27$^-$ population that was described by Wang et al. in SLE (64). The peripheral composition of plasmablasts was shared with CD27$^-$ and CD27$^+$ MCs with the highest and lowest frequencies in SLE, respectively. Toapanta et al. reported the induction of CD27 plasmablasts after Shigella LPS treatment, with a correlation between IgA and IgG production (65). However, limited data are available on CD27$^-$ plasmablasts in SLE. Lesco et al. showed that CD14^{bright}CD16$^-$ classic monocytes were increased in SSc patients compared with HCs (66). A subpopulation of classic monocytes was identified by our research group, MC10 (CD16$^-$CD25$^+$CD127$^-$HLA-DR$^-$), with elevated levels in all investigated SADs compared with HCs. Additionally, we found two intermediate (CD14^{bright}/CD16$^+$) monocyte populations, MC11 (CD16$^+$CD25$^+$CD183$^-$) and MC12 (CD16$^+$CD25$^+$CD183$^+$), which were higher in SSc than in HCs, RA, and SLE.

In summary, we highlight seven metaclusters, each differentiating one group from the other three. In HCs, compared with patients with SADs, the following subpopulations showed significantly lower subpopulation percentages: MC08 (CD27$^+$/CD28$^+$/CD38$^-$CD127$^-$/CD197^{dim}) in CD4$^+$/CD57$^-$ T cells, and the SLE group also differed from the other two SAD groups. The subpopulations MC04 (CD45RO^{dim}/CD45RA^{dim}/CD57$^-$) of TCRγ/δ$^+$ T cells and MC10 (CD16$^-$/CD25$^+$/CD127$^-$/HLA-DR$^-$) of monocytes had the lowest percentage in HCs. In contrast, the following subpopulation percentages were significantly higher in HCs than in SADs: MC06 (CD27$^+$/CD28$^+$/CD38$^-$CD57$^+$/CD127$^-$) in CD8a$^+$/CD161$^-$ T cells and MC03 (CD38$^-$/CD57$^-$/CD161) in NK cells. In patients with SLE, we detected a significantly higher subpopulation percentages of MC07 (CD38$^+$/CD196$^-$/IgD$^-$) in B cells and MC01 (CD27$^-$) in plasmablasts compared with the other three groups. The findings of our study showed that the peripheral immune landscape demonstrated circulating immune cell attributes that discriminated the three SADs, therapy-naive RA, SSc, and SLE, from each other, as well as from HCs.

This study is based on several years of patient sample collection. For all inflammatory rheumatic diseases, the time between the initial symptoms and the actual diagnosis can be years. In addition, patients are almost invariably admitted to specialist care centers following a certain form of anti-inflammatory or immunosuppressive treatment. Both the

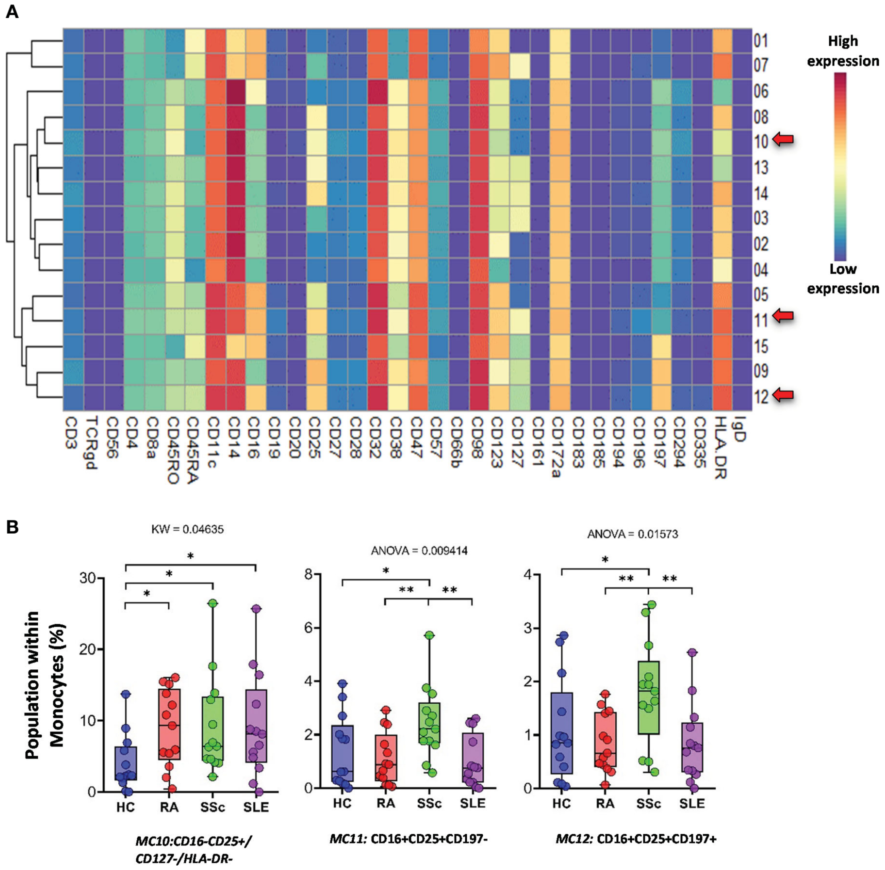

FIGURE 13
The subpopulations of monocytes. **(A)** Marker expression heatmap of the monocytes divided into 15 MCs by the FlowSOM algorithm. Coloration indicates the intensity of the cell surface marker density. Dark red refers to high expression; dark blue refers to low expression. Red arrows highlight the MCs with significant differences among the studied groups. **(B)** Chart diagrams of the MCs with significantly different frequencies among the studied groups. The differences between the groups were evaluated using the Kruskal–Wallis (KW) test or one-way ANOVA (ANOVA), and the results are shown on the top of each column bar. Significance was determined when the *q*-value of the false discovery rate (FDR) was below 0.1 and $p < 0.05$; $^*p < 0.05$, $^{**}p < 0.01$. The values shown on the column bar from the bottom to the top: lower bar = minimum value, bottom line of the chart = lower quartile (Q1), middle line = median, top line of the chart = upper quartile (Q3), upper bar = maximum value.

prolonged duration of illness and the treatments used can significantly alter the patient's immunophenotype. Mapping the immunophenotype of early and untreated patients can be of importance in several ways. In the early stages of the disease, there can be a lot of overlap between different syndromes. In many cases, they are identified as an undifferentiated autoimmune syndrome. Early mapping of the immunophenotype can help in early diagnosis. Knowledge of the immunophenotype prior to therapy can also be a prognostic marker for subsequent response to therapy. Changes in disease activity can be used to identify markers of disease severity. This may provide the basis for further prospective analysis following the current study. Identifying difficult-to-treat patient groups is another major clinical challenge. Furthermore, the results of our present study may help to map this patient group, including various possible organ-specific immunological processes. Our results, including significant differences in several main cell populations, marker expression intensities, and metaclusters, may contribute to clarify the prior described, challenging autoimmune diseases. Additionally, our dataset about early, untreated patients may show overt disease pathology related to the etiology of the disease unveiling potential therapeutic targets that could contribute to the development of novel therapies.

Data availability statement

The raw data supporting the conclusions of this article will be made available by the authors, without undue reservation.

Ethics statement

Details about the study design and handling of biological materials were submitted to the Human Investigation Review Board of the University of Szeged under the 149/2019-SZTE Project Identification code. The studies were conducted in accordance with the local legislation and institutional requirements. The participants provided their written informed consent to participate in this study.

Author contributions

JB: Conceptualization, Data curation, Formal Analysis, Investigation, Methodology, Software, Validation, Visualization, Writing – original draft. ÁZ: Investigation, Methodology, Writing – original draft. VB: Investigation, Writing – original draft. LP: Conceptualization, Funding acquisition, Project administration, Resources, Writing – original draft. AB: Conceptualization, Funding acquisition, Investigation, Resources, Supervision, Writing – original draft, Writing – review & editing. GS: Conceptualization, Funding acquisition, Project administration, Resources, Supervision, Visualization, Writing – original draft, Writing – review & editing.

Funding

The author(s) declare that financial support was received for the research, authorship, and/or publication of this article. This research was funded by the GINOP-2.3.2-15-2016-00030, 2020-1.1.6-JÖVŐ–2021-00003, 2022-1.2.6-TÉT-IPARI-TR-2022-00023, and 142877 FK22 grants from the National Research, Development, and Innovation Office (NKFI), Hungary. This work was supported by an SZTE OK-KKA Hetényi 2020 grant (AB). This work was supported by the János Bolyai Research Scholarship of the Hungarian Academy of Sciences BO/00582/22/8 (GS) and the ÚNKP-23-5-SZTE-694 New National Excellence Program of the Ministry for Innovation and Technology (GS).

Acknowledgments

We would like to acknowledge the excellent assistance of Szilvia Pördi és Cynthia Szabó. We would like to thank Editage (www.editage.com) for English language editing.

Conflict of interest

GS is an employee of Astridbio Technologies Ltd.

The remaining authors declare that the research was conducted in the absence of any commercial or financial relationships that could be construed as a potential conflict of interest.

Publisher's note

Supplementary material

The Supplementary Material for this article can be found online at: https://www.frontiersin.org/articles/10.3389/fimmu.2024.1376933/full#supplementary-material

SUPPLEMENTARY FIGURE 1

Determination of live single cells and debarcoding of the CyTOF FCS files. Cells were gated first negative for 140Ce and 142Ce calibration bead specific metal tags (upper row on the left). Singlets were gated based on 191Ir DNA labeling (upper row in the middle). Live cells were gated based on negativity for 103Rh cationic nucleic acid intercalator Live/Dead reagent (Fluidigm) (upper row on the right). Debarcoding of the patients was carried out using the gating on CD45+ positive cells such as the following: HC: 116Cd CD45+, RA: 89Y CD45+, SSc: 114Cd CD45+, SLE: 106Cd CD45+.

SUPPLEMENTARY FIGURE 2

Data clarification of CyTOF FCS files based on manual gating excluding cell doublets. Double negative cells were processed further during the data analysis for CD56-/CD294-, CD3-/CD14-, CD19-/CD14-, CD19-/CD3-, CD56-/CD19-, CD20-/CD16-.

SUPPLEMENTARY FIGURE 3

The percentage of the main immune subsets within the matured living peripheral CD45+ leukocytes. The non-significant differences are demonstrated here, significant differences are demonstrated in Figures 2. The values shown on the column bar are from the bottom to the top: lower bar = minimum value, bottom line of the chart = lower quartile (Q1), middle line = median, top line of the chart = upper quartile (Q3), upper bar = maximum value.

SUPPLEMENTARY FIGURE 4

The tSNE plots of the expression profile of 34 markers. The areas of the tSNE plots corresponds to the main 17 immune subset described in Figures 1A. The red coloration is proportional with the higher, the blue coloration is proportional with the lower expression levels within the 17 immune subsets. Aggregated data of the 52 cases.

SUPPLEMENTARY FIGURE 5

The significant differences in the marker expression profile (median metal intensity) of CD4+/CD57- T-cells (upper row) and the CD8a+/CD161- T-cells (lower row). The statistical method (WA = Welch-ANOVA, or ANOVA = one way ANOVA) is shown on the top of each column bar. Significance was accepted when the q value of the false discovery rate (FDR) was below 0.1 and $*p<0.05$, $**p<0.01$. The values shown on the column bar are from the bottom to the top: lower bar = minimum value, bottom line of the chart = lower quartile (Q1), middle line = median, top line of the chart = upper quartile (Q3), upper bar = maximum value.

SUPPLEMENTARY FIGURE 6

The significant differences in the marker expression profile (median metal intensity) of CD8+/CD161+/CD28+ T-cells (upper row) and the CD8a+dim T-cells (lower row). The statistical method (KW= Kruskal Wallis test; WA = Welch-ANOVA, or ANOVA = one way ANOVA) is shown on the top of each column bar. Significance was accepted when the q value of the false discovery rate (FDR) was below 0.1 and $*p<0.05$, $**p<0.01$, $***p<0.001$, $****p<0.0001$. The values shown on the column bar are from the bottom to the top: lower bar = minimum value, bottom line of the chart = lower quartile (Q1), middle line = median, top line of the chart = upper quartile (Q3), upper bar = maximum value.

SUPPLEMENTARY FIGURE 7

The significant differences in the marker expression profile (median metal intensity) of CD3+/CD4-/CD8a-T-cells. The statistical method (KW= Kruskal Wallis test; WA = Welch-ANOVA, or ANOVA = one way ANOVA) is shown on the top of each column bar. Significance was accepted when the q value of the false discovery rate (FDR) was below 0.1 and $*p<0.05$, $**p<0.01$, $***p<0.001$, $****p<0.0001$. The values shown on the column bar are from the bottom to the top: lower bar = minimum value, bottom line of the chart = lower quartile (Q1), middle line = median, top line of the chart = upper quartile (Q3), upper bar = maximum value.

SUPPLEMENTARY FIGURE 8

The significant differences in the marker expression profile (median metal intensity) of TCRgd+ T-cells (upper row), CD4+ NKT, or CD8a+ NKT cells (lower row). The statistical method (KW= Kruskal Wallis test; WA = Welch-ANOVA, or ANOVA = one way ANOVA) is shown on the top of each column bar. Significance was accepted when the q value of the false discovery rate (FDR) was below 0.1 and *p<0.05, **p<0.01, ***p<0.001, ****p<0.0001. The values shown on the column bar are from the bottom to the top: lower bar = minimum value, bottom line of the chart = lower quartile (Q1), middle line = median, top line of the chart = upper quartile (Q3), upper bar = maximum value.

SUPPLEMENTARY FIGURE 9

The significant differences in the marker expression profile (median metal intensity) of NK cells (upper row), CD56dim/CD98 dim cells (lower row). The statistical method (KW= Kruskal Wallis test; WA = Welch-ANOVA, or ANOVA = one way ANOVA) is shown on the top of each column bar. Significance was accepted when the q value of the false discovery rate (FDR) was below 0.1 and *p<0.05, **p<0.01, ***p<0.001, ****p<0.0001. The values shown on the column bar are from the bottom to the top: lower bar = minimum value, bottom line of the chart = lower quartile (Q1), middle line = median, top line of the chart = upper quartile (Q3), upper bar = maximum value.

SUPPLEMENTARY FIGURE 10

The significant differences in the marker expression profile (median metal intensity) of B-cells (upper and middle rows), plasmablasts (lower row). The statistical method (KW= Kruskal Wallis test; ANOVA = one way ANOVA) is shown on the top of each column bar. Significance was accepted when the q value of the false discovery rate (FDR) was below 0.1 and *p<0.05, **p<0.01, ***p<0.001, ****p<0.0001. The values shown on the column bar are from the bottom to the top: lower bar = minimum value, bottom line of the chart = lower quartile (Q1), middle line = median, top line of the chart = upper quartile (Q3), upper bar = maximum value.

SUPPLEMENTARY FIGURE 11

he significant differences in the marker expression profile (median metal intensity) of Monocytes (upper row), CD11cdim/ CD172adim cells (middle and lower rows). The statistical method (KW= Kruskal Wallis test; WA = Welch-ANOVA, or ANOVA = one way ANOVA) is shown on the top of each column bar. Significance was accepted when the q value of the false discovery rate (FDR) was below 0.1 and *p<0.05, **p<0.01, ***p<0.001, ****p<0.0001. The values shown on the column bar are from the bottom to the top: lower bar = minimum value, bottom line of the chart = lower quartile (Q1), middle line = median, top line of the chart = upper quartile (Q3), upper bar = maximum value.

SUPPLEMENTARY FIGURE 12

The significant differences in the marker expression profile (median metal intensity) of mDCs cells (upper row), pDCs cells (lower row). The statistical method (KW= Kruskal Wallis test; WA = Welch-ANOVA, or ANOVA = one way ANOVA) is shown on the top of each column bar. Significance was accepted when the q value of the false discovery rate (FDR) was below 0.1 and *p<0.05, **p<0.01, ***p<0.001. The values shown on the column bar are from the bottom to the top: lower bar = minimum value, bottom line of the chart = lower quartile (Q1), middle line = median, top line of the chart = upper quartile (Q3), upper bar = maximum value.

SUPPLEMENTARY FIGURE 13

Visualizations, tSNE maps of the subpopulations (metaclusters, MCs) defined by the FlowSOM analysis. **(A)** The 2−dimensional viSNE plots of the 20 MCs of CD4+/CD57- T-cells (left). **(B)** The 2−dimensional viSNE plots of the 16 MCs of CD8+/CD161- T-cells (left). **(C)** The 2−dimensional viSNE plots of the 10 MCs of CD8adim/CD47dim T-cells (left). One dot corresponds to one cell (left). The different colors represent the different MCs (left). The red arrows highlight the significant differences in the distribution of MCs among the studied groups. The cell density plots demonstrate the number of cells in the MCs within the studied groups (right). Red color is proportional with high, blue color is proportional with low cell density (right). Red boxes and Arabic numbers demonstrate the distribution of MCs with significant differences among the studied groups.

SUPPLEMENTARY FIGURE 14

Visualisations, viSNE maps of the subpopulations (metaclusters, MCs) defined by the FlowSOM analysis. **(A)** The 2−dimensional viSNE plots of the 6 MCs of CD4-/CD8- T-cells (left). **(B)** The 2−dimensional viSNE plots of the 12 MCs of TCRgd+T-cells (left). **(C)** The 2−dimensional viSNE plots of the 14 MCs of NK cells (left). One dot corresponds to one cell (left). The different colors represent the different MCs (left). The red arrows highlight the significant differences in the distribution of MCs among the studied groups. The cell density plots demonstrate the number of cells in the MCs within the studied groups (right). Red color is proportional with high, blue color is proportional with low cell density (right). Red boxes and Arabic numbers demonstrate the distribution of MCs with significant differences among the studied groups.

SUPPLEMENTARY FIGURE 15

Visualisations, viSNE maps of the subpopulations (metaclusters, MCs) defined by the FlowSOM analysis. **(A)** The 2−dimensional viSNE plots of the 7 MCs of CD56dim/CD98dim cells (left). **(B)** The 2−dimensional viSNE plots of the 19 MCs of B-cells (left). **(C)** The 2−dimensional viSNE plots of the 2 MCs of plasmablasts (left). One dot corresponds to one cell (left). The different colors represent the different MCs (left). The red arrows highlight the significant differences in the distribution of MCs among the studied groups. The cell density plots demonstrate the number of cells in the MCs within the studied groups (right). Red color is proportional with high, blue color is proportional with low cell density (right). Red boxes and Arabic numbers demonstrate the distribution of MCs with significant differences among the studied groups.

SUPPLEMENTARY FIGURE 16

Visualisations, viSNE maps of the subpopulations (metaclusters, MCs) defined by the FlowSOM analysis. The 2−dimensional viSNE plots of the 15 MCs of Monocytes (left). One dot corresponds to one cell (left). The different colors represent the different MCs (left). The red arrows highlight the significant differences in the distribution of MCs among the studied groups. The cell density plots demonstrate the number of cells in the MCs within the studied groups (right). Red color is proportional with high, blue color is proportional with low cell density (right). Red boxes and Arabic numbers demonstrate the distribution of MCs with significant differences among the studied groups.

References

1. Moutsopoulos HM. Autoimmune rheumatic diseases: One or many diseases? *J Transl Autoimmun*. (2021) 4:100129. doi: 10.1016/j.jtauto.2021.100129

2. Mariani FM, Martelli I, Pistone F, Chericoni E, Puxeddu I, Alunno A. Pathogenesis of rheumatoid arthritis: one year in review 2023. *Clin Exp Rheumatol*. (2023) 41:1725–34. doi: 10.55563/clinexprheumatol/sgjk6e

3. Ko J, Noviani M, Chellamuthu VR, Albani S, Low AHL. The pathogenesis of systemic sclerosis: the origin of fibrosis and interlink with vasculopathy and autoimmunity. *Int J Mol Sci*. (2023) 24:14287. doi: 10.3390/ijms241814287

4. Crow MK. Pathogenesis of systemic lupus erythematosus: risks, mechanisms and therapeutic targets. *Ann Rheum Dis*. (2023) 82:999–1014. doi: 10.1136/ard-2022-223741

5. Mitratza M, Klijs B, Hak AE, Kardaun J, Kunst AE. Systemic autoimmune disease as a cause of death: mortality burden and comorbidities. *Rheumatol (Oxford)*. (2021) 60:1321–30. doi: 10.1093/rheumatology/keaa537

6. Taylor PC, Atzeni F, Balsa A, Gossec L, Muller-Ladner U, Pope J. The key comorbidities in patients with rheumatoid arthritis: A narrative review. *J Clin Med*. (2021) 10:509. doi: 10.3390/jcm10030509

7. Radu AF, Bungau SG. Management of rheumatoid arthritis: an overview. *Cells*. (2021) 10:2857. doi: 10.3390/cells10112857

8. Pope JE, Denton CP, Johnson SR, Fernandez-Codina A, Hudson M, Nevskaya T. State-of-the-art evidence in the treatment of systemic sclerosis. *Nat Rev Rheumatol*. (2023) 19:212–26. doi: 10.1038/s41584-023-00909-5

9. Lazar S, Kahlenberg JM. Systemic lupus erythematosus: new diagnostic and therapeutic approaches. *Annu Rev Med*. (2023) 74:339–52. doi: 10.1146/annurev-med-043021-032611

10. Watanabe R, Okano T, Gon T, Yoshida N, Fukumoto K, Yamada S, et al. Difficult-to-treat rheumatoid arthritis: Current concept and unsolved problems. *Front Med (Lausanne)*. (2022) 9:1049875. doi: 10.3389/fmed.2022.1049875

11. Bobeica C, Niculet E, Tatu AL, Craescu M, Vata D, Statescu L, et al. Old and new therapeutic strategies in systemic sclerosis (Review). *Exp Ther Med*. (2022) 23:134. doi: 10.3892/etm

12. Fanouriakis A, Tziolos N, Bertsias G, Boumpas DT. Update on the diagnosis and management of systemic lupus erythematosus. *Ann Rheum Dis*. (2021) 80:14–25. doi: 10.1136/annrheumdis-2020-218272

13. Baharlou H, Canete NP, Cunningham AL, Harman AN, Patrick E. Mass cytometry imaging for the study of human diseases-applications and data analysis strategies. *Front Immunol*. (2019) 10:2657. doi: 10.3389/fimmu.2019.02657

14. Zhang T, Warden AR, Li Y, Ding X. Progress and applications of mass cytometry in sketching immune landscapes. *Clin Transl Med*. (2020) 10:e206. doi: 10.1002/ctm2.206

15. Mulhearn B, Barton A, Viatte S. Using the immunophenotype to predict response to biologic drugs in rheumatoid arthritis. *J Pers Med*. (2019) 9:46. doi: 10.20944/preprints201908.0242.v1

16. Papadimitriou TI, van Caam A, van der Kraan PM, Thurlings RM. Therapeutic options for systemic sclerosis: current and future perspectives in tackling immune-mediated fibrosis. *Biomedicines*. (2022) 10:316. doi: 10.3390/biomedicines10020316

17. Nagafuchi Y, Shoda H, Fujio K. Immune profiling and precision medicine in systemic lupus erythematosus. *Cells*. (2019) 8:140. doi: 10.3390/cells8020140

18. Nakayamada S, Tanaka Y. Immune phenotype as a biomarker for systemic lupus erythematosus. *Biomolecules*. (2023) 13:960. doi: 10.3390/biom13060960

19. Buckner JH. Translational immunology: Applying fundamental discoveries to human health and autoimmune diseases. *Eur J Immunol*. (2023) 53:e2250197. doi: 10.1002/eji.202250197

20. Nagafuchi Y, Shoda H, Sumitomo S, Nakachi S, Kato R, Tsuchida Y, et al. Immunophenotyping of rheumatoid arthritis reveals a linkage between HLA-DRB1 genotype, CXCR4 expression on memory CD4(+) T cells, and disease activity. *Sci Rep*. (2016) 6:29338. doi: 10.1038/srep29338

21. Takeshita M, Suzuki K, Kondo Y, Morita R, Okuzono Y, Koga K, et al. Multi-dimensional analysis identified rheumatoid arthritis-driving pathway in human T cell. *Ann Rheum Dis*. (2019) 78:1346–56. doi: 10.1136/annrheumdis-2018-214885

22. Bader L, Gullaksen SE, Blaser N, Brun M, Bringeland GH, Sulen A, et al. Candidate markers for stratification and classification in rheumatoid arthritis. *Front Immunol*. (2019) 10:1488. doi: 10.3389/fimmu.2019.01488

23. Koppejan H, Hameetman M, Beyrend G, van Unen V, Kwekkeboom JC, van der Helm-van Mil AH, et al. Immunoprofiling of early, untreated rheumatoid arthritis using mass cytometry reveals an activated basophil subset inversely linked to ACPA status. *Arthritis Res Ther*. (2021) 23:272. doi: 10.1186/s13075-021-02630-8

24. Paleja B, Low AHL, Kumar P, Saidin S, Lajam A, Nur Hazirah S, et al. Systemic sclerosis perturbs the architecture of the immunome. *Front Immunol*. (2020) 11:1602. doi: 10.3389/fimmu.2020.01602

25. van der Kroef M, van den Hoogen LL, Mertens JS, Blokland SLM, Haskett S, Devaprasad A, et al. Cytometry by time of flight identifies distinct signatures in patients with systemic sclerosis, systemic lupus erythematosus and Sjogrens syndrome. *Eur J Immunol*. (2020) 50:119–29. doi: 10.1002/eji.201948129

26. Fox DA, Lundy SK, Whitfield ML, Berrocal V, Campbell P, Rasmussen S, et al. Lymphocyte subset abnormalities in early diffuse cutaneous systemic sclerosis. *Arthritis Res Ther*. (2021) 23:10. doi: 10.1186/s13075-020-02383-w

27. Agarbati S, Benfaremo D, Viola N, Paolini C, Svegliati Baroni S, Funaro A, et al. Increased expression of the ectoenzyme CD38 in peripheral blood plasmablasts and plasma cells of patients with systemic sclerosis. *Front Immunol*. (2022) 13:1072462. doi: 10.3389/fimmu.2022.1072462

28. Hu S, Tao D, He P. Immunophenotyping of lymphocyte T and B in the peripheral blood of systemic lupus erythematosus. *J Tongji Med Univ*. (2001) 21:108–9. doi: 10.1007/BF02888069

29. Perry DJ, Titov AA, Sobel ES, Brusko TM, Morel L. Immunophenotyping reveals distinct subgroups of lupus patients based on their activated T cell subsets. *Clin Immunol*. (2020) 221:108602. doi: 10.1016/j.clim.2020.108602

30. Lee JM, Chen MH, Chou KY, Chao Y, Chen MH, Tsai CY. Novel immunoprofiling method for diagnosing SLE and evaluating therapeutic response. *Lupus Sci Med*. (2022) 9:e000693. doi: 10.1136/lupus-2022-000693

31. Sasaki T, Bracero S, Keegan J, Chen L, Cao Y, Stevens E, et al. Longitudinal immune cell profiling in patients with early systemic lupus erythematosus. *Arthritis Rheumatol*. (2022) 74:1808–21. doi: 10.1002/art.42248

32. Aletaha D, Neogi T, Silman AJ, Funovits J, Felson DT, Bingham CO 3rd, et al. 2010 Rheumatoid arthritis classification criteria: an American College of Rheumatology/European League Against Rheumatism collaborative initiative. *Arthritis Rheum*. (2010) 62:2569–81. doi: 10.1002/art.27584

33. van den Hoogen F, Khanna D, Fransen J, Johnson SR, Baron M, Tyndall A, et al. 2013 classification criteria for systemic sclerosis: an American College of Rheumatology/European League against Rheumatism collaborative initiative. *Arthritis Rheum*. (2013) 65:2737–47. doi: 10.1002/art.38098

34. LeRoy EC, Black C, Fleischmajer R, Jablonska S, Krieg T, Medsger TA Jr., et al. Scleroderma (systemic sclerosis): classification, subsets and pathogenesis. *J Rheumatol*. (1988) 15:202–5.

35. Petri M, Orbai AM, Alarcon GS, Gordon C, Merrill JT, Fortin PR, et al. Derivation and validation of the Systemic Lupus International Collaborating Clinics classification criteria for systemic lupus erythematosus. *Arthritis Rheumatol*. (2012) 64:2677–86. doi: 10.1002/art.34473

36. Neuperger P, Szalontai K, Gemes N, Balog JA, Tiszlavicz L, Furak J, et al. Single-cell mass cytometric analysis of peripheral immunity and multiplex plasma marker profiling of non-small cell lung cancer patients receiving PD-1 targeting immune checkpoint inhibitors in comparison with platinum-based chemotherapy. *Front Immunol*. (2023) 14:1243233. doi: 10.3389/fimmu.2023.1243233

37. Gemes N, Balog JA, Neuperger P, Schlegl E, Barta I, Fillinger J, et al. Single-cell immunophenotyping revealed the association of CD4+ central and CD4+ effector memory T cells linking exacerbating chronic obstructive pulmonary disease and NSCLC. *Front Immunol*. (2023) 14:1297577. doi: 10.3389/fimmu.2023.1297577

38. Balog JA, Honti V, Kurucz E, Kari B, Puskas LG, Ando I, et al. Immunoprofiling of drosophila hemocytes by single-cell mass cytometry. *Genomics Proteomics Bioinf*. (2021) 19:243–52. doi: 10.1016/j.gpb.2020.06.022

39. Neuperger P, Balog JA, Tiszlavicz L, Furak J, Gemes N, Kotogany E, et al. Analysis of the single-cell heterogeneity of adenocarcinoma cell lines and the investigation of intratumor heterogeneity reveals the expression of transmembrane protein 45A (TMEM45A) in lung adenocarcinoma cancer patients. *Cancers (Basel)*. (2021) 14:144. doi: 10.3390/cancers14010144

40. Fish M, Ellis R, Bishop C, Todd K, Petrov N, Singer M, et al. Utilising mass cytometry with CD45 barcoding and standardised leucocyte phenotyping for immune trajectory assessment in critically ill patients. *Br J Anaesth*. (2021) 126:e149–e52. doi: 10.1016/j.bja.2021.01.006

41. Balog JA, Hackler L Jr., Kovacs AK, Neuperger P, Alfoldi R, Nagy LI, et al. Single cell mass cytometry revealed the immunomodulatory effect of cisplatin via downregulation of splenic CD44+, IL-17A+ MDSCs and promotion of circulating IFN-gamma+ Myeloid cells in the 4T1 metastatic breast cancer model. *Int J Mol Sci*. (2019) 21:170. doi: 10.3390/ijms21010170

42. Crowell HL, Chevrier S, Jacobs A, Sivapatham S, Tumor Profiler C, Bodenmiller B, et al. An R-based reproducible and user-friendly preprocessing pipeline for CyTOF data. *F1000Res*. (2020) 9:1263. doi: 10.12688/f1000research

43. Weber LM, Robinson MD. Comparison of clustering methods for high-dimensional single-cell flow and mass cytometry data. *Cytomet A*. (2016) 89:1084–96. doi: 10.1002/cyto.a.23030

44. Nowicka M, Krieg C, Crowell HL, Weber LM, Hartmann FJ, Guglietta S, et al. CyTOF workflow: differential discovery in high-throughput high-dimensional cytometry datasets. *F1000Res*. (2017) 6:748. doi: 10.12688/f1000research

45. Cole S, Walsh A, Yin X, Wechalekar MD, Smith MD, Proudman SM, et al. Integrative analysis reveals CD38 as a therapeutic target for plasma cell-rich pre-disease and established rheumatoid arthritis and systemic lupus erythematosus. *Arthritis Res Ther*. (2018) 20:85. doi: 10.1186/s13075-018-1578-z

46. Ye X, Zhao Y, Ma W, Ares I, Martinez M, Lopez-Torres B, et al. The potential of CD38 protein as a target for autoimmune diseases. *Autoimmun Rev*. (2023) 22:103289. doi: 10.1016/j.autrev.2023.103289

47. Yalcin Mutlu M, Wacker J, Tascilar K, Taubmann J, Manger B, Kronke G, et al. Effective and safe treatment of anti-CD38 therapy in systemic lupus erythematosus-associated refractory cerebral vasculitis induces immune tolerance. *Rheumatol (Oxford)*. (2023) 62:e21–e3. doi: 10.1093/rheumatology/keac393

48. Liu X, Gao N, Li M, Xu D, Hou Y, Wang Q, et al. Elevated levels of CD4(+)CD25(+)FoxP3(+) T cells in systemic sclerosis patients contribute to the secretion of IL-17 and immunosuppression dysfunction. *PloS One*. (2013) 8:e64531. doi: 10.1371/journal.pone.0064531

49. Radstake TR, van Bon L, Broen J, Wenink M, Santegoets K, Deng Y, et al. Increased frequency and compromised function of T regulatory cells in systemic sclerosis (SSc) is related to a diminished CD69 and TGFbeta expression. *PloS One*. (2009) 4:e5981. doi: 10.1371/journal.pone.0005981

50. Burns M, Ostendorf L, Biesen R, Grutzkau A, Hiepe F, Mei HE, et al. Dysregulated CD38 expression on peripheral blood immune cell subsets in SLE. *Int J Mol Sci*. (2021) 22:2424. doi: 10.3390/ijms22052424

51. Lima G, Trevino-Tello F, Atisha-Fregoso Y, Llorente L, Fragoso-Loyo H, Jakez-Ocampo J. Exhausted T cells in systemic lupus erythematosus patients in long-standing remission. *Clin Exp Immunol*. (2021) 204:285–95. doi: 10.1111/cei.13577

52. Comte D, Karampetsou MP, Yoshida N, Kis-Toth K, Kyttaris VC, Tsokos GC. Signaling lymphocytic activation molecule family member 7 engagement restores defective effector CD8+ T cell function in systemic lupus erythematosus. *Arthritis Rheumatol*. (2017) 69:1035–44. doi: 10.1002/art.40038

53. Yuan S, Zeng Y, Li J, Wang C, Li W, He Z, et al. Phenotypical changes and clinical significance of CD4(+)/CD8(+) T cells in SLE. *Lupus Sci Med*. (2022) 9:e000660. doi: 10.1136/lupus-2022-000660

54. Cho YN, Kee SJ, Kim TJ, Jin HM, Kim MJ, Jung HJ, et al. Mucosal-associated invariant T cell deficiency in systemic lupus erythematosus. *J Immunol*. (2014) 193:3891–901. doi: 10.4049/jimmunol.1302701

55. Bank I. The role of gamma delta T cells in autoimmune rheumatic diseases. *Cells*. (2020) 9:462. doi: 10.3390/cells9020462

56. Nguyen CT, Maverakis E, Eberl M, Adamopoulos IE. gammadelta T cells in rheumatic diseases: from fundamental mechanisms to autoimmunity. *Semin Immunopathol*. (2019) 41:595–605. doi: 10.1007/s00281-019-00752-5

57. Chalan P, Bijzet J, Kroesen BJ, Boots AM, Brouwer E. Altered natural killer cell subsets in seropositive arthralgia and early rheumatoid arthritis are associated with autoantibody status. *J Rheumatol.* (2016) 43:1008–16. doi: 10.3899/jrheum.150644

58. Benyamine A, Magalon J, Sabatier F, Lyonnet L, Robert S, Dumoulin C, et al. Natural killer cells exhibit a peculiar phenotypic profile in systemic sclerosis and are potent inducers of endothelial microparticles release. *Front Immunol.* (2018) 9:1665. doi: 10.3389/fimmu.2018.01665

59. Schepis D, Gunnarsson I, Eloranta ML, Lampa J, Jacobson SH, Karre K, et al. Increased proportion of CD56bright natural killer cells in active and inactive systemic lupus erythematosus. *Immunology.* (2009) 126:140–6. doi: 10.1111/j.1365-2567.2008.02887.x

60. Lu Z, Tian Y, Bai Z, Liu J, Zhang Y, Qi J, et al. Increased oxidative stress contributes to impaired peripheral CD56(dim)CD57(+) NK cells from patients with systemic lupus erythematosus. *Arthritis Res Ther.* (2022) 24:48. doi: 10.1186/s13075-022-02731-y

61. Amu S, Tarkowski A, Dorner T, Bokarewa M, Brisslert M. The human immunomodulatory CD25+ B cell population belongs to the memory B cell pool. *Scand J Immunol.* (2007) 66:77–86. doi: 10.1111/j.1365-3083.2007.01946.x

62. Rincon-Arevalo H, Wiedemann A, Stefanski AL, Lettau M, Szelinski F, Fuchs S, et al. Deep phenotyping of CD11c(+) B cells in systemic autoimmunity and controls. *Front Immunol.* (2021) 12:635615. doi: 10.3389/fimmu.2021.635615

63. Mouat IC, Goldberg E, Horwitz MS. Age-associated B cells in autoimmune diseases. *Cell Mol Life Sci.* (2022) 79:402. doi: 10.1007/s00018-022-04433-9

64. Wang S, Wang J, Kumar V, Karnell JL, Naiman B, Gross PS, et al. IL-21 drives expansion and plasma cell differentiation of autoreactive CD11c(hi)T-bet(+) B cells in SLE. *Nat Commun.* (2018) 9:1758. doi: 10.1038/s41467-018-03750-7

65. Toapanta FR, Simon JK, Barry EM, Pasetti MF, Levine MM, Kotloff KL, et al. Gut-homing conventional plasmablasts and CD27(-) plasmablasts elicited after a short time of exposure to an oral live-attenuated shigella vaccine candidate in humans. *Front Immunol.* (2014) 5:374. doi: 10.3389/fimmu.2014.00374

66. Lescoat A, Lecureur V, Roussel M, Sunnaram BL, Ballerie A, Coiffier G, et al. CD16-positive circulating monocytes and fibrotic manifestations of systemic sclerosis. *Clin Rheumatol.* (2017) 36:1649–54. doi: 10.1007/s10067-017-3597-6

frontiers | Frontiers in Immunology

TYPE Original Research
PUBLISHED 08 May 2024
DOI 10.3389/fimmu.2024.1383358

OPEN ACCESS

EDITED BY
Shiang-Jong Tzeng,
National Taiwan University, Taiwan

REVIEWED BY
Imelda Balboni,
Stanford University, United States
Xiaojing Chu,
Changping Laboratory, China
Ana Campar,
University of Porto, Portugal

*CORRESPONDENCE
Anastasia Filia
✉ afilia@bioacademy.gr
Ioannis Kokkinopoulos
✉ ikokkinopoulos@bioacademy.gr

†These authors have contributed equally to this work

RECEIVED 07 February 2024
ACCEPTED 18 April 2024
PUBLISHED 08 May 2024

CITATION
Filia A, Mitroulis I, Loukogiannaki C, Grigoriou M, Banos A, Sentis G, Giannouli S, Karali V, Athanasiadis E, Kokkinopoulos I and Boumpas DT (2024) Single-cell transcriptomic analysis of hematopoietic progenitor cells from patients with systemic lupus erythematosus reveals interferon-inducible reprogramming in early progenitors. *Front. Immunol.* 15:1383358.
doi: 10.3389/fimmu.2024.1383358

Single-cell transcriptomic analysis of hematopoietic progenitor cells from patients with systemic lupus erythematosus reveals interferon-inducible reprogramming in early progenitors

Anastasia Filia[1*†], Ioannis Mitroulis[2†], Catherine Loukogiannaki[1], Maria Grigoriou[1,2], Aggelos Banos[1], George Sentis[1], Stavroula Giannouli[3], Vassiliki Karali[4], Emmanouil Athanasiadis[5], Ioannis Kokkinopoulos[1*†] and Dimitrios T. Boumpas[1,4†]

[1]Laboratory of Autoimmunity and Inflammation, Center of Clinical, Experimental Surgery and Translational Research, Biomedical Research Foundation Academy of Athens, Athens, Greece, [2]1st Department of Internal Medicine, University Hospital of Alexandroupolis, Democritus University of Thrace, Alexandroupolis, Greece, [3]2nd Department of Internal Medicine, Ippokrateion Hospital, National and Kapodistrian University of Athens, Athens, Greece, [4]4th Department of Internal Medicine, Attikon University Hospital, National and Kapodistrian University of Athens Medical School, Athens, Greece, [5]Medical Image and Signal Processing Laboratory, Department of Biomedical Engineering, University of West Attica, Athens, Greece

Introduction: Immune cells that contribute to the pathogenesis of systemic lupus erythematosus (SLE) derive from adult hematopoietic stem and progenitor cells (HSPCs) within the bone marrow (BM). For this reason, we reasoned that fundamental abnormalities in SLE can be traced to a BM-derived HSPC inflammatory signature.

Methods: BM samples from four SLE patients, six healthy controls, and two umbilical cord blood (CB) samples were used. CD34+ cells were isolated from BM and CB samples, and single-cell RNA-sequencing was performed.

Results: A total of 426 cells and 24,473 genes were used in the analysis. Clustering analysis resulted in seven distinct clusters of cell types. Mutually exclusive markers, which were characteristic of each cell type, were identified. We identified three HSPC subpopulations, one of which consisted of proliferating cells (*MKI67* expressing cells), one T-like, one B-like, and two myeloid-like progenitor subpopulations. Differential expression analysis revealed i) cell cycle-associated signatures, in healthy BM of HSPC clusters 3 and 4 when compared with CB, and ii) interferon (IFN) signatures in SLE BM of HSPC clusters 3 and 4 and myeloid-like progenitor cluster 5 when compared with healthy controls. The IFN signature in SLE appeared to be deregulated following

TF regulatory network analysis and differential alternative splicing analysis between SLE and healthy controls in HSPC subpopulations.

Discussion: This study revealed both quantitative—as evidenced by decreased numbers of non-proliferating early progenitors—and qualitative differences—characterized by an IFN signature in SLE, which is known to drive loss of function and depletion of HSPCs. Chronic IFN exposure affects early hematopoietic progenitors in SLE, which may account for the immune aberrancies and the cytopenias in SLE.

KEYWORDS

single cell RNA sequencing, SLE, bone marrow, hematopoiesis, interferon signaling

1 Introduction

Hematopoietic stem and progenitor cells (HSPCs) represent a primitive multipotent population that gives rise to all blood cell types (1). HSPCs reside in the bone marrow (BM) niche and remain in a quiescent state. Under hematopoietic stress, including inflammation, these cells respond with proliferation and differentiation, in order to replenish any progeny needed (2, 3).

HSPCs are an integral part of the immune response with the ability to sense inflammatory stimuli in infectious and chronic inflammatory diseases, since they are equipped with receptors for pathogen-derived stimuli, several cytokines, such as interferons and IL-1β, or myeloid-related growth factors. Studies in animal models have shown that HSPCs are important players in the initiation and perpetuation of the inflammatory processes in systemic lupus erythematosus (SLE) (4), rheumatoid arthritis (5), and spondyloarthritis (6).

A prolonged exposure to inflammatory stimuli during chronic inflammatory diseases has long-lasting effects on the BM cell output's nature through epigenetic modifications in HSPCs (1, 7, 8). The reprogramming of HSPCs by inflammatory stimuli can alter mature cell output, resulting in the generation of effector cells with inflammatory properties (7, 9, 10).

It has been demonstrated that an interplay between environmental, genetic, and epigenetic factors promotes SLE (11). A key observation in SLE is that most cells participating in its pathogenesis such as lymphocytes, monocytes, and neutrophils originate from HSPCs (11). We have reasoned that the fundamental molecular aberrations in SLE may be traced back in the HSPCs within the BM. To this direction, we collected human $CD34^+$ cells from healthy and SLE patients as well from newborn umbilical cord blood (CB) and we performed deep RNA sequencing analysis, at the single-cell level. We report that interferon signaling, which is a major player in disease pathogenesis, already affects early hematopoietic progenitors in SLE. Differential mRNA splicing analysis underscored alterations in the cell cycle and DNA repair machineries in SLE BM-derived HPSCs, when compared with healthy-derived HSPCs. These data suggest that HSPCs act as sensors of interferon-related inflammatory signals, initiating the inflammatory process that characterizes SLE.

2 Methods

2.1 Human samples

BM aspirates were obtained from four SLE individuals and six age- and sex-matched healthy volunteers. Patients' clinical and serological characteristics are summarized in Supplementary Table 1. Informed consent was obtained from all patients prior to sample collection (Athens, Greece, protocol 10/22-6-2017). Two umbilical CB samples were donated from the Hellenic Cord Blood Bank, Biomedical Research Foundation of Academy of Athens (BRFAA).

2.2 Isolation of human CD34+ progenitor cells

Human heparinized BM aspirate (10 ml) was collected from healthy and SLE patients and subjected to density gradient centrifugation using Histopaque-1077 (Sigma-Aldrich). Briefly, blood was diluted 1:3 PBS and carefully layered over Histopaque medium. Tubes were centrifuged at 500 g for 30 min (no break) at room temperature. BM mononuclear cells were isolated using Histopaque-1077 (Sigma-Aldrich). BM mononuclear cells were washed, and erythrocytes were lysed with RBC buffer (420301, BioLegend). $CD34^+$ cells were isolated using EasySep™ Human CD34 Positive Selection Kit II (18056, StemCell Technologies). Purity was tested and was >95%.

Abbreviations: SLE, systemic lupus erythematosus; HSPCs, hematopoietic stem and progenitor cells; BM, bone marrow; CB, cord blood; IFN, interferon; TF, transcription factor; GSEA, gene set enrichment analysis; FDR, false discovery rate; DAS, differential alternative splicing; PSI, percent spliced in.

2.3 Single cell RNA sequencing data processing

Human CD34^{+} cells were loaded on Fluidigm C1 IFC. Single-cell capture and RNA extraction were performed on the IFC. Reverse transcription and amplification were performed using the SMART-Seq v.4 cDNA synthesis kit, and libraries were prepared using the Illumina Nextera XT kit. Libraries were sequenced 75 bp or 150 bp paired-end on the Illumina MiSeq or NextSeq500 platforms. Single-cell RNA-sequencing experiments were carried out at the Greek Genome Center, BRFAA.

Sequencing files were demultiplexed and converted to FASTQ format using Illumina bcl2fastq software. FASTQC v.0.11.7 software was used for quality control. Adapters and low-quality bases ($Q<30$) were trimmed from the 3′ end of the reads using Cutadapt v.1.18 (12). Alignment was performed against the primary assembly of GRCh38 using STAR v.2.6.1b (13), and quantification was performed using gencode_v29 annotation using HTSeq v.0.11.1 (14).

Quality control analysis was performed in order to remove poor-quality cells, which could be dead or dying. Cells were excluded if the alignment rate was <50%, the numbers of detected genes (at least one count) were <200 and >6,000, and the percentage of reads mapping to mitochondrial genes was >20%. Following filtering with the above criteria, 426 were used for further analysis.

The Seurat R package (v.4) (15) and harmony (16) were used for normalization and graph-based clustering. A resolution of 0.7 was used for UMAP clustering. The FindMarkers function was used for marker identification using the wilcox.test method (cell fraction in each subpopulation >0.2, logFC >0.2, and $p < 0.01$). The cell-cycle state of each cell was predicted by scoring cells for their cell cycle phase using Seurat's CellCycleScoring function. The stemness score of each cell was calculated using the UCell R package (17) with a gene set as reported elsewhere (18). Pairwise Mann–Whitney rank-sum tests were performed for the stemness score between clusters. The interferon (IFN) score was calculated accordingly using a gene set, which is a union of modules M1.2, M3.4, and M5.12 as reported elsewhere (19).

2.4 Gene regulatory network analysis

The single-cell RNA-seq data were further analyzed by using SCENIC (20). SCENIC is a computational method that reconstructs gene regulatory networks and identifies cell states from single-cell RNA-seq data. There are three major R/Bioconductor packages that SCENIC depends on GENIE3 (21), RcisTarget (20), and AUCell (20). GENIE3 identifies potential transcription factor (TF) targets that are coexpressed with those TFs. Then, RcisTarget identifies the direct targets via cis-regulatory motif analysis and creates the regulons (transcription factor regulatory networks). Lastly, AUCell scores the activity of each regulon on single cells. It should be noted that all graphs except violin plots were constructed using the binary values of the AUCell algorithm. Specifically, SCENIC was utilized to create the regulons, estimate the transcription factors' activity scores, and perform an enrichment analysis on them. Differential regulon activity analysis between SLE and healthy controls was performed in each regulon cluster. Differential regulon activity was considered significant when $p < 0.05$. Results were visualized by UMAPs, heatmaps, pie charts, and violin plots. Scripts were based on the work of Zhu et al. (22) and the SCENIC vignettes offered by Aibar et al. (20).

2.5 Differential expression

The Seurat FindMarkers function was used for differential expression analysis using the wilcox.test method between a) SLE and H controls and b) H vs. CB in each cluster. No DE was performed If cells per condition per cluster were less than 10. Gene set enrichment analysis (GSEA) (23) was performed in order to reveal enriched signatures in our gene sets based on the Molecular Signatures Database v.2022.1.Hs collections (Hallmark gene sets, GO Biological Processes, KEGG, and REACTOME pathways). Gene sets were ranked by taking the –log10 transform of the p-value multiplied by the fold change. Significantly upregulated genes were at the top and significantly downregulated genes were at the bottom of the ranked list. GSEA pre-ranked analysis was then performed using the default settings. Enrichment was considered significant when false discovery rate (FDR) < 0.05.

2.6 Differential alternative splicing

Differential alternative splicing (DAS) was performed between SLE and healthy controls for each cluster separately using rMATS turbo v4.1.2 (24). BAM files were merged for each participant per cluster and used as input for the detection of differential alternative splicing (DAS) events between SLE and healthy controls in each cluster. Briefly, the number of supporting reads was counted by the junction reads only. For each event, the difference in the percent-spliced-in (PSI) values, which represent the fraction of transcripts that include a particular exon or spliced site, between SLE and healthy controls was calculated. A likelihood ratio test within rMATS was performed, and DAS events between SLE and healthy controls were considered significant when FDR <0.05. Enrichment analysis was performed using the gene names showing significant DAS events using enrichR (25). Enrichment was considered significant when FDR <0.05. Sashimi plots were created to visualize the splicing patterns of genes between SLE and healthy controls using the function rmats2sashimiplot (https://github.com/Xinglab/rmats2sashimiplot#usage).

3 Results

3.1 Single-cell transcriptomes of HSPCs in CB and BM

We sought to assess the molecular changes that take place in the HSPC signature from early life to adulthood, as well as to address the effect of SLE-dependent inflammation in this modulation at the single-cell level. To this end, single-cell RNA sequencing was performed in isolated CD34$^+$ umbilical cord blood (CB) (n = 2) and bone marrow (BM) cells from healthy adult individuals (n = 6) and patients with SLE (n = 4) (Figure 1A). The use of CB-derived cells would be acting as a "naive" CD34+ hematopoietic progenitor cell population that has not been affected by the BM microenvironment, therefore providing a reference point for BM-derived CD34+ HPSC intrinsic differences between healthy and SLE patients. In total, we obtained transcriptomes of 426 single cells following quality control filtering (see Methods), 177 of which were healthy BM, 141 were SLE BM, and 108 were CB cells. The median number of reads was 1,259,063 (range 73,279–6,281,814). There was no statistically significant difference in the total number of reads between the three sample types (Kruskal–Wallis chi-squared = 0.33, p = 0.85, Supplementary Figure 1). However, there was a statistically significant difference in the total number of detected genes between the three sample types (Kruskal–Wallis chi-squared = 14.7, $p < 0.001$) with SLE samples expressing more genes compared with the other two sample types (Supplementary Figure 2).

Unsupervised clustering partitioned the cells in seven clusters (Figure 1B). Clusters were further defined based on the expression of lineage markers (26, 27), differentially expressed genes in each cluster compared with all others (Figure 1C; Supplementary Table 2) as well as annotation against a reference dataset (Supplementary Figure 3). Specifically, we identified a cluster characterized by T-cell markers (cluster 0; T-like progenitors instead of T-like prog), including *IL32*, *CD3E*, *TRBC1*, and *TRBC2*; three clusters that comprised cells expressing HSPC-related genes (cluster 2, 3, 4; HSPCs), such as *CD164*, *MSI1*, *IKFZ1*, *GATA2*, and *CD34*; two clusters characterized by the expression of myeloid-related genes (clusters 1 and 5; myeloid-like progenitors instead of myeloid-like prog), such as *MP8*, *CLEC4C* and *CD117*, *LGALS1*, *CSF2RB*, *IRF8*, *FCER1G*, and *ANXA2*; and finally a cluster characterized by B-cell markers (cluster 6; B-like progenitors instead of B-like prog), such as *CD79A*, *CD79B*, *VPREB3*, *CD22*, *CD19*, and *CD10* (Figure 1C). Of note, HSPC cluster 4 was characterized by the expression of the cell-cycle genes *MKI67* and *CCND2*, suggesting characterization of proliferating HSPCs (Figure 1C). Based on the expression of genes associated with HSPC stemness (stemness score), we were able to confirm that clusters 2, 3, and 4 included cells that were characterized by a stem cell signature (Figure 1D). We then focused on these three HSPC clusters and assessed the cell-cycle state of each cell, by scoring cells for their cell-cycle phase (see Methods). This analysis revealed that HSPC cluster 4 was formed by proliferating cells (Figure 1E). For instance, increased frequency of cells expressing *MKI67*, *CDK4*, *CDK6*, *CDKN2C*, and *TP53* and higher expression of these genes was observed in HSPCs cluster 4 ($p < 0.01$, Figure 1F).

3.2 Single-cell transcriptomes of HSPC subpopulations in SLE BM

We then studied whether SLE-dependent inflammatory signals act specifically to subpopulations of progenitor cells in the BM. To do so, we initially assessed the distribution of CB, healthy BM, and SLE BM CD34$^+$ cells (Figure 2A). Regarding the HSPC clusters 2, 3, and 4, CD34$^+$ cells from healthy adults were equally distributed to the three HSPC clusters, whereas the majority of CD34$^+$ CB cells and only few SLE cells were present in HSPC cluster 2 compared with clusters 3 and 4, suggesting that this cluster corresponds to a primitive cell population (Figures 2A, B). Additionally, there was an

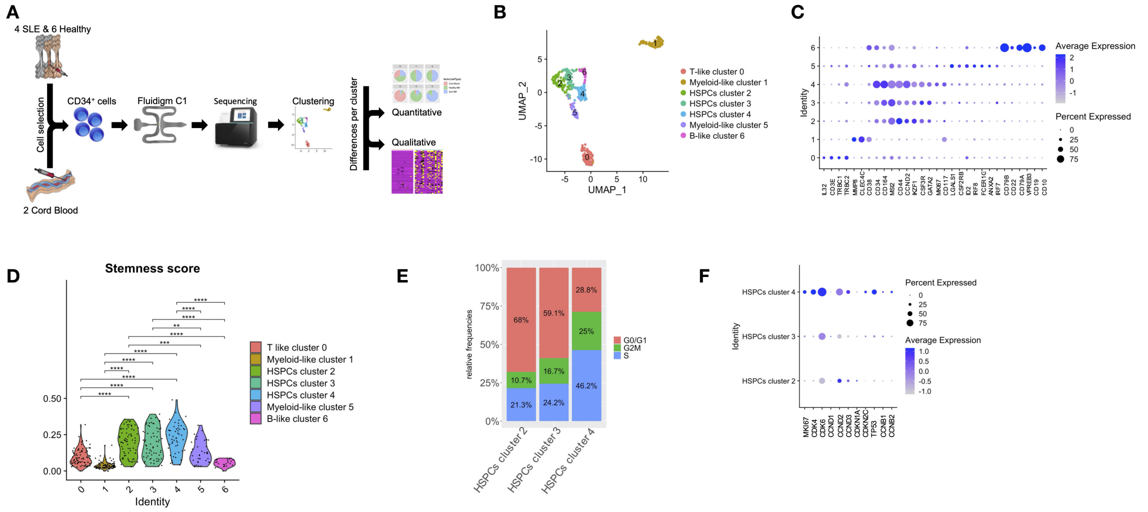

FIGURE 1
Lineage-specific alterations in HSPCs using single-cell transcriptomics in patients with SLE. **(A)** Diagram of analysis pipeline. **(B)** Uniform manifold approximation and project (UMAP) visualization of HSPC cells (CD34$^+$) irrespective of disease or developmental stage (cord blood, n = 2, healthy bone marrow (BM), n = 6, SLE BM, n = 4) based on single-cell transcriptomes. Each dot represents a single cell; colors indicate cell clusters with numbered labels and cell type annotations. **(C)** Dot plot of selected marker genes in each identified cluster. **(D)** Violin plots of stemness signature score of each cluster (Mann–Whitney rank-sum test p values, $^{**}p < 0.01$, $^{***}p < 0.001$, $^{****}p < 0.0001$). **(E)** Bar plot of cell-cycle phase assignments for captured cells in the HSPC clusters 2, 3, 4. **(F)** Dot plot of selected cell-cycle genes in HSPC clusters 2, 3, 4.

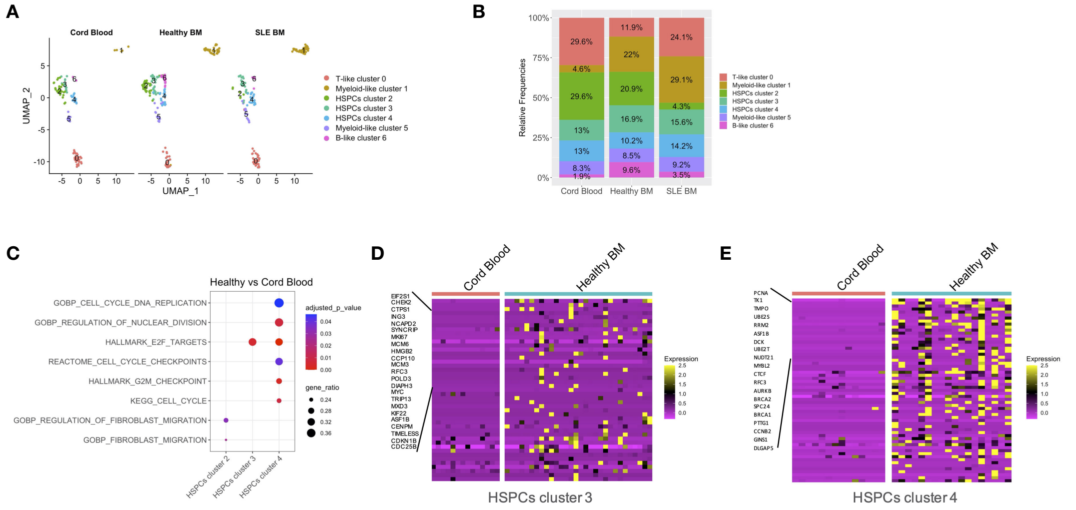

FIGURE 2

Quantitative differences per condition and qualitative differences in patients with SLE versus CB. **(A)** Uniform manifold approximation and project (UMAP) visualization of HSPC cells (CD34+) per sample type (cord blood, n = 2, healthy bone marrow (BM), n = 6, SLE BM, n = 4) based on single-cell transcriptomes. **(B)** Bar plot of cluster assignments for captured cells in each sample type. **(C)** Dot plot of GSEA-enriched terms following differential expression analysis between healthy controls and CB samples in HSPC clusters 2, 3, 4. **(D, E)** Heatmap of genes supporting the enriched cell-cycle-related pathways in healthy controls vs. CB in HSPC clusters 3 and 4.

underrepresentation of $CD34^+$ SLE and CB cells in B-like cluster 6. Taken together, from the naive state of CB cells to HSPCs derived from the BM of control subjects and then of patients with SLE, there is an underrepresentation of the primitive cells of cluster 2. In parallel to these quantitative changes, we addressed whether there are changes in gene expression within different clusters of HSPCs using differential expression analysis. GSEA showed a positive enrichment of cell-cycle-associated signatures, including cell cycle and DNA replication, regulation of nuclear division, E2F targets, and G2M checkpoints in healthy BM of HSPCs cluster 4 (Figures 2C, D; Supplementary Table 3) and E2F targets in healthy BM of HSPCs cluster 3 when compared with CB of HSPCs cluster 4 and 3, respectively (Figures 2C, E; Supplementary Table 3).

GSEA between SLE and healthy cells per cluster showed a positive enrichment of interferon signatures in the SLE HSPCs cluster 3 and 4 and myeloid-like cluster 5 cells (Figures 3A–D; Supplementary Table 4; Supplementary Figure 4). This was accompanied by a positive enrichment of proliferation and differentiation in HSPCs, including oxidative phosphorylation and G2-M checkpoint signatures in the SLE myeloid-like cluster 5 cells (Figure 3A). Of note, when we compared the cell-cycle state of control and SLE HSPCs in clusters 3 and 4, we observed that the vast majority of SLE HSPCs in cluster 4 was in the S/G2-M phase (Figure 3E), whereas the gene expression and the frequency of cells expressing the cell-cycle-associated genes *CDK4*, *CDK6*, *CCND2*, and *TP53* were increased in SLE HSPCs within cluster 4 compared with healthy HSPCs although these changes did not reach statistical significance (Figure 3F).

Transcription factors (TFs) are critical regulators of HSPC phenotype and lineage bias. In order to study the TFs that could act as regulators of the transcriptomic changes observed in patients with SLE, we performed TF regulatory network analysis of the single-cell data, which resulted in the identification of six clusters–regulons (Figure 4A). Regulon 0 included the HSPC clusters 2, 3, 4 (Figure 4A). Regarding the distribution of cells in the regulons, regulon 4 was enriched with healthy cells (mainly B-like cluster 6), which is characterized by the *SMAD1, EBF1, LEF1, FOXO1*, and *KLF6*-regulated networks. Regulon 5 was enriched with SLE cells (mainly myeloid-like cluster 5 cells), characterized by *SPIB* and the interferon-inducible *IRF7, IRF8, IRF9*-regulated networks (Figures 4B, C). Differential TF activity analysis between SLE and healthy controls within regulon 0, which includes the HPSC clusters, showed increased predicted activity of the TFs *IRF7* and *IRF9* as regulators of transcriptomic changes in SLE ($p < 0.05$, Figure 4D; Supplementary Table 5), further supporting that HSPCs in SLE are targeted by IFNs.

3.3 Differential alternative splicing in SLE HSPCs

Alternative splicing represents a vital component of the gene regulation process through the reduction of mRNA translation or the production of non-functional or malfunctional proteins. Previous studies have shown that SLE-related genes are subject to alternative splicing (28, 29). Therefore, we sought to identify whether alternative splicing events might affect hematopoiesis in patients with SLE. In total, we observed a larger number of splicing events in HSPC cluster 4 compared with other clusters (Figure 5A). Significant differential alternative splicing events between patients with SLE and healthy controls was observed in HSPC cluster 4 cells only with the most frequent type of event being skipped exon (Figure 5B). There were 383 genes affected by differential alternative

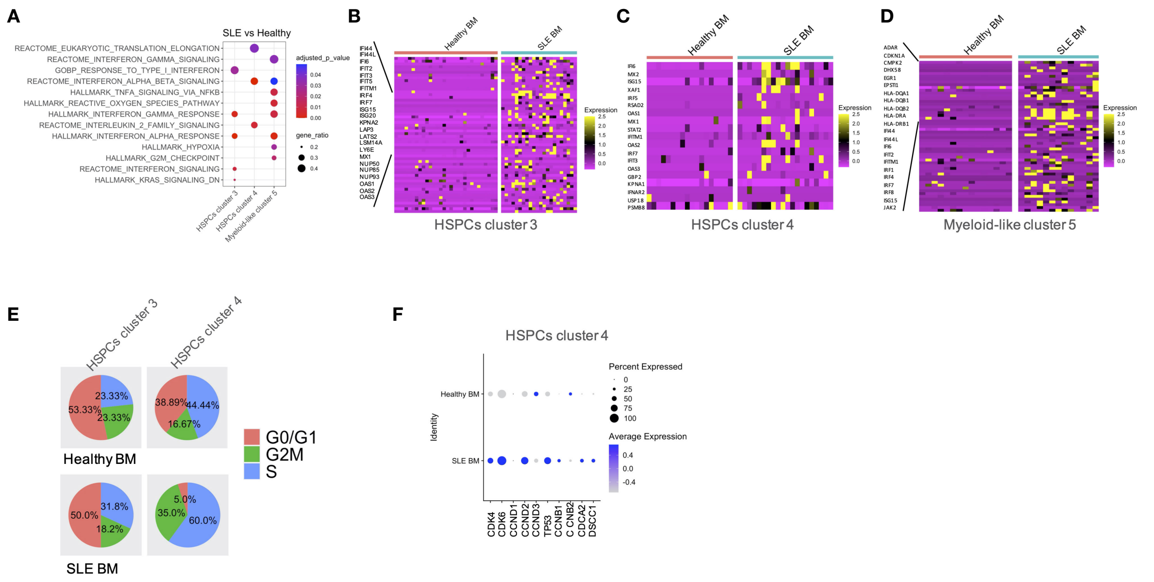

FIGURE 3
Qualitative differences in patients with SLE compared with healthy controls. **(A)** Dot plot of GSEA enriched terms following differential expression analysis between SLE and healthy controls in HSPC clusters 3 and 4 and myeloid-like cluster 5. **(B–D)** Heatmaps of genes supporting the enriched IFN-related pathways in SLE BM vs. healthy controls in HSPC clusters 3 and 4 and myeloid-like cluster 5, respectively. **(E)** Pie charts showing the composition of each cell-cycle phase in healthy BM and SLE BM in HSPC clusters 3 and 4. **(F)** Dot plot of selected cell-cycle genes in healthy BM and SLE BM in HSPC clusters 4.

splicing (DAS) in HSPC cluster 4, and these genes were enriched in pathways associated with cell proliferation, such as G2-M checkpoint, replication, translation and DNA repair, and interferon pathways (Figure 5C), providing supportive evidence that these mechanisms are dysregulated in SLE HSPCs. Particularly, IFN-related genes such as *SELL* and *CD74* were found to be affected by DAS giving rise to different proportions of two isoforms per gene in SLE when compared with healthy controls (Figures 5D, E).

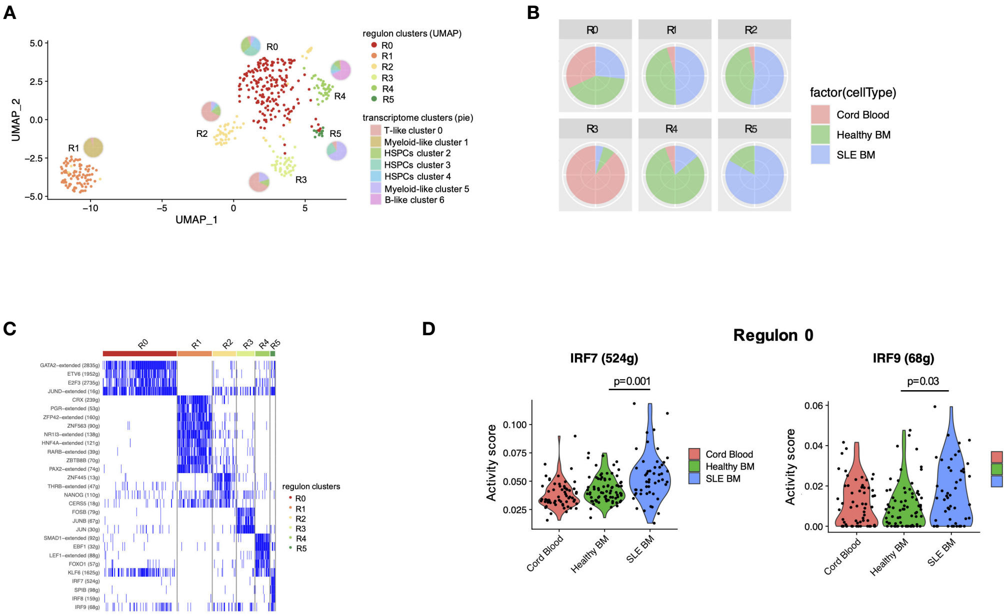

FIGURE 4
Transcription factor regulatory network analysis in HSPCs. **(A)** UMAP visualization of HSPC clustering based on regulons. Each pie chart shows the composition of each regulon cluster by cell type (defined based on single-cell gene expression). **(B)** Pie charts showing the composition of each regulon cluster by sample type. **(C)** Representative display of transcription factor regulon activity as binary outcome (blue: present, white = non-present) in each regulon. **(D)** Violin plots of IRF7 and IRF9 activity scores per sample type in regulon 0 (mainly HSPC clusters 2, 3, 4).

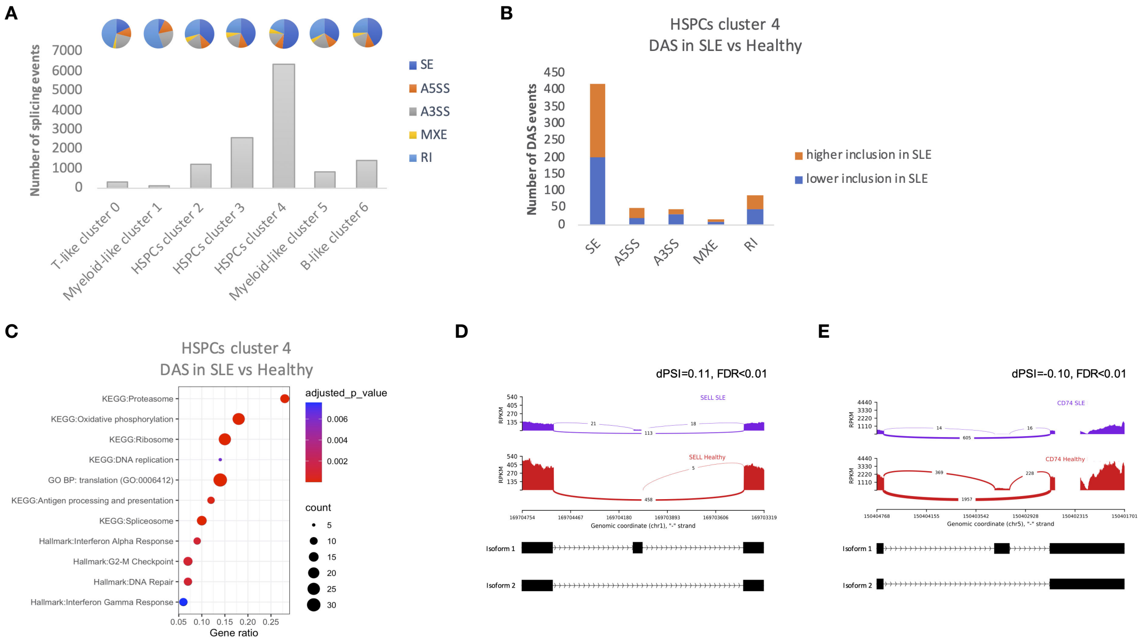

FIGURE 5

Alternative splicing events in HSPCs. **(A)** Number of total alternative splicing events in each cluster irrespective of disease or developmental stage. Each pie chart shows the composition of each cluster by alternative splicing event types (SE, skipped exon; RI, retained intron; MXE, mutually exclusive exons; A5SS, alternative 5′ splicing site; A3SS, alternative 3′ splicing site). **(B)** Number of differential alternative splicing (DAS) events in HSPC cluster 4 for each event type. Orange color represents the DAS events with higher inclusion level of exons in SLE and blue DAS events with lower inclusion level in SLE **(C)** Dot plot of EnrichR-enriched terms following differential alternative splicing analysis between SLE and healthy controls in HSPCs cluster 4. **(D, E)** Representative display of differential SELL and CD74 (IFN-related genes) exon usage in SLE versus healthy controls, respectively. The arcs connecting exons in the plot represent splice junctions, and their thickness provides a visual representation of the read coverage supporting those junctions. Differential splicing is measured in terms of the difference in the per cent spliced in dPSI. For example, the inclusion level of the splice site of *SELL* is 11% higher in SLE; therefore, the difference in PSI (SLE vs. healthy; dPSI) is 0.11.

4 Discussion

Hematopoietic progenitor cells are considered important players in the regulation of inflammation, being responsive to several inflammatory stimuli (7). Previous studies in preclinical mouse models of rheumatic diseases have shown that HSPCs are activated giving rise to inflammatory cells of the myeloid lineage (4–6, 10). Herein, we engaged single-cell RNA-seq to study, at the single-cell level, the molecular changes of human bone marrow-derived CD34+ progenitor cells in SLE. Based on the transcriptomic profile of this heterogeneous cell population (27), which includes both hematopoietic and myeloid progenitors, we were able to identify three clusters of cells with HSPC-like molecular profile. We observed that cells derived from two of these clusters, clusters 3 and 4, were enriched for genes associated with IFN signaling. Additionally, analysis for upstream regulators identified the interferon-dependent TFs IRF7 and IRF9 as possible TFs that drive the transcriptional modulation of HSPCs in SLE. Interestingly, there was a decrease in the number of cells in cluster 2 in SLE, which includes cells with increased quiescence, suggesting a transition of the HSPCs toward a proliferative state. Also, there was a decrease in the number of B-like cluster 6 cells in SLE and CB compared with healthy adults. In SLE, this is possibly due to the inflammation-driven myelopoiesis bias. On the other hand, in CB, due to the lack of exposure in environmental factors and inflammation, this is possibly due to the fact that these cells are more lineage primed based on their decreased stemness score.

Type I interferons (IFNs) are key players in steady state and autoimmunity. Interferon signaling is important for functional innate immunity, whereas various cell types produce interferons and express ISGs (interferon-stimulated genes) (30, 31). Terminally differentiated cells such as monocytes/macrophages, dendritic cells, and plasmacytoid cells produce IFNs in infection and autoimmunity. The type I-IFN pathway is genetically and mechanistically important for lupus pathogenesis (32–34). Transcriptomic analyses, both bulk and single-cell, have shown that high ISG expression represents a key signature for lupus pathogenesis (35–37). Interferon-targeted therapies (e.g., anifrolumab) (38) or cell-targeted therapies toward types producing type-I IFNs (e.g., belimumab) (39) have a constantly augmenting role in the armamentarium against SLE.

HSPCs are affected by IFN signaling, as shown in animal models (40–42). Chronic exposure to IFN-α is known to induce cell cycle entry and impair the stem cell activity in hematopoietic stem cells by inducing DNA damage (41), whereas dormant HSCs are protected from IFN-induced attrition by a circular RNA that binds and blocks the activity of the DNA sensor cGAS (43). To this direction, we show in the present study that SLE-dependent IFN signaling results in enhanced expression of cell cycle-related genes in cluster 4, a cluster that includes cells with enhanced proliferative potential. Except for the effect of type I interferons in cell-cycle entry, they can drive epigenetic changes in progenitor cells, which are reflected in their progeny. For instance, type I interferon signaling in progenitor cells in response to induction of trained immunity imprinted an inflammatory signature, which resulted in the generation of granulocytes with inflammatory and tumor suppressing properties (44). Based on this observation, we show herein that IFN signaling in SLE acts on bone marrow HSPCs, which could drive the generation of inflammatory cells of the myeloid lineage that can fuel disease activity and prime them to respond to secondary stimuli, contributing in the development of disease flares.

Even though peripheral destruction is the main cause of cytopenias in SLE, bone marrow failure has been also described. IFN signaling is the causal factor of aplastic anemia (AA), a prototypic autoimmune bone marrow failure disorder (45, 46). In AA, IFN-γ released in the bone marrow inflicts damage and attrition of CD34+ progenitor cells, causing pancytopenia (22, 46). Based on the effect of chronic IFN signaling in the suppression of HSC function, our data support a possible contribution of HSC dysfunction in SLE-associated cytopenias. Interestingly, altered alternative splicing events have been observed in HSPCs from patients with AA (22), further supporting a possible shared mechanism between the two disorders.

In addition to HSPCs, we identified a cluster of cells with myeloid transcriptomic features (myeloid-like cluster 5) that was significantly altered in patients with SLE. Specifically, within this cluster, genes associated with pathways associated with inflammation, including IFN and TNF signaling, the cell cycle-related pathway G2/M transition and hypoxia, and reactive oxygen species pathway, were upregulated in SLE. Previous studies have shown that there is a myeloid cell signature in bone marrow progenitor cells in SLE (4), whereas neutrophils and monocytes are critical effector cell populations in the pathogenesis of severe disease complications, such as nephritis (32). In this direction, in addition to HSPCs, we show that progenitor cells with a myeloid bias based on the transcriptomic signature are affected by IFN, whereas other clusters of cells such as cells with a T- and B-like signature are unaffected.

A fundamental question is whether the IFN-related signature in HSPCs acts as the initiator of disease phenotype, or it is a secondary effect that further amplifies the cascade of events that characterize SLE-dependent inflammation. This study cannot be addressed by our experimental setting, since BM samples from asymptomatic subjects that will develop SLE in the future are needed to distinguish whether HSPCs are the starting point of the inflammatory process in SLE, which makes this type of experimental process not possible.

Taken together, single-cell analysis of BM cells from patients with SLE demonstrated that interferon signaling, a major player in disease pathogenesis, affects early hematopoietic progenitors. Early imprinting of the interferon signature in HSPCs is likely to affect their progeny downstream, promoting the initiation and progression of the disease. Together, these data suggest that the fundamental aberrancies in SLE could be traced back to the HSPCs. Whether novel therapies that target IFNs can reverse the imprinted inflammatory signature in HSPCs and to what extent this reversal can result in the modulation of the function of the generated immune cells is to be shown.

Data availability statement

The dataset has been deposited at the EGA controlled-access repository (EGAS00001007317).

Ethics statement

The studies involving humans were approved by Attikon University Hospital Research Ethic Committee (Athens, Greece, protocol 10/22-6-2017). The studies were conducted in accordance with the local legislation and institutional requirements. The participants provided their written informed consent to participate in this study.

Author contributions

AF: Writing – original draft, Writing – review & editing, Formal analysis, Investigation, Methodology, Validation. IM: Writing – original draft, Writing – review & editing, Investigation, Methodology. CL: Methodology, Writing – review & editing. MG: Methodology, Writing – review & editing. AB: Investigation, Writing – review & editing. GS: Methodology, Writing – review & editing. SG: Resources, Writing – review & editing. VK: Resources, Writing – review & editing. EA: Methodology, Writing – review & editing. IK: Investigation, Methodology, Writing – original draft, Writing – review & editing. DB: Conceptualization, Funding acquisition, Resources, Supervision, Writing – original draft, Writing – review & editing.

Funding

The author(s) declare that financial support was received for the research, authorship, and/or publication of this article. This work was supported by a research grant from the European Research Council (ERC) under the European Union's Horizon 2020 research and innovation program (grant agreement no. 742390). AF, IM, and MG were supported by the Hellenic Foundation for Research and Innovation (HFRI) and the General Secretariat for Research and Technology (GSRT), under the HFRI "Research Projects to Support Faculty Members & Researchers and Procure High-Value Research Equipment" grant (GA. 452). IM was supported by VolkswagenStiftung under the "Life?" program (96732).

Acknowledgments

We thank Dr. Ioannis Vatsellas from the Greek Genome Center (BRFAA) for the next-generation sequencing service and Dr Efstathios Michalopoulos from the Hellenic Cord Blood Bank, BRFAA, for providing cord blood samples. We also thank the healthy participants and the patients and their referring physicians and nurses at the Attikon Rheumatology and Ippokrateion Hematology Units. Computational time granted from the National Infrastructures for Research and Technology S.A. (GRNET S.A.) in the National HPC facility - ARIS - under project IDs pr007035_thin-SLE_BIO and pr011006_taskp-BIOSLE.

Conflict of interest

The authors declare that the research was conducted in the absence of any commercial or financial relationships that could be construed as a potential conflict of interest.

The author(s) declared that they were an editorial board member of Frontiers, at the time of submission. This had no impact on the peer review process and the final decision.

Publisher's note

Supplementary material

The Supplementary Material for this article can be found online at: https://www.frontiersin.org/articles/10.3389/fimmu.2024.1383358/full#supplementary-material

References

1. King KY, Goodell MA. Inflammatory modulation of HSCs: viewing the HSC as a foundation for the immune response. *Nat Rev Immunol*. (2011) 11:685–92. doi: 10.1038/nri3062

2. Baldridge MT, King KY, Goodell MA. Inflammatory signals regulate hematopoietic stem cells. *Trends Immunol*. (2011) 32:57–65. doi: 10.1016/j.it.2010.12.003

3. Trumpp A, Essers M, Wilson A. Awakening dormant haematopoietic stem cells. *Nat Rev Immunol*. (2010) 10:201–9. doi: 10.1038/nri2726

4. Grigoriou M, Banos A, Filia A, Pavlidis P, Giannouli S, Karali V, et al. Transcriptome reprogramming and myeloid skewing in haematopoietic stem and progenitor cells in systemic lupus erythematosus. *Ann Rheum Dis*. (2020) 79:242–53. doi: 10.1136/annrheumdis-2019-215782

5. Hernandez G, Mills TS, Rabe JL, Chavez JS, Kuldanek S, Kirkpatrick G, et al. Pro-inflammatory cytokine blockade attenuates myeloid expansion in a murine model of rheumatoid arthritis. *Haematologica*. (2020) 105:585–97. doi: 10.3324/haematol.2018.197210

6. Regan-Komito D, Swann JW, Demetriou P, Cohen ES, Horwood NJ, Sansom SN, et al. GM-CSF drives dysregulated hematopoietic stem cell activity and pathogenic extramedullary myelopoiesis in experimental spondyloarthritis. *Nat Commun*. (2020) 11:155. doi: 10.1038/s41467-019-13853-4

7. Chavakis T, Mitroulis I, Hajishengallis G. Hematopoietic progenitor cells as integrative hubs for adaptation to and fine-tuning of inflammation. *Nat Immunol*. (2019) 20:802–11. doi: 10.1038/s41590-019-0402-5

8. Mitroulis I, Hajishengallis G, Chavakis T. Trained immunity and cardiometabolic disease: the role of bone marrow. *Arterioscler Thromb Vasc Biol*. (2021) 41:48–54. doi: 10.1161/ATVBAHA.120.314215

9. Caiado F, Pietras EM, Manz MG. Inflammation as a regulator of hematopoietic stem cell function in disease, aging, and clonal selection. *J Exp Med*. (2021) 218: e20201541. doi: 10.1084/jem.20201541

10. Li X, Wang H, Yu X, Saha G, Kalafati L, Ioannidis C, et al. Maladaptive innate immune training of myelopoiesis links inflammatory comorbidities. *Cell*. (2022) 185: S0092–8674(22)00393-2. doi: 10.1016/j.cell.2022.03.043

11. Crow MK. Pathogenesis of systemic lupus erythematosus: risks, mechanisms and therapeutic targets. *Ann Rheumatic Dis*. (2023) 82:999–1014. doi: 10.1136/ard-2022-223741

12. Martin M. Cutadapt removes adapter sequences from high-throughput sequencing reads. *EMBnet J*. (2011) 17:10–2. doi: 10.14806/ej.17.1

13. Dobin A, Davis CA, Schlesinger F, Drenkow J, Zaleski C, Jha S, et al. STAR: ultrafast universal RNA-seq aligner. *Bioinformatics*. (2013) 29:15–21. doi: 10.1093/bioinformatics/bts635

14. Anders S, Pyl PT, Huber W. HTSeq—a Python framework to work with high-throughput sequencing data. *Bioinformatics*. (2015) 31:166–9. doi: 10.1093/bioinformatics/btu638

15. Hao Y, Hao S, Andersen-Nissen E, Mauck WM, Zheng S, Butler A, et al. Integrated analysis of multimodal single-cell data. *Cell*. (2021) 184:3573–3587.e29. doi: 10.1016/j.cell.2021.04.048

16. Korsunsky I, Millard N, Fan J, Slowikowski K, Zhang F, Wei K, et al. Fast, sensitive and accurate integration of single-cell data with Harmony. *Nat Methods*. (2019) 16:1289–96. doi: 10.1038/s41592-019-0619-0

17. Andreatta M, Carmona SJ. UCell: Robust and scalable single-cell gene signature scoring. *Comput Struct Biotechnol J*. (2021) 19:3796–8. doi: 10.1016/j.csbj.2021.06.043

18. Wang X, Wen Y, Xie X, Liu Y, Tan X, Cai Q, et al. Dysregulated hematopoiesis in bone marrow marks severe COVID-19. *Cell Discovery*. (2021) 7:1–18. doi: 10.1038/s41421-021-00296-9

19. Chiche L, Jourde-Chiche N, Whalen E, Presnell S, Gersuk V, Dang K, et al. Modular transcriptional repertoire analyses of adults with systemic lupus erythematosus reveal distinct type I and type II interferon signatures. *Arthritis Rheumatol*. (2014) 66:1583–95. doi: 10.1002/art.38628

20. Aibar S, González-Blas CB, Moerman T, Huynh-Thu VA, Imrichova H, Hulselmans G, et al. SCENIC: Single-cell regulatory network inference and clustering. *Nat Methods*. (2017) 14:1083–6. doi: 10.1038/nmeth.4463

21. Huynh-Thu VA, Irrthum A, Wehenkel L, Geurts P. Inferring regulatory networks from expression data using tree-based methods. *PloS One*. (2010) 5:e12776. doi: 10.1371/journal.pone.0012776

22. Zhu C, Lian Y, Wang C, Wu P, Li X, Gao Y, et al. Single-cell transcriptomics dissects hematopoietic cell destruction and T-cell engagement in aplastic anemia. *Blood*. (2021) 138:23–33. doi: 10.1182/blood.2020008966

23. Subramanian A, Tamayo P, Mootha VK, Mukherjee S, Ebert BL, Gillette MA, et al. Gene set enrichment analysis: a knowledge-based approach for interpreting genome-wide expression profiles. *Proc Natl Acad Sci U.S.A.* (2005) 102:15545–50. doi: 10.1073/pnas.0506580102

24. Shen S, Park JW, Lu Z, Lin L, Henry MD, Wu YN, et al. rMATS: robust and flexible detection of differential alternative splicing from replicate RNA-Seq data. *Proc Natl Acad Sci U.S.A.* (2014) 111:E5593–5601. doi: 10.1073/pnas.1419161111

25. Chen EY, Tan CM, Kou Y, Duan Q, Wang Z, Meirelles GV, et al. Enrichr: interactive and collaborative HTML5 gene list enrichment analysis tool. *BMC Bioinf*. (2013) 14:128. doi: 10.1186/1471-2105-14-128

26. Velten L, Haas SF, Raffel S, Blaszkiewicz S, Islam S, Hennig BP, et al. Human haematopoietic stem cell lineage commitment is a continuous process. *Nat Cell Biol*. (2017) 19:271–81. doi: 10.1038/ncb3493

27. Pellin D, Loperfido M, Baricordi C, Wolock SL, Montepeloso A, Weinberg OK, et al. A comprehensive single cell transcriptional landscape of human hematopoietic progenitors. *Nat Commun*. (2019) 10:2395. doi: 10.1038/s41467-019-10291-0

28. Dam EM, Habib T, Chen J, Funk A, Glukhova V, Davis-Pickett M, et al. The BANK1 SLE-risk variants are associated with alterations in peripheral B cell signaling and development in humans. *Clin Immunol*. (2016) 173:171–80. doi: 10.1016/j.clim.2016.10.018

29. Papanikolaou S, Bertsias GK, Nikolaou C. Extensive changes in transcription dynamics reflected on alternative splicing events in systemic lupus erythematosus patients. *Genes (Basel)*. (2021) 12:1260. doi: 10.3390/genes12081260

30. Jiang J, Zhao M, Chang C, Wu H, Lu Q. Type I interferons in the pathogenesis and treatment of autoimmune diseases. *Clin Rev Allergy Immunol*. (2020) 59:248–72. doi: 10.1007/s12016-020-08798-2

31. Crow MK, Ronnblom L. Type I interferons in host defence and inflammatory diseases. *Lupus Sci Med*. (2019) 6:e000336. doi: 10.1136/lupus-2019-000336

32. Caielli S, Wan Z, Pascual V. Systemic lupus erythematosus pathogenesis: interferon and beyond. *Annu Rev Immunol*. (2023) 41:533–60. doi: 10.1146/annurev-immunol-101921-042422

33. Rönnblom L, Leonard D. Interferon pathway in SLE: one key to unlocking the mystery of the disease. *Lupus Sci Med*. (2019) 6:e000270. doi: 10.1136/lupus-2018-000270

34. Bradford HF, Haljasmägi L, Menon M, McDonnell TCR, Särekannu K, Vanker M, et al. Inactive disease in patients with lupus is linked to autoantibodies to type I interferons that normalize blood IFNα and B cell subsets. *Cell Rep Med*. (2023) 4:100894. doi: 10.1016/j.xcrm.2022.100894

35. Panousis NI, Bertsias GK, Ongen H, Gergianaki I, Tektonidou MG, Trachana M, et al. Combined genetic and transcriptome analysis of patients with SLE: distinct, targetable signatures for susceptibility and severity. *Ann Rheum Dis*. (2019) 78:1079–89. doi: 10.1136/annrheumdis-2018-214379

36. Nehar-Belaid D, Hong S, Marches R, Chen G, Bolisetty M, Baisch J, et al. Mapping Systemic Lupus Erythematosus heterogeneity at the single-cell level. *Nat Immunol*. (2020) 21:1094–106. doi: 10.1038/s41590-020-0743-0

37. Banchereau J, Pascual V. Type I interferon in systemic lupus erythematosus and other autoimmune diseases. *Immunity*. (2006) 25:383–92. doi: 10.1016/j.immuni.2006.08.010

38. Vital EM, Merrill JT, Morand EF, Furie RA, Bruce IN, Tanaka Y, et al. Anifrolumab efficacy and safety by type I interferon gene signature and clinical subgroups in patients with SLE: *post hoc* analysis of pooled data from two phase III trials. *Ann Rheum Dis*. (2022) 81:951–61. doi: 10.1136/annrheumdis-2021-221425

39. Wilkinson C, Henderson RB, Jones-Leone AR, Flint SM, Lennon M, Levy RA, et al. The role of baseline BLyS levels and type 1 interferon-inducible gene signature status in determining belimumab response in systemic lupus erythematosus: a *post hoc* meta-analysis. *Arthritis Res Ther*. (2020) 22:102. doi: 10.1186/s13075-020-02177-0

40. Essers MAG, Offner S, Blanco-Bose WE, Waibler Z, Kalinke U, Duchosal MA, et al. IFNalpha activates dormant haematopoietic stem cells *in vivo*. *Nature*. (2009) 458:904–8. doi: 10.1038/nature07815

41. Walter D, Lier A, Geiselhart A, Thalheimer FB, Huntscha S, Sobotta MC, et al. Exit from dormancy provokes DNA-damage-induced attrition in haematopoietic stem cells. *Nature*. (2015) 520:549–52. doi: 10.1038/nature14131

42. Pietras EM, Lakshminarasimhan R, Techner J-M, Fong S, Flach J, Binnewies M, et al. Re-entry into quiescence protects hematopoietic stem cells from the killing effect of chronic exposure to type I interferons. *J Exp Med*. (2014) 211:245–62. doi: 10.1084/jem.20131043

43. Xia P, Wang S, Ye B, Du Y, Li C, Xiong Z, et al. A circular RNA protects dormant hematopoietic stem cells from DNA sensor cGAS-mediated exhaustion. *Immunity*. (2018) 48:688–701.e7. doi: 10.1016/j.immuni.2018.03.016

44. Kalafati L, Kourtzelis I, Schulte-Schrepping J, Li X, Hatzioannou A, Grinenko T, et al. Innate immune training of granulopoiesis promotes anti-tumor activity. *Cell*. (2020) 183:771–785.e12. doi: 10.1016/j.cell.2020.09.058

45. Lin F, Karwan M, Saleh B, Hodge DL, Chan T, Boelte KC, et al. IFN-γ causes aplastic anemia by altering hematopoietic stem/progenitor cell composition and disrupting lineage differentiation. *Blood*. (2014) 124:3699–708. doi: 10.1182/blood-2014-01-549527

46. Smith JNP, Kanwar VS, MacNamara KC. Hematopoietic stem cell regulation by type I and II interferons in the pathogenesis of acquired aplastic anemia. *Front Immunol*. (2016) 7. doi: 10.3389/fimmu.2016.00330

Frontiers in
Immunology

Explores novel approaches and diagnoses to treat immune disorders.

The official journal of the International Union of Immunological Societies (IUIS) and the most cited in its field, leading the way for research across basic, translational and clinical immunology.

Discover the latest Research Topics

See more →

frontiers

Frontiers in
Immunology

Frontiers

Avenue du Tribunal-Fédéral 34
1005 Lausanne, Switzerland
frontiersin.org

Contact us

+41 (0)21 510 17 00
frontiersin.org/about/contact